R. Vaira Vignesh
R. Padmanaban
M. Govindaraju *Editors*

Advances in Processing of Lightweight Metal Alloys and Composites

Microstructural Characterization and Property Correlation

Springer

Materials Horizons: From Nature to Nanomaterials

Series Editor

Vijay Kumar Thakur, School of Aerospace, Transport and Manufacturing, Cranfield University, Cranfield, UK

Materials are an indispensable part of human civilization since the inception of life on earth. With the passage of time, innumerable new materials have been explored as well as developed and the search for new innovative materials continues briskly. Keeping in mind the immense perspectives of various classes of materials, this series aims at providing a comprehensive collection of works across the breadth of materials research at cutting-edge interface of materials science with physics, chemistry, biology and engineering.

This series covers a galaxy of materials ranging from natural materials to nanomaterials. Some of the topics include but not limited to: biological materials, biomimetic materials, ceramics, composites, coatings, functional materials, glasses, inorganic materials, inorganic-organic hybrids, metals, membranes, magnetic materials, manufacturing of materials, nanomaterials, organic materials and pigments to name a few. The series provides most timely and comprehensive information on advanced synthesis, processing, characterization, manufacturing and applications in a broad range of interdisciplinary fields in science, engineering and technology.

This series accepts both authored and edited works, including textbooks, monographs, reference works, and professional books. The books in this series will provide a deep insight into the state-of-art of Materials Horizons and serve students, academic, government and industrial scientists involved in all aspects of materials research.

Review Process

The proposal for each volume is reviewed by the following:

1. Responsible (in-house) editor
2. One external subject expert
3. One of the editorial board members.

The chapters in each volume are individually reviewed single blind by expert reviewers and the volume editor.

R. Vaira Vignesh · R. Padmanaban ·
M. Govindaraju

Editors

Advances in Processing of Lightweight Metal Alloys and Composites

Microstructural Characterization and Property Correlation

🐴 Springer

Editors
R. Vaira Vignesh
Department of Mechanical Engineering
Amrita School of Engineering
Amrita Vishwa Vidyapeetham
Coimbatore, India

R. Padmanaban
Department of Mechanical Engineering
Amrita School of Engineering
Amrita Vishwa Vidyapeetham
Coimbatore, India

M. Govindaraju
Department of Mechanical Engineering
Amrita School of Engineering
Amrita Vishwa Vidyapeetham
Coimbatore, India

This book is dedicated to

Dr. S. Thirumalini
(1971–2021)
Formerly, Professor and Chairperson
Department of Mechanical Engineering
Amrita School of Engineering, Coimbatore
Amrita Vishwa Vidyapeetham, India

Foreword by Dr. T. Ram Prabhu

The last decade has witnessed remarkable research and development of novel lightweight alloys for automotive, aviation, and structural components. The editors Dr. R. Vaira Vignesh, Dr. R. Padmanaban, and Dr. M. Govindaraju have made a timely book on *Advances in Processing of Lightweight Metal Alloys and Composites*. The book has touched upon the essentials of lightweight metal alloys processing, post-processing, joining methodologies, and the industry's future trends.

The salient features of the book are as follows:

- Detailed documentation of promising and novel research trends in the solid-state welding and processing of lightweight metallic materials.
- Overview of recent additive manufacturing trends in the industry for aluminum, magnesium, and titanium alloys.
- Comprehensive analysis of the microstructural evolution and properties of aluminum and magnesium alloys subjected to solid-state welding/processing.

A significant effort has been made to elucidate the future trends of materials research. The book will benefit researchers, academicians, scientists, and engineers who want to delve deeper into the subject.

I wish all the best to the editors in all their endeavors.

Dr. T. Ram Prabhu
Joint Director, Defence Research
Development Organization,
Ministry of Defence
Government of India
Bengaluru, Karnataka, India

Foreword by Dr. Shantanu Bhowmik

The rapid progress of and the numerous research conducted under the aegis of materials science and manufacturing make it challenging to interpret the facts accumulated over a decade.

This book on *Advances in Processing of Lightweight Metal Alloys and Composites*, edited by Dr. R. Vaira Vignesh, Dr. R. Padmanaban, and Dr. M. Govindaraju, provides a number of chapters that are excellent examples of research work applied to relevant metallurgical problems. This book covers the critical areas in lightweight metallic materials, including the recent advancements in additive manufacturing processes.

I believe the book would extract the technical fundamentals of processing lightweight metal alloys and composites. The authors have presented the modern engineering problems associated with the processing and characterizing of advanced materials.

This book forms a valuable addition to the existing body of knowledge. It is primarily intended for the students, scholars, and researchers devoting themselves to researching lightweight materials, composites, and solid-state welding and processing.

The authors and editors of the book deserve appreciation for shaping a sensible and applied book.

<div style="text-align: right">

Dr. Shantanu Bhowmik
Professor, Department of Aerospace
Engineering
Amrita Vishwa Vidyapeetham
Coimbatore, India

Adjunct Professor, Center for Future
Materials
University of Southern Queensland
Toowoomba, Australia

</div>

Foreword by Dr. A. Srinivasan

I am happy to extend my good wishes to Dr. R. Vaira Vignesh, Dr. R. Padmanaban, and Dr. M. Govindaraju for their book *Advances in Processing of Lightweight Metal Alloys and Composites.*

The compiled chapters cover a range of areas, including an overview, liquid and solid-state processing, and machinability characteristics of lightweight alloys and composites. The thematic information in the book provides a comprehensive base on innovative ideas and technologies developed by eminent researchers working on lightweight metal alloys and composites.

The curated book chapters will serve the research community with current trends in friction stir welding and processing aluminum and magnesium alloys. An inclusive analysis of the resulting microstructure, properties, and mechanisms is presented. An overview of the recent trends in solid-state joining, processing, and additive manufacturing in the industry is presented.

I hope this book will enhance the conceptual understanding of young scientists and the research community. The book editors deserve my huge appreciation for their effort in bringing out the valuable and useful book.

<div align="right">

Dr. A. Srinivasan
Principal Scientist, CSIR—National
Institute for Interdisciplinary
Science and Technology (NIIST),
Council of Scientific and Industrial
Research (CSIR), Ministry of Science
and Technology
Government of India
Thiruvananthapuram, Kerala, India

</div>

Preface

This book is a compilation of the collective knowledge of students, instructors, and researchers on the subject of lightweight materials (alloys and composites) and their uses, in both academic and professional contexts. Several industries currently use lightweight materials extensively as a critical component in creating cutting-edge products. As a result, the need for understanding and using lightweight materials has multiplied, as has the number of users in this field.

In order to introduce both new and established users to this field, there was a need for organized learning material. Several renowned, widely acknowledged, and excellent texts in lightweight materials exist. However, almost all of these texts are advanced and go into great detail about fabrication techniques. As a result, a substantial unmet demand for high-quality educational materials that emphasize the characterization of lightweight material remains open. This book aims to satisfy that need. We hope this book would offer the reader a clear, comprehensive, and useful introduction to the processing and characterization of lightweight materials.

The first five chapters (Chaps. 1–5) of this book introduce the essentials of lightweight materials to a novice reader. The following six chapters (Chaps. 6–11) deal with the essence of existing knowledge on liquid state processing and solid-state welding of lightweight alloys. The subsequent seven chapters (Chaps. 12–18) are dedicated to some relatively recent topics in the solid-state processing of lightweight alloys and composites. The next three chapters (Chaps. 19–21) deal with the machinability characteristics of lightweight alloys and composites. The last four chapters (Chaps. 22–25) provide a brief account of current trends in additive manufacturing of lightweight materials.

Researchers working in various disciplines, including metallurgy, materials science and engineering, manufacturing engineering, and production engineering, will find this book as a handy reference. Using the content wisely, this book can also be used as a text for one-semester undergraduate and graduate courses in lightweight materials. The contributions of many people fruition a book of this caliber. Without the teamwork of members from our respective research groups, this book would

have not been possible. We appreciate each person's contribution to this manuscript, individually and collectively.

Coimbatore, India   R. Vaira Vignesh
                                                                               R. Padmanaban
                                                                              M. Govindaraju

Acknowledgements

Contents

Editors and Contributors

About the Editors

Dr. R. Vaira Vignesh obtained his bachelor's degree in Mechanical Engineering (First Class with Distinction) from Karpagam College of Engineering, an autonomous institution affiliated with Anna University, India. He obtained his Ph.D. under the Faculty of Engineering from Amrita Vishwa Vidyapeetham for his research on Magnesium Alloy Surface Composites for Biodegradable Implants. He was involved in the indigenization of laser surface texturing technology for reducing the frictional losses in automotive components and the development of wind turbine brake pads with gradient composition, and functionality that were funded by the Department of Science and Technology, Government of India. Subsequently, he joined as Assistant Professor at Amrita Vishwa Vidyapeetham. In the field of advanced materials and processing, his research and development span solid-state processing, solid-state welding, surface engineering, and powder metallurgy processing. He has one patent, 10+ book chapters, 35+ conference publications, and 50+ research publications in peer-reviewed international journals to his credit. He received the Amrita Vishwa Vidyapeetham—Chancellor's Publication Award for his eminent contribution to the field of solid-state welding and processing of lightweight materials. He is the recipient of the prestigious Amrita Innovation and Research Awards (Publication Merit Award) for his distinction in research publications. Appreciating his excellence in the curricular and technical field, he received Henry Ford Award and Best Academic Performer award from Karpagam College of Engineering, and the Best Student Award from the Indian Society for Technical Education, New Delhi (Tamil Nadu and Puducherry). He currently serves as an Assistant Professor in the Department of Mechanical Engineering, Amrita School of Engineering, Amrita Vishwa Vidyapeetham, India.

Dr. R. Padmanaban is a mechanical engineer with specialization in engineering design. He completed his doctoral research in the area of friction stir welding. He is currently working as Associate Professor in the Department of Mechanical

engineering, Amrita School of Engineering, India. He has two decades of teaching experience and is teaching undergraduate and postgraduate students and supervising doctoral students. He has successfully guided more than fifty bachelor's and master's students' projects, and one Ph.D. candidate. He has published several articles in reputed international journal and conferences. His areas of interest include welding and joining, fatigue and fracture behavior of materials, application of finite element method to analyze manufacturing processes, simulating microstructural evolution and resultant properties. He also specializes in the application of artificial intelligence and statistical techniques to build regression models and analyze manufacturing processes to optimize process parameters, maximize output and process efficiency. He has conducted seminars, organized workshops and presented talks on finite element methods and applications, welding, and friction stir welding. He is an active reviewer for several national and international journals, and a life member in the Indian Society for Technical Education (ISTE) and Indian Welding Society.

Dr. M. Govindaraju completed B.E. in Metallurgical Engineering from Government College of Engineering, Salem, in 2001 and joined as Engineer at Nonferrous Materials Technology Development Center (NFTDC), Hyderabad. He served there for 15 years up to 2016 in various capacities including as Principal Scientist, before moving to Amrita Vishwa Vidyapeetham in July 2016 as Assistant Professor at Department of Mechanical Engineering. After joining in NFTDC, he completed M.Tech. (Welding) and Ph.D. from Indian Institute of Technology Madras subsequently. His Ph.D. thesis is on friction stir processing of magnesium alloys. He has industry and research exposure of over ~20 years in various capacities, in the field of advanced welding and brazing technology, design, and fabrication of furnaces, leak testing, non-destructive testing, new and advanced materials (super alloys, ultra-pure metals, magnesium alloy, aluminum alloy, and ceramic to metal joins). He has developed technologies for sheet brazing of automotive components and diffusion brazing of honeycomb structures which are transferred to industries. In addition, he is involved in building and indigenization of various process equipment, mainly high technology furnaces for processing of materials for Indian Space Research Organization, Bhabha Atomic Research Center, Defence Research and Development Organization and other national programs. He has completed 12 projects and 2 projects are ongoing; published more than 40 articles in international journals and conferences. He has indigenized more than 15 techniques/equipment for various applications in India. He has delivered 100 guest lectures in various colleges and universities across India. He currently serves as an Associate Professor in the Department of Mechanical Engineering, Amrita School of Engineering, Amrita Vishwa Vidyapeetham (Coimbatore Campus), India.

Contributors

Agarwal Pankaj Department of Mechanical Engineering, Samrat Ashok Technological Institute, Vidisha, India

Alagarsamy S. V. Department of Mechanical Engineering, Mahath Amma Institute of Engineering and Technology, Pudukkottai, Tamil Nadu, India

Amantayeva Akniyet Department of Mechanical and Aerospace Engineering, School of Engineering and Digital Sciences, Nazarbayev University, Astana, Kazakhstan

Amos P. G. Kubendran Theoretical Metallurgy Group, Department of Metallurgical and Materials Engineering, National Institute of Technology Tiruchirappalli, Tiruchirappalli, Tamil Nadu, India

Arulmurugan B. Department of Mechanical Engineering, KPR Institute of Engineering and Technology, Coimbatore, Tamil Nadu, India

Babu S. Ramesh Department of Mechanical Engineering, KPR Institute of Engineering and Technology, Coimbatore, Tamil Nadu, India

Bag S. Indian Institute of Technology Guwahati, Guwahati, Assam, India

Baghad Abd Euromed Research Center, Euromed Polytechnic School, Euromed University of Fes, Route de Meknes, Rond-point de Bensouda, BP 51, Fes, Morocco

Balaji S. Department of Aeronautical Engineering, Nehru Institute of Engineering and Technology, Coimbatore, India

Bamini A. M. Anusha Department of Computer Science and Engineering, Karunya Institute of Technology and Sciences, Coimbatore, India

Bhagyanathan C. Department of Mechanical Engineering, Sri Ramakrishna Engineering College, Coimbatore, India

Boopathi Sampath Department of Mechanical Engineering, Muthayammal Engineering College (Autonomous), Rasipuram, Namakkal (District), India

Bricha Meriame Euromed Research Center, Euromed Polytechnic School, Euromed University of Fes, Fes, Morocco

Chanakyan C. Department of Mechanical Engineering, R.V.S. College of Engineering and Technology, Kumaran Kottam Campus, Coimbatore, Tamil Nadu, India

Chitra R. Department of Computer Science and Engineering, Karunya Institute of Technology and Sciences, Coimbatore, India

Das Kalyan Department of Metallurgy and Materials Engineering, Indian Institute of Engineering Science and Technology, Shibpur, Howrah, India

Dennison Milon Selvam Department of Mechanical Engineering, Kampala International University, Kampala, Uganda

Dewangan Saurabh Department of Mechanical Engineering, Manipal University Jaipur, Dehmi Kalan, Jaipur, Rajasthan, India

El Baakili Salwa Euromed Research Center, Euromed Polytechnic School, Euromed University of Fes, Fes, Morocco

El Mabrouk Khalil Euromed Research Center, Euromed Polytechnic School, Euromed University of Fes, Fes, Morocco

Erturk A. T. Department of Mechanical Engineering, Kocaeli University, Izmit, Turkey

Frankin V. Alfred Mechanical and Industrial Engineering Section, University of Technology and Applied Sciences-Ibri, Ibri, Oman

Ghosh Abhishek Department of Metallurgy and Materials Engineering, Indian Institute of Engineering Science and Technology, Shibpur, Howrah, India

Ghosh Manojit Department of Metallurgy and Materials Engineering, Indian Institute of Engineering Science and Technology, Shibpur, Howrah, India

Glivin Godwin Department of Energy and Environment, National Institute of Technology, Trichy, India

Govindaraju M. Department of Mechanical Engineering, Amrita School of Engineering, Amrita Vishwa Vidyapeetham, Coimbatore, India

Jagadeesh Kumar S. Department of Mechanical Engineering, Amrita School of Engineering, Amrita Vishwa Vidyapeetham, Coimbatore, India

Jain Sanjay Department of Mechanical Engineering, Samrat Ashok Technological Institute, Vidisha, India

Jebabalan Kirubanidhi Department of Mechanical Engineering, Division of Materials Technology, Technical University of Liberec, Liberec, Czech Republic

Jegan T. M. Chenthil Department of Mechanical Engineering, St. Xaviers Catholic College of Engineering, Chunkankadai, India

Kaasi Viswanath J. Department of Mechanical Engineering, Amrita School of Engineering, Amrita Vishwa Vidyapeetham, Coimbatore, India

Kamaleshwar S. Department of Mechanical Engineering, Amrita School of Engineering, Amrita Vishwa Vidyapeetham, Coimbatore, India

Karuppuswamy P. Department of Mechanical Engineering, Sri Ramakrishna Engineering College, Coimbatore, India

Keerthana S. Department of Mechanical Engineering, Amrita School of Engineering, Amrita Vishwa Vidyapeetham, Coimbatore, India

Kumar A. Indian Institute of Technology Guwahati, Guwahati, Assam, India

Kumar M. Indian Institute of Technology Guwahati, Guwahati, Assam, India

Kumar S. Dharani Department of Mechanical Engineering, KPR Institute of Engineering and Technology, Coimbatore, Tamil Nadu, India

Lokesh Kumar R. Department of Mechanical Engineering, Amrita School of Engineering, Amrita Vishwa Vidyapeetham, Coimbatore, India

Maniarasan P. Department of Aeronautical Engineering, Nehru Institute of Engineering and Technology, Coimbatore, India

Mashinini P. M. Department of Mechanical and Industrial Engineering, University of Johannesburg, Johannesburg, South Africa

Mathew Adarsh Abi Pimpri Chinchwad College of Engineering, Pune, Maharashtra, India

Meiirbekov Arshyn Department of Mechanical and Aerospace Engineering, School of Engineering and Digital Sciences, Nazarbayev University, Astana, Kazakhstan

Memon Shabbir Department of Mechanical Engineering, Wichita State University, Wichita, KS, USA

Mondal D. P. CSIR—Advanced Materials and Processes Research Institute, Bhopal, India

Muralimanokar M. Department of Mechanical Engineering, Amrita School of Engineering, Amrita Vishwa Vidyapeetham, Coimbatore, India

Murmu Uttam Kumar Department of Metallurgy and Materials Engineering, Indian Institute of Engineering Science and Technology, Shibpur, Howrah, India

Muthu N. Indian Institute of Technology Guwahati, Guwahati, Assam, India

Muthukumaran N. Department of Mechanical Engineering, KPR Institute of Engineering and Technology, Coimbatore, Tamil Nadu, India

Narayanan R. G. Indian Institute of Technology Guwahati, Guwahati, Assam, India

Nath Ananya Department of Mechanical Engineering, National Institute of Technology, Durgapur, India

Naveen Kumar K. Department of Mechanical Engineering, Amrita School of Engineering, Amrita Vishwa Vidyapeetham, Coimbatore, India

Padmanaban R. Department of Mechanical Engineering, Amrita School of Engineering, Amrita Vishwa Vidyapeetham, Coimbatore, India

Prabhakaran P. Department of Mechanical Engineering, J. J. College of Engineering and Technology, Trichy, Tamil Nadu, India

Puri Asit Baran National Institute of Technology Durgapur, Durgapur, India

Radha R. School of Mechanical Engineering, Vellore Institute of Technology, Chennai, India

Ramesh M. R. Department of Mechanical Engineering, National Institute of Technology Karnataka, Mangalore, India

Ray Debajyoti Sanaka Educational Trust's Group of Institutions, Durgapur, India

Sahu Shrishty Department of Metallurgy and Materials Engineering, Indian Institute of Engineering Science and Technology, Shibpur, Howrah, India

Saikia P. J. Indian Institute of Technology Guwahati, Guwahati, Assam, India

Samuel Ratna Kumar P. S. Department of Mechanical and Industrial Engineering, University of Johannesburg, Johannesburg, South Africa

Sarfraz Shoaib Department of Manufacturing, School of Aerospace, Transport and Manufacturing, Cranfield University, Cranfield, Bedford, UK

Sathish S. Department of Mechanical Engineering, Sri Ramakrishna Engineering College, Coimbatore, India

Senthamarai K. Department of Mechanical Engineering, Sri Raaja Raajan College of Engineering and Technology, Karaikudi, Tamil Nadu, India

Shakya J. P. Department of Mechanical Engineering, Samrat Ashok Technological Institute, Vidisha, India

Sharma Anirudh Automotive Systems Engineering, University of Michigan, Dearborn, USA

Shehab Essam Department of Mechanical and Aerospace Engineering, School of Engineering and Digital Sciences, Nazarbayev University, Astana, Kazakhstan

Singh Pradeep Department of Mechanical Engineering, Samrat Ashok Technological Institute, Vidisha, India

Sivakandhan C. Department of Mechanical Engineering, Nadar Saraswathi College of Engineering and Technology, Theni, India

Sreekanth D. School of Mechanical Engineering, Vellore Institute of Technology, Chennai, India

Srinath M. S. Department of Industrial and Production Engineering, Malnad College of Engineering, Hassan, India

Suleimen Aidar Department of Mechanical and Aerospace Engineering, School of Engineering and Digital Sciences, Nazarbayev University, Astana, Kazakhstan

Suresh G. Department of Mechanical Engineering, Vignan's Institute of Information Technology, Visakhapatnam, India

Tewary Arpan Central University of Jharkhand, Ranchi, Jharkhand, India

Tokbolat Serik School of Architecture, Design and the Built Environment, Nottingham Trent University, Nottingham, UK

Upadhyay Chandan Dr. R. M. L. Avadh University Ayodhya, Uttar Pradesh, Ayodhya, India

Vaira Vignesh R. Department of Mechanical Engineering, Amrita School of Engineering, Amrita Vishwa Vidyapeetham, Coimbatore, Tamil Nadu, India

Verma Karan Singh Mechanical Engineering Department, Oriental College of Technology, Bhopal, India

Vohra Siddharth NewSpace Research and Technologies, Bengaluru, India

Yadav Rahul Kumar Indian Institute of Technology Indore, Indore, Madhya Pradesh, India

Yadav Ramneek Delhi Technological University (East Campus), Delhi, India

Yadav Ravindra Nath Department of Mechanical Engineering, BBD National Institute of Technology and Management, Lucknow, India

Yashwanth Kumar B. G. Department of Mechanical Engineering, Amrita School of Engineering, Amrita Vishwa Vidyapeetham, Coimbatore, India

List of Abbreviations

3D	Three dimensional
AA	Aluminum alloy
AFM	Atomic force microscope
AI	Artificial intelligence
AM	Additive manufacturing
AMMCs	Aluminum metal matrix composites
ANFIS	Adaptive neuro-fuzzy inference system
ANN	Artificial neural network
ANOVA	Analysis of variance
ARB	Accumulative roll bonding
AS	Advancing side
ASME	American Society of Mechanical Engineers
ASTM	American Society for Testing and Materials
BJ	Binder jetting
BM	Base metal
BMG	Bulk metallic glass
BPNN	Back propagation neural network
CAD	Computer-aided design
CDFW	Continuous drive friction welding
CF	Carbon fiber
CFD	Computational fluid dynamics
CFRP	Carbon fiber-reinforced polymers
CLIP	Continuous liquid interface production
CT	Compact tension
DDFW	Direct drive friction welding
DED	Direct energy deposition
DED	Directed energy deposition
DM	Direct manufacturing
DMD	Direct metal deposition
DMLS	Direct metal laser sintering
DOD	Drop on demand

DOE	Design of experiment
EBM	Electron beam melting
EBSD	Electron backscatter diffraction
EBW	Electron beam melting
ECAP	Equal channel angular pressing
EDM	Electro-discharge machine
EDS	Energy-dispersive X-ray spectroscopy
EWR	Electrode wear ratio
F	Fabricated
FBP	Fluidized bed process
FDM	Fused deposition modeling
FEA	Finite element analysis
FFF	Fused filament fabrication
Fig.	Figure
FS	Friction stir
FSP	Friction stir processing
FSW	Friction stir welding
FSWed	Friction stir welded
FW	Friction welding
GA	Genetic algorithm
GHG	Greenhouse gas
GRA	Gray relational analysis
GRG	Gray relational grade
GWP	Global warming potential
H	Strain hardened
HAZ	Heat affected zone
HCP	Hexagonal closed pack structure
HIP	Hot isostatic pressing
HPT	High-pressure torsion
HRC	Rockwell hardness
IFW	Inertia friction welding
LCA	Life cycle assessment
LCI	Life cycle inventory
LENS	Laser-engineered net shaping
LFW	Linear friction welding
LOM	Laminated object manufacturing
LPBF	Laser powder bed fusion
MCDM	Multiple criteria decision making
ME	Material extrusion
MF	Membership function
MJ	Material jetting
MMC	Metal matrix composite
MRR	Material removal rate
NZ	Nugget zone
O	Annealed

ODP	Ozone depletion potential
OFW	Orbital friction welding
OM	Optical microscopy
PBF	Powder bed fusion
PSD	Particle size distribution
PSO	Particle swarm optimization
RAR	Redundant articulated robot
RBFNN	Radial basis function neural network
rCF	Recycled carbon fiber
RFW	Rotary friction welding
RNN	Recurrent neural network
RS	Retreating side
RSM	Response surface methodology
RT	Room temperature
SAED	Selected area electron diffraction
SCW	Solvolysis using supercritical water
SEM	Scanning electron microscope
SL	Sheet lamination
SLA	Stereolithography apparatus
SLM	Selective laser melting
SLS	Selective laser sintering
SN	Signal-to-noise ratio
SPD	Severe plastic deformation
SR	Surface roughness
SSW	Solid-state welding
T	Thermally treated
TEM	Transmission electron microscopy
TMAZ	Thermo-mechanically affected zone
TO	Topology optimization
TRL	Technology readiness level
TWI	The Welding Institute
TWR	Tool wear rate
UFG	Ultra-fine grain
UTS	Ultimate tensile strength
VP	Vat photopolymerization
W	Solution heat treated
WAAM	Wire arc additive manufacturing
WCZ	Weld center zone
WEDM	Wire cut electric discharge machining
YS	Yield strength

List of Symbols/Formula/Notation

μ	Frictional coefficient
μm	Micrometer
μs	Microseconds
A	Cross-sectional area
A_c	Clad area
Al	Aluminum
Al_2O_3	Aluminum oxide
A_m	Fusion area
AM	Aluminum-manganese
amps	Ampere
AS	Aluminum-silicon-manganese
AZ	Aluminum-zinc-manganese
B4C	Boron carbide
$CaAl_2O_4$	Calcium aluminate
$CaCO_3$	Calcium carbonate
CaO	Calcium oxide
Co	Cobalt
CO_2	Carbon dioxide
Cp-Ti	Commercially pure titanium
Cr	Chrome
Cu	Copper
d	Depth of cut
EZ	Rare earth metal-zirconium
f	Feed
F	Powder flow rate
Fe	Iron
F_x	Feed force
F_y	Radial force
F_z	Tangential force
GRA	Gray relational analysis
h	Uncut chip thickness

H13	High-speed steel
Ip	Discharge current or pulse current
l	Bid overlap ration
Li	Lithium
M	Interfacial torque
m_2 UES	Area of an unprotected ecosystem
Mg	Magnesium
MgH_2	Magnesium hydride
MJ	Mega joules
mm/min	Millimeter/minute
Mn	Manganese
Mo	Molybdenum
MRR	Material removal rate
N	Spindle speed
n	Rotational frequency
Na_2CO_3	Sodium carbonate
Nb	Niobium
Ni	Nickel
P	Power
P	Fracture load
P	Laser power
P	Axial pressure
$P(r)$	Pressure distribution across interface
P_n	Normal pressure
q	Heat generation rate
q_0	Net power
r	Chip thickness ratio
R	Radius
R_p	Radius of pin
RPM	Rotations per minute
Rs	Radius of shoulder
S	Flatness ratio
s	Second
Si	Silicon
SiC	Silicon carbide
Sn	Tin
SO_2	Sulfur dioxide
Sr	Strontium
SS	Stainless steel
Ta	Tantalum
Ti	Titanium
TiH_2	Titanium hydride
TiO_2	Titanium dioxide
T_{off}	Pulse off time
T_{on}	Pulse on time

Uk	Input of kth neuron
umax	Max. surface velocity
V	Vanadium
V	Scan speed
W	Deposited width
W_e	Experimental result
W_{jk}	Momentum constant
W_p	Predicted result
X	Denormalized value
X_j	Process parameters
X_{max}	Maximum value
X_{min}	Minimum value
X_{norm}	Normalized value
Y	Yttrium
Y_k	Output of kth neuron
ZC	Zinc-copper-manganese
ZE	Zinc-zirconium-rare earth metal
ZK	Zinc-zirconium
Zn	Zinc
Zr	Zirconium
ZrH_2	Zirconium hydride
α	Momentum parameter
α	Offset distance for linear velocity
β	Regression coefficient
δ	Dimensionless sliding factor
ΔK	Stress intensity factor
ε	Experimental error
η	Learning rate
ν	Rubbing velocity
σ_n	Normal stress at interface surface
τ	Shear stress
ω	Angular velocity

Overview of Lightweight Materials

Chapter 1
Design of Light-Metal Alloys Using Machine Learning Techniques

P. G. Kubendran Amos

1 Introduction

The term light metals can, at times, be misleading. It seems that this category of materials includes metals which, in a given shape or form, weigh less when compared to others. In other words, metals with significantly low density can apparently be categorised as light metals. If this description holds true, then lithium would be a prime example for light metal, owing to its minimal density. However, for engineering and technological, intents and purposes, it is magnesium and aluminium which are primary considered as the light metals, despite their relatively greater density when compared to lithium [1]. The treatment of magnesium and aluminium, in spite of other 'lighter' option(s), highlights the key feature dictating the categorisation of the light metals. Accordingly, light metals and alloys, besides their low density, are characterised by superior mechanical properties which allows them to serve in structural applications [2].

With the technological advancements, the properties reputed as 'superior' are progressively varying. Therefore, more efficient behaviour of light metals and alloys, under specific mechanical conditions, is expected without compromising their characteristically high strength-to-weight ratio. A principal processing technique that caters to this ever-demanding material needs is alloy development or alloy design, which ensures that the desired response is induced by achieving appropriate mechanical properties [3].

The conventional approach to design an alloy with desired properties involves considering different base metals and various combination of alloying elements. The material with suitable properties is subsequently identified by individually analysing the behaviour of the wide range of alloys, with its diverse chemical compositions.

P. G. K. Amos (✉)
Theoretical Metallurgy Group, Department of Metallurgical and Materials Engineering, National Institute of Technology Tiruchirappalli, Tiruchirappalli, Tamil Nadu, India
e-mail: prince@nitt.edu

Considering that this trial and error technique mirrors the one adopted by Edison to realise a suitable filament material, it is generally referred to as the Edisonian approach [4]. Even though, at least in the early days, this technique proved to be admissible for designing alloys, the material advancements have expanded the range of base metals, and corresponding alloying elements, thereby making the adoption of Edisonian approach practically impossible. While the material research considerably expands the 'search space' for alloy design, it also enhances the understanding of the effect of alloying elements on the behaviour of base metals. These insights on the influence of alloying elements on the material properties have been exploited to refine the extremely arduous Edisonian technique [5]. The refined approach, despite being efficient than the conventional treatment, is hugely dependent on, and is rather restricted by, the gradually progressing investigations of existing alloys, thereby inadequately exploring the wide range of possible options (search space). In this context, the advent and adoption of machine learning techniques is increasing proving to be a godsend for alloy design [6].

Simply put, stemming from well-established statistical concepts, machine learning attempts to unravel meaningful information from a given data set, irrespective of the enormity of its size and dimensionality [7]. Machine learning techniques, in general, are distinguished into different types primarily based on the nature of the data set they handle. However, considering that data sets of analogous structure are investigated for designing alloys, a treatment referred to as *supervised machine learning* is extensively employed [8].

Lately, over the past few years, machine learning techniques have increasingly been adopted to refine and/or develop light-metal alloys with magnesium or aluminium as base metal. In this chapter, an attempt is made to give an overview of the approach which has thus far been adopted to develop light-metal alloys using machine learning. Though there are numerous articles discussing the application of machine learning in the field of material science [9–11], particularly the discovery of materials and alloy design [12–15], these reviews generally encompass a wide range of systems and often assume a certain level of understanding on machine learning as whole, or certain techniques in specific. In contrast, the present chapter exclusively focuses on the development of light-metal alloys, while at the same time rendering a generalised and pedagogical deliberation on the various machine learning treatments that are employed. Given that the association of machine learning with alloy design commenced quite recently, the corresponding works handling light-metal alloys are rather limited. Therefore, when compared to a conventional review, the present article includes relatively fewer reports. Nevertheless, interestingly, each of these works is unique and definitively varies from one another, either in the alloy(s) they handle and/or in the adopted machine learning procedure. Consequently, despite the apparent restriction in volume, there is absolutely no shortage in the wealth of knowledge offered by the existing works on light-metal alloys.

2 Generalised Framework

The approach of employing machine learning to design alloys, in its entirety, comprises distinguishable steps. These steps, often sequentially pursued, yield a framework that elucidates the role of machine learning in realising the desired alloy composition [15]. The generalised framework that exploits machine learning techniques to develop alloys is schematically illustrated in Fig. 1.

The outcome of any machine learning analyses typically, and to a significant extent, relies on the data set it handles. Additionally, the characteristic nature of a data set, along with its volume (at times), dictates the choice of machine learning technique for a given investigation. Owing to its pivotal role, the approach of machine learning-based alloy design begins with gathering the relevant data. This initial step that inaugurates the entire treatment of identifying a definite alloy is referred to as data acquisition. In the framework of alloy design, the generated data set primary includes varying compositions of different alloys and the corresponding properties of interest it yields [16].

Following acquisition, the approach proceeds by analysing the data set to develop a surrogate model with the capability of predicting the properties of an alloy based on its composition. These predictive surrogate models are construed through machine learning technique(s) [17]. It is not an uncommon practice to consider different techniques, and to determine the most efficient one, for the given data set, based on their individual performance [18, 19]. In order to identify an appropriate technique, the
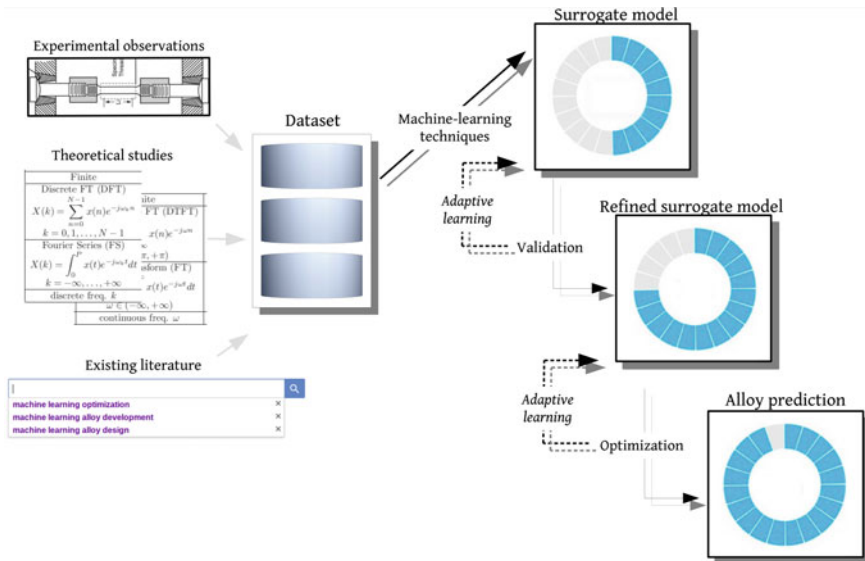
Fig. 1 Schematic representation of the general framework adopted for designing alloys using machine learning techniques

predictive model rendered by the difference machine learning treatments is closely examined. This examination which validates the machine learning models, developed through different techniques, constitutes the next step of the generalised framework. Besides, in approaches, wherein an individual technique is exclusively pursued, this step facilitates the refinement of the model [20, 21]. In other words, when the validation indicates that the performance of a given machine learning technique is rather unconvincing, the corresponding data can be augmented to the existing one, thereby facilitating the improvement of the model. This method of improving the accuracy of the model through validation is generally referred as adaptive learning [22].

The realisation of an efficient predictive surrogate model consciously lends itself to the treatment which ultimately enables the alloy design. Irrespective of the approach, the development of alloy generally involves arriving at a specific composition which delivers the desired set of properties. Correspondingly, as opposed to the predictive model, the final and characteristic step of machine learning-based alloy design framework intakes the desired properties and yields the chemical composition, which is likely to render them [23]. To that end, this alloy design step handles the existing datapoints through the surrogate model developed in the previous step.

The generalised machine learning framework which ultimately leads to the realisation of alloys rendering desired combination of properties will be expanded in the subsequent section, in order to explicate their role in efficiently identifying new light-metal alloys.

3   Data for Light-Metal Alloy Design

3.1   Acquisition

A survey of machine learning-based material analyses indicates that a wide range of techniques are adopted to build the necessary data set. These techniques include both theoretical and experimental investigations. Besides, the required data are also gathered from the existing relevant reports.

Increase in the availability of the computational resources has enhanced the role of the theoretical techniques in building up the data set [24]. Ab-initio calculations [25, 26], atomistic simulation [27, 28] and multiphase-field modelling [29] are some of the approaches which are utilised to render the desired outcome which could subsequently be analysed in the machine learning framework. Despite their efficiency, these techniques often impose considerable computational burden to yield accurate outputs. Considering that, for a given approach, numerous identical calculations are performed to yield a reliable data set, the correspondingly computational cost gets proportionally compounded. Therefore, a reasonable trade-off is achieved between the sophistication of the technique and the accuracy of the datapoint it yields. In this context, while the term 'throughput' indicates the amount of data generated by a technique, the accuracy of it is discussed as the 'fidelity'. In other words,

often the fidelity of the outcome of a high-throughput treatment is relatively compromised when compared to the fidelity of the data set built using conventional or low-throughput approach [15]. Given the seminal nature of the output, the data set generated through the experimental studies can be understandably treated as high-fidelity information.

Though theoretical techniques play a critical role in establishing the data set, in machine learning-based development of light-metal alloys, their role has thus far been rather marginal. Alternatively, the required information for light-metal alloy design is gathered either by experimental techniques [30, 31] or from the existing works [32, 33]. Moreover, since the data acquired from the literature are largely outcomes of experimental observations, almost all of the analyses on the development of light metal stems from high-fidelity information.

3.2 Refinement

Approaches largely employed to generate the principal data set for light-metal alloy design directly or indirectly stems from experimental observation. Consequently, the relevant information is sufficiently accurate, irrespective of the technique used. However, despite the accuracy, reports indicate that the data acquired from existing investigations require additional degree of 'cleaning' when compared to the ones, wherein the experimental treatment is implicitly included. In other words, the alloy design approach which is characterised by machine learning framework with experimental observations playing an integral role in data acquisition, and the acquired information is generally suitable for subsequent treatment without the need for any extensive pre-processing [34, 35]. This directly applicable structure of the data set is a primary reason for including the experimental studies in the machine learning approach for light-metal alloy development. Accordingly, since the primary goal of the light-metal alloy design is to arrive a composition that renders the desired combination of properties, the experimental investigations invariably establish a data set that relates the concentration of the alloying elements with the resulting properties. In addition to conventional mechanical factors typifying light-metal alloys, like yield strength, related properties including resistance to stress corrosion cracking are also considered for the development [30]. However, generating a data set with properties which are not straightforward to measure is an arduous task. Therefore, in those cases, material behaviour that principally influences the interested property is conveniently measured and the required information is built [30, 31].

Besides the need for an alternate measurable behaviour, the alloy design approach that relies on experimental studies for data acquisition experiences an additional constraint. Given that the experimental investigations are generally more laborious when compared to the theoretical analyses, the amount of corresponding data generated is rather restricted. In order avoid any significant influence of this restriction, an appropriate treatment called 'bootstrapping' is adopted before the data is transmitted for subsequent analysis [34, 36]. A superfluous insight of this treatment can
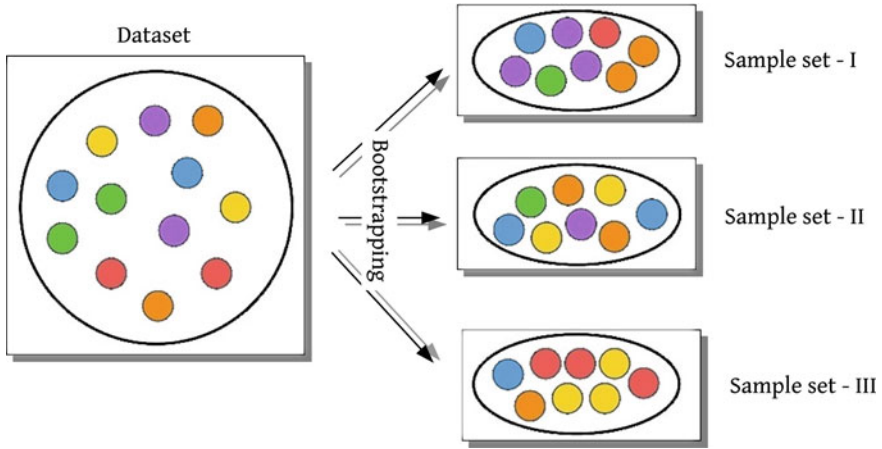
Fig. 2 Schematic representation of bootstrapping technique where several sample sets are generate from a given data

be gained from the terminology *bootstrap*, and the context in which it is usually used. Bootstrapping, in general, refers to the attempt to make the best use of the available resources [37]. Correspondingly, bootstrapping in machine learning-based light-metal alloy design ensures that the rather limited but high-fidelity principal data set built by the experimental observations is efficiently used to develop the surrogate model [34, 36]. Limitation in the amount of information rendered by the experimental studies is surmounted by the bootstrapping technique through seemingly increasing the number of datapoints [38]. This apparent increase in the wealth of available information is achieved by the concept of resampling, wherein several sets of samples are generated from a given principal data set with the provision of duplicating a datapoint both within and across the sample sets (Fig. 2). The surrogate model is subsequently developed based on the different sample sets which collectively comprises an increased number of datapoints, in relation to the original data set, resulting from the experimental observations.

When compared to machine learning framework with experimental studies, relatively extensive pre-processing or cleaning is required in the approach, wherein the information is gathered from existing works [33, 36, 39]. Since these existing works invariably have their own ends to meet, additional cleaning efforts become necessary to efficiently employ the emerging data in alloy design. Therefore, ultimately, the labour that is saved by circumventing the direct involvement of experimental investigation is spent in preparing the gathered data set.

The pre-processing of the externally gained information (data gathered from existing studies), in light-metal alloy design, begins with identifying and removing the 'outliers' [36]. As considered earlier, since the works contributing the necessary data are almost always oriented towards addressing a specific question much different from alloy design, the corresponding information includes datapoints that do not

comply with the general trend. These datapoints exhibiting considerable deviation from the rest are referred to as outliers [40]. Owing to the undesired influence of the outliers on the predictive surrogate model, the pre-processing of the externally acquired data begins with the elimination of these stray points.

The removal of the outliers though increases the applicability of the externally gathered data set, it does not adequately address the difficulties introduced by the difference in the objectives of the original works, which offer the required information, and the present goal of light-metal alloy design. This perceived gap is bridged by identifying, and at times formulating, appropriate 'features' in the data set built from the external sources. Features, in machine learning context, are the independent variables that serve as the input for the predictive model [41]. Despite considering similar base metal, experimental studies, that yield the data, generally report on wide range of alloying elements with varying concentration. For instance, traces of certain elements found in a given investigation would be completely absent in the rest. Furthermore, besides chemical composition, experimental works often include different processing techniques which ultimately effect the behaviour of materials. Realising definite set of independent variables called features, which would act as the input for predictive surrogate model, ensures the efficient use of information gathered from the experimental investigation. In light-metal alloy design, the features are identified by comprehending the relative influence of different variables on the desired material properties. Relating the wide range of variables, including both concentration and processing parameters, to the resulting behaviour of the material, and developing a *Pearson correlation matrix* has thus far been a successful approach for unravelling optimal features and ultimately, developing light-metal alloys [30, 33, 35]. This correlation matrix by encompassing all corresponding coefficients quantifies the linear relation between a given variable and the rest along with the output. Though a linear relation cannot always be expected between a feature and the output, the correlation matrix aides in gaining a qualitative understanding on the relative degree of influence a variable imposes on the behaviour of the material.

4 Surrogate Model

An elegant realisation of predictor (input) and target (output) variables, either innately or through appropriate pre-processing, in a given data set, lends itself to the formulation of predictive model. Numerous techniques exist, within the machine learning framework, which are sufficiently capable of rendering predictive model. Accordingly, the task of developing a surrogate model begins with selecting an appropriate machine technique. Often the nature of the data set effect the choice of the technique adopted for model development. A predictive model from high-fidelity data set with limited datapoints is devised using sophisticated techniques, whereas in general, less rigorous approach is employed to handle huge, accessible and relatively compromised low-fidelity information [15]. As opposed to this common conception, attempts to design light-metal alloys rarely follow a definite pattern in finalising a

technique for formulating the surrogate model. However, it is not an uncommon practice, particularly in light-metal alloy design, to expose the data to several machine learning techniques and identify the optimal one by verifying the predictability of the resulting model [33, 35, 36]. This approach of simultaneously considering different techniques to handle the same information, and deciding based on the corresponding outcomes, is accompanied by a common perception that there are 'No Free Lunch Theorem' [42]. In other words, even though for a given set of information, one technique might appear to render a better model than the rest, and this observation is largely indicative of the nature of the data than technique itself. Correspondingly, preference of a technique, in a given investigation, cannot be directly extended to the next, despite the similarity in the structure of the data set which is handled. To that end, in considerable proportion of the works on light-metal alloy design, several machine learning techniques are individually considered, although they handle analogous information towards a common objective. In this section, a succinct description of these different techniques that are employed in developing surrogate model is offered. Furthermore, the approach adopted to validate the developed model is briefly elucidated.

Linear regression Regression approach, in principle, attempts to relate the predictor variables to the target parameters. Correspondingly, surrogate model rendered by this technique can be conveniently expressed as a discernible function. In a data set, where information of a specific feature is associated with the output, regression analysis construes a model by fitting a line through the points in the two-dimensional space of the respective dependent and independent variables. Considering that, in light-metal alloy design, the features include composition of several alloying elements, regression involves fitting a *hyperplane in a multidimensional space* [43]. The best fit ensures that the deviation of the function from the datapoints, which is estimated as 'mean-squared error', is the least.

Predictor variables for surrogate model, in alloy design framework, typically include concentration of various multicomponent alloys. Consequently, each datapoint is characterised by a specific position in the multidimensional space, which is represented by a vector, $\mathbf{X}_i$ with i indicating one of the N alloy concentrations. The resulting surrogate model rendered by regression technique is expressed as

$$\hat{\mathbf{Y}} \equiv F_\beta(\mathbf{X}) = \beta_0 + \boldsymbol{\beta}\mathbf{X} + \epsilon, \tag{1}$$

where β_0 and β_1 are fitting coefficients with $\mathbf{X}$ encompassing all alloy composition, $\{\mathbf{X}_1, \mathbf{X}_2 \ldots \mathbf{X}_N\}$. In keeping with the conventional representation, the surrogate model is represented by $\hat{\mathbf{Y}}$. There is an unexplained error associated with the regression model, largely owing to its dependence on the data set. This error, in Eq. (1), is indicated by ϵ.

4.1 Random Forest

Owing to the nature of the data set typically handled in light-metal alloy design, techniques besides linear regression are sought after to formulate surrogate model [36]. Random forest is one such approach which elegantly handles multidimensional information. A schematic sketch depicting random forest is shown in Fig. 3. As indicated in the illustration, the performance of random forest relies on the efficient role of its components called 'regression tree' [44].

A regression tree typically comprises several nodes. Each of these nodes can be classified as root, branch (decision) or leaf nodes. The principal node from which the entire tree extends is referred to as the root node. On the other hand, leaf node indicates the end of the regression tree, with branch node constituting the major section. Definite thresholds are assigned to root and decision nodes which sequentially leads to the prediction offered by the tree in the leaf node. For a given data set, characterised by several distinct features, different combination of thresholds is assigned to the root and branch nodes. To accommodate a given combination, the number of decision nodes is varied. The residual error, indicating the disparity in the actual and predicted value, from each combination is estimated based on the corresponding information, and one rendering the least deviation is fixed. Ultimately, the prediction is made in the leaf node, augmenting necessary *bias*, in order to avoid *overfitting*.

A random forest comprises numerous regression trees, which are built based on different sets of sample extracted from the original data. The non-uniformity in the sample ensures the heterogeneity in the trees and avoids overfitting. Predictive efforts of random forest begins with the activation of appropriate trees with thresholds satisfying the input conditions. These regression trees are allowed to formulate their own individual outcomes, which are subsequently averaged and rendered as the single prediction of the random forest technique [45].
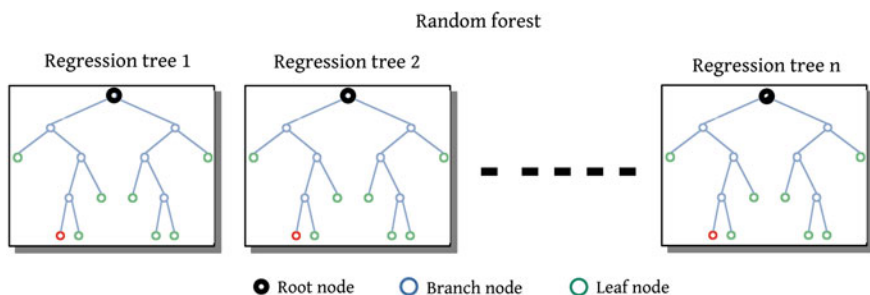
Fig. 3 Graphical illustration of the random forest technique indicating the regression trees and the characteristic nodes

4.2 Gradient Boost Tree

Besides random forest, gradient boost trees offer an alternate approach to develop a predictive surrogate model from the convoluted multidimensional data set [32, 35]. Though the prediction of this technique combines the individual output of different tress, similar to that of random forest, the approach is distinct and relatively more rigorous [46].

Gradient boost technique begins with the realisation of a differentiable *loss function* capable of quantifying the disparity between the predicted and actual data. This function could be as straightforward as

$$L(\mathbf{Y}, F(\mathbf{X})) = \frac{1}{2}(\mathbf{Y} - F(\mathbf{X}))^2, \tag{2}$$

where $L(\mathbf{Y}, F(\mathbf{X}))$ is the loss function, with $\mathbf{Y}$ and $F(\mathbf{X})$ indicating the actual and predicted data, respectively. Irrespective of its form, a loss function should be differentiable with respect to the predicted value. Based on the loss function, a gradient boost model is initialised by devising a leaf node with definite common prediction. This prediction is estimated by

$$F_0(\mathbf{X}) = \underset{\gamma}{\operatorname{argmin}} \sum_{i=1}^{N} L(\mathbf{Y}_i, \gamma), \tag{3}$$

where γ is the constant which yields the minimal sum of difference between the actual and predicted value. For a loss function of the form in Eq. (2), the definite prediction that initialises the gradient boost approach is the average of all target values in the data set.

Estimation of a constant common prediction for all input variables is subsequently followed by ascertaining the deviation of this parameter from the actual value. This disparity between the predicted and observed value is referred to as 'pseudoresidual'. Once the pseudoresidual for each input data is assessed, a regression tree to predict the respective disparity between the respective actual and constant value is formulated. The pseudoresidual rendered by the tree is combined with its existing counterpart and the constant prediction of the initial leaf to offer a revised expected value. Deviations of the actual data from these devised values are determined, and regression trees are progressively instituted to reduce the pseudoresidual. Ultimately, the prediction of the gradient boost tree includes the summation of the pseudoresiduals predicted by the individual regression trees and constant value of the initial leaf node. Often a definite learning rate is augment to this approach, in order to uniformly regulate the contribution of individual trees to the final prediction. Pseudoresiduals for data i emerging from nth-regression tree are expressed as

$$r_{in} = -\left[\frac{\partial L(\mathbf{Y}_i, F(\mathbf{X}_i))}{\partial F(\mathbf{X}_i)}\right]_{F_n(\mathbf{X}_i)=F_{n-1}(\mathbf{X}_i)}, \tag{4}$$

which for straightforward loss function would be difference in the actual and predicted value. Since the prediction made by the technique is largely dependent on the pseudoresidual of the gradient form in Eq. (4), which result from several individual regression trees, this approach is referred to as gradient boost.

4.3 XGBoost Regression

The fundamental framework of the XGBoost approach in developing a predictive surrogate model is identical to that of the previously discussed gradient boost [47]. This technique, similar to gradient boost, initiates the modelling attempt by identifying a constant prediction for all input variables. By relating this prediction to the respective input values, the corresponding pseudoresiduals are calculated. Estimation of these residuals are followed by the formulation of regression trees which are intended to predict the deviation between the realised constant and actual data. These trees are sequentially devised to gradually minimise the pseudoresiduals and make predictions that are closer to the observed value. This treatment ultimately renders a combination a principal leaf and several trees that can potentially offer a reasonable prediction for any given set of input variables. Even though all these aspects indicate that XGBoost adopts the general approach of the gradient boost, there are certain key differences that set the former apart.

The difference between XGBoost and gradient boost technique is evident in the very first step of initialisation. While a definite treatment is employed to arrive at the initial constant prediction for gradient boost, a default value is readily assumed for XGBoost. Moreover, as opposed to a conventional regression tree, XGBoost builds characteristic trees, called 'XGTrees', to predict the disparity between the assumed constant and actual value [48].

The formulation of the XGTree starts with a leaf node that encompasses all pseudoresiduals, which are difference between the constant prediction and actual value. 'Similarity score' for this leaf is subsequently estimated by

$$\text{Similarity Score} = \frac{[\text{Sum of residuals}]^2}{\text{Number of residuals} + \lambda} \tag{5}$$

where the regularisation parameter, λ, monitors the influence of an individual datapoint on the entire model. Following the determination of the similarity score for the principal leaf, attempts are made to cluster the corresponding set of pseudoresiduals. Different combinations of clusters are separately realised through suitable thresholds, which are assigned to the original leaf, thereby transforming it to root node. Similarity score for each cluster is individually ascertained, and the overall clustering is evaluated by calculating 'gain' which is difference between the similarity score of the clustered leaf nodes and the root. The cluster with maximum gain is transformed to the first branch node, while the rest is overlooked. The set of residuals in these branch nodes is subsequently clustered, by ensuring the maximum gain,

which ultimately yields a typical XGTree. The output of a XGTree, whose leaves characteristically comprise cluster of individual residuals, is determined by

$$\text{XGTree output} = \frac{[\text{Sum of residuals}]}{\text{Number of residuals} + \lambda}, \tag{6}$$

where λ is the regularisation parameter that avoids overfitting. This output, which varies with the predictor variables, along with existing pseudoresidual and constant prediction is collectively adopted to calculate the revised prediction. Following the framework, similar XGTrees are progressively built to reduce the deviation between actual and predicted data. Generally, a learning rate, represented by η, is augmented to the formulation to uniformly regulate the contribution of individual trees to the final prediction [36].

4.4 Artificial Neural Network

Deemed to operate akin to the human neurological system, this technique gets its name artificial neural network. The approach adopted by neural network to develop a predictive model can be described in numerous ways. However, a rather straightforward way of perceiving the working of neural network would be relating it to the regression technique. Similar to regression, it can be stated that the neural network forms the surrogate model by fitting hyperplane through the datapoints in the multidimensional space.

The *architecture* of the neural network approach that lends itself to the development of predictive surrogate model from convoluted data set is schematically illustrated in Fig. 4. Besides the input and output nodes, which respectively intakes the multidimensional predictor variables and yield targets, there are 'hidden layers' comprising of several characteristic nodes. The number of hidden layers and nodes associated with each layer can be suitably varied to yield the desired outcome in an efficient manner. The nodes of input, output and hidden layers are intricately *linked*. In the hidden layers, where the input variables are processed, the corresponding nodes are associated with a specific function called *the activation function*. There are few options available for the activation function, and a specific choice is made for the given data set. The hyperplane that elegantly fits through the datapoints is formulated by appropriately manipulating the input variables and relating it to the activation functions. Therefore, the accuracy of the model hugely relies on treatment of input data within the hidden layers which yields the hyperplane from the activation functions. This manipulation of the predictor variables is achieved by suitable hyperparameters called *weights* and *biases*. For a given data set and a neural network framework, an efficient predictive model is developed only when the appropriate combination of these hyperparameters is realised [35, 36]. Often *back propagation* treatment involving several iterations or *epochs* is employed to prefect and arrive at a seemingly ideal combination of weights and biases. Ultimately, an artificial neural
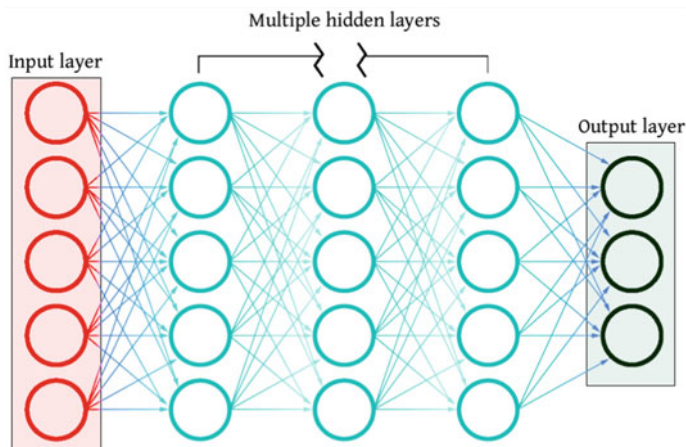
Fig. 4 Schematic illustration of neural network comprising of input, output and multiple hidden layers with each comprising of several nodes

network cumulatively exploits the hyperparameters and the activation functions to predict outcomes for a given set of input variables [39].

4.5 Support Vector Regression

Support vector machines are predominantly adopted for classifying data with intricate distribution and noticeable overlap. However, this technique has been suitably extended to develop models that could render definite value for a given set of input. Akin to the conventional regression approach, support vector regression aims to formulate a surrogate model by fitting hyperplane through the datapoints in multidimensional space. Despite the similarity, while the regular regression ensures the best fit by minimising the *least-squared error*, square of the difference between predicted and observed value, support vector regression achieves it through appropriate *kernel functions*.

In light-metal alloy designs, support vector regression invariably adopts 'radial basis' function, as the kernel, to build the predictive surrogate model [33]. Radial basis functions are of the form similar to Gaussian distribution, in that they monotonically increase (or decrease) towards the centre. In order to realise a hyperplane that fits best with the data, several of the kernel functions with identical form, centred at the respective datapoints in multidimensional space, are considered. The form of the radial basis function is generally expressed as $\psi(||\mathbf{X} - \mathbf{X}_i||)$ with $\mathbf{X}_i$ indicating the multidimensional datapoint on which the kernel is centred. The distribution or(deviation) of the function is fixed by $||\mathbf{X} - \mathbf{X}_i||^2$, which indicates the L_2 norm (Euclidean distance). Kernel functions of this form are NOT always assigned to every

datapoints. By suitably varying the weights, the radial basis functions are efficiently placed. Surrogate model from the radial basis functions is ultimately formulated by linear superposition, which is expressed as

$$\hat{F}(\mathbf{X}) = \sum_{i=1}^{N} w_i \psi(||\mathbf{X} - \mathbf{X}_i||), \tag{7}$$

where w_i is the weight that effects the contribution made by the function centred at i to the hyperplane that reflects the predictive model. When compared to regular regression, w_i is equivalent to the fitting coefficient. Moreover, in Eq. (7), the function $\psi(\cdot)$ dictates form of the radial basis kernel. Besides linear and cubic, this function can be suitably varied to render a form similar to that of the Gaussian distribution.

4.6 Kriging Technique

When surrogate models are built from limited high-fidelity data, generally, exhaustive and sophisticated approach called *Gaussian Process* is employed [15]. Kriging is one variant of the Gaussian process technique which has been used in light-metal alloy design. Despite being relative sophisticated, Kriging shares certain features with the radial basis function based support vector regression. In other words, the latter can be viewed as the less rigorous form of Kriging. Moreover, the expression that describes the approach to develop the surrogate model in Kriging would be similar to Eq. (7), which is associated with radial basis function.

Despite the similarity with the previous approach, there are key characteristic features associated with Kriging that distinguishes it from other techniques, and makes it most suitable for alloy design studies [30, 31]. The principal difference stems from the form of the function involved in Kriging, which is written as

$$\psi(|\mathbf{X} - \mathbf{X}_i|) = \exp\left(-\sum_{i=1}^{N} \theta_i |\mathbf{X} - \mathbf{X}_i|^{p_i}\right). \tag{8}$$

When a constant value is assumed for $\theta_i \equiv \theta$, and $p_i = 2$, in above relation, the resulting function transforms to the radial basis function. However, in Kriging, the parameter p_i, which penalises the function in relation to the distance $|\mathbf{X} - \mathbf{X}_i|$, varies with the individual data. Similarly, instead of assuming identical distribution for all functions, as in the previous technique, function width is specifically varied for each datapoints through θ_i. This parameter by considering the correlation between the target variables, and the predictors through them, assumes a value that varies with the position of the data. Therefore, along the points of higher correlation, the function assumes a sharper form when compared to the rest. The inclusion of correlation in the formulation of the function, through θ_i, facilitates in individually quantifying

the unexplained error associated with the prediction. In conventional regression, as indicated in Eq. (1), there is an unexplained error originating from the definite nature of the data set. This error is generally described as a Gaussian function with identical features irrespective of the its position on the hyperplane. However, in Kriging, the correlation-based estimation of θ_i enables a more rigorous delineation of the unexplained error, which is dependent on the position of the datapoints. This feature plays a critical role in *optimization process*, which is key for alloy design.

4.7 Model Validation

Before the surrogate model rendered by the machine learning technique is exhaustively manipulated, to design alloys with desired combination of properties, their outcomes are sufficiently analysed to ensure the relevance and consistency. Depending on the wealth of information available, one of the various validation technique has been adopted to study the predictability of the model. As described earlier, in light-metal alloy design, data set employed in model development is either implicitly built through dedicated experimental works or from suitable external sources. The wealth of information gathered from the external sources are often noticeably greater than the experimentally arrived. Correspondingly, the approach adopted to validate the model varies with the source of the data which was used to establish it [35, 36].

Cross validation Predictability of surrogate model, particularly when internally developed data set is involved, is investigated through a technique called 'cross validation'. This technique verifies the output rendered by the model against a portion of the existing data set. In other words, in the context of light-metal alloy design, cross validation technique feeds in a composition of *known* properties to the model and cross verifies the accuracy of the model by comparing it to the corresponding output. The known datapoint which is used in cross validation is generally not involved in the model development. This cross validation approach, primarily adopted in light-metal alloy design framework wherein implicit experimental studies are involved to generate data, is called leave-p-out validation [30, 31].

In leave-p-out validation, 'p' indicates the number of datapoints which are initially left in model development solely for the purpose of being utilised in cross verifying the predictability of the emerging model. Since this technique is largely employed in alloy design framework with internally developed experimental information, often only one datapoint is set apart for the validation ($p = 1$, Fig. 5). This datapoint, though not involved in model development, will be used for validation. The left-out datapoint is sequentially changed, and the validation is iterated, to gain a sufficient understanding on the predictability of the surrogate model [39]. Therefore, ultimately, leave-one cross validation ensures the predictability of the surrogate model in light-metal alloy design attempts which are characterised by direct involvement of experimental studies.
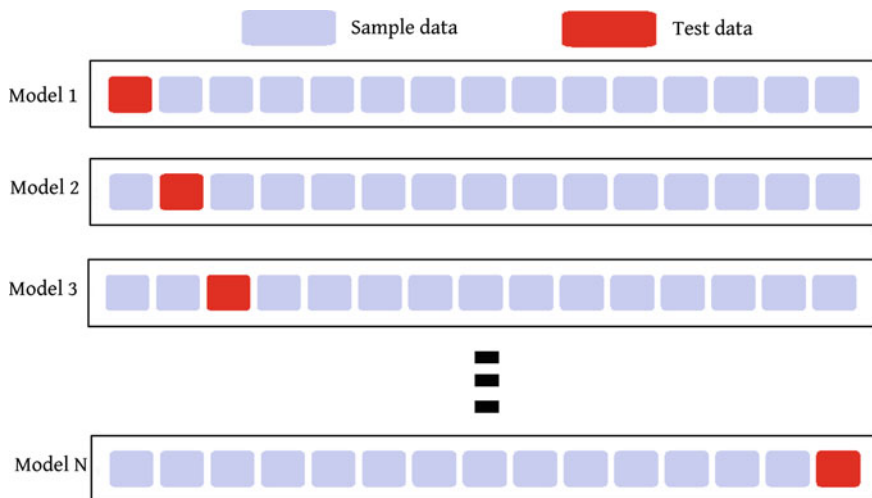
Fig. 5 Graphical representation of leave-one-out cross validation technique

Splitting data Amount of data externally gathered from existing resources, particularly for light-metal alloy design, is significantly higher when compared to the information built from implicit experimental studies. This increased wealth of information lends itself to be split into different sets of data which can then be separately employed for model development and validation. In light-metal alloy design, the gathered data is split into '60-20-20' with the predominant portion of it (60%) assumes the role of training data, while the rest is treated as validation (20%) and testing (20%) set [35]. The surrogate model is built primarily based on the training data. However, during the formulation, the validation data is infused to refine the model parameter and enhance its predictability. Finally, the developed and refined model is verified against the test data set to complete the validation.

Comparison with experimental results The possibility of data splitting validation stems, in principle, from the wealth of the available information. The data set gathered from relevant external sources allows for another form of validation as well. In light-metal alloy design, since the information is gathered invariably from experimental studies, these are characteristically associated with accurate outputs. Therefore, once a surrogate model is developed based on this gather data set, its prediction is 'statistically' compared to the corresponding experimental results. This statistical comparison involves correlating the output of the surrogate model to the corresponding experimental outcomes and quantifying the compliance through the correlation coefficient. This validation approach of correlating the model prediction with experimental result is utilised to identify the best surrogate model in studies, where numerous machine learning techniques are involved [33, 36].

5 Alloy Design

The final aspect of the light-metal alloy design involves realising the composition that could potentially render the combination of desired properties. The methodology associated with this step is principally in contrast to the one involved in the development of surrogate models. In other words, the composition of the alloys is treated as the predictor variables, with the corresponding properties turning into target, when the model is devised. However, in alloy design, the roles of these variables get reversed, with the desired properties fed in as the input. Owing to the approach that is involved, the attempts of identifying the alloy concentration with preferred behaviour, based on the surrogate model, are referred to as optimisation [49, 50].

The optimisation pursued in light-metal alloy design, in keeping with the convention, can be categorised into two [15]. When the focus is restricted to a specific property, and efforts are directed towards realising an alloy with this improved feature, the corresponding approach is referred to as target objective optimisation. In contrast, multi-objective optimisation attempts to realise composition capable of rendering a definite combination of properties. Depending on the type of the optimisation, the corresponding nature of the technique appropriately varies. In other words, despite being collectively referred as optimisation, approach associated with target objective varies noticeably from multi-objective investigations.

Even though the technique varies depending on number of properties that are sought, the optimisation approach can, in general, be delineated by considering two critical aspects. *Exploitation* and *exploration* are characteristic features which form the integral part of any optimisation efforts. In light-metal alloy design exploitation involves focusing on the concentration, within the data set, which renders properties close to the desired behaviour. Contrastingly, chemical composition much different from the ones encompassed in the data set is analysed in the exploration aspect of alloy design. An efficient optimisation scheme attempts to achieve a right balance between these aspects of exploration and exploitation.

5.1 Target Objective Optimisation

In light-metal alloy design, when focus is restricted to a specific property, different optimisation treatments are adopted to realise the suitable alloy composition [30, 31]. Most of these technique, despite the difference in the methodology, hugely rely on the surrogate model, particularly the uncertainties brought about by the unexplained error. Expect for Kriging, since all other machine learning techniques assume a homogeneous form of unexplained errors, bootstrapping is involved to provide a characteristic description for the uncertainties [36].

Random strategy As the name indicates, random strategy looks for different compositions in the *search space*, in an indistinct manner, and ascertains the corresponding properties through the surrogate model. The data gained from this trial and error

search is examined, and the composition offering the best of the required property is assumed to be the suitable candidate. Moreover, the predominant portion of the concentration that does not enhance the property is subsequently used to refine the surrogate model. The technique of strengthening the model from the data gathered from optimisation, and subsequently using it for analysing further random concentration is called *active learning*. Besides random strategy, active or adaptive learning is involved in other optimisation treatments as well. Though random search fails to render a reliable output, this technique does not employ a dedicated optimisation scheme and is primarily dependent on surrogate model alone.

Response surface optimisation Besides using the surrogate model to predict the property associated with a randomly chosen datapoint, an informed choice of the concentration can be made based on it. In other words, stemming from the surrogate model, concentration which could offer the desired property can be identified and further analysed. This approach is adopted in response surface optimisation. In this technique, the surrogate model is extensively studied to realise datapoints capable of yielding the expected behaviour of alloy. This realisation is followed by the investigation of the concentrations surrounding the existing data. As opposed to the random search, this approach restricts the focus to a specific section of the search space, adjacent to the hyperplane that reflects the surrogate model. Given that this model is developed based on available datapoints, with a particularly focus on the concentrations surrounding them, this scheme is essentially biased towards the exploitation aspect of optimization.

Efficient global optimisation As opposed to the aforementioned techniques, efficient global optimisation neither looks for the concentration rendering the desired property randomly or primarily exploits the model reflecting the existing data. However, by involving a dedicated scheme, this approach attempts to realise the desired concentration yielding the preferred behaviour by appropriately balancing the exploitation and exploration aspect of optimisation. To that end, efficient global optimisation scheme begins with the formulation of an *acquisition (or utility) function* that encompasses both the surrogate model and the respective confidence interval, which reflects the unexplained error. The acquisition function directs towards the next optimal point which could render the desired property. Once this point is explored, through adaptive learning the utility function is refined, and another potential composition is subsequently realised based on the updated function. This process is iterated till the improvement is desired property is less than 1% [35]. In light-metal alloy design, the *expected improvement* for a choice of concentration rendered by the acquisition function is expressed as

$$E[I(\mathbf{x})] = (f_{\min} - \hat{Y})\Phi\left(\frac{f_{\min} - \hat{Y}}{s}\right) + s\phi\left(\frac{f_{\min} - \hat{Y}}{s}\right), \tag{9}$$

where $f_{\min} = \min(y_1, y_2, \ldots, y_N)$ is function of relevant datapoint, and $\hat{Y}$ is the prediction made by the surrogate model [30]. Moreover, the standard deviation of

uncertainties associated with the predicted value is represented by s. In Eq. (9), $\Phi(\cdot)$ and $\phi(\cdot)$ respectively indicate the standard normal density and distribution function which correspond to the cumulative distribution and probability density function.

5.2 Multi-objective Optimisation

Though perfecting one property through appropriate composition is relevant, technological advancements often demand development of alloys with complementing. Evolution of the different generation of automotive materials is a prime example where attempts are made design materials with seemingly mutually exclusive properties. In machine learning-based alloy design, multi-objective optimisation is employed to realise concentration capable of yielding more than one desired behaviour. In light-metal alloy design, few techniques have been adopted to arrive at a alloy composition with the potential to render multiple target [34, 39].

Pareto front Considering that multi-objective optimisation scheme characteristically attempts to realise a candidate with multiple target features, a multidimensional space can be built based on these desired properties. The development of such multidimensional space initiates the multi-objective optimisation scheme using Pareto front. Information of the data set can be positioned in this space by focusing of the target properties rendered by the alloy composition. The distribution of the points in the space generated by properties is referred to as the Pareto plot. Moreover, the set of datapoints in the *properties-search space* that represent the boundary of the plot is called Pareto front. Owing to its configuration, the Pareto front captures the trade-off between the different properties constituting the space. Therefore, the target that ideally combines these different properties is estimated based on the Pareto front. In order to arrive at this target, two vectors are introduced. While both stem from the origin of the properties space, one connects to the perceived target with efficient behavioural combination, while other relates to the Pareto front. The progress towards the target is made by reducing the angle between the two vectors.

Scalarization technique A relatively straightforward and less rigorous approach, when compared to Pareto front, is employed by the scalarization technique for multi-objective optimisation. In principle, this approach transforms the multi-objective optimisation problem to a target objective one. This is achieved by formulating a new target that includes all the necessary properties needed to characterise the alloy development. In order to describe this all-encompassing feature, the Euclidean distances between the target properties in corresponding space are ascertained. Based on the distance between the desired properties, the replacing feature is realised. The realisation subsequently facilitates the involvement of target optimisation techniques to yield the respective alloy composition.

6 Summary

Arriving at an alloy composition, which would render a set desired properties, through conventional experimental approach is an arduous task. Involvement of machine learning technique in materials engineering has significantly curtailed the efforts associated with alloy development. In the recent years, these techniques have increasingly been adopted to design light-metal alloys.

Irrespective of the base metal, the machine learning approach for alloy development begins with the generation of the relevant data set. The characteristic structure of the data includes the composition of the alloying elements and resulting material properties. In light-metal alloy designs, this data set is internally generated through suitable experimental works or gathered from existing external resources. Based on this data, using machine learning techniques, predictive surrogate models are formulated as a next step towards the light-metal alloy design. Amongst the different stages of the alloy development process, it is in the formulation of the surrogate models, and the machine learning algorithms are extensively employed. Before proceeding to the alloy design, the working of the surrogate models is sufficiently verified against the existing data set and experimental observations. Only the validated predictive models are exploited to develop light-metal alloys. Suitable optimisation techniques, which would respectively treat the properties and composition as the predictor and target variables, are formulated and adopted to realise the light-metal alloy composition capable of offering the desired behaviour from the surrogate models.

References

1. Polmear I, StJohn D, Nie JF, Qian M (2017) Light alloys: metallurgy of the light metals. Butterworth-Heinemann
2. Monteiro WA (ed) (2014) Light metal alloys applications. BoD-Books on Demand
3. Tien J (ed) (2012) Alloy and microstructural design. Elsevier
4. Amis EJ, Xiang XD, Zhao JC (2002) Combinatorial materials science: what's new since Edison? MRS Bull 27(4):295–300
5. Haidemenopoulos GN (2018) Physical metallurgy: principles and design. CRC Press
6. Suzuki A, Shen C, Kumar NC (2019) Application of computational tools in alloy design. MRS Bull 44(4):247–251
7. Alpaydin E (2020) Introduction to machine learning. MIT Press
8. Kotsiantis SB, Zaharakis I, Pintelas P (2007) Supervised machine learning: a review of classification techniques. Emerg Artif Intell Appl Comput Eng 160(1):3–24
9. Butler KT, Davies DW, Cartwright H, Isayev O, Walsh A (2018) Machine learning for molecular and materials science. Nature 559(7715):547–555
10. Jain A, Hautier G, Ong SP, Persson K (2016) New opportunities for materials informatics: resources and data mining techniques for uncovering hidden relationships. J Mater Res 31(8):977–994
11. Mueller T, Kusne AG, Ramprasad R (2016) Machine learning in materials science: recent progress and emerging applications. Rev Comput Chem 1(29):186–273
12. Liu Y, Zhao T, Ju W, Shi S (2017) Materials discovery and design using machine learning. J Mater 3(3):159–177

13. Takahashi K, Tanaka Y (2016) Materials informatics: a journey towards material design and synthesis. Dalton Trans 45(26):10497–10499
14. Lu W, Xiao R, Yang J, Li H, Zhang W (2017) Data mining-aided materials discovery and optimization. J Mater 3(3):191–201
15. Gubernatis JE, Lookman T (2018) Machine learning in materials design and discovery: examples from the present and suggestions for the future. Phys Rev Mater 2(12):120301
16. Hart GL, Mueller T, Toher C, Curtarolo S (2021) Machine learning for alloys. Nat Rev Mater 6(8):730–755
17. Pandey A, Pokharel R (2021) Machine learning based surrogate modeling approach for mapping crystal deformation in three dimensions. Scr Mater 1(193):1–5
18. Wu CT, Chang HT, Wu CY, Chen SW, Huang SY, Huang M, Pan YT, Bradbury P, Chou J, Yen HW (2020) Machine learning recommends affordable new Ti alloy with bone-like modulus. Mater Today 1(34):41–50
19. Arisoy YM, Özel T (2015) Machine learning based predictive modeling of machining induced microhardness and grain size in Ti-6Al-4V alloy. Mater Manufact Process 30(4):425–433
20. Malinov S, Sha W, McKeown JJ (2001) Modelling the correlation between processing parameters and properties in titanium alloys using artificial neural network. Comput Mater Sci 21(3):375–394
21. Trochu F, Sacepe N, Volkov O, Turenne S (1999) Characterization of NiTi shape memory alloys using dual kriging interpolation. Mater Sci Eng A 15(273):395–399
22. Zhang Y, Wen C, Wang C, Antonov S, Xue D, Bai Y, Su Y (2020) Phase prediction in high entropy alloys with a rational selection of materials descriptors and machine learning models. Acta Mater 15(185):528–539
23. Tran A, Tranchida J, Wildey T, Thompson AP (2020) Multi-fidelity machine-learning with uncertainty quantification and Bayesian optimization for materials design: application to ternary random alloys. J Chem Phys 153(7):074705
24. Friederich P, Häse F, Proppe J, Aspuru-Guzik A (2021) Machine-learned potentials for next-generation matter simulations. Nat Mater 20(6):750–761
25. Huang B, von Lilienfeld OA (2021) Ab initio machine learning in chemical compound space. Chem Rev 121(16):10001–10036
26. Li Y, Li H, Pickard FC IV, Narayanan B, Sen FG, Chan MK, Sankaranarayanan SK, Brooks BR, Roux B (2017) Machine learning force field parameters from ab initio data. J Chem Theory Comput 13(9):4492–4503
27. Mortazavi B, Rajabpour A, Zhuang X, Rabczuk T, Shapeev AV (2022) Exploring thermal expansion of carbon-based nanosheets by machine-learning interatomic potentials. Carbon 1(186):501–508
28. Wang Y, Xie T, France-Lanord A, Berkley A, Johnson JA, Shao-Horn Y, Grossman JC (2020) Toward designing highly conductive polymer electrolytes by machine learning assisted coarse-grained molecular dynamics. Chem Mater 32(10):4144–4151
29. Teichert GH, Garikipati K (2019) Machine learning materials physics: surrogate optimization and multi-fidelity algorithms predict precipitate morphology in an alternative to phase field dynamics. Comput Methods Appl Mech Eng 1(344):666–693
30. Xinyu C, Yingbo Z, Jiaheng L, Hui C (2020) Composition design of 7XXX aluminum alloys optimizing stress corrosion cracking resistance using machine learning. Mater Res Exp 7(4):046506
31. Li J, Zhang Y, Cao X, Zeng Q, Zhuang Y, Qian X, Chen H (2020) Accelerated discovery of high-strength aluminum alloys by machine learning. Commun Mater 1(1):1
32. Chaudry UM, Hamad K, Abuhmed T (2021) Machine learning-aided design of aluminum alloys with high performance. Mater Today Commun 1(26):101897
33. Xu X, Wang L, Zhu G, Zeng X (2020) Predicting tensile properties of AZ31 magnesium alloys by machine learning. JOM 72(11):3935–3942
34. Chen Y, Tian Y, Zhou Y, Fang D, Ding X, Sun J, Xue D (2020) Machine learning assisted multi-objective optimization for materials processing parameters: a case study in Mg alloy. J Alloys Compd 5(844):156159

35. Shariati M, Weber WE, Bohlen J, Kurz G, Letzig D, Höche D (2020) Enabling intelligent Mg-sheet processing utilizing efficient machine-learning algorithm. Mater Sci Eng A 9(794):139846
36. Liu Y, Wang L, Zhang H, Zhu G, Wang J, Zhang Y, Zeng X (2021) Accelerated development of high-strength magnesium alloys by machine learning. Metall Mater Trans A 52(3):943–954
37. Wen C, Zhang Y, Wang C, Xue D, Bai Y, Antonov S, Dai L, Lookman T, Su Y (2019) Machine learning assisted design of high entropy alloys with desired property. Acta Mater 15(170):109–117
38. Didona D, Romano P (2014) On bootstrapping machine learning performance predictors via analytical models. arXiv preprint arXiv:1410.5102
39. Mi X, Tian L, Tang A, Kang J, Peng P, She J, Wang H, Chen X, Pan F (2022) A reverse design model for high-performance and low-cost magnesium alloys by machine learning. Comput Mater Sci 1(201):110881
40. Tian L, Fan Y, Li L, Mousseau N (2020) Identifying flow defects in amorphous alloys using machine learning outlier detection methods. Scr Mater 1(186):185–189
41. Padula D, Simpson JD, Troisi A (2019) Combining electronic and structural features in machine learning models to predict organic solar cells properties. Mater Horiz 6(2):343–349
42. Wolpert DH (1996) The lack of a priori distinctions between learning algorithms. Neural Comput 8(7):1341–1390
43. Chen SH, Hsu CH (2021) Using uniform design and regression methodology of turning parameters study of nickel alloy. Int J Adv Manufact Technol 116(11):3795–3808
44. Juez-Gil M, Erdakov IN, Bustillo A, Pimenov DY (2019) A regression-tree multilayer-perceptron hybrid strategy for the prediction of ore crushing-plate lifetimes. J Adv Res 1(18):173–184
45. Liuyang ZH, Xiaohong MA, Weiqi FA, Rui WA, Zesheng LI, Yang SO, Huafeng ZH (2019) A rapid classification method of aluminum alloy based on laser-induced breakdown spectroscopy and random forest algorithm. Plasma Sci Technol 21(3):034018
46. Krishna YV, Jaiswal UK, Rahul MR (2021) Machine learning approach to predict new multiphase high entropy alloys. Scr Mater 1(197):113804
47. Chen T, He T, Benesty M, Khotilovich V, Tang Y, Cho H (2015) Xgboost: extreme gradient boosting. R package version 0.4-2 1(4):1–4
48. Chen T, Guestrin C. Xgboost: A scalable tree boosting system. In: Proceedings of the 22nd ACM SIGKDD international conference on knowledge discovery and data mining, pp 785–794
49. Zhang H, Fu H, Zhu S, Yong W, Xie J (2021) Machine learning assisted composition effective design for precipitation strengthened copper alloys. Acta Mater 15(215):117118
50. Qiao L, Bao A, Lai Z, Liu Y, Zhu J, Wang Y (2021) Alloy design and properties optimization of multi-component alloy based on solidification characteristics. Mater Sci Eng A 23(805):140576

Chapter 2
Environmental Assessment of Recycling Carbon Fibre-Reinforced Composites: Current Challenges and Future Opportunities

Arshyn Meiirbekov, Akniyet Amantayeva, Serik Tokbolat, Aidar Suleimen, Shoaib Sarfraz, and Essam Shehab

1 Introduction

Carbon fibre-reinforced polymers (CFRP) are a commonly used type of material amongst car and aircraft manufacturers. It contributes to 65% and 20% weight reduction, respectively, leading to a reduction in terms of fuel demand [1]. The range of products made from CFRP is rapidly increasing, thus increasing the amount of waste to be accumulated in landfill sites unless treated properly. According to Lefeuvre et al. [2], nearly 500 thousand tonnes of scrap and end-of-life carbon fibre composite waste are projected to be accumulated from the aerospace industry alone by 2050. Polymer matrix composite materials have existed for a long time but there are no effective and global solutions for recycling this type of waste. Both scientists and industries are constantly attempting to improve the existing CFRP waste treatment methods, but not all are functioning at an industrial scale. Although landfilling and incineration are common practices in this context, recycling is becoming a more strategic way due to economic, environmental, and legislative considerations [3]. At the same time, the production of virgin carbon fibre requires large financial and energy inputs making the recycled carbon fibre more attractive [4]. However, unlike landfilling

A. Meiirbekov · A. Amantayeva · A. Suleimen · E. Shehab (✉)
Department of Mechanical and Aerospace Engineering, School of Engineering and Digital
Sciences, Nazarbayev University, Astana, Kazakhstan
e-mail: essam.shehab@nu.edu.kz

S. Tokbolat
School of Architecture, Design and the Built Environment, Nottingham Trent University,
Nottingham NG1 4FQ, UK

S. Sarfraz
Department of Manufacturing, School of Aerospace, Transport and Manufacturing, Cranfield
University, Cranfield MK43 0AL, Bedford, UK

and incineration, the environmental impacts or benefits of existing CFRP recycling techniques still need to be quantified [1].

Although recycling is perceived to be environmentally advantageous, it also causes environmental damage through the collection, sorting, transportation, and processing of the material [5]. Therefore, environmental and economic feasibility studies are needed for the evaluation of recycling processes. One of the main impact criteria considered in environmental impact assessment studies is the climate change (kg CO_2 equivalent). However, many other impact indicators make the environmental assessment inaccurate and challenging to apply to different scenarios [6, 7]. Therefore, this paper summarizes the common life-cycle inventories (LCI) in different CFRP recycling techniques.

In the case of CFRP waste, there are few papers on environmental impact assessment with reliable and scalable results. The commonly used LCA method is still in the early stage of application for CFRP materials. This is mainly due to the shortage of data on CFRP recycling processes at an industrial scale. These and other issues hinder the advancement of sustainable recycling strategies, particularly in the context of understanding the supply chain for CFRP recycling. Therefore, this study aims to review the scientific literature on the environmental impact assessment of CFRP recycling techniques and analyze the related challenges to provide further directions for the assessment design of CFRP recycling processes and sustainable supply chain networks.

2   Methods

This paper used a narrative literature review method proposed by Mayer [8]. The review considers the recent environmental impact works related to recycling CFRPs. This study focusses on an overview of the intersection of environmental assessment and recycling CFRPs in the context of the current situation and perspectives. The primary databases used are Scopus, Science Direct, and Research gate. The publication date of papers included in the study is limited by the last 20 years. Also, only papers written in English with clear references were included in this work. The keywords for the search were "environmental impact", "environmental assessment", "LCA", "life-cycle assessment", "LCI", "environmental impact categories" combined with "recycling carbon fibres", "recycling CFRPs", "recovery of carbon fibre composites". Finally, all the relevant articles were selected after thoroughly reading the abstracts.

3 CFRP Waste Recycling Methods

Currently, the most common CFRP waste recycling methods are mechanical, thermal, and chemical. Whilst mechanical recycling methods are based on mechanical treatment (shredding, milling, and sieving), the most popular and mature thermal recycling method is pyrolysis. Solvolysis with fluid in supercritical conditions (such as water, alcohol, and acetone) is a promising chemical recycling method too [9]. In this section, these methods will be discussed to analyze the inputs and outputs of the system that contribute to the damage in the context of environmental assessment.

3.1 Mechanical Recycling

Mechanical recycling is the cheapest but the least preferable way of recycling. This method implies waste size reduction to very small particles (10–50 mm) and using it as a filler material, for example, for concrete reinforcement [10]. Mechanical cutting, shredding, milling, and sieving are done by the rotating equipment. In this process, the higher the output of the machine the less the energy demand per unit of recycled CF, thus causing less environmental impact. Other than that, these machines can only process small size waste (e.g. 3 mm thickness), therefore, may require additional work such as dismantling and downsizing of composites. These processes might entail additional electrical energy and human health impact, therefore, need to be considered in the life-cycle inventory phase.

3.2 Pyrolysis

Thermal recycling method such as pyrolysis uses heat to decompose carbon fibre. It is widely adopted at an industrial scale due to its efficiency. The important role in pyrolysis recycling is played by the parameters of the process (temperature, pressure, heating rate, etc.). They influence the mechanical properties of reclaimed fibres. This means that depending on the required application process optimization is needed which in turn will affect the energy demand [11]. Figure 1 represents LCI for the pyrolysis process.

3.3 Fluidized Bed Process

Fluidized bed process (FBP) is the thermal process that uses silica sand to decompose the composite waste into the fibres and reinforcing material. During the process, a hot stream of air runs through a bed at a temperature >500 °C. After that fibres
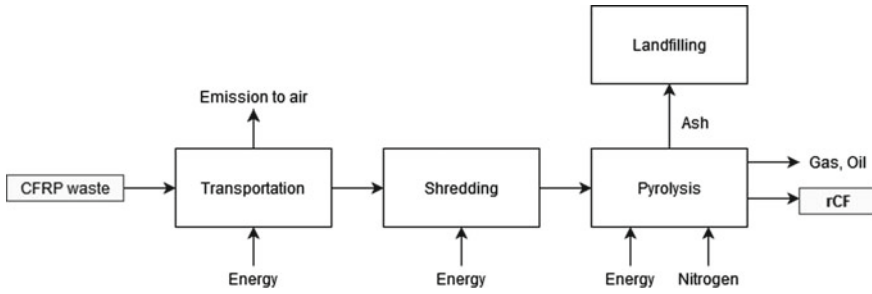
Fig. 1 Life-cycle environmental impact of pyrolysis process
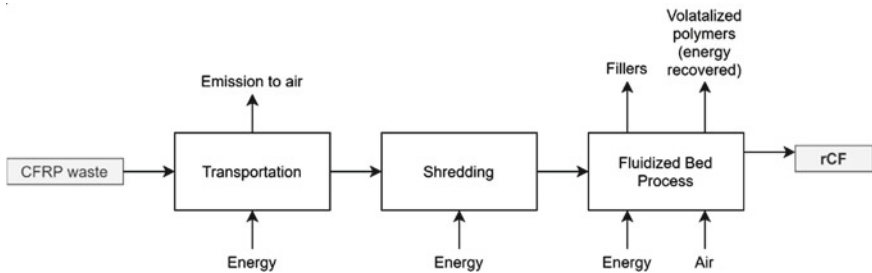
Fig. 2 LCI of fluidized bed process

are discharged by a cyclone from the stream of the gas. The degraded components remain in the bed. The method has its advantages such as tolerance to contaminants and moderately preserved fibre characteristics, indicating a technology readiness level (TRL) of 6 at Nottingham University, UK [12]. The schematic representation of LCI of FBP is represented in Fig. 2.

3.4 Solvolysis

Chemical recycling process or solvolysis is utilized to decompose polymer matrix with the help of chemical components. Based on the solvent's state, the method is subdivided as solvolysis with (1) lower temperatures and (2) supercritical fluids. During the process, the waste is shredded initially to increase the surface of interaction with the chemical and then dissolved using solvents (Fig. 3). The range of used chemicals is wide starting from supercritical water and ending with solvents such as ethanol, acetone, and methanol [13]. The method is not still applied at the industry scale, though the results were validated at the laboratory level [14].
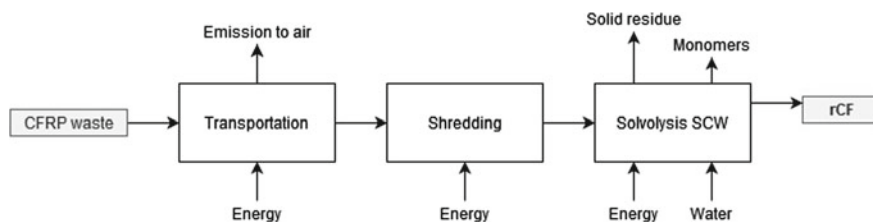
Fig. 3 LCI of solvolysis process

4 Life-Cycle Assessment

LCA is one of the widely applied methods for the environmental assessment of a product. This method is ISO 14000 standardized and is conducted following the established procedures [15]. LCA assessment is performed in several steps. These steps include identifying the aim and defining the system of the LCA, quantifying the input and output flow of the system, evaluating the life-cycle impact, and classifying their impact categories to the environment and improving assessment [5]. Throughout the life cycle of a product, different process stages require a different number of resources and have varying levels of impact on the environment. As a part of the LCA study, the assessor needs to delineate the system boundaries and scope of the study. After that, inventory analysis is carried out on emissions and waste generated during the process. Then, their environmental impact is quantified in terms of ozone depletion, eco- and human toxicity, and so on [15]. Depending on the chosen scope, LCA analysis can cover the whole life cycle of a system or only a part of it [16]. "Gate-to-gate" LCA covers partial LCA which considers only a single process. In our work, gate-to-gate indicated studies are those which covered only the recycling process itself. "Cradle to grave" is a standard full-cycle LCA which covers all production phases, use, and disposal phase. "Cradle to cradle" or closed LCA is a type of "cradle to grave" LCA, but it also includes the recycling process. This whole life-cycle assessment allows relevant stakeholders to manage the product and drive its production and disposal in a more sustainable way.

5 Life-Cycle Inventory

The life-cycle inventory (LCI) analysis stage is an important and challenging step in the LCA process. It is challenging because it requires appropriate data which usually tends to be limited in the early-stage development of a process or a product. Inventory refers to all direct and indirect environmental impacts of a process such as inputs (raw stock material, energy, etc.) and outputs (emissions, waste, etc.) [17]. It is also possible to include social considerations such as health and safety, risks as well as human health impact. Depending on the chosen set of inputs/outputs during the

Table 1 Energy consumption levels by different CFRP recycling methods

Recycling method	Reported energy consumption (MJ/kg)	References
Mechanical recycling	2.03 (10 kg/h)	[19]
Pyrolysis	2.8 30	[20] [21]
Solvolysis	63–91 19	[22] [23]

LCI, the accuracy and validity of the LCA results will vary. Moreover, the inventory data (e.g. energy, material, emission, etc.) is aggregated to quantify the specific environmental concerns, for example, global warming and resource depletion. There are far more examples of environmental impact categories. However, no standard method or criteria exists for selecting the "right" impact category. The decision is mostly dependent on the studied sector, scope, and authors' judgement [18].

Another important deliberation is the availability of several impact categories to quantify one environmental concern. For example, global warming indicators could be a global warming potential (GWP, kg CO_2 eq.), the climate change impact (kg CO_2 eq.), greenhouse gas emissions (kg CO_2 eq.), CO_2 emission (kg CO_2 eq.), and others. According to general observations, the recycling CFRP sector tends to evaluate GWP as a function of energy required to recycle by one of the aforementioned methods. There are several works published that quantify and compare the energy consumption of CFRP recycling techniques. However, they use different functional units and experimental setups and make different assumptions. Therefore, the data usually varies from one study to another. The indicative energy consumption by methods is shown in Table 1.

In addition, sometimes, one impact category can be measured with different units which also confuses relevant stakeholders [1]. For example, acidification can be expressed as kg SO_2 eq. or m^2 UES (area of an unprotected ecosystem) or as the number of extinct species per year. The list of commonly used impact categories and their units is presented in Table 2.

According to [5], the environmental impact assessment is three-step process: classification, characterization, and evaluation. First, the data or inventory needs to be classified into the environmental issue (e.g. global warming), the scale of the impact (e.g. local, global), and impact media (e.g. air). Second, characterization refers to quantifying the impact of the inventory to determine environmental issues. Some of the terms to quantify such contributions can be GWP and ozone depletion potential (ODP). Similarly, recycling CF from CFRP entails unique environmental impacts which are summarized in Fig. 4. These are the main impact categories that are widely reported in the literature [32].

Although LCA is a very useful tool, users should be aware of its sources of uncertainty which might lead to different outcomes [7]. For example, as was discussed before, some steps of the analysis require personal judgement (determining system boundary, analyzing the recycling process, choosing quantifiable impact categories,

Table 2 List of impact categories for LCI analysis of CFRP material

Name	Abbreviation	units	Comment	Sources
Global warming potential (climate change)	GWP	kg CO_2 eq/kg	If the process emits gas, it will have GWP, which compares the energy absorbed by 1 tonne of gas over time with the emissions of 1 tonne of CO_2	[24]
Greenhouse gas emissions	GHG	kg CO_2 eq/kg	The most widely used environmental impact assessment category	[1]
Cumulative energy demand	CED	MJ/kg	The energy required to make the product, process, or service	[25]
Energy intensity	EI	MJ/kg	Equivalent to cumulative energy demand (CED) corresponding to primary energy	[25]
Ozone layer depletion	OLD	kg CFC-11 eq	The function of the emission of ozone depleting gas	[26]
Human toxicity (cancer causing and non-cancer effect)	HTP	CTUh	The function of the number of toxic releases to humans in water, air, and soil media	[27]
Acidification potential	AP	kg SO_2 eq	The function of soil acidity due to sulphates, nitrates, and phosphates (NO_x, NH_3, and SO_2) in the atmosphere	[28]
Eutrophication potential	EP	kg N-Eq	Nutrient enrichment of marine ecosystem	[29]
Ecotoxicity (freshwater, marine, terrestrial)	ET	kg O_3-Eq	The function of exposure level to released toxic substances to the environment	[30]
Resource depletion (water, natural resources)	RD	m^3 water/oil eq	Depletion of non-renewable natural resources	[31]
Photochemical oxidation	POCP	kg Sb eq	Also known as summer smog, the air pollution resulted from the reaction of emissions with sunlight	[30]
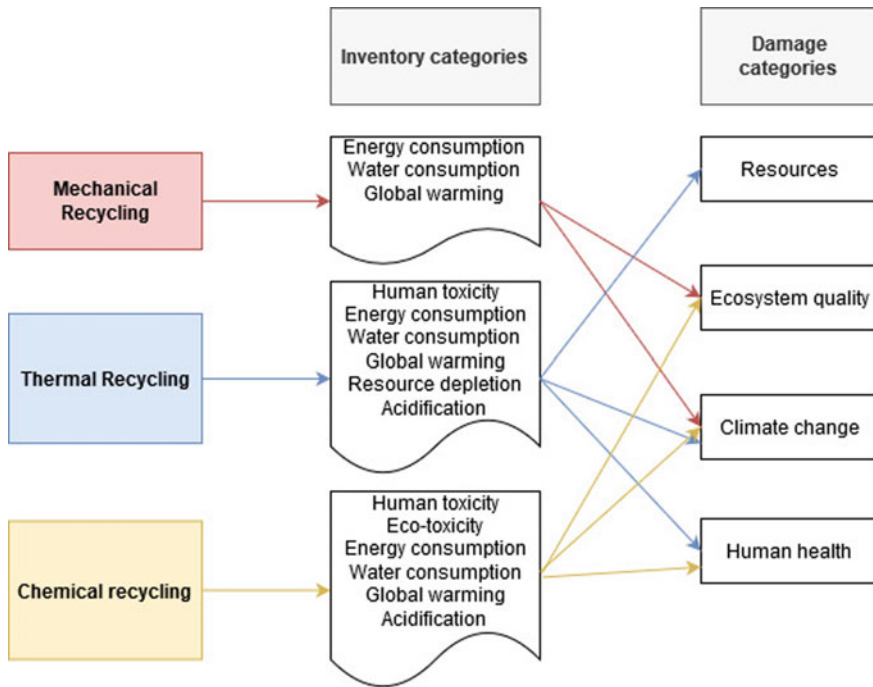
Fig. 4 Environmental inventory and damage categories of CFRP recycling methods

etc.). This and other challenges in the environmental analysis of CF recycling will be discussed in the next sections.

6 Environmental Assessment of CFRP Recycling: Current Status

The works related to the environmental assessment of CFRP recycling methods are listed in Table 3. Most of the authors compared different recycling options according to their global warming potential, acidification, and ecotoxicity potential. Also, as data plays a crucial role in the LCA analysis. The authors used databases of well-known platforms such as Simapro, Ecoinvent, and Gabi. The research work presented in Table 3 are grouped according to the recycling methods included.

From Table 3, it is clear that numerous research attempts have been made to discover the environmental impacts of recycling CFRPs. Most studies rely on LCA/LCI databases and follow similar procedures. However, the studies tend to be different in terms of considered recycling methods, life-cycle phases included in the investigation, assessed impact indicators, and databases used. Also, the studies mainly considered energy impact and GWP in terms of assessed impact categories.

Table 3 Environmental assessment of recycling CFRP

References	Year	Approach used	Recycling process	Main impact categories	Database	Comments/Main findings
[33]	2017	Review of indicators	n/a	GWP, EI, AP, OLD, HTP	n/a	The authors state that the most relevant indicators for the CFRP recycling sector are GWP, human toxicity, and acidification
[34]	2021	MCDM	Pyrolysis, FBP, Microwave pyrolysis, Solvolysis SCW	End-of-life index	n/a	The authors proposed end-of-life index to support decisions in choosing a recycling process. The index includes the quality, cost, and environmental aspects of recycling methods
[1]	2020	Review	n/a	n/a	n/a	The authors proposed an LCA framework for composite recycling applicability review, including all phases. The authors state that the use phase is the greatest potential for CFRP in terms of emissions savings. Authors believe that different LCA databases affect negatively cross comparison between different study outputs

(continued)

Table 3 (continued)

References	Year	Approach used	Recycling process	Main impact categories	Database	Comments/Main findings
[25]	2017	Review	n/a	n/a	n/a	The authors provided an extensive LCA review of composites use in aviation including bio-based fibres, bio-based thermoset resins, and recycled CFRPs; also, LCA studies in pyrolysis usage for CFRP recycling were briefly discussed
[35]	2011	Manufacture, use, end-of-life	Mechanical	Climate change, HTP, ET, RD	Ecoinvent, IDEMAT LCI database, literature	Currently, automotive manufacturers are concerned only about reducing emissions during the useful life and increasing the recovery rate of end-of-life waste. Authors suggest that these two requirements are not enough to decide on an environmentally friendly strategy for transportation. Instead, the whole life cycle is needed to be considered

Table 3 (continued)

References	Year	Approach used	Recycling process	Main impact categories	Database	Comments/Main findings
[19]	2014	Gate-to-gate (end-of-life)	Mechanical	EI	Experiment	The energy demand for mechanical recycling was estimated: the energy intensity for the milling process was defined to be between 0.27 and 2.03 MJ/kg
[36]	2016	Gate-to-gate (end-of-life)	Mechanical	GWP, EI	Ecoinvent	The environmental impacts of landfilling, incineration, and mechanical recycling were assessed. Mechanically recycled CFRP may offer great GHG reductions if used instead of virgin glass fibre (-378 CO$_2$ eq./t.), though the costs of recycling are an obstacle to prompting the method to a larger scale
[37]	2020	Gate-to-gate (end-of-life)	Mechanical	GWP, EI	Simpro 9.0.0	The authors provided environmental considerations of rCF coprocessing in cement kilns, which showed a positive trend. 1% of added rCF replacing 10% of cement with silica fume allowed to reduce GWP impact by 14%

(continued)

Table 3 (continued)

References	Year	Approach used	Recycling process	Main impact categories	Database	Comments/Main findings
[38]	2017	Gate-to-gate	Fluidized bed process	GWP, EI	Gabi, Ecoinvent, experiment	The authors evaluated the life-cycle environmental impact of FBP recycling followed by manufacturing from rCF using the wet papermaking process. Results demonstrate that rCF energy demand and GHG emissions can be reduced by 32–50% and 33–51%, respectively
[12]	2020	Gate-to-gate	Fluidized bed process	GWP, EI	Gabi, Ecoinvent, GREET	The work assesses the environmental impact of rCF utilization for aviation applications using the FBP recycling. The phases start with a collection of rCF, manufacturing components, and use phase. The environmental impact reductions are between 4 and 31% compared to virgin glass fibre productions

(continued)

Table 3 (continued)

References	Year	Approach used	Recycling process	Main impact categories	Database	Comments/Main findings
[39]	2018	Gate-to-gate (end-of-life)	Pyrolysis vs solvolysis SCW	AP, ET, EP, GWP, HTP (non-carcinogenics, carcinogenics), ODP, smog	Gabi	ODP is the most responsive impact category to variations in the energy inputs of grinding. The ET is the least sensitive category to variations in the grinding energy
[40]	2015	Gate-to-gate (end-of-life)	Solvolysis (supercritical fluid)	GWP, RD, HTP, OLD, AP, ET	Ecoinvent 3.0	The realignment and the cleaning rCF have a small environmental impact, and supercritical water solvolysis and remanufacturing have a substantial impact. Electricity and natural gas account for more than 33% of the impact
[41]	2014	Cradle–cradle (without use phase)	Solvolysis SCW		Experimental data, Simapro, Ecoinvent, recipe midpoint (H) method	Using recovered carbon reinforcement by aqueous, solvolysis results in an 80% gain for all impact categories compared to landfilling

(continued)

Table 3 (continued)

References	Year	Approach used	Recycling process	Main impact categories	Database	Comments/Main findings
[42]	2016	Production and recycling of the (CF) (gate-to-gate)	Chemical treatment	CED, GWP, AP, OLD, HTP, ET, POCP	Simapro 8.01, Ecoinvent v3, laboratory data	Recycling is environmentally beneficial because recovered fibres could be used instead of virgin fibres for different applications. The avoided energy consumption for vCF production is the main influencing positive factor in the environmental assessment of chemical treatment for CFRP. Laboratory data was used in the study, but plant data is planned to be integrated into the LCA study
[43]	2021	Cradle-to-gate and use phase	Pyrolysis	Primary energy demand (PED), GWP	Gabi, GREET model, and literature studies	The environmental benefits vary from country to country and for different fibre mass content in recycled carbon fibre. 13% and 34% decrease in GWP can be achieved with a 40% recovery rate in cradle-to-gate and use phases, respectively. In Europe, the positive effect on GWP is larger than in the United States

(continued)

Table 3 (continued)

References	Year	Approach used	Recycling process	Main impact categories	Database	Comments/Main findings
[21]	2013	End-of-life recycling	Pyrolysis	RD, GWP, HTP, ET	Simapro	This study is one of the pioneers in LCA analysis for recycling CFRPs. Results indicated that when rCF is used instead of virgin CF, the recycling via pyrolysis has less impact by 78, 84, and 82% on climate change, resource, and ecosystem quality compared to landfilling
[44]	2010	Gate-to-gate (end-of-life)	Acid, pyrolysis in oxygen and nitrogen, organic solvents, supercritical process	Energy footprint, GHG footprint	Simapro 7.0.0. and Ecoinvent	The overall footprint (energy + GHG) is 5 times larger for pyrolysis compared to acids. The overall potential of recycling with acid was shown by the authors
[45]	2017	Gate-to-gate (only recycling)	Mechanical, high voltage fragmentation (HVF), solvolysis	Energy footprint	Ecoinvent 3, European life-cycle database	Experiment and LCA were conducted by the authors. HVF has the highest energy demand (60 MJ per kg) in comparison with chemical (12.3 MJ/kg) and mechanical (0.37 MJ/kg)

(continued)

Table 3 (continued)

References	Year	Approach used	Recycling process	Main impact categories	Database	Comments/Main findings
[46]	2018	Gate-to-gate	Mechanical, pyrolysis, fluidized bed, and chemical recycling process)	GWP, EI	Gabi and Ecoinvent	Four recycling methods were compared to landfilling option in terms of environmental impact. According to the authors, all recycling methods propose GWP reductions from −19 to −27 CO_2 eq and energy reductions from 395 to 520 MJ per 1 kg. The study notes that the net PED and GHG impact categories are more affected by replacing vCF, which are 10–20 times more effective than the recycling process itself
[47]	2018	Gate-to-gate (end-of-life recycling)	Mechanical, pyrolysis, microwave, supercritical water	GWP	Ecoinvent v 2.2	The authors considered the difference of GWP impact between substituted virgin fibre and process impact. All recycling methods have beneficial GWP impacts from recycling, though grinding showed only minor improvements

(continued)

Table 3 (continued)

References	Year	Approach used	Recycling process	Main impact categories	Database	Comments/Main findings
[48]	2021	Gate-to-gate (recycling content approach)	Pyrolysis (assumed)	GHG, EI	Ecoinvent, GREET,	The main focus on the analysis of the production of subframes from recycled CFs. According to the authors, CFRP subframe may reduce GHG emissions in combination with increasing life-cycle distance compared to the conventional subframe
[15]	2020	Cradle to cradle	Landfilling, incineration, pyrolysis	GWP, OLD, HTP, etc	Ecoinvent, experimental data	LCA analysis was conducted with the experiment of prototypes such as sailing boats and handbrake levers. According to the authors, pyrolysis allows up to 40% impact savings because of recovered material

The research interest in determining the environmental aspects of recycling CFRPs is robust and notable work has already been done in this field. All the recycling methods mentioned in this study were examined to some extent to see if the positive environmental implications compared to traditional disposal ways are observed. Despite numerous research efforts that have been highlighted in this review, there are still other challenges associated with the effective and accurate estimation of environmental impacts of recycling CFRPs. These challenges are tightly tied with the research gaps which were formulated based on the conducted literature review. The following subsections provide information on challenges related to this field.

(a) **Variability of methodologies**

Although ISO 14044 documentation stipulates specific standards for the LCA assessment, there is still a great variability within an inventory (LCI) and impact analysis (LCIA) [49]. First, the modelling approach may vary as some modellers can use the attributional LCA method. In attributional LCA, the functional units or phases of the product are attributed according to average retrospective data within a specific period. Conversely, consequential LCA is conducted to determine the change in the environment due to the effects of inputs and outputs of the product [49].

Overall, LCA methodologies have evolved significantly in the last 30 years and have different classification and characterization methods. For instance, the midpoint level indicators might vary from method to method. Some of the methodologies might include completely different indicators compared to the others [50].

(b) **Comparability—functional and system boundaries, oversimplification**

It is critical to determine the functional and system boundaries in the assessment as it directly influences the final interpretation of the assessment results. Ambiguous or unclear definitions of the functions and processes in the recycling chain (not mentioning the usage of accompanied products during the recycling process and other similar omissions) may result in an inaccurate estimation of the final impact. It may seem that comparing recycling methods in terms of an environmental impact are sufficient to examine only the primary processes, however, it may jeopardize the purpose of the environmental assessment [51]. The recycling processes differ in terms of functions (some of them are multifunctional), and the byproducts they produce. It is a challenging task to split the environmental impact within multifunctional recycling methods [52]. For instance, the fluidized bed and pyrolysis process result in byproducts that can be transformed into energy, whereas mechanical recycling does not recover energy [53].

The mentioned challenges in terms of comparability methods are accompanied by the challenge related to the LCA methodology itself. For example, an oversimplification, during which the model limitations and simplify cations result in significant

influence on the outputs [16]. The oversimplification challenge is highly tied to small companies which struggle to implement the LCAs due to the lack of amplitude [52].

(c) Scaling the results

Not all recycling processes have reached the readiness level to be exploited at an industrial scale. Only pyrolysis and mechanical grinding for recycling CFRPs have shown technology readiness levels (TRLs) of 8 and 6.5, respectively. Whereas solvolysis and fluidized bed processes are still at the validation phase in the laboratory environment [14]. This indicates that these methods do not consider the complexity of the industrial scale equipment, management, and additional investment [51]. Hence, scaling the results by using common practices or just by normalization may not result in accurate results for processes that are still at the laboratory scale.

(d) Data-related challenges

Data for LCI/LCA approach is systematically summarized and publicly available in Ecoinvent and Simapro for various materials and processes [54, 55]. However, those databases do not contain specific information for processes related to composite manufacturing, recycling, and disposal. For instance, [47] extract data for a landfilling process from Simapro v7.3 and Ecoinvent 2.2 for mixed polymer plastics instead of composites, as there is no specific data on the environmental effects of composites landfilling. Other parameters of a model for LCI in the studies are also accompanied by the great extent of impreciseness, e.g. energy consumption levels of recycling processes. In the analysis done by Witik [21], the authors examined the product manufacturing phase which is assumed to be using 162 MJ for electricity and 191 MJ of heat from gas. On the other hand, the manufacturing of virgin carbon fibres varies between 183 and 286 MJ per kg [56]. This all demonstrate that the data used in models is not accurate with uncertainty factors embedded in input parameters. Thus, missing datasets for specific processes are a challenge to some extent that has to be overcome by conducting experiments and investing time [51]. In addition, other circumstances negatively affect the reliability of data such as the quality of data in terms of the geographical source, consistency, the compatibility of data from different sources, reasonable assumptions, and reproducibility [52].

(e) Uncertainty

Any LCA study will have results affected by a degree of uncertainty. During the assessment, all the factors will influence the accuracy of results, for example, how model data is arranged and which scope is selected [57]. In fact, most of the studies considered in this work agree with the uncertainty of the LCA method to a certain degree. The difference in methodologies, the discrepancy between lab test results vs implementation of an industrial project, and data quality in combination create a snowball effect. This causes the level of uncertainty of a study to be too high to be used for decision-making. Given that the LCA analysis for new emerging recycling methods is conducted for further decision-making, determining, and leveraging the uncertainty of conducted studies is essential [51]. Figure 5 demonstrates the level of uncertainty and technology readiness level relationship. Composites recycling
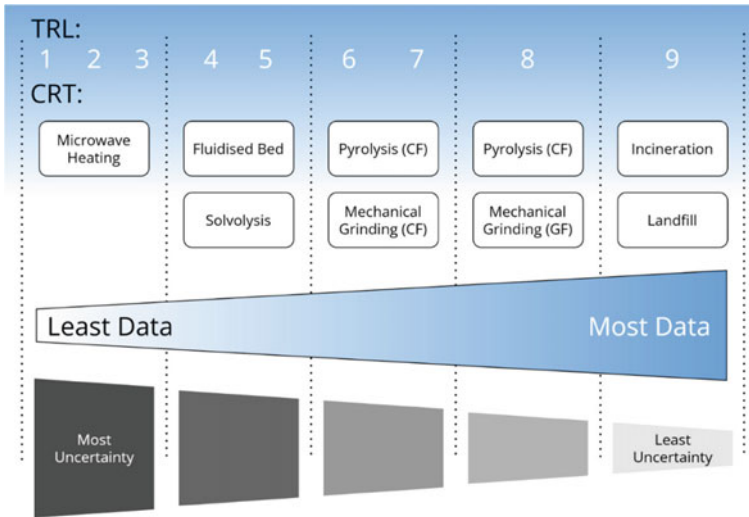
Fig. 5 Uncertainty level representation with respect to TRL of the CFC recycling process

technologies (CRT) on the technology readiness (TRL) scale are adapted from [14]. The more data is available to conduct LCA, and the more accurate results will be obtained during the assessment.

(f)   **Resource demanding assessment**

Although there is no minimum threshold for assessing product sustainability [52], the LCA methodology allows approximating the environmental impact of supply chain operations by analyzing the data. However, environmental assessment is a time and resource-consuming activity for the industry. It requires expertise, knowledge, and financial support as well as adequate environmental data to conduct an LCA study [52]. Moreover, the information and data need to be updated accordingly, especially for products with a long life cycle due to economic and environmental conditions changing over time [49].

7   Conclusions and Future Directions

The processes for recycling CFRPs such as mechanical recycling, pyrolysis, fluidized bed process, and solvolysis result in different qualities of recovered fibres and vary in terms of costs and environmental impacts. This work provided a brief overview of studies that covered the theme of environmental assessment aspects of recycling CFRPs. At present, this field has several studies that mainly investigated CFRP recycling in the context of LCA frameworks. Several works were published assessing the environmental challenges including different life-cycle phases for different methods.

This study has identified the main challenges such as the variability of methodologies, comparability, scaling results, data, uncertainty, and resource demands. The further developments in the environmental assessment of CFRP recycling can be fulfilled through the following future directions:

- A combined methodology should be used with a preliminary agreement with the studies considered in this research. Standardization of the LCA framework for CFRPs within the industries (automotive and aerospace) will help to unite and compare statements from different authors.
- Promoting data availability for CFRP in current databases could be a critical action to bring potential benefits to various stakeholders instantly. However, no accurate data on CFRP manufacturing and recycling is present in databases. The quality of data and availability is the key factors which define the reliability of results. Therefore, it is highly recommended to improve current databases with specific composite materials data.
- LCA studies convey a lot more information as they include the use phase. Some industries benefit from weight savings (for instance, in the automotive industry), therefore consume less fuel in the use phase.
- The collaboration between researchers and recycling industry-related stakeholders will increase the reliability of conducted studies. Because simply scaling the laboratory output does not provide reliable data. The LCA studies conducted within the laboratories using existing databases could be integrated into plant-level studies to demonstrate real-time cases.

Design informed thinking should be promoted. The LCA proves that the positive environmental effects during the production and use phases could be achieved if the design of a product is known beforehand. Though composite material components are usually produced with specific shapes and parameters, it is always possible to incorporate into the design features. This would further allow reuse/remanufacturing of the component in less demanding applications. The opportunities for secondary applications of recycled CFRP shall be rigorously researched to reduce landfilling impacts and avoid an intensive increase in manufacturing rates of virgin CFRPs. This statement is especially critical that the effect of replacing virgin carbon fibre has the dominating positive environmental effect due to avoided energy consumption.

References

1. Tapper RJ, Longana ML, Norton A, Potter KD, Hamerton I (2020) An evaluation of life cycle assessment and its application to the closed-loop recycling of carbon fibre reinforced polymers. Compos B Eng 184:107665. https://doi.org/10.1016/j.compositesb.2019.107665

2. Lefeuvre A, Garnier S, Jacquemin L, Pillain B, Sonnemann G (2017) Anticipating in-use stocks of carbon fiber reinforced polymers and related waste flows generated by the commercial aeronautical sector until 2050. Resour Conserv Recycl 125:264–272. https://doi.org/10.1016/j.resconrec.2017.06.023

3. Lefeuvre A, Yerro X, Jean-Marie A, Vo Dong PA, Azzaro-Pantel C (2017) Modelling pyrolysis process for CFRP recycling in a closed-loop supply chain approach. In: 27th European symposium on computer aided process engineering. Barcelona, pp 2029–2034. https://doi.org/10.1016/B978-0-444-63965-3.50340-8

4. Gopalraj SK, Kärki T (2020) A review on the recycling of waste carbon fibre/glass fibre-reinforced composites: fibre recovery, properties and life-cycle analysis. SN Appl Sci 2(433). https://doi.org/10.1007/s42452-020-2195-4

5. Craighill AL, Powell JC (1996) Lifecycle assessment and economic evaluation of recycling: a case study. Resour Conserv Recycl 17(2):75–96. https://doi.org/10.1016/0921-3449(96)01105-6

6. Guo M, Murphy RJ (2012) LCA data quality: sensitivity and uncertainty analysis. Sci Total Environ 435–436:230–243. https://doi.org/10.1016/j.scitotenv.2012.07.006

7. Ylmén P, Berlin J, Mjörnell K, Arfvidsson J (2020) Managing choice uncertainties in life-cycle assessment as a decision-support tool for building design: a case study on building framework. Sustainability 12(12):5130. https://doi.org/10.3390/su12125130

8. Mayer P (2009) Guidelines for writing a review article: a good to know about review articles. Zurich-Based Plant Science Center, pp 1–10

9. Pimenta S, Pinho ST (2011) Recycling carbon fibre reinforced polymers for structural applications: Technology review and market outlook. Waste Manage 31(2):378–392. https://doi.org/10.1016/j.wasman.2010.09.019

10. Ogi K, Shinoda T, Mizui M (2005) Strength in concrete reinforced with recycled CFRP pieces. Compos A Appl Sci Manuf 36(7):893–902. https://doi.org/10.1016/j.compositesa.2004.12.009

11. Meyer LO, Schulte K, Grove-Nielsen E (2009) CFRP-recycling following a pyrolysis route: process optimization and potentials. J Compos Mater 43(9):1121–1132. https://doi.org/10.1177/0021998308097737

12. Meng F, Cui Y, Pickering S, McKechnie J (2020) From aviation to aviation: environmental and financial viability of closed-loop recycling of carbon fibre composite'. Compos B Eng 200:108362. https://doi.org/10.1016/j.compositesb.2020.108362

13. Krauklis AE, Karl CW, Gagani AI, Jørgensen JK (2021) Composite material recycling technology—state-of-the-art and sustainable development for the 2020s. J Compos Sci 5(28). https://doi.org/10.3390/jcs5010028

14. Rybicka J, Tiwari A, Leeke GA (2016) Technology readiness level assessment of composites recycling technologies. J Clean Prod 112:1001–1012. https://doi.org/10.1016/j.jclepro.2015.08.104

15. Petrakli F et al (2020) End-of-life recycling options of (nano) enhanced CFRP composite prototypes waste—a life cycle perspective. Polymers 12(9):2129. https://doi.org/10.3390/polym12092129

16. da Silva TR et al (2021) Application of plastic wastes in construction materials: a review using the concept of life-cycle assessment in the context of recent research for future perspectives. Materials 14(13). https://doi.org/10.3390/ma14133549

17. Mansor MR, Mastura MT, Sapuan SM, Zainudin AZ (2019) The environmental impact of natural fiber composites through life cycle assessment analysis. In: Durability and life prediction in biocomposites, fibre-reinforced composites and hybrid composites. Elsevier, pp 257–285. https://doi.org/10.1016/B978-0-08-102290-0.00011-8

18. Reyes T, Gouvinhas RP, Laratte B, Chevalier B (2020) A method for choosing adapted life cycle assessment indicators as a driver of environmental learning: a French textile case study. Artif Intell Eng Des Anal Manuf 34(1):68–79. https://doi.org/10.1017/S0890060419000234

19. Howarth J, Mareddy SSR, Mativenga PT (2014) Energy intensity and environmental analysis of mechanical recycling of carbon fibre composite. J Clean Prod 81:46–50. https://doi.org/10.1016/j.jclepro.2014.06.023

20. Song YS, Youn JR, Gutowski TG (2009) Composites: part a life cycle energy analysis of fiber-reinforced composites. Compos A 40(8):1257–1265. https://doi.org/10.1016/j.compositesa.2009.05.020

21. Witik RA, Teuscher R, Michaud V, Ludwig C, Månson JAE (2013) Carbon fibre reinforced composite waste: an environmental assessment of recycling, energy recovery and landfilling. Compos A Appl Sci Manuf 49(2013):89–99. https://doi.org/10.1016/j.compositesa.2013.02.009

22. Shibata K, Nakagawa M (2014) CFRP recycling technology using depolymerization under ordinary pressure. Available at: https://www.mc.showadenko.com/english/report/056/56_sou01.pdf

23. Keith MJ, Leeke GA (2016) Optimisation of solvolysis for recycling carbon fibre reinforced composites. In: ECCM17—17th European conference on composite materials, pp 26–30

24. Vallero DA (2019) Air pollution biogeochemistry. In: Air pollution calculations. Elsevier, pp 175–206. https://doi.org/10.1016/B978-0-12-814934-8.00008-9

25. Bachmann J, Hidalgo C, Bricout S (2017) Environmental analysis of innovative sustainable composites with potential use in aviation sector—a life cycle assessment review. Sci China Technol Sci 60(9):1301–1317. https://doi.org/10.1007/s11431-016-9094-y

26. Bałdowska-Witos P, Piasecka I, Flizikowski J, Tomporowski A, Idzikowski A, Zawada M (2021) Life cycle assessment of two alternative plastics for bottle production. Materials 14(16):4552. https://doi.org/10.3390/ma14164552

27. Imbeault-Tétreault H, Jolliet O, Deschênes L, Rosenbaum RK (2013) Analytical propagation of uncertainty in life cycle assessment using matrix formulation. J Ind Ecol 17(4):485–492. https://doi.org/10.1111/jiec.12001

28. Geisler G, Hellweg S, Hungerbühler K (2005) Uncertainty analysis in life cycle assessment (LCA): case study on plant-protection products and implications for decision making (9 pp + 3 pp). Int J Life Cycle Assess 10(3):184–192. https://doi.org/10.1065/lca2004.09.178

29. Thiel C, Campion N, Landis A, Jones A, Schaefer L, Bilec M (2013) A materials life cycle assessment of a net-zero energy building. Energies 6(2):1125–1141. https://doi.org/10.3390/en6021125

30. Frischknecht R et al (2005) The ecoinvent database: overview and methodological framework (7 pp). Int J Life Cycle Assess 10(1):3–9. https://doi.org/10.1065/lca2004.10.181.1

31. Ciroth A, Fleischer G, Steinbach J (2004) Uncertainty calculation in life cycle assessments. Int J Life Cycle Assess 9(4):216. https://doi.org/10.1007/BF02978597

32. Bulle C et al (2019) IMPACT world+: a globally regionalized life cycle impact assessment method. Int J Life Cycle Assess 24(9):1653–1674. https://doi.org/10.1007/s11367-019-01583-0

33. Pillain B, Gemechu E, Sonnemann G (2017) Identification of key sustainability performance indicators and related assessment methods for the carbon fiber recycling sector. Ecol Ind 72:833–847. https://doi.org/10.1016/j.ecolind.2016.08.056

34. Markatos DN, Katsiropoulos CV, Tserpes KI, Pantelakis SG (2021) A holistic end-of-life (EoL) index for the quantitative impact assessment of CFRP waste recycling techniques. Manuf Rev 8:18. https://doi.org/10.1051/mfreview/2021016

35. Witik RA, Payet J, Michaud V, Ludwig C, Månson JE (2011) Composites: part A assessing the life cycle costs and environmental performance of lightweight materials in automobile applications. Compos A 42(11):1694–1709. https://doi.org/10.1016/j.compositesa.2011.07.024

36. Li X, Bai R, Mckechnie J (2016) Environmental and financial performance of mechanical recycling of carbon fibre reinforced polymers and comparison with conventional disposal routes. J Clean Prod 127(2016):451–460. https://doi.org/10.1016/j.jclepro.2016.03.139

37. Akbar A, Liew KM (2020) Assessing recycling potential of carbon fiber reinforced plastic waste in production of eco-efficient cement-based materials. J Clean Prod 274:123001. https://doi.org/10.1016/j.jclepro.2020.123001

38. Meng F, McKechnie J, Turner T, Pickering SJ (2017) Energy and environmental assessment and reuse of fluidised bed recycled carbon fibres. Compos A Appl Sci Manuf 100:206–214. https://doi.org/10.1016/j.compositesa.2017.05.008

39. Khalil YF (2018) Comparative environmental and human health evaluations of thermolysis and solvolysis recycling technologies of carbon fiber reinforced polymer waste. Waste Manage 76:767–778. https://doi.org/10.1016/j.wasman.2018.03.026

40. Dauguet M, Mantaux O, Perry N, Zhao YF (2015) Recycling of CFRP for high value applications: effect of sizing removal and environmental analysis of the supercritical fluid solvolysis. Procedia CIRP 29:734–739. https://doi.org/10.1016/j.procir.2015.02.064

41. Prinçaud M, Aymonier C, Loppinet-Serani A, Perry N, Sonnemann G (2014) Environmental feasibility of the recycling of carbon fibers from CFRPs by solvolysis using supercritical water. ACS Sustain Chem Eng 2(6):1498–1502. https://doi.org/10.1021/sc500174m

42. La Rosa AD, Banatao DR, Pastine SJ, Latteri A, Cicala G (2016) Recycling treatment of carbon fibre/epoxy composites: materials recovery and characterization and environmental impacts through life cycle assessment. Compos B Eng 104:17–25. https://doi.org/10.1016/j.compositesb.2016.08.015

43. He D, Soo VK, Kim HC, Doolan M (2021) Life cycle primary energy demand and greenhouse gas emission benefits of vehicle light weighting with recycled carbon fibre. Procedia CIRP 98:43–48. https://doi.org/10.1016/j.procir.2021.01.003

44. Lee CK, Kim YK, Pruitichaiwiboon P, Kim JS, Lee KM, Ju CS (2010) Assessing environmentally friendly recycling methods for composite bodies of railway rolling stock using life-cycle analysis. Transp Res Part D: Transp Environ 15(4):197–203. https://doi.org/10.1016/j.trd.2010.02.001

45. Shuaib NA, Mativenga PT (2017) Carbon footprint analysis of fibre reinforced composite recycling processes. Procedia Manuf 7:183–190. https://doi.org/10.1016/j.promfg.2016.12.046

46. Meng F, Olivetti EA, Zhao Y, Chang JC, Pickering SJ, McKechnie J (2018) Comparing life cycle energy and global warming potential of carbon fiber composite recycling technologies and waste management options. ACS Sustain Chem Eng 6(8):9854–9865. https://doi.org/10.1021/acssuschemeng.8b01026

47. Vo Dong PA, Azzaro-pantel C, Cadene A (2018) Economic and environmental assessment of recovery and disposal pathways for CFRP waste management. Resour Conserv Recycl 133(2018):63–75. https://doi.org/10.1016/j.resconrec.2018.01.024

48. Ghosh T, Chul H, Kleine RD, Wallington TJ, Bakshi BR (2021) Life cycle energy and greenhouse gas emissions implications of using carbon fiber reinforced polymers in automotive components: Front subframe case study. Sustain Mater Technol 28:e00263. https://doi.org/10.1016/j.susmat.2021.e00263

49. Kousemaker TM, Jonker GH, Vakis AI (2021) Lca practices of plastics and their recycling: a critical review. Appl Sci (Switzerland) 11(8):1–17. https://doi.org/10.3390/app11083305

50. Bekker ACM, Verlinden JC, Galimberti G (2016) Challenges in assessing the sustainability of wire + arc additive manufacturing for large structures. In: 27th Annual international solid freeform fabrication 2016: an additive manufacturing conference, pp 406–416

51. Hetherington AC, Borrion AL, Griffiths OG, McManus MC (2014) Use of LCA as a development tool within early research: challenges and issues across different sectors. Int J Life Cycle Assess 19(1):130–143. https://doi.org/10.1007/s11367-013-0627-8

52. Heidrich O, Tiwary A (2013) Environmental appraisal of green production systems: challenges faced by small companies using life cycle assessment. Int J Prod Res 51(19):5884–5896. https://doi.org/10.1080/00207543.2013.807372

53. Pickering SJ (2006) Recycling technologies for thermoset composite materials-current status. Compos A Appl Sci Manuf 37(8):1206–1215. https://doi.org/10.1016/j.compositesa.2005.05.030

54. Ecoinvent (2021) Ecoinvent. Available at: ecoinvent.org

55. Simapro (2021) SimaPro: LCA software to help you drive change. Available at: https://sim apro.com/
56. Giorgini L, Benelli T, Brancolini G, Mazzocchetti L (2020) Recycling of carbon fiber reinforced composite waste to close their life cycle in a cradle-to-cradle approach. Curr Opinion Green Sustain Chem 26:100368. https://doi.org/10.1016/j.cogsc.2020.100368
57. Heinzle E, Weirich D, Brogli F, Hoffmann V, Koller G, Verduyn M, Hungerbühler K (1998) Ecological and economic objective functions for screening in integrated development of fine chemical processes. 1. Flexible and expandable framework using indices. Ind Eng Chem Res 37:3395–3407

Chapter 3
Synthesis of Lightweight Metallic Foam and Their Applications in Various Engineering Sectors

Pradeep Singh, J. P. Shakya, Pankaj Agarwal, Sanjay Jain, D. P. Mondal, and Karan Singh Verma

1 Introduction

The role of lightweight materials in the field of automobile, aerospace, construction, marine, medical, defence and electronics industries is accelerating day by day. Lightweight porous materials of Al, Mg and their alloys are already used in the manufacturing of vehicles and aeroplanes bodies to reduce the fuel consumption [1]. Porous Al foam alloy foams have the potential to absorb impact energy and sound which can efficiently work as the bumper of vehicles as well as blast resistance material [2, 3]. The use of porous materials in the area of aerospace is being started for the reduction of weight of the aeroplane. Porous materials like Ti alloys and Mg alloys foams are also employed in the field of biomedical to prepare the stents and the orthopaedic scaffold. The area of porous materials is vast, and it is essential to explore the different synthesizing processes and specific applications of the synthesized product.

P. Singh (✉) · J. P. Shakya · P. Agarwal · S. Jain
Department of Mechanical Engineering, Samrat Ashok Technological Institute, Vidisha 464001, India
e-mail: erpradeep3408@gmail.com

D. P. Mondal
CSIR—Advanced Materials and Processes Research Institute, Bhopal 462026, India

K. S. Verma
Mechanical Engineering Department, Oriental College of Technology, Bhopal 462021, India

1.1 Materials Used for Synthesizing Foam

Materials having low density due to gas filling pores in their bulk are called foam [4]. Materials for making foam may be metallic as well as for non-metallic. Nowadays metal foams are made from aluminium alloy [5], stainless steel [6], magnesium and its alloy [7], tantalum, nickel alloy [8, 9], titanium and its alloy [10, 11], while carbon [12], polymer [13], ceramic [14], starch [15] and zinc [16] are used as non-metallic foams. In recent times, open cell metal foams are prepared through the infiltration of the melted metal in the non-metallic cellular precursor of plastic, ceramic, etc.

1.2 Types of Foam

There are broadly three classes of metal foam that can be categorized following.

    1.2.1. Open cell foam.
    1.2.2. Closed cell foam.
    1.2.3. Composite foam.

1.2.1 Open Cell Foam

When gas-filled cells or pores which are found in the bulk of foam are interconnected to each other, such that a fluid can pass through it, called open cell foam. The microstructure of open cell foam is shown in Fig. 1 [17]. The shape and size of the pores depend on the process of preparation of the foam. For example, the shape and size of pores for open cell foam synthesized through the powder metallurgy route using a space holder material are depending on the morphology and size of the space holder powder particles [18].

Pores of the open cell foam are surrounded by metallic ligaments called edges. The relative density of the foam depends on the ratio of the thickness of the edge and pore size. For containing high porosity, the ratio of the edge thickness and pore size should be minimum. Mechanical properties such as compressive stress and young modulus depend on the porosity of the material [19, 20]. The open cell foam is used as the heat exchanger, filter, impact energy absorber, etc.

1.2.2 Closed Cell Foam

When each pore of the foam is covered by the thin wall of the metal, and there is no interconnectivity among them then it is known as closed cell foam. The relative density of the foam depends on the cell wall thickness and cell size. The microstructure of closed cell foam is shown in Fig. 2 [17].

Fig. 1 Microstructure of open cell foam; it can be seen that the pores are interconnected in nature [17]
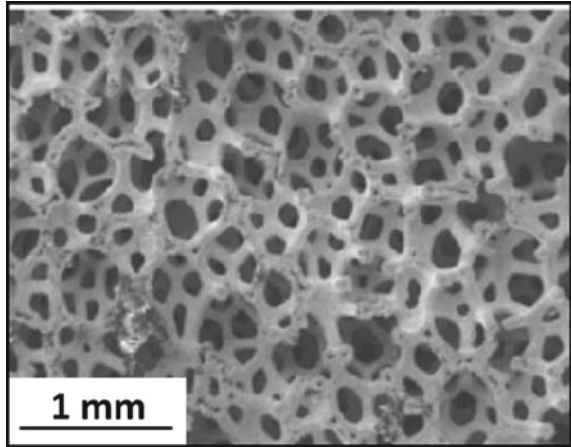
Fig. 2 Alporas closed cell aluminium foam [17]
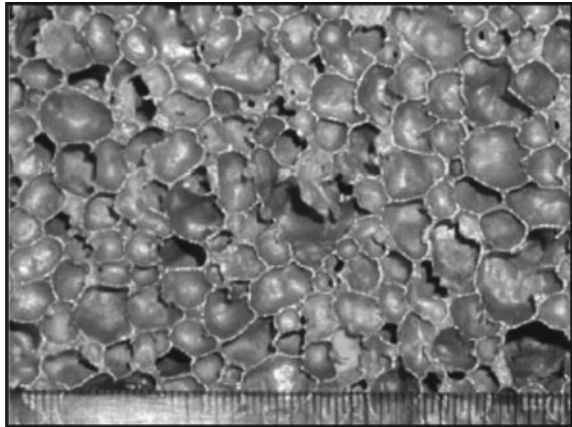
Cell shape, size and relative density of the closed cell foam play an important role in tailoring the mechanical properties [21]. Generally, closed cell foam has a higher relative density and strength compared to open cell foam. So, it can be used for structural purposes like sandwich panels, automobile bumpers, blast resistance boxes, aircraft bodies, insulation, etc.

1.2.3 Composite Foams

Composite foams are a new class of materials synthesized by adding the solid reinforcement in the metal matrix before foaming or the addition of hollow spheres (cenosphere) in the metal melt or powder. The composite foam may be closed or open cell type. Two major classifications of composite foam are following.
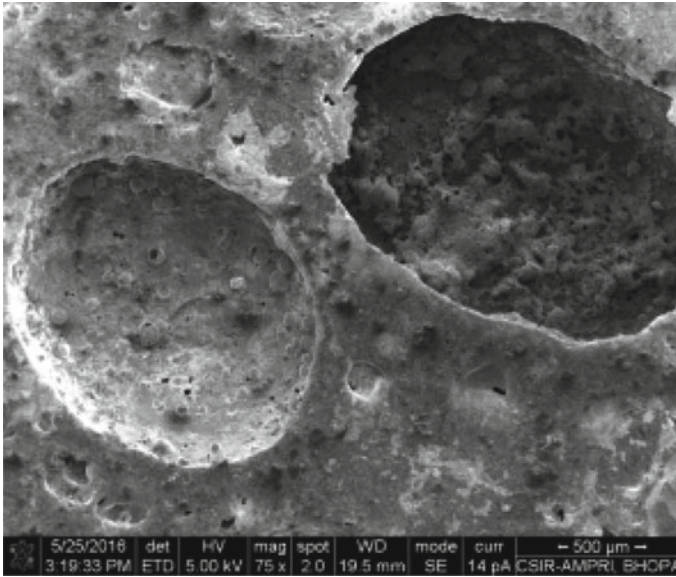
Fig. 3 Syntactic foam made through the liquid metallurgy route [24]

Hollow Particle Reinforced Composite Foam (Syntactic Foam)

Hollow particles called cenosphere are added as reinforcement in the metal matrix. The addition of the cenosphere in the metal matrix is done by liquid metallurgy or powder metallurgy route [22, 23]. Syntactic foam has higher compressive strength and stiffness than other foam of similar metal manufactured through conventional processes. The relative density and properties of the foam depending on the amount of cenosphere addition in the metal matrix [23]. A microstructure of syntactic foams manufactured through the liquid metallurgy route is shown in Fig. 3 [24].

Aluminium, iron, titanium, nickel, magnesium, zinc, lead, etc., can be used as matrix material in syntactic foam as found in literature, but the aluminium alloy is well known. Hollow particles of alumina, carbon, steel, glass, aluminium and fly ash that has the size in the range of a few mm to micron level are used as the particulate reinforcement. At present, fly ash cenosphere is the main concern due to its low density, low cost, environmental protection and easy availability from the combustion products of the power plant.

Hybrid Foam

When two or more two methods are used to generate porosity in the metal matrix, then it is known as hybrid foam. Hybrid foam is synthesized to incorporate extra porosity by adding foaming agents such as TiH_2 and ZrH_2 in the melt of the syntactic foam.

2 Synthesizing Techniques of Metal Foams

Metal foams are generally synthesized through two popular routes. These are liquid and powder metallurgy. The well-established process to make the porous or foam material are represented in the flow chart shown in Fig. 4. Some other methods like electrochemical, rapid prototyping and vapour deposition are also used for the production of foam [25].

2.1 Synthesizing of Foam Through Liquid Metallurgy Route

In the liquid metallurgy route, pores are created by direct injection of gas or by adding the substance that decomposes at a certain temperature to release gas in the molten metal or by infiltration of melt in the open cell cellular decomposable perform or by spraying the melt at a substrate to obtain the droplets form. Because metals have to be melted in this route, so only those metals are synthesized precisely that have lower melting points such that Al, Mg, Zn, etc. Although the metals like Fe, Ni, Ti, etc., that have high melting points can also be synthesized through this route, much sophistication is required due to more chance of oxidation at high temperatures.
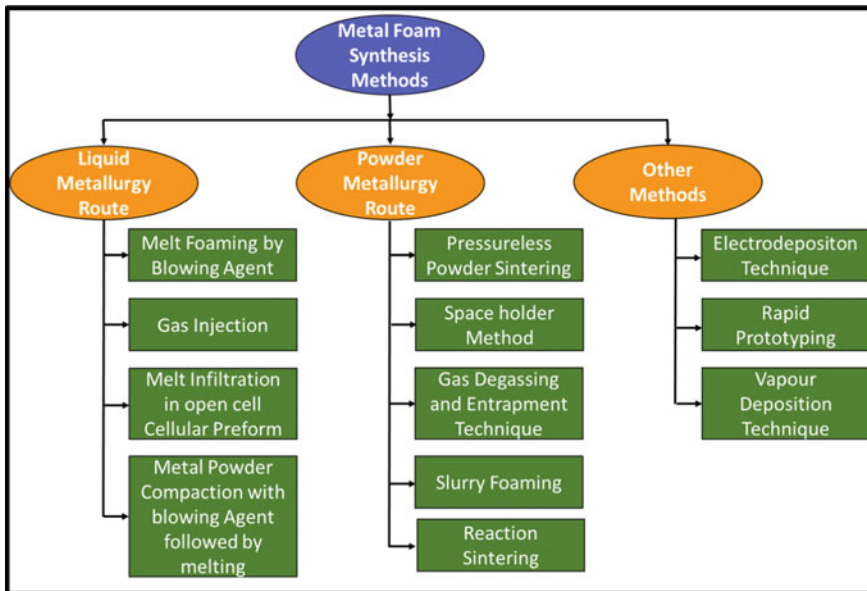
Fig. 4 Flow chart of foam synthesis methods

2.1.1   Melt Foaming by Blowing Agent

The schematic diagram of the overall procedure of generating the foam by blowing agent technique is shown in Fig. 5 [26]. The materials that decompose due to heating above a certain temperature and release a gas called foaming or blowing agent MgH_2, Na_2CO_3, $CaCO_3$, TiH_2 and ZrH_2 are well-known blowing agents for synthesizing the foam which decomposes above a definite temperature and releases carbon dioxide or hydrogen gas [27–29]. The blowing agent is added to the melt to decompose. The melting point of the metal should be greater than the decomposing temperature of the blowing agent.

   The procedure of production of foam by using a blowing agent is following:

(1) Metal is melted in a crucible and a thickening agent like Ca is added to the melt to increase the melt viscosity followed by stirring for several minutes. During the stirring process, Ca form the intermetallic compounds due to oxidation or the melt reaction, so the viscosity of the melt increases. For example, if Ca is added to the aluminium melt, the formation of intermetallic compounds such that CaO, $CaAl_2O_4$, Al_4Ca, etc., takes place [30, 31]. The increment of the viscosity of the melt depends on the amount of Ca addition and stirring time. It has been seen that a 1.5% Ca addition in the aluminium melt at 680 °C increases the viscosity of the melt up to the five times stirred for 9 min [32]. Variation of melt viscosity with the amount of Ca addition and stirring time is shown in Fig. 6a [33]. The viscosity of the melt increases with stirring time and the amount of calcium addition.

(2) After the addition of Ca, TiH_2 is added to the melt and continuously stirred to the formation of pores due to the release of hydrogen gas by decomposition at the higher temperature. Pore size and relative density of the foam depending on
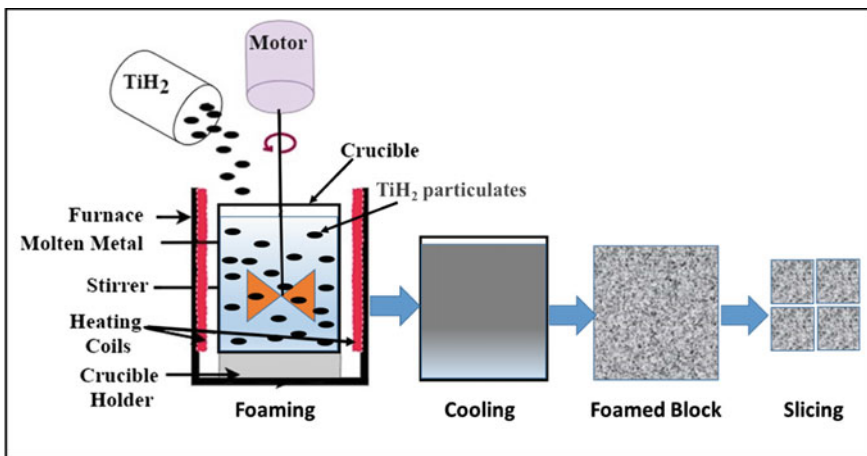
Fig. 5   Schematic diagram of foam making by blowing agent technique

Fig. 6 a Influence of amount of Ca addition and stirring time on the viscosity of the melt [33], **b** variation of pore number per unit cross-sectional area with stirring time [34]

(a)

(b)
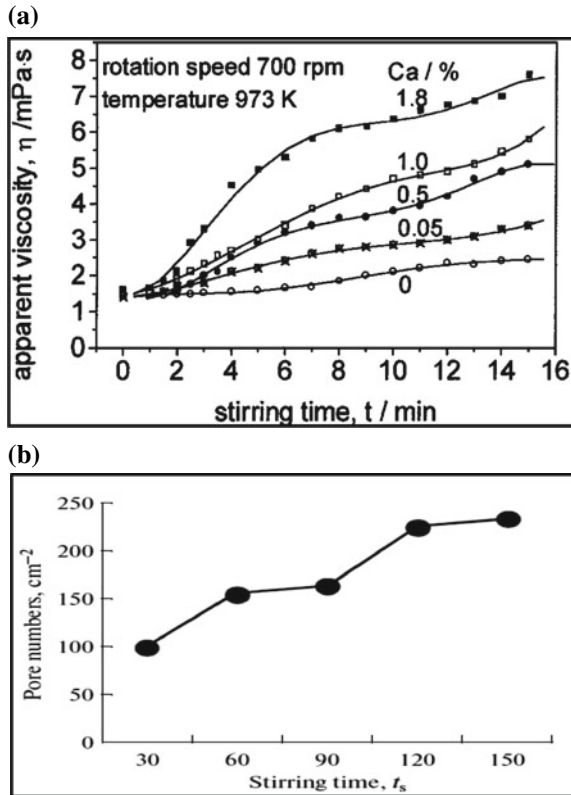
the amount of blowing agent and stirring time [28]. The number of pores per unit cross-sectional area for 1.0 wt% TiH_2 for varying stirring times is given in Fig. 6b [34].

(3) After the addition of TiH_2, stirring is stopped and the melt is kept at a furnace temperature to allow decomposing of the blowing agent for a time. This time is known as holding time. Holding time also plays an important role in tailoring the properties of the foam.

2.1.2 Foaming by Injecting the Gas into the Melt

Generally, aluminium alloy foams are synthesized and supplied by NORSK HYDRO and CYMAT Company of Norway and Canada by adopting this method that was patented by ALCAN international company Canada [25]. The whole procedure of producing the foam through this method is given in Fig. 7. According to this method, gas is injected into the molten metal and stirred by using an impeller to create the uniformly distributed fine bubbles of gas in the melt. Commonly used gases for bubbling are air, nitrogen, argon, carbon dioxide, etc. [35]. Pure aluminium foam

could not be manufactured directly due to insufficient viscosity of the aluminium melt, because if the internal pressure of the creating bubbles is more than the surface tension of the melt then bubbles could not be longer stable due to bubble bursting and drainage of the melt takes place. To increase the surface tension of the melt, its viscosity should be increased for the stability of the formed bubbles. Ceramic particles like silicon carbide, zirconium oxide, titanium carbide, aluminium oxide, etc., are added to the melt to increase its viscosity. Ceramic particles are accumulated around the wall of the bubbles and increase the strength and stability because of enhancement in surface tension. Melt viscosity depends on the volume fraction and the particle size of the ceramic material which is to be added to the melt. Volume fraction and particle size should be in a preferred range to obtain limited viscosity of the melt to find desired pore size of the foam. If the ceramic particles are very fine, it will be difficult to disperse in the melt due to high surface energy and if they are large in size, settled down in the melt. So particle size and amount of the ceramic material should be properly selected. Wettability between the reinforced particles and melt also significantly influences the properties of the foam. For stability of the bubbles, wettability should be optimum. Generated bubbles float upward due to buoyancy. The size of the bubbles increases when float from downward to upward. This may cause due to reduction in the viscosity of the melt.

Floating bubbles start to solidify at the melt surface. Time taken for solidification depends on the thermal gradient of the walls of the bubbles. A conveyor belt is used for pulled off the solidified bubbles.

The controlling factors to obtain the desired property of the foam by gas injection method are the temperature of the melt, volume fraction and size of the reinforced ceramic particles, speed of the injected gas, the rotational speed of the stirring paddle, rate of the solidification of the bubbles, etc.
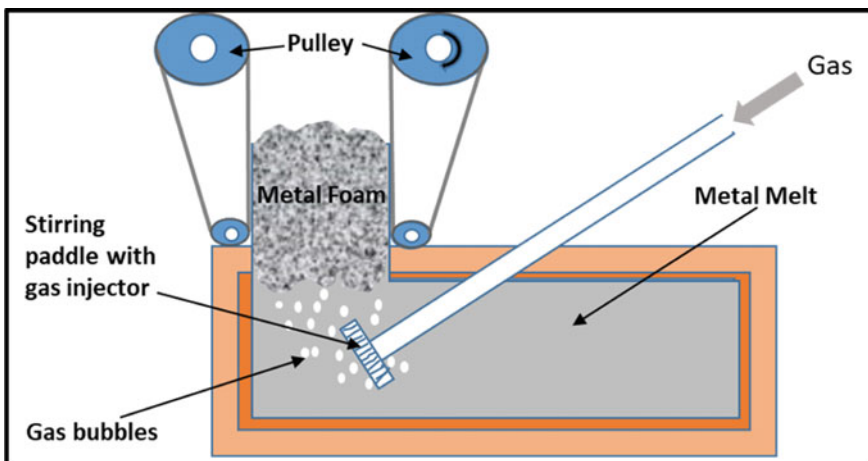
Fig. 7 Schematic diagram of making aluminium foam through the gas injection method

2.1.3 Compaction of Metal Powder with Blowing Agent Followed by Melting Technique

The method was developed to find the well-distributed pores in the bulk of the foam by the Fraunhofer Institute of Germany [25]. It is a combined method of powder and liquid metallurgy but foaming is performed by the pressure of gas generated due to the decomposition of the blowing agent in the semi-solid melt, so it is kept in the category of liquid metallurgy route. The whole procedure of manufacturing the foam through this method is shown in Fig. 8. The method is started with proper mixing of aluminium alloy powder and the blowing agent material such that TiH_2. The mixture is cold compacted and extruded to obtain a density of the compact near to the theoretical density as possible because any defect or residual porosity in the product deteriorates the property of the foam significantly. The extruded product should be in the form of a bar or cylinder to perform further operations. The extruded bar is cut into small pieces and kept in a tightly sealed mould. Mould is heated above the solidus temperature of aluminium alloy to find the semi-solid melt. The solidus temperature of aluminium alloy is more than the decomposition temperature of the TiH_2. Above the decomposition temperature, hydrogen gas evolved from the blowing agent creates voids in the semi-solid melt due to the generation of local internal pressure that causes expansion of the semi-solid melts in the mould thus highly porous mould shape structured material is found.

The melt temperature and size of the product decide the time taken for the full expansion of the foam. The pore shape and size of the foam depending on the time required for expansion of the melt in the mould. The density of the foam can be adjusted by controlling the amount and particle size of the blowing agent [36], atmosphere and compaction pressure in which the blowing agent decomposes [37, 38], the temperature of the melt and the heat supplied per second [39] to the mould for converting the pieces of the extruded bar in the semi-solid melt.

Aluminium, zinc, magnesium and their alloys, steel, etc., can be synthesized by adopting this technique. Other materials that can be manufactured in the form of foam are lead, tin, brass, gold, etc., but the controlling parameters like melt temperature, rate of heat supplied, blowing agent, etc., should be chosen according to the matrix material.

2.1.4 Investment Casting Using Polymer Foam Performs

Open cell foam of well-controlled pore size can be generated by using this technique. The overall procedure of preparation of open cell foam by investment casting using open cell polymer foam perform is shown in Fig. 9. The process is started with polymer like polyurethane open cell foam perform. Mixture of ceramic materials like phenolic resin, calcium carbonate, and mullite in the form of slurry is infiltrated in the open cell polymeric preform. The slurry of simple plaster can be also used to infiltrate [40]. After infiltration, the mould is heated above the evaporating temperature of the polymeric foam to be drawn out. The heating process also hardened the ceramic
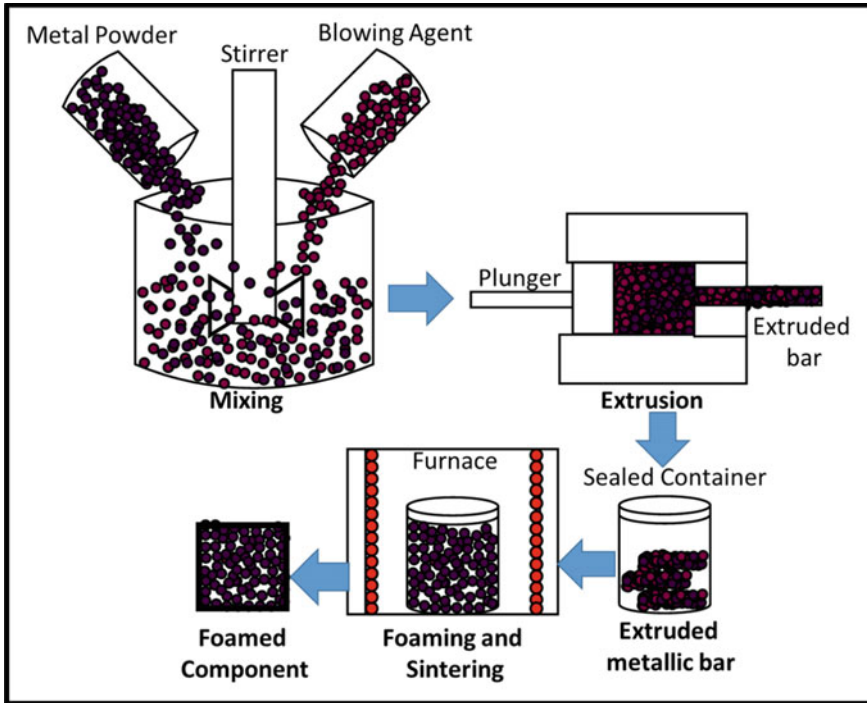
Fig. 8 Procedure of preparing the foam through compaction of metal powder with blowing agent followed by melting technique

mixture and gives strength to it. Due to drawn off the polymeric foam from the mould, open cell foam of ceramic materials with a negative image of started polymeric foam is found. Now the molten metal is infiltrated into the ceramic foam. Pressure or gravity infiltration can be used depending on the size of the pores of the ceramic foam. If the pores are narrow then pressure infiltration is used otherwise gravity infiltration will be economical. The ceramic mould material is removed by impact or direct imposing the stream of pressurized water on it after solidification of the melt. This is how a perfect replica of polymeric foam made of metallic material is obtained. The main problems that occur in this method are perfect filling of materials in the pores, controlling the directional solidification of molten metal and removing the finished product from the ceramic mould without damage.

2.1.5 Foam Making by Using Metal Melt and Space Holder

Space holders are organic or inorganic materials that are added in the melt to generate pores in the bulk of the materials by leaching in an appropriate solvent or vaporizing at a low temperature or micro-hollow spheres that become an integral part of the
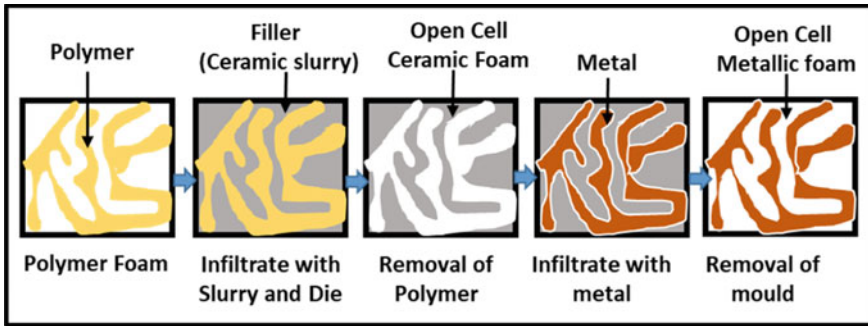
Fig. 9 Procedure of investment casting using open cell polymer foam perform

product after melt solidification. Salts are used as space holders that can be leachable in an appropriate solvent [41]. Syntactic foam is made by using space holders like aluminium oxide hollow spheres and fly ash that is entrapped in the product after solidification of the melt, and porosity generates due to the hollow balloons type structure of the space holder particles [42–44].

Before mixing in the metal melt, preheating of the space holder is performed to prevent the premature solidification of the melt. Preheating is essential, especially for the space holder which has a large heat capacity and the operation is carried out at low infiltration pressure [45]. There might be a problem with wetting of space holder by the metal melt due to the high contact angle between them. Hence, the melt cannot reach the interstitial position of the space holder. To overcome this problem, the space holder particles are coated with an appropriate coating to reduce the contact angle or a vacuum is created in the crucible or high pressure is applied to the melt to infiltrate the interstices of the granules of the space holder [24, 46].

Syntactic foam can be made by using the stir casting method, pressure or vacuum infiltration method. The stir casting method is used when the volume fraction of the hollow space holder is small. For a high-volume fraction of the space holder, the pressure or vacuum infiltration method is used. The overall procedure of making syntactic foam through the pressure infiltration method is shown in Fig. 10.

Metal is melted in a crucible by using an electric heater above 30–50 °C of its melting temperature to obtain the supersaturated condition of melt. Die filled with hollow spheres (space holder) is infiltrated in the evacuated melt by applying pressure. The melt infiltrates the interstitial voids of the hollow spheres. After solidification, foam containing a high-volume fraction of space holder is obtained.
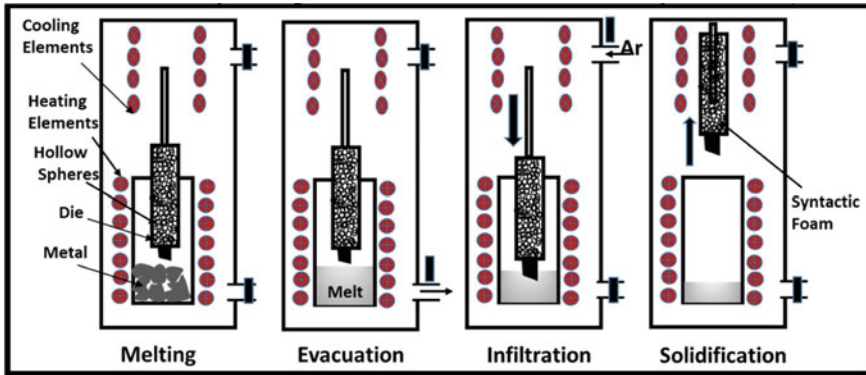
Fig. 10 Making of syntactic foam through pressure infiltration method

2.2 Manufacturing of Cellular Materials by Powder Metallurgy Route

Foam can be manufactured by using the powder metallurgy route. The main difference between the liquid and powder metallurgy route is that metal powder is used for the synthesis. Melting of this metal powder is not required in the powder metallurgy route. The methods which are adopted for synthesizing the foam by this route are gas entrapment method, slurry foaming, space holder technique, loose powder sintering, mixing of metal powder with polymer binder method, reaction sintering, etc.

2.2.1 Foam Making by Gas Entrapment Method

The foam is manufactured by entrapment of gas in the compacted metal powder. In this method, foam is obtained without melting the metals and without using any blowing agent. Metal powder is compacted at high pressure in a precursor and gas is allowed to entrap in it as shown in Fig. 11. In the second step, the compacted powder is heated and allowed to expand the entrapped gas due to increasing pressure causing the incorporation of porosity in the compacted powder.

Aircraft manufacturer boing (USA) has adopted this method for synthesizing the titanium foam [47]. First of all the precursor is evacuated and titanium powder is filled in it. The precursor is refilled by an inert gas like argon at a pressure of 3–5 atm [26]. The filled powder with argon gas is compacted by hot isostatic pressing to obtain a dense structure. Due to high isostatic pressure, argon gas distributes uniformly in the pores of the titanium powder. The structure can be further extruded to find the extra densification. In the second stage, densify structure is annealed at a temperature of $0.6\ T_m$ for 20–46 h. The entrapped gas expands during the annealing and pores are created in the structure. Theoretically, it has been considered that up to 50% porosity can be found by using this technique [48].
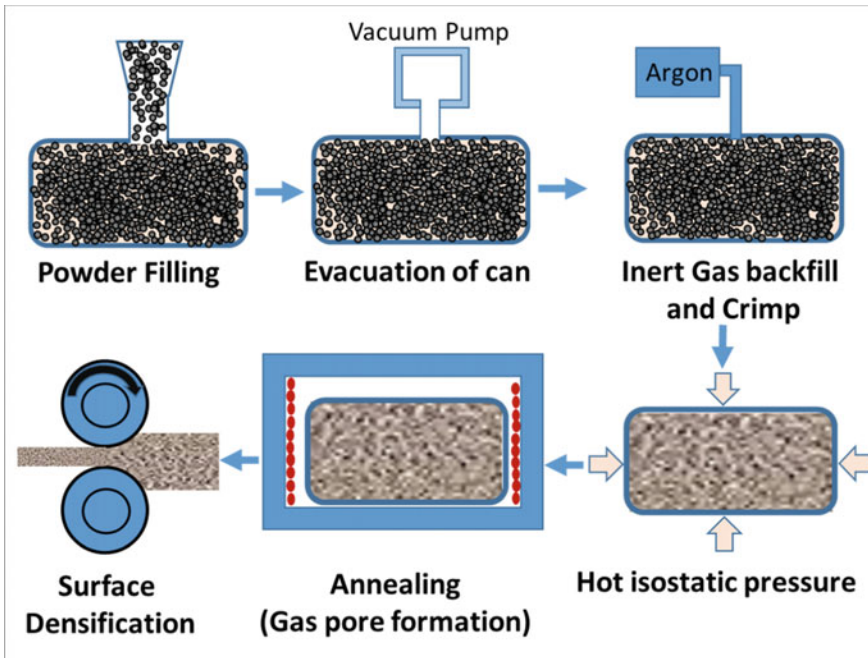
Fig. 11 Manufacturing process of metal foam by gas entrapment technique

2.2.2 Slurry Foaming Method

There are two methods of synthesizing the metal foam through slurry foaming. In the first method, a slurry is made by mixing the metal powder, blowing agent and additives [49]. The mixture is thoroughly blended and poured in to mould at a high temperature. Due to the presentation of blowing agent and additive, the state of slurry becomes viscous and evaluation of gas takes place. Due to gas evolving, the pores are created in the viscous slurry. Green foam is kept at an elevated temperature for drying. The aluminium foam was manufactured by using this method with orthophosphoric acid as a binder and hydrochloric acid as a blowing agent. Up to 7% relative density of the foam can be achieved by using this method but the strength is small and the chance of cracking in the foam may increase.

The second method of manufacturing the foam by using slurry is the template or matrix method. A matrix with interconnected pores and having low melting points or being easy to remove is selected. Generally, polyurethane foam of interconnected pores is selected as a matrix because its decomposition temperature is about 400 to 600 °C which decomposes during sintering [50]. The slurry of metal powder and the additives is made by sufficient blending and the matrix is dipped in it. So, the slurry is impregnated in the pores of the matrix. During sintering above the decomposition temperature of the matrix, metal foam of open cell with interconnected pores (counter pores of the matrix) is generated.

2.2.3 Loose Powder Sintering

Loose powder or gravity sintering is generally used for bronze, stainless steel, titanium and superalloys. The powders of the metals are packed loosely in a chamber and allowed to sinter [51]. During sintering atoms are diffused among the particles of the powder and bonding takes place. Generally, loose powder of bronze is sintered at 820 °C and 20–50% porosity levels are achieved but the strength of the sintered product is lower. The strength can be increased by compaction or rolling the packed powder prior to sintering but the porosity of the structure reduces [52].

2.2.4 Foam Making Through Powder Metallurgy Route and Space Holder Technique

It is an important method of manufacturing the Ti foam through the powder metallurgy route using fugitive materials as a space holder. There are various advantages of this method. The shape, size, porosity and the distribution of the pores in the porous material can be adjusted easily by using the different shapes, sizes and volume fractions of the space holder in the metal powder [10, 53, 54]. The process of making the foam through the powder metallurgy route using a space holder is shown in Fig. 12. There are four major processes of this technique as given below:

(1) Mixing: First of all, metal powder and space holder should be selected in appropriate amounts. The amount of space holder should be according to the desire for porosity incorporation in the material. The metal powder and space holder are mixed thoroughly to obtain the homogeneous mixture. A small amount of polyvinyl alcohol is also added for sufficient binding during compaction.
(2) Compaction: The mixture is compacted in a die by applying sufficient pressure to obtain the green compact in desired shape and size. The shape and size are controlled by the use of a die.
(3) Pre-sintering or baking: Pre-sintering or baking is performed for the debinding or removal of the space holder. The pre-sintering temperature and the time depend on the type of space holder used. If the space holder is evaporative type, then it evaporates during the baking or sintering; otherwise, it is leached out in an appropriate solvent.
(4) Sintering: Baked sample is sintered in a suitable furnace for sufficient time at the applicable temperature. The sintering process is employed to obtain the strength in the green compact due to diffusion among the particles of the matrix powder. Due to diffusion, the bonding strength among the particles increases causing the increment in the total strength of the sample by small shrinkage in the volume of the sample.

There are several materials that can be used as space holders. The materials used as space holders by the researchers are ammonium bicarbonate [55], urea [56], sodium chloride [57], polymer granules [58] and magnesium [59]. The material that can be
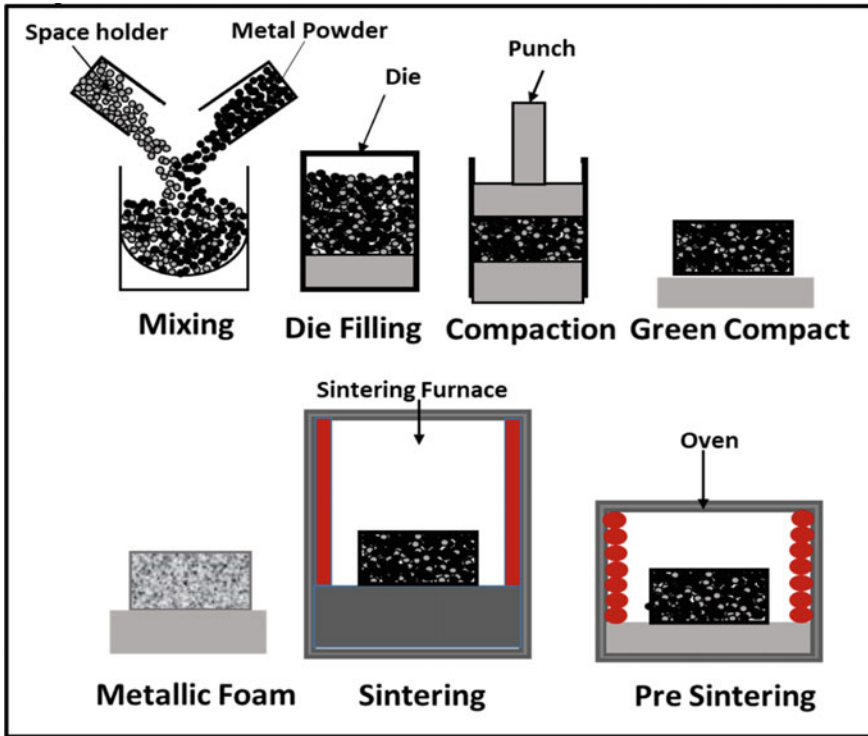
Fig. 12 Making of Ti foam through powder metallurgy route and space holder technique

used as a space holder should have some specific properties like unreactivity with the matrix powder, no or minute residue left after the removal, easy processibility, etc. The general difficulty of the space holder technique is the removal of the space holder. For biomedical applications, any residue left in the material causes adverse effects on the human body. So, the space holder material should be either bioinert or biocompatible. It is reported that sodium chloride is a better choice as a space holder for making the porous titanium implant through the powder metallurgy route because it is biocompatible and easily remove from the sintered material by leaching in the water. Panic et al. explore the advantage of the use of sodium chloride as a space holder such that low cost has fast leachable properties in water and is less toxic for the human body [60].

In recent years, the trend of ammonium bicarbonate and urea as space holder materials is increasing to form the titanium foam of controlled porosity and pore shape and size. Because the melting points of ammonium bicarbonate and urea are low, it decomposes rapidly during the pre-sintering which causes difficulty in controlling the pore structure and porosity [61].

2.2.5 Combustion Synthesis

The overall schematic diagram of the combustion synthesis process is shown in Fig. 13. Combustion synthesis is a recently developed method of producing porous materials effectively. The particles of the metal powder fused due to the generation of vast heat by the exothermic reaction of mixed product. There are two stages of combustion synthesis: (a) Gradually heating of the reactants until a reaction takes place in the whole sample; (b) Self-propagation of high-temperature synthesis. Due to the exothermic reaction heat is generated and propagated in a direction throughout the mixture without any additional energy [62]. The porosity of the final product depends on the particle size of the powder, type of binder used, compaction pressure, etc.

Porous Ni–Ti alloys are successfully made by several researchers by using the combustion synthesis method [63]. The main drawback of the method is that the generated porosity in the foam is limited. Li et al. observed that the Ni–Ti foam made by using this technique has a porosity of 54% with anisotropic pore [64].
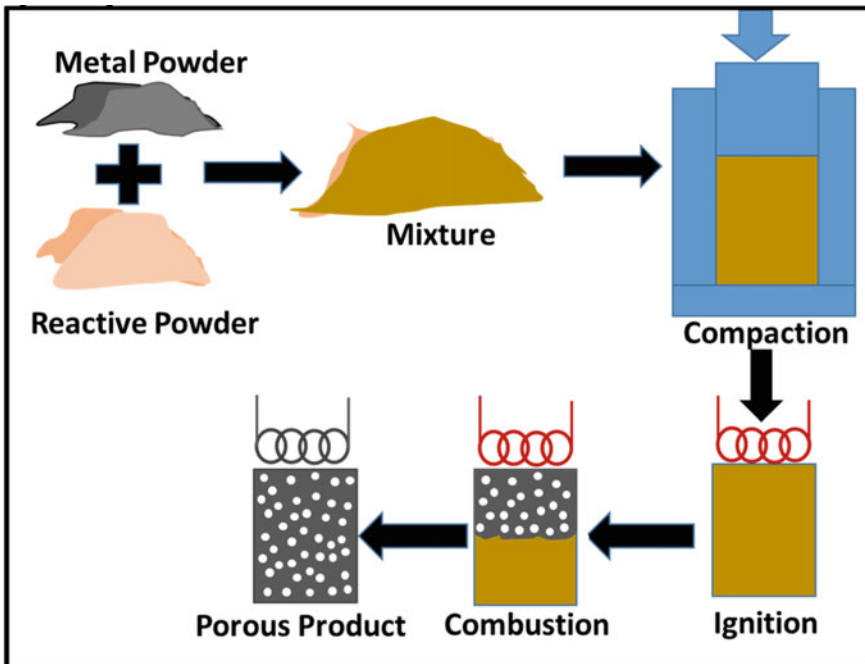
Fig. 13 Schematic diagram of combustion synthesis process

2.2.6 Gel Casting

Gel casting was initially used for processing the porous ceramic product of high porosity and interconnected pores [65]. In this process, the slurry is prepared by mixing the metal powder, dispersing agent and an organic monomer in a solvent (generally distilled water is used as solvent [66]). The porosity of the foam depends on different process parameters such as the amount of organic monomer, dispersing agent, initiator, etc. The mixture is properly homogenized to form uniformity. A mechanical stirrer is used for homogenization. Ball milling can be also used for obtaining high uniformity. The polymerization process initiates by adding the appropriate initiator to the homogenized mixture (some catalysts are also added to the mixture before the addition of the initiator) and further stirring is performed. In situ polymerization process takes place because of cross-linking reaction in the mixture due to the presence of an initiator to form the foamed gel. After thoroughly stirring, the mixture is poured into a mould for casting in a shape and allows cooling at room temperature. Cast product is removed from the mould and dried at a higher temperature for the evaporation of the solvent. After drying, the green product is capable to bind the powder to retain the shape of the cast due to the polymer formed by the polymerization. Green product is further sintered in the appropriate furnace at a suitable temperature and time. The schematic diagram of overall procedure is shown in Fig. 14 [67].

Ti alloy foam and ceramic foam like hydroxyapatite can be processed easily by using the gel casting method. Yang et al produce porous Ti–Mo and Ti–Nb alloy of three-dimensional open cell structure by using the gel casting method and sintered at 900 and 1050 °C for 2 h [67]. Obtained foams have up to 50% porosity with elastic modulus 5–18 GPa and compressive strength in the range of 141–286 MPa.

2.3 Other Useful Methods of Foam Manufacturing

Rather than the liquid and powder metallurgy route, some useful methods were also developed by applying specific techniques to generate the porosity in the final product. Electro deposition technique, rapid prototyping and vapour deposition are the methods that are recently used for processing the porous product.

2.3.1 Electrodeposition Technique

Electrodeposition is a technique of depositing the metal ions on the substrate by the method of the creation of a reverse galvanic or electrolytic cell. It is a type of electrochemical cell in which redox reaction occurs by the application of electrical energy. The metal that is to be deposited is made the anode while the substrate on which the metal ion deposition takes place works as a cathode. The anode and cathode both are dipped in an electrolyte that contains ions to flow the electric charges. When
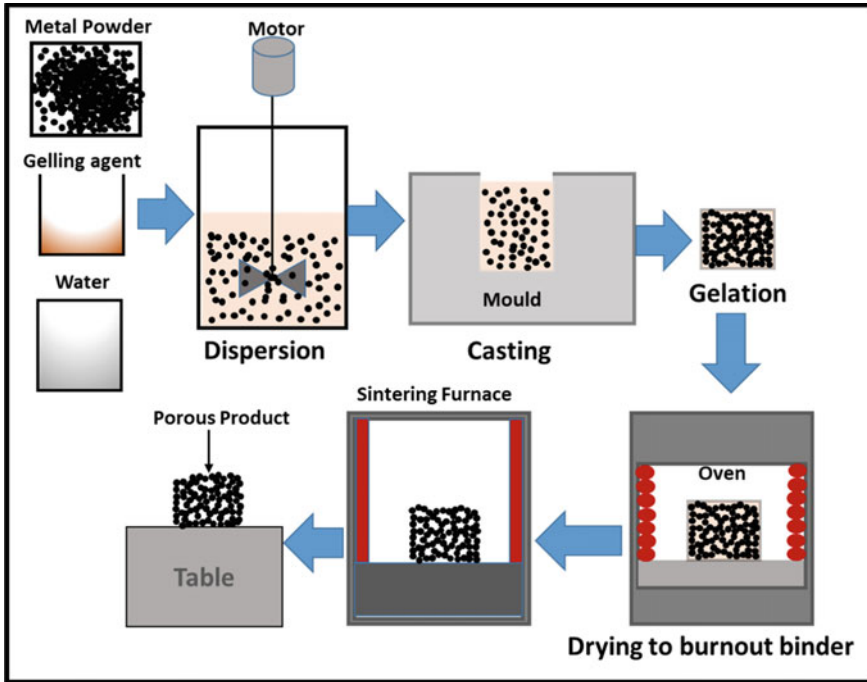
Fig. 14 Process of gel casting for processing the porous titanium alloy foam

electrical energy is applied in the cell then metal releases its ion in the electrolyte due to oxidation reaction and is deposited at the cathode through the electrolyte due to reduction reaction on the cathode.

For making the porous metal foam, the metal ion is deposited on the open cell conductive polymeric foam by the electrodeposition technique [68]. There are some polymeric materials like polyacetylene, polyphenylene vinylene, etc., which have the property of electrical conductivity. The polymers that are the insulator can be made electrically conductive by dipping them into an electrically conductive slurry of graphite or carbon or polymer coating by the thin layer of electrically conductive materials by using a cathode sputtering method. The procedure of the technique is shown in Fig. 15. Three-dimensional interconnected (reverse image of the open cell polymeric foam that was used as a substrate for deposition of metal ion) pores metal foam is found by adopting the electrodeposition technique.

2.3.2 Rapid Prototyping

Rapid prototyping is a very useful method of manufacturing the product in an extensively controlled manner by the combination of computer-aided design (CAD) and computer-aided manufacturing (CAM) [69]. The product can be manufactured
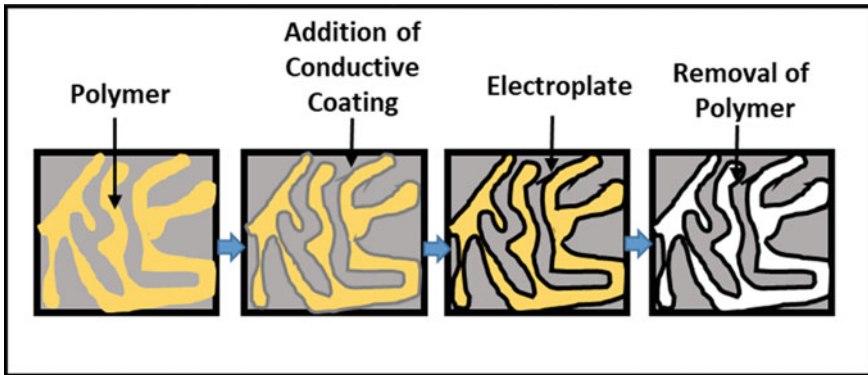
Fig. 15 Overall procedure of making the open cell metal foam through electrodeposition technique

according to the desired shape and size with desired properties with perfection [70]. The processing of porous materials by the use of the rapid prototyping technique is limited till now. Selective Electron Beam Melting (SEBM), Laser Engineered Net Shaping (LENS), 3D fibre deposition (3DF) and Selective Laser Sintering are the different processes of the Rapid Prototyping method.

Selective electron beam melting (SEBM)

The process for the manufacturing of porous titanium products by using a selective electron beam melting process is shown in Fig. 16. First of all, a 3D CAD model of the desired product is generated and divided into layers of uniform thickness to specify the information about the layer. A programme is installed about the information of the single layer to perform computer-aided manufacturing. The selective electron beam melting process initiates by applying a single layer of metal powder to the working table. The single layer of loose powder particles is scanned by the electron beam. Due to the high energy of the electron beam, loose powder particles fuse and create a solid single layer of the product that is to be manufactured. After this, the working platform is lowered by the thickness of one layer, and a new powder layer is applied to the presented layer and scanned by the electron beam to fuse the loose powder particles of the newly applied layer. The process is repeated up to the formation of a 3D solid product. Interconnected porosity is found due to the layer-by-layer addition to form the final product. [14].

Laser-engineered net shaping (LENS)

The internal structure and property of the product can be improved significantly by using the manufacturing process of laser engineering net shaping (LENS). The schematic diagram of the manufacturing process by the adoption of LENS is near similar to the SEBM process, but a laser beam is employed for the heat energy at the place of the electron beam. Near net shape and Ti-based alloy foam with superior
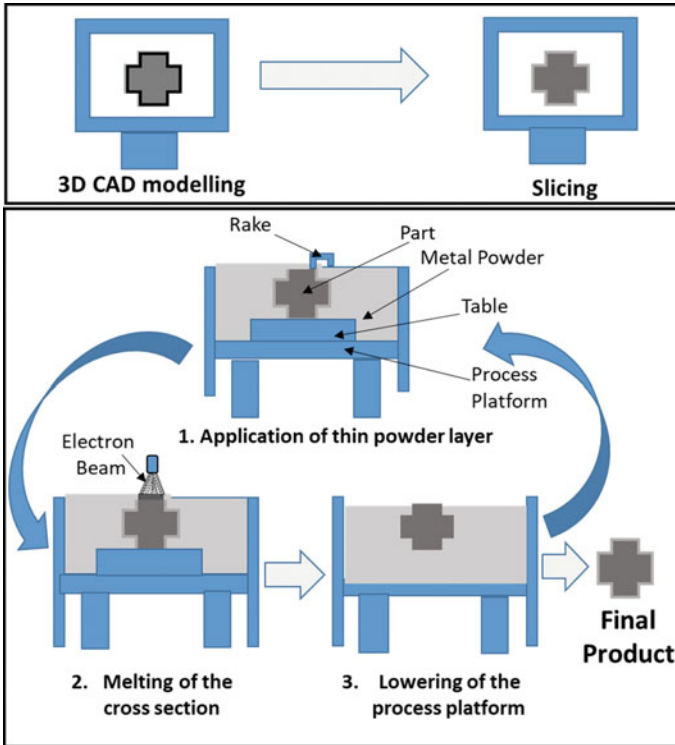
Fig. 16 Manufacturing of porous titanium product from through SEBM process

mechanical properties can be manufactured by the implementation of the LENS method [71].

Selective Laser Sintering (SLS): SLS is a rapid prototyping process for processing complex 3D products by using powder materials. Recently, this method is used for synthesizing the biocompatible scaffold of polymer and polymeric/ceramic composite.

2.3.3 Vapour Deposition Technique

The cellular structure of the metal can be found by condensing the metal vapour on the cold substrate. First of all, metal is vaporized in the vacuum chamber and vapour is allowed to cool on the cold polymeric foam precursor. The metal vapour condenses in the pores of the polymeric foam and comes in a solid state. After solidification of the metal vapour, the precursor is removed by the thermal and chemical treatment. Generally, nickel foam is synthesized by the vapour deposition method.

3 Summary and Conclusion

Metallic cellular materials or foams have drawn the attention of researchers to synthesize through economical and property control ways due to their applications in various engineering filed. Metallic foams can be synthesized through the melting route or powder metallurgy route. In the melting route, metal is melted in a furnace and then pores are created by the mixing of gas creating agent, injection of gas or addition of porous spacer materials in the melt. The important gas creating agents are CaH_2 and TiH_2 which are added to the melt to generate hydrogen gas due to their dissociation at the melt temperature. Hydrogen gas is entrapped in the melt and creates pores in the bulk material after solidification. Another method is to feed the gases like N_2, H_2 or air in the melt through a blower which creates the small-sized pores in the material when solidified. In the space holder method, porous spacer particles like fly ash are added to the melt and stirred to uniform distribution of the fly ash. After solidification, a porous spacer creates closed cell foam. This type of foam is also known as syntactic foam. One of the methods to synthesize open cell porous through the foam is the polymer perform the method. In this method, first, a cellular polymer prepared is prepared and metal melt is infiltrated in the pore of the polymer preform. After that, the infiltrated polymeric preform is kept in the furnace above the evaporation temperature of the polymer. Therefore, polymer gets vaporized and ceramic/metallic open cell foam is obtained.

In the powder metallurgy route, metallic powders are used to synthesize the porous structure. The gas entrapment method, slurry foaming and space holder method are the important processes to create pores without melting the material. In these techniques, partially open and partially closed cell foams are found. Gas entrapment technique and slurry foaming provide limited porosity in the material, while porosity, as well as pore size can be easily controlled through the space holder technique. Some special types of foam manufacturing processes are rapid prototyping, electrodeposition and vapour deposition techniques. Porous products can be manufactured with perfection and controlled properties via rapid prototyping. This method is used to create complex porous medical products like sophisticated stents, skull scaffolds and prostheses.

References

1. Bisht A, Patel VK, Gangil B (2019) Future of metal foam materials in automotive industry. Automotive Tribology, Springer pp 51–63
2. Fan Z, Liu Y, Xu P (2019) Blast resistance of metallic sandwich panels subjected to proximity underwater explosion. Int J Impact Eng 93:128–135
3. Meghana M, Shashikanth C (2016) Impact analysis of bumper and car chassis frame due to frontal collision for different materials. Int J Eng Manage Res (IJEMR) 6:131–135
4. Ashby MF, Evans T, Fleck NA, Hutchinson J, Wadley H, Gibson L (2000) Metal foams: a design guide. Elsevier

5. Yadav B, Singh P, Mondal D (2020) Fabrication of ultra-light LM13 alloy hybrid foam reinforced by MWCNTs and SiC through stir casting technique. Mater Lett 279:128271

6. Kaya AC (2020) In situ shear behavior of open-cell austenitic 316L steel foams. Mater Chem Phys 252:123303

7. Yang D, Guo S, Chen J, Qiu C, Agbedor S-O, Ma A et al (2021) Preparation principle and compression properties of cellular Mg–Al–Zn alloy foams fabricated by the gas release reaction powder metallurgy approach. J Alloy Compd 857:158112

8. Li H, Yao Z, Zhang J, Cai X, Li L, Liu G et al (2020) The progress on physicochemical properties and biocompatibility of tantalum-based metal bone implants. SN Appl Sci 2:1–14

9. Niu W, Xiao Y, Wan C, Li D, Fu H, He H (2020) Ultrasonic bonding of 2024 Al alloy using Ni-foam/Sn composite solder at ambient temperature. Mater Sci Eng, A 771:138663

10. Singh P, Shrivastava V, Abhash A, Yadav B, Singh I, Mondal D (2021) Compressive deformation and corrosion behaviour of moderate to highly porous Ti_4Al_4Co (wt%) alloy foam. Mater Chem Phys 257:123718

11. Aguilar C, Aguirre T, Martínez C, De Barbieri F, San Martín F, Salinas V et al (2020) Improving the mechanical strength of ternary beta titanium alloy (Ti–Ta–Sn) foams, using a bimodal microstructure. Mater Des 195:108945

12. Feng Y, Chen S, Wang J, Lu B (2020) Carbon foam with microporous structure for high performance symmetric potassium dual-ion capacitor. J Energy Chem 43:129–138

13. Jiang H, Ziegler H, Zhang Z, Meng H, Chronopoulos D, Chen Y (2020) Mechanical properties of 3D printed architected polymer foams under large deformation. Mater Des 194:108946

14. da Costa FP, da Silva Morais CR, Rodrigues AM (2020) Sustainable glass-ceramic foams manufactured from waste glass bottles and bentonite. Ceram Int 46:17957–17961

15. Machado CM, Benelli P, Tessaro IC (2020) Effect of acetylated starch on the development of peanut skin-cassava starch foams. Int J Biol Macromol 165:1706–1716

16. Rajaei M, Elahi SH, Asefi A (2020) Modal properties of closed-cell zinc foam. Structures, Elsevier, pp 1380–1383

17. Onck P, Van Merkerk R, Raaijmakers A, De Hosson JTM (2005) Fracture of open-and closed-cell metal foams. J Mater Sci 40:5821–5828

18. Tuncer N, Arslan G (2009) Designing compressive properties of titanium foams. J Mater Sci 44:1477–1484

19. Singh P, Singh I, Mondal D (2019) A comparative study on compressive deformation and corrosion behaviour of heat treated Ti_4 wt% Al foam of different porosity made of milled and unmilled powders. Mater Sci Eng, C 98:918–929

20. Orbulov IN, Szlancsik A, Kemény A, Kincses D (2020) Compressive mechanical properties of low-cost, aluminium matrix syntactic foams. Compos A Appl Sci Manuf 135:105923

21. Duan Y, Ding Y, Liu Z, Hou N, Zhao X, Liu H et al (2020) Effects of cell size vs. cell-wall thickness gradients on compressive behavior of additively manufactured foams. Compos Sci Technol 199, 108339

22. Neville B, Rabiei A (2008) Composite metal foams processed through powder metallurgy. Mater Des 29:388–396

23. Birla S, Mondal D, Das S, Kashyap DK, Ch VA (2017) Effect of cenosphere content on the compressive deformation behaviour of aluminum-cenosphere hybrid foam. Mater Sci Eng, A 685:213–226

24. Birla S, Mondal D, Das S, Khare A, Singh JP (2017) Effect of cenosphere particle size and relative density on the compressive deformation behavior of aluminum-cenosphere hybrid foam. Mater Des 117:168–177

25. Banhart J (2001) Manufacture, characterisation and application of cellular metals and metal foams. Prog Mater Sci 46:559–632

26. Schwartz DS, Shih DS, Evans AG, Wadley HN (1998) Materials research society. In: symposium proceedings, porous and cellular materials for structural applications. Warrendale PA, p 521

27. Badkul A, Saxena S, Mondal D (2020) A numerical solution to accurately predict deformation behaviour of metallic foam material up-to densification region for the possible use in composite structures. Compos Struct 246:112419

28. An J, Chen C, Zhang M (2021) Effect of $CaCO_3$ content change on the production of closed-cell aluminum foam by selective laser melting. Opt Laser Technol 141:107097
29. Bisht A, Gangil B, Patel VK (2020) Selection of blowing agent for metal foam production: a review. J Metals, Mater Miner 30
30. Simone A, Gibson LJ (1998) Aluminum foams produced by liquid-state processes. Acta Mater 46:3109–3123
31. Park C, Nutt S (2000) PM synthesis and properties of steel foams. Mater Sci Eng, A 288:111–118
32. Miyoshi T, Itoh M, Akiyama S, Kitahara A (2000) ALPORAS aluminum foam: production process, properties, and applications. Adv Eng Mater 2:179–183
33. Song Z-L, Ma L-Q, Wu Z-J, He D-P (2000) Effects of viscosity on cellular structure of foamed aluminum in foaming process. J Mater Sci 35:15–20
34. Sarajan Z (2015) A356 alloy foaming by titanium hydride. Russian J Non-Ferrous Metals 56:516–521
35. Wang N, Maire E, Chen X, Adrien J, Li Y, Amani Y et al (2019) Compressive performance and deformation mechanism of the dynamic gas injection aluminum foams. Mater Charact 147:11–20
36. An J, Chen C, Zhang M (2021) Effect of TiH_2 oxidation treatment on foamed aluminum alloys produced by selective laser melting. Phys Metals Metall 1–18
37. García-Moreno F, Banhart J. Influence of gas pressure and blowing agent content on the formation of aluminium alloy foam. Adv Eng Mater
38. Kumar N, Bharti A (2021) Review on powder metallurgy: a novel technique for recycling and foaming of aluminium-based materials. Powd Metall Metal Ceram 1–8
39. Kennedy A (2002) The effect of TiH_2 heat treatment on gas release and foaming in Al–TiH_2 preforms. Scripta Mater 47:763–767
40. Yamada Y, Shimojima K, Sakaguchi Y, Mabuchi M, Nakamura M, Asahina T et al (2000) Processing of cellular magnesium materials. Adv Eng Mater 2:184–187
41. Erryani A, Greenita C, Lestari FP, Utomo MS, Kartika I, Nugraha T (2021) Casting technique of NaCl space-holder using 3D printed PLA template for manufacture porous Mg alloy. In: AIP conference proceedings. AIP Publishing LLC, 030004
42. Meng J, Liu T-W, Wang H-Y, Dai L-H (2021) Ultra-high energy absorption high-entropy alloy syntactic foam. Compos B Eng 207:108563
43. Zhang B, Wang L, Zhang J, Jiang Y, Wang W, Wu G (2021) Deformation and energy absorption properties of cenosphere/aluminum syntactic foam-filled circular tubes under lateral quasi-static compression. Int J Mech Sci 192:106126
44. Kannan S, Pervaiz S, Alhourani A, Klassen RJ, Selvam R, Haghshenas M (2020) On the role of hollow aluminium oxide microballoons during machining of AZ31 magnesium syntactic foam. Materials 13:3534
45. Vishwakarma A, Mondal D, Birla S, Das S, Prasanth N (2017) Effect of cenosphere size on the dry sliding wear behaviour LM13-cenosphere syntactic foam. Tribol Int 110:8–22
46. Afolabi LO, Mutalib NAA, Ariff ZM (2019) Fabrication and characterization of two-phase syntactic foam using vacuum assisted mould filling technique. J Market Res 8:3843–3851
47. Murray N, Schuh C, Dunand D (2003) Solid-state foaming of titanium by hydrogen-induced internal-stress superplasticity. Scripta Mater 49:879–883
48. Queheillalt DT, Wadley HN, Choi BW, Schwartz DS (2000) Creep expansion of porous Ti_6-Al_4-V sandwich structures. Metall Mater Trans A 31:261–273
49. Kulkarni S (1973) Foamed aluminium
50. Kumar R, Jain H, Sriram S, Chaudhary A, Khare A, Ch VA et al (2020) Lightweight open cell aluminum foam for superior mechanical and electromagnetic interference shielding properties. Mater Chem Phys 240:122274
51. Davari HR, Gholamzadeh H, Dehghan SA, Paydar MH (2017) Effect of sintering parameters (time and temperature) upon the fabrication process of organic binder-based metallic hollow sphere. Powder Metall 60:363–370
52. Eisenmann M (1998) Metal powder technologies and applications. ASM Handbook 7:171–221

53. Singh P, Abhash A, Nair P, Khare A, Singh I, Mondal D (2019) Effect of space holder size on microstructure, deformation and corrosion response of Ti4Al4Co (wt%) alloy foam. Appl Innov Res (AIR) 1:41–47
54. Bekoz N, Oktay E (2012) Effects of carbamide shape and content on processing and properties of steel foams. J Mater Process Technol 212:2109–2116
55. Abhash A, Singh P, Kumar R, Pandey S, Sathaiah S, Shafeeq MM et al (2020) Effect of Al addition and space holder content on microstructure and mechanical properties of Ti$_2$Co alloys foams for bone scaffold application. Mater Sci Eng, C 109:110600
56. Jain H, Gupta G, Kumar R, Mondal D (2019) Microstructure and compressive deformation behavior of SS foam made through evaporation of urea as space holder. Mater Chem Phys 223:737–744
57. Bansiddhi A, Dunand D (2008) Shape-memory NiTi foams produced by replication of NaCl space-holders. Acta Biomater 4:1996–2007
58. Jin F-L, Zhao M, Park M, Park S-J (2019) Recent trends of foaming in polymer processing: a review. Polymers 11:953
59. Cetinel O, Esen Z, Yildirim B (2019) Fabrication, morphology analysis, and mechanical properties of Ti foams manufactured using the space holder method for bone substitute materials. Metals 9:340
60. Patnaik P (2003) Handbook of inorganic chemicals. McGraw-Hill, New York
61. Li D, Zhang Y, Ma X, Zhang X (2009) Space-holder engineered porous NiTi shape memory alloys with improved pore characteristics and mechanical properties. J Alloy Compd 474:L1–L5
62. Farley C, Turnbull T, Pantoya ML, Hunt EM (2011) Self-propagating high-temperature synthesis of nanostructured titanium aluminide alloys with varying porosity. Acta Mater 59:2447–2454
63. Biswas A (2005) Porous NiTi by thermal explosion mode of SHS: processing, mechanism and generation of single phase microstructure. Acta Mater 53:1415–1425
64. Li B-Y, Rong L-J, Li Y-Y, Gjunter V (2000) A recent development in producing porous Ni–Ti shape memory alloys. Intermetallics 8:881–884
65. Wu Z, Sun L, Pan J, Wang J (2018) Highly porous Y$_2$SiO$_5$ ceramic with extremely low thermal conductivity prepared by foam-gelcasting-freeze drying method. J Am Ceram Soc 101:1042–1047
66. Sepulveda P, Binner J, Rogero S, Higa O, Bressiani J (2000) Production of porous hydroxyapatite by the gel-casting of foams and cytotoxic evaluation. J Biomed Mater Res Offic J Soc Biomater Japanese Soc Biomater 50:27–34
67. Yang D, Guo Z, Shao H, Liu X, Ji Y (2012) Mechanical properties of porous Ti–Mo and Ti–Nb alloys for biomedical application by gelcasting. Procedia Eng 36:160–167
68. Usman M, Pan L, Farid A, Khan AS, Yongpeng Z, Khan MA et al (2020) Carbon nanocoils-Fnickel foam decorated with silver nanoparticles/sheets using a novel stirring assisted electrodeposition technique for non-enzymatic glucose sensor. Carbon 157:761–766
69. Hutmacher DW, Sittinger M, Risbud MV (2004) Scaffold-based tissue engineering: rationale for computer-aided design and solid free-form fabrication systems. Trends Biotechnol 22:354–362
70. Yang S, Leong K-F, Du Z, Chua C-K (2002) The design of scaffolds for use in tissue engineering. Part II, Rapid Prototyp Tech Tissue Eng 8:1–11
71. Krishna BV, Bose S, Bandyopadhyay A (2007) Low stiffness porous Ti structures for load-bearing implants. Acta Biomater 3:997–1006

Chapter 4
Overview of Lightweight Metallic Materials

P. S. Samuel Ratna Kumar, P. M. Mashinini, and R. Vaira Vignesh

1   Introduction

Lightweight materials are widely employed in a variety of industries that require high performance with less weight, including biomedical, automobile, aviation, power generation, batteries, electronic devices, and the marine industries [1–3]. Several manufacturers are constantly looking for new materials that have the technological and economic capacity to compete successfully on the marketplace. There are reasonable grounds for examining a component's desirable action at the outset of manufacturing and changing the part's manufacturing as well as in properties to fit the needs of the system. It is feasible to detect and leverage potent impacts between the various aspects using concurrent engineering technique. By making judicious use of innovation, a specific structural module can be optimized so that the engineering criteria are met but not surpassed by a massive margin above other specified safety aspect. For the engineer, the result is a design strategy that allows for the most efficient use of all the attributes of significant individual components with the intention of establishing lightweight materials with superior metallic properties [4, 5]. Using lighter materials like aluminum, magnesium, titanium, and its alloys or foams or composites to replace standard ferrous material options has proven to be a cost-effective and effective way to meet weight goals. These metal alloys and its composite material constitute a reasonable alternative for these objectives with a good property

P. S. Samuel Ratna Kumar (✉) · P. M. Mashinini
Department of Mechanical and Industrial Engineering, University of Johannesburg, Johannesburg, South Africa
e-mail: skumar@uj.ac.za; samuelrathish@live.com

R. Vaira Vignesh
Department of Mechanical Engineering, Amrita School of Engineering, Amrita Vishwa Vidyapeetham, Coimbatore, Tamil Nadu, India

such as strength-to-weight ratio, mechanical, thermal, electrical, tribological, corrosion, and bio-compact ability. The material and its properties were selected based on their applications [6–8]. Like aluminum alloys are among the lightweight materials that have been widely used in automobile structures and aircraft body components. Automotive panel sections, which make up a considerable amount of the weight of body structures, have been the focus of extensive research [9, 10]. In industry revolution 5.0, the major motive is to have large extent of productiveness when robot and human work together. The role of material in designing a robot is crucial in improving its mechanical and dynamic performance. This robot requires high torque, strength, stiffness, durable, vibration resistant, wear, corrosion resistance, and cost-effective. The mentioned properties can be attained with the help of metal alloys and composite material [11].

Some of the major lightweight metallic material properties which influence the designing of automobile and aviation industries are listed here. The non-ferrous materials like aluminum (Al) and its alloys have good strength, flexibility, and resistant to corrosion. These materials have good thermal and electrical conductivity and are utilized in steel/magnesium/titanium alloys as an alloying material. They are also incredibly versatile and lightweight than titanium, yet it lacks the strength when compared to titanium. These alloys offer great stiffness and elasticity, which improves as the temperature is reduced. Most aluminum alloys show a minor change in tensile and impact properties, when exposed to subzero temperatures.

Similarly, magnesium (Mg) and its alloys are also non-ferrous materials with decent strength, strong ductile, less weight, and great resistant to corrosion. The strength and other material properties are determined by a variety of elements, including the conditions, chemical composition, surface heat treatment, manufacturing characteristics, and so on. Magnesium seems to have no defined elastic modulus, and its alloys are vulnerable to notch and many other strains, which reduces their durability ranges significantly [12, 13].

Titanium (Ti) and its alloys offer great corrosion protection, superior strength-to-weight ratios, with good fatigue performance. It also known as a temperamental material, which signifies it is wear and temperature resistant. This material is highly resistant to sea water corrosion and non-magnetic. The heat conduction property of the material is very low compared to the aluminum and magnesium. Temperature will greatly influence the basic properties of the material, and its alloys can maintain high tensile strength even at the higher temperatures compared to pure material. Also, it has an excellent high cycle fatigue strength. Toughness of the material is determined by the interplay of surface morphology, micrograph, strength, and chemical composition [14, 15]. This chapter will briefly explain the present implementations of these metals, as well as their properties and behaviors, to improve the study and assessments of different procedures for creating these metals.

2 Aluminum Alloys

In general, aluminum (Al) alloys of heat treatable as well as non-heat treatable are preferred options for the aerospace and automobile applications [16]. At ambient temperature and considerably increased temperature, the heat-treated alloys contain an element whose solid solubility decreases with decreasing temperature and in concentrations that exceed their equilibrium solid solubility. Magnesium, copper, lithium, and zinc seem to be the most significant alloying elements in this category. To material property development, a significant variety of different compositions depends on strain hardening using physical reduction, frequently in addition to different annealing methods were used. Hence, these materials were known as non-heat-treatable alloys.

2.1 Types of Alloying Elements

Based on the types of alloying elements, it has been differentiated into two primary groups of aluminum alloys, cast, and wrought aluminum alloys. Cast aluminum alloys (AAs) have more than 20–23% alloy elements in composition; however, wrought aluminum alloys possess less than 3–5%. Although it may appear to be a minor distinction, the proportion of alloy elements seems to have a major effect on materials characteristics. When more alloy elements are introduced, aluminum reduces its ductility, rendering many cast alloys vulnerable to brittle fractures [17]. Wrought alloys, on the other hand, have enabled manufacturers to improve the stiffness, resistance to corrosion, conduction, and other properties of aluminum while maintaining ductility and other desirable properties. Compared to wrought aluminum, cast aluminum alloys having lower melting temperatures and strength properties; frequently used aluminum alloy is Al–silicon material, which contains high quantities of silicon and simple to cast. The most of aluminum components, like those made by extruded or rolled, are made of wrought aluminum. Several wrought aluminum alloy classifications are defined by alloying materials such as manganese, copper, silicon, zinc, magnesium, and lithium [18].

Aluminum cast alloys are identified by 4 numbers, with a decimal between the 3rd and 4th digits. The alloys present in the material are indicated by the first three digits, while the product's shape is indicated by the fourth digit [19]. Table 1 shows the many varieties of cast aluminum and also its frequently chosen alloy elements and base material qualities.

Grade 1 cast alloys were extensively pure aluminum, provide excellent resistance to corrosion, machining attributes, and welding features. Grade 1 alloys are frequently used to make blades or to enclose highly corrosive materials.

Grade 2 cast alloys, Cu is the primary alloying element although Mg, Mn, and Cr are frequently incorporated. These are heat treatable, this implies materials could

Table 1 Various cast aluminum grades

Grade	Major elements	Material strengthening
1xx.x	Unalloyed	Non-heat treatable
2xx.x	Cu	Heat treatable
3xx.x	Si, Mg, Cu	Heat treatable
4xx.x	Si	Heat treatable
5xx.x	Mg	Non-heat treatable
6xx.x	NA	NA
7xx.x	Zn	Heat treatable
8xx.x	Sn, Cu, Ni	Heat treatable

get added strength by heating them. Across all cast alloy materials, it has the greatest strength and toughness, particularly at high-range temperatures.

Grade 3 cast alloys have Si, Cu, and Mg are the principal alloying components, having Ni and Be added as needed. These are heat treated, do have excellent mechanical properties, excellent wear and crack resistance; also, it is machinable.

Grade 4 cast alloys have Si as the only alloying element. They are heat treated and have excellent casting properties, weldable, high resistance to wear and corrosion.

Grade 5 cast alloys have Mg as their major alloying element, and it is non-heat-treated material. Once it is anodized, they offer a fantastic surface appeal, good resistance to corrosive environment, and machinability.

Grade 7 cast alloys are heat-treated and contain Zn as the principal alloying element. The ability to cast the material is poor although they have better dimensional stability, machinability, and final properties, as well as decent resistance to corrosion.

Grade 8 cast alloys are heat treated, which contains large amount of Sn, with minor amounts of Cu and Ni. It has poor strength; however, excellent machinability and resistance to wear define such material.

Wrought aluminum alloys use the same 4-digit indication as cast aluminum alloys, but there are no decimals. By examining the construction of the term, it is simple to distinguish a cast from a wrought aluminum alloy. The 1st digit identifies the category of aluminum alloys which include metal alloys, with differing ratios of substances particular to every blends in each alloy within a category. Because of their enhanced qualities, wrought alloys are more adaptable than cast alloys [19]. Table 2 displays the various wrought alloy categories, their strengthening methods, and their enhanced attributes, and Table 3 shows the basic types of tempers used for wrought alloys.

Grade 1xxx wrought alloys are not real alloys because they are 99% pure form of aluminum. They are great for electrical and chemical applications because they are corrosion resistant and easy to work. The 1100 aluminum alloy, which is economically pure aluminum, is a common alloy in this category. The material is malleable and ductile and has high operability, making it appropriate for hard-forming operations. It is a non-heat-treatable material and easy to weld by any type of method.

Table 2 Various wrought aluminum grades

Grade	Major elements	Material strengthening
1xxx	99% Al	Non-heat treatable
2xxx	Cu	Heat treatable
3xxx	Mn	Non-heat treatable
4xxx	Si	Based on alloy element
5xxx	Mg	Non-heat treatable
6xxx	Mg, Si	Heat treatable
7xxx	Zn	Heat treatable
8xxx	Others	Limited

Table 3 Types of tempers for wrought alloys

Letter	Indications
F (Fabricated)	The temperature during the operating or strain-hardening process to produce certain material qualities does not necessitate any additional control
O (Annealed)	To obtain maximum workability, toughness, and ductility, the material is exposed to high treatment
H (Strain-hardened)	Used to maintain the strength of non-heat-treatable alloys that have been cold wrought using the strain-hardening process
W (Solution heat treated)	After the solution heat treatment, the treatment is applied to alloys that have been subjected to natural aging. The categorization is kind of narrow
T (Thermally treated)	Heat-treatable alloys that have been aged naturally or artificially in order to maintain a steady tempers other than F, O, or H

Grade 2xxx wrought alloys which primarily use Cu as an alloying element, with modest quantities of Mg thrown in for good measure. Once heat treated, they develop excellent strength, surpassing low carbon steels although they are susceptible to corrosion owing to their Cu component.

Grade 3xxx wrought alloys which primarily use Mn as an alloying element. It has a moderate strength, strong corrosion protection, dimensional stability, and suitability for use at extreme temperature. Compare to the Grade 1xxx non-heat-treated alloys, it has a good mechanical strength, and this material can be extruded, twisted, fused, or bonded.

Grade 4xxx wrought alloys which primarily use Si are used as an alloying element to reduce melting temperature without sacrificing ductility. They are widely used to combine different types of aluminum as welding wires and brazing alloys. Some Grade 4xxx wrought alloys could be heat treated to a restricted extent, but they are not heat treatable in general.

Grade 5xxx wrought alloys which primarily use Mg are the most common alloying ingredient, having trace levels of Mn present in some alloys. These materials are non-heat-treatable, with good weldability, and have excellent corrosion resistance,

particularly in marine conditions. Due to the obvious possibility for reactivity and consequent tendency to stress corrosion cracking, materials in this category with more than 3% Mg are not advised for higher temperatures operation beyond 150 °F.

Grade 6xxx wrought alloys which primarily use Mg and Si are the most common alloying ingredient. Heat treatment improves their mechanical strength, and though they are not as robust as Grade 2 and 7 alloys, they offer good ductility, weldability, processability, and resistance to corrosion.

Grade 7xxx wrought alloys, Zn, are used as the principal alloying ingredient. Due to this alloying composition, these alloys are still the dominant among all wrought alloys, with properties surpassing certain steels. The presence of Zn reduces reliability and processability, but the material's excellent strength compensates for such drawbacks.

Grade 8xxx alloys are made up of a variety of alloying elements that are used for a variety of purposes, including high-temperature performance, reduced density, increased stiffness, and other special features.

3   Applications

The inclusion of alloying elements is what causes the physical characteristics of different metals to vary its properties. Although AA2-series alloys have greater diameters of intermetallic phases, they possess less fracture toughness over AA7-series alloys with equal yield strength values. To prevent the production of big and fragile combinations, the quantities of ferrous, cooper, or silicon can be lowered to increase fracture toughness [20]. To make up for the lack of strength, non-heat-treatable aluminum-based alloys such as AA5754, AA5025 (Al–Mg) are often used for interior body structures. These alloys are strengthened by cold working and solution hardening process at the time of manufacturing. As a result, AA5-series sheet parts are often cold pressed in annealing (O), forged (F), or strain-hardening (H) environments to increase ductility. The widespread use of AA5-series aluminum alloys is due to its softness and ease of forming. The usage of greater Mg containing alloy in automobiles in applications such as sub-frames, wheel rims, and chassis when the importance of welding material strength is emphasized. As Al alloys are widely used, these alloys will be used in parts of the vehicle structures where surface quality, operating temperatures, and resistance to corrosion must be carefully considered [21]. In contrast, mid or great strength Al alloys, such as AA6-series and AA7-series, could be used for exterior panel construction. The precipitation hardening gives these alloys its strength, which is arrived from the standard heat (T6) treatment used in the automobile sector. Due to its great strength and resistance to corrosion, AA7-series and AA2-series are the key material choices in the aviation sector. The corrosion rate of AA7-series is high with good mechanical at T6 heat treatment condition, such alloys are typically used in an over-aged state, such like T73. These materials were used in brake shoes, piston ring, structural frames, pressure cabin, stabilizers, fuselage, landing gears, lower and upper wings. Presently, the building industry consumes

25% of worldwide manufacturing because of its favorable properties. The easiness of extrusion, aluminum alloys are an adaptable structural material that may be used to create complicated cross-sectional geometries that aren't possible with more traditional structural materials like steel or concrete. They are well-suited for usage in marine conditions without protective coating and with high reliability due to their high resistance to corrosion. Their high resilience enables buildings to preserve their special characteristics even when exposed to extreme temperatures [22].

The very first aluminum–lithium (Al–Li) alloys were created in the early twentieth century. To present, the third version of Al–Li alloys is matured and suitable of being implemented to real-time world. When related to many other aviation alloys, these Al–Li alloys have less density, higher stiffness, and high fatigue life are commonly employed in wing sections [23].

4 Magnesium Alloys

Magnesium (Mg) and its alloys possess very less density compared to aluminum (30%), steel (70%), and titanium (60%). This is a promising material, which can replace the abovementioned material for possible applications. Magnesium also has several other advantages, like great formability, high absorption capacity, superior electromagnetic shielding, seems to be the most conveniently machinable of all metal alloys, and requiring less power to produce than aluminum [24–26]. Moreover, it has a significant flaw in that it is subject to corrosion and by addition of reinforcement or any coating methods that have been used to solve this limitation. Pure Mg is readily available and acceptable for most of the applications, with a least impurity of 99.8%. On the other hand, it provides perfect for metallurgy and chemical applications, limited to engineering and structural applications. As a result, for an engineering and structural applications, pure metals need to enhance its inferior properties without compromising its essential characteristics by adding alloying elements. The structure and chemical composition of alloying elements will have an impact on the increased mechanical properties of Mg alloys [27]. The addition of alloying elements continues to make up about two-third of a Mg alloy. Zinc and aluminum are the most prevalent and preferable alloying components, with aluminum serving as the core for most Mg alloys.

4.1 Types of Alloying Elements

Similar to aluminum, magnesium alloys are also classified into two groups such as cast and wrought alloys. Al, Mn, and Zn are common alloying constituents in Mg cast alloys, with quantities ranging from 1 to 10%. Further alloying elements, including as zirconium (Zr) and rare-earth metals, also lately been employed to improve creep resistance. Heat treatments also improve the mechanical characteristics of cast alloys.

Table 4 ASTM Identification for Mg alloys

Main alloying element	ASTM identification
Manganese	M
Aluminum–manganese	AM
Aluminum–zinc–manganese	AZ
Zirconium	K
Zinc–zirconium	ZK
Zinc–zirconium–rare earth metal	ZE
Rare earth metal–zirconium	EZ
Zinc–copper–manganese	ZC
Aluminum–silicon–manganese	AS

Wrought Mg alloys have been mechanically worked to get the required shape, such as forging, extrusion, and rolling processes. Al, Mn, and Zn are common alloying elements as of the cast alloys. Mg wrought alloys are differentiated based on heat treatable and non-heat treatable [28].

To identify the proportions of alloy, identification schemes displaying the alloying elements and its related information have been developed. Mg alloys were identified and classified according to their primary alloying components within ASTM identification system. The main alloying elements and its respective identities are shown in Table 4.

In Mg alloys, Zn is an efficient solid solution strengthener. Zn further counteracts the negative impacts of Fe or Ni contaminants on Mg alloy corrosion resistance. To increase the time of life properties of Mg–RE–Zr or Mg–Th–Zr alloys, Zn is added directly. By raising the recrystallization temperature and changing the shape of the eutectic phase from separated to enables easier, adding Cu to Mg–Zn increases the alloy's tensile properties, allowing for greater homogeneity of the alloys upon solution treatment.

The addition of Zr is maximal soluble at ambient temperature is less than 0.28 wt%; it is a highly potent grain refiner in Mg alloys including RE/Ag/Th combinations and Zn. Zr's efficiency as a powerful grain refiner in Mg is attributable to the fact that it fits three conditions. The addition of Zr is greater than 0.5 wt%, i.e., the maximum solubility of Zr in Mg at 653 °C, is required for improved grain refining. With Zr additions below the solubility limit, however, grain refinement in Mg has been reported. The active intervention of coarse, 0.5–2 μm, prismatic Zr granules (found in grain refiners) in the germination process and consequently grain refinement has been attributed to this disparity. Including elements such as Al, Fe, Si, C, and the gases O_2, H_2, N_2, Zr in Mg alloys may lose their grain refining capacity since it forms intermetallic with metals.

Solid solution strengthening enhances the strength and ductility of Al in Mg alloys. The inclusion of 6% Al gives the strongest and most ductile material. In both wrought and cast Mg alloys, Al is the principal alloying element, and up to 10%, Al

is employed. The increase in addition of Al in Mg alloys will form an intermetallic bonding and reduces the ductility of the material.

Didymium or mischmetal is used to add rare-earth metals (RE) to magnesium alloys. In creep-resistant sand-casting alloys, those elements are the main alloying elements. RE enhances Mg alloy creep strength by keep improving intergranular eutectics which bind the boundary layer and prevent intergranular movement. The RE additions further limit the crystallization range, which aim to minimize micro-shrinkage porous structure in casting and welding cracks.

Mn may not enhance Mg alloys, but it is an efficient scavenger in Mg–Al and Mg–Al–Zn alloys, where it combines with harmful heavy elements to generate harmless intermetallic. Mn considerably enhances creep resistance in Mg–Sc alloys, according to recent research.

Si contributes to the wettability of Mg alloys. As a result, all cast Mg alloys have significant Si. Even in tiny levels, transition elements are detrimental because they weaken the corrosion protection of Mg alloys. Cu, Fe, and Ni in Mg alloys have maximum permissible limits of 0.05 wt% Cu and 0.005 wt% Fe and Ni, respectively.

5 Applications

The AZ91 and AZ31 Mg alloys are popular magnesium-based alloys containing aluminum as a core alloying element. AZ31 Mg alloy is commonly applied in the aviation sector because of its low density and strong mechanical characteristics. Mg and its alloys entered into the commercial aviation industry because it has significant economic and environmental advantages when used in aircraft structural construction. Most interestingly, replacing harder materials with lightweight materials like Mg will enhance the aircraft fuel efficiency and minimize air pollutants. The use of Mg in aviation and automobile industry was a great debate; due to its flammability, surface endurance and resistance to corrosion are the most important factors to consider [28]. Despite recent developments in Mg exploration, it is now feasible to solve these challenges. Regardless of the fact that it has numerous automobiles, its overall proportion of metals in the automobile sector is negligible in comparison to steel and aluminum [29]. Molded Mg alloys are still the most popular choice for automobiles owing to its superior properties. Mg–Al alloy series, like AM and AZ alloys, Mg alloyed with rare-earth material is the most common forms of molded Mg alloys used in the automobile industry. Due to various advantageous properties like biocompatibility, degradability, and mechanical qualities, Mg alloys have emerged as attractive biomedical metallic materials. The cells may adhere, disseminate, and multiply successfully on Mg alloys with respect to cytotoxicity. Also, Mg and its alloys have a minimal number of applications in cardiovascular therapy at the moment because they are mostly investigational or preliminary. Mg and its alloys are now being studied to see whether they can substitute bio-inert metals implantation in common cardiovascular therapy procedures [30].

For two reasons, lithium is an essential alloying ingredient in magnesium alloys: (1) Li density is lesser than Mg; (2) Li transforms Mg crystal structure to bcc with only 10% addition of Li, improving the processability of Mg–Li alloys. The reduction in density is beneficial to lightweight buildings. Such alloys have specified bending stiffness two times that of typical Al alloys and five times those of traditional Mg alloys due to their lightweight properties [31].

6 Titanium Alloys

Titanium alloy is the most used in the aerospace industries, nuclear industries, etc., because of its superior mechanical properties (high strength and toughness), low density, and excellent corrosion protection properties. Titanium alloys due to their combination of enhanced strength and fatigue characteristics, high-temperature corrosion resistance (low reactivity) stands out as advantageous in providing reliable service in manufacturing titanium products under different loading conditions [32–34]. In addition, all of the phases present usually precipitate as a result of the designated heat treatment or processing condition and contain titanium as one of the major constituents of the phase. If pure titanium is heated above 882.5 °C, the low-temperature hexagonally close-packed (hcp) phase (α) will transform to the high-temperature, body-centered cubic phase (β). Upon cooling, the transformation is reversed. Alloying additions are classified as α stabilizers or β stabilizers. Examples of the former include gallium, tin, zirconium, and aluminum; examples of the latter include molybdenum, vanadium, chromium, and iron. Commercial titanium alloys may be broadly classified as α, ($\alpha + \beta$), or β types, depending on the predominant phase present [35, 36].

In α titanium alloys, the effect of alloying element would be to increase mechanical characteristics of the hcp structure. The major α-stabilizer elements being aluminum and oxygen. Commercially, pure titanium, which is alloyed with oxygen comes under α titanium alloys, is divided into four grades of titanium from Grades 1 to 4 based upon the iron content and interstitial elements, but in particular, it is oxygen content that increases from 0.18% (Grade 1) to 0.40% (Grade 4) [37]. Grade 1 being the most ductile also possesses high formability among all the titanium alloys. Grade 2, also known as workhorse, is widely produced and used pure titanium due to its significant increase in the unit yield load from all the properties it shares with Grade 1. Grade 3 and Grade 4 are the evolutions of Grade 1 and 2 with a slight improvement in their mechanical strength. Some of the key characteristics of these α-alloys, which are non-heat treatable, offer are high-temperature creep strength and oxidation resistance. In ($\alpha + \beta$) and β titanium alloys, β-stabilizer elements such as vanadium, molybdenum, iron, and chromium play a useful in the annealing heat treatment. ($\alpha + \beta$) titanium alloys do have varying from medium to high levels of strength and hardness but are not good as α-alloys when it comes to creep strength and cold formability. β titanium alloys are readily heat transferable [37].

7 Applications

Presently, aerospace applications use 50% of all titanium alloys produced. The very first sector to benefit of titanium's exceptional strength-to-weight is aviation [38]. The landing gear on the Boeing 777, 787, and Airbus A380 all uses near β titanium alloy [39]. Due to the obvious potential for combustion, titanium alloy Ti–6Al–4 V, which is used to build turbine compressor blades for jet engines, is not employed in environments with temperatures above 400 degrees. Titanium is indeed the preferred material in offshore oil platforms because of its strength and corrosion resistance, which makes it perfect for prolonged exposure to sea water and corrosive materials [40]. Titanium is the most popular material used in biomedical field in which developing a strong, biodegradable, and biocompatible metal that is inert is essential [41].

8 Conclusion

Aluminum, magnesium, and titanium alloys have formed the backbone of the aviation and automobile industry for almost a century due to their special mix of lightweight, high strength, and simplicity of manufacturing. Some known shortcomings of alloys, such as their high cost and production-related environmental problems, must now be given considerable thought. The different alloying elements will improvise the base materials and allow it use for all the applications. The processing methods also play a major role in deciding the properties of the material. Hence, the usage of these lightweight materials in the applications will have the major impact on the less weight–high strength durability, bio-compactable, fuel economy, and environmental pollution.

References

1. Samuel Ratna Kumar PS, Jyothi S, John Alexis S (2020) Corrosion behavior of aluminum alloy reinforced with MWCNTs. In: Rajendran S, Nguyen TANH, Kakooei S, Yeganeh M, Li Y (eds) In micro and nano technologies, corrosion protection at the nanoscale. Elsevier, pp 47–61, ISBN: 9780128193594. https://doi.org/10.1016/B978-0-12-819359-4.00004-0
2. Ali Y, Qiu D, Jiang B, Pan FS, Zhang MX (2015) Current research progress in grain refinement of cast magnesium alloys: a review article. J Alloys Compd 619:639–651. https://doi.org/10.1016/j.jallcom.2014.09.061
3. Shahadat M, Teng TT, Rafatullah M, Arshad M (2015) Titanium-based nanocomposite materials: a review of recent advances and perspectives. Coll Surf B: Biointerf 126:121–137. https://doi.org/10.1016/j.colsurfb.2014.11.049
4. Reitz W. Review of: "metallic materials for lightweight applications". In: Wells MGH, Kula EB, Beatty JH (eds) Materials and manufacturing processes, vol 11(2), pp 315–316. https://doi.org/10.1080/10426919608947484

5. Haber D (2015) Lightweight materials for automotive applications: a review. SAE Technical Paper. 2015-6-0219. https://doi.org/10.4271/2015-36-0219

6. Sivasankaran S (ed) Aluminium alloys—recent trends in processing, characterization, mechanical behavior and applications. London, United Kingdom, IntechOpen. Available from: https://www.intechopen.com/books/6071. https://doi.org/10.5772/68032

7. Song JF, She J, Chen D, Pan FS (2020) Latest research advances on magnesium and magnesium alloys worldwide. J Magnes Alloys 8:1–41. https://doi.org/10.1016/j.jma.2020.02.003

8. Sudhakar KV, Wood E (2016) Superplastic grade titanium alloy: comparative evaluation of mechanical properties, microstructure, and fracture behavior. J Mater 2016:1–7.https://doi.org/10.1155/2016/2309232

9. Peters M, Leyens C (2009) Materials science and engineering. In: Aerospace and space materials, vol III

10. Samuel Ratna Kumar PS, Mashinini P, John Alexis S (2022) Metal matrix nanocomposites, nanotechnology in the automotive industry. Elsevier, ISBN: 9780323905244. https://doi.org/10.1016/B978-0-323-90524-4.00010-4

11. Saravana Mohan M, Samuel Ratna Kumar PS (2021) Influence of CNT-based nanocomposites in dynamic performance of redundant articulated robot. Robotica 39:153–164. https://doi.org/10.1017/S0263574720000272

12. Loukil N (2021) Alloying elements of magnesium alloys: a literature review. In: Tański T, Jarka P (eds) Magnesium alloys structure and properties [internet]. IntechOpen, London. [cited 2022 Apr 26]. Available from: https://www.intechopen.com/chapters/75298. https://doi.org/10.5772/intechopen.96232

13. Li SB, Yang XY, Hou JT, Du WB (2020) A review on thermal conductivity of magnesium and its alloys. J Magnes Alloys 8:78–90. https://doi.org/10.1016/j.jma.2019.08.002

14. Ogawa A, Niikura M, Ouchi C, Minikawa K, Yamada M (1996) Development and applications of titanium alloy SP-700 with high formability. J Test Eval 24(2):100–109. https://doi.org/10.1520/JTE12683J

15. Welsch G, Boyer R, Collings EW (1993) Ti-3Al-8V-6Cr4Mo-4Zr (beta C). In: Materials properties handbook: titanium alloys, p 797, ASM International

16. Kumar PSSR, Mashinini PM (2021) Dry sliding wear behaviour of AA7075—Al_2SiO_5 layered nanoparticle material at different temperature condition. SILICON 13:4259–4274. https://doi.org/10.1007/s12633-020-00728-3

17. Davis JR (1994) Aluminum and aluminum alloys. ASM speciality handbook, ASM international, Materials Park, OH, USA

18. Vasudevan AK (1989) Doherty RD aluminum alloys—contemporary research and applications. Academic Press Inc., Cambridge, MA, USA

19. Rambabu P, Eswara Prasad N, Kutumbarao VV, Wanhill RJH. Aluminium alloys for aerospace applications. In: Eswara Prasad N, Wanhill RJH (eds) Aerospace materials and material technologies. Indian Institute of Metals Series. https://doi.org/10.1007/978-981-10-2134-3_2

20. Aamir M, Giasin K, Tolouei-Rad M, Vafadar A (2020) A review: drilling performance and hole quality of aluminium alloys for aerospace applications. J Mater Res Technol 9(6):12484–12500. https://doi.org/10.1016/j.jmrt.2020.09.003

21. Campbell FC (2008) Aluminum, elements of metallurgy and engineering alloys. ASM international 1:487–508. https://doi.org/10.31399/asm.tb.emea.t52240487

22. Varshney D, Kumar K (2021) Application and use of different aluminium alloys with respect to workability, strength and welding parameter optimization. Ain Shams Eng J 12(1):1143–1152. https://doi.org/10.1016/j.asej.2020.05.013

23. Starke EA (2014) Historical development and present status of aluminum–lithium alloys. In: Eswara Prasad N, Gokhale AA, Wanhill RJH (eds) Aluminum-lithium alloys. Butterworth-Heinemann, pp 3–26, ISBN: 9780124016989, https://doi.org/10.1016/B978-0-12-401698-9.00001-X

24. Shand MA (2006) History of magnesia. In: The chemistry and technology of magnesia. John Wiley & Sons, Inc., Hoboken, NJ, USA, pp 1–4

25. Dobrzanski LA (2019) The importance of magnesium and its alloys in modern technology and methods of shaping their structure and properties. In: Magnesium and its alloys. CRC Press, Boca Raton, FL, USA, pp 1–28
26. Song GL, Atrens A (1999) Corrosion mechanisms of magnesium alloys. Adv Eng Mater 1:11–33. https://doi.org/10.1002/(SICI)1527-2648(199909)
27. Moosbrugger C (2017) Engineering properties of magnesium alloys. ASM Int 1–10, ISBN: 978-1-62708-143-6
28. Ram Prabhu T, Vedantam S, Singh V. Aluminium alloys for aerospace applications. In: Eswara Prasad N, Wanhill RJH (eds) Aerospace materials and material technologies. Indian Institute of Metals Series. https://doi.org/10.1007/978-981-10-2134-3_2
29. Kainer KU (ed). Magnesium alloys and their applications. WILEY-VCH Verlag GmbH, Weinheim. ISBN: 3-527-30282-4
30. Dong J, Lin T, Shao H, Wang H, Wang X, Song K, Li Q (2022) Advances in degradation behavior of biomedical magnesium alloys: a review. J Alloys Compounds 908:164600. https://doi.org/10.1016/j.jallcom.2022.164600
31. Bach FW, Schaper M, Jaschik C (2003) Influence of lithium on HCP magnesium alloys. Mater Sci Forum 419–422:1037–1042
32. Lütjering G, Williams JC (2007) Titanium: engineering materials and processes, 2nd edn. Springer, Berlin, Germany
33. Zarkades A, Larson FR (1970) Elasticity of titanium sheet alloys. In: The science, technology and application of titanium. Pergamon Press, Oxford, UK, pp 933–941
34. Boyer R, Welsch G, Collings EW (eds) (1994) Materials properties handbook: titanium alloys. ASM International, Materials Park, OH, USA
35. Partridge PG (1967) The crystallography and deformation modes of hexagonal close-packed metals. Metall Rev 12(1):169–194
36. Yoo HM (1981) Slip, twinning, and fracture in hexagonal-close packed metals. Metall Trans A 12A:409–418
37. Bhattacharjee A, Saha B, Williams JC. Titanium alloys: part 1—physical metallurgy and processing. In: Eswara Prasad N, Wanhill RJH (eds) Aerospace materials and material technologies. Indian Institute of Metals Series, https://doi.org/10.1007/978-981-10-2134-3_2
38. Boyer RR (1995) Titanium for aerospace: rationale and applications. Adv Perform Mater 2:349–368
39. Zhao W, Wang S, Han Z, He N (2015) Cutting performance evaluation of end mills for titanium aircraft components. Procedia CIRP 35:1–7
40. Tardelli JDC, Bolfarini C, dos Reis AC (2020) Comparative analysis of corrosion resistance between beta titanium and Ti–6Al–4V alloys: a systematic review. J Trace Element Med Biol 62:126618
41. Suntharavel Muthaiah VM, Indrakumar S, Suwas S, Chatterjee K (2022) Surface engineering of additively manufactured titanium alloys for enhanced clinical performance of biomedical implants: a review of recent developments. Bioprinting 25:e00180

Chapter 5
Surface Engineered Titanium Alloys for Biomedical, Automotive, and Aerospace Applications

G. Suresh, M. R. Ramesh, and M. S. Srinath

1 Introduction

Innovative technologies that are automatic, smart, and possess effective, rapid, and economic superiority to existing technologies are constantly needed for continued technical advances in various fields. New design and material applications are two major ways to broaden the titanium alloy applications. The adoption of new technologies and materials, in particular, are critical factors in extending the applications of titanium alloys. The advanced materials used for surface modification have the potential to bring about revolutionary change. Metallic biomaterials are an important category of materials used in biomedical devices for bearing mechanical loads, bone substitutes, dental implants, hip joints, and stents. 316L stainless steel, cobalt-chromium alloys, titanium, and other metallic materials are examples. The modulus of cobalt-chromium and stainless steel materials is slightly higher than bone, resulting in stress shielding. They were used clinically for many years, but these alloys possess toxic effects due to the release from the prosthetic implants of Ni, Cr, and Co in stainless steel and cobalt-chromium alloys.

G. Suresh (✉)
Department of Mechanical Engineering, Vignan's Institute of Information Technology, Visakhapatnam 530049, India
e-mail: gsuresham@gmail.com

M. R. Ramesh
Department of Mechanical Engineering, National Institute of Technology Karnataka, Mangalore 575025, India

M. S. Srinath
Department of Industrial and Production Engineering, Malnad College of Engineering, Hassan 573202, India

Titanium alloys outperform stainless steel and cobalt-chromium alloys in mechanical and chemical properties due to their superior high specific strength, good corrosion resistance, and low young's modulus. Furthermore, unlike the other materials, these alloys are completely inert to the body environment. Due to these benefits, titanium and its alloys are the most widely used biomaterials among all metals. On the other hand, titanium alloys tend to wear when in motion against themselves or with other materials [1]. The removal of accessible materials in these alloys raises the coefficient of friction. In the process, the formed wear debris causes pain and implant loosening. Although the normal formation of TiO_2 prevents metal ion release from the matrix into the human body, the TiO_2 surface layer formation of 5–20 nm thickness is insufficient to sustain biological conditions. The surface modification of titanium-based biomaterials is discussed in this chapter.

Over the last fifty years, titanium alloys have been subjected to a variety of modifications. Shot peening [2, 3], alkali treatment [4, 5], thermal spraying [6, 7], and other traditional methods are used. These methods, however, have limited properties and some geometry complications. Friction stir processing [6], ion implantation [7], electron beam treatment [8], laser shock peening [9], sol–gel [10], physical vapor deposition [11], chemical vapor deposition [12], selective laser melting [13], and other advanced surface modification methods effectively improved the surface properties of the titanium alloy. Each of these surface modification techniques had a distinct effect on the surface of titanium alloy. So, the choice of the modification method mainly depends on specific operating conditions and the required application of the material being used.

Lightweight structural materials are increasing, particularly in the aerospace, electronics, and automotive industries [14–16]. In addition, there is a broad scope for developing low-density titanium alloys, particularly for the aerospace sector. According to recent research, magnesium hydrides are promising materials for industrial applications because they store hydrogen in the solid form [16]. Titanium alloys combined with materials such as Mg and Al produce good results. Because of their compatible physical and mechanical properties, Mg alloys distinguished themselves from other materials, particularly biomedical applications. Furthermore, the rapid development of Mg parts in the biomedical sector influences commercial parts to be introduced directly to the market, which may be possible in the near future. The addition of magnesium to titanium alloy reduces density while increasing modulus and strength three to five times [17]. Other research has shown that adding Sr and Mg to titanium alloys improves their mechanical and biological properties [18]. Metallic biomaterials like 316 L stainless steel, Ti–6Al–4V, and Co–Cr alloys are commonly used. Titanium alloys were discovered to be effective in biomedical applications among these alloys. However, due to their higher elastic modulus than bone, pure Ti and Ti–6Al–4V cause stress shielding issues.

2   Potential Applications on Surface Engineered Titanium Alloys

2.1   Biomedical

Before World War II, titanium was used in medical, dental, and surgical devices due to the aerospace and military industry demand. Titanium alloys have a lower modulus, superior biocompatibility, and superior corrosion resistance when compared to stainless steel and cobalt-based alloys. These titanium alloy properties are the driving force behind the early introduction of alloys such as (cpTi) and +(Ti–6Al–4V) and other orthopedic metastable titanium alloys. The biomedical applications can be classified based on their biomedical functionalities. Accidents, aging, and other factors frequently cause hard tissue damage. Hard tissues are typically replaced surgically with artificial implants. Titanium alloys can be used as artificial bones, joints, and dental implants in these applications. Because of the low elastic modulus, it produces significantly less stress yielding. The most common application is hip replacement, in which titanium alloys are used as artificial hip joints, which include an articulating bearing and a stem. Titanium alloys are also commonly used in dental implants, which are classified as subperiosteal, transosteal, or endosseous based on position and shape. Transosteal implants are widely used in the lower frontal jaw, whereas endosseous implants can be used in upper and lower jaws. The best solution is to anchor the prosthesis directly to the bone, which improves future developments. Compared with cementing, direct cementless anchoring of the prosthesis through osseointegration is a more recent technique.

Wear occurs due to the mixed lubrication regime used in artificial joints. During the motions of artificial hip joints, billions of microscopic particles are produced. Foreign body reactions may occur due to these trapped particles in the tissues [19]. To avoid adverse reactions in the body, it is preferable to use a bio-inert material that is stable in the human body and does not react with body fluids or tissues. Bioactive materials such as hydroxyapatite and bioactive glasses are preferred to improve bonding between implants and bone tissues. These materials can bond to living bones without forming fibrous tissues. Titanium has better bio-inert properties due to its native surface oxides. Even so, it is difficult to achieve good bonding in the early stages of implantation in order to create new bones. Hence, titanium and its alloys cannot be considered ideal materials. The current trend is to use surface modification techniques due to the ever-increasing clinical demands. Titanium alloys can be used in cardiac and cardiovascular applications because of their unique properties. Titanium alloys can be used in artificial hearts, prosthetic heart valves, and circulatory devices. Shape-memory nickel-titanium alloys have recently been used in stents, occlusion coils, and intravascular devices. Metals in prosthetic heat are typically coated with a carbon film to improve blood compatibility. Because of the shape memory effects, nickel-titanium was the most commonly used material for vascular tents. Titanium and its alloys are frequently used in osteosynthesis, in addition to artificial bones and

joints. These materials can be used to repair bone fractures. Bone screws, maxillofacial implants, and bone plates are common osteosynthesis implants. By depositing thermal spray coatings, osteointegration would improve, aiding in reducing relative motions. When selecting materials for a specific biomedical application, bulk properties such as non-toxicity, modulus of elasticity, non-toxicity, and fatigue strength must be considered. The material surface is critical in responding to biological and artificial material surfaces to their environments. Normal manufacturing methods in titanium implants can result in an oxidized and contaminated surface layer that is frequently stressed and plastically deformed. Another important reason for the surface modification of titanium alloys is that the specific surface properties are different from the bulk material often required. The surface modification techniques retain bulk attributes of the titanium and its alloys and improve the specific surface properties like modulus, fatigue strength, and machinability for various clinical applications.

The primary surface chemical treatments are typically performed with acid, alkali, H_2O_2, and heat treatment and are based on chemical reactions at the interface between titanium and the solution. The sol–gel method is also widely used to deposit thin ceramic coatings on titanium alloy substrates. Compared to traditional thin film processes, the sol–gel process allows for greater control over the chemical composition, microstructure of the coating, and homogeneous films. Furthermore, these precursors can be combined at the molecular level. The uniform mixing allows for a high degree of homogeneity in the films. The microstructure of the resulting sol–gel films is primarily determined by the relative rates of condensation and evaporation. Coatings such as titanium oxide (TiO_2), calcium phosphate (CaP), and TiO_2–CaP have recently been prepared on titanium alloys for various biomedical applications. The sol–gel technique also applies some silica-based coatings to titanium alloys. Also, for optical, electrical, and catalytic fields, titania coatings are typically synthesized using the sol–gel process [20, 21]. The experiments revealed that titania-rich Ti–OH groups aid in the formation of calcium phosphate. This formation also contributed to improved bone bonding. The sol–gel titania could also aid in the osteogenesis of bone precursor cells [22]. Similarly, calcium phosphate coatings, particularly hydroxyapatite (HA), are widely used in orthopedic applications. Kim et al. observed that HA and FHA coated Ti substrates had higher ALP expression levels than pure Ti, indicating improved cell activity and functionality [23]. Titania/hydroxyapatite sol–gel synthesized are typically bioactive but poorly adhesion to the titanium substrate. TiO_2 coatings, on the other hand, exhibit good bonding with the titanium substrate but less bioactivity than hydroxyapatite coating. Titania/hydroxyapatite coatings can be created to provide both bioactivity and adhesion. Ramires et al. investigated the biocompatibility of titania/hydroxyapatite coatings prepared by sol–gel. TiO_2/HA coatings are bioactive because they promote calcium and phosphate precipitation, which improves interaction with osteoblastic cells. Recently, many researchers have investigated bone-like apatite formation with silica gel coating. Hench et al. found that the Si–OH groups in the coating were sufficient to attract Cao and P_2O_5 from the body fluids for better nucleation and growth of the apatite layer. Earlier, diamond films were deposited using CVD at pressures lower than 1 atm. Diamond CVD films have a high potential in the biomedical field due to superior properties such as high

hardness, low friction coefficient, and fracture toughness. However, due to the high thermal expansion mismatch, poor adhesion to the substrate can be observed even without any surface treatment. Stress values can be reduced by 2 Gpa by grit blasting the titanium substrate. On the TiC buffer layer, Baek et al. deposited a continuous diamond film. The deposition of polycrystalline diamond films on titanium substrates improved tribological performance [24]. Ianno et al. used PECVD and PACVD to deposit DLC coatings on titanium alloy to use hip and knee prostheses. The adhesion strength obtained from the PACVD coating was much lower than that obtained from DC magnetron sputtering [25]. Biochemical modification techniques such as silanized titania, photochemistry, self-assembled monomers, and protein immobilization are introduced for titanium and its alloys. Self-assembled monolayers (SAMs) have emerged as a critical research technique for creating surfaces with well-defined chemical compositions. Self-assembled monolayers of phosphonates or alkane phosphates have been used in recent studies to improve the surface's physicochemical properties. SAMs are typically used as model surfaces for biological assays such as cell-surface interaction and spontaneous mineralization caused by contact with simulated body fluid. Some surface modification techniques, such as physical vapor deposition and thermal spraying, do not involve chemical reactions. In this case, kinetic, thermal, and electrical energy will be used to create a modified layer or coating on titanium and its alloys. Previous research found that plasma-sprayed HA coating could form a strong connection with bone tissue in a short period. In addition, high residual stress developed at the interface due to the greater thermal mismatch between the titanium and the coating. Several studies [26–31] developed HA coatings using the plasma spraying technique. HA coatings also degrade quickly in a biological environment, resulting in coating disintegration. The amorphous and metastable compounds are more soluble than the HA coating, but due to excessive dissolution, these compounds over-mast. It may affect the long-term reliability of the implants. In 1985, the first clinical trials were reported. With bone apposition, most components become stable in 3 months. Similarly, plasma-sprayed calcium silicate coatings are biocompatible. The bioactivity of the $CaO–SiO_2$ coating components was very high in the study. The bioactive glass retains its amorphous properties and its behavior in a hydrolytic environment. Titanium coatings sprayed with plasma typically have porous structures. Coated implants are also used in the knee, hip, root, and shoulder. The formation of apatite on the coating surface can be used to assess bioactivity or bone conductivity. Plasma-sprayed titanium coatings may also show promise in the tooth root, hip, shoulder, and knee implants. Recently, ion plating processes like plasma immersion ion plating and arc ion plating were used to deposit hard films such as BN, TiC, and TiN on titanium substrates for dental applications. The ion implantations such as oxygen, nitrogen, carbon, and metal ion implantation showed good bioactivity.

2.2 *Aerospace*

Nowadays, there is a greater demand for efficient and cost-effective commercial transportation. Material characteristics such as low weight and improved performance are critical. Titanium alloys are becoming increasingly crucial in proposed applications and missions like supersonic transport operating at Mach 2 or higher speeds. The main difficulties arise when dealing with the degradation properties of titanium alloys. Each class of titanium alloy has unique material properties and is helpful for a specific application. Understanding the benefits and drawbacks of particular titanium alloys is critical for maximizing structural and operational efficiency. Various types of and titanium alloys can be used for aircraft structures.

In comparison, α-β alloys can be effective with fewer effects of temperature rise than the β alloys. Titanium alloy material chemistry has improved in recent decades, resulting in improved material performance. Furthermore, material performance development for emerging high-speed aircraft is a new concept. In some studies developed by Boeing defense, two titanium sheets were the first laser welded in the appropriate pattern. With partial penetration welding, the third sheet was attached to the top. The total pack is then kept in a sandwich configuration tool, resulting in a triangular cell structure. Laser welding has been widely used to create three and four-sheet processes for efficient applications. The main advantage of laser welding is that it can be easily programmed to create weld patterns in core geometries. Most titanium alloys can be formed into core sandwich structures using superplastic forming. The candidates designed are primarily used in aircraft applications. The main two processes, resistance welding/superplastic forming/diffusion bonding and laser welding/superplastic forming/diffusion bonding were typically used to fabricate the truss core test panels.

Some issues must be considered to meet the aviation industry's current and future framework conditions, such as technological developments, innovative materials, design, and the effective new fabrication process. Recently, additive manufacturing has emerged as a viable option for producing components with innovative designs and optimal geometries. Based on CAD data input, the SLM process can be used to create complex structures. These titanium alloy lightweight structures can improve efficiency by lowering aircraft fuel consumption and gas emissions [32]. Continuous quality improvement in microstructure and post-processing of parts is critical for the aerospace industry to progress and meet upcoming requirements. Due to the lower thermal expansion like other composite materials and superior corrosion resistance, titanium alloys can be extensively used in aerospace applications.

Recently, titanium alloys such as Ti–6Al–4V, Ti–3Al–8V–6Cr–4Mo–4Zr, Ti–15Mo–2.7Nb–3Al–0.2Si, Ti–10V–2Fe–3Al, Ti–5.0Al–5.5Mo–2Cr–1Ni–0.1Mo, Ti–5Al–2Sn, Ti–6Al–2Sn–2Zr–2Cr–2Mo–(Si), Ti–6Al–2Sn–4Zr–2Mo–0.08Si, Ti–4Al–4Mo–2Sn–0.5Sn, Ti–15Mo–2.7Nb–3Al–0.2Si, Ti–4.5Fe–6.8Mo–1.6Al, Ti–4.5Al–2Fe–2Mo–3V, Ti–6Al–1.7Fe–0.1Si–4Mo–2Zr–2Cr–1Fe were used in airframe structures. Furthermore, several surface modification techniques were used on these titanium alloys to improve their performance levels in terms of wear and

corrosion. Significant progress has been made in developing surface chemistry that improves material performance significantly over commercial titanium alloys.

2.3   Automotive Applications

The demand for environmentally friendly and fuel-efficient vehicles has grown. Titanium alloys were used to improve the performance of many applications due to their low modulus and excellent resistance to corrosion and oxidation. Titanium alloys are used in a variety of automotive applications, including valve springs, exhaust systems, steering gear, valve retainers, suspension linkages, rocker arms, torsion bars, gudgeon pins, Suspension springs, wheels, cam belt wheels, connecting rods, high strength fasteners, bumper supports, gearbox housings, and so on. One of the significant challenges that today's design engineers face is reducing the weight of motor vehicles and private cars. The obvious challenge is to reduce the weight of the car without sacrificing space. The weight reduction also minimizes the fuel consumption contributes to the 'green' image of the manufacturer. It was discovered that a 1% reduction in vehicle weight is claimed to reduce fuel consumption by 0.7%. Furthermore, reducing the weight of the engine's moving parts would be more beneficial and effective in achieving fuel economy than reducing body weight.

On the other hand, titanium alloys have a density that is 60% that of steel and an elastic modulus that is 50% that of steel. To improve performance levels in automotive applications, replacing steel with titanium would be a better option than a weight reduction of 40%. Titanium has higher specific strength, toughness, and fatigue limits than steel and aluminum alloys. Table 1 shows a comparison of titanium alloys with other engineering alloys. The springs made of titanium alloy have high strength, low density, and modulus. Spring made of titanium alloy has a very lightweight, 60–70% lighter than steel. The use of titanium alloys in the suspension springs increases carrying capacity reduces weight and reduces fuel consumption. These will most likely increase operating range and revenue. Because corrosion fatigue is the primary cause of failures in steel suspension springs, replacing them with titanium alloys provides better corrosion resistance even in aggressive conditions. When space is at a premium, the ability to reduce engine size is advantageous. The use of titanium valves in conjunction with valve retainers helps prevent 'valve bounce' at high engine speeds, increasing savings even further. Surface-treated titanium alloys can improve overall performance in valve train applications. Exhaust valves can still be effective for oxidation and creep at high temperatures. Pure titanium sheets and tubes are also preferred for silencers and pipework in exhaust systems. To reduce the weight and cost of the exhaust systems, the thinnest gauges of materials will be chosen while engineering and acoustic requirements are taken into account. On the other hand, titanium alloys may not be suitable for the entire system but are limited to components where the temperature does not exceed 400 °C for an extended period.

Multi-materialization has advanced in recent years, primarily in aircraft and high-end motorcycles. Aircrafts such as the Boeing B787 and Airbus A350, for example,

Table 1 The specific strength of the various engineering alloys

Material	Density (Kg/l)	Young's modulus (GPa)	Yield strength (Mpa)	Specific strength
Aluminum alloy	2.8	70	100–330	35–120
Steel	7.8	200	350–450	45–60
CP-Titanium	4.5	105	250–450	50–100
Ti–6Al–4V	4.4	110	900–1050	200–250

were made up of roughly 50% composite materials, 20% aluminum, 15% titanium, and 10% steel. Titanium has been used three to five times more than in previous generations of aircraft. Because of the increased composite material ratio, titanium's specific strength, corrosion resistance, and thermal expansion coefficient all increased. The titanium alloy outperformed steel in terms of strength, density, shear modulus, and relative weight. Because titanium alloy has high corrosion resistance, no anti-corrosion treatments, coatings, or paints are required. Estimated savings of 2–4% can be achieved by using titanium parts in the engine. Researchers focused primarily on three different areas to improve components' financial and life cycles in the recent past, such as the development of lower cost alloys, low-cost manufacturing methods, and surface treatments to improve wear resistance. Fuel tank weight reduction is also an essential consideration for two-wheeled vehicles. The stabilization and reduction of the vehicle's center of gravity can also affect fuel consumption. Lightweight materials have been introduced instead for surface-treated steel sheets in recent years.

On the other hand, titanium sheets are known to have better deep drawability than carbon steels and aluminum alloys. Furthermore, due to its higher conductivity, heat input for aluminum welding cannot be concentrated. Because the strength of titanium alloy is comparable to that of stainless steel, commercially pure titanium is the best material for two-wheeler fuel tanks. Resistance welding, like steel welding, can be used to make pure titanium fuel tanks. The weight of connecting rods can be reduced to improve engine response and rotation speeds for motorcycles, where temperatures exceed 350 °C, the specific fatigue strength of the connecting rods is significantly higher. Ti–6Al–4V was previously used as the connecting rod for the first time in 1987. Ti–3Al–2.5V-REM-S was later used in the HONDA NSX, a four-wheeler vehicle [33]. Because titanium alloys have lower thermal conductivity than steel, sliding heat accumulates, and titanium alloys react with other metals, causing severe adhesive wear. Surface coatings can be applied using thermal spraying and other arc-assisted surface engineering methods to avoid material removal and resist wear. CrN, NiP, and TiAlN coatings were recently applied to the connecting rods of the YAMAHA YZF-R1 [34]. The young's modulus of titanium alloys is much higher than that of steel, roughly half that of steel. To attain the same rigidity as steel, the connecting rods' thickness needs to be increased.

The reduction of weight by reducing the engine valves leads to improving driving response. Recently, the Ti–5Al–2Fe–3Mo alloy, which is stronger than Ti–6Al–4V

alloy, was used for intake engine valves in motorcycles. Engine intake valves made of Ti–6Al–4V can be used in temperatures from 300 to 400 °C. Nb, Mo, and Si encapsulated titanium alloys can be used because the strength of titanium alloys decreases with temperature. Titanium alloys such as Ti–5.8Al–4sn–3.5Zr–2.8Mo–0.7Nb–0.35Si–0.06C and Ti–7Al–2Mo–0.2Si–0.15C–0.2Nb can also be used in exhaust valves, where high fatigue and creep strength is typically required at high temperatures. Because sliding wear is common in engine valves, coatings with increased oxidation and wear resistance can be used. Surface treatment or modification of titanium alloy is required to improve the wear and fatigue resistance of engine valves made with titanium alloy. Due to weight savings and design considerations, titanium has been used in automobile mufflers. However, the heat resistance of commercial ASTM grade 2 and pure titanium became insufficient due to the high exhaust temperatures.

In addition to heat and oxidation resistance, titanium's press formability at room temperature enables it to be used in exhaust systems. Ti–0.5Si–Fe, Ti–0.1Fe–0.35Si, Ti–1.5Al, Ti–0.5Al–0.45Si–0.2Nb, Ti–1Cu–1Sn–0.35Si–0.2Nb, Ti–1Cu, and Ti–1Cu–0.5Nb are some of the heat resistant titanium alloys developed [35, 36]. The addition of Al, Si, Sn, and Cu improves high-temperature strength. The addition of Nb and Si to the alloy improves oxidation resistance and corrosion resistance at high temperatures. Ti–1Cu, for example, was used in the NISSAN GTR Spec-V, and Ti–0.5Al–0.45Si–0.2Nb was used in the TOYOTA LEXUS LFA. Even when the cost is considered, titanium alloys may be the best choice in some automotive applications. For example, savings can offset high-cost titanium alloys in CAFÉ penalties and fuel economy in valve train components. Automobile manufacturers consider style and performance to be the most important sales factors. In recent years, environmentally conscious customers have prioritized improved safety, lower noise, improved fuel economy, and lower harmful emissions. As the demand for fuel-efficient and environmentally friendly vehicles grows, affordability becomes less consideration. These factors allow for a greater emphasis on corrosion resistance, weight, and fuel consumption. Savings on fuel costs in mass production are estimated to be $2.20, corporate average fuel efficiency (CAFÉ) is in the range of $4.50–$7.70, and vehicle produced with specialty and luxury is estimated to be $8.50.

2.4 Case Studies of Surface Engineered Titanium Alloys for Biomedical, Aerospace, and Automotive Applications

The titanium alloys were widely used in aviation, aerospace, and automotive applications due to their low density and excellent corrosion resistance. However, there are some drawbacks, such as high friction coefficients, low hardness, and poor wear resistance, reducing component life. In addition, replacing the parent material resulted in higher operating costs. The preparation of hard coating on the surface is one of

the effective methods to solve problems of surface hardness, wear, and corrosion resistance to reduce operating costs and increase the service life of the components.

Hatem et al. [37] used plasma-enhanced magnetron sputtering to deposit Ti–Si–C–N nanocomposite coatings. The tribocorrosion and biocompatibility of the coatings were also evaluated. The reciprocal tribocorrosion tests are repeated in PBS solution and compared to untreated titanium alloy. Compared to the titanium alloy, the corrosion resistance of all samples was improved to some extent. Previously, similar corrosion enhancement was observed in TiSiC–Zr and TiSiC–Cr coatings [38]. The deposited Ti–(Si)–C–N composite coatings on titanium alloy demonstrated a 97% reduction in wear rate. Furthermore, the coated samples' tribocorrosion performance is primarily governed by Ti(C)N nanocrystallites in the Si_3N_4 amorphous matrix. Moreover, carbon in the coating acted as a self-lubricant to improve performance levels. The Ti–Si–C–N coating experienced cohesive and adhesive failures. Within the arc tensile cracks, the coating sample has many lateral cracks. Spallation occurs at the Ti(Si)CN film interface and the inter-bonding layer when these cracks overlap critical length.

Bansal et al. [39] used HA/ZnO plasma spray coatings to improve the surface properties and corrosion resistance of Ti13Nb13Zr titanium alloy. Microhardness values gradually increased as ZnO percentage increased. In comparison to other samples, HA + 12% ZnO had the highest hardness. On the other hand, surface roughness was gradually reduced as the ZnO percentage was increased. Furthermore, all coating samples were found to be hydrophilic. The addition of ZnO to pure HA improves the surface properties and corrosion resistance of Ti13Nb13Zr samples. The SEM and EDS analyses show that the HA and ZnO are distributed uniformly in the coating. According to the electrochemical and morphological findings, HA/ZnO coatings may be compatible with bio-implants.

Jiang et al. [40] investigated the biocompatibility of hydroxyapatite coatings that were hydrothermally deposited on titanium alloy. The results show that the prepared HA coating on titanium alloy demonstrated superior corrosion resistance. Furthermore, antibacterial studies yielded promising results and acted as a carrier for antibiotics to inhibit bacterial growth. In vitro studies revealed that the cells grow well on the surface of the sample. The in vitro and in vivo experiments showed that HA coated titanium alloys had promoted better biocompatibility and osteoconductivity. HA coated titanium alloy showed more new bone formations than the uncoated titanium alloy.

Yuan et al. [41] used a duplex treatment (DT) of laser surface texturing (LST) and thermal oxidation (TO) on the Ti–6Al–4V alloy surface to improve mechanical properties and wear performance. TO treatment improved the surface hardness and elastic modulus of the Ti–6Al–4V alloy. According to the specific wear rate results, the untreated Ti–6Al–4V alloy had a higher wear rate than the duplex treated titanium alloy, attributed to the better LST and TO treatments. Because of its higher hardness and elastic modulus, the wear performance of DT–Ti–6Al–4V coating was particularly good. Because of the microstructure transformation, the TO-treated coating performed better. The results show that excellent wear resistance was achieved as a

result of the LST and TO treatments. These modified alloys can be used in aerospace and automotive applications in the future.

Zhao et al. [42] used laser cladding to create TiO_xN_y/Ti composite coatings on Ti–6Al–4V alloy. The effect of laser power was investigated further in order to improve microstructural and mechanical properties. Higher laser power was found to cause thermal cracks and other thermal defects. The phase TiO_xN_y predominated in the clad, resulting in higher microhardness values. At a laser power of 200 W, the highest microhardness value of 1613 HV was obtained, which was 4.7 times higher than the Ti–6Al–4V alloy. The wear results revealed that the composite coating's wear depth and friction coefficient were significantly lower than those of the Ti–6Al–4V alloy. To summarize, to improve the wear performance of the coating, the optimal laser parameters should be carefully chosen.

Lu et al. [43] developed Ni60-hBN composite laser claddings by varying hBN content for high-temperature tribological applications. Clads were found to be metallurgically bonded to the substrate and to have no cracks or pores. The self-lubricating laser clads had an average microhardness three times that of the titanium substrate. Due to the formation of hBN, γ-NiCrAlTi, TiC, and TiB_2 phases, composite coatings exhibited outstanding wear resistance compared to titanium alloy. The wear mechanism of Ni60 coatings was primarily abrasive, whereas solid lubricant encapsulated coatings were a combination of brittle fracture and transfer layer breakdown. The coatings developed above can withstand harsh conditions in automotive and aerospace applications by encapsulating solid lubricants.

3   Future Trends

The above sections highlight the key advancements in surface engineered titanium alloys that can enhance the surface properties for biomedical, automotive, and aerospace applications. Despite the progress, there is significant scope for continued research. The use of numerical simulations and artificial intelligence for parametric sensitivity and optimization is the emerging trend toward increasing the effectiveness of the treatments. Studies on specific conditions such as higher temperature, dynamic loading, oxidation, corrosion, and wear are required to maximize the efficiency under severe conditions. Several surface engineering techniques on titanium alloys have shown promising in vitro results in cytotoxicity and osteogenic differentiation. Similarly, surface-modified titanium alloys have shown better performance in automotive and aerospace applications. Many surface engineering techniques have emerged for modifying titanium alloys in recent years, but they remain unexplored for additively manufactured titanium alloys. The combination of dealloying and additive manufacturing is also an emerging process for the controlled formation of hierarchically porous structures. Hybrid surface treatments could also provide a pathway to explore and concurrently leverage the benefits of individual post-processes. Surface treatments used as in-situ correcting methods, combined with non-destructive testing and advanced analysis, will provide very good near-net-shape geometry.

4 Summary

Titanium alloys provide a unique strength-to-weight ratio, favorable high-temperature mechanical properties, and better corrosion resistance. From the design perspective, titanium alloys offer numerous automotive applications, including lower vehicle weight performance stability. With the surface engineering techniques, the surface properties of titanium alloys can be enhanced, thereby decreasing fuel consumption and CAFÉ penalties. Also, surface modification of titanium alloys can increase the working temperature of titanium alloys without any surface deterioration. The development of surface treatments to engineer the properties of titanium alloy is receiving enormous attention. This chapter presents a detailed review of the recent advancements in this field, especially for titanium alloys for aerospace, automotive, and biomedical applications. Applying surface treatments to the titanium alloys is essential for maximizing clinical outcomes in biomedical and lifetime for various applications in the automotive and aerospace field.

References

1. Miller PD, Holladay JW (1958) Friction and wear properties of titanium. Wear 59:133–140
2. Thomas M, Lindley T, Rugg D et al (2012) The effect of shot peening on the microstructure and properties of a near-alpha titanium alloy following high temperature exposure. Acta Mater 60:5040–5048
3. Chen X, Zhu R, Gao H et al (2020) A high bioactive alkali-treated titanium surface induced by induction heat treatment. Surf Coat Technol 385:125362
4. Pierlot C, Pawlowski L, Bigan M et al (2008) Design of experiments in thermal spraying: a review. Surf Coat Technol 202:4483–4490
5. Urlea V, Brailovski V (2017) Electropolishing and electropolishing-related allowances for powder bed selectively laser-melted Ti-6Al-4V alloy components. J Mater Process Technol 242:1–11
6. Farias A, Batalha GF, Prados EF et al (2013) Tool wear evaluations in friction stir processing of commercial titanium Ti-6Al-4V. Wear 302:1327–1333
7. Poltavtseva VP, Ghyngazov SA, Satpaev DA (2012) The influence of high-energy krypton ion implantation temperature on structure and properties of Ni–Ti alloy. Russ Phys J 61:2012–2018
8. Zaguliaev D, Gromov V, Rubannikova Y et al (2020) Structure and phase states modification of AL-11SI-2CU alloy processed by ion-plasma jet and pulsed electron beam. Surf Coat Technol 383:125246
9. Okipnyi IB, Maruschak PO, Zakiev VI et al (2014) Fracture mechanism analysis of the heat-resistant steel 15Kh2MFA(II) after laser shock-wave processing. J Fail Anal Prev 14:668–674
10. Wu LK, Wu JJ, Wu WY et al (2020) Sol–gel-based coatings for oxidation protection of TiAl alloys. J Mater Sci 55:6330–6351
11. Hussein M, Adesina A, Kumar M et al (2019) Investigations of in vitro corrosion, and wear properties of TiN PVD coating on Ti6Al4V alloy for dental application. Key Eng Mater 813:1–6
12. Grenadyorov AS, Solovyev OKV et al (2020) Modifying the surface of a titanium alloy with an electron beam and a-C:H:SiOx coating deposition to reduce hemolysis in cardiac assist devices. Surf Coat Technol 381:125113
13. Konovalov S, Osintsev K, Golubeva A et al (2020) Surface modification of Ti-based alloy by selective laser melting of Ni-based superalloy powder. Integr Med Res 9:8796–8807

14. Matli PR, Krishnan AV, Manakari V et al (2020) A new method to lightweight and improve strength to weight ratio of magnesium by creating a controlled defect. J Mater Res Technol 9:3664

15. Basheer AA (2020) Advances in the smart materials applications in the aerospace industries. Aircraft Eng Aero Technol 92:1027e35

16. Malahayati M, Yufita E, Ismail I et al (2021) Hydrogen desorption properties of $MgH_2 + 10$ wt% $SiO_2 + 5$wt% Ni prepared by planetary ball milling. Bull Chem React Eng Catal 16:280e5

17. Salleh EM, Ramakrishnan S, Hussein Z (2016) Development of biodegradable Mg-Ti alloy synthesized using mechanical alloying. Adv Mater Res 1133:75e9

18. Berglund IS, Brar HS, Dolgova N et al (2012) Synthesis and characterization of Mg-Ca-Sr alloys for biodegradable orthopedic implant applications. J Biomed Mater Res B Appl Biomater 100:1524e34

19. Howie DW (1990) Implant-bone interface. Springer, London

20. Samuneva B, Kozhukharov V, Trapalis C et al (1993) Sol-gel processing of titanium containing thin coatings. J Mater Sci 28:2353

21. Trapalis C, Kozhukharov V, Samuneva B, Stefanov P (1993) J Mater Sci 28:1276

22. Dieudonne SC, van den Dolder J, de Ruijter JE et al (2002) Osteoblast differentiation of bone marrow stromal cells cultured on silica gel and sol-gel-derived titania. Biomaterials 23:304

23. Kim HW, Kim HE, Knowlesb JC et al (2004) Hydroxyapatite/poly (ε-caprolactone) composite coatings on hydroxyapatite porous bone scaffold for drug delivery. Biomaterials 25:3351

24. Baek SH, Choi Y, Choi W (2015) Large-area growth of uniform single layer MoS2 thin films by chemical vapor deposition. Nano res lett 10:388

25. Ianno NJ, Dillon RO, Ali A (1995) Deposition of diamond-like carbon on a titanium biomedical alloy. Thin Solid Films 270:275

26. Khor KA, Yip CS, Cheang P (1997) Ti-6Al-4V/hydroxyapatite composite coatings prepared by thermal spray techniques. J Therm Spray Technol 6:109

27. Chang E, Chang WJ, Wang BC et al (1997) Plasma spraying of zirconia-reinforced hydroxyapatite composite coatings on titanium: part I phase, microstructure and bonding strength. J Mater Sci Mater Med 8:193–200

28. Khor KA, Cheang P, Wang Y (1998) Plasma spraying of combustion flame spheroidized hydroxyapatite (HA) powders. Therm Spray Technol 7:254

29. Silva PL, Santos JD, Monteriro FJ et al (1998) Adhesion andmicrostructural characterization of plasma-sprayed hydroxy-apatite/glass ceramic coatins onto Ti-6Al-4V substrates. Surf Coat Technol 102:191–196

30. Wang Y, Khor KA, Cheang P (1998) Thermal spraying of functionally graded calcium phosphate coatings for biomedical implants. J Therm Spray Technol 7:50

31. Tsui YC, Doyle C, Clyne TW (1998) Plasma sprayed hydroxyapatite coatings on titanium substrates. Part 1: mechanical properties and residual stress levels. Biomaterials 19:2015

32. Uhlmann E, Kersting R, Borsoi T (2015) Additive manufacturing of titanium alloy for aircraft components. Procedia CIRP 35:55–60

33. Matsubara T, Sato Y, Kimura K et al (1991) HONDA R&D Tech Rev 3:12–26

34. Kubota T, Takahashi K (2018) Bull Iron Steel Inst Jpn 23:585–590

35. Wagner L, Schauerte O (2007) Ti-2007 science and technology. Jpn Inst Metals:1371–1378

36. Kosaka Y, Fox SP, Faller K (2007) Ti-2007 science and technology. Jpn Inst Metals:1383–1386

37. Hatem A, Lin J, Wei R et al (2018) Tribocorrosion behavior of low friction TiSiCN nanocomposite coatings deposited on titanium alloy for biomedical applications. Surf Coatings Technol 347:1–12

38. Schroeder V, Gilbert CJ, Ritchie RO (1998) Comparison of the corrosion behavior of a bulk amorphous metal, Zr41.2Ti13.8Cu12.5Ni10Be 22.5, with its crystallized form. Scr Mater 38:1481–1485

39. Bansal P, Singh G, Sidhu HS (2021) Improvement of surface properties and corrosion resistance of Ti13Nb13Zr titanium alloy by plasma-sprayed HA/ZnO coatings for biomedical applications. Mater Chem Phys 257:123738

40. Jiang J, Han G, Zheng X et al (2019) Characterization and biocompatibility study of hydroxyapatite coating on the surface of titanium alloy. Surf Coatings Technol 375:645–651
41. Yuan S, Lin N, Zou J et al (2020) In-situ fabrication of gradient titanium oxide ceramic coating on laser surface textured Ti6Al4V alloy with improved mechanical property and wear performance. Vacuum 176:109327
42. Zhao Y, Lu M, Fan Z et al (2020) Laser deposition of wear-resistant titanium oxynitride/titanium composite coatings on Ti-6Al-4V alloy. Appl Surf Sci 531:147212
43. Lu XL, Liu XB, Yu PC et al (2016) Synthesis and characterization of Ni60-hBN high temperature self-lubricating anti-wear composite coatings on Ti6Al4V alloy by laser cladding. Opt Laser Technol 78:87–94

Liquid State Processing and Solid State Welding of Lightweight Alloys

Chapter 6
Solid-State Welding of Aluminium Alloys

Kirubanidhi Jebabalan and Milon Selvam Dennison

1 Introduction

Since the dawn of human civilization, materials have been the backbone of human society and the initial period of human evolution has been denoted only by materials, e.g. stone age, bronze age, copper age, iron age, etc. At present due to the digital revolution, we call it as silicon age. In the seventeenth century, industrial revolution led to the discovery and application of various metals, and these metals had to be joined for a variety of applications leading to the revival of metal joining techniques popularly known as welding. Metal joining techniques have been practised since time immemorial and the historical records have stated that the Greeks have used welding in the fifth century. This technique had proper entry into the manufacturing sector only in 1801 when Sir Humphry Davy discovered the short-pulse electrical arc. After this discovery, there had been serious inventions by various scientists, but the demand for welded products had a surge during World War 1 as various nations needed a variety of products for various applications as the demand for reliable high-performing structure components was the need of the hour.

These joining techniques are classified as fusion welding, soldering, brazing, adhesion bonding, and solid-state welding. Amongst these processes, our interest lies in the most recently developed solid-state welding technique in that we will discuss a process known as friction stir welding (FSW). The classification of the metal joining process is shown in Fig. 1. In this subsection, we will see why and how

K. Jebabalan (✉)
Department of Mechanical Engineering, Division of Materials Technology, Technical University of Liberec, Liberec, Czech Republic
e-mail: kiruprod@gmail.com

M. S. Dennison
Department of Mechanical Engineering, Kampala International University, Western Campus, Kampala, Uganda
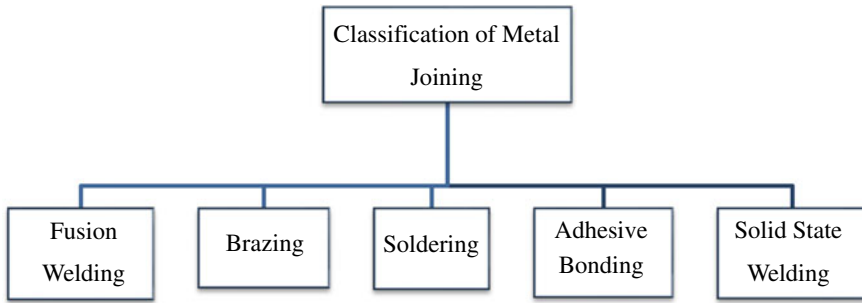
Fig. 1 Classification of metal joining process

FSW developed what is the shortcoming in the conventional fusion welding process when applied to aluminium alloys and the science behind it.

FSW was developed and patented by The Welding Institute (TWI) in the year 1991 a process that has proved to be energy efficient, environmentally friendly and dubbed green technology these characteristics made it attractive in the following sectors automotive, aerospace, shipbuilding and electronic industry [1]. It is a combination of frictional heating and mechanical deformation caused due to the rotating tool therefore it is a thermo-mechanical process [2].

2 Why Friction Stir Welding (FSW)?

High-strength Aluminium alloys belonging to 2XXX, 6XXX, 7XXX series finds its application in aerospace components such as fuselages, wing structures these were difficult to weld using conventional fusion welding process [2].

These alloys are non-weldable in the fusion welding process due to defects like the formation of brittle phase, solidification cracking, liquidation cracking, uneven heating and cooling leading to stress build-up and porosity in the fusion zone leads to the decrease in mechanical properties. Due to these degradative actions, conventional fusion welding is least preferable, but there are exceptions, such as resistance spot-welding, but the surface preparation is quite expensive with the formation of aluminium oxide being a major deterrent [2].

2.1 Tool

In FSW, the process of metal joining is made very simple by moving a non-consumable tool moving across the butt joint the function of the tool is to heat the workpiece and to move/throw the material as the tool moves forward to produce the joint [2]. The tool is mostly cylindrical in geometry and has a tapered pin at
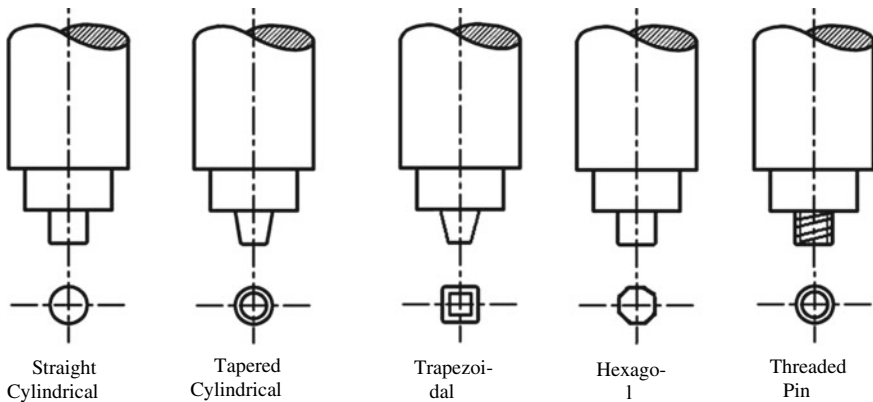
| Straight
Cylindrical | Tapered
Cylindrical | Trapezoi-
dal | Hexago-
l | Threaded
Pin |

Fig. 2 Various geometry of FSW tools

the bottom. The major design specification here is the (D/d) ratio where the tool shoulder (D) and the pin diameter (d) should be in the ratio of 3:1 and the length of the pin should not exceed the plate thickness. For example, if the plate thickness is 5 mm the pin length should be 4.7 mm [3] the tool material used for FSW of Al alloys are tool steels which are denoted usually by H13 these tool steels possesses high-temperature strength, toughness and can withstand high temperatures. Since Al alloys have an operating temperature between (400 °C–500 °C) tools steels with tempering temperatures above 500 °C will be an ideal choice [2]. With the effect of high temperature coupled with extreme levels of plastic deformation (due to the flow of materials around the tool) a significant grain refinement takes place due to dynamic re-crystallization Mishra et al. [2] tabulated the grain size of FSW aluminium alloys and observed that they vary in the range of 1–20 μm. The various geometry of FSW tools is shown in Fig. 2.

2.2 Process

To describe the process in a bit more detailed manner the cylindrical shouldered tool with a pin profile is inserted into the joint and it moves across the workpiece. The workpieces to be welded are held by a pair of clamps placed below the weld line as the tool moves it causes heat the heat is generated due to friction caused due to the relative motion between the tool and workpiece this leads to the temperature rise as a result the metal below the tool comes to a plasticized state neither solid nor liquid the localized heating results in softening the material around the pin until here the first objective of the tool is meet now to second part the combination of tool rotation and translation leads to movement of material from the front end of the pin to the back of the pin resulting in the formation of the joint since there is no melting involved as in fusion welding this process is known as solid-state welding.

Fig. 3 AA6061 base alloy at
500×
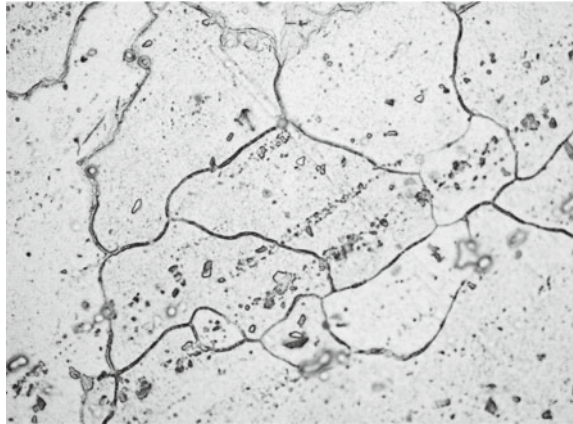
2.3 Microstructure and Grain Formation

The microstructure is a small-scale structure/cluster of atoms in a metal, ceramic, polymer, or composite that determines the physical property of the materials such as toughness, wear, and corrosion resistance. These structures can be viewed only with the help of an electron microscope having 25× magnification. When any material is subjected to welding, there will be significant microstructural changes that will reflect in determining the strength of the weld joint [2]. In early 2000, a technology for microstructural modification based on the fundamental principle of FSW was developed by Prof R. S. Mishra known as friction stir processing (FSP) [2].

During the FSW process, due to elevated temperature, the material undergoes intense plastic deformation and this results in the formation of fine equiaxed recrystallized grains [4, 5]. Grains are defined as the orientation of atoms, and the line separating the orientation is known as grain boundaries [2].

When FS is welded, and components are viewed under the microscope, we see fine grains which in turn produce sound mechanical properties. At this junction, our readers have to understand the relationship between the microstructure, grain, grain boundary and mechanical property. In any welding process, the properties and performance of the weld are determined by these features in a microstructure [2]. For the understanding purpose, the microstructure of the base material AA6061 is shown in Fig. 3, and the microstructure of FS welded AA6061 is shown in Fig. 4.

2.4 Process Parameters

The next stage for the readers to understand the FSW process parameters as it is crucial to produce sound and defect-free weld as well as in microstructure formation for any manufacturing process. The parameters play an important role the following

Fig. 4 Microstructure of welded AA6061 at 500×
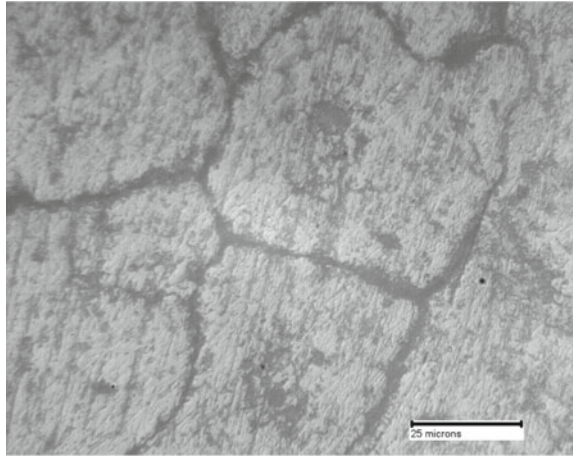
Table 1 Process variables of FSW

Tool design variables	Machine variables	Other variables
Shoulder diameter	Welding speed	Workpiece dimension
Pin diameter	Axial load	Work piece properties
Pin length	Spindle speed/rotation	Formation of oxides
Tool material	Angle of tilt	

are the parameters axial load (kN), tilt angle (deg), tool rotation speed (rpm) and tool traverse rate (mm/min) for the process to get completed. We need to follow a certain operational sequence in the joining process there are four phases. The selection of process parameters is very critical for getting the best possible microstructure leading to welds that are free from defects and other detrimental features. The process variables of FSW are given in Table 1 to enhance a better understanding of our readers [6].

2.5 The Sequence of Operations

The main objective of this introduction is to make our readers aware that there is a solid-state welding process, and it is the most significant metal joining process of the 20th century as we go through the various topics to be discussed, we will try to unravel the science behind the process in a general manner and more particularly about how aluminium alloys have responded to this state-of-the-art process (Fig. 5).
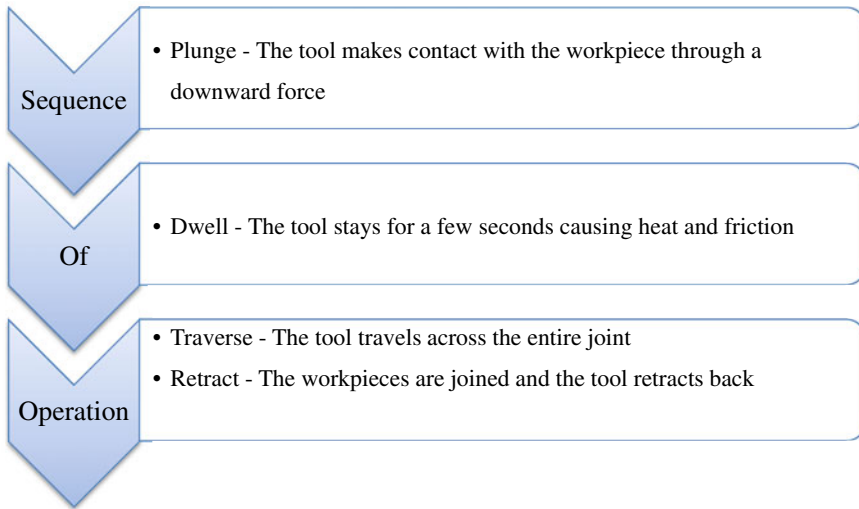
Fig. 5 Sequence of operation

2.6 Aluminium Alloys—Solid-State Welding

Before the readers, goes into the depth of understanding about Al alloys they have to know the metallurgical differences in weld zones. In fusion welding, we have two distinct zones one is the fusion zone and another is the heat affected zone (HAZ) but in FS welded joints there are three distinct microstructural zones known as weld nugget zone also known as the stirred zone, thermo-mechanically affected zone (TMAZ) and heat affected zone (HAZ) [7].

2.7 Welding Zones in FSW

Threadgill in 1997 made the first attempt to classify FSW microstructures His attempts were focussed only on Al alloys but were limited to features that were only visible by light electron microscopy. This was soon replaced in 2001 by American Welding Society Standard D17/3M [8]. These microstructural terms are defined below:

- *Parent material*: Material in the weld, which has not been affected by the weld thermal cycle there are no visible changes in microstructure or properties.
- *Heat Affected Zone (HAZ)*: In this zone, there is a significant modification of the microstructure and properties of the material but there is no significant plastic deformation.

- *Thermomechanically Affected Zone (TMAZ)*: This zone is a distinct region when compared to the fusion welding process because here the material has been plastically deformed due to the tool and subsequent heat generated. In the case of aluminium, the plastic strain will be generated without undergoing dynamic recrystallization. When observed under an electron microscope, we can see a distinct boundary between the dynamically recrystallized zone and the deformed zone [8].
- *Weld Nugget/ nugget zone*: The centre of the weld is referred to as the nugget zone dynamic recrystallization (grain refinement) takes place resulting in the formation of finer grain which is less than 4 μm resulting in the superior mechanical property as we move from the weld nugget towards the HAZ we can see an increase in grain size [2, 8]. Nugget zone can be classified into two types basin shape and elliptical nugget, basin shape nugget zone is formed due to lower tool rotation speed (300–500 rpm), whereas elliptical nugget zone is formed for tool rotation for higher speeds (> 700 rpm).

These microstructural zones are considered individual entities and exhibit characteristics like grain size, texture, precipitate size and residual stress. Based on the weld zones only the properties of the material are decided as it serves as direct evidence of characteristic material transport phenomena occurring during FSW [2].

Aluminium alloy is one of the most abundant elements present in the earth's crust and the second-highest consumed metal next to ferrous-based alloys due to its superior property like high specific strength, high wear resistance, static strength, thermal diffusivity, etc. due to which it finds its application in various sectors like aerospace, automotive, marine, armour, etc. As we have seen in our previous discussions, the low weldability and formation of oxides make cost-effective fusion-based joining methods inefficient to use the arrival of FSW has transformed this situation making Al alloy joining a much simpler activity [9] till date the predominant focus of FSW has been for welding aluminium alloy both in academia as well as in the area of critical application another factor that makes Al alloys an attractive option is its working temperature the maximum temperature reached during the processing of aluminium is around 500 °C the range of operating temperature lies between 425–500 °C when measured using thermocouple [10]. In this sub topic, there will be a discussion on the FSW of different Al alloys and the microstructural/mechanical/corrosion characteristics of such joints followed by its application across various domains.

3   Commercial Designation of AL alloys

The commercial designation of Al alloys their alloying element and their subsequent effect are tabulated in Table 2 [9].

Initially, FSW was applied on AA2024 and AA7075 alloy, and the results showed that there was a decrease in the tensile strength, but it proved that un-weldable Al

Table 2 Commercial designation of Al alloys

Aluminium grades	Alloying elements	Effect of alloying element
1xxx	Unalloyed 99% Al pure aluminium	Since no alloying element is found no effect is observed
2xxx	The principal alloying element is copper	An increase in strength allows precipitation hardening
3 xxx	The principal alloying element is manganese	Increases strength through solid solution strengthening
4 xxx	The principal alloying element is silicon	Increases strength and ductility
5 xxx	The principal alloying element is magnesium	Increases Strength through solid solution strengthening and also increases work hardening ability
6 xxx	The principal alloying element is magnesium and silicon	Produces precipitation hardening when magnesium combines with silicon
7 xxx	The principal alloying element is magnesium and zinc	Increases strength, enables precipitation hardening, A major defect in stress corrosion
8 xxx	The principal alloying element is lithium	Increases strength and Young's modulus

Table 3 Case studies

Base alloy	Temper designation	Tensile strength (parent material) in MPa	Tensile strength (FS welded) in MPa
2024	T3–Solution heat treated naturally aged	485	432 (89% strength achieved)
7075	T6–Solution heat treated artificially aged	585	468 (80% strength achieved)

alloys can be welded so that is how this technology was introduced to weld Al alloys [9]. The details of the case study are presented in Table 3.

3.1 Microstructure

Microstructure plays an important role in deciding the property of a material it affects all materials, ranging from pure single crystals to complex engineering alloys. It can change, by orders of magnitude, a material's mechanical behaviour (e.g. strength, toughness and hardness ductility), electrochemical effect (e.g. stress corrosion and charging behaviour) and functional properties (e.g. magnetic hysteresis and electrical conductivity). With the distinct microstructural regions/zones present the evolution

of the grains takes place in the nugget zone but each region shows a distinct characterization. It is a well-established fact that a grain refinement mechanism known as dynamic recrystallization takes place in the nugget zone of the joint resulting in finer grain than the parent material grain [2, 7, 9]. This refining of grains is possible due to the action of the tool and specifically, its geometry resulting in producing ultrafine-grained (UFG) microstructure less than 1 μm smaller than the grain difficult is the deformation process and crack propagation [2].

As we have discussed the microstructure zone, we will discuss the recrystallization mechanism there are three major mechanisms discontinuous dynamic recrystallization (DDRX) continuous dynamic recrystallization (CDRX) and geometric dynamic recrystallization (GDRX) [11–13]. Initially, researchers stated that aluminium alloy normally doesn't undergo DDRX, since Al alloys have a high rate of recovery; however, DDRX is found in alloys having grain sizes larger than 0.6 μm [13, 14].

Su et al. [15] investigated the FSW of AA 7050Al-T651 suggested that the CDRX mechanism is responsible for dynamic recrystallization in the nugget zone, but this was proved wrong by two investigators Su et al. [16] and Rhodes et al. [17] in 2003 who investigated AA7075–T76 by the plunge and extract technique and subjected it to rapid cooling and found out that recrystallized grain in the nugget zone is caused by DDRX mechanism for aluminium alloys. Thus, DDRX mechanism is responsible for nanostructure evolution in the nugget zone.

3.2   Mechanical Properties

FSW results in significant microstructural evolution around the nugget zone, TMAZ and HAZ leading to a significant change in mechanical properties when examined post-weld certain properties like ductility, fatigue, strength and fracture toughness are properties, which are examined. Research has also shown that on subjecting FSW samples to tensile tests the mechanical properties are significantly higher than those of MIG and TIG welded ones [11]. A case study on how strength and ductility react to FS welded Al alloy has responded.

3.3   Strength and Ductility

Mahoney et al. [7] investigated FSW AA7075–T651 (T-refers to thermal ageing) the nugget zone was identified from that tensile specimen was machined in two different directions longitudinal and transverse. The longitudinal section contains only fully recrystallized grains from the nugget zone, whereas the transverse section contains grains from all the four weld zones in the Table 4, we will be comparing the tensile strength yield strength across both directions and how it has responded to FSW. The FSW sample was taken and subjected to post-weld thermal ageing treatment heat-treated at 121 °C for 24 hrs

Table 4 Tensile strength of FSW AA7075–T651 (longitudinal cross section)

Conditions	Ultimate tensile strength (MPa)	Yield strength (MPa)	Elongation (%)
Base metal	622	571	14.5
After FSW	525	365	15
Post weld thermal aging	496	455	3.5

Table 5 Tensile strength of FSW AA7075–T651 (transverse cross section)

Conditions	Ultimate tensile strength (MPa)	Yield strength (MPa)	Elongation (%)
Base metal	622	571	14.5
After FSW	468	312	7.5
Post-weld thermal aging	447	312	3.5

Tensile strength across the nugget zone across the longitudinal cross-section FSW AA7075–T651.

Tensile strength across the nugget zone across the transverse cross-section FSW AA7075–T651.

From the Table 5, we can conclude that the samples tested in the longitudinal cross section exhibited a decrease in tensile and yield strength but exhibited an increase in ductility, whereas in the transverse section there has been a decrease in strength and ductility. This proves that there will be an increase in ductility in nugget zone. Factors affecting the Tensile strength of FSW 2024Al-T4 was studied and presented in the proceedings of the first international symposium on FSW. Was studied and presented at the proceedings of the first international symposium on FSW from that study we can conclude that for a constant ratio of tool traverse speed, yield, and ultimate strengths increase with increasing tool rotation rate and ductility also improves [2].

3.4 Corrosion Properties and Corrosion Characteristics

The various microstructural zones will reveal different corrosion resistance for materials under applications; it is therefore very significant to know the corrosion behaviour of the FSW welds and reveal the fundamental mechanisms for corrosion in various FSW alloys across the various zones.

Corrosion studies were studied extensively in recent years to understand the effect of FSW on corrosion and stress corrosion cracking. Pitting and stress corrosion were investigated by Frenkel et al. [18] on AA5454 and its corrosion tests were compared against FSW, base material and gas tungsten arc welded (GTAW) samples the following observation was summarily noted.

Corrosion pits in FSW were found in the HAZ region, whereas in the GTAW process large dendrites inside the fusion zone. When compared to base metal FSW welds showed greater resistance when compared to parent material and GTAW weld. Frenkel et al. [18] stated that FSW weld showed greater resistance consistently next these samples were subjected to stress corrosion cracking through U-bent test the samples were kept in 0.5 M NaCl solution for 20 days and polarized at + 60 mV post the test results showed that FSW, base metal samples did not show signs of stress corrosion cracking, whereas GTAW sample cracked at the same condition. Samples obtained were subjected to another test know as slow strain rate tests (SSRT) in this test the anodically polarized samples of FSW, GTAW welds, the base metal reported a loss in ductility indicating a possible stress corrosion cracking still the loss in ductility for FSWwelds was lower when compared to GTAW welds.

AA2024 a common heat treatable aviation-grade aluminium alloy was investigated by a researcher by Corral et al. [19] he clearly stated that the pitting and stress corrosion cracking resistance of FSW welds was superior to that of the base material. Despite these advantages, high-strength Al alloys do show certain susceptibility towards corrosion researchers Corrals et al. [19], Davenport et al. [20] and Jariyaboon et al. [21] investigated FSW welds in 2024Al-T351 and 7010Al-T651 after welding these samples were subjected to post-weld treatments to improve corrosion resistance the post-weld heat treatment was excimer laser treatment this treatment leads to a remarkable improvement in corrosion resistance of FSW samples leading to higher pitting potential this improvement was due to reduction in the undesirable precipitate, suppressing of intergranular corrosion within HAZ and a change in the grain boundary chemistry.

4 Application of FSW in Al Alloys

Commercial application of FSW has been reported across various sectors in our chapter some selected examples will be discussed to our readers to illustrate the growing appeal of this technology as discussed before the first welded alloys were high-strength Al alloys this acted as a catalyst leading to increased awareness amongst the research community [2] our list is not a comprehensive one rather it is just an illustration of examples that have been implemented using this technology. Readers should be aware that new appear of applications do emerge over some time FSW doesn't restrict the operating temperature range of aluminium alloy with Al alloy finding applications in sectors working at cryogenic temperature (e.g. oxygen tanks and rocket fuel tanks) and to slightly higher temperature applications (e.g. heat exchanger) this technology can be used, users should be aware of a difference here the process doesn't have an operating temperature but the material does have one in case of Al alloys we have to be careful not exceed 500 °C if there an excess it will lead to serious microstructural modifications. Most FS weld joints are butt weld joints with increased frequency in the usage of lap weld and friction stir spot welds being observed [8].

Below we have discussed comprehensively the sectors in which FSW finds its way toward applying itself as an alternative technology.

4.1 Armour

High-strength aluminium alloys due to their combination of strength and extraordinary ballistic performance have been used as armour. UK armed forces used an Al alloy grade known as DEFENSE STANDARD 95-022 aluminium alloy. It was based on AA7017 grade (Al–Mg–Zn), these served as armour plate in the tank for the gunner to mount their guns since the early 70s its thickness varies between 6 mm and 120 mm [22]. These armour alloys were welded using a fusion welding process like MIG welding using Al–Mg fillers. However, over a period the joints experienced stress corrosion failure coupled with liquidation cracking along the grain boundaries of the heat-affected zone [2, 23]. With the invention of FSW these alloys were again welded in 1995 and tested for weld quality and failure analysis FSW performed better against the conventional welding process, since then FSW has been incorporated to increase the speed of welding and the thickness of plates that can be joined [23].

In the US infantry division, the U.S. Marine Corps has used a vehicle known as amphibious assault vehicle (AAV) whose structural members are made up of AA2519-T87 the main structural component known as the hull was welded using a conventional fusing process like gas metal arc welding (GMAW) and gas tungsten arc welding (GTAW), this process produced low ductility due to which the combat vehicles couldn't pass the important ballistic test. To overcome this shortcoming, a company is known as concurrent technologies corporation (CTC) FS welded one-inch-thick AA 2519-T87 alloy and proved that this alloy exhibited a tensile strength of 389 MPa which was 124 MPa than the GMAW process and a 300% increase in ductility theses enhanced features helped it pass the ballistic test with ease [24]. This has been the role of FSW in this sector and T—Refers to thermally aged.

4.2 Aerospace

In the initial years, FSW was implemented to weld aerospace alloys high strength aluminium alloys like 2XXX and 7XXX series this was the classical example of the technique known as technology pull these aluminium alloys are used as structural members in aircraft components like fuselage, wings, etc., thereby leading to producing lightweight components as it reduced the usage of fasteners thereby reducing weight and cost [2]. Reducing rivets by nearly 60–70% has been the major takeaway in this sector [8].

Eclipse aviation an aerospace company pioneered the use of FSW in aircraft structures, using it extensively in the primary structure of Eclipse 500 in the year 1998 in this aircraft nearly 7300 fasteners were replaced by 263 welds [2, 8, 25].

This technology to a greater extent replaced fusion welding process like variable polarity plasma arc (VPPA) which had induced thermal stress. Using FSW Boeing aerospace manufactured rocket fuel tanks for delta II and IV rockets the end users reported zero defects leading to huge cost saving over the previous process. They also reported that the tensile strength improved from 270 to 300 MPa [2, 9, 26]. Large fuel tanks for the space shuttle launch vehicle and military aircraft C-17 Globemaster III are all-welded using the FSW technique by using the same technology the Japanese were able to send the H2B rocket for space exploration [2, 8, 27, 28].

Thus, the role of the FSW joint is using Al alloys in aerospace structure for various explorative activities is comprehensive just a brief explanation with examples is given above.

4.3 Marine

5XXX Aluminium series alloys are used to construct ships as they have to proved to be highly resistive against corrosive attacks. The scandinavian fishermen were the pionerrs in this sectors as they used FS welded freezer panels in their fishing trawlers. Is used as one of the main construction materials in shipbuilding as it has high corrosion resistance to seawater [2, 9]. The first commercial application of FSW in the marine sector was the joining of the 6xxx series which was used as hollow deep freezer panels in fishing trawlers the trendsetters being Scandinavian fishermen [29]. High-speed coast guard boats, fishing boats, and cruise ships have used aluminium alloy 6xxx series as bulkheads and in decks of ships, cruise ship by the name seven seas has extensively used lightweight aluminium superstructures and have been welded by FSW it has replaced MIG welding since MIG welding had defect like blowhole formation and produced cracking defect at HAZ zone due to intergranular corrosion [6, 30]. Japanese engineering conglomerate Mitsui engineering 2004 launched a fast ferry between Tokyo to Ogasawara Island it was at that time known as the world's largest aluminium vessel and it had made extensive use of FSW in its superstructure. Shipbuilding using the FSW process has also been the earliest application in Europe to regularize its process shipbuilding standards were developed by Lloyd's Register of Shipping issued a guideline for approval of FSW. BS EN ISO 151614-2:2005 prefabricated FSW panels in shipbuilding reduced 15% of labour time [6].

4.4 Automotive

The automotive industry extensively uses FSW in manufacturing components like light-alloy wheels, fuel tanks, suspension components engine chassis, tailor welded blanks, car body structures, seat frames, etc. [1]. Since lightweight structures are the need of the hour in this sector high strength low alloy steels are replaced with Al alloys and magnesium alloys [2]. A Norwegian company called SAPA (manufacturer of

extruded aluminium profiles) manufactured a prototype of an engine cradle through FSW to reduce weight in the front end of the car the aluminium component weighed 16 kgs as compared to the 23 kgs of steel [6]. Since 1998 FSW has been used to manufacture structural components in automotive right from tailor blanks indoor panels up to structural components supporting the chassis of sports car variant of Ford slowly a variant of FSW known as friction stir spot welding (FSSW) is now being used in the series production of aluminium automotive components for several automotive companies [1].

4.5 Railways

Passenger rail vehicles are manufactured using, stainless steel or aluminium. The joining technique used is metal inert gas welding (MIG) this process produces high heat which distorts welds [1, 2]. Researchers suggested FSW as an alternative process as it produces low heat input and produces less distortion when coupled with high welding speeds using this technology long weld up to 25 in in length, complex structures with varying thickness up to 12 mm are welded [1].

High-speed aluminium railway coaches were first used by the Japanese rail company shinkansen bullet train using FSW technique using aluminium alloy 6xxx series now the Japanese manufacturer Hitachi has now begun to export FSW trains to Europe [2, 6].

The Japanese railway firms used FSW to build their railway coaches this propeeled other firms like Alstom, CAF, Hsbc Rail etc. to implement this process when they built railway coaches. This was instrumental in transforming FSW from research laboratories into industrial appplication. In railways alone the total lenght of components welded amounts to nearly 3000Kms and in the next decade 2000 new coaches are planned to be built using this process [6].

5 Advantages of FSW

- Since it is a solid-state process defect like hot cracking, porosity, etc., which occurs during the fusion welding process is completely avoided.
- Alloys considered non-weldable could be welded.
- As the process is heavily mechanized, the need for skilled and manual intervention is less required.
- Processing time is greatly reduced when compared to fusion welding as joining can be achieved in a single pass [6].
- Very few variables/parameters are there to be controlled, whereas in fusion welding we have 8–9 parameters that have to be controlled.
- Unlike fusion welding, two clean metal plates can be easily joined in the form of butt or lap joints without worrying about the surface conditions of the plates.

Table 6 Flaws occurring during FS welding

Flaws	Position of flaws	Reasons as to which the flaw happens
Voids	On the advancing side of the nugget zone	The welding speed is too high
Hooking	Advancing side of the TMAZ	Issues in tool design
Root flaw	At the root of the nugget zone	The tool pin has insufficient length
Plate thinning	Retreating side of TMAZ	Issues in tool design
Joint line residue	Interface/joining side of the plate	Improper removal of oxides from the plate

- Lead to the production of defect-free welds, with lower residual stresses and lower distortion these advancements lead to weld low strength Al alloys.

6   Flaws/Limitations in FSW

- There is a certain limitation of FSW it can be seen in a less constructive light in certain circumstances. For example, due to the lack of a filler wire, the process cannot use for making fillet welds [8].
- As the process is heavily mechanized, it cannot be used to make complex weld shapes [11].
- The cost of machines at times is too high making it impossible for everyone to buy.
- The cost of licencing fees is quite exorbitant [6].

  The flaws occurring during FS welding are given below [8] (Table 6).

7   Conclusion Remarks

Prof. Thomas W. Eagar of the Massachusetts Institute of Technology, a pioneer in the field of metal joining had clearly stated that any welding process that is invented is commercialized for mass production even before the scientist and researchers understand the basics of physics and chemistry underlying the joining process this has been true with FSW technology which has only three decades of arriving in the manufacturing scenario has had a lot of takers in the transportation sector e.g. shipbuilding with the commercialization overtaking the research aspect [2].

In this chapter critical issues and processes, and modelling of FSW Al alloys are addressed in detail. However, a few areas are left unaddressed in our research community. These relevant areas whose work has gone unnoticed limitations in the current research and recommendations for future work in the area of FSW for aluminium alloys have been summarized below:

- Few topics like grain growth, recovery, recrystallization, and grain growth, kinetics of grain growth, microstructural stability, thermomechanical simulation have been less explored [9].
- Since this chapter is limited to the exploration of aluminium alloys, our readers should not think FSW doesn't have scope beyond this material. Very hard (concerning density) materials like nickel-based super-alloys, and cobalt-based super-alloys have been less explored by the contemporary researchers [9].
- Al alloys which were once considered to be un-weldable have become weldable using FSW process, thermoplastics and hightemperature materials can also be joined using FSW by developing appropriate tools at a low cost due to which we have very few findings in this area here the research gap would be developing a low-cost tool for high-temperature applications [2].
- Post-weld heat treatment and study of stress corrosion cracking in Al alloys have been less investigated [6].
- The main factor that acts as an obstacle to the growth of FSW for Al alloys is the cost of the machine researchers on machine design can work on this to produce a cost-effective machine [8].
- Analysis of material flow within the weld during FSW is a very complex issue, which has not been studied/researched properly and is still poorly understood.
- Auxiliary energy-assisted methods like adding additional energy sources like a laser (laser-assisted friction stir welding) pre-welding heating sources, etc., have also been less explored these areas of research can be further explored because these drastically reduce mechanical effort thereby enhancing tool life and achieving sustainable manufacturing process [11].
- Theoretical models have to be developed to understand the underlying physics behind the joint formation in FSW by using these models we can optimize welding parameters to suit the required joint characteristics [11].
- The latest development in allied FSW processes like underwater, vibration assisted, laser assisted, electrical current-aided and ultrasonic vibration assisted. FSW has not been studied extensively these processes do provide a serious research gap that researchers can explore [11].
- There has been a lack of work, reported on FSW of recycled Al alloys or Al MMCs [11].

Conflict of Interest The authors confirm that they have no conflict of interest and this article complies with ethical standards prescribed by the scientific community.

Reference

1. https://www.twi-global.com/technical-knowledge/job-knowledge/friction-stir-welding-147. (https://www.twi-global.com/technical-knowledge/published-papers/friction-stir-welding-a-competitive-new-joining-option-for-aluminium-rolling-stock-manufacturers-october-2002)

2. Mishra RS, Ma ZY (2005) Friction stir welding and processing. Materials Sci Eng R Rep 50(1–2):1–78
3. Padmanaban G, Balasubramanian V (2009) Selection of FSW tool pin profile, shoulder diameter and material for joining AZ31B magnesium alloy—an experimental approach. Mater Design 30(7):2647–2656
4. Jata KV, Semiatin SL (2000) Continuous dynamic recrystallization during friction stir welding of high-strength aluminium alloys. Air force research lab wright-Patterson of materials and manufacturing directorate
5. Benavides S, Li Y, Murr LE, Brown D, McClure JC (1999) Taguchi optimization of process parameters in friction stir welding of 6061 aluminium alloy: a review and case study. Scripta Mater 41:809
6. Daniela L, Chen Z (eds) (2009) Friction stir welding: from basics to applications. Elsevier
7. Mahoney MW, Rhodes CG, Flintoff JG, Bingel WH, Spurling RA (1998) Properties of friction-stir-welded 7075 T651 aluminium. Metall Mater Trans A 29(7):1955–1964
8. Threadgill PL, Leonard AJ, Shercliff HR, Withers PJ (2009) Friction stir welding of aluminium alloys. Int Mater Rev 54(2):49–93
9. Rajiv Sharan M, Sarathi De P, Kumar N (2014) Friction stir processing. In: Friction stir welding and processing. Springer, Cham, pp 259–296
10. Reynolds AP, Lockwood WD, Seidel TU (2000) Processing-property correlation in friction stir welds. In: Materials science forum, vol 331. Trans Tech Publications Ltd, pp 1719–1724
11. Christy JV, Mourad AHI, Sherif MM, Shivamurthy B (2021) Review of recent trends in friction stir welding process of aluminium alloys and aluminium metal matrix composites. Trans Nonferr Metals Soc China 31(11):3281–3309
12. Rollett A, Rohrer GS, Humphreys J (2017) Recrystallization and related annealing phenomena. Newnes
13. Sunil, BR (2019) Surface engineering by friction-assisted processes: methods, materials, and applications. CRC Press
14. Bowen AW (1990) Texture development in high strength aluminium alloys. Mater Sci Technol 6(11):1058–1071
15. Su J-Q, Nelson TW, Mishra R, Mahoney M (2003) Microstructural investigation of friction stir welded 7050-T651 aluminium. Acta Materialia 51(3):713–729
16. Su J-Q, Nelson TW, Sterling CJ (2003) A new route to bulk nanocrystalline materials. J Mater Res 18(8):1757–1760
17. Rhodes CG, Mahoney MW, Bingel WH, Calabrese M (2003) Fine-grain evolution in friction-stir processed 7050 aluminium. Scripta Materialia 48(10):1451–1455
18. Frankel GS, Xia Z (1999) Localized corrosion and stress corrosion cracking resistance of friction stir welded aluminium alloy 5454. 55(02)
19. Corral J, Trillo EA, Li Y, Murr LE (2000) Corrosion of friction-stir welded aluminium alloys 2024 and 2195. J Mater Sci Lett 19(23):2117–2122
20. Davenport AJ, Ambat R, Jariyaboon M, Connolly BJ (2004) The corrosion susceptibility of friction stir welds (FSW) in the aerospace. In: Corrosion and protection of light metal alloys: proceedings of the international symposium, vol 2003. The Electrochemical Society, p 403
21. Jariyaboon M, Davenport AJ, Ambat R, Connolly BJ, Williams SW, Price DA (2007) The effect of welding parameters on the corrosion behaviour of friction stir welded AA2024–T351. Corrosion Sci 49(2):877–909
22. https://standards.globalspec.com/std/13498970/DEF%20STAN%2095-022
23. Bassett JC, Birley SS (2000) Proceedings 2nd international symposium on 'friction stir welding'. Gothenburg, Sweden, TWI
24. Colligan KJ, Fisher JJ, Gover JE, Pickens JR (2002) Friction stir welding in the AAAV. Adv Mater Processes 160:39–41
25. Christner B, McCoury J, Higgins S (2003) Development and testing of friction stir welding (FSW) as a joining method for primary aircraft structure. In: Fourth international symposium on friction stir welding, pp 12–14

26. Wang G, Zhao Y, Hao Y (2018) Friction stir welding of high-strength aerospace aluminium alloy and application in rocket tank manufacturing. J Mater Sci Technol 34(1):73–91
27. Du B, Sun Z, Yang X, Cui L, Song J, Zhang Z (2016) Characteristics of friction plug welding to 10 mm thick AA2219-T87 sheet: Weld formation, microstructure and mechanical property. Mater Sci Eng A 654:21–29
28. Nimura K, Akiyama K, Egawa K, Ujino TAKUMI, Sato TOSHIAKI, Oowada YOUICHI (2013) Technologies and prospects of the H-IIB launch vehicle. Mitsubishi Heavy Ind Tech Rev 50(1):63
29. Midling OT, Kvale JS, Dahl O (1999) TWI 1st international symposium on friction stir welding. Thousand Oaks, California, USA, pp 14–16
30. Gesto D, Pintos V, Vazquez J, Rasilla J, Barreras S (2008) TWI seventh international symposium on friction stir welding, May 20–22, 2008. Awaji Island, Japan

Chapter 7
Solid-State Welding of Magnesium Alloys

Arpan Tewary, Chandan Upadhyay, and Rahul Kumar Yadav

1 Introduction

The element magnesium (Mg) is considered to be the sixth most plentiful element on the planet, with a nearly limitless supply in saline water bodies such as the seas and oceans. With an approximate concentration of 0.14%, it is the third most prevalent element dissolved in seas and oceans. Magnesium alloys have seen a nearly 20% yearly rise in industrial output in recent years. Magnesium and its alloys are 40% lighter than aluminum (Al) and 78% lighter than steel as the lightest building material. When compared to other materials, using magnesium alloys results in weight savings of 22 to 70%. Magnesium alloys provide high specific strength, strong sound dampening properties, electromagnetic interference shielding, good castability, hot workability, machinability, and recyclability. Furthermore, because of its large heat capacity, magnesium is difficult to ignite in the air. Based on the following, several drawbacks of magnesium are presented: low elasticity modulus; high solidification shrinkage; high chemical reactivity. Furthermore, at high temperatures, these alloys exhibit low fatigue and creep strength. Magnesium alloys have low ductility and cold workability at ambient temperature owing to their hexagonal close-packed (HCP) crystal assembly.

Alloys of magnesium provide outstanding specific strength, soundproofing capabilities, hot workability, good castability, and recyclability due to their lightweight qualities. Magnesium alloys have reduced strength, fatigue, and creep resistance at

A. Tewary
Central University of Jharkhand, Ranchi, Jharkhand, India

C. Upadhyay
Dr. R. M. L. Avadh University Ayodhya, Uttar Pradesh, Ayodhya, India

R. K. Yadav (✉)
Indian Institute of Technology Indore, Indore, Madhya Pradesh, India
e-mail: getrahul.yadav@gamil.com

increased temperatures due to their hexagonal close-packed (HCP) crystal structure, as well as low stiffness, restricted ductility, and cold workability under ambient conditions. Alloys of magnesium have low hardness, wear resistance, and resistance to corrosion, as well as significant reduction during solidifying and strong chemical reactivity in the molten state.

Alloys of magnesium (Mg) contain other metals such as manganese, zinc, copper aluminum, silicon, zirconium, and other rare earth metals. The hexagonal lattice structure of magnesium alloys affects the basic characteristics of these alloys. Magnesium alloys are primarily utilized as-cast alloys due to the hexagonal lattice's more sophisticated plastic deformation than cubic lattice metals such as aluminum, copper, and steel; however, research on wrought alloys has been increasingly widespread since 2003. Mg casting alloys are utilized for numerous components in current vehicles and have been employed in some high-performance vehicles; magnesium die casting is also used for the fabrication of lens components and camera bodies. Short codes (specified in ASTM B275) that specify approximate chemical content by weight are used to identify magnesium alloys. AS41, for example, contains 4% aluminum (Al) and 1% silicon (Si), while AZ81 contains 7.5% aluminum (Al) and 0.7% zinc (Zn).

In most conditions, these alloys are approximate as corrosion resistant as mild steel although they are not as corrosion resistant as aluminum alloys. As a result of their poor ability for corrosion resistance and ductility, the usage of magnesium alloys has been restricted. To address these issues, new alloys with enhanced corrosion resistance, such as Mg-AZ91D, have been developed. The property profiles required by automobiles and other potential large numbers of magnesium consumers have highlighted the requirement for the development of alloy. Magnesium is an alkaline earth element with abundant availability on the planet's surface. Due to its hexagonal close-packed (HCP) type crystal morphology, magnesium (Mg) has low ductility and machinability at room temperature; its castability is also limited. Magnesium has a lower melting point of roughly 650 °C. As a result, issues relating to creep phenomena are fairly widespread. The inclusion of thorium has been suggested as a viable remedy although there are significant radiation concerns. Rare earth elements, on the other hand, can be employed as alloying elements although their scarcity remains an issue. Furthermore, due to their weak corrosion resistance, Mg alloys have been found to have restricted uses. This is primarily owing to impurities or the second phase.

Despite the associated restrictions and other production challenges, the usage of magnesium alloys is favored by certain industries. Magnesium has a density of 1.738 gcm^{-3}, which is lower than that of high-density materials such as aluminum (2.7 gcm^{-3}) and steel (7.86 gcm^{-3}). Alloys of Mg are also acknowledged for their enhanced specific strength, stiffness, and damping capacity, as well as their ease of recycling and machinability. The current use of magnesium per vehicle in the automotive sector is 2 kg, but by 2030, it is expected to rise to 100 kg. Aerospace, ground transportation, shipbuilding, shipping, civil engineering, electronic components, and biomaterials all employ magnesium alloys. Mg alloys have found usage in nuclear power plants due to their low proclivity for absorbing neutrons, good aversion to carbon dioxide, and excellent thermal conductivity. Magnesium may be alloyed with

other elements to increase its physical and mechanical characteristics; however, the behavior is highly dependent on the composition.

Alloys of Mg are appealing engineering materials for constructing lightweight structures. These alloys have grown in industrial manufacturing faster than any other metal in recent years. Because the majority of magnesium alloy components are created via die casting, the problem of welding Mg alloys has received minimal attention. However, due to their increased ductility and manufacturing flexibility, wrought Mg alloys have recently received interest for lightweight structural applications in the substitution of Mg alloy die castings. This necessitates the creation of appropriate welding methods for Mg alloys including other metals. When Mg alloys are fusion welded with other light metals like aluminum, hazardous intermetallic compounds are formed, the majority of which are brittle. To weld these materials, a solid-state welding method must be utilized. Because the heat-affected zone might be restricted to a very narrow zone, explosion welding, as one of the solid-state welding procedures, is considered to be one of the most effective alternatives for connecting this combination.

Zinc, aluminum, thorium, and rare earth metals make up the majority of commercial magnesium alloys. Aluminum is the major alloying element in the ternary Mg–Al family, which includes the AS (Mg–Al–Si), AZ (Mg–Al–Zn), and AM (Mg–Al–Mn) alloys. The alloys of Mg may be divided into two categories: ambient condition, i.e., room temperature and enhanced temperature. Rare earth metals and thorium (Th) are employed as elements of alloying in high-temperature alloys, whereas aluminum (Al) and zinc (Zn) are used as alloying elements in room-temperature alloys. These magnesium alloys are now identified using the American Society for Testing Materials (ASTMs) standard. The major code for the most significant alloying elements is indicated by the first two letters in sequence. The concentration of the most essential alloying elements is indicated by two numbers after these two letters. The fifth sign is a letter that indicates how the alloy has been modified. This alloy code is sometimes followed by a hardness indication that is comparable to that of aluminum alloys: "H" cold worked, "O" annealed, "F" as manufactured, "T4" solution treatment and natural aging, "T5" artificial aging, and "T6" solution treatment followed by artificial aging welding by the tool's direction of rotation is referred to as the forward side, and welding by the tool's direction of rotation is referred to as the reverse side.

2 Solid-State Welding

Solid-state welding (SSW) is the process of joining two metals without the use of an external source such as heat. On the other hand, the mobility of a stationary constituent relative to a moving constituent generates heat from the contact surfaces. This method is largely motivated by the applied pressure and at any temperature lower than the counter alloy's melting point. The interfacial atoms diffuse to accomplish the bonding. The main advantage of SSW is that it does not have the normal welding defects and porosities that occur with traditional fusion welding processes.

Because little or no heat is applied during welding, any phase shift due to microstructural evolution is insignificant. The welded joints have better surface quality and mechanical properties than the utmost trivial fusion processes.

The major drawback is that it is difficult to attach more than two components at the same time. Since the use of filling materials can be dispensed with, very wide root gaps must also be covered. SSW does not involve melting, and weld appearance is excellent, along with enhanced mechanical qualities at the weld joint. There are several categories of the SSW technique. Examples of this technique are roller welding, ultrasonic welding, forge welding, cold welding, pressure welding, friction stir welding, diffusion welding, friction welding, and explosion welding. The friction stir welding (FSW) is commonly used because this is versatile and can also join a variety of metals.

Metals that are soft and difficult to weld, such as magnesium, aluminum, copper, and zinc, are welded with good mechanical qualities and minimal flaws. Several other solid-state welding approaches like friction welding, explosion welding, and roller welding have also received significant attention, but these come with their own demerits. This embrace inflicts serious injury and pollutes the atmosphere. A brief discussion of the interaction between processing parameters and microstructural properties is provided. The progression of microstructural properties like grain sizes across specific zones is used to explain relevant mechanical properties. This is done to determine the appropriateness of the product for a precise application of engineering. SSW is a process of welding that joins two workpieces at a pressure that ensures intimate contact and at a temperature significantly below the melting point of the base material, without the use of brazing alloy. The materials combine through the proliferation of their contact atoms.

Advantages

- No structural defects in the weld (bond) (precipitation of alloying elements, non-metallic inclusions, and pores).
- The weld's mechanical characteristics are alike to those of the base metals.
- Additives materials like fluxes and protective gases are not required.
- Foreign metals are joined (steel—copper alloy and steel—aluminum alloy).
- Metallurgical purity is maintained, and liquid phases are eliminated.

Disadvantages

- Intensive surface planning such as oxide repulsion, brushing or sanding, and degreasing is needed.
- The equipment is significantly costly.
- Non-destructive inspection and joint design are limited.

Applications

- Stainless-steel liners bonded to aluminum fry pans.
- Aluminum cladding bonded to uranium fuel rods.
- In the microelectronics sector, ultrasonic and thermo-compression bonding is used.

- In aeronautical and automotive applications, friction welding is used.
- Manufacturing of automatic intake/exhaust valves.

2.1 Cold Welding (CW)

It is a type of solid-state welding that can be accomplished at an ambient condition, i.e., room temperature and pressure to produce a metal combination with significant distortion at the weld. Welding involves the application of very high pressures to extremely clean interface materials. When joining very thin materials, sufficient pressure can be achieved with simple hand tools. Cold welding heavier parts often require the use of a press to apply enough pressure for a successful weld. Dimples are commonly formed in cold-welded parts. The technique can be easily modified to combine ductile metals (Fig. 1).

Salient features

- A cold weld is frequently stronger and has the same electrical characteristics as the parent material.
- At the very least, one of the metals should be ductile and not overworked.
- The importance of the preparation of the surface cannot be overstated.
- Metals that are similar or dissimilar can be used for both workpieces.
- It is necessary to clean both workpieces, with short sections sheared off.
- There is no heat applied at all.

Advantages

- Pieces being connected are not subjected to any temperature impacts, and the operation is quick.
- There are no thermal impacts on the pieces being connected because the procedure is carried out at room temperature.
- The procedure is quick, and there is hardly any distortion.
- Not only is the weld zone metallurgically uniform but also stronger than the surrounding areas. It is also worth mentioning that the metal is work hardened as well.

Fig. 1 Schematic diagram of cold welding
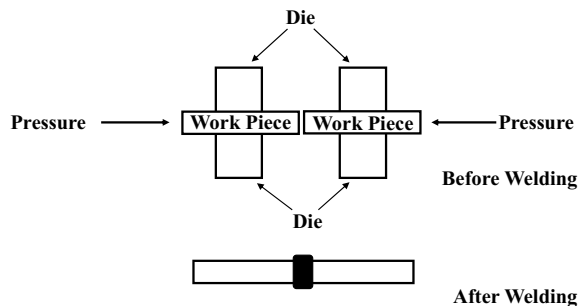
- Once the die is manufactured, it is easy and affordable to operate.
- There is no need to prepare the ends of the wire or rod before welding, and when the material is placed on the die, the two butt ends are automatically aligned.
- Pieces are bonded without being contaminated by sparks, dust, or vapors.

Disadvantages

- Inspection is challenging since the welds are done in a solid state.
- The contact surfaces are sheared together at the weld, and the thickness of the components is greatly decreased.
- It is a sort of welding that is extremely specialized in terms of joint design and welded materials.
- Though speed is a benefit to assemblers, it can also be a constraint.
- When two bodies traveling at the same speed collide, the faster body will attempt to displace the slower one.

Applications

- It is utilized for wire joining, a foil to wire joining, bi-metal wire joining, and scaling of heat-sensitive containers like explosives canisters.
- Butt-welded rod coils enable post-weld drawing to lower diameters while maintaining consistency.
- It is being used to connect components that cannot be heated, such as magnets.
- Cold welding procedures are used in the electronics sector for the manufacturing of heat-sensitive semiconductor devices using cans copper packages and sealed tin-plated steel crystals.

2.2 Diffusion Welding (DFW)

Diffusion welding is an solid-state welding (SSW) process that is employed to weld abutting surfaces utilizing pressure and high temperatures. There is no melting, microscopic deformation, or relative movement of the components in this procedure. Filler metal can be used or not. Galvanized surfaces might be used for this. Titanium alloys, for example, are frequently diffusion bonded because at temperatures exceeding 850 °C; the thin oxide layer may disintegrate and diffuse away from the bonding surfaces.

Salient features

- There is very little residual stress, and the bonding process creates no contamination.
- Plastic deformation is either absent or minimal in these materials.
- It may theoretically be conducted on any size joint surface with no increase in dispensation time, but, in practice, the surface is restricted by the pressure needed and physical constraints.

- Identical and unidentical metals, reactive and refractory metals, and pieces of varied thicknesses can all be used in diffusion bonding.
- Diffusion bonding is most commonly employed for operations that are difficult or impossible to weld with conventional methods because of its comparatively high cost. Welding materials that are normally impossible to join via liquid fusion, such as zirconium and beryllium; materials with extremely high melting points, such as tungsten; alternating layers of different metals that must maintain strength at extremely high temperatures, and very thin, honeycombed metal foil structures are just a few examples.
- This type of bonding is done by gripping the two parts to be welded with their surfaces abutting one other when uniting two materials with comparable crystalline structures. Prior to welding, these surfaces must be machined to the smoothest finish possible while remaining free of chemical impurities and other debris. Any substance between the two metallic surfaces might obstruct proper material dispersion. To match the welder to the workpieces, specific equipment is designed for each welding application. Pressure and heat are applied to the components after they have been clamped, generally for many hours. The heated surfaces are either heated in a furnace or heated by electrical resistance. A hydraulic press may be used to apply pressure at a certain temperature; this approach enables precise load readings on the pieces. Differential thermal expansion can be utilized to provide load in circumstances when the pieces must have no temperature gradient.

The quantity of diffusion flux that flows across the cross-sectional area of the mating surfaces determines steady-state diffusion.

The first law of diffusion states, according to Fick:

$$J = -D\left(\frac{dC}{dx}\right)$$

where "J" denotes the diffusion flux, "D" denotes diffusion coefficient, while "dC/dx" represents the concentration gradient through the materials in question. Here, the negative symbol signifies the product of the gradient.

Diffusion bonding takes place in three steps at the microscopic level:

- Micro-asperity deformities before the surfaces wholly contact, asperities on the two surfaces contact and plastically deform. These asperities entangle and establish interfaces between the two surfaces as they deform.
- Material creep is increased by diffusion-controlled mass movement at a higher pressure and temperature; grain boundaries and raw material migrate and gaps between the two surfaces are narrowed to isolated pores.
- Material initiates to spread over the border between the neighboring surfaces, merging the material boundaries and forming a connection.

Combining refractory metals at temperatures that do not impact their metallurgic characteristics is done using this method. Resistive, inductive, or oven heating are
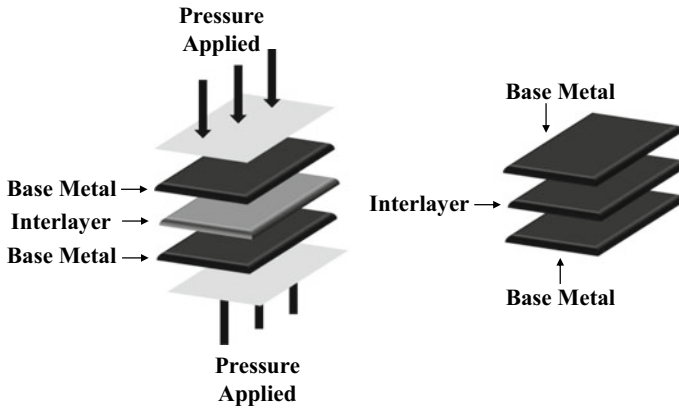
Fig. 2 Schematic diagram of diffusion welding

the most common methods of heating. Most refractory metals require a protected inert environment; therefore, vacuum and atmosphere furnaces are used. Welds on refractory metals were performed at temperatures just above half of the metals' usual melting point. This sort of bonding necessitates bond preparation with extremely tight tolerances and the use of a vacuum or inert environment. The process is often used to join incompatible metals. When a layer of filler material is placed between the mating surfaces of the components to be joined, the technique is known as diffusion brazing (Fig. 2).

Advantages

- Welding of dissimilar materials like ceramics, glass, and metals is possible.
- High-quality welds with no distortions, inclusions, pores, and chemical segregation are produced.
- There are no restrictions on the thickness of the workpiece.

Disadvantages

- The process that takes a long time and yields small results,
- Before beginning the welding process, thorough surface preparation is necessary,
- The mating surfaces must be perfectly aligned with one another,
- Initial equipment costs are rather expensive.

Applications

- Bonding different metals that are tough to weld using other welding methods, such as stainless steel to titanium (Ti), steel to niobium (Nb), steel to tungsten (W), gold (Au) to copper (Cu) alloys.
- Manufacturing of composite materials.
- In rocketry and aeronautical/aerospace industries, this process finds a major use.
- Used in the electronics sector.

2.3 Explosion Welding (EXW)

Explosive welding is a type of SSW process in which the combination of the parts to be welded together is affected by high-velocity motion caused by controlled detonation. Even if no heat is used for a blast weld, the metal at the point of contact appears to have melted during the welding process. This heat is generated by several factors, including the impact shock wave and the energy consumed during the contact. Heat is released as a result of the plastic deformation associated with jetting and the development of waviness at the interface between the pieces to be welded. With surface jetting, the plastic interaction between the metal surfaces is very clear. It has been shown that for a high-quality weld it is important to allow the metal to flow plastically.

Salient features

- Considerable high velocities are promoted by carefully detonating the explosives.
- This process is usually conducted under a vacuum for reducing the intensity of the sound and blast.
- Only high-velocity explosives are utilized with angled interfaces.
- Typical impact pressures are millions of psi.
- The velocity of detonation must not be more than 120% of the metal's sonic velocity.
- Welding has a limited speed over which the heat effects degrade the joints.
- The explosive kinds, explosive composition, and thickness of the explosive layer all influence detonation velocity.
- If two materials are brought near enough together, a molecular bond will form.
- Explosives with high velocity necessitate minor gaps between plates; therefore, rubber, as well as Plexiglass, are utilized as buffers.
- The critical angle, standoff distance, and critical velocity are all important parameters.
- For brittle metals with a tensile elongation of 5% and a Charpy V notch value of 10 ft. lb, this technique does not function effectively.
- When heat welded, metals that are prone to brittle seams, such as Al and Ti on steel, are well suited.
- To efficiently use the explosives, the plate separation should be 0.5–1 times the cladding plate thickness.
- Typical explosives used are cast shapes, powder/granular, pressed shapes, cord, plastic flexible sheer.
- Sonic velocity of the cladding material can be calculated by the given equation:

$$V_s = \sqrt{\frac{k}{s}} \quad k = \frac{E}{3(1 - 2v)}$$

  where K is the adiabatic bulk modulus, ρ is the density of the cladding material, E is the Young's of cladding material, v is the poisons ratio of the cladding material.
- Types of bonds produced during explosive welding

Fig. 3 Schematic diagram
of explosion welding
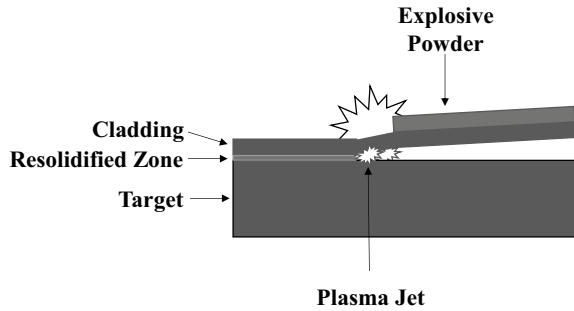
- **Direct metal to metal bond**—such a strong bond is produced when collision velocity is less than the critical velocity.
- **Continuous layer bond**—a weak bond is formed when the impact velocity is too great and the alloy bonds are strong.
- **Wavy**—they are produced when the interface is strong and has a wave.

There are three categories of detonation wave welds.

- **Shock waves**—they form if the sonic velocity is more than 120% of the material's sonic velocity.
- **Detached shock wave**—they occur when the velocity of detonation is between 100 and 120% of the sonic velocity of the material.
- **No shock waves**—they form or occur when the detonation velocity of the material is smaller than the substance's sonic velocity (Fig. 3).

Advantages

- It provides higher bonding, with no distortions, porosity, or changes in the metal microstructure.
- There isn't any diffusion at all.
- Welding incompatible metals such as copper (Cu) to stainless steel, aluminum (Al) to steel, or titanium (Ti) to steel are simple.
- Only limited melting takes place.
- Apart from the weld surface, there is no heat-affected zone (HAZ).
- The final product is unaffected by differences in melting temperatures and thermal expansion coefficients.
- Explosive welding is well suited to cladding applications, and the process is straightforward and quick. It also has a close tolerance for thickness.

Disadvantages

- Materials that are brittle cannot be treated.
- Only, basic form pieces are permitted to be bonded.
- The thickness of the flier plate is restricted.
- The cladding plate must not be excessively big.
- Storing and handling explosives safely and securely is challenging.

- Metals must be ductile yet sufficiently resistant to impact.
- Workers may need to be protected from noise and blasts by using vacuum chambers or being buried in sand or water.
- The noises and ground vibrations induced by an explosion will limit the usage of explosives in industrial locations.
- Licenses are required to possess and use explosives, and the area should be cleansed and well-grounded before the explosion.

Applications

- In heat exchangers, boiler tubes, and feedwater heaters, this method is used to clad tube plates and weld tubes and tube plates.
- Naval brass tube plates are made of steel, brass, aluminum, copper, bronze tubes, and stainless steel, as well as brass and bronze tubes.
- It is used to create pipes and clad tubes, aerospace structures, heat exchangers, pressure vessels, ship structures, bi-metal sliding bearings, and weld transitions.
- It is utilized to coat thick plates in corrosion-resistant layers when roll bonding like other methods isn't feasible.
- It is utilized for remote joining in hazardous situations, as well as for securing cooling fins and in cryogenic sectors.

2.4 Forge Welding (FOW)

It is also a type of solid-state welding procedure that involves heating metals in a forge and application of enough pressure or impact to permanently distort the interface. Previously, known as hammer welding, this is an earlier welding method. Forge welds were created by heating the components to be connected to a red heat that was significantly lower than the melting point. Flux was the typical procedure at the interface. The smith was able to achieve coalescence by applying enough pressure to the abutting surfaces using a hammer and anvil. This method isn't very important in the modern industrial world (Fig. 4).

Fig. 4 Schematic diagram of forge welding
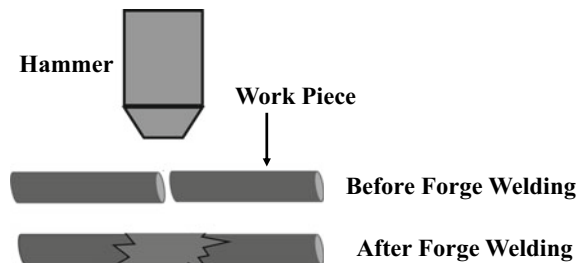
Salient features

- As we discussed, this is also a type of solid-state welding technique in which both plates are heated to temperatures much below their melting points. The workpieces are plastically deformed as a result of the heating. These plates are now subjected to repetitive hammering or a high pressurize load. Inter-molecular diffusion occurs at the interface surface of the plates as a result of the high pressure and temperature, resulting in a strong weld connection.
- A clean interface surface, devoid of oxide or other contaminating particles, is one of the essential prerequisites of this form of welding. Flux is used to prevent oxidation of the welding surface by mixing with the oxide and lowering its melting temperature and viscosity. During the heating and hammering operation, this causes the oxide layer to flow out.
- To begin, both work plates are preheated at the same time. The heating temperature is approximately 50% to 90% of the melting temperature. Flux has been applied to both plates.
- Making a joint now requires physical pounding with a blacksmith hammer. This procedure is done until the joint is complete.
- Mechanical hammering, which is either operated by an electric motor or by hydraulic means, is used for welding huge workpieces. Dies are sometimes used to create a polished surface.

Advantages

- It is a simple and easy technique commonly used to join steel and iron.
- Welding tiny components does not need expensive equipment.
- It can weld metals that are comparable and different.
- Filler material is not required since the weld joint's properties are comparable to those of the base material.

Disadvantages

- Welding is limited to tiny items. Larger things necessitated the use of enormous presses and heating furnaces, both of which are costly.
- Excessive hammering might damage the welding plates; thus, high competence is essential.
- There are a lot of welding errors, and the welding process is slow.
- It can't be used in large manufacturing.
- It is best for iron and steel.

Applications

- As previously indicated, it is typically used to connect steel or iron.
- It is used to construct gates, prison cells, and other things.
- It is a popular component in cookware.
- Before the introduction of alternative welding methods, it was employed to join boilerplates.
- It was used to forge weapons such as swords and other blades.
- Used to join shotgun barrels together.

2.5   *Friction Welding (FRW)*

Friction welding is a solid-state welding technique that utilizes the heat generated by mechanically induced sliding motion between friction surfaces to achieve material coalescence. Under pressure, the workpieces are kept together. To create frictional heat at the joint, this method usually includes rotating components against each other. The circular movement is stopped, and extra pressure is applied when a suitable high temperature is obtained, resulting in coalescence.

Friction welding can be done in two different ways. In the original method, one component is maintained immobile, while the other is spun by a motor that maintains a nearly persistent rotational speed. The two components are pressed together at a predetermined pressure for a predetermined period. The torque of the rotating parts is interrupted, and the pressure is increased. The weld is finished when the rotating part comes to a standstill. When speed, pressure, and time are closely monitored, this process can be precisely controlled.

The other type of welding is known as flywheel welding. A motor spins a flywheel until it achieves a specified speed. This turns one of the components to be welded. The engine is separated from the flywheel, and the second part to be welded is brought into physical interaction with the rotating part under pressure. The flywheel is brought to an abrupt stop, and additional pressure is applied to complete the weld during the predefined time as the rotation speed of the parts is reduced. Both methods use frictional heat to create high-quality welds. The original technique is said to have slightly better control. Friction welding has several advantages, including the ability to generate high-quality welds in a fast cycle time. There is no need for a filler metal, and no flux is necessary. The method may be used to join the most common metals. This may also be utilized to link a variety of metals that aren't the same. Friction welding necessitates the use of somewhat costly machine tool-like equipment. When creating a friction weld, three important factors play a role:

- **The speed of rotation**—This has to do with the weldable material and the diameter of the weld at the contact.
- **The pressure between the two parts to be welded**—During the welding process, the pressure changes. During the welding procedure, the pressure varies. It is initially extremely modest, but it is gradually raised to produce frictional heat. As the revolution comes to a halt, the pressure is swiftly raised, allowing for forging to occur either before or after the rotation comes to a halt.
- **The welding time**—The length of time is determined by the form, kind, and finish of the metal. It usually just takes a few seconds. The machine's actual operation is fully automated, with a sequence controller that can be programmed to match the welding schedule for the components to be connected. In the case of friction welding, one of the components to be welded must generally have a round cross-section; however, this is not always the case. The burr that appears around the perimeter of the weld can be used to visually check the weld quality. Usually, this ridge extends beyond the part OD and loops back to the part, but the joint extends beyond the part OD. If the flash comes out of the joint fairly straight, it
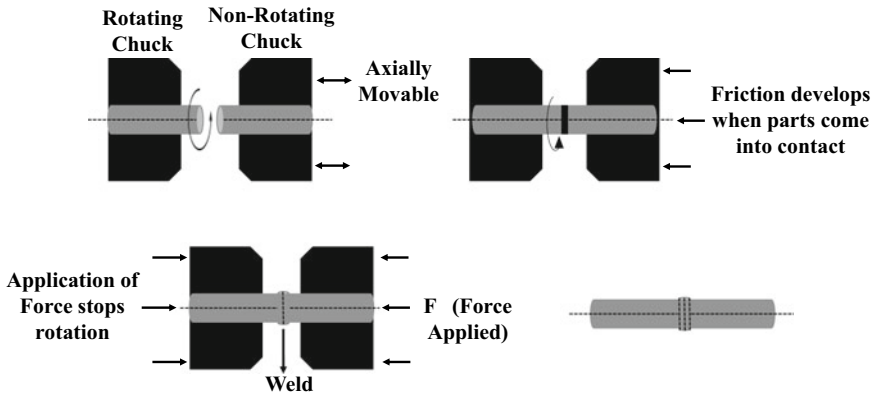
Fig. 5 Schematic diagram of friction welding

means the time was too short; the pressure was too low, or the speed was too high. These joints can break. If the burr bends back too much on the OD, it means the time was too long, and the pressure was too high. The ideal lightning shape falls somewhere in the middle of these two extremes (Fig. 5).

Salient features

- Friction stir welding) is a solid-state joining procedure that involves attaching two facing workpieces using a non-consumable tool without melting the workpiece material.
- Heat is produced through mechanical friction among workpieces in relative motion to one another, with the addition of a lateral force called "upset" to plastically displace and fuse the materials.
- Heat is generated by friction between the spinning tool and the workpiece material, resulting in a softened zone around the FSW tool.
- The tool mechanically intermixes the two pieces of metal and forges the heated and softened metal with the tool's mechanical pressure as it moves along the connection line, similar to how clay or dough is bonded.
- There are several zones in friction welding: HAZ–TMAZ–thermo-mechanically affected zone, heat-affected zone, WCZ–weld center zone, BM–base material, parent material, and flash.
- Furthermore, ways where high temperature impacted zone happened, as well as modifying the grain structure during metal joining cycles, are phase transformation's structure. For example, steel, austenite, martensite, pearlite, ferrite, cementite, and bainite are diverse types of minerals.
- Solid-state welding may be desirable to prevent changes, and a wide heat-affected zone is not required if it weakens the material qualities.

Advantages

- Filler metal, flux, or shielded gases are not required.

- It is a non-polluting method that does not produce smoke, fumes, or gases.
- The process is in a solid state with a minimal HAZ since no material is melted.
- After the welding process, the oxides can be eliminated.
- The operation is quite efficient, and welds are done in a very small period.
- The weld strength is superior to that of the weaker of the two materials being connected.

Disadvantages

- The method can only be used to connect round bars or tubes of the same diameter.
- Welding is not possible with dry bearing and non-forgeable materials. (In other words, one of the materials must be ductile). Welding free machining alloys is also tough.
- For producing consistent rubbing and heating, the workpiece's preparation and alignment may be crucial.
- The cost of equipment and tooling is expensive.
- Free machining alloys are difficult to weld.

Applications

- Critical airplane engine components are held in place by tongs.
- Engine valves and shock absorbers are examples of automotive components manufactured using friction welding.
- In agricultural machinery, hydraulic piston rod and track roller.
- Friction-welded components are frequently employed in place of costly castings and forgings.

2.6   Hot-Pressure Welding (HPW)

Hot-pressure welding is a solid-state welding process in which heat is applied to materials and sufficient pressure is applied to cause macro-deformation of the base metal. At the boundary between the pieces, heat and pressure cause coalescence, which goes together with visible distortion. The surface deformation breaks down the surface oxide deposit, allowing the cleaner metal to be exposed. Diffusion across the interface is used to weld this metal to the clean metal of the adjacent section, resulting in a merger of the faying surface. This type of procedure is often performed in sealed chambers using shielding or a vacuum medium. It is mainly utilized in the aerospace industry to make welded parts. One variant is the hot isostatic pressure welding process. Herein, a heated inert gas in a pressure vessel is used for pressurization (Fig. 6).

Salient features

- The torches are abruptly removed as soon as the two bodies facing ends attain the right temperature, so as not to obstruct the process. Hydraulic equipment is used

Fig. 6 Schematic diagram
of hot-pressure welding
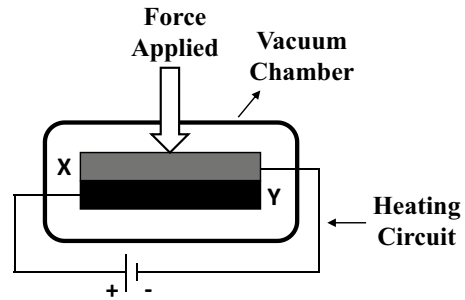
to bring the bodies together and upset them under pressure. The open joint proce-
dure is the proper name for this type. The closed joint process occurs when two
pieces make contact under pressure before being heated from the outside. In either
situation, flash material is ejected from the joint, resulting in a bulge. Although the
source of heat is different, hot-pressure welding is comparable to both flash and
friction welding in several ways. Surfaces should be machined straight and clean
to provide the greatest results. To reduce the amount of upheaval, some beveling
can be applied. The procedure mentioned here is carried out manually.

- The weldable materials must have hot ductility or enforceability. As a result,
  cast iron cannot be welded at high pressure. Low alloy steels, carbon steels, and
  several nonferrous metals are routinely connected via hot-pressure welding. This
  welding technique can be used to weld some incompatible material combinations.
  This technique cannot readily weld materials that produce adherent oxides on the
  surface shortly after heating. Aluminum alloys and stainless steel are common
  examples. The experiments were performed out in a void chamber.
- The pressure sequence cycle is the most essential parameter, which may have
  been produced by trial and error. A pressure range of 40–70 MPa is required.
- Hot-pressure welding can be done in closed chambers with a vacuum or a shielding
  media for use in the manufacturing of weldments for the aerospace sector using
  delicate materials.
- Mechanical characteristics are similar to those of basic materials; however, they
  are affected by the composition, cooling rate, and quality of the components.
- If the materials are easily weldable, hot-pressure welding can be a cost-effective
  and successful procedure for creating butt joints of basic forms.

Advantages

- Easy to follow the procedure.
- Joint preparation is simple.
- Low-cost equipment.
- Faster weld manufacturing.
- Enhanced quality of welds.
- No requirement for filler metal.
- Low-skilled operators are sufficient for operation.

Disadvantages

- This method cannot be used for welding all metals.
- This method is not readily automated.
- Cycle length is depending on the heating duration.
- After welding, flash and bulge must be removed.
- Only, basic portions can be butted and welded.

Applications

- Butt hot-pressure welding of railroad rails sections and steel reinforcing bars is a common use recorded, notably in Japan.
- For use in the manufacture of weldments for the aerospace industry with delicate materials.

2.7   Roll Welding (ROW)

Roller welding is also a type of solid-state welding process in which metals flow together with rollers by heating and applying sufficient pressure to generate deformities at the faying surfaces. This procedure is similar to forge welding, except that instead of hammer blows, the pressure is applied by rollers. Diffusion at the butting surfaces causes coalescence at the contact between the two sections. Cladding low-alloy or mild steel with stainless steel which is a high-alloy material is one of the most common applications for this process. It is also used in the instrument field for the production of bimetallic materials (Fig. 7).

Salient features

- This procedure is identical to forge welding, except that instead of hammer blows, pressure is delivered with rolls.
- Diffusion at the faying surfaces causes coalescence at the contact between two sections. Weldable parts must be ductile and free of work hardening.
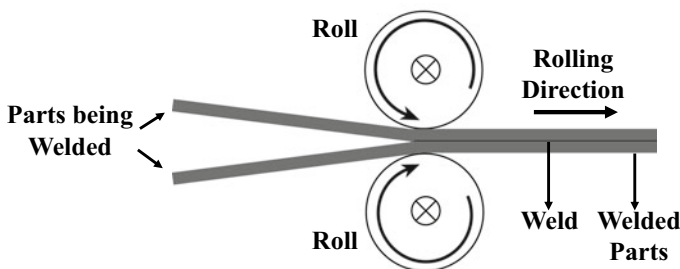- The surface to be joined should be cleaned before welding takes place.

Fig. 7   Schematic diagram of roll welding

- When the parts to be welded are tiny, simple hand-operated instruments are used to apply the pressure applied by rolls.
- Power presses are used to apply pressure to larger pieces.
- If the welding is done without the use of heat, it is termed cold roll welding, and if the heat is utilized, it is called hot roll welding.
- Two forms of roll welding are commonly used. The components to be welded are simply piled and sent through the rolls in the first. Pack rolling is the second method, which entails sealing the parts to be rolled in a pack or sheath and then roll welding the pack assembly.
- In the first method, the parts to be welded are completely enclosed in a pack that is sealed (typically by fusion welding) and often evacuated to provide a vacuum atmosphere, whereas in the second method, the parts to be welded are completely enclosed in a pack that is sealed (typically by fusion welding) and often evacuated to provide a vacuum atmosphere.

Advantages

- Roll welding is a simple way to join metals like soft gold, silver, copper, and aluminum.
- There is no need for flux or filler metal, and the operation is straightforward.
- The process is environmentally beneficial, as no fumes, vapors, or smoke are produced.
- It is a quick and easy process that even takes less time to perform the desired activity.

Disadvantages

- The welding process necessitates great pressure, and the cost of equipment is significant.
- Quality of weld is lower than with fusion welding.
- It can only be used to solder flat shapes.

Applications

- It is used to make bimetallic strips.
- It is also used to clad stainless steel to mild steel for corrosion resistance.
- Toto transform sandwich strips into coins, roll welding is utilized.
- One of the major uses of the roll welding process is the cladding of mild or low-alloy steel with a high-alloy material such as stainless steel.

2.8 Ultrasonic Welding (USW)

It is a type of solid-state welding process in which union is achieved by providing high-frequency vibrational energy locally to the workpieces, while they are held together under pressure. Welding occurs when the energy coupling device, an ultrasonic tip or electrode, is clamped against the workpieces and caused to oscillate in

Fig. 8 Schematic diagram
of ultrasonic welding
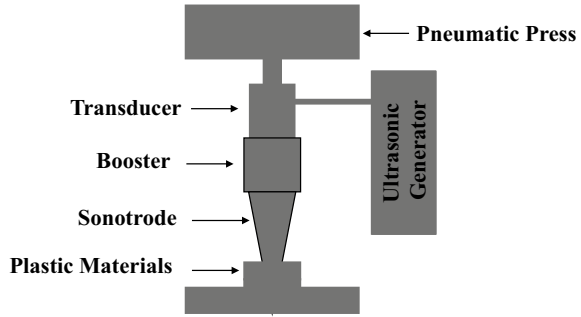
a plane parallel to the weld interface. The base material is dynamically stressed by
the clamping pressure and oscillating forces. This causes tiny deformations in the
base metal, resulting in a slight rise in temperature in the weld zone. This, combined
with the fastening pressure, causes union across the interface resulting in a weld.
Ultrasonic energy can help clean the weld area by breaking up oxide coatings and
causing them to be dissolved (Fig. 8).

High-frequency alternating electrical energy is converted into mechanical energy
using a transducer, which creates the vibrational energy that causes the tiny deforma-
tion. Various types of tools are used to bond the transducer to the workpiece, ranging
from resistance welding tips to electrode wheels for resistance roller welding. The
lap seam is the most common weld seam. There is no nugget as the temperature at the
weld is not raised to the melting point as in resistance welding. The strength of the
weld corresponds to the strength of the base metal. Welding can be used to join most
ductile metals, and there are several combinations of dissimilar metals that can be
welded. The process is limited to relatively thin materials such as foils or ultra-thin
thicknesses.

Salient features

- The major technological parameters of ultrasonic welding are the vibration dura-
  tion, the vibration amplitude and the (normal) force perpendicular to the vibration
  direction.
- Performance requirements for vibration generation and maintenance are given by
  the equation:

$$P = F \cdot A \cdot f = S_{mh} \cdot p_\ell \cdot \eta \cdot A \cdot f$$

where P is the performance [W], F is the force [N], A is the amplitude [μm], f
is the frequency [Hz], S_{mh} is the cross-sectional area of the pneumatic cylinder
[m^2], p_ℓ is the compressed air pressure [Pa], η is the mechanical efficiency [$-$].
- Then, the energy demand for a welding cycle is given by the equation:

$$E = P \cdot \Delta t = F \cdot A \cdot f \cdot \Delta t = S_{mh} \cdot p_\ell \cdot \eta \cdot A \cdot f \cdot \Delta t$$

where E is the energy [J], Δt the cycle time or weld time [s]. This time for most bindings is less than one second. If more energy is needed and all other technological parameters remain unchanged, the welding time should be increased.

- The resonator—acoustic transformer—sonotrode unit requires unimpeded minimum electrical power to initiate and maintain vibration motion. As the mechanical load increases, the power requirement required to maintain mechanical vibration increases. Friction due to pressure results in the welding by diffusion or local "stirring" of the base material.
- By increasing the pressure—keeping the other parameters at a constant value—the mechanical load of the welding zone increases and the power, and power required to maintain the vibration also increases.
- By increasing the pressure—keeping the other parameters at a constant value—the mechanical load of the welding zone increases, and the power and performance required to maintain the vibration also increases.
- Ultrasonic equipment is a resonant acoustic device. Its amplitude is the difference in longitudinal extent and contraction (5 … 35 μm) with which the tool actively vibrates.
- Ultrasonic welding results in a localized temperature increase due to the collective effects of flexible hysteresis, friction, and plastic deformation. The welding surfaces reach roughly one-third of the metal's melting temperature so that the physical properties of the welded materials practically do not change. As the ultrasonic welding process is an exothermic (heat-producing) reaction, the welding time increases the welding temperature.

Advantages

- Because the workpieces are not heated in bulk, there is no risk of mechanical or metallurgical damage.
- It is a great way to bind thin and thick sheets together.
- Sound welds originate from local plastic deformation and mechanical mixing.
- It is possible to combine dissimilar metals.
- The weld produced is of appreciably high quality.
- The method can be incorporated into automated manufacturing lines.
- A moderate level of operator competence is sufficient to run the process.
- It ensures enhanced flexibility and variety by being quick, cost-effective, and automated.
- It creates extremely strong joints.
- Welding can be done on very thin materials.
- It can produce up to 60 components per minute in mass manufacturing.

Disadvantages

- Welding is limited to tiny and thin pieces.
- Equipment and workpieces and components may become fatigued as a result of ultrasonic vibration's reciprocating stresses.
- Because ductile materials yield under stress, it is not ideal for them.

- It necessitates the use of specially constructed joints.
- Electrical components can be damaged by ultrasonic vibrations.
- Fixture tooling expenses are considerable.

Applications

- This type of welding is mostly used to join small components in electronics, communication devices, medical devices, and timepieces.
- It is utilized in manufacturing automobiles, medical devices, and toys.
- Hermetic sealing can be achieved with ring-type continuous welds.
- It is utilized in airplanes, missiles, and nuclear component production, among other things.
- It is also utilized in armatures, starter motor armatures, slotted commuters, braded brush wire connecting, wire terminals, and brush plates, among other things.
- Dashboards, headlamp parts, switches and buttons, fuel filters, fluid vessels, seat-belt locks, electronic key fobs, light assemblies, and air ducts are all made with ultrasonic welding.
- Ultrasonic welding is used to create electronic appliances such as data storage keys switches and sensors.
- Because of its clean welds, it is used in the healthcare industry. Medical items such as filters, catheters, medical garments, and masks are also made using ultrasonic welding.
- It is used in solar panels to join tubes and sheets together.
- Ultrasonic welding can be used to create blister packs, tubes, pouches, carton spouts, and storage containers, among other packaging uses.
- The ultrasonic welding process is widely used in the instrument, aerospace, and electronics industries.
- This process is also used to make packaging and containers and to seal them.

3   Summary

Joining and welding magnesium alloys have developed significantly in the last ten years. New technologies and hybrids are being developed to improve traditional fusion welding techniques. Fusible welding processes, on the other hand, can help reduce a few metallurgical imperfections. Among the various processes of welding, laser welding, as well as friction stir welding, are likely to develop into efficient joining methods for magnesium as well as its alloys. Some magnesium alloys, especially wrought alloys, can produce laser-welded joints without any cracks along with minimal porosity including good surface quality. Most of the problems encountered in fusion welding have been solved by friction stir welding. However, limitations in weld design, high mechanical stresses on tie plates, and the consequent need for stronger attachment may have limited its use. Since magnesium has poor formability, particularly in cast alloys such as AZ91, joining methods that need localized deformation are not entirely efficacious. In this scenario, scientific research is still

desirable to fully comprehend and override the fundamental weldability issues that plague alloys of magnesium.

4 Conclusion

In conclusion, we can accomplish that magnesium alloy solid-state welding techniques are of great importance given the contemporary needs of mankind. Magnesium alloys are attractive engineering materials for making lightweight structures. The desirable material properties such as excellent specific strength, sound deadening capabilities, recyclability, good castability, and hot workability. Alloys of magnesium have reduced strength, creep resistance, and fatigue at increased temperatures owing to their hexagonal close-packed (HCP) crystal assembly, as well as low stiffness, restricted ductility, and cold workability at ambient temperature. Alloys of magnesium have meager hardness, corrosion resistance, and wear qualities, considerable reduction during solidification and may readily develop enhanced chemical reactivity. You will find maximum use in aerospace applications and unlimited uses for various other purposes in various household and industrial sectors. We can say unreservedly that a few other applications will certainly be attributed to these alloys in the future.

References

1. Troughton MJ (2008) Handbook of plastics joining, 2nd edn. Elsevier, William Andrew Inc, New York
2. Bralla JG (1998) Design for manufacturability handbook, 2nd edn. McGraw-Hill Education, New York
3. Singh K, Singh G, Singh H (2018) Review on friction stir welding of magnesium alloys. J Magnes Alloy 6:399–416
4. Rubino F, Parmar H, Esperto V, Carlone P (2020) Ultrasonic welding of magnesium alloys: a review. Mater Manuf Process 35:1051–1068
5. Sanders PG, Keske JS, Leong KH, Korneck G (1999) High power Nd: YAG and CO_2 laser welding of magnesium. J Laser Appl 11
6. Ghaderi SH, Mori A, Hokamoto K (2008) Explosion joining of magnesium alloy AZ31 and aluminum. Mater Sci Forum 566:291–296
7. Fernandez GJ, Murr L (2004) Characterization of tool wear and weld optimization in the friction-stir welding of cast aluminum 359+20% SiC metal-matrix composite. Mater Charact 52:65–75
8. Schrader GF, Elshennway AK (2000) Manufacturing processes and materials, 4th edn. Industrial Press, Inc., pp 319–320, ISBN: 0872635171
9. Pastor M, Zhao H, DebRoy T (2000) Continuous wave Nd: yttrium–aluminium–garnet laser welding of AM60B magnesium alloys. J Laser Appl 12: 91–100
10. Chawla KK (1998) Composite materials: science and engineering. Materials research and engineering, 2nd edn (Corr. 3rd printing). Springer, New York, Heidelberg Dordrecht London, p 174. ISBN: 0387984097

11. Kainer KU, Mihriban AK, Pekguleryuz O (2013) Fundamentals of magnesium alloy metallurgy. Elsevier Science, United Kingdom. ISBN: 9780857097293
12. Diffusion bonding. Welding fundamentals and processes, vol 06A. In: ASM international, Materials Park, Ohio. Handbook Committee, pp 682–689. ISBN: 978-0-87170-377-4.im
13. Asadi P, Kazemi-Choobi K, Elhami A (2012) Welding of magnesium alloys in new features on magnesium alloys. Intech Open, pp 121–154. ISBN: 978-953-51-0668-5
14. Black JT, Kohser RA (2019) DeGarmo's materials and processes in manufacturing, 13th ed. John Wiley and Sons Inc, ISBN: 978-1-119-49282-5
15. Akca E, Gürsel A (2016) Solid state welding and application in aeronautical industry. Period Eng Nat Sci 4
16. Bayraktar E, Isac N, Arnold G (2005) An experimental study on the forming parameters of deep-drawable steel sheets in automotive industry. J Mater Process Technol 162–163:471–476
17. Meriç C, Sinan Köksal N, Karlik B (1997) An investigation of deep drawing of low carbon steel sheets and applications in artificial neural networks. Math Comput Appl 2:119–125
18. Tomitz A, Kaspar R (2000) Deep-drawable thin-gauge hot strip of steel as a substitution for cold strip. ISIJ Int 40:927–931
19. Kulekci MK (2008) Magnesium and its alloys applications in automotive industry. Int J Adv Manuf Technol 39:851–865
20. Kainer KU (2000) Magnesium alloys and their applications. WILEY-VCH Verlag GmbH, Weinheim 3-527-30282-4
21. Callister WD, Rethwisch DG (2016) Materials science and engineering: an introduction, 9th edn. John Wiley & Sons, Inc.
22. Bettles C, Gibson M (2005) Current wrought magnesium alloys: strengths and weaknesses. JOM 57:46–49
23. Dixit US, Yadav V, Pandey PM, Roy A, Silberschmidt VV (2020) Modeling of friction in manufacturing processes. In: Silberschmidt PT (eds) Elsevier series in mechanics of advanced materials. Elsevier, pp 415–444. ISBN: 9780128182321
24. Dhanapal A, Boopathy SR, Balasubramanian V, Chidambaram K, Zaman ART (2013) Experimental investigation of the corrosion behaviour of friction stir welded AZ61A magnesium alloy welds under salt spray corrosion test and galvanic corrosion test using response surface methodology. Int J Met 1–17
25. Wang W, Han P, Qiao K, Li T, Wang K, Cai J, Wang L (2020) Effect of the rotation rate on the low-cycle fatigue behaviour of friction-stir welded AZ31 magnesium alloy. Eng Fract Mech 228:106925
26. Klenam DEP, Ogunwande GS, Omotosho T et al (2021) Welding of magnesium and its alloys: an overview of methods and process parameters and their effects on mechanical behaviour and structural integrity of the welds. Manuf Rev 8:29
27. Balachandar K et al (2021) Friction stir welding tool condition prediction using vibrational analysis through machine learning—a review. J Phys Conf Ser 1969:012051
28. Santhi KA, Srinivas C (2020) Comparative study of light weight materials in analysis of chassis. Int J Adv Sci Technol 29(05):10480–10489
29. Mordike BL, Ebert T (2001) Magnesium: properties—applications—potential. Mater Sci Eng A 302:37–45
30. Dobrzański LA, Totten GE, Bamberger M (eds) (2019) Magnesium and its alloys: technology and applications, 1st ed. CRC Press
31. Sillekens WH, Hort N (2013) Magnesium and magnesium alloys. In: Lehmhus D, Busse M, Herrmann AS, Kayvantash K (eds) Structural materials and processes in transportation, pp 113–150
32. Loukil N (2021) Alloying elements of magnesium alloys: a literature review. In: Tański T, Jarka P (eds) Magnesium alloys structure and properties. IntechOpen, London.
33. Sankaran KK, Mishra RS (2017) Magnesium alloys. In: Metallurgy and design of alloys with hierarchical microstructures. Elsevier, pp 345–383
34. Papenberg NP, Gneiger S, Weißensteiner I, Uggowitzer PJ, Pogatscher S (2020) Mg-alloys for forging applications—a review. Materials (Basel) 22;13(4):985

Chapter 8
Solid-State Friction Welding Technology for Joining of Lightweight Metal and Alloys

Ravindra Nath Yadav

1   Introduction

Lightweight metal and alloys become a preferable material for advanced industries because of weight reduction and cost saving. The weight reduction significantly enhances the fuel efficiency, and 10% weight reduction leads to decrease of fuel consumption as 3–7% [1–3]. Hence, the automobiles and aerospace industries focus their attention to use of lightweight materials for structural works. The most common lightweight metals for structural works are aluminum (Al), magnesium (Mg), titanium (Ti) and its alloys [1–4]. The Al and its alloys show their potential for automobile, aerospace and naval industries because of better mechanical properties and easy formability [5]. The Al and Mg metals and their alloys are significantly replaced the steel and cast iron from the manufacturing sectors [3]. In existing materials, the Mg is the lightest metal and not only replacing the heavy dense materials as cast iron and steels but also copper (Cu), Al and its alloys from the automobiles sectors [6]. The another lightweight metal such as Ti and its alloys is preferred by aerospace, biomedical and petrochemical industries by reason of low density, high strength, corrosion resistance and biocompatibility [4, 7–10].

Lightweight materials are gaining growth to replace the heavier objects made of iron and steels because of low volume and high mechanical strength with non-corrosive nature. The joining of these materials is critical issues to achieve the strength of joint equal to base metals for the manufacturer and assembly units. In existing joining processes, the fusion/arc welding is broadly used for joining of ferrous and non-ferrous materials with high weld strength. Hence, it is widely accepted by aerospace, automobile, naval, railways and military industries. The requirement

R. N. Yadav (✉)

Department of Mechanical Engineering, BBD National Institute of Technology and Management, Lucknow 226028, India
e-mail: mechrny@gmail.com

of heat source, filler rod, flux materials, generation of high heat and fume, cracks formation and heat-affected zone (HAZ) in fusion welding limits its applicability [11–13]. In addition to this, joining of dissimilar metal and alloys also becomes challenging for fusion welding causes of variation in the melting temperature and metallurgical incompatibility, lack of fusion, cracking, porosity and harmful gaseous environment [9, 13–15]. In such situation, the solid-state welding (SSW) has been found more appropriate joining process for similar/dissimilar materials.

In SSW process, the welding can be achieved without melting by applying pressure with or without heat. In this process, the welding temperature is always less than melting temperature of joining objects, and weld quality is higher than fusion welding. It shows strength for welding of similar/dissimilar materials significantly at low heat input [16, 17]. In general, weld joints are achieved because of plastic deformation of base materials by mean of different form of mechanical energies. In SSW, no phase transformation occurs as which problems associated with fusion welding can be eliminated. It shows several other advantages like narrow HAZ, less distortion and residual stress [18]. In manufacturing sectors, various SSW processes like friction welding, diffusion welding, ultrasonic welding and explosion welding are utilized to achieve quality welds. Among these processes, the friction welding is found more appropriate to weld the similar and dissimilar metal and alloys by utilizing frictional energy as a heat source in presence of pressure.

2 Friction Welding

Friction welding (FW) is a SSW process where neither external heat nor filler material is required to achieve the weld joints. It can be defined as a joining process that utilizes friction energy and pressure to get quality welds of two similar or dissimilar components [14, 16]. Generally, heat is mechanically generated between two rubbing surfaces having relative motion between them. Once sufficient heat is generated, then pressure is applied axially through stationary object [19]. Hence, material is displaced at interface surface and fused together resulting weld joints. The main advantages of FW process are shorter weld time, no need of filler materials, effective welding of similar and dissimilar metal/alloys and also suitable for welding of pipes and rod [14, 17].

The preparation of surface before FW is not required as fusion welding, and mostly, saw cut surface is preferred. It is an energy-efficient welding process without application of flux or shielding gas and filer material. The requirement of energy for FW is low as which it becomes a cost-efficient for joining of lightweight metal and alloys. There is not spattering of metal, radiation and electrical hazardous. Hence, it is safer in operation and healthy work environment for operator because of no fume generation [20]. The automation is applicable for FW, and no certification is required for welder. Several metal and alloys of medium and high carbon steel are difficult for fusion/arc welding, while such materials are preferred for FW process. In same way, lightweight metals such as copper, Al, Mg and Ti are extensively used in FW

for joining without scarifying the weld strength and product integrity. It shows their potential to get the 100% airtight weld at interface of joint without risk of porosity, cracks, voids and other welding defects.

Of course, FW significantly meets the demand of manufacturing industries for welding of similar and dissimilar materials. However, it suffers with several limitations that affect the process capabilities. The most important factor is the plastically deformable characteristic of at least one material for particular welding [20]. It is not suitable for the complex profiles and non-uniform materials. Hence, the profile should be easier in clamping with relative motion ability to generate friction. The clamping devices and workpiece are having ability to sustain the pressure and torque for welding. In general, the FW process is limited to the butt and flat welding.

The FW is applied in different sectors such as automobile, aerospace, agricultural, marine, railway and petroleum industries [14, 20]. It is used to manufacture butt joints for drive shafts and oil drilling pipe for components of aircraft engines. It is used to produce gears, valves and axles for automobiles, piston rods and track rollers for agricultural industries. It is also applied for welding of turbine blades to disk of aircraft and electrical motor shafts of power plant industries [20]. The boiler grade tubes/plates and composite materials can be effectively welded by it [21, 22].

3   Mechanism of FW Process

The basic principle of FW is the friction which is utilized to generate the heat at interface of joining objects. Such friction for heat generation is continued till plastic forming temperature. The plastic temperature depends upon material properties and varies material to material. Once heating phase achieved, the increasing axial force is applied till permanent joint of objects causes of thermo-mechanical treatment at interface surface. In general, the FW process is completed in four phases as shown in Fig. 1.

- Initial phase
- Contact/friction phase
- Thermal/heating phase
- Forging phase.

In initial phase, the workpieces are prepared for joining, and one of them is clamped with rotor for rotating, while other is kept stationary. The rotor rotates at high speed as which workpiece starts rotate with same speed. Mostly, electric motor is used to rotate the rotor during welding. In second (contact/friction) phase, a slight pressure is applied to stationary object to make contact with rotating part. Initially, the contaminated materials (dust, dirt, etc.) are cleaned from faying surfaces by rubbing phenomena.

The heat is generated by utilizing friction energy between faying surfaces during thermal or heating phase. For this, higher pressure is applied through stationary
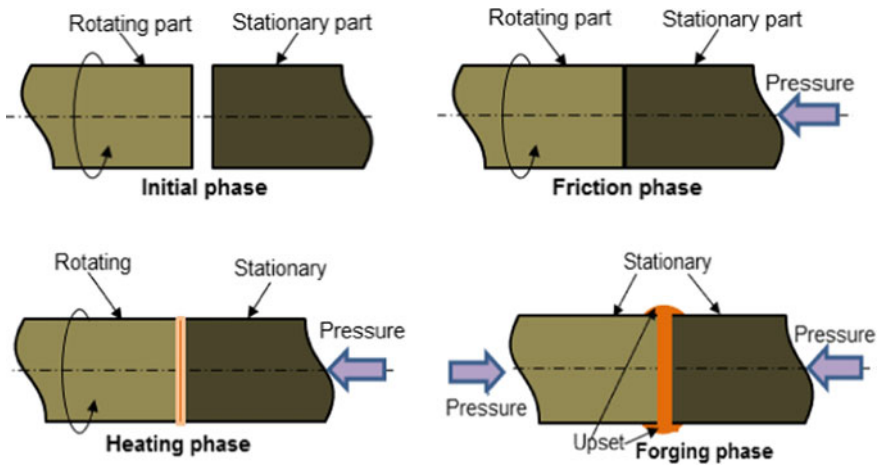
Fig. 1 Different phases of FW process

element to create a high friction between faying surfaces. Due to this, heat is generated at interface surface as which temperature of material rises at rubbing surfaces and simultaneously decreases in flow stress of material with axial shorting [20, 23]. Hence, the material is found incapable to sustain the applied pressure resulting upsetting and material plastically flows outward as a flash. Such phenomenon is known as burn-off stage. The major advantages of flash formation are removal of contaminations and oxide layers from the flying surfaces [20]. In the forging phase, the rotor is stopped, while the application of high pressure continues as which bonding between faying surfaces and finally get a weld joint.

3.1 Heat Generation

In fact, the friction plays important role in FW process, and heat generation depends upon it. Generally, two surfaces (one stationary and other rotating) having relative motion are used for joining by FW process. The relative motion means rubbing action at interface surface when they make contact to each other resulting generation of heat energy. The temperature increases at rubbing surface means loss of kinetic energy into thermal energy and finally reaches the plastic temperature of materials. In FW process, two phenomena as heating and plastic deformation occur simultaneously. Initially, the strain rate is low, and deformation of material occurs at high temperature. The material is reached at fully plasticized region where rate of strain may exceed 10^{-3}/s because of axially displacement of material with application of pressure [24].

The pressure, rotating speed and time are significantly affected the heat generation during FW process. In FW process, the heat transfer at faying interface and
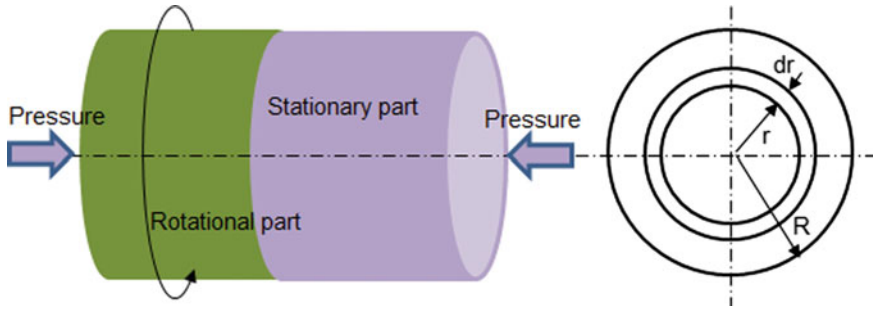
Fig. 2 Circular objects under FW process

energy input are difficult to explain clearly because of variation in friction coefficient throughout process. In friction, the axial pressure increases as which shear stress induces during FW process. The applied axial pressure assumed to be constant. Hence, the shear stress exerted on interface will be also constant and determined as [20]:

$$\left.\begin{array}{c} \tau = \mu P_n \\ \text{and } q = \tau v \end{array}\right\} \tag{1}$$

where τ = shear stress, P_n = axial (normal) pressure, v = rubbing velocity, q = heat generation rate/interfacial area per cycle and μ = coefficient of friction.

In general, the frictional coefficient (μ) varies from $\mu > 1$ (at dry sliding) to zero when temperature for asperity melting is reached at interface. However, it is considered as constant for analysis purpose only. In FW, the torque force is required to rotate the rotating elements (Fig. 2) under influence of axial pressure which can be determined as [25].

$$\left.\begin{array}{c} M\,(\text{Nm}) = \displaystyle\int_0^{M(R)} dM = \int_0^R \mu\ P(r) \times\ 2\pi r^2 dr \\[4mm] = \dfrac{2}{3}\pi\ \mu P R^3 \end{array}\right\} \tag{2}$$

where M = interfacial torque, R = surface radius, P = axial pressure and $P(r)$ = pressure distribution across the interface.

Generally, different types of relative motion are used to generate friction between flying objects. Hence, the rotary friction welding (RFW), linear friction welding (LFW), orbital friction welding (OFW) and friction stir welding (FSW) come into existence based on relative motion. On other hand, heat generation depends upon frictional energy which varies according to the frictional coefficient. For simplicity, the frictional coefficient is considered constant throughout weld process, and all

frictional energy is transformed into heat. Hence, average heat energy per unit area
with respect to time is computed as [24].

$$
\begin{aligned}
\frac{q_0}{A}\,(\text{W/mm}^{-2}) &= \frac{1}{A}\int_0^{M(R)} \omega\,\mathrm{d}M = \int_0^R \mu\,Pu\,\mathrm{d}A \\
&= \frac{1}{A}\int_0^R \mu\,Pu_{\max}\frac{r}{R}2\pi r\,\mathrm{d}r \\
&= \frac{2}{3}vPu_{\max}
\end{aligned} \tag{3}
$$

where q_0 = net power, P = friction pressure, A = cross-sectional area, $u_{\max}$ = max.,
surface velocity at outer edge, ω = angular velocity, v = rubbing velocity.

Equation (3) is used to determine average heat per unit area with time for RFW
process (Fig. 2) where rotary motion of objects is responsible for heat generation.
Similar to RFW, heat generation in LFW also depends upon relative motion between
faying surfaces, but the nature of motion is reciprocating. In practical, the rubbing
velocity in LFW is not a function of angular velocity (ω). The angular velocity comes
from linear oscillating when distance from center is considered as function of time.
The heat generation is considered as function of angular velocity and time which
can be determined as [20, 26].

$$
\left.
\begin{aligned}
v &= \alpha\omega\cos(\omega t) \\
\text{where, } \omega &= 2\pi n \\
\text{and} \quad q_{\text{lfw}} &= \mu P_n\alpha\omega\cos(\omega t)
\end{aligned}
\right\} \tag{4}
$$

where α = offset distance for linear velocity and n = rotational frequency in rev/s.

The average heat generation rate for LFW can be determined by integrating Eq. (4)
over a cycle with a consideration as annular velocity is a function of frequency (where
n in Hz). Hence, the motion is taken as cyclic in nature and integrated four times a
quarter of cycle for average heat generation rate as [20].

$$
\begin{aligned}
q_{\text{lfw}} &= \frac{1}{T}\int_0^T q\,\mathrm{d}t = \frac{4}{T}\int_0^{T/4} q\,\mathrm{d}t \\
&= \frac{4}{T}\int_0^{T/4} \mu P_n\alpha\omega\cos(\omega t)\,\mathrm{d}t = 4\mu P_n\alpha n
\end{aligned} \tag{5}
$$

The generation of frictional heat in OFW is more uniform than the RFW and
LFW processes. This is because of unidirectional uniform relative velocity between
rubbing surface of two elements over whole interfacial area as which high weld

integrity associated with the OFW process [24]. Similar to other FW processes, the rate of heat generation in OFW is a function of rubbing velocity, offset distance of axes (α), frictional coefficient and angular velocity, which can be determined using following equations [20, 27].

$$\left. \begin{array}{l} v = \alpha\ \omega \\ \text{where, } \omega = 2\pi n \\ \text{and} \quad q_{\text{ofw}} = 2\pi n \times \mu P_n \alpha \end{array} \right\} \tag{6}$$

where α = axes offset for orbital motion and n = rotational speed (rev/s).

The FSW is another process for joining of objects that utilizes plasticized region of materials but in different way as compared to RFW, LFW and OFW processes. In this process, heat is generated between shoulder of rotating tool and joining objects. The heat generated between tool shoulder and plate interface is calculated as [28].

$$q_{\text{fsw}} = \frac{2}{3}(1 - \delta) \times \pi \omega P \mu \sigma_n (R_s^3 - R_p^3)(1 + \tan\theta) \tag{7}$$

where σ_n = normal stress at interface surface, μ = friction coefficient, θ = angle between vertical and tool axes, δ = dimensionless sliding factor ($\delta = 1$ for sticking, $\delta = 0$ for sliding and δ = between zero to one for partially sliding/sticking), R_s and R_p = radius of shoulder and pin.

3.2   Heat-Affected Zone and Microstructure

In FW process, the frictional energy is utilized for heating of objects within a very short period of time, while longer cooling time is responsible for weld joint in presence of load. In general, the interface temperature plays significant role in weld characteristics which is significantly affected by rotation speed, frictional coefficient, applied load, contact period, material properties and geometry. Due to this, the joining temperature differs material to material, and joints are made below melting temperature of objects. Hence, heat-affected zone (HAZ) becomes difficult for researchers to define appropriately. In general, the temperature change and gradient of strain and strain rate lead to microstructural into weld joint. Such phenomena refer as HAZ and categorized into three different regions as contact/rubbing region, fully plasticized, partially deformed and undeformed regions [20, 29].

The various regions of HAZ for FW process are graphically presented in Fig. 3. The contact region refers as interface surface where faying surfaces make contact to each other. It is considered as a severe plastic deformation region where rubbing and metal transfer phenomena occur from one surface to other surface. The rotational speed is responsible to control the strain energy. The grain structure of weldment of this region is very fine causes by the recrystallization and severe straining.

Fig. 3 Various regions of
HAZ in FW process
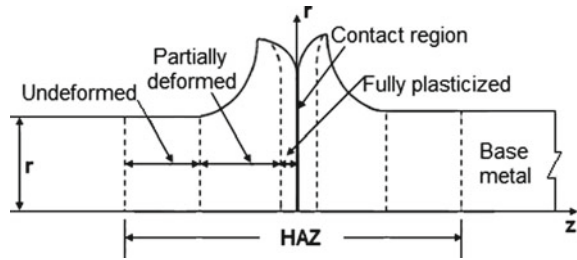
The second region refers as fully plasticized region where object is subjected to significant amount of plastic deformation. It is also considered as dynamic recrystallization region. In this region, neither rubbing nor metal transfer phenomena occur between faying surfaces. The weld of such region is under influence of dynamic recrystallization because of high temperature as which fine and equiaxed grain structures of joints are obtained [30].

In third region or partly deformed region, the significant parameters of joining such as plastic deformation, temperature, strain and strain rate are smaller than amount of fully plasticized region. Due to the reduction in strain and strain rate, the grain structure of this region becomes coarser. In undeformed region, the material may undergo the phase transformation. In this region, plastic deformation doesn't take place, but grain growth may occur. After this region, the material lying at room temperature and there is no any change occurs in grain structure of base materials.

The microstructure of weld joints depends upon solidification rate and time. The different zones of weld joint for Ti–4Al–6V are as weld center zone (WCZ), thermo-mechanically affected zone (TMAZ) and base metal. The different zones and microstructures of weld joints are as shown in Fig. 4a–d [31]. The microstructure of WCZ is either martensitic or Widmanstatten pattern as shown in Fig. 4b. The material of TMAZ is mechanically deformed and significantly affected by heat, but the grains of this zone are not significantly recrystallized because presence of original grains of the parent metal as shown in Fig. 4c. In most of the cases, the weld experiences a small amount (approx. 1 mm) of burn-off by reason of surface impurities like oxides along interface of weld as shown in Fig. 4d. Such phenomena of burn-off is significantly affected the quality of weld joints and needs to better control of process parameters to minimize it.

4 Variants of FW Process

In early efforts, the FW process is broadly used in automobiles and aerospace industries to join the axial symmetry objects where one of them is circular profile [20]. To remove such limitation, the FW has been developed in the different configurations (Fig. 5) as listed here.
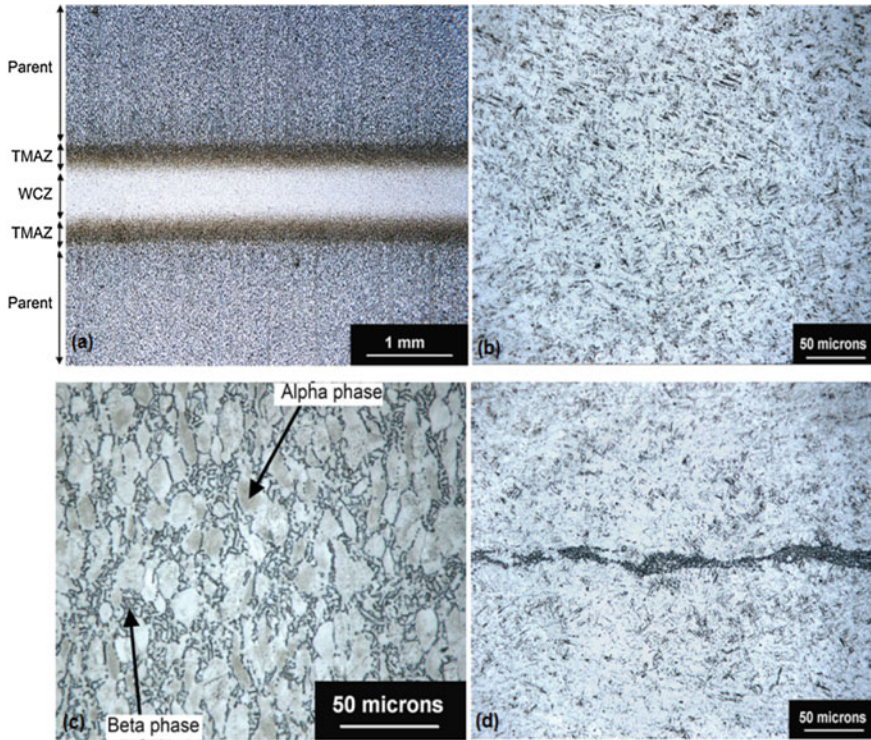
Fig. 4 Microstructure and different zones of weld joint; **a** different zones of weld; **b** microstructure of TMAZ; **c** parent metal grain structure; **d** surface impurity in weld due to the low burn-off [31]

- Direct drive friction welding (DDFW)
- Inertia friction welding (IFW)
- Linear friction welding (LFW)
- Orbital friction welding (OFW)
- Friction stir welding (FSW).

DDFW or continuous drive friction welding (CDFW) is the RFW technique where electrical motor is utilized to maintain the constant speed of rotational object, while other is kept stationary. The stationary object put through in contact with rotating body resulting friction at interface raised temperature to plasticize the materials. Once desired temperature is obtained, then rotation is stopped, and axial pressure is maintained or increased to get a weld joint. It is used for joining of tubular structures such as axel, valves, pressure vessels, pipelines for the automobiles and marine applications [32, 33].

IFW is another development of RFW, and its mechanism of heat generation is almost similar to DDFW process rather than rotational speed as shows in Fig. 6a, b. In IFW, the rotational speed continuously decreases during frictional phase under influence of inertia force of flywheel and axial force, while it is constant for DDFW
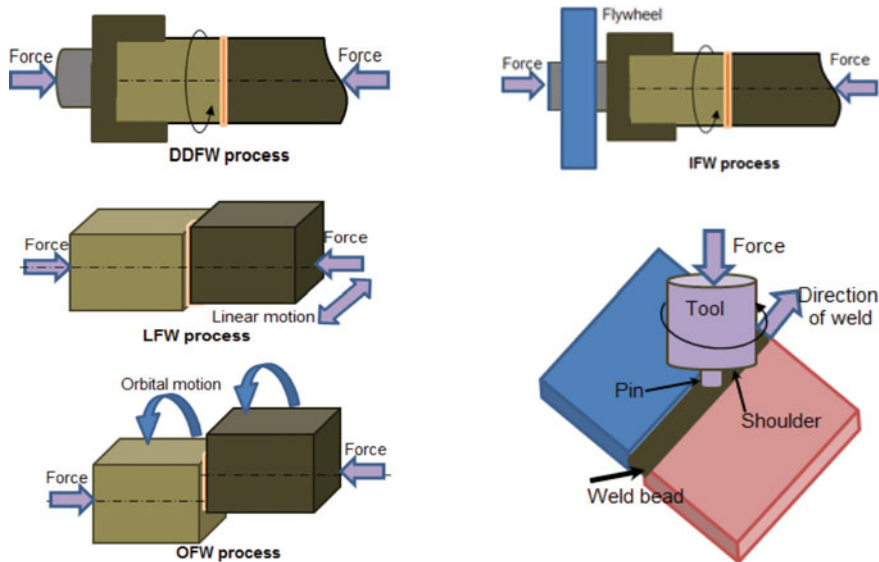
Fig. 5 Variants of FW process

process. In IFW process, one object is held stationary, while other is attached with flywheel. The flywheel is attached with an electrical motor to acquire the desired speed. The flywheel is disengaged with rotary motor when it stored the predetermined energy [34]. The energy stored by flywheel is utilized to generate heat at faying surfaces when they come in contact and axial pressure is applied. Due to heat, the metals are plasticized at interface and finally get a weld joint when maintained the absolute pressure till cooling. Similar to DDFW, the IFW process is also suitable for joining of circular objects having equal cross-sections. It is preferred by automotive industries for manufacturing of aero-engines causes by higher energy input than CCDFW process [17].

To overcome the drawbacks of RFW, the LFW come into existence where linear reciprocating motion is utilized to generate the heat rather than the rotational speed of
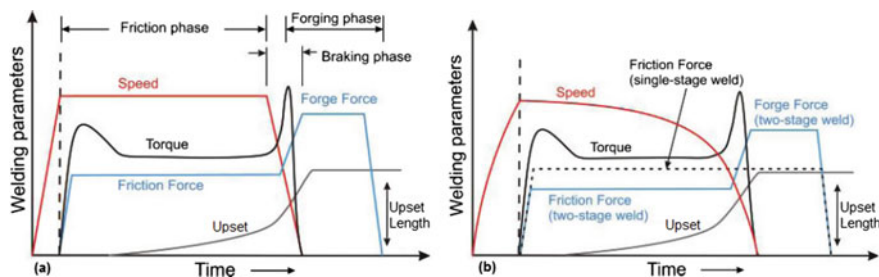

Fig. 6 Variation of parameters with time; **a** for DDFW process; **b** for IFW process [20]

the object. In this process, the stationary object is pushed against reciprocating object to create friction at the interface of faying surfaces. Due to this, heat is generated to plasticize at interface and finally get the weld joint after cooling with application of absolute pressure [35]. The plasticized layer at interface is expelled outside from weld region which is known as a flash. Due to this, reduction in length of specimen during joining. It is a suitable welding technique for various geometrical profiles rather than round profiles and provides uniform heat generation at constant speed.

The OFW is most suitable for joining of non-circular objects where workpiece does not rotate its central axis. In this, the both objects rotate in same direction, but their axis is offset about 3 mm [36]. The orbital motion delivers steady tangential velocity over entire area at interface resulting homogeneous weld structures. The OFW shows many benefits such as constant heat generation, suitability for non-circular objects and extra heat generated in weld zone as compared to LFW process.

FSW is the recent development of FW process which is widely applied for joining of dissimilar metal with application of rotating tool. The application of tool is mainly used to differentiate the FSW with other FW processes. In FSW, the friction stir tool is used to generate the heat rather than other processes. It is a most acceptable joining technique for lightweight metal and alloys such as aluminum, titanium, magnesium and polymer composites. It is broadly used for welding of lightweight boats, hulls, car bodies, deck panels, frames, airplane wings, fuel tanks, electronic circuits and devices [37, 38].

Generally, tool is key element of FSW which is rotated by electrical motor and having two parts as shoulder and pin. A typical schematic view of FSW process is as shown in Fig. 7 [38]. The purpose of shoulder is to create friction at tool-workpiece interface for generation of sufficient heat at junction and also prevention of molten metal from weld region. However, the pin absolutely penetrates along the thickness of specimen to maintain the contact of shoulder with specimen throughout welding [38–41]. Once adequate heat is generated, then tool is traversed in the weld direction and extruded fused material in a specific flow pattern as which plasticized metals bonded together to make weld joints. The FSW is a versatile joining process that provides better quality of welds and applicable for variety of geometry such as butt, lap, fillet and tee joints.

Fig. 7 Schematic view of FSW process [38]
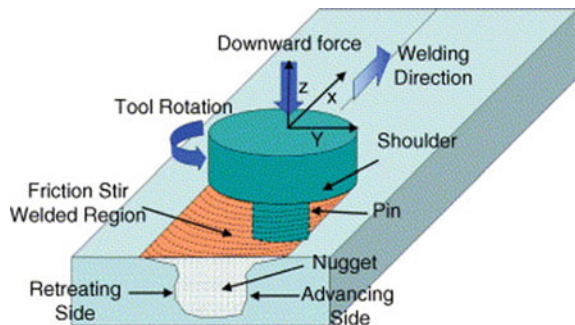
5 Process Parameters

In FW process, the rotational speed, transverse velocity, friction pressure, forge pressure, burn-off length, friction time and forge time are important factors that significantly affected the heat generation in FW and also heat transfer for quality weld. The tensile strength, yield strength, ultimate strength, micro-hardness and grain structures are evaluated quality of weld joints.

The effect of control parameters on responses related to FW process is shown in Fig. 8a–h. Figure 8a shows that the rotational speed is the predominant factor and significantly affected the parameters of OFW process [20]. The effects of the friction force, upset force and friction time on tensile strength are shown in Fig. 8b–d [42]. With increase of friction force, tensile strength of weld is increased within a limit because of better weld joint at higher temperature, while the upset force shows negative effect on the tensile force. Similar to friction force, the friction time also have positive effect of tensile strength, but initial tensile strength of weld joint decreases with increase of time because of insufficient availability of time for generation of adequate heat energy.

Figure 8e, f show the effect of rotational speed and rime on relative friction coefficient, friction coefficient (μ) and temperature [20]. As increase of rotational speed, the frictional coefficient decreases caused by softening of metal at higher temperature generated at higher speed. On other hand, the welding temperature increases with increase of time, while friction coefficient increases with time initially and then decreases refers Fig. 8f. The effect of rotational and travel speeds on failure load is presented in Fig. 8g, h and observed that failure load is higher at rotational speed as 900 rev/min and travel speed as 120 mm/min for Al–Mg metal [43]. Hence, the failure location and microstructure for FSW of Al–Mg is analyzed at such condition and presented in Fig. 9a–d.

Figure 9a shows the location of failure at rotational speed = 900 rev/min and transverse speed = 120 mm/min, while Fig. 9b shows the failure location at same conditions after 60 min heat treatment of weld. The formations of intermetallic compounds (IMC) are basic reason of failure of weld as shown in Fig. 9c, d. It is difficult to fully remove the formation of IMC during joining of similar/dissimilar metal materials by FW process. In general, the facture occurs in base metal as observed during welding of AlMg3–X10CrNiTi189 steel (diameter = 30 mm and tensile strength = 207 MPa). However, the bending angles within few degrees have been achieved during technological bending test with application of bending mandrel [44]. Such phenomena presented in Fig. 10a–d. Therefore, selection of appropriate parameters becomes necessary to reduce the formation of IMC during FW process.
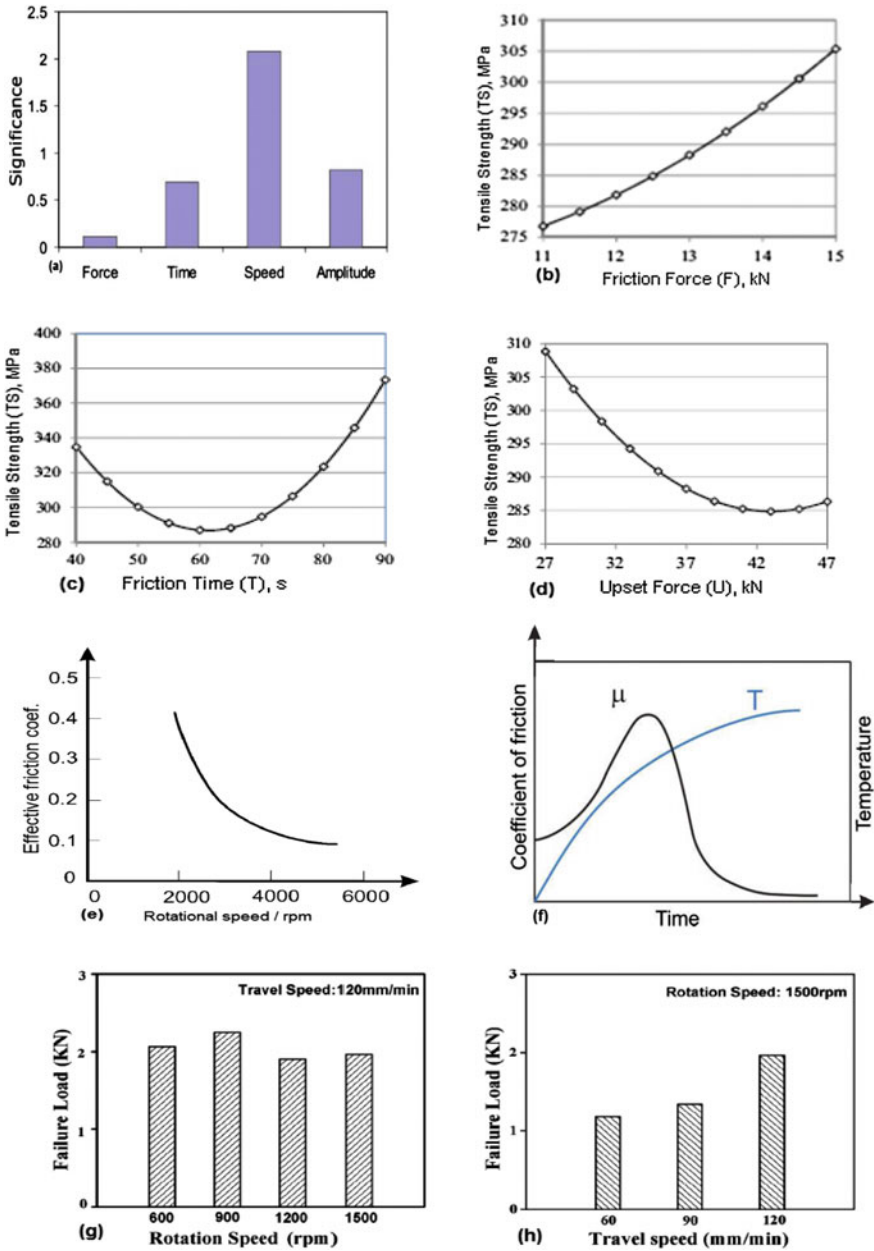
Fig. 8 Effect of process parameters; **a** significance of parameters for OFW process [20]; **b** effect of friction force on tensile strength [41]; **c** effect of friction time on tensile strength [41]; **d** effect of upset force on tensile strength [41]; **e** effect of rotational speed on relative friction coefficient [20]; **f** effect of friction time on friction coefficient and temperature; **g** effect of rotational speed on failure rate [42]; **h** effect of travel speed on failure rate [42]
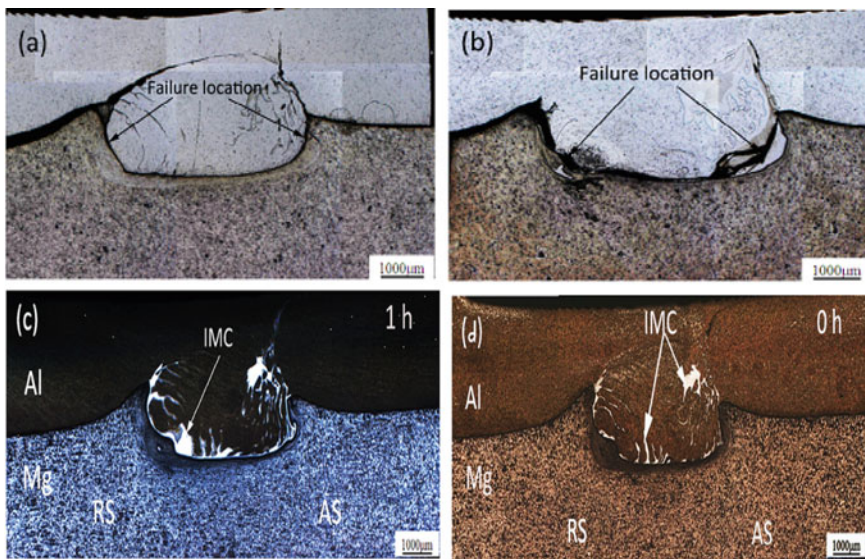
Fig. 9 Failure location in FSW joint of Al–Mg; **a** welded by 900 rpm–120 mm/min; **b** welded by 900 rpm–120 mm/min and after 1 h heat treatment; **c** microstructure of the samples after heat treatment at 400 °C of 0.5 h; **d** microstructure of samples after one hour heat treatment at 400^0C [42]
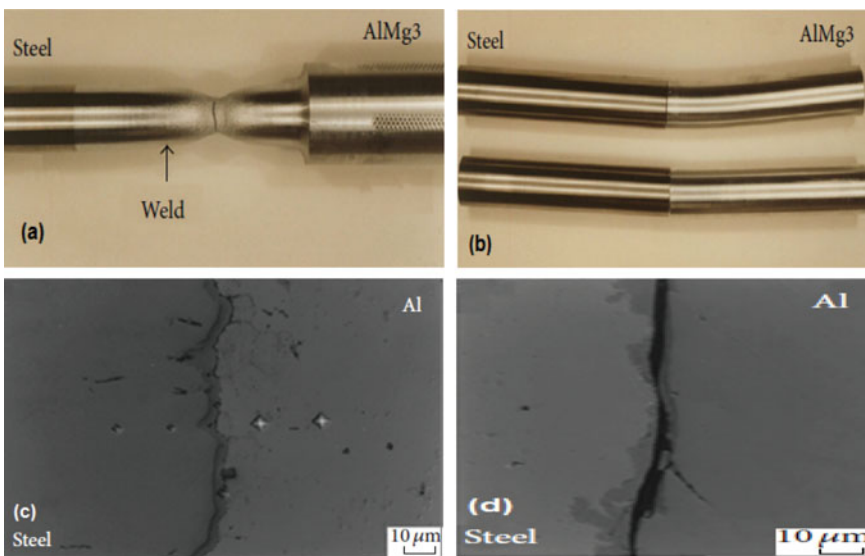

Fig. 10 FW of AlMg3–X10CrNiTi189 austenitic steel; **a** weld joint after static tensile weld; **b** technological bend test with mandrel; **c** microstructure of weld under static test; **d** microstructure of weld after technological bend test [43]

6 Process Capabilities

FW process shows many advantages over fusion welding process because of conversion of friction energy into thermal energy at interface of joint with small HAZ. The entire joining process is completed in order of second without application of shielding gas, filler rod or flux material [20, 23]. It is used to weld the variety of similar and dissimilar metal and alloys which makes challenge for various fusion/arc welding processes without sacrificing the weld strength and quality.

Due to low HAZ and rapid weld joints, it is applied to make a variety of parts related to the automobile and aerospace for joining of shaft, gears, axels and engine parts of aircraft. The plates and tubes of boilers and the components made of composite materials are effectively welded by FW process [14, 21, 22]. The RFW is applied in automobiles and marine application for joining of tubes, axels, pressure vessels, valves and pipe networks [32, 33]. The circular objects and aero-engines are preferred IFW process over DDFW and significantly applicable in automobiles industries [17]. The non-circular objects can be welded together by OFW process [36]. The lightweight items such as boats, hulls, car bodies, deck panels, frames, airplane wings, fuel tanks, electronic circuits and devices can be manufactured by FSW process [37]. The joining of boiler tube and plate is also preferred the FW process [21]. It is also applicable for joining of variety of objects and profiles including butt joint, lap joint, fillet and tee joints.

It is mostly used to weld lightweight metal and alloys like Al, Mg, Ti and nickel [26, 31, 34, 39]. Now, it is broadly accepted for joining of variety of dissimilar materials like Al and Mg [3], Al and SS [12, 30], Ti and SS [20]. It shows their potential for welding of ceramics also as Al and SiC [15, 22], Al–Mg and Si and Al–SiC [29]. Of course, variety of industries like automobile, marine, aerospace, agricultural and electronics offer FW process for making different objects which are difficult for fusion welding processes.

However, FW process has several limitations like one object must be plastically deformable under welding conditions. Generally, flash is formed during RFW because of plastic deformation at higher temperature which requires further machining to get desire profile as shown in Fig. 11a–c [45]. Instead of this, the thin objects and highly complex profiles are difficult to weld by it. The strong fastening and clamping devices are also limiting the applicability of FW process. Generally, non-uniform heat is generated in RFW welding as which non-uniform HAZ, and it also limited to circular objects [20]. The most common issues with FW process are its applicability for flat and angular butt joints.

7 Discussion and Future Directions

Of course, FW process is a unique method for joining of lightweight metal and alloys. The rapid joining with less HAZ without application of flux and filler material
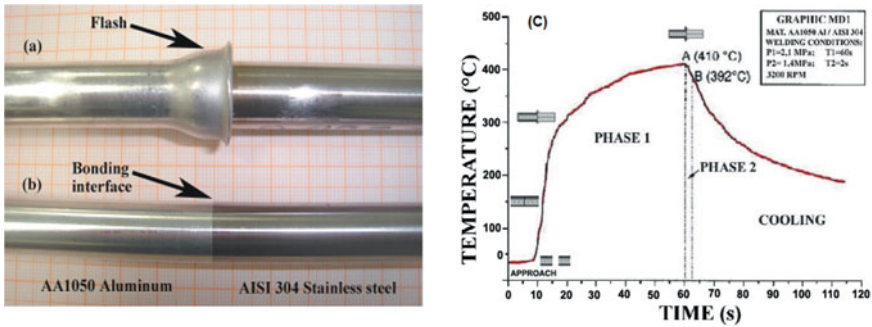
Fig. 11 Flash formation in FW of Al and stainless steel; **a** actual flash during RFW; **b** weld surface after machining; **c** time–temperature distribution with phase transformation during RFW of for Al and stainless steel with total time 62 s [44]

attracts the manufactures with wide acceptability for joining of similar/dissimilar materials. Hence, FW process becomes a demanding joining method for various industries like automobiles, aerospace, marine and railways. Many parameters such as rubbing velocity, rotational speed, friction pressure, coefficient of friction, forge pressure, burn-off length and friction time are significantly affected quality weld. Hence, the better combination of parameters are always preferred for quality weld. For this, optimization of parameters becomes a better tool to meet such criteria and also minimizes the cost.

In FW, the heat generation depends upon friction coefficient between rubbing bodies which vary throughout the process. Initially, sliding friction is considered when workpiece makes contact with rotational body. In this situation, heat generation is low, while higher high frictional stress causes of plastic deformation. On other hand, sticking condition is considered for higher temperature where shear stress is lower than frictional stress. Hence, it is difficult to find the exact/more appropriate frictional coefficient for FW process. For this, modeling becomes more appropriate tools for particular analysis.

Generally, mechanical bonding and diffusion play important role for joining of objects during FW process. In case of dissimilar metals, the melting at higher temperature material is difficult to achieve during FW which needs more realist study and analysis to identify the appropriate solution in same situations.

In FW, the materials are subjected to axial load as a result bending can take place. Hence, the materials are deformed or upset form their axial location. To minimize the axial deformation or upsetting, the comprehensive analysis becomes necessary to identify the loading conditions. In same way, the rotation torque also leads in upsetting and bending. Such phenomenon also needs to minimize during FW process.

Mostly, flash can be formed during forge/upset phase of FW process which requires secondary processing like machining. To minimize it, more analysis is required to identify the applied load capacity in different conditions for various

materials. In case of FSW process, the tool is influenced by thermal and mechanical loads during joining process, but mostly thermal behavior is mostly taken into consideration for analysis, while mechanical load is not clearly discussed in literatures. Hence, such area also needs analysis of mechanical behavior during FSW as well as FW process.

8 Summary

In solid-state welding processes, the FW is gaining importance for joining of the lightweight similar and dissimilar metal and alloys without external heat and filler material. Due to low heat energy, it makes welding process easier and eco-friendly and broadly applicable in modern industries like automobile and aerospace. The different variant of FW process is developed to meet the needs of advanced industries. The present chapter covers the basic concept of FW process with mechanism of heat generation, developed variants, effect of control parameters and process capabilities. Of course, the entire chapter presents in such a way that it makes easier and interesting for readers to understand different aspect of the FW process and their industrial applications.

References

1. Baqer YM, Ramesh S, Yusof F, Manladan SM (2018) Challenges and advances in laser welding of dissimilar light alloys: Al/Mg, Al/Ti, and Mg/Ti alloys. Int J Adv Manuf Technol 95(5):4353–4369
2. Manladan S, Yusof F, Ramesh S, Fadzil M (2016) A review on resistance spot welding of magnesium alloys. Int J Adv Manuf Technol 86(5–8):1805–1825
3. Liu L, Ren D, Liu F (2014) A review of dissimilar welding techniques for magnesium alloys to aluminum alloys. Materials 7(5):3735–3757
4. Auwal ST, Ramesh S, Yusof F, Manladan SM (2018) A review on laser beam welding of titanium alloys. Int J Adv Manuf Technol 97:1071–1098
5. Abhay Jha K, Sreekumar K (2008) Metallurgical studies on cracked Al-5.5 Zn-2.5Mg-1.5Cu aluminum alloy injector disc of turbine rotor. J Failure Anal Prevent 8(4):327–332
6. Mordike B, Ebert T (2001) Magnesium: properties-applications-potential. Mater Sci Eng, A 302(1):37–45
7. Yadav RN (2018) An experimental study and parameters optimization on duplex turning of titanium alloy. Mater Perform Characterization 7(1):423–444
8. Kumar S, Yadav RN, Kumar R (2020) Modelling and optimisation of duplex turning of titanium alloy (grade 5) using Taguchi methodology-response surface methodology. Int J Indus Syst Eng 35(4):463–481

9. Kumar C, Das M, Paul CP, Singh B (2017) Experimental investigation and metallographic characterization of fiber laser beam welding of Ti-6Al-4V alloy using response surface method. Opt Laser Eng 95:52–68

10. Donachie MJ (2000) Titanium: a technical guide, 2nd edn. ASM International, Ohio, USA

11. Alves EP, Neto FP, An CY (2010) Welding of AA1050 aluminum with AISI 304 stainless steel by rotary friction welding process. J Aerosp Technol Manag 2(3):301–306

12. Little RL (2017) Welding and welding technology. McGraw Hill Education, USA

13. Parmar RS (2013) Welding engineering and technology. Khanna Publishers, New Delhi, India

14. Meshram SD, Mohandas T, Reddy GM (2007) Friction welding of dissimilar pure metals. J Mater Process Technol 184:330–337

15. Sreenivasan KS, Kumar SS, Katiravan J (2019) Genetic algorithm based optimization of friction welding process parameters on AA7075-SiC composite. Eng Sci Technol 22(4):1136–1148

16. Rajak DK, Pagar DD, Menezes PL, Eyvazian A (2020) Friction-based welding processes: friction welding and friction stir welding. J Adhes Technol 34(24):2613–2637

17. Li W, Vairis A, Preuss M, Ma T (2016) Linear and rotary friction welding review. Int Mater Rev 61(2):71–100

18. Mllieswaran K, Padmanabhan R, Balasubramanian V (2018) Friction stir welding parameters optimization for tailored welded blank sheets of AAl 100 with AA 6061. Adv Mater Process Technol 4(1):142–157

19. Muralimohan CH, Ashfaq M, Ashiri R, Muthupandi V, Sivaprasad K (2016) Analysis and characterization of the role of Ni interlayer in the friction welding of Titanium and 304 austenitic stainless steel. Metal Mater Trans A 47(1):347–359

20. Maalekian M (2007) Friction welding-critical assessment of literature. Sci Technol Weld Joining 12(7):738–759

21. Kumaran SS, Das AD (2018) An investigation of boiler grade tube and tube plate without block by using friction welding process. Mater Today: Proc 5:8267–8276

22. Zuo L, Zhao X, Li Z, Zuo D, Wang H (2020) A review of friction stir joining of SiCp/Al composites. Chin J Aeronaut 33(3):792–804

23. Masaaki K, Kenji S, Masahiro K, Akiyoshi F (2003) Observation of joining phenomena in friction stage and improving friction welding method. JSME Int J, Ser A 46(3):384–390

24. Uday MB, Fauki MNA, Zuhailawati H, Ismail AB (2010) Advances in friction welding processes: a review. Sci Technol Weld Joining 15(7):534–558

25. Grong O (1997) Metallurgical modelling of welding, 2nd edn. Institute of Materials, London, UK

26. Vairis A, Frost M (2000) Modelling the linear friction welding of titanium blocks. Mater Sci Eng, A 292(1):8–17

27. Maalekian M (2007) Friction welding of high carbon steel in large cross section. PhD Thesis, Graz University of Technology, Graz, Austria

28. Moraitis GA, Labeas GN (2010) Investigation of friction stir welding process with emphasis on calculation of heat generated due to material stirring. Sci Technol Weld Joining 15(2):177–184

29. Midling OT, Grong O (1994) A process model for friction welding of Al-Mg-Si alloys and Al-SiC metal matrix composites-I. HaZ temperature and strain rate distribution. Acta Metall Mater 42(5):1595–1609

30. Lee WB, Yeon YM, Kim DU, Jung SB (2003) Effect of friction welding parameters on mechanical and metallurgical properties of aluminium alloy 5052–A36 steel joint. Mater Sci Technol 19(6):773–778

31. McAndrew AR, Colegrove PA, Addison AC, Flipo BCD, Russell MJ (2014) Energy and force analysis of Ti-6Al-4V linear friction welds for computational modeling input and validation data. Metall Mater Trans A 45:6118–6128

32. Kalsi NS, Sharma VS (2011) A statistical analysis of rotary friction welding of steel with varying carbon in workpieces. Int J Adv Manuf Technol 57(9–12):957–967

33. Schmicker D, Naumenko K, Strackeljan J (2013) A robust simulation of direct drive friction welding with a modified carreau fluid constitutive model. Comput Methods Appl Mech Eng 265:186–194

34. Liu C, Zhu HY, Dong CL (2014) Internal residual stress measurement on inertia friction welding of nickel-based superalloy. Sci Technol Weld Joining 19(5):408–415

35. Vaziri M, Lindgren O, Pizzi A (2012) Influence of machine setting and wood parameters on crack formation in scots pine joints produced by linear friction welding. J Adhes Sci Technol 26(18–19):2189–2197

36. McAndrew AR, Colegrove PA, Buhr C, Flipo BCD, Vairis A (2018) A literature review of Ti-6Al-4V linear friction welding. Prog Mater Sci 92:225–257

37. Venu B, Swathi IB, Raju LS, Santhanam G (2019) A review on friction stir welding of various metals and its variables. Mater Today: Proc 18(1):298–302

38. Mishra RS, Ma ZY (2005) Friction stir welding and processing. Mater Sci Eng R Rep 50(1–2):1–78

39. Li Y, Qin F, Liu C, Wu Z (2017) A review: effect of friction stir welding on microstructure and mechanical properties of magnesium alloys. Metals 7(12):524–538

40. Zens A, Zaeh MF, Marstatt R, Haider F (2019) Friction stir welding of dissimilar metal joints. Mater Sci Eng 50(8):949–957

41. Mohanty HK, Mahapatra MM, Kumar P, Biswas P (2012) Effect of tool shoulder and pin probe profiles on friction stirred aluminum welds-a comparative study. J Mar Sci Appl 11(2):200–207

42. Winiczenko R (2016) Effect of friction welding parameters on the tensile strength and microstructural properties of dissimilar AISI 1020-ASTM A536 joints. Int J Adv Manuf Technol 84(5–8):941–955

43. Tan S, Zheng F, Chen J, Han J, Wu Y, Peng L (2017) Effects of process parameters on microstructure and mechanical properties of friction stir lap linear welded 6061 aluminum alloy to NZ30K magnesium alloy. J Magnesium Alloys 5(1):56–63

44. Ambroziak A, Korzeniowski M, Kustron P, Winnicki M, Sokowski P, Harapinska E (2014) Friction welding of aluminium and aluminium alloys with steel. Adv Mater Sci Eng. https://doi.org/10.1155/2014/981653

45. Alves EP, Neto FP, An CY, Silva EC (2012) Experimental determination of temperature during rotary friction welding of AA1050 aluminum with AISI 304stainless steel. J Aerosp Technol Manag 4(1):61–68

Chapter 9
Fractographic Analysis of Friction Stir Welded Aluminium Alloy

A. Kumar, P. J. Saikia, M. Kumar, S. Bag, N. Muthu, and R. G. Narayanan

1 Introduction

In this modern era, fuel plays an essential role in the economic development of any nation. Fuel demands are increasing day by day, yet their sources are limited and rapidly shrinking. Therefore, there is a need to reduce fuel consumption. One of the ways of achieving this goal is to reduce the overall weight of the structure whilst ensuring access to affordable and reliable material. Under such requirements in aerospace and automobile sectors, joining various lightweight materials such as aluminium [1, 2] or magnesium [3, 4] is necessary to produce parts with complex geometries. In the conventional welding process, such lightweight materials cannot be joined due to inherent disadvantages such as high residual stresses, porosity, cracking during solidification, and heat-affected zones (HAZs).

The friction stir welding (FSW) process was developed at The Welding Institute (TWI) by Wayne Thomas in 1991 [5, 6]. The FSW produces good quality welds in

A. Kumar · P. J. Saikia · M. Kumar · S. Bag · N. Muthu (✉) · R. G. Narayanan
Indian Institute of Technology Guwahati, Guwahati, Assam 781039, India
e-mail: nelsonm@iitg.ac.in

A. Kumar
e-mail: avneesh.kumar@iitg.ac.in

P. J. Saikia
e-mail: pranj176103002@iitg.ac.in

M. Kumar
e-mail: munnakr2861rj@gmail.com

S. Bag
e-mail: swarupbag@iitg.ac.in

R. G. Narayanan
e-mail: ganu@iitg.ac.in

materials such as aluminium, and therefore, it has become a favoured approach for developing lightweight structures in practically all industrial applications. The FSW provides several advantages over the traditional joining processes, and it was first used to weld aluminium alloy sheets in butt joints [7, 8]. A schematic of the FSW process is shown in Fig. 1. A non-consumable rotating tool with a specially designed pin and shoulder is placed between two plates to be welded and simultaneously traversed along the joint line in this operation. The plates must be fastened to a backing bar so that the adjacent joint faces are not pushed apart or displaced out of place. The first contact is made when the pin is put into the joint. As a result of friction between the tool and the workpiece, wear-resistant welding tools heat up a metal column with a cylindrical shape surrounding the pin and the area immediately below the pin. This localized heating due to the friction between the tool and the workpiece causes the workpiece to deform micro-plastically [9], and the material around the pin gets softer. Softened material allows the tool to travel along the weld line more easily without exceeding the melting point. The plasticised material is moved from the front part to the rear part of the tool pin rotation and translation [10]. As a result of the procedure, a solid joint is formed. Depending on the tool pin's length, the penetration thickness into the plates is controlled [11]. The shoulder generates an extra amount of frictional heat to the weld zone during welding, which is essential for keeping highly plastic materials from being evacuated. The softened zone of the material is more prominent at the upper surface of the material that comes into direct contact with the shoulder and progressively tapers to the pin diameter [12]. The tool pin and tool shoulder are sufficiently heated as a result of the heat due to friction to form a plastic state around the submerged pin and on the contact area between the workpiece and the tool shoulder [13–15]. In the welding process, the welding tool rotates and moves on both surfaces simultaneously, creating a specific imbalance between the two surfaces. An advancing side of the welding tool is characterised by rotation and translation of the welding tool in the same direction. On the other hand, the retreating side results from a tool rotation and translation motions counteracting each other [16].

The tool pin profile plays an essential role in a good joint. Tikader et al. [17] used straight cylindrical and tapered cylindrical pin profile tools to the friction stir
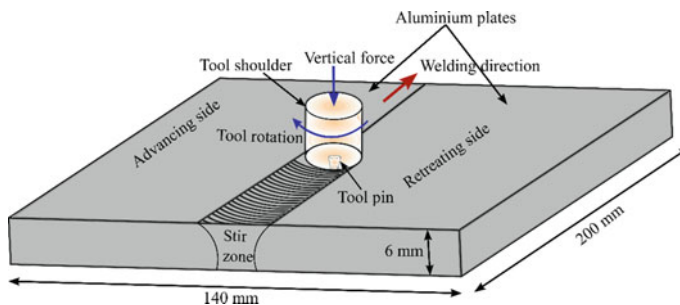

Fig. 1 Schematic of FSW process

(FS) weld of AA 1100 plates and found that the heat produced by the tool with the tapered pin was less than that produced by the straight cylindrical pin. As a consequence of welding samples with tapered cylindrical tools, greater toughness values were achieved. They also stated that an increase in shoulder diameter has no major effect on heat generation. It is recommended that the diameter be kept as small as effective ways to minimize the emergence of worm-hole defects. Yaduwanshi et al. [18] performed the FSW of AA1100 with and without preheating and achieved joint strengths of around 89% and 95%, respectively, compared to the un-welded base metal strength. The elongation of FS welded specimens differed significantly from that of the base material. The material experiences constant dynamic recrystallization, resulting in fine grains with Al_2O_3 particles at the stirred zone. The elongation was reduced for preheated FS welds compared to the non-preheated FS welds and the base metal specimens.

The fracture toughness of the material is an important parameter in aerospace, automobile, and structural applications under service loading conditions. Sutton et al. [19] investigated the AA2024-T3 plates and found that all welded samples showed less fracture toughness than the un-welded sample. Pirondi and Collini [20] studied the fracture toughness of two aluminium-based metal matrix composite (MMC) reinforced with Al_2O_3 particles, namely 6061 aluminium having 20 vol.% of Al_2O_3 (W6A20A), and another one was 7005 having 10 vol.% of Al_2O_3 (W7A10A). Fracture toughness value in the case of W6A20A, the welded joint was 25% lower than the parent material, whilst it was 10–20% higher for the W7A10A.

The fractographic analysis is concerned with the study of fractured surface topographies to determine the causal stress and process. Whilst macro-fractography deals with the research of surface morphologies by visual inspection, micro-fractography deals with the study of surface morphologies by optical microscope or high-definition scanning electron microscope (SEM) [21]. The fracture study of the friction stir welded specimens is essential to estimate the toughness of the welded sample and estimate the quality of the weld. The material fracture due to crack propagation is primarily influenced by inhomogeneity, grain size, crystal structure, and loading conditions [22]. The fracture modes can be ductile or brittle depending on the aforementioned parameters. Whereas a ductile fracture is characterised by relatively larger plastic deformation, formation of the shear lip with fibrous fracture surface, a brittle fracture has minimal plastic deformation and a flat fracture surface perpendicular to the loading plane; chevron or granular-like surface structures are the characteristic features of brittle fracture [23].

In the present study, the effects of rotational speed at constant welding speed on the tensile strength of FS welded joints made of 1100 aluminium alloy are analysed. Further, the standard test method for mode I crack involving a CT specimen was fabricated, and fracture toughness was estimated to study the effects of rotational speed. Finally, the SEM analysis was used to investigate the fracture surfaces using fractured tensile and CT test samples to understand the nature of the failure.

2   Experimental Procedure

As-received AA1100 is used for FSW experiments. The dimensions of aluminium plates are 200 mm × 70 mm × 6 mm. Before welding, the sides of the aluminium plates were machined with a grinding machine. This made it easier for the mating surfaces to make good contact when arranged in a butt configuration. Acetone was used to clean the workpieces to eliminate dirt, debris completely, and small particles left after the machining process. A commercial high-speed steel (H13) tool with a tapered cylindrical threaded pin (Fig. 2) of 5.7 mm length, 6 mm base diameter, 4 mm minor diameter, and 16 mm shoulder diameter was employed. The FSW experiments were performed at 1100 and 1500 rpm, with 98 mm/min traverse speed.

2.1   Tensile Testing

Standard tensile specimens were cut according to the ASTM standard E8 [24] with gauge lengths of 32 mm and width of 6 mm from the welded plates as shown in Fig. 3, normal to the weld, with an electro-discharge machine (EDM). The gauge length of the tensile samples includes weld zone and parent material. Tensile tests were conducted in a 100 kN UTM machine at a cross-head speed of 1 mm/min.

2.2   Fracture Testing

The fracture tests were carried out as per the standard ASTM E647, as shown in Fig. 4 with the stated dimensions [25]. Using wire EDM cutting, an initial seam of 2 mm in length and 0.5 mm in width was produced ahead of the notch tip with the understanding that wire EDM has effect on the fracture toughness [26]. All the specimens were subjected to fatigue loading with a stress intensity factor range $\Delta K = 4.7 \, \text{MPa} \sqrt{\text{m}}$ under a stress ratio $R = 0.2$ to extend the pre-crack length by another 2 mm. The crack growth direction is along the weld line for all the CT specimens. The crown side of the specimens was machined to remove the flush and to ensure the proper alignment of the base plate. All the specimens were subjected to quasi-static loading with 0.25 mm/min cross-head speed until rupture.
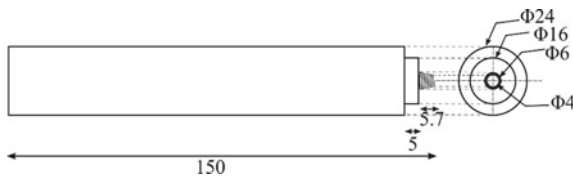

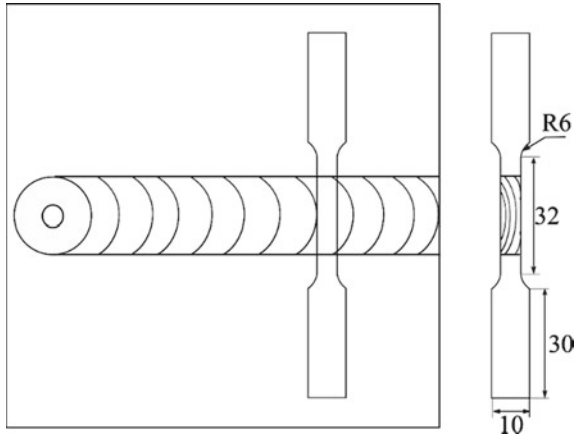**Fig. 2** Tool dimensions (in mm)

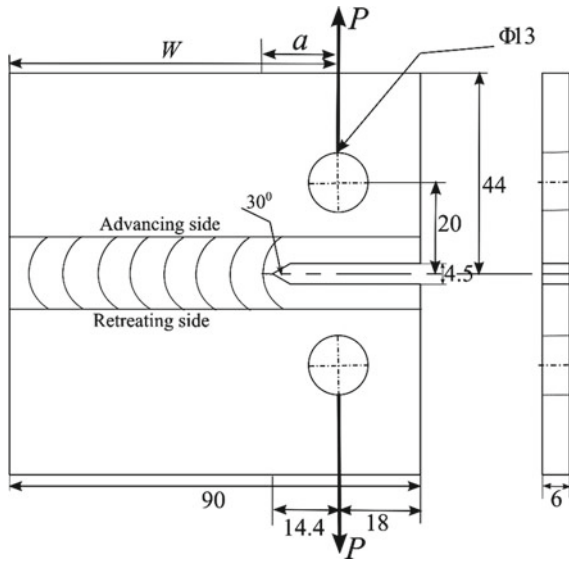**Fig. 3** Schematic of the tensile test specimen (all dimensions are in mm)

Fig. 4 Schematic of the CT test specimen (all dimensions are in mm)

3 Results and Discussions

3.1 Failure and Fracture Surface Analysis of Tensile Tested Specimens

The tensile characteristics of the base material and the FS welded specimens are shown in Table 1. Identical fracture patterns were observed in the base metal (A) and the welded specimens (B and C) at 1100 rpm. A rapid fracture was observed in specimens B and C in two directions: first, upwards at 45°, bending slightly towards the stir zone, then vertically upwards in the stir zone. Secondly, the tool marks caused the fracture to progress downward vertically (Fig. 5—B and C). Specimens D and E made from 1500 rpm fractured almost at the joint line. Specimens D and E had a tiny hole in the nugget area that determined the fracture position. The sharp edges of the tiny hole served as stress concentrators, which allowed the weld nugget to fracture quickly. According to Liu et al. [27], tensile failures around weld nugget contact are commonly caused by significant variances in their internal structures, making the interface a weaker area. All the FSW samples are less ductile as compared to the base material.

Table 1 Tensile testing results of the base specimen and FS welded specimens

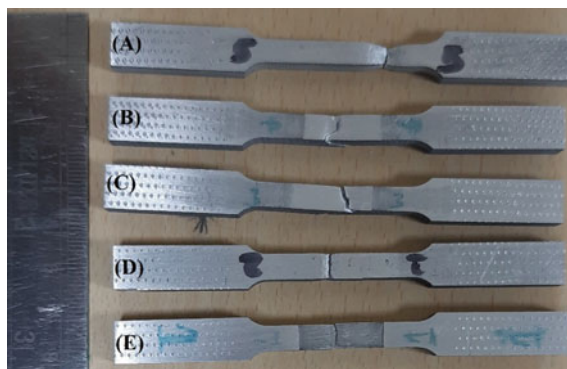| Specimen					
Properties	(A)	(B)	(C)	(D)	(E)
Ultimate tensile strength (UTS), MPa	148	128	121	101	95
Percentage of elongation	13.7	8.55	9.21	6.25	5.3
Joint efficiency (%)	100	86.4	81.8	68.2	64.2

Fig. 5 Fractured tensile specimen of (A) base metal, (B and C) welded specimens at 1100 rpm, and 98 mm/min, (D and E) welded specimens at 1500 rpm and 98 mm/min

Figures 6a, b show dimple ruptures characterized by high amounts of plastic deformation prior to fracture. Images of tensile fracture surfaces captured using scanning electron microscopy (SEM) showed several voids of various shapes and sizes scattered randomly on the fracture surface. Fracture is initiated by micro-void coalescence observed as distinctly elongated dimples in Fig. 6b. Dimples of different shapes and sizes throughout the overload zone resembled localized ductile failures [12].

Figure 6(ii) shows the fractured features at 1100 rpm. Figure 6c shows that the overall morphology of the material was ductile and brittle. On closer inspection, lots of new cracks could be seen in the form of multilayered cliffs, which resembled locally brittle failures (Fig. 6d). The transgranular area was characterised by ridges of tear and microscopic cracks, suggesting a locally brittle and ductile failure process. An isolated distribution of voids and elongated dimples indicated local ductility in the tensile overload zone.

The fracture morphology of the FS welded sample made at 1500 rpm is shown in Fig. 6(iii). The morphology at high resolution was predominantly rock candy fracture (low-energy fracture) regions and transgranular. High magnification shows characteristics identical to those seen in the base metal part in the transgranular zone with several small voids as well as cracks of different forms and sizes.

3.2   Failure and Fracture Surface Analysis of CT Specimens

The load-extension behaviour of all the CT specimens is shown in Fig. 7, indicating a better performance from base material as compared to FSW plates. On a similar note, the welded specimen made at 1100 rpm has a higher load-bearing capacity than that made at 1500 rpm.

Another critical parameter in fracture mechanics is the resistance of a material against crack propagation, popularly termed as fracture toughness. It serves as a basis for quality assurance and selection of material for proper design. The fracture toughness (K_{IC}) of a material can be evaluated as per the standard ASTM E399-09E2 [28]

$$K_{IC} = \frac{P}{B\sqrt{W}} f\left(\frac{a}{W}\right) \tag{1}$$

where $f\left(\frac{a}{W}\right)$ is a geometrical parameter depending on the crack length and the width of the specimen mentioned in Fig. 4. For a CT specimen,

$$f\left(\frac{a}{W}\right) = \frac{\left(2 + \frac{a}{W}\right)}{\left(1 - \frac{a}{W}\right)^{\frac{3}{2}}}$$
$$\left[0.886 + 4.64\left(\frac{a}{W}\right) - 13.32\left(\frac{a}{W}\right)^2 + 14.72\left(\frac{a}{W}\right)^3 - 5.60\left(\frac{a}{W}\right)^4\right] \tag{2}$$

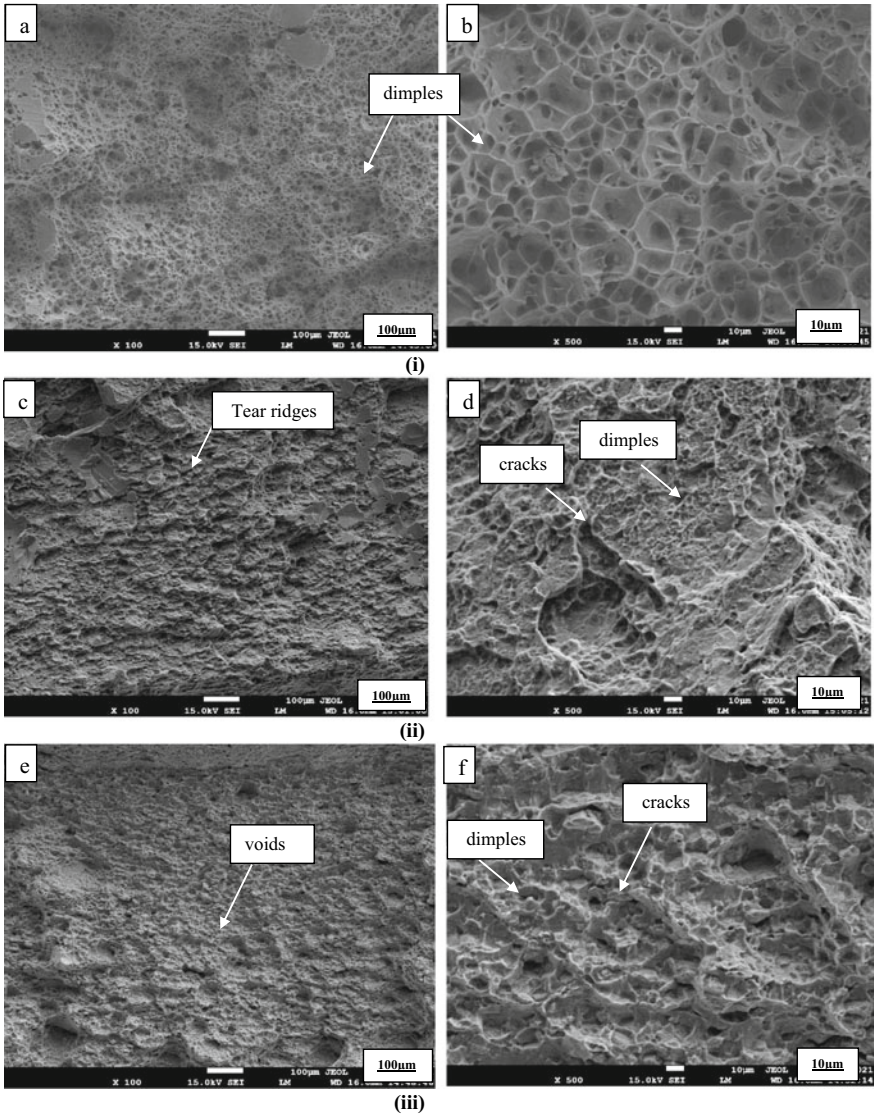**Fig. 6** SEM images of the fractured surface of (**i**) base metal [specimen (A)], (**ii**) welded specimen at 1100 rpm and 98 mm/min [specimen (B)], (**iii**) welded specimen at 1500 rpm and 98 mm/min [specimen (D)]
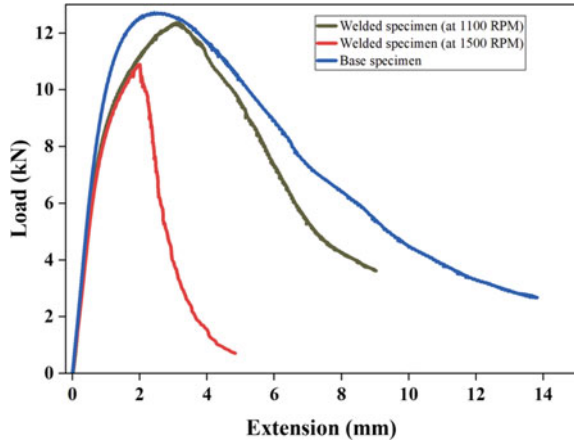
Fig. 7 Load-extension behaviour of CT specimen

Table 2 Estimated values of fracture toughness

Specimen	Estimated fracture toughness, $K_{IC}(MPa\sqrt{m})$
Base material	36.59
FS welded (rpm = 1100)	35.58
FS welded (rpm = 1500)	31.33

The calculated values of fracture toughness for all base and welded specimens are mentioned in Table 2.

From Fig. 7, the maximum fracture load (P) obtained for the base metal is 12.7 kN, which is higher than the welded specimens. The fracture toughness value of the welded CT specimens compared to the base metal is 97.24% and 85.62% for 1100 rpm and 1500 rpm, respectively. As the rotational speed increases, fracture toughness values decrease due to the loss of ductility and likelihood increase in the worm-hole defects [29].

SEM was used to investigate the fracture surfaces of the base metal and the FS welded samples. The observation was considered at three specific places parallel to the rolling plane: the notch tip, middle, and end, as shown in Fig. 8. All of the quantitative data were collected on a sample size of 4×4 mm^2, with appropriate microscope resolution.

The fracture surfaces of the base material consisted of rough surface textures with a combination of void and dimples, as shown in Fig. 9a–c. Due to dimple coalescence, the tiny shallow dimples grow and create large voids. A series of V-shaped chevron patterns are observed across the fracture surface, as shown in Fig. 9d–h, irrespective of the rotational speeds. Intergranular fracture is observed in Fig. 9(i).
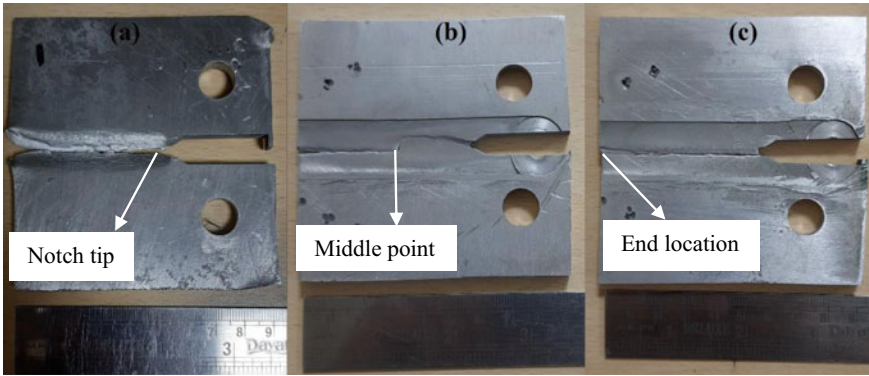
Fig. 8 Fractured CT specimen of **a** base metal, **b** welded specimen at 1100 rpm, **c** welded specimen at 1500 rpm
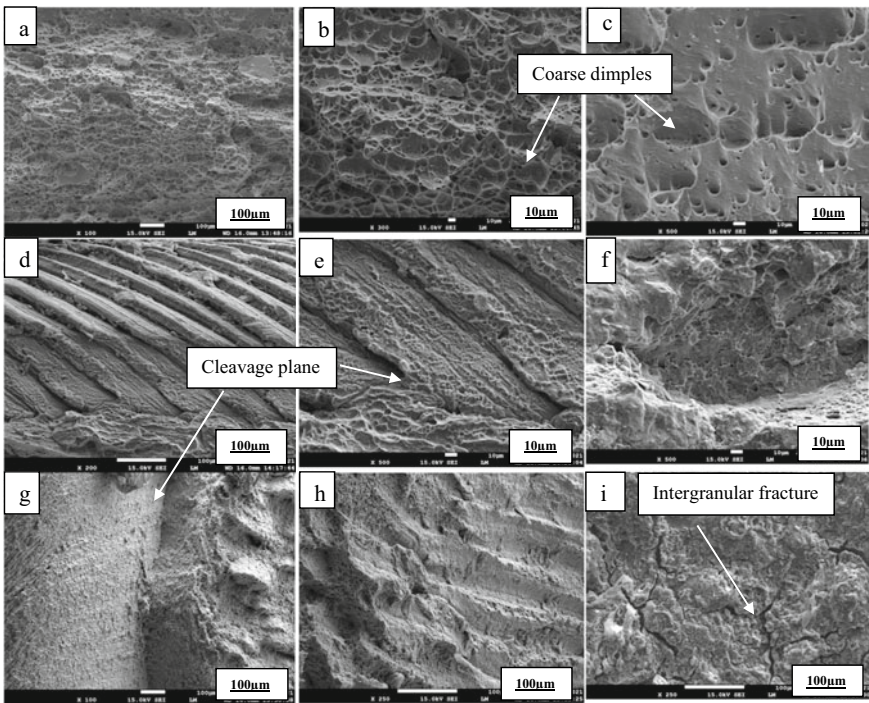

Fig. 9 Fracture morphology of CT specimen **a–c** base material, **d–f** welded specimen made at 1100 rpm, **g–i** Welded specimen made at 1500 rpm

4 Conclusions

An experimental investigation was conducted to investigate the FS welded aluminium alloy's (AA1100) fracture and quasi-static deformation behaviour.

The following are the conclusions made from the results obtained:

- As compared to the base specimen, FS welded specimens failed at significantly lower strain levels. This is due to localized strain in regions that FSW has softened.
- UTS of the FSW specimens decreased by 12.6% and 31.8%, respectively, for 1100 rpm and 1500 rpm rotational speed.
- Compared to the base metal, the fracture toughness of welded CT specimens is 97.24% for 1100 rpm and 85.62% for 1500 rpm.
- In the base metal specimen under tensile fracture, several voids were scattered in various directions on the fracture surface during tensile tests. Dimples and voids of varying sizes and shapes were found throughout the overload zone, resembling localized ductile failures. The fracture surface of the FS welded tensile specimen at 1100 rpm showed that the overall morphology of the material was ductile and brittle, with the failure axis parallel to the stress axis. On closer inspection, the transgranular area was characterized by ridges of tear and microscopic cracks, suggesting a locally brittle and ductile failure process. The fracture surface of the FS welded tensile specimen at 1500 rpm at the high magnification reveals predominantly rock candy fracture regions and transgranular zone with several small voids and cracks of various shapes and sizes.
- The fractured surfaces of welded CT specimens are negligible plastic deformation irrespective of the process parameters. The fracture surfaces were relatively brighter than the base metal, with more pronounced peaks and valleys. The granular and brilliance surfaces are indicative of a brittle fracture. The fracture surfaces of the base material consist of rough surface textures with a combination of void and dimples.

References

1. El-Danaf EA, El-Rayes MM (2013) Microstructure and mechanical properties of friction stir welded 6082 AA in as welded and post weld heat treated conditions. Mater Des 46:561–572. https://doi.org/10.1016/j.matdes.2012.10.047
2. Sonne MR, Tutum CC, Hattel JH et al (2013) The effect of hardening laws and thermal softening on modeling residual stresses in FSW of aluminum alloy 2024–T3. J Mater Process Technol 213:477–486. https://doi.org/10.1016/j.jmatprotec.2012.11.001
3. Cao X, Jahazi M (2011) Effect of tool rotational speed and probe length on lap joint quality of a friction stir welded magnesium alloy. Mater Des 32:1–11. https://doi.org/10.1016/j.matdes.2010.06.048

4. Chowdhury SM, Chen DL, Bhole SD, Cao X (2010) Tensile properties of a friction stir welded magnesium alloy: effect of pin tool thread orientation and weld pitch. Mater Sci Eng A 527:6064–6075. https://doi.org/10.1016/j.msea.2010.06.012

5. Thomas WM, Staines DG, Norris IM, De Frias R (2003) Friction stir welding tools and developments. Weld World 47:10–17. https://doi.org/10.1007/BF03266403

6. Thomas WM (1991) Improvements relating to friction welding

7. Dawes C, Thomas WM (1996) Friction stir process welds aluminium alloys: the process produces low-distortion, high-quality, low-cost welds on aluminium. Weld J 75:41–45

8. Threadgilll PL, Leonard AJ, Shercliff HR, Withers PJ (2009) Friction stir welding of aluminium alloys. Int Mater Rev 54:49–93. https://doi.org/10.1179/174328009X411136

9. Nègre P, Steglich D, Brocks W (2004) Crack extension in aluminium welds: a numerical approach using the Gurson-Tvergaard-Needleman model. Eng Fract Mech 71:2365–2383. https://doi.org/10.1016/j.engfracmech.2004.01.007

10. Cavalier P, Nobile R, Panella FW, Squillace A (2006) Mechanical and microstructural behaviour of 2024–7075 aluminium alloy sheets joined by friction stir welding. Int J Mach Tools Manuf 46:588–594. https://doi.org/10.1016/j.ijmachtools.2005.07.010

11. Zeng W (2006) Effect of tool wear on microstructure, mechanical properties and acoustic emission of friction stir welded 6061 Al ALLOY. Acta Metall Sin (english Lett) 19:9–19

12. Srivatsan TS, Vasudevan S, Park L (2007) The tensile deformation and fracture behavior of friction stir welded aluminum alloy 2024. Mater Sci Eng A 466:235–245. https://doi.org/10.1016/j.msea.2007.02.100

13. Mishra RS, Ma ZY (2005) Friction stir welding and processing. Mater Sci Eng R Reports 50:1–78. https://doi.org/10.1016/j.mser.2005.07.001

14. Sidhu MS, Chatha SS (2012) Friction stir welding—process and its variables: a review. Int J Emerg Technol Adv Eng 2:275–279

15. Ma ZY (2008) Friction stir processing technology: a review. Metall Mater Trans A Phys Metall Mater Sci 39(A):642–658. https://doi.org/10.1007/s11661-007-9459-0

16. Nandan R, Roy GG, Debroy T (2006) Numerical simulation of three dimensional heat transfer and plastic flow during friction stir welding. Metall Mater Trans A Phys Metall Mater Sci 37:1247–1259. https://doi.org/10.1007/s11661-006-1076-9

17. Tikader S, Biswas P, Puri AB (2018) A study on tooling and its effect on heat generation and mechanical properties of welded joints in friction stir welding. J Inst Eng Ser C 99:139–150. https://doi.org/10.1007/s40032-016-0325-y

18. Yaduwanshi DK, Bag S, Pal S (2014) Effect of preheating in hybrid friction stir welding of aluminum alloy. J Mater Eng Perform 23:3794–3803. https://doi.org/10.1007/s11665-014-1170-x

19. Sutton MA, Reynolds AP, Yang B, Taylor R (2003) Mode I fracture and microstructure for 2024–T3 friction stir welds. Mater Sci Eng A 354:6–16. https://doi.org/10.1016/S0921-5093(02)00078-3

20. Pirondi A, Collini L (2009) Analysis of crack propagation resistance of Al–Al2O3 particulate-reinforced composite friction stir welded butt joints. Int J Fatigue 31:111–121. https://doi.org/10.1016/j.ijfatigue.2008.05.003

21. Lynch SP, Moutsos S (2006) A brief history of fractography. J Fail Anal Prev 6:54–69. https://doi.org/10.1361/154770206X156231

22. Pradhan PK, Dash PR, Robi PS, Roy SK (2012) Micro void coalescence of ductile fracture in mild steel during tensile straining. Frat ed Integrita Strutt 19:51–60. https://doi.org/10.3221/IGF-ESIS.19.05

23. der Voort GF (1987) Visual examination and light microscopy. ASM Handbook 12:91–165

24. ASTM E8 (2010) ASTM E8/E8M standard test methods for tension testing of metallic materials 1. Annu B ASTM Stand 4(i):1–27. https://doi.org/10.1520/E0008

25. ASTM E647−13 (2014) Standard test method for measurement of fatigue crack growth rates. Am Soc Test Mater 03:1–50

26. Madyira DM (2015) Effect of wire EDM on microstructure and fracture toughness of 7075–T6511 aluminum alloy. Lect Notes Eng Comput Sci 2218:1038–1042

27. Liu HJ, Fujii H, Maeda M, Nogi K (2003) Tensile properties and fracture locations of friction-stir-welded joints of 2017–T351 aluminum alloy. J Mater Process Technol 142:692–696. https://doi.org/10.1016/S0924-0136(03)00806-9

28. Factor S (1997) Standard test method for plane-strain fracture toughness of metallic materials 1. Configurations 90:1–31

29. Moghadam DG, Farhangdoost K (2016) Influence of welding parameters on fracture toughness and fatigue crack growth rate in friction stir welded nugget of 2024–T351 aluminum alloy joints. Trans Nonferrous Met Soc China 26:2567–2585. https://doi.org/10.1016/S1003-6326(16)64383-2

Chapter 10
Production of Al–TiB$_2$ Composites with Grain Modification by Strontium and Magnesium

C. Bhagyanathan, P. Karuppuswamy, and S. Sathish

1 Introduction

Metal matrix composites (MMCs) are highly engineered materials that find specific applications based on extreme needs in the automotive, aerospace, nuclear, and energy sectors. As per Surappa [1], metal matrix composites using low-density and low-cost reinforcing materials have garnered increased attention. There is a need to enhance the properties of aluminium that can be used as secondary alloys after end-of-life utility. Bhowmik et al. [2], the trace addition of reinforcements could be a crucial factor in enhancing the properties of the base alloy. The observations of Moazami et al. [3] showed that a uniform distribution of the reinforcing particles is needed to avoid changes in property. For the homogeneous scattering of strengthening particles, wetting the particles with the melt in the case of stir casting during liquid processing is necessary, followed by the creation of a strong reinforcement-matrix connection following solidification. This is required to ensure that the additions are transferred throughout the matrix during liquid processing. However, since the majority of elements are not wetted by aluminium, it is difficult to distribute the reinforcing particles equally throughout the liquid and solid phases, as discussed by Ali et al. [4] and Dey [5]. The development of MMCs is hampered by a number of obstacles, including poor wettability, porosity, and uneven reinforcement distribution. From the research works of Poria et al. [6], it was observed that the TiB$_2$ particles have the advantage of enhancing the properties through uniform dispersal in aluminium melts and can be totally wetted by aluminium among other properties. TiB$_2$ particles are also purposely inserted into aluminium melts, and according

C. Bhagyanathan (✉) · P. Karuppuswamy · S. Sathish
Department of Mechanical Engineering, Sri Ramakrishna Engineering College, Coimbatore 641022, India
e-mail: bhagyanathan@srec.ac.in

to Senthil Kumar et al. [7], AlTi-B master alloys act as nucleation spots for segregating grain. Kumar et al. [8] and Yu et al. [9] have confirmed that the best suited ceramic reinforcement for aluminium-based melts has been TiB_2 Samuel et al. [10]. Sulardjaka et al. [11] have shown that the addition of TiB_2 to a variety of aluminium alloys enhanced the tensile behaviour by reducing the porosity formation sites in the aluminium alloy. Strengthening characteristics of aluminium-copper, aluminium-manganese, and aluminium-silicon alloys increase with TiB_2 addition according to the findings of Sulardjaka et al. [11], Anand et al. [12], and Syahrial et al. [13].

However, due to particle pushing during solidification, homogenous scattering of TiB_2 particles in aluminium alloys remains a challenge. Ramadhan and Zulfia [14] and Radhika et al. [15] claimed that due to the exothermic bio-chemical developments involved in the liquefied salt procedure, there are problems in controlling the proportions and structure of the Al–Si alloys and composites. Sumalatha et al. [16] and Tamuly et al. [17] stated that the addition of grain refiners and modifiers to the molten aluminium modifies the interactions between the particles and the aluminium, which results in the development of modified grain structures. Ali et al. [18], Zulfia et al. [19], Kumar et al. [20] stated that a really solid solution of titanium dioxide and aluminium dioxide formation in the melt is very much dependent on the contents of titanium and boron particles. TiB_2 particles are solid solutions of titanium dioxide and aluminium dioxide [21]. The particles have a hexagonal disc form in general, which is rather prevalent in the industry. The TiB_2 particles (grain size) are equivalent in size to the master alloys of aluminium-titanium-boron [22, 23] and have a crystalline structure. Indarsari et al. [23] used sub-micrometre TiB_2 particles that were generated using ultrasonic vibration at relatively low temperatures, in an attempt to reduce the size of in situ TiB_2 particulates.

Specifically, the effects of TiB_2, Sr, and Mg on ADC12 (Fig. 1a) are being explored in this study. TiB_2 is one of the reinforcements with low-density (4.52 g/cm^3) used in composites, and it is one of these discontinuous reinforcements that provide more advantageous qualities than the others. Composites containing TiB_2 as reinforcement are thus appropriate for a broad range of applications, such as automotive and small engine applications, and are becoming more popular. Thus, the results of the interaction between TiB_2 particles (Fig. 1c) and other components in the aluminium matrix should get specific attention. Metal matrix composites with a high degree of reinforcement based on iron are utilized in durable functions (Fig. 1b) like mining and construction. Braking systems, railway wagon wheels, and other heavy-duty equipment are all examples of applications for this material.

2 Materials and Methods

The Al–Si10Cu2Fe (ADC12) aluminium alloy with the elementary structure (Table 1) was chosen as the base material to be used in the experiments for its wide utilization as a primary and secondary processed alloy in various industries. Titanium diboride (TiB_2) was chosen for its grain refining properties and its ability to reinforce the
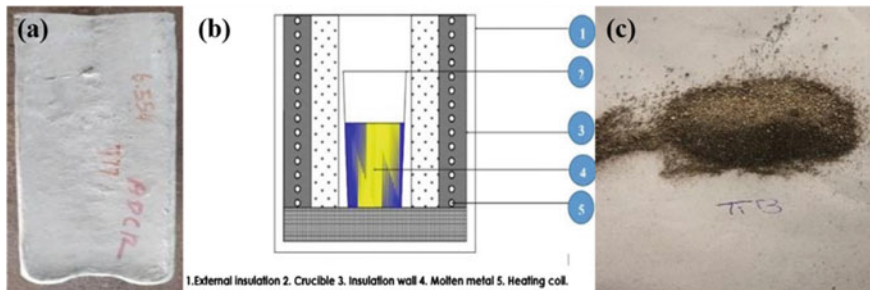
Fig. 1   **a** ADC12 ingot; **b** stir casting furnace; and **c** TiB$_2$ powder

Table 1   Composition of ADC12 alloy

Alloy	Si	Fe	Cu	Mn	Mg	Ni	Sn	Zn	Al
%	10.5–12	1.3	3–4.5	0.5	0.10	0.5	0.35	3.0	73–86

metal matrix composite structure. Strontium (Sr) and magnesium (Mg) were added as reinforcements to wet the TiB$_2$ particulates to the melt.

2.1   Fabrication Process

Graphite crucibles were used to hold the aluminium alloy inside the stir casting furnace, with a maximum loading capacity of 5 kg to melt the alloy and composites. The ADC12 ingots were cut to the required weights and placed inside the graphite crucible, which was preheated to a temperature of 200 ± 10 °C. The entire setup was then transferred to an electrical stir casting furnace. The initial sample was melted without the addition of any composites at temperatures above the melting point of aluminium.

The sample was manually poured into a preheated die at a pouring temperature of 670 ± 10 °C. For the remaining experiments, TiB$_2$ powders were added at 1 wt% to the melt. The reinforcements were added when the melt was in a semisolid state at a temperature of 500 ± 10 °C. The melt was stirred for up to 10 min by a metal stirrer (Fe) at 45 rpm by a motor-powered stirring unit. Strontium and the wetting agent Mg were added in varying proportions as per the details shown in Table 2.

The melt was then poured into a top-pouring cylindrical mould (50 mm diameter × 70 mm height). Efforts were made to maintain the same pouring temperature and stirring speed for the unreinforced alloy and the composites.

The samples were then sectioned and machined to ASTM specifications for analysis of elementary composition, tensile, and hardness behaviour. The OES of the samples was determined by using the Optical Emission Spectroscopy machine (Spectromaxx F model). An Optical Microscopy (Metagraph I) with a magnification up

Table 2 Method of experimental works

Trial	Base material	Description	Load (kg)	Added materials	% Additions	Stirring speed (RPM)
1	ADC12	ADC12	2	–	–	45
2	ADC12	M1	2	TiB_2: Mg: Sr	1:0: 0	45
3	ADC12	M2	2	TiB_2: Mg: Sr	1:1:0	45
4	ADC12	M3	2	TiB_2: Mg: Sr	1: 0: 1	45
5	ADC12	M4	2	TiB_2: Mg: Sr	1: 1: 1	45

to 100x, FESEM (Zeiss FESEM SIGMA VP 03-04), and X-ray diffraction (XRD) (Bruker D8 Advance, Germany) with High-Intensity Ka1,2 Parallel Beam are used to study the dispersion of TiB_2, Sr, and Mg in the aluminium alloy ADC12. The tensile analysis was done using a servo-controlled UTM with a 400 KN capacity. A 10 mm steel-ball indenter was used in a Brinell hardness machine to determine the hardness of the materials. Wear analysis was carried out using the pin-on-disc apparatus, which has a steel base. The sliding distance was maintained at 90 mm, and the wear loss of the MMCs was determined at an RPM of 300.

3 Results and Discussion

3.1 Optical Emission Spectroscopy and Microstructural Characterization

The results shown in Table 2 indicate that there was a rise in the composition values of Ti, Sr, and Mg in the aluminium melt. It was also observed that not all the particles that were added diffused but only about half of the added elements adhered to the melt. This could be attributed to the diffusion coefficients of the elements, as Mg has a diffusion coefficient of 6.2 to 6.3×10^{-6} m^2/s and that of Ti is 1.12×10^{-1} m^2/s. It also highlights the fact that only 50% of the added composites bonded with the base alloy. The dispersion of the added reinforcements (Table 3) was further confirmed by the microstructural characterization (Fig. 2).

The microstructure of the sample M1 has an unmodified grain structure consisting of the Al–Si particles as shown in Fig. 2a, which is similar to the results obtained by Poria et al. [6]. It can be observed that the microstructure of aluminium ADC12 alloy with the reinforced TiB_2 and Sr particles and the wetting agent Mg shows the presence of α-AlTi structures in the grain boundaries of the eutectic silicon (Fig. 2b).

Table 3 Composition of various trials

Alloy	Si	Fe	Cu	Mn	Mg	Ni	Zn	Sr	Ti	Al
ADC12	10.6	0.808	2.52	0.175	0.093	0.04	0.458	0.002	0.2	86
M1	10.9	1.07	2.68	0.14	0.425	0.091	0.737	0.002	0.2	85.4
M2	10.07	0.76	2.35	0.09	0.342	0.096	0.401	0.081	0.2	86.2
M3	10.38	0.417	2.25	0.148	0.512	0.106	0.418	0.002	0.58	84.8
M4	11.06	0.475	1.98	0.157	0.448	0.127	0.421	0.075	0.62	84.6
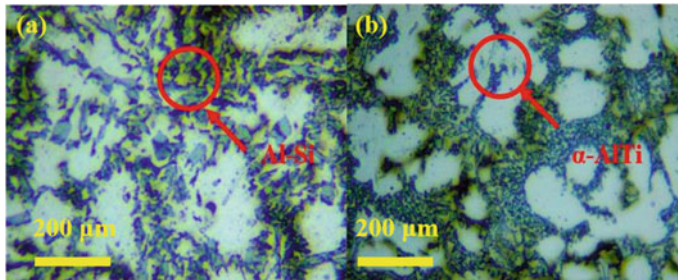
Fig. 2 Microstructures of alloys **a** without Mg, Sr, and TiB$_2$ (ADC12); **b** with Mg, Sr, and TiB$_2$ additions (M4)

The composites modified with the additions of magnesium and strontium have better grain refined structure where grain shape and phase structure change from coarse dendrites to homogeneous and polished grains of aluminium. This can be attributed to the addition of strontium. The mentioned phenomenon has an impact on both the tensile and hardness behaviour of samples.

The SEM-EDS analysis carried out using the FESEM technique showed the presence of titanium particles spread in the interface between the aluminium-silicon phases. The existing phase is correlated with the chemical composition of the composite, which is highlighted in the EDS analysis of the composite material. As given in Fig. 3, the added particles were not uniformly distributed but had formed clusters with certain portions of the aluminium alloy.

The composite of ADC12 reinforced with TiB$_2$ showed the presence of Mg and Sr along with the titanium. The added magnesium powder was mostly present in the form of MgO, which might be due to the oxidation of the topmost layer, which interacts with the atmosphere (Table 4).

The results also concord with the findings of Vivekananda and Prabu [24]. They stated that the formation of Al$_3$Ti is a result of the exothermic reaction between the compounds of the added titanium particles and the aluminium alloy ADC12 (Fig. 4).

The phase composition through the X-ray diffraction shows the formation of the Al$_3$Ti phases in the aluminium composite, which were indicated as smaller peaks in the XRD analysis.
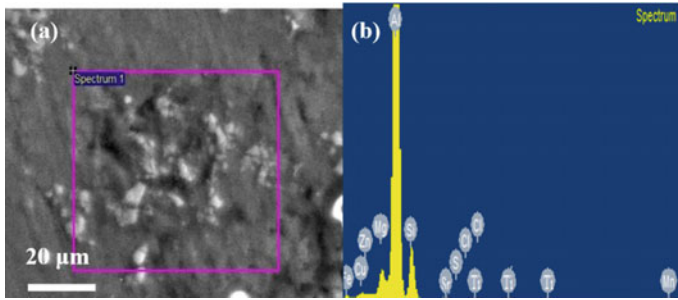
Fig. 3 SEM–EDS of the sample with TiB_2, Sr, and Mg additions (M4)

Table 4 Composition of the sample from the EDS analysis of sample M4

Element	Weight%	Atomic%
O K	15.43	24.03
Mg K	1.78	1.82
Al K	67.76	62.57
Si K	11.10	9.85
Sr K	0.16	0.13
Cl K	0.20	0.14
Mn K	0.34	0.15
Fe K	1.83	0.82
Cu K	0.74	0.29
Zn K	0.34	0.13
Ti K	0.32	0.07
Total	100.00	

3.2 Mechanical Behaviour of the Samples

The results showed that the tensile strength of the materials gradually increased. However, there was a constant reduction in the yield strength of the materials, and the elongation was good for the samples with the addition of TiB_2, Sr, and Mg to the melt.

It is also clear from the tensile results (Fig. 5) that with an increase in the amount of reinforcement, tensile strength increases while ductility decreases. The undesirable needle-like shape of unaltered eutectic silicon works as a stress concentrator, lowering its strength and ductility. It corresponded with the findings of Prasad and Radhika [25]. The results also highlighted the loss in the elongation percentage when the matrix was present with Sr alone. Strontium had refined the eutectic structures, which enhanced the hardness but affected the elongation. The fact that the titanium particles spread at the interface between the aluminium-silicon phases had enhanced the elongation of the composites [26, 27].
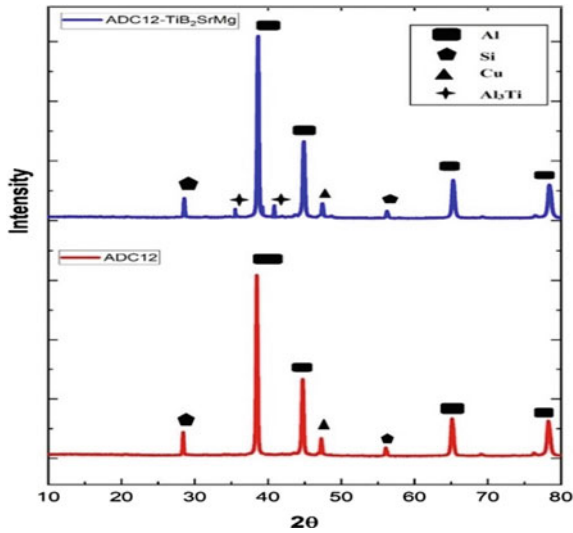
Fig. 4 XRD wave pattern of ADC12 with TiB$_2$, Sr, and Mg addition (M4) and unreinforced alloy (ADC12)
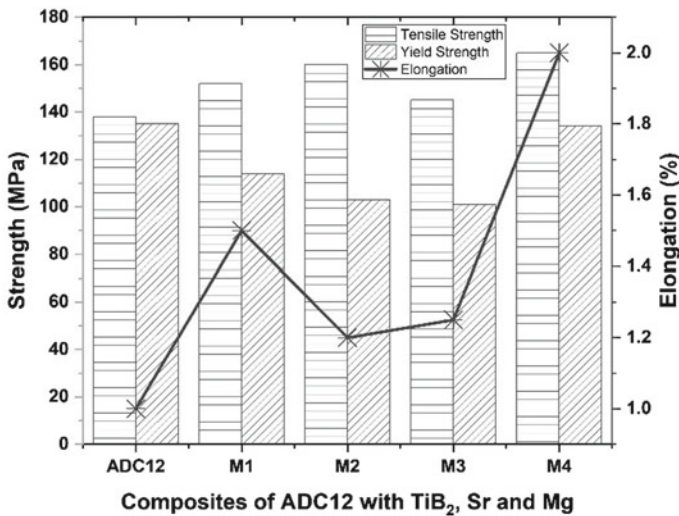
Fig. 5 Tensile properties versus composite of ADC12

The hardness values plotted in the graph are the three-point averages of the samples as shown in Fig. 6. A notable rise in the hardness of the alloy matrix can be seen with the addition of TiB$_2$, Sr, and Mg particles compared to the values obtained with the unreinforced alloy and other composites. The primary reason that could be obtained from the rise in hardness is the existence of particulates in the matrix. These
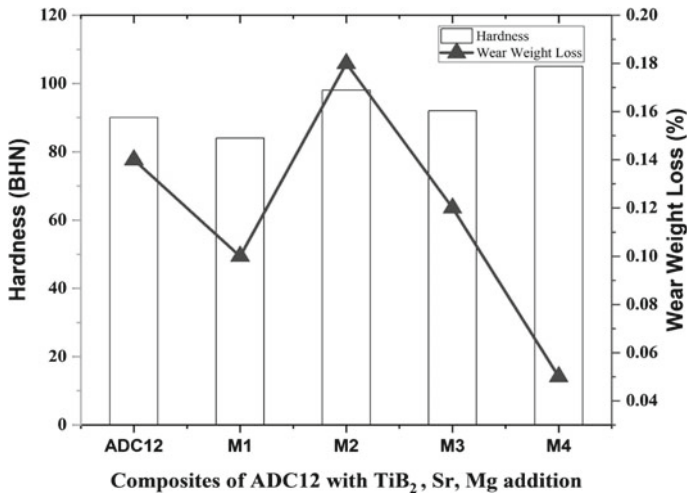
Fig. 6 Variation of hardness and wear with variation in the reinforcements

particulates of TiB_2, which have led to the formation of Al_3Ti, have improved the overall hardness of the composites [24, 28].

The results from the wear analysis demonstrate that the wear resistance of the Al–TiB_2 composite rises in the presence of both Mg and Sr (M4). It was also revealed that the presence of Sr alone lowered the hardness values as it functions as a material strengthening agent, enhancing the UTS features of the material alone, as indicated by Panov et al. [29]. As shown in Fig. 6, the weight loss percentage of the composite is smaller compared to the aluminium alloy as the particles enhance the wear resistance of the MMC.

3.3   Fractography Analysis

The fractured surfaces of the tensile specimens were examined using a scanning electron microscope (SEM), which gives the fracture propagation of the tensile specimens. Figure 7a shows the fractured SEM image of ADC12. The fracture surfaces showed a surface consisting of small dimples to be ductile and of order 3.5–5 µm in diameter. The fractured SEM images of the composite of ADC12 and TiB_2 show flat tear ridges and wear tracks. As per the statements of Maleque et al., fracture occurs in composite material by crack initiation, which follows immediately at the boundary between aluminium alloy and reinforcement, as the added particles of TiB_2 settle on the junctions of the silicon clusters in the aluminium alloy and this serves as a crack initiation point [17, 30].
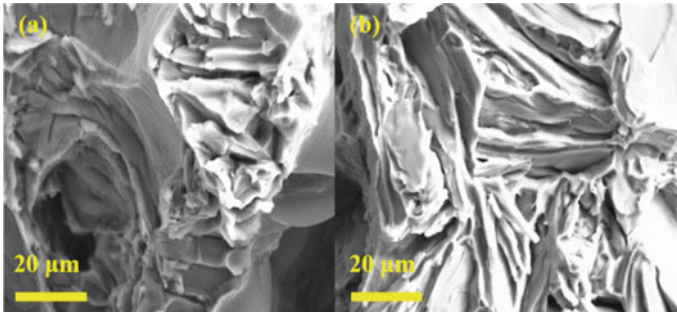
Fig. 7 Fractography of tensile specimens **a** without Mg, Sr, and TiB$_2$ (ADC12); **b** with Mg, Sr, and TiB$_2$ additions (M4)

4   Conclusion

The behaviour of the ADC12 alloy, ADC12–TiB$_2$ aluminium MMC, and the MMC reinforced with strontium and manganese was investigated. The research demonstrates that adding TiB$_2$ increases aluminium's tensile and hardness properties when done in the presence of strontium and magnesium. Furthermore, adding reinforcement to aluminium increases the material's hardness value. As a consequence of the finding, it was observed that the performance of TiB$_2$ in the aluminium would increase when reinforced with strontium and magnesium.

- It was found that the Mg dissolved into the vacancies of the Sr grain refined α-AlTi lattice to form solid solution strengthening, which enhances the properties of the MMC.
- Results from the tensile graph show an improvement in the tensile characteristics with an increase in the elongation of up to 2% in the Al–TiB$_2$ composite with Sr and Mg modification.
- The results of the wear tests were also in correspondence with the findings of Ale et al. [18], and Pongen et al. [31], and the wear resistance of the composite with Sr and Mg was nearly two times higher compared to other composites and unreinforced ADC12 alloy.
- The results show that the inclusion of reinforcement TiB$_2$ and Sr will improve the mechanical properties of the aluminium composite. Thus, we conclude that the developed composites exhibit superior wear resistance and properties compared to the alloy.

References

1. Surappa MK (2003) Aluminium matrix composites: challenges and opportunities. Sadhana 28(1–2):319–334
2. Bhowmik A, Dey D, Biswas A (2021) Comparative study of microstructure, physical and mechanical characterization of SiC/TiB2 reinforced Aluminium matrix compo site. SILICON 13(6):2003–2010
3. Moazami MR, Razaghian A, Mirzadeh H, Emamy M (2022) Tailoring the mechanical properties of hypereutectic in situ Al–Mg2Si composites via hybrid TiB2 reinforcement and hot extrusion. Arch Civ Mech Eng 22(2):1–9
4. Ali KS, Mohanavel V, Ravichandran M, Arungalai Vendan S, Sathish T, Karthick A (2021) Microstructure and mechanical properties of friction stir welded SiC/TiB2 reinforced aluminum hybrid composites. Silicon:1–11
5. Dey D, Biswas A (2021) Comparative study of physical, mechanical and tribological properties of Al2024 alloy and SiC-TiB2 composites. SILICON 13(6):1895–1906
6. Poria S, Sahoo P, Sutradhar G (2016) Tribological characterization of stir-cast aluminium-TiB2 metal matrix composites. SILICON 8(4):591–599
7. Senthil Kumar P, Kavimani V, Soorya Prakash K, Murali Krishna V, Shanthos Kumar G (2020) Effect of TiB2 on the corrosion resistance behavior of in situ Al composites. Int J Metalcast 14(1):84–91
8. Kumar N, Gautam G, Gautam RK, Mohan A, Mohan S (2016) Synthesis and characterization of TiB2 reinforced aluminium matrix composites: a review. J Inst Eng (India): Ser D, 97(2):233–253
9. Yu W, Chen J, Li Y, Zuo Z, Chen D, An Q, Chen M, Wang H (2021) Comprehensive study on the cutting spe- cific energy and surface roughness of milled in situ TiB2/Al composites and Al alloys. Int J Adv Manuf Technol 112(9):2717–2729
10. Samuel A, Zedan Y, Doty H, Songmene V, Samuel F (2021) A review study on the main sources of porosity in Al–Si cast alloys. Adv Mater Sci Eng
11. Sulardjaka S, Nugroho S, Iskandar N (2021) Mechanical properties of AlSiMg/SiC and AlSiMgTiB/SiC produced by semi-solid stir casting and high pressure die casting. Mater Phys Mech Т. 47. N. 1. С. 31–39. https://doi.org/10.18149/MPM.4712021_3
12. Anand SH, Venkateshwaran N (2021) Effect of heat treatment and biosilica on mechanical, wear, and fatigue behavior of Al–TiB2 in situ metal matrix composite. Biomass Convers Biorefinery:1–13
13. Syahrial AZ, Putro EC, Aditya RM, Andiva S (2018) The role of Sr and TiB on mechanical properties of aluminium 6061 composites produced through stir casting route. Mater Sci Forum 929:63–69
14. Ramadhan R, Zulfia A (2020) Study on the effect of volume fraction (Vf%) SiC addition to the characteristics of Mg-Al-Sr/SiC composites using stir casting method. IOP Conf Ser: Mater Sci Eng 924(1):012022
15. Radhika N, Sasikumar J, Jojith R (2021) Effect of grain modifier on mechanical and tribological properties of Al–Si alloy and composite. SILICON 13(3):841–855
16. Sumalatha C, Rao PV, Rao VV, Deepak MSK (2022) Influence of grain refiner, modifier and graphene on the dry sliding wear of hypereutectic Al–Si alloys. Metall Microstruct Anal:1–11
17. Tamuly R, Behl A, Borkar H (2022) Effect of addition of grain refiner and modifier on microstructural and mechanical properties of squeeze cast A356 alloy. Trans Indian Inst Metals:1–14
18. Ali MM, Omran ANM, Mohamed MAEH (2021) Prediction the correlations between hardness and tensile properties of aluminium-silicon alloys produced by various modifiers and grain refineries using regression analysis and an artificial neural network model. Eng Sci Technol Int J 24(1):105–111
19. Zulfia A, Muhammad S, Budi U (2019) Effect of aging time on characteristics of ADC12/SiC composite with addition of Sr modifier and Al-5TiB grain refiner. IOP Conf Ser: Mater Sci Eng 547:012029. https://doi.org/10.1088/1757-899X/547/1/012029

20. Kumar DT, Kumar KG, Pattanaik A, Mukherjee M (2020) Improvement of Al–Si hypoeutectic cast alloy properties by forging with grain refiner and modifier. Trans Indian Inst Met 73(12):3105–3112
21. Sunitha K, Gurusami K (2021) Study of Al–Si alloys grain refinement by inoculation. Mater Today: Proc 43:1825–1829
22. Yang L, Yu F, Li P, Yan Q, Cui J (2022) The effects of Al-5ti-1b and Sr interaction on microstructure and properties of Zl101. http://dx.doi.org/10.2139/ssrn.4102981
23. Indarsari A, Syahrial AZ, Utomo BW (2019) Characteristics of Aluminium ADC 12/SiC Composite with the addition of TiB and Sr modifier. In: E3S web of conferences, vol 130, p 01004. EDP Sciences
24. Vivekananda AS, Prabu SB (2018) Wear behaviour of in situ Al/TiB2 composite: influence of the microstructural instability. Tribol Lett 66(1):1–14
25. Prasad PHD, Radhika N (2020) Comparative study of microstructure, mechanical and reciprocating wear properties of unmodified and Sr-modified A383 alloy and composite. Trans Indian Inst Met 73(7):1939–1950
26. Vaishnav V, Kumar RP, Venkatesh C (2022) Influence of nano MoS2 particle on the mechanical and tribological properties of Al–TiB2-Gr hybrid composite. J Mech Sci Technol 36(2):857–867
27. Wang H, Li G, Zhao Y, Chen G (2010) In situ fabrication and micro-structure of Al$_2$O$_3$ particles reinforced aluminum matrix composites. Mater Sci Eng, A 527(12):2881–2885
28. Chaudhury SK, Panigrahi SC (2007) Role of processing parameters on microstructural evolution of spray formed Al–2Mg alloy and Al–2Mg–TiO$_2$ composite. J Mater Process Technol 182:343–351
29. Panov I, Dochev B, Dimova D (2021) Investigation of the influence of the modifiers P, Sr, Ti and combinations of them on the structure and mechanical properties of AlSi25 alloy. In: Environment. Technologies. Resources. Proceedings of the international scientific and practical conference, vol 3, pp 256–260
30. Prema S, Chandrashekharaiah TM, Begum F (2019) Study of improvement in mechanical properties and microstructure of LM25 alloy with the addition of grain refiners/modifier. Int J Appl Eng Res 14(6):1297–1300
31. Pongen R, Birru AK, Parthiban P (2019) Study of microstructure and mechanical properties of A713 aluminium alloy having an addition of grain refiners Al-3.5 Ti-1.5 C and Al-3Cobalt. Results Phys 13:102105

Chapter 11
Stir Casting Process Parameters and Their Influence on the Production of AA6061/B$_4$C Metal Matrix Composites

R. Chitra, T. M. Chenthil Jegan, A. M. Anusha Bamini, Godwin Glivin, and V. Alfred Frankin

1 Introduction

Emerging trends in the industry increase the need for novel materials and their components. Safri et al. [1] stated that composites are providing good and reliable performance for current social and industrial benefits. Due to the excellent properties of the aluminium matrix composites (AMCs), many researches have been carried out in the last two decades. Because of its light weight characteristics, aluminium is used for many applications, but it cannot meet the demand of high performance [2]. Yigezu et al. [3] reported that AMCs are promoted to be superior because of their significant properties like high strength, lower coefficient of thermal expansion and higher wear resistance. The reinforcement materials are selected based on the need and applications where they are used [4–6]. Singh et al. [5, 6], Rahmana and Al Rashed [7], Jha et al. [8] suggested that commonly used reinforcements are alumina, SiC, B$_4$C, TiO$_2$, TiC and TiB$_2$. High tensile strength and hardness were obtained by using alumina. Due to their good mechanical properties, AMCs are used to produce automobile components such as cylinder heads and connecting rods, brake discs

R. Chitra · A. M. A. Bamini
Department of Computer Science and Engineering, Karunya Institute of Technology and Sciences, Coimbatore, India

T. M. C. Jegan (✉)
Department of Mechanical Engineering, St. Xaviers Catholic College of Engineering, Chunkankadai, India
e-mail: chenthiljegantm@gmail.com

G. Glivin
Department of Energy and Environment, National Institute of Technology, Trichy, India

V. A. Frankin
Mechanical and Industrial Engineering Section, University of Technology and Applied Sciences-Ibri, Ibri, Oman

and pistons [9]. SiC reinforced AMCs produce high hardness, excellent stiffness and good thermal properties. Because of its good thermal and wear properties, it is used to produce engine components like piston connecting rods, drive shafts and high wear resistance components such as brake rotors, callipers and liners [10, 11]. Ravichandran and Dineshkumar [12] proved that strong bonding, high tensile and impact strength, as well as great hardness are achieved by using TiO_2 as a reinforcement. TiC reinforced AMCs are used to produce pistons and connecting rods due to their high wear resistance by Jamwal et al. [13], Veeravalli et al. [14]. Suresh et al. [15] informed that TiB_2 reinforced AMCs possess high strength and wear resistance and thus these AMCs are used in very technical, structural and functional applications like aerospace, automotive and defence. Among the reinforcements, B_4C reinforced AMCs possess high strength and hardness—which are excellent chemical behaviours. Yield, as well as ultimate tensile and compressive strength values also increased in B_4C reinforced AMCs. Because of this nature, these AMCs are used in automotive and chemical applications [16–18]. For better improvement of mechanical properties, reinforcement materials such as Al_2O_3, SiC and B_4C are also used. The strength of the composites is increased because of the bonding between the matrix and reinforcement (Researchers, Moona et al. [19]). Nai and Gupta [20], Naher et al. [21] found that the stir casting is the promising technique for the production of MMCs. Many researches were conducted on the production of aluminium-based SiC metal matrix composites. But very little research has been done on the optimization of process parameters influencing the even dispersal of a particle in the matrix and mechanical characterization of aluminium with B_4C metal matrix composites.

AMCs are commonly fabricated using stir casting, a direct melt oxidation process, powder metallurgy and compo casting. Even though the stir casting process was pondered upon by many researchers, only limited study has been carried out to analyse the parameters that influence stir casting. The uniform dispersion of reinforcement particle is increased by the stirring speed. Prabu et al. [22], Ravi et al. [23] identified that low stirring speed and minimum stirring time cause un-uniform particle distribution among the matrix materials in SiC reinforced AMCs. Akhlaghi et al. [24], Amirkhanlou and Niroumand [25] noticed that the casting temperature is also a significant factor in obtaining uniform particle dispersal of AMCs. Soundararajan et al. [26] detected that lower casting temperatures provide good distribution and mechanical characteristics. Empirical relationship between the stirring parameters such as stirring angle, stirring speed, casting temperature and the tensile strength was also analysed, and the influencing parameters were investigated by Khosravi et al. [27], Akbari et al. [28]. In most of the papers, the influencing parameters of stir casting are analysed with a few experimental runs. The process parameters are analysed by tensile strength and microscopic observations. Mathematical models are not used to analyse the stir casting parameters for more than one output response variables for a wide range. The salient process parameters that significantly influence the AMCs properties are (A) stirrer speed, (B) stirring time, (C) holding temperature and (D) percentage of reinforcement. These parameters are selected based on extensive literature survey.

In this paper, a mathematical model is developed to correlate the stir casting variables to predict the tensile strength and hardness in B_4C reinforced AMCs. The influence of input variables on the response variables is identified from the developed mathematical model and correlated with the detected microstructure. The experiments are conducted according to the central composite design (CCD) using response surface methodology. Sathiskumar et al. [29], Vettivel et al. [30], Rostamiyan et al. [31] used CCD for predicting the suitable process parameters on the response output variables. Vaira Vignesh et al. [32] stated the need of magnesium alloys which is used for bio-medical application. Vaira Vignesh and Padmanaban [33] modelled the parameter influencing the stir casting process using aluminium-based composites. Vaira Vignesh et al. [34] reported the synthesis and characterization magnesium alloys which is used for bio-medical application and studied parameters for stir casting process. The objective of the paper is to attain the appropriate process parameters influencing the uniform distribution of B_4C particles in the AMCs and to ensure better values of tensile strength and hardness.

2   Materials and Methods

2.1   Stir Casting

In the present study, stir casting (SC) technique is employed for the fabrication of the specimens. It is also known as vortex casting technique in some literatures as the vortex is created for homogenous mixture of reinforcing material during solidification. In SC process, reinforcing material is distributed into molten matrix using mechanical stirring. Mechanical stirring in the furnace is vital for producing homogeneity of reinforcement in AMCs. Further, the molten alloy is used for die casting in order to get required shape of the specimen. The stir casting setup used for the production of AA6061/B_4C reinforced composite is shown in Fig. 1.

The dispersal of reinforcement particles in the composites depends on properties of the material and stir casting process parameters. The process parameters of stir casting include:- stirrer speed, stirring time, stirring temperature, blade angle of stirrer, pre-heat temperature of mould, pre-heat temperature and feed rate of reinforcement particles. Particle dispersal in the composite material through the molten phase of the casting procedure also depends on the viscosity of the slurry. In SC, the pre-heated ceramic particles are mixed into the vortex of molten metal produced by the rotating impeller. AA6061 is situated inside the crucible and the maximum temperature is set at 800 °C. 1% of the degasser Hexachloroethane has been added to the molten AA6061. The purpose of degasser is to avoid the porosity of the molten metal during the solidification and post solidifying processes. The molten metal is stirred holding the crucible with forks to eliminate the gases. The same process is repeated for various levels of process parameters with different weight percentages of B_4C reinforced AMC. Stir casting control panel setup used for experimentation is shown in Fig. 2.

Fig. 1 Stir casting setup

In stir casting, the ceramic reinforcement particles are merged into a molten metal by different methods, followed by mixing which results in the casting of AMCs. High processing temperature is used for developing the strong bond between the matrix and reinforcement, and it can be intermingled with the reinforcement to fabricate the composites with increased wettability in AMCs.

The steps involved in enhanced stir casting techniques are given below:-

- The AA6061 is kept in the crucible pre-heated to 800 °C temperature in the aluminium melting furnace. To achieve better wettability between matrix and reinforcements, the reinforcements are also pre-heated to high temperatures around 10000 to 12000 °C.
- After a few minutes, 1% of degasser Hexachloroethane is added to the molten content in the crucible. The poisonous gases of carbon, nitrogen, etc., that
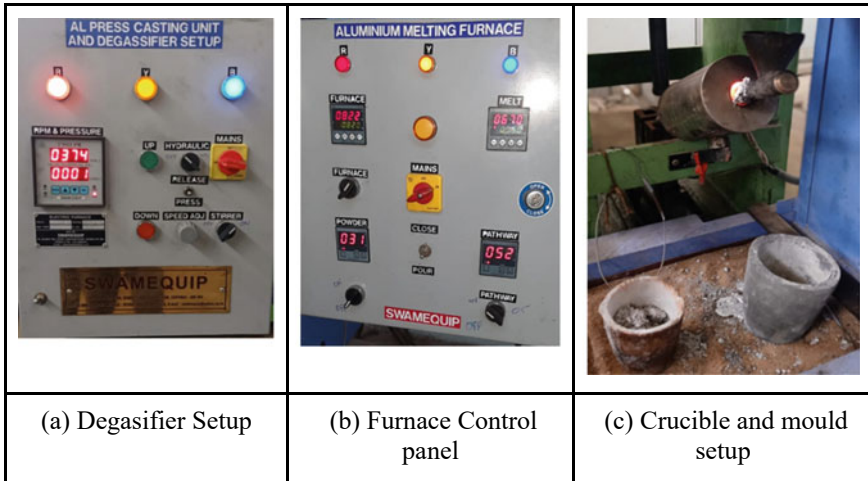
(a) Degasifier Setup	(b) Furnace Control panel	(c) Crucible and mould setup

Fig. 2 Stir casting control panel setup

may cause porosity of the molten matrix throughout and after the process of solidification were engaged with the molten matrix. It can be reduced by degasser.

- The pre-heated reinforcement particles are added to the molten metal simultaneously, with the motor-powered stirring act for 2–10 min at the speed of around 300 rpm to 400 rpm in order to ensure the uniform dispersal.
- Further, the molten metal is chilled slowly to reduce its liquids' temperature and to maintain it in a semisolid condition. Finally, the melt is maintained at the temperature range of $600 \pm 150\,°C$ while pouring it into the required dimensional mould.

2.2 Experimental Design

The process parameters are analysed using response surface methodology. Response surface method (RSM) facilitates the computation of the association between more computed responses and the very important parameters. In this experimentation, four input factors are considered which require a two-level factorial screening design. In any case, a number of the factors for RSM have to be measurable. The goal is to discover an attractive position in the design space. This may perhaps be the highest, the lowest or an area in which the response is steady above a variety of factors. Targets might comprise gathering a group of specifications for some response tensile strength and hardness.

RSM is used to identify the performance of the Al/B_4C composites. In design of experiments (DOE), various designs like central composite design, Box-Behnken design, pentagon design, small central composite design, hexagon design and distance-based design are available. Among various options available in DOE, the

Table 1 Design factors for stir casting process

Input parameters	Code	Various levels				
		−2	−1	0	1	2
Stirring speed (rpm)	A	300	320	340	360	380
Stirring time (min)	B	2	4	6	8	10
Holding temperature (°C)	C	640	660	680	700	720
% of reinforcement (weight fraction)	D	0	2.5	5	7.5	10

second-order full fraction central composite design with five levels for the input parameters is considered in the present study.

Design-Expert version 12 is used for the modelling of the stir casting variables. The input parameters considered are stirring speeds, stirring time, holding temperature and percentage of reinforcement, while the response variables are tensile strength and hardness. The levels of the variables used to design the experiment for the modelling are given in Table 1.

Based on the output of the DOE, the 30 combinations of various input parameters have been chosen to carry out the experiments over B_4C reinforced AMC specimens and coded from R01 to R30. The chosen experimental parameters with their experimental codes are presented in Table 2.

Tensile strength and hardness are the two output parameters which decided the performance of the stir casting process. Tensile strength is a mechanical behaviour that comprises the individual features of materials and portrays their behaviour in the circumstance of action of exterior forces.

The tensile examination is the most straightforward investigation method employed to characterize the mechanical characteristics of the material. To obtain accurate data in distinctive construction composites, specialized devices are employed for tensile examination. The machine used for tensile test is digital tensometer shown in Fig. 3. The tensile samples are tested in room temperature. The specimens before and after tensile testing are shown in Fig. 3. The Brinell hardness number evaluates the global response of the material and is comparatively inattentive to contained outcomes and display hardness values straightforwardly, hence averting tiresome computations concerned in other hardness evaluation methods. The results of tensile strength (Mpa) and hardness (BHN) at different experimental runs from R01 to R30 are presented in Table 3.

The best value of tensile strength within the selected experimental runs is obtained for R10 (stirrer speed of 360 rpm, stirring time of 8 min, holding temperature of 700 °C and weight fraction of 7.5), whereas good hardness value is obtained corresponding to R16 (stirrer speed of 340 rpm, stirring time of 6 min, holding temperature of 680 °C and weight fraction of 10).

Table 2 Experimental run code with input parameters

Sl. No.	Experimental run code	A	B	C	D
1	R1	1	−1	1	1
2	R2	0	0	0	0
3	R3	0	0	0	0
4	R4	1	−1	−1	−1
5	R5	1	−1	1	−1
6	R 6	−1	1	−1	−1
7	R7	0	−2	0	0
8	R8	−1	−1	1	1
9	R9	−1	1	1	−1
10	R10	1	1	1	1
11	R11	0	0	−2	0
12	R12	0	0	0	−2
13	R13	−1	1	−1	1
14	R14	0	0	2	0
15	R15	0	0	0	0
16	R16	0	0	0	2
17	R17	0	0	0	0
18	R18	0	0	0	0
19	R19	−1	−1	−1	1
20	R20	1	1	−1	−1
21	R21	−1	−1	−1	−1
22	R22	1	−1	−1	1
23	R23	0	2	0	0
24	R24	0	0	0	0
25	R25	−1	−1	1	−1
26	R26	−2	0	0	0
27	R27	−1	1	1	1
28	R28	1	1	−1	1
29	R29	1	1	1	−1
30	R30	2	0	0	0

3   Development of Mathematical Model

The modelling of stir casting parameters in order to evaluate the output responses is carried out in this section. The concepts of design of experiments (DOE) and the basics of response surface methodology (RSM) have been described. RSM quadratic model is used for modelling the relationship between a scalar variable and one or more explanatory variables. In quadratic model, a smooth interpolating function is

(a) Digital Tensometer

(b) Specimens before tensile test

(c) Specimens after tensile test

Fig. 3 Tensile test

usually used, and it generally includes quadratic and interaction effects. The standard quadratic model is defined by Eq. (1).

$$Y = \beta 0 + \Sigma(\beta i X i) + \Sigma(\beta(i \neq j) X i X j) + \Sigma(\beta i i X i^2) \tag{1}$$

where Y is the dependent variable and $(X\_1, X\_2, ..., X\_j)$ are non-stochastic variables. Developed regression equation for tensile strength and hardness is represented in Eqs. (2) and (3), respectively.

$$
\begin{aligned}
\text{Tensile strength} = {} & 226.46 + 12.68A + 6.71B + 0.53C + 1.92D \\
& + 0.60AB + 3.82AC + 3.33AD - 1.69BC \\
& + 0.56BD + 1.47CD - 1.86A2 - 2.85B2 \\
& - 1.51C2 - 1.55D2
\end{aligned}
\tag{2}
$$

Table 3 Experimental run code with response variables form experimentation

Sl. No	Run code	Tensile strength (Mpa)	Hardness (BHN)
1	R01	244.18	72
2	R02	222.18	66
3	R03	226.32	67
4	R04	218.94	61
5	R05	220.86	60
6	R06	212.42	57
7	R07	198.86	64
8	R08	192.51	71
9	R09	208.54	58
10	R10	246.46	72
11	R11	219.18	64
12	R12	217.25	55
13	R13	215.37	70
14	R14	223.33	65
15	R15	227.79	66
16	R16	224.95	78
17	R17	223.35	67
18	R18	228.28	68
19	R19	201.89	74
20	R20	234.49	60
21	R21	204.62	56
22	R22	216.75	69
23	R23	232.95	69
24	R24	230.87	66
25	R25	200.26	58
26	R26	196.84	63
27	R27	204.57	72
28	R28	239.83	75
29	R29	231.19	59
30	R30	242.87	67

$$
\begin{aligned}
\text{Hardness} = {}& 66.67 + 0.84A + 0.5B + 0.08C + 6.34D + 0.38AB \\
& - 0.25AC - 0.63AD - 0.13BC + 0.25BD - 0.13CD \\
& - 0.48A2 - 0.11B2 - 0.62C2 - 0.11D2
\end{aligned}
\tag{3}
$$

3.1   Validation of Regression Equation

The regression equation (RE) for tensile strength and hardness is validated with the experimental data as the equations are further used for the optimization process. The values of experimental runs from R01 to R230 have been incorporated in the corresponding REs of tensile strength and hardness. The predicted value is compared with the experimentally arrived values. Thus, the comparisons of the results are presented with their percentage deviation. Table 4 shows the tensile strength and hardness values obtained using RE and experiments.

The experimental results from the experimentation and predicted values from RE are validated. The results of tensile strength with experimentation and RE are shown as graph in Fig. 4a to show the close agreement between them. In a similar way, the values of hardness are also shown as graph in Fig. 4b. It is noted that the closeness is observed for both MRR and SR.

4   Result and Discussion

The influence of process parameters on tensile strength and hardness is discussed in this section, and the microstructure is analysed using scanning electron microscopy and EDAX.

4.1   Influence of Process Parameters

The significance of RE is discussed with ANOVA table and normal plot for all the AMCs produced in the stir casting. The equations thus formed are validated with experimental results obtained in the experimentation. The influence of process parameters is analysed using three-dimensional surface plots.

4.1.1   Influences on Tensile Strength

The influencing parameters in the stir casting are analysed with three-dimensional response plot. It is plotted against two input variables in x and y axes, respectively, with output parameter tensile strength in z axis. Other two parameters are kept at the centre point of the design.

Three-dimensional response plot for tensile strength on the stirrer speed and stirring time is shown in Fig. 5a. Here, the holding temperature and percentage of reinforcement on stir casting are kept at the centre point of the design. When the stirrer speed is low, the tensile strength of the AMC is low, and it gradually increases with increase of stirrer speed. The higher the value, the better is the tensile strength.

Table 4 Comparison of tensile strength and hardness for various experimental runs

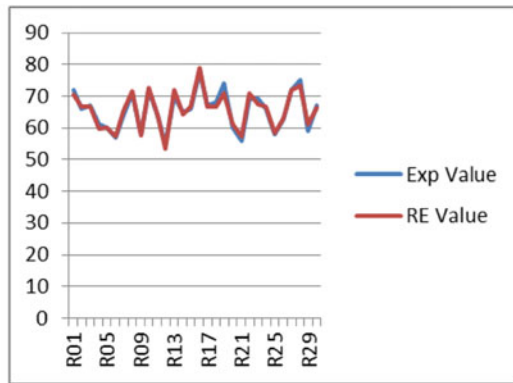| Sl. No.	Exp. run	Tensile strength			Hardness		
		Exp	RE	%Dev	Exp	RE	%Dev
1	R01	244.18	236.26	3.24	72.00	70.62	1.92
2	R02	222.18	226.47	−1.93	66.00	66.67	−1.02
3	R03	226.32	226.47	−0.07	67.00	66.67	0.49
4	R04	218.94	214.86	1.86	61.00	59.79	1.98
5	R05	220.86	223.98	−1.41	60.00	59.96	0.07
6	R06	212.42	219.45	−3.31	57.00	57.13	−0.23
7	R07	198.86	201.67	−1.41	64.00	65.25	−1.95
8	R08	192.51	197.79	−2.74	71.00	71.46	−0.65
9	R09	208.54	206.55	0.95	58.00	57.79	0.36
10	R10	246.46	248.63	−0.88	72.00	72.62	−0.86
11	R11	219.18	219.39	−0.1	64.00	64.08	−0.12
12	R12	217.25	216.48	0.35	55.00	53.58	2.58
13	R13	215.37	214.78	0.27	70.00	71.79	−2.56
14	R14	223.33	221.49	0.82	65.00	64.42	0.89
15	R15	227.79	226.47	0.58	66.00	66.67	−1.02
16	R16	224.95	224.09	0.38	78.00	78.92	−1.18
17	R17	223.35	226.47	−1.4	67.00	66.67	0.49
18	R18	228.28	226.47	0.79	68.00	66.67	1.96
19	R19	201.89	198.07	1.89	74.00	70.79	4.34
20	R20	234.49	231.74	1.17	60.00	61.29	−2.15
21	R21	204.62	204.98	−0.18	56.00	57.13	−2.02
22	R22	216.75	221.27	−2.09	69.00	70.96	−2.84
23	R23	232.95	228.51	1.91	69.00	67.25	2.54
24	R24	230.87	226.47	1.91	66.00	66.67	−1.02
25	R25	200.26	198.82	0.72	58.00	58.29	−0.5
26	R26	196.84	193.66	1.62	63.00	63.08	−0.13
27	R27	204.57	207.75	−1.55	72.00	71.96	0.06
28	R28	239.83	240.38	−0.23	75.00	73.46	2.05
29	R29	231.19	234.12	−1.27	59.00	60.96	−3.32
30	R30	242.87	244.42	−0.64	67.00	66.42	0.87

From Fig. 5a, it is clear that tensile strength is proportional to rate of change of speed of the stirrer and stirring time.

Three-dimensional response plot for the influence of holding temperature and stirring time on tensile strength is shown in Fig. 5b. Here, the weight fraction and stirrer speed on stir casting are kept at the centre point of the design. For the consideration of holding temperature, best value of tensile strength occurs at the midpoint value.

Fig. 4 Experimental versus predicted values
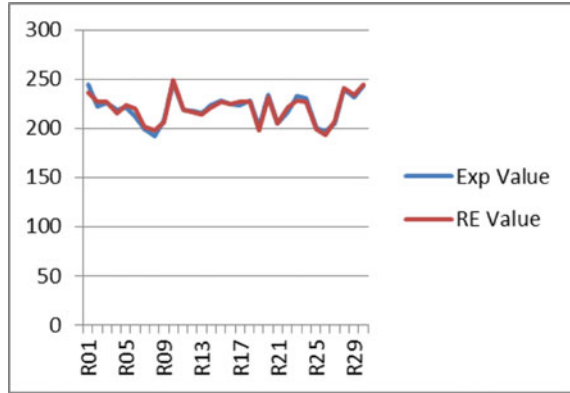
(a) Tensile Strength

(b) Hardness

Three-dimensional response plot for the influence of weight fraction and stirring time on tensile strength is shown in Fig. 5c. Here, the stirrer speed and holding temperature on stir casting are kept at the centre point of the design. Weight fraction of reinforcement plays a vital role in tensile strength. Hence, good tensile strength of material removal can be obtained from the optimum weight fraction of B_4C reinforcement.

Three-dimensional response plot for the influence of stirrer speed and holding temperature on tensile strength is shown in Fig. 5d. Here, the stirring time and weight fraction of reinforcement in AMC are kept at the centre point of the design. If the stirrer speed increases, the tensile strength increases, whereas good tensile strength is obtained in midpoint values.

Three-dimensional response plot for the influence of stirrer speed and weight fraction of reinforcement on tensile strength is shown in Fig. 5e. Here, the stirring time and holding temperature on stir casting are kept at the centre point of the design. If the stirrer speed increases, the tensile strength increases, whereas the best value
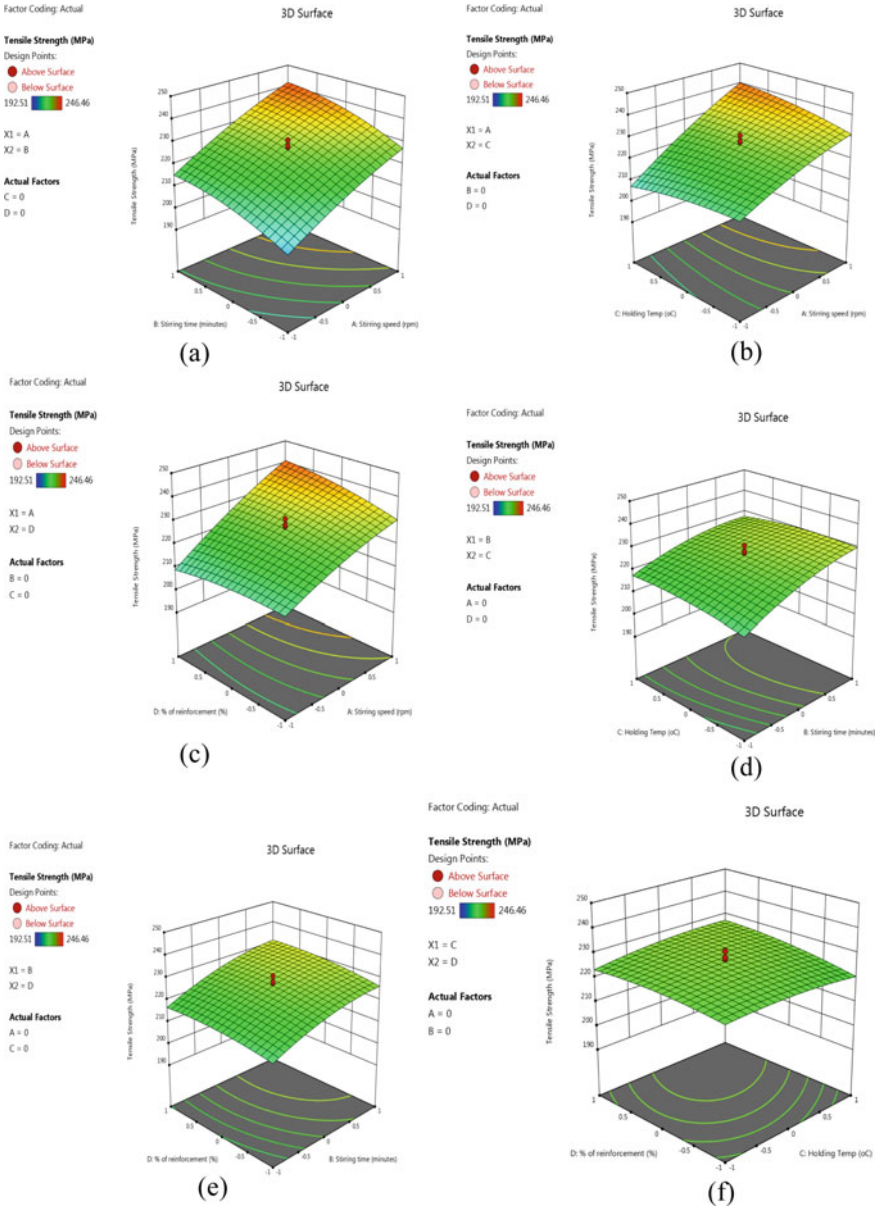
Fig. 5 Input parameters influencing on tensile strength

of tensile strength is obtained in midpoint values. From Fig. 5e, it is found that the weight fraction of reinforcement in AMC and stirrer speed are the major influencing factors in the production of B_4C reinforced AMCs using stir casting method.

Three-dimensional response plot for the influence of weight fraction of reinforcement and holding temperature on tensile strength is shown in Fig. 5f. Here, the stirring time and stirrer speed on stir casting are kept at the centre point of the design. If the weight fraction of reinforcement increases, the tensile strength increases, whereas good tensile strength is obtained in midpoint values.

4.1.2 Influence on Hardness (BHN)

The influence of input parameters on BHN in the fabrication of B_4C reinforced AMCs using stir casting is analysed with three-dimensional response plot. It is plotted against two input variables in x and y axes, respectively, with output parameter BHN in z axis. The other two parameters are kept at the centre point of the design.

Three-dimensional response plot BHN of AMC is shown in Fig. 6. Influence of stirrer speed and stirring time on BHN is shown in Fig. 6a. Here, the holding temperature and weight fraction of reinforcement in AMCs using stir casting are kept at the centre point of the design. For improved stir casting indices, elevated accuracy, and enhanced hardness, it is necessary to select the appropriate stirrer speed. In low values of stirrer speed, efficiency may reveal an inability to select the optimum casting conditions that show the way to elevated tensile strength and hardness. If the time taken for the stirring action is very high, then good BHN can be achieved from the aluminium B_4C reinforced composites.

At low stirring time, BHN is low and is slightly increased. Then, it gets smoothly reduced with increase in stirring time. Three-dimensional response plot for the influence of holding temperature and stirring time on BHN is shown in Fig. 6b. Here, the weight fraction of B_4C reinforcement and stirrer speed on stir casting are kept at the centre point of the design.

Hardness of the B_4C reinforced composites and holding temperature in the molten metal of the crucible are directly proportional to each other. If the holding temperature is low, hardness is also low. It gets increased with increase in the holding temperature in the furnace. Three-dimensional response plot for the influence of weight fraction of B_4C reinforcement and stirring time on BHN is shown in Fig. 6c. Here, the stirrer speed and holding temperature stir casting are kept at the centre point of the design. Optimal value of weight fraction of reinforcement will be giving the best value of BHN. Minimum weight fraction of reinforcement will produce minimum tensile strength, and hence provide minimum BHN values.

Three-dimensional response plot for the influence of stirrer speed and holding temperature on BHN is shown in Fig. 6d. Here, the weight fraction of B_4C reinforcement and stirring time on stir casting are kept at the centre point of the design. From the figure, it is noticed that the influence of holding temperature is less than that of stirrer speed. Three-dimensional response plot for the influence of weight fraction of B_4C reinforcement and holding temperature on BHN is shown in Fig. 6f. Here, the
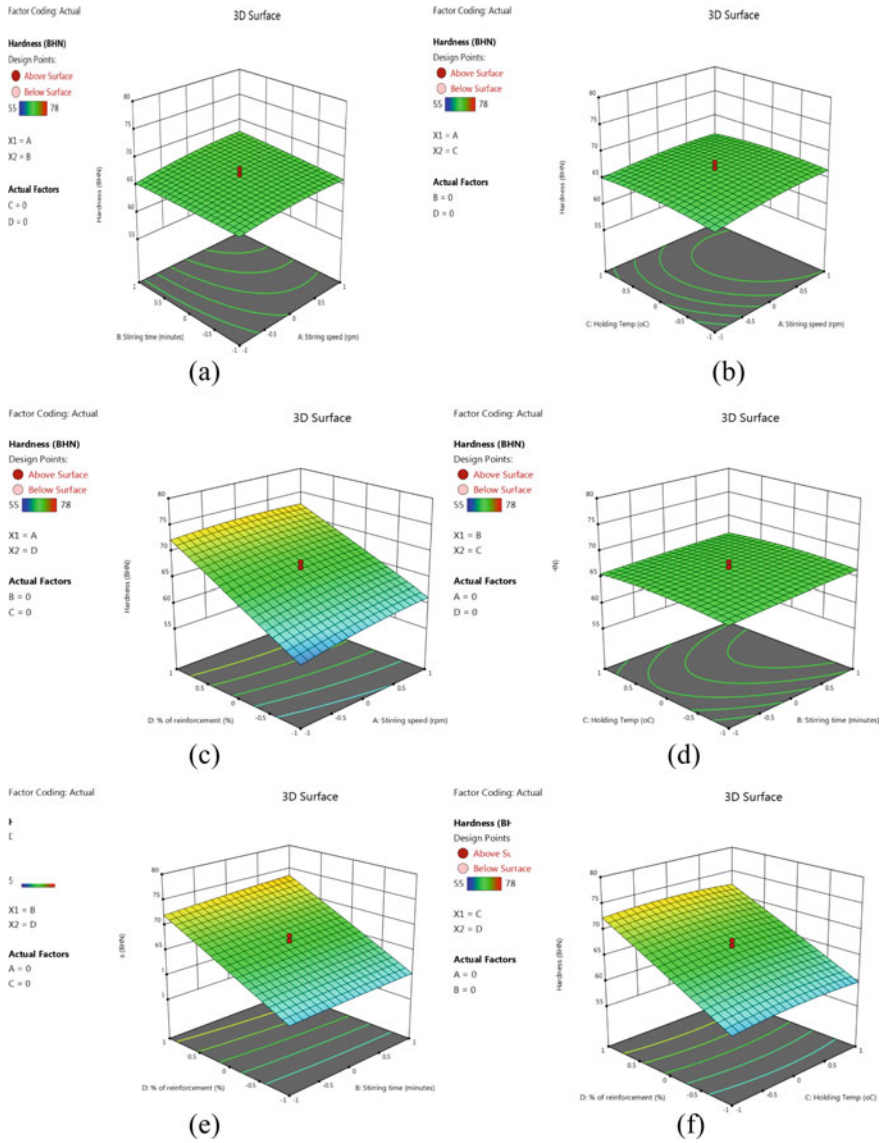
Fig. 6 Input parameters influencing on hardness

stirring time and stirrer speed on fabrication of AMCs using stir casting are kept at the centre point of the design. If weight fraction of B_4C reinforcement is increased, BHN also increases, but the influence of holding temperature is minimum compared with another parameter as concerned to BHN.

Table 5 ANNOVA results of tensile strength for B_4C reinforced AMCs

Source	df	Mean square	F-value	p-value
Model	14	419.03	18.68	< 0.0001
A-Stirring speed	1	3865.37	172.27	< 0.0001
B-Stirring time	1	1080.58	48.16	< 0.0001
C-Holding Temp	1	6.57	0.2929	0.5963
D-% of reinforcement	1	86.79	3.87	0.0680
Residual	15	22.44		
Lack of fit	10	28.40	2.70	0.1420
Pure error	5	10.51		
Cor total	29			

4.2 ANOVA Results

The analysis of variance is used to validate the model for deriving inference and the results. Since the response is nonlinear, the quadratic model has been selected for modelling.

4.2.1 ANOVA Results of Tensile Strength

The ANOVA result of tensile strength for B_4C reinforced AMCs is shown in Table 5. The model F-value of 18.68 and the p-value of <0.0001 represent that the selected quadratic model developed in DOE is good for deriving inference.

From ANOVA analysis, it is evident that the stirrer speed is the most influencing factor for maximizing the tensile strength because the F-value is 172.27. The stirring time has also a dominant influence on tensile strength (F-value 48.16). The other two parameters holding temperature and weight fraction of reinforcement are less influential factors on tensile strength. There are significant interactive effects (p-value < 0.0001) on stirrer speed and stirring time in the process which cannot be inferred by simple experiments. The p-value of the selected model is <0.0001, and hence, it can be a significant model for the experimental design for fabricating B_4C reinforced AMCs. The model F-value of 18.68 implies that the model is significant. Hence, this model can be used to navigate the design space.

4.2.2 ANOVA Results of BHN

The ANOVA table for BHN is given in Table 6. F-value of 25.74 implies that the model is significant for the modelling of predominant process parameter BHN. The p-value of selected model is <0.0001, and hence, it can be a significant model for

Table 6 ANNOVA results of BHN for B$_4$C reinforced AMCs

Source	df	Mean square	F-value	p-value
Model	14	72.21	25.74	< 0.0001
A-Stirring speed	1	16.67	5.94	0.0277
B-Stirring time	1	6.00	2.14	0.1643
C-Holding Temp	1	0.1667	0.0594	0.8107
D-% of reinforcement	1	962.67	343.13	< 0.0001
Residual	15	2.81		
Lack of fit	10	3.87	5.81	0.0329
Pure error	5	0.6667		
Cor total	29			

stir casting process for the fabrication process related to B$_4$C reinforced AMCs. The model F-value of 25.74 implies that the model is significant.

From ANOVA analysis, it is evident that the weight fraction of the B$_4$C presented in the AMC is the most influencing factor for good BHN, because the F-value is 343.13. The stirrer speed and stirring time have also an influence on BHN (F-value 5.94 and 2.14). The remaining parameter holding temperature is less influential on BHN. There are significant interactive effects (p-value < 0.0001) on the model as well as the weight fraction of the reinforcement in the process.

4.3 Regression Analysis

The normal probability plot is used for regression analysis. The normal plot of tensile strength and hardness of B$_4$C reinforced AMCs is shown in Fig. 7. From Fig. 7a, it is inferred that there exists a close agreement between the predicted R^2 of 0.7241 and adjusted R^2 of 0.8951 because the difference is less than 0.2. Hence, adequate precision processes the signal-to-noise ratio is achieved. A ratio of more than 4 is desirable. Model for the tensile strength, ratio of 16.412 indicates an adequate signal. This model can be used to navigate the design space.

From Fig. 7b, it is noticed that the predicted R^2 of 0.7835 is in close agreement with the adjusted R^2 of 0.9227. It shows that the difference is less than 0.2. Hence, adequate precision indicates good the signal-to-noise ratio. A ratio of more than 4 is desirable. In the current model, the ratio of 21.389 indicates an adequate signal. This model can be used to navigate the design space. The R-squared value of BHN is 0.9227, which means the regression model offers superior connection between the process parameters and response in hardness. The spread revealed in Fig. 7 indicates that the error in tensile strength and hardness is of normal spread, and the regression model is well integrated with the observed values.
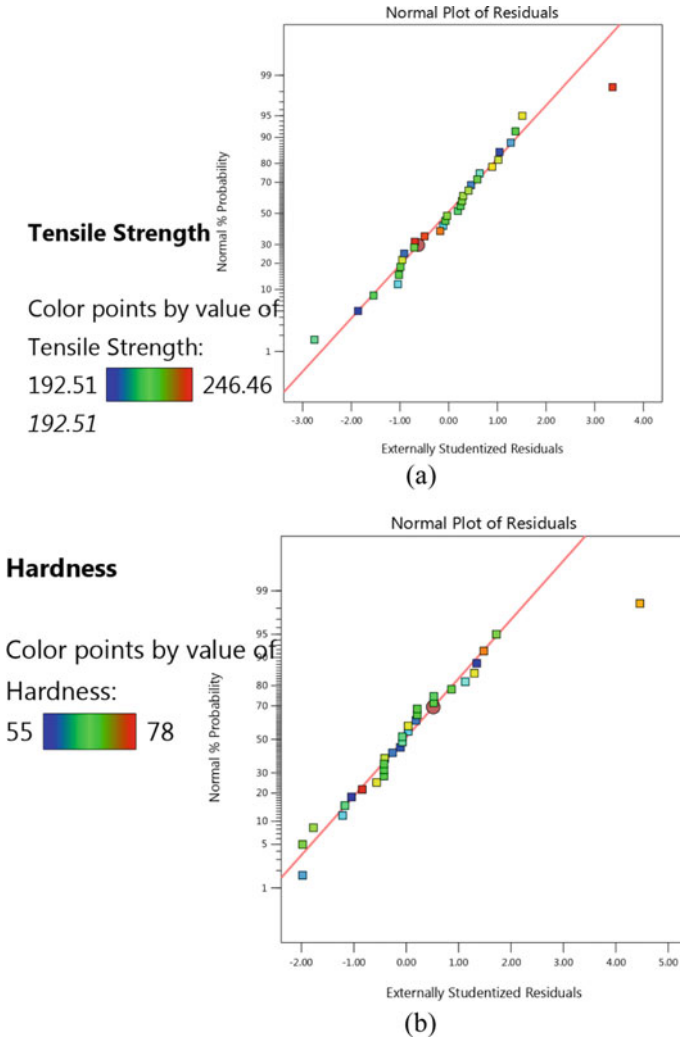
Fig. 7 Normal plot of B$_4$C reinforced AMC

The RSM model is developed for stir casting to map the relationship between process parameter and output variables. RE is formulated using the RSM model to predict the value of the output parameter. The experimental values are compared with the predicted values from RE. It has been observed that the predicted values are in close agreement with experimental values of tensile strength and hardness. The significance of RSM model is analysed with ANOVA and from the p-value and F-value it is concluded that the selected model is good for stir casting. The developed RE is also validated using normal plot. From normal plot, it has been noticed that

the developed regression model is significant for the experimentation of stir casting. The optimal values obtained from RSM is further used for microstructure analysis.

4.4   Microstructure Analysis

The SEM microstructure of AMCs is shown in Fig. 8. From the figure, it is observed that the B_4C particles were distributed homogeneously in AA6061. During the initial stage of the production of the metal matrix composites, the molten stage AA6061 flows with B_4C particles. A rotating action of the stirrer provides a rapid stirring which causes ceramic particles getting uniformly distributed in aluminium matrix. Most of the ceramic particles were found within the grain boundaries. Aluminium metal matrix composites were formed in the solid state, and the free movement of particles is absent because of the heavy density of the material. The particles were distributed by axial force induced by the rotating tool. The distribution of the particles becomes intra-granular. The basic structure of AA6061 is body centred cubic so that the B_4C particles were bonded together in reinforcement. Hence, the elongation was comparatively high for applied load. The ductility also improved because of the bonding nature of B_4C.

Specimens for microstructure analysis are carried at different portion of cast piece. Metallographic specimens are prepared by polishing. Microstructure study on the AMCs revealed the distribution of reinforcement particles throughout the matrix and occurrence of porosity. Figure 8 represents the microstructure images of AMC/B_4C specimens. From the figure, it was noticed that the input parameters which shows the distribution of reinforcements among the matrix. At higher speeds, the homogeneous distribution of the reinforcement has been attained. It is identified that the stirring time is also the influencing factor in addition to the stirrer speed.

It has been acknowledged that the spreading of reinforcement particle in Fig. 9. It is noticed that in some areas particle concentration is more and in some areas there is less concentration of the particles. Hence, the uniform particle reinforcement can
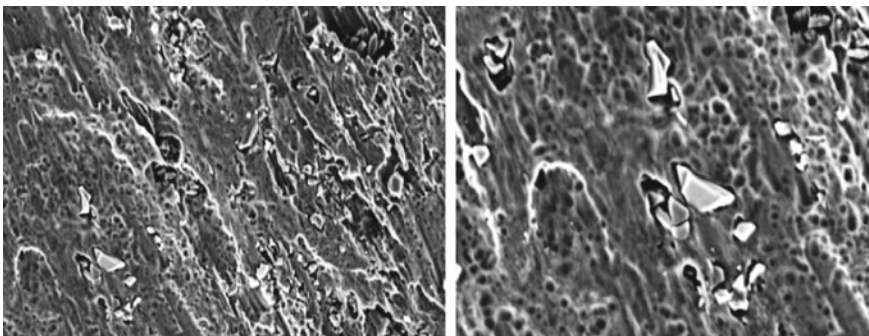

Fig. 8 SEM images

be attained by optimal stirring time of 6 min and just above. Some regions were identified without B$_4$C presence at stirring time of 6 min . If the stirring time is increased from 8 to 10 min, the reinforcement particle distribution becomes high which is compared with 6 min stirring. Hence, it is concluded that the better uniform distribution of the particle can be obtained from optimal stirring time and increasing the speed of the stirrer.

Some porosity areas were also recognized in the microstructure investigation. It may be due to poor wettability of the reinforcement with the matrix. If the temperature of the reinforcement is low, porosity associated with the B$_4$C reinforcement occurs in clusters. These porosity regions were well identified in SEM and EDAX pictures. AA6061 is generally a soft material, and the addition of particle reinforcement could increase the hardness of the AMCs. It is due to the presence of hard particles such as B$_4$C that tends to increase the plastic deformation of the matrix in the hardness test. It is also identified that in some places, the hardness value is more and some places its value is low. It is due to the absence of reinforcement particles in that region at the various locations in the tested specimen. It was exposed that the effect of stirrer
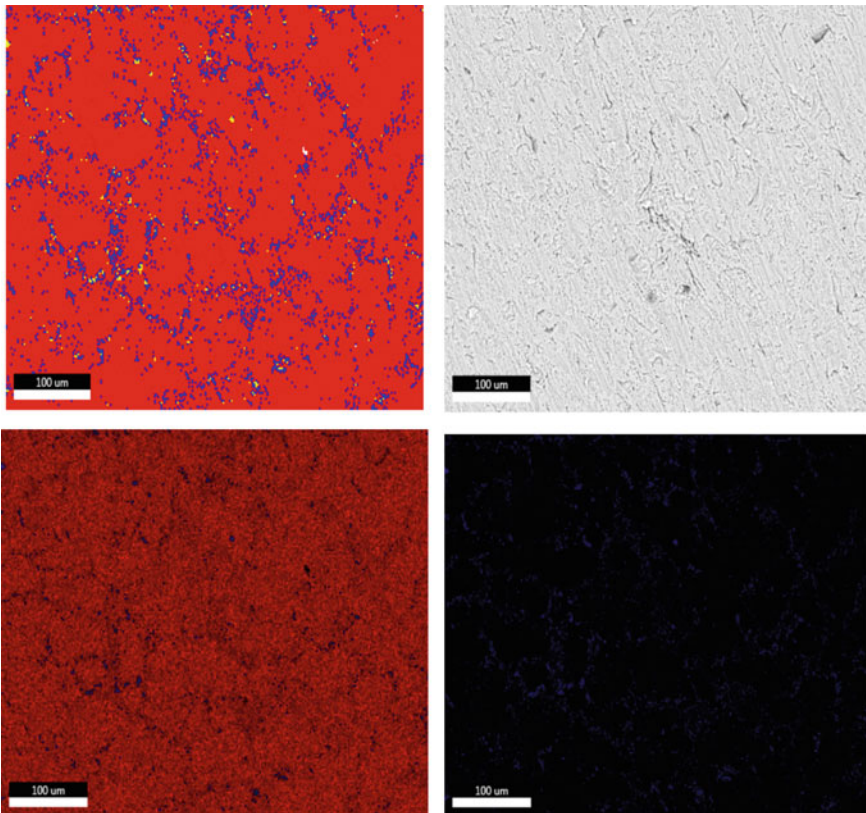

Fig. 9 EDAX results for AA6061/B$_4$C composites

speed and weight fraction of reinforcements mostly influenced the hardness value. The stirrer speed influenced the hardness value. At minimum stirrer speed, the values of hardness at certain places are low and, in some places, it was observed high. It is noticed from the areas where the B_4C particles were absent that minimum value of hardness is acquired. It is also observed that some areas where the particle gathering is high, maximum hardness values were obtained.

The hardness is non-uniform for low stirrer speeds and low stirring time. Due to this non-uniform distribution of the particles, some places were identified with high hardness and some places with low value of it. It is also observed that the stirring time and holding temperature do not make any improvement on hardness. When the stirrer speed is increased to 380 rpm, maintaining the stirring time of 6 min yields better results in hardness. It has been resolved from the microstructure that 6 min stirring and high weight fraction of reinforcement yield respectable hardness composite.

5   Conclusion

The composite specimens are fabricated at different experimental conditions using CCD, and the tensile strength and hardness in AA6061/B_4C are observed. The input parameters considered are stirrer speed, stirring time, holding temperature and percentage of reinforcement. The mathematical model using RSM is developed, and the regression equations are obtained for tensile strength and hardness. From the experimental outcomes and the developed models, the following conclusions are made:

- The simplest and the most economical way to produce good quality AA 6061/B_4C composites is stir casting technique.
- From the analysis, it is shown that the values obtained from regression equation are in close agreement with experimental model. The R^2 value of the regression equation is in significant fit. ANOVA analysis revealed that the mathematical model is in reasonable agreement for tensile strength as well as hardness.
- It was found from the tensile test that the stirrer speed and stirring time influence the ultimate strength of the composite. Higher stirring speed and stirring time give better strength and good hardness to composite of AMC. Better tensile strength and hardness composites were obtained from 360 rpm and 6 min stirring time with 700° holding temperature and 7.5% weight fraction of reinforced B_4C.
- In the microstructure study, it has been revealed that lowering the stirrer speed and minimum stirring time tends to non-uniform distribution of reinforcement particles and some places were recognized without B_4C addition. At maximum stirrer speed and high stirring time has given healthier and homogeneous distribution of B_4C in the Al matrix which was obtained. Uniform distributions of B_4C were obtained at 360 rpm and 8 min stirring time condition.

- Opportunity of crowding of the reinforcements increases with increasing weight fraction of reinforcements which will increase the ultimate tensile strength and hardness of AA6061/B_4C composites.

References

1. Safri SNA, Sultan MTH, Jawaid M, Jayakrishna K (2018) Impact behaviour of hybrid composites for structural applications: a review. Composites Part B Eng 133:112–121. https://doi.org/10.1016/j.compositesb.2017.09.008
2. Gladston JAK, Sheriff NM, Dinaharan I, Selvam JDR (2015) Production and characterization of rich husk ash particulate reinforced AA6061 aluminum alloy composites by compocasting. Trans Nonferrous Metals Soc China 25(683–691):2242–2247
3. Yigezu BS, Venkateswarlu D, Mahapatra MM, Jha PK, Mandal NR (2014) On friction stir butt welding of Al + 12Si/10 wt% TiC in situ composite. Mater Des 54:1019–1027
4. Kainer KU (2006) Metal matrix composites: custom-made materials for automotive and aerospace engineering.https://doi.org/10.1002/3527608117
5. Singh N, Banerjee S, Parkash O, Kumar D (2018) Tribological and corrosion behavior of (100–x)(Fe70Ni30)-(x) ZrO_2 composites synthesized by powder metallurgy. Mater Chem Phys 205:261–268
6. Singh N, Parkash O, Kumar D (2018) Phase evolution, mechanical and corrosion behavior of Fe (100–x) Ni (x) alloys synthesized by powder metallurgy. J Phys Chem Solids 114:8–20
7. Rahmana MH, Al Rashed HMM (2014) Characterization of carbide reinforced aluminium matrix composites. Procedia Eng 90:103–109
8. Jha P, Gupta P, Kumar D, Parkash O (2014) Synthesis and characterization of Fe–ZrO_2 metal matrix composites. J Comp Mater 48(17):2107–2115
9. Sajjadi SA, Ezatpour HR, Torabi Parizi M (2012) Comparison of microstructure and mechanical properties of A356 aluminum alloy/Al_2O_3 composites fabricated by stir and compo-casting processes. Mater Des 34:106–111. https://doi.org/10.1016/j.matdes.2011.07.037
10. Bandil K, Vashisth H, Kumar S, Verma L, Jamwal A, Kumar D et al (2019) Microstructural, mechanical and corrosion behavior of Al–Si alloy reinforced with SiC metal matrix composite. J Comp Mater
11. Reddy PS, Kesavan R, Vijaya RB (2017) Investigation of mechanical properties of aluminium 6061-silicon carbide, boron carbide metal matrix composite. SILICON. https://doi.org/10.1007/s12633-016-9479-8
12. Ravichandran M, Dineshkumar S (2014) Synthesis of Al-TiO2 composites through liquid powder metallurgy route. SSRG Int J Mech Eng 1:12–17
13. Jamwal A, Vates UK, Gupta P, Aggarwal A, Sharma BP (2019) Fabrication and characterization of Al_2O_3–TiC-reinforced aluminum matrix composites. In: Advances in industrial and production engineering. Springer, Singapore, pp 349–356
14. Veeravalli RR, Nallu R, Mohammed Moulana Mohiuddin S (2016) Mechanical and tribiological properties of AA7075-TiC metal matrix composites under heat treated (T6) and cast conditions. J Mater Res Technol 5:377–383. https://doi.org/10.1016/j.jmrt.2016.03.011
15. Suresh S, Shenbag N, Moorthi V (2012) Aluminium-titanium diboride (Al-TiB2) metal matrix composites: challenges and opportunities. Procedia Eng 38:89–97. https://doi.org/10.1016/j.proeng.2012.06.013
16. Dao V, Zhao S, Lin W, Zhang C (2012) Effect of process parameters on microstructure and mechanical properties in AlSi9Mg connecting-rod fabricated by semi-solid squeeze casting. Mater Sci Eng A 558:95–102
17. Harichandran R, Selvakumar N (2015) Effect of nano/micro B_4C particles on the mechanical properties of aluminium metal matrix composites fabricated by ultrasonic cavitation-assisted solidification process. Arch Civ Mech Eng 6:1–12. https://doi.org/10.1016/j.acme.2015.07.001

18. Taylor P, Mazahery A, Shabani MO (2013) Existence of good bonding between coated B$_4$C reinforcement and Al matrix via semisolid techniques: enhancement of wear resistance and mechanical properties. Tribol Trans 3:37–41. https://doi.org/10.1080/10402004.2012.752552

19. Moona G, Walia RS, Rastogi V, Sharma R (2018) Aluminium metal matrix composites: a retrospective investigation. Indian J Pure Appl Phys 56:164–175

20. Nai SML, Gupta M (2002) Influence of stirring speed on the synthesis of Al/SiC based functionally gradient materials. Compos Struct 57:227–233

21. Naher S, Brabazon D, Looney L (2003) Simulation of the stir casting process. J Mater Process Technol 143–144:567–571

22. Prabu SB, Karunamoorthy L, Kathiresan S, Mohan B (2006) Influence of stirring speed and stirring time on distribution of particles in cast metal matrix composite. J Mater Process Technol 171:268–273

23. Ravi KR, Sreekumar VM, Pillai RM, Mahato C, Amaranathan KR, Arul Kumar R, Pai BC (2007) Optimization of mixing parameters through a water model for metal matrix composites synthesis. Mater Des 28:871–881

24. Akhlaghi F, Lajevardi A, Maghanaki HM (2004) Effects of casting temperature on the microstructure and wear resistance of compocast A356/SiCp composites: a comparison between SS and SL routes. J Mater Process Technol 155–156:1874–1880

25. Amirkhanlou S, Niroumand B (2010) Synthesis and characterization of 356−SiCp composites by stir casting and compocasting methods. Trans Nonferrous Metals Soc China 20(S):s788−s793

26. Soundararajan R, Sivasankaran S, Al-Mufadi FA, Akilesh M, Elango PR (2019) Investigation on A356-20wt% SiC composites through mechanical stirring and ultra-sonic-assisted cavitation. Mater Res Exp 6(9). https://doi.org/10.1088/2053-1591/ab3082

27. Khosravi H, Bakhshi H, Salahinejad E (2014) Effects of compocasting process parameters on microstructural characteristics and tensile properties of A356−SiCp composites. Trans Nonferrous Metals Soc China 24:2482–2488

28. Akbari MK, Mirzaee O, Baharvandi HR (2013) Fabrication and study on mechanical properties and fracture behavior of Nano metric Al$_2$O$_3$ particle-reinforced A356 composites focusing on the parameters of vortex method. Mater Des 46:199–205

29. Sathiskumar R, Murugan N, Dinaharan I, Vijay SJ (2014) Prediction of mechanical and wear properties of copper surface composites fabricated using friction stir processing. Mater Des 55:224–234

30. Vettivel SC, Selvakumar N, Narayanasamy R, Leema N (2013) Numerical modelling, prediction of Cu−W nano powder composite in dry sliding wear condition using response surface methodology. Mater Des 50:977–996

31. Rostamiyan Y, Fereidoon A, Rezaeiashtiyani M, Mashhadzadeh AH, Salmankhani A (2015) Experimental and optimizing flexural strength of epoxy-based nanocomposite: effect of using nano silica and nano clay by using response surface design methodology. Mater Des 69:96–104

32. Vaira Vignesh R, Padmanaban R, Mohan Das K, Govindaraju M (2020) Research and development in magnesium alloys for industrial and biomedical applications: a review. Metals Mater Int 26:409–430

33. Vaira Vignesh R, Padmanaban R (2017) Modelling corrosion behavior of friction stir processed aluminium alloy 5083 using polynomial: radial basis function. Trans Indian Inst Metals 70:2575–2589

34. Vaira Vignesh R, Padmanaban R, Govindaraju M (2019) Synthesis and characterization of magnesium alloy surface composite (AZ91D—SiO$_2$) by friction stir processing for bioimplants. Silicon 5:2619–2633

Solid State Processing of Lightweight Alloys and Composites

Chapter 12
Microstructure and Mechanical Properties of Severely Deformed Aluminum Alloys

Shrishty Sahu, Abhishek Ghosh, Uttam Kumar Murmu, Kalyan Das, and Manojit Ghosh

1 Introduction

Nowadays, the use of aluminum and its alloys is progressively increasing in the aerospace and automobile industries owing to their high specific strength, excellent formability, and cost-effectiveness [1]. Various researchers have worked on improving the mechanical properties of these alloys and came up with the idea of refining the coarse-grained structures, which could be accomplished through severe plastic deformation (SPD). SPD is a novel method that produces grain sizes below sub-micrometer or even nanometer ranges in fully dense bulk metals [2]. This is achieved by imposing a very high strain without bringing any noteworthy change in the general dimensions of the materials [3]. It is already known that metals' average grain size and microstructural characteristics are quite responsible for modifying their mechanical properties [3]. Thus, two main advantages of ultra-fine grain (UFG) structures can be obtained from the SPD techniques. Firstly, the reduction in grain size up to the nanometer range (100 nm [4]) consequently the material behaving stronger following the Hall–Petch relationship. Secondly, the polycrystalline materials with UFGs subjected to a tension test at rapid rates and higher temperatures can exhibit super plasticity [2]. The conventional deformation methods (such as rolling and drawing, pressing) are much inferior to the SPD processes as they refrain the metals from achieving high strain and, consequently, grain refinement. They are even responsible for reducing the cross-sectional area of the materials, which is not the case with SPD techniques. The structures thus obtained after SPD processes possess

S. Sahu · A. Ghosh (✉) · U. K. Murmu · K. Das · M. Ghosh (✉)
Department of Metallurgy and Materials Engineering, Indian Institute of Engineering Science and Technology, Shibpur, Howrah 711103, India
e-mail: abhishek.me.08@gmail.com; abhishek.me.rs2015@metal.iiests.ac.in

M. Ghosh
e-mail: mghosh.metal@faculty.iiests.ac.in

UFGs, low density of free dislocations, high strain, high angle of misorientation in grains, high energy, high strength, increased wear resistance, increased strain rate, and decreased dynamic recrystallization [4]. Therefore, the following sections will introduce the readers to various SPD processes with respective microstructures developed.

2 Relevant Topics

2.1 *Principles of Severe Plastic Deformation (SPD) Processing*

Out of the numerous available SPD processing techniques, the most developed ones are accumulative roll bonding (ARB), equal-channel angular processing (ECAP), and high-pressure torsion (HPT) [2]. Hence, they have been discussed here in detail due to their broad applicability, high degree of homogeneity, excellent mechanical properties, etc. These techniques have various applications for the SPD processed materials, such as biomedical appliances, sports equipment (for example high-performance bicycles), extreme environmental conditions, and dental and orthopedic surgeries. [5]. ARB is the simplest and most cost-effective of these three techniques, while HPT results in greater refinement of microstructures. However, all processes do have their demerits as well. Some of the significant difficulties encountered with ECAP are its non-continuous and labor-intensive nature, high initial set-up cost, the possibility of formation of cracks, usage of relatively small-sized billets, amount of wastage and employment of rod or bar samples instead of the commonly used sheet metals in the industry. However, HPT is a continuous process, but the use of thin disk samples is one of its drawbacks. Thus, ECAP and HPT processes are not so helpful for processing larger volumes of materials [5]. Nevertheless, ARB has proved to be one of the best SPD processes in the industry because, along with several other benefits, it did not require many changes in its conventional design [1]. ECAP and HPT processes still find industrial applications due to the generation of negligible porosity and contamination [2]. The UFG alloys so produced are homogenous and possess equiaxed microstructures with grain boundaries mostly having high angles of misorientation [3]. The other advantages in mechanical properties of these alloys include better strength at low temperatures, greater hardness and ductility, improved formability at elevated temperatures, and superior fatigue life [6, 7].

2.1.1 ARB Process

In the ARB processing technique, large fine-grained sheets can be continuously produced without changing the dimensions of the specimen. First, the material is divided into strips parallel to the rolling direction. The next step is to remove any
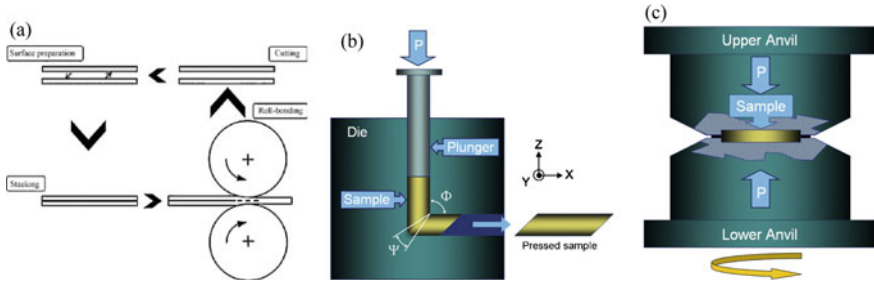
Fig. 1 Schematic diagrams of **a** ARB, **b** ECAP, **c** HPT processes [8, 9]. Reprinted from Ref. [9] with permission from Elsevier

contaminants from the surface of the strips that are to be bonded together. After the surface preparation, the surfaces are fixed tightly with the help of copper wires. Then they are rolled out by 50% of their thickness without using any lubricants at ambient temperature. After each cycle, these roll-bonded strips are cut in half and then rolled again (Fig. 1a) [8].

2.1.2 ECAP Process

ECAP is known to be developed by Segal et al. in Russia during the 1970s [7]. This method is well capable of introducing large plastic strains without substantially changing the overall geometry of the sample [7]. In this process, a workpiece in the form of a bar or rod is pushed through two channels that intersect at an angle close to 90° (Fig. 1b). The sample is pushed with the help of a plunger by applying an external pressure P. [2] In the sample shown in Fig. 1b, the two channels intersect at $\varphi = 90°$, and the angle at which their outer arc of curvature meets is $\Psi = 0°$. These angles act as the deciding factor for the strain produced in the work metal in a single pass. To introduce different slip systems during ECAP, the samples can be rotated about their longitudinal axis between each pass. Based on the rotation of the sample billet, three types of processing routes can be recognized: Route A (no rotation), Route B_C (90° clockwise rotation), and Route C (180° rotation between passes). On comparing all the routes, Route B_C has proved to be the best because it produces equiaxed arrays of UFGs having high-angle grain boundaries in the three orthogonal planes [10].

2.1.3 HPT Process

HPT is another SPD processing technique that uses pure shear to deform thin disks of metals. These disks are placed between two anvils which rotate against each other (Fig. 1c). Since the deformation produced is non-uniform across the diameter; hence, it is difficult to provide an exact estimation of the strain produced. Another factor

responsible for affecting the value of the strain is the thickness of the disks used. Hence, the strain must be measured in terms of the number of turns of the disks. According to the literature, various experiments confirmed that HPT is better than ECAP because it can produce a very fine grain size (~450 nm [11]) in the sample. However, the size of the samples being too small is one of its disadvantages [2, 5].
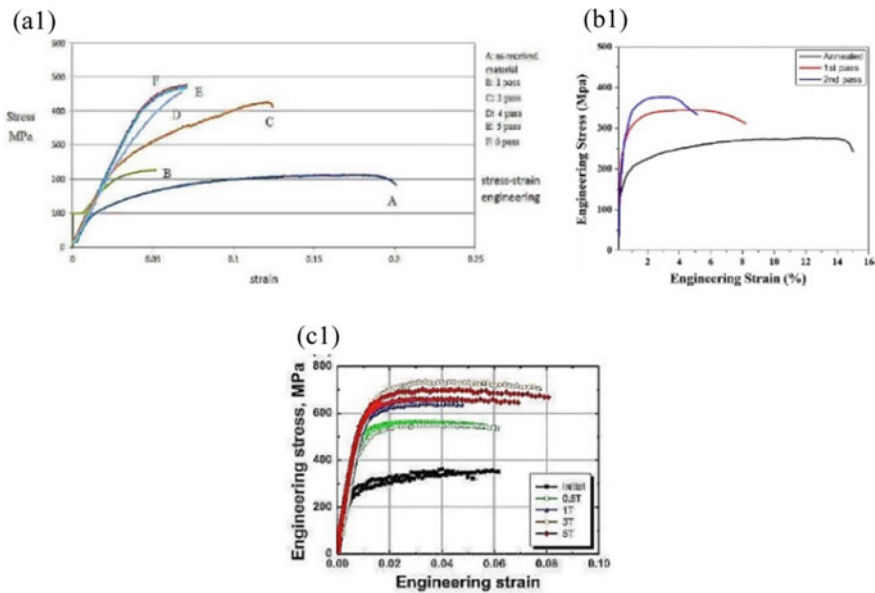
2.2 Mechanical Properties After SPD Processes

See Fig. 2 and Table 1.

Fig. 2 Engineering stress–strain curves for Al-7075 alloy for **a1** ARB, **b1** ECAP and **c1** HPT processed sheets [12–14]. Reprinted from Refs. [13] and [14] with permission from Springer Nature and Elsevier, respectively

Table 1 Mechanical properties of ARB, ECAP and HPT processes [11–17]

Process	Equivalent strain	YS (MPa)	UTS (MPa)	% El	Hardness (Hv)	Grain size
ARB	0.055	235	305	18	55	1.3 μm
ECAP	0.082	255	330	7	125	1 μm
HPT	0.048	550	650	20	255	450 nm

2.2.1   Strength and Ductility

On observing the engineering stress–strain curve for Al-7075 alloys for all three processes, it can be concluded that after one pass, the specimen's yield strength (YS) and ultimate tensile strength (UTS) increase the most for the HPT process and the least for ARB process. This proves that all SPD processes increase the strength of the material while lowering its ductility. The YS and UTS of the Al-7075 alloy increase by 30% and 20%, respectively, after the ARB process. While for the ECAP process, the YS and UTS increase by 94% and 43%, respectively, after the second ECAP pass. And for the HPT process, the YS and UTS increase by 100% and 90%, respectively. Strengthening mechanisms due to dislocations, grain refinement, precipitation and solid solution are responsible for enhancing strength after the SPD processes [17, 18].

The YS and UTS of the Al-6061 alloy increase by 22% and 19.5%, respectively, for the ARB process after 5 cycles [19]. While for the ECAP process, both YS and UTS increase by 40% [20] and by 60% and 55%, respectively, for the HPT process.

2.2.2   Hardness

Hardness can be described as the resistance of a material against plastic deformation. The hardness of the Al-7075 alloy increases after every pass [15]. For the ARB process, the hardness of the specimen increases by 100% after a single ARB cycle and becomes constant after the third ARB cycle [16]. Considering the ECAP process for the Al-7075 alloy, the hardness increases by approximately 71% due to the fragmentation of the precipitates, increase in dislocation density and grain refinement [13, 18]. However, the mechanical properties of the specimens after ECAP increase significantly up to 120 °C only. From 120 to 180 °C, the size of the grains and precipitates increase, due to which the mechanical properties decrease [17]. The hardness of the material also increases after HPT processing. The distribution of microhardness in the case of HPT processed specimens is the least in the central zone and keeps increasing while moving away from the center. Similar results are obtained for other aluminum alloys.

2.3   Microstructural Evolution After SPD Processing

Primarily the Al alloys can be divided into age-hardenable (2xxx, 6xxx, 7xxx, etc.) alloys and non-age hardenable (1xxx, 3xxx, 5xxx) alloys. Among the different kinds of Al alloys, the age hardenable 6xxx and 7xxx series alloys have gained a special interest in many industrial applications due to their excellent mechanical properties. Thus, a detailed overview of the microstructural evolution of 6xxx and 7xxx series alloys after the three novel SPD processes: ARB, ECAP and HPT processes, has been discussed in this section.

2.3.1 Grain Size and Shape

On observing the microstructural evolution after the ARB process, the average grain size of an Al-7075 alloy is observed to reduce to 1.3 μm from the initial grain size consisting of both equiaxed and elongated grains with varying volume fractions (Fig. 3) [15, 21]. The grains become more elongated and flatter by increasing the number of cycles [16]. Apart from ARB, the microstructural evolution after the ECAP process illustrated significant grain refinement (60–1 μm). From the TEM and EBSD figures (Fig. 4), it can be concluded that the grains become almost equiaxed, and with an increase in ECAP temperature, an increase in grain size with equiaxed structure and a decrease in dislocation density can be observed [17]. In the case of the HPT process, a better refinement occurred in grains (~500 nm in the center and ~250 nm near the edge [22]) (Fig. 5) when the process is carried out at RT rather than at high temperatures (200 °C). At RT, the refinement in grains after two revolutions becomes negligible due to an increase in dislocation density. While after 200 °C, the grain refinement increases with an increase in temperature due to a decrease in dislocation density. Generally, after two revolutions, a mixture of equiaxed and elongated UFGs is observed during HPT. While the number of equiaxed UFGs increases after multiple HPT cycles [7].
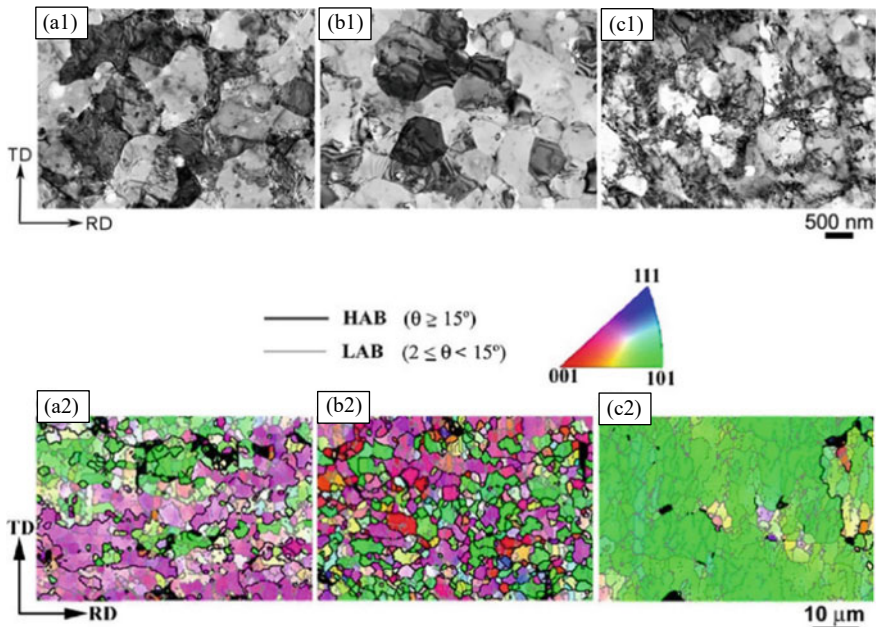

Fig. 3 Microstructures after processing by ARB for Al-7075 samples by TEM at **a1** 300 °C, **b1** 350 °C, and **c1** 400 °C and EBSD at **a2** 300 °C, **b2** 350 °C, and **c2** 400 °C [26]. Reprinted from Ref. [26] with permission from Springer Nature
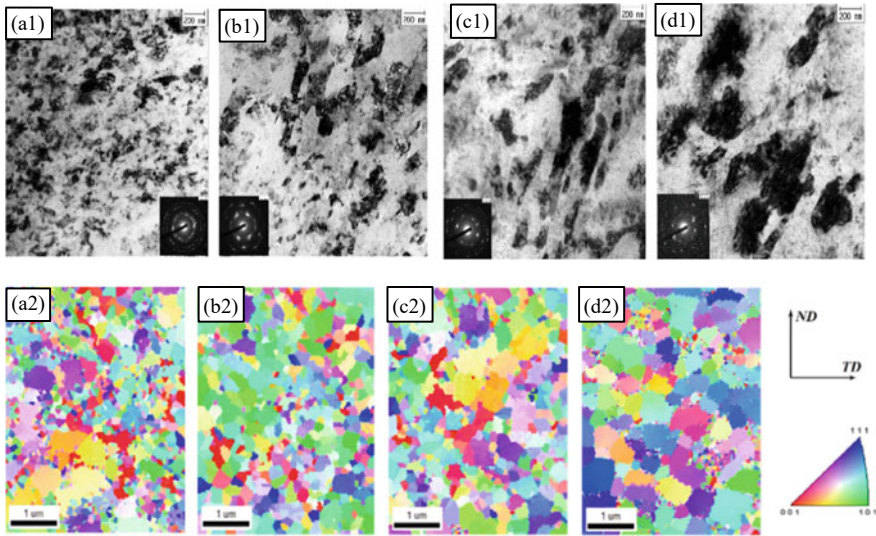
Fig. 4 Microstructures after processing by ECAP for Al-7075 alloys at different temperatures: TEM micrographs and corresponding SAED patterns for **a1** 3 passes RT, **b1** 3 passes 120 °C, **c1** 4 passes at 150 °C, **d1** 4 passes at 180 °C and EBSD for **a2** 3 passes RT, **b2** 3 passes 120 °C, **c2** 4 passes at 150 °C, **d2** 4 passes at 180 °C [17]
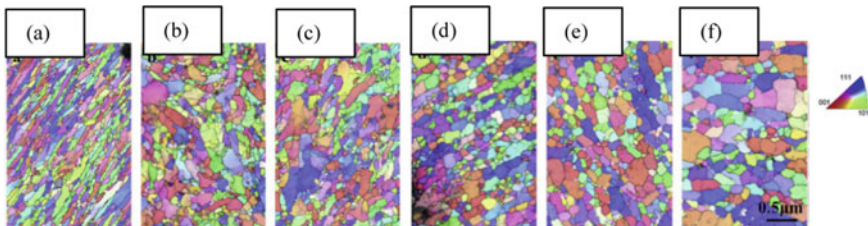

Fig. 5 EBSD orientation color maps of Al-7075 alloy disks processed by HPT after **a** 2 revolutions, **b** 5 revolutions, **c** 10 revolutions at RT; and after **d** 2 revolutions, **e** 5 revolutions, **f** 10 revolutions at 200 °C [27]. Reprinted from Ref. [27] with permission from Elsevier

On observing the microstructural evolution after the 12-cycle ARB process at RT (Fig. 6), the average grain size of an Al-6061 alloy is observed to reduce to 500 nm from the initial grain size. An increase in the number of cycles further decreases the size of the UFGs [23]. In the case of the ECAP process, the mean grain size reduces to 300–400 nm after 4 ECAP passes (Fig. 7) [24]. While in the case of the HPT process, the mean grain size of the UFG structure is observed to reduce to 100 nm (Fig. 8) [25].
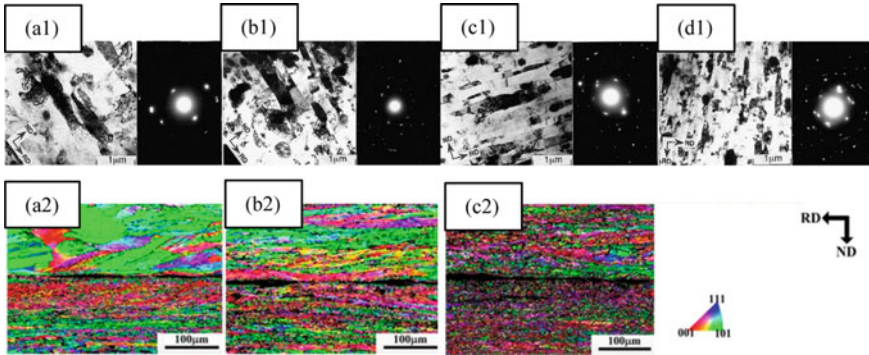
Fig. 6 Microstructures after processing Al-6061 alloys by ARB: TEM micrographs and corresponding SAED patterns at the rolling plane after **a1** two, **b1** four, **c1** six, **d1** eight cycles and EBSD for **a2** one, **b2** two, **c2** three cycles [1, 23]. Reprinted from Ref. [23] with permission from Elsevier
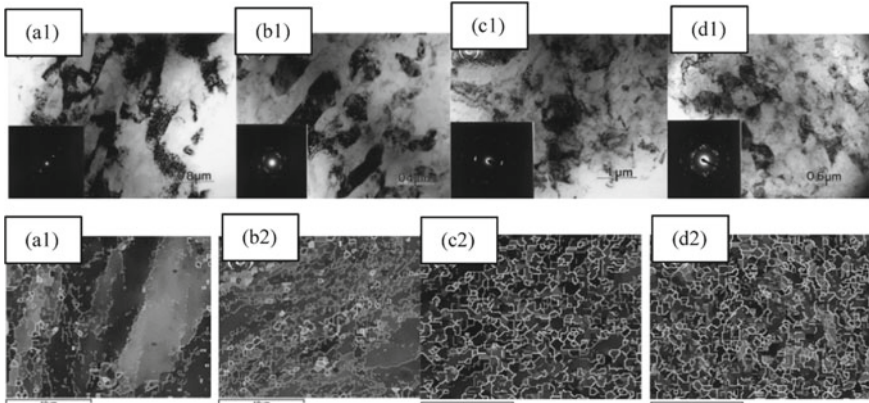

Fig. 7 Microstructures after processing Al-6061 alloys by ECAP: TEM micrographs and corresponding SAED patterns for **a1** 1 pass, **b1** 4 passes, **c1** 8 passes, **d1** 12 passes and EBSD for **a2** 1 pass, **b2** 4 passes, **c2** 8 passes, **d2** 12 passes [28]. Reprinted from Ref. [28] with permission from Elsevier

2.3.2   Development of Precipitates

The SPD processes are responsible for accelerating the formation of precipitates in Al-7xxx and 6xxx alloys since high-density dislocations are introduced by these processes. High-density dislocations provide heterogeneous nucleation sites for precipitates [29]. During the ARB processing at elevated temperatures, the precipitates become larger due to coarsening of the material in the heating steps (Fig. 9a–d). As the temperature of the process is increased, a further increase in the size of precipitates is observed (Fig. 9b–d) [16, 26]. The precipitation characteristics through TEM
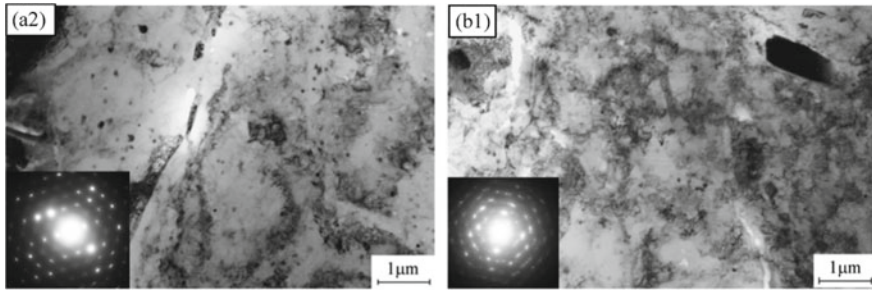
Fig. 8 Microstructures after processing Al-6061 alloys by HPT: TEM micrographs and their corresponding SAED patterns for **a1** the center and **b1** at the edge [25]. Reprinted from Ref. [25] with permission from Elsevier

figures (Fig. 10) of the ECAP process show that no precipitate is formed at RT after 3 ECAP passes. However, with the increment of temperature to 120 °C, the precipitates of small spherical (3–5 nm) sizes are formed. On further increasing the temperature to 150 °C, the size of the precipitates increases to 10–20 nm, while the shape remains the same. Alternatively, the morphology of the precipitates changes to plate-like, and the size increases to 14–45 nm when the alloy is ECAPed at 180 °C. [17]. In the case of the HPT process, the formation of precipitates (<7 nm in size) of irregular shapes takes place during deformation at RT. By contrast, the development of coarse globular precipitates (>10 nm in size) is noticeable at the time of the high-temperature HPT process [27].

3   Future Directions

It is a well-known fact that the UFG Al alloys produced by SPD processes have a grain size lying in the sub-micrometer range along with various excellent mechanical properties such as high hardness and strength but low ductility. Hence, some extensive research in the fields of microstructural evolution, processing routes, etc., was required to enhance the ductility of SPD-produced materials. The recently developed 3rd generation Al-Li alloys with high strength and ductility can be tried with SPD refinement to produce UFG materials.
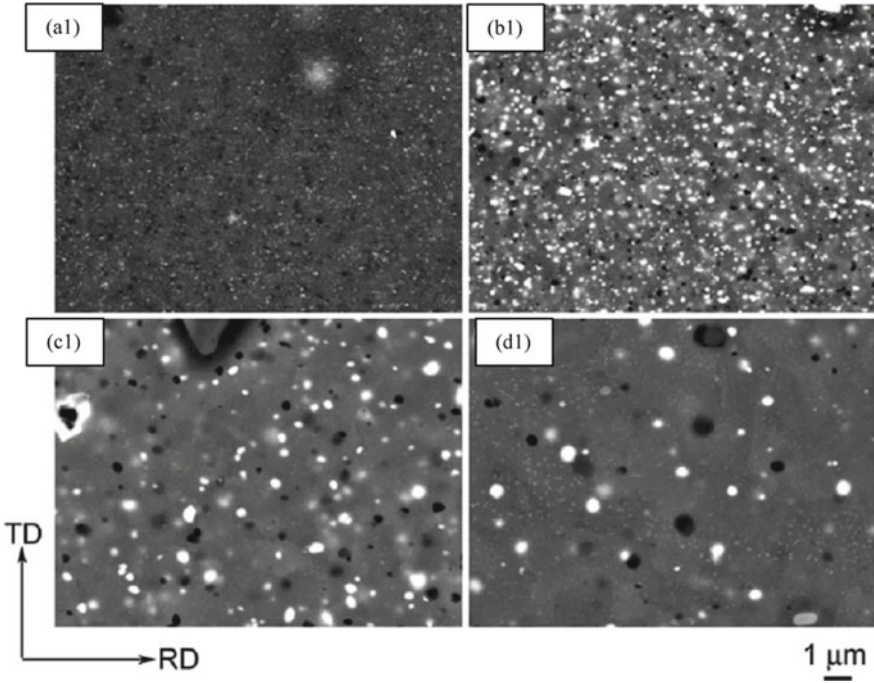
Fig. 9 Comparative TEM images subjected to ARB process showing the precipitates in Al-7075 alloy **a1** as-received, **b1** 300 °C, **c1** 350 °C, and **d1** 400 °C [26]. Reprinted from Ref. [26] with permission from Springer Nature
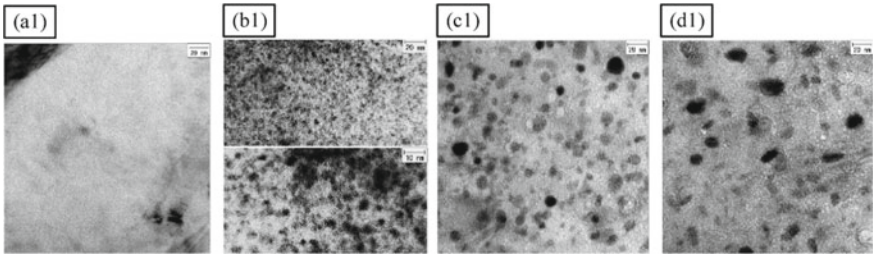

Fig. 10 Depiction of precipitates in Al-7075 alloy put through ECAP process for 3 passes **a1** at RT, **b1** at 120 °C and 4 passes **c1** at 150 °C and **d1** at 180 °C [17]

4   Summary and Conclusion

To sum up, the following points may be considered:

- The mechanical properties of aluminum alloys can be improved by refining the coarse-grained structures through SPD, whose average size lies in the sub-micrometer range.
- On observing the microstructural evolution after the ARB, ECAP and HPT processes, it can be concluded that the average grain size of the specimen reduces significantly for all SPD processes. These processes are also responsible for accelerating the formation of precipitates which become coarser on increasing the temperature.
- Among the three SPD processes, ultrafine grains were achieved in HPT, followed by ECAP and ARB. The same trend was followed in the case of mechanical properties such as YS, UTS, and hardness.

References

1. Li Z, Jiang H, Wang M, Jia H, Han H, Ma P (2021) Microstructure and mechanical properties of Al–Mg–Si similar alloy laminates produced by accumulative roll bonding. Materials (Basel) 14(15). https://doi.org/10.3390/ma14154200
2. Langdon TG (2006) Processing of aluminium alloys by severe plastic deformation. Mater Sci Forum 519–521:45–54. https://doi.org/10.4028/www.scientific.net/msf.519-521.45
3. Valiev RZ, Langdon TG (2006) Principles of equal-channel angular pressing as a processing tool for grain refinement. Prog Mater Sci 51(7):881–981. https://doi.org/10.1016/j.pmatsci.2006.02.003
4. Dobatkin SV, Zrnik J, Mamuzić I (2006) Nanostructures by severe plastic deformation of steels: advantages and problems. Metalurgija 45(4):313–321
5. Ghalehbandi SM, Malaki M (2019) Accumulative roll bonding—a review. Appl Sci
6. Ghosh A, Ghosh M (2021) 3D FEM simulation of Al-Zn-Mg-Cu alloy during multi-pass ECAP with varying processing routes. Mater Today Commun 26(Feb):102112. https://doi.org/10.1016/j.mtcomm.2021.102112
7. Srinivasan R, Chaudhury PK, Cherukuri B, Han Q, Swenson D, Gros P (2006) Continuous severe plastic deformation processing of aluminum alloys. Final Tech Rep Forg 513:1–59
8. Rezaei MR, Toroghinejad MR, Ashrafizadeh F (2011) Production of nano-grained structure in 6061 aluminum alloy strip by accumulative roll bonding. Mater Sci Eng A 529(1):442–446. https://doi.org/10.1016/j.msea.2011.09.057
9. Huang Y, Langdon TG (2013) Advances in ultrafine-grained materials. Mater Today 16(3):85–93. https://doi.org/10.1016/j.mattod.2013.03.004
10. Valiev RZ, Estrin Y, Horita Z, Langdon TG, Zehetbauer MJ, Zhu Y (2016) Producing bulk ultrafine-grained materials by severe plastic deformation: ten years later. JOM 68(4):1216–1226. https://doi.org/10.1007/s11837-016-1820-6
11. Loucif A, Figueiredo RB, Baudin T, Brisset F, Langdon TG (2010) Microstructural evolution in an Al-6061 alloy processed by high-pressure torsion. Mater Sci Eng A 527(18–19):4864–4869. https://doi.org/10.1016/j.msea.2010.04.027
12. Alvandi H, Farmanesh K (2015) Microstructural and mechanical properties of nano/ultra-fine structured 7075 aluminum alloy by accumulative roll-bonding process. Procedia Mater Sci 11:17–23

13. Ghosh A et al (2020) Development of ultrafine grained Al–Zn–Mg–Cu alloy by equal channel angular pressing: microstructure, texture and mechanical properties. Arch Civ Mech Eng 20(1). https://doi.org/10.1007/s43452-019-0003-y
14. Kim H et al (2021) Outstanding mechanical properties of ultrafine-grained Al7075 alloys by high-pressure torsion. Mater Sci Eng A 810(March):141020. https://doi.org/10.1016/j.msea.2021.141020
15. Anne G, Ramesh MR, Nayaka HS, Arya SB, Sahu S (2017) Microstructure evolution and mechanical and corrosion behavior of accumulative roll bonded Mg-2% Zn/Al-7075 multilayered composite. J Mater Eng Perform 26(4):1726–1734
16. Velázquez-Carrillo OA, García-Pastor FA (2021) Thermal stability of microstructure, mechanical properties, formability parameters and crystallographic texture in an Al-7075 alloy processed by accumulative roll bonding. J Market Res Technol 11:2208–2220. https://doi.org/10.1016/J.JMRT.2021.02.041
17. Shaeri MH, Shaeri M, Ebrahimi M, Salehi MT, Seyyedein SH (2016) Effect of ECAP temperature on microstructure and mechanical properties of Al-Zn-Mg-Cu alloy. Prog Nat Sci Mater Int 26(2):182–191. https://doi.org/10.1016/j.pnsc.2016.03.003
18. Ghosh A, Ghosh M (2020) Effect of heat treatment and severe plastic deformation on microstructure and texture evolution of 7075 alloy. Mater Today Proc 33:5239–5242. https://doi.org/10.1016/j.matpr.2020.02.947
19. Sahli A et al (2021) Effect of an addition of vanadium on the mechanical properties of the A6061 alloy deformed by accumulative roll bonding. J Mater Eng Perform. https://doi.org/10.1007/s11665-021-05882-2
20. Kim JK, Jeong HG, Hong SI, Kim YS, Kim WJ (2001) Effect of aging treatment on heavily deformed microstructure of a 6061 aluminum alloy after equal channel angular pressing. Scr Mater 45(8):901–907
21. Ghazanlou SI, Eghbali B, Petrov R (2021) Microstructural evolution and strengthening mechanisms in Al7075/graphene nano-plates/carbon nano-tubes composite processed through accumulative roll bonding. Mater Sci Eng A 807:140877
22. Sabbaghianrad S, Kawasaki M, Langdon TG (2012) Microstructural evolution and the mechanical properties of an aluminum alloy processed by high-pressure torsion. J Mater Sci 47(22):7789–7795. https://doi.org/10.1007/s10853-012-6524-x
23. Lee SH, Saito Y, Sakai T, Utsunomiya H (2002) Microstructures and mechanical properties of 6061 aluminum alloy processed by accumulative roll-bonding. Mater Sci Eng A 325(1–2):228–235. https://doi.org/10.1016/S0921-5093(01)01416-2
24. Hirosawa S, Hamaoka T, Horita Z, Lee S, Matsuda K, Terada D (2012) Methods for designing concurrently strengthened severely deformed age-hardenable aluminum alloys by ultrafine-grained and precipitation hardenings. Metall Mater Trans A Phys Metall Mater Sci 44(8):3921–3933. https://doi.org/10.1007/s11661-013-1730-y
25. Xu C, Horita Z, Langdon TG (2008) The evolution of homogeneity in an aluminum alloy processed using high-pressure torsion. Acta Mater 56(18):5168–5176
26. Hidalgo P, Cepeda-Jiménez CM, Ruano OA, Carreño F (2010) Influence of the processing temperature on the microstructure, texture, and hardness of the 7075 aluminum alloy fabricated by accumulative roll bonding. Metall Mater Trans A Phys Metall Mater Sci 41(3):758–767. https://doi.org/10.1007/s11661-009-0138-1
27. Zhang Y et al (2019) Dynamic precipitation, segregation and strengthening of an Al-Zn-Mg-Cu alloy (AA7075) processed by high-pressure torsion. Acta Mater 162:19–32. https://doi.org/10.1016/j.actamat.2018.09.060
28. Kim WJ, Sa YK, Kim HK, Yoon US (2008) Plastic forming of the equal-channel angular pressing processed 6061 aluminum alloy. Mater Sci Eng A 487(1–2):360–368. https://doi.org/10.1016/j.msea.2007.10.069
29. Chen X et al (2020) Ultrafine-grained Al–Zn–Mg–Cu alloy processed via cross accumulative extrusion bonding and subsequent aging: Microstructure and mechanical properties. J Alloys Compd 846:156306

Chapter 13
A Comprehensive Survey on Friction-Based Processing of AZ Series Magnesium Alloys

S. Dharani Kumar, B. Arulmurugan, N. Muthukumaran, and S. Ramesh Babu

Nomenclature

mm/min	Millimetre/minute
RPM	Rotations per minute
HAZ	Heat-affected zone
BM	Base metal
HCP	Hexagonal closed pack structure
MMC	Metal matrix composite

1 Introduction

Because of the lightweight and desirable specific strength, magnesium (Mg) and its alloys will be extensively used in the automotive and aerospace sectors in future. While aluminium is still the most popular choice for lightweight structural components, magnesium and magnesium alloys are significantly lighter, weighing around 40% less than aluminium and 78% less than steel. Mg, one of the world most popular and available engineering metals, has a lower density than other structural materials like aluminium (2.7 g/cm^3) and steel (7.86 g/cm^3). Increasing the use of Mg alloys has been difficult due to the high cost of these materials. Mg costs up to six times as much as steel and twice as much as aluminium on a mass basis, despite being readily available in seawater (0.13%). Mg alloys are critical in the transportation, aviation,

S. D. Kumar (✉) · B. Arulmurugan · N. Muthukumaran · S. R. Babu
Department of Mechanical Engineering, KPR Institute of Engineering and Technology, Coimbatore, Tamil Nadu 641407, India
e-mail: sdharanikumarmech@gmail.com

and logistics industries because they reduce weight, maximise energy efficiency, and emit fewer pollutants into the environment.

AZ31 alloy is the most widely employed in industries within this context. The exceptional properties of magnesium make it a viable alternative to aluminium and steel in a wide range of applications. For example, AZ31 alloy is an ideal wrought magnesium alloy, used in automobile industry due to its high damping capacity, low density, and high stiffness to weight ratio, high strength at room temperature, strong corrosion resistance, and ease of availability. It is also known as the AZ series of commercial Mg–Al–Zn alloys, and they have an Al percentage of 1–10 wt%, with the Zn content being lower. General application of Mg alloy is shown in Fig. 1.
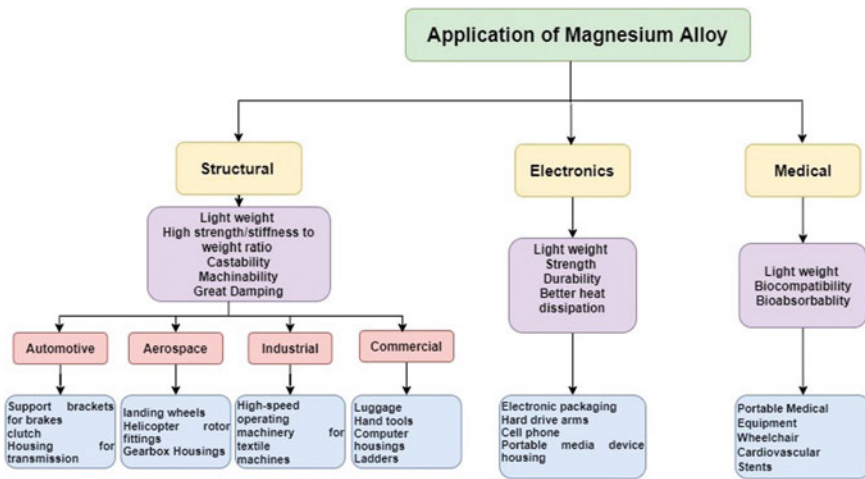

Fig. 1 Applications of Mg alloy

In addition, magnesium (Mg) is prone to galvanic corrosion [1], an electron that flows between two different materials due to its potential difference while a contact in a solution is conductive or corrosive [2]. The higher active metal then turns into anodic and is corroded, and the lower active metal comes to be cathodic and is protected [3]. Galvanic corrosion easily wears out the components made by Mg alloys because magnesium has the lowest standard potential of all the engineering metals [4], so the fabrication industries strive to overcome this major drawback. Processing of Mg alloys using conventional method like welding and casting supplies higher heat input and processing difficulties. This drastically modify the microstructure of Mg alloy plates, causing a wider heat-affected zone and significant distorting effects as well as affects the service life of the component. However, friction-based solid-state processes could be the better alternative which effectively controls the microstructure as well as reduces deformation and residual stress. Producing surface composite by FSP is a novel approach in friction assists methods such as friction stir welding (FSW) and friction welding (FW). FSW and FSP are being used largely for

industrial applications. The present study aims to give comprehensive review of the work reported by several researchers in the field of friction-based processing of AZ series Mg alloys.

2   Friction-Based Processing

FSW and FSP are the major processing method that is adopted for AZ series Mg alloy by many researchers. The year 1991 was a boon to fabrication industries for developed friction stir welding (FSW), by Wayne Thomas at TWI Ltd. [5]. The friction stir welding process is termed green technology welding because of its energy effectiveness and environmentally friendliness. This process aids to overwhelm numerous problems related to traditional joining techniques especially lightweight materials like aluminium and Mg alloys [6] and also dissimilar materials such as titanium alloy joining with magnesium alloy [7]. Friction stir welding (FSW) is one of the solid-state welding techniques [8]. The tool used in FSW is harder than workpiece material. It is used to rotate while plunging the line of joining to be welded [9]. At that point, the non-consumable tool swirled over the welding line creates heat, which causes the material to be welded to melt [10]. The FSW process is depicted in Fig. 2 is a schematic diagram with nomenclature.

Fig. 2   FSW process [11]
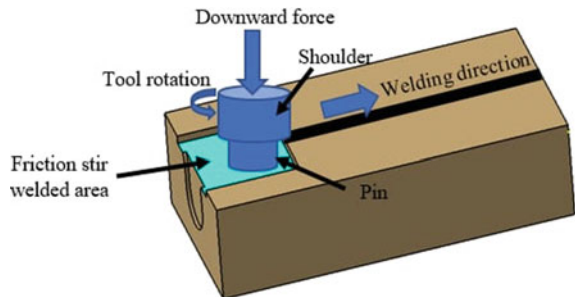
2.1   Influence of Process Parameters in FSW

FSW processes are well established in fabrication industries incorporated with the automobile and aircraft manufacturing sector [12]. The quality of weld and microstructure of the base metal is significant in the assembly of their products. The weld quality has a significant impact on the process parameters of friction stir welding. These characteristics also have an impact on the microstructure of identical or dissimilar base materials. Table 1 shows the FSW process parameters and their

Table 1 Summary of FSW process parameters for Mg alloy and its effects

Process parameter		Material	Influencing properties	References
Rotational speed		AZ31, AZ31D, AZ61, AZ91D, Al 6061, 6063, 6061Al AZ31BMg, Ti	Joint strength such as tensile and compressive microstructure and hardness	[7]
Transverse speed			Hardness and homogeneous texture	[13]
Tool material			Hardness and homogeneous weldment	[14]
Tool shank diameter		AZ31	Tensile strength	[15]
Shoulder diameter				
Shoulder length		AMX602	The microhardness and tensile strength	[16]
Pin profile	Cylindrical–straight	AZ91, AZ61	Microstructure and tensile strength	[17]
	Cylindrical–fluted			
	Truncated	Al and Mg alloys	Homogeneous microstructure and weld density	[18]
	Conical			
Pin diameter		Al and Mg alloys	Tensile strength and weld density	[19]
Pin length				
Tool tilt angle		Al, Cu, and Mg alloys	Tensile strength and microstructure	[20]
Tool offset		Aluminium and copper	Tensile strength and microhardness	[21]
Downward welding force		AA5454-H22 and AZ91	Hardness and intermetallic phase structure	[22]

impact on weld quality and microstructure, as well as other mechanical qualities including tensile strength and hardness. Rotational speed and tool transverse speed are the most influential parameters.

2.2 Effects of Rotational and Transverse Speed

In FSW, the rotational and transverse speeds are critical criteria for obtaining weldment quality. Firouzdor et al. [23] used AA6061 and AZ31B Mg alloys in their experiments. The rotating speed was varied from 1000 to 2200 rpm, while the transverse speed was varied from 38 to 305 mm/min. They noticed that lot of intermetallic

compounds (IMC) in the microstructure; they also found that these two characteristics cause the temperature to be created, which impacts mechanical attributes like hardness and tensile strength. They concluded from their experiments that a slower rotational speed combined with a faster transverse speed produces less temperature but poor weldment, whereas a faster rotational speed combined with a slower transverse speed produces a higher temperature and better weldment. Because higher temperatures impact the microstructure of the BM, they proposed that the ideal parameters for the AZ31B and AA6061 dissimilar joint are average rotating speed and modest transverse speed. The effects of tool rotational and transverse speeds on mechanical properties are shown in Table 2.

Table 2 Parameters influencing Mg FSW joints

Properties	Transverse speed (mm/min)	Rotational speed (RPM)	AZ31B FSW joints	AZ31B BM	References
Ultimate tensile	100	1200	260 MPa	240 MPa	[24, 25]
Hardness	60	800	75–90	50–70 HV	[26]
Yield strength	70	1070	202 MPa	185 MPa	[27]

The non-consumable FSW tool geometry is immensely affecting the weldment area and microstructure of base metal (BM) also heat affected zone (HAZ). Chen et al. [26] in their experimental work they used Mg alloy grade AZ31B and steel plates as work pieces, and process parameters of FSW were rotational speed 25 rad/s (234 rpm) and 1.65 mm/s (99 mm/min) as transverse speed. The cylindrical shape tool was used the shoulder and probe diameter of the tool kept 15 and 5 mm, respectively. The probe length is maintained at1.5 and 1.8 mm. After their experimental work, they reveal the tool geometry such as profile, tool shoulder diameter; shoulder pin diameter and length greatly affect the microstructure of the BM and HAZ. Motalleb-nejad et al. [28], they used three different FSW tool profiles such as straight pin, screw threaded, and taper pin for joining AZ31B FSW joints. The taper pin FSW tool produced fine microstructure and superior mechanical properties compared other two tool profile. During FSW, the taper pin tool has less contact surface with the BM compared with the cylindrical and screwed tool profile. The less contact surface produces low level of material flow and heat input. Hence, it helps to refine the grain structure and enhanced the hardness of the FSW joint.

Many of the fabrication industries are tied up with the automobile and aerospace manufacturing sector. They mainly adopt the FSW process exclusively working with light weight metal like Al and Mg alloys [27]. The defence sector utilizes the benefits of FSW for fabricating lightweight materials such as aluminium and magnesium alloys. Kumar et al. [29] incorporate the FSW technique to fabrication and analyse the ballistic performance of AZ31B Mg alloy. They established the alloy increased the microhardness and increase the ballistic resistance after post weld heat treatment. In the magnesium alloy family, the AZ31 series is most suitable for fabricating

the defence sector products by the FSW process. It is extensively obtainable when compared with other magnesium grades. Some of the researchers suggest that the ballistic behaviour of this particular alloy is significantly improved using the shot peening process to fabricating [30]. Subramani et al. [31] used five different volume fractions of micro-silicon carbide particles in AZ31B Mg FSW joints. The inclusion of nano silicon carbide particles improved the tensile and microhardness properties of the FSW joint. The addition of 12% Si particles in the nugget zone greatly increased the tensile strength (21%) when compared to the FSW joint without Si particles, according to the findings. The insertion of reinforcement particles during FSW increased joint strength, as shown in this work. It is, however, a revolutionary way for increasing Mg FSW joint strength. FSW allows for the inclusion of reinforcing particles, which increases the strength and hardness. Using a recent friction stir surface processing technology, the mechanical characteristics of Mg can be improved. In future, the publication will include a discussion of friction-based surface composites made from AZ series Mg alloys.

3   Fabrication Methods of Mg-based Composites

Metal matrix composites (MMCs) are an important subset of todays engineered materials that have proven to be capable of a variety of structural applications [32]. The inclusion of a proper proportion of secondary phase particles can improve the specific strength of pure metals. Particles improved the wear and corrosion resistance qualities as well [33–35]. Magnesium, aluminium, and titanium are some examples of non-ferrous matrix materials and carbon nanotubes, TiC, Al_2O_3, SiC, NbC, and SiO_2 are some examples of reinforcement particles. The MMCs can be found in a wide variety of applications such as automobile, aerospace, biomedical, and marine applications [36, 37]. Figure 3 shows the common manufacturing methods used for producing MMCs. In recent times, magnesium alloys are found to be good substitution materials for fabricating structures parts in aerospace, automobile, defence, and electronics applications because of less density, superior damping properties, high specific strength, good castability, and machinability [38]. However, in comparison with aluminium, Mg alloy is highly brittle due to its hexagonal closed pack structure (HCP). Mg-based MMCs are a new non-ferrous metals material that can solve the difficulty associated with pure Mg alloys.

There are only a few situations where surface characteristics are critical. However, an incorrect surface property has an impact on the parts performance and life. The characteristics of the base material (BM) were improved via surface composites [39]. Surface composites are the best illustration of such materials since they only contain the scattered reinforcing particles on the surface while leaving the base material at the core intact. As a result, the surface exhibits greater hardness and wear resistance, but the material toughness is unaffected at higher thicknesses [34, 35]. Surface composites are manufactured using a variety of processes, including plasma spraying, laser surface processing, and centrifugal casting [40]. The material phase

Fig. 3 Common
manufacturing method
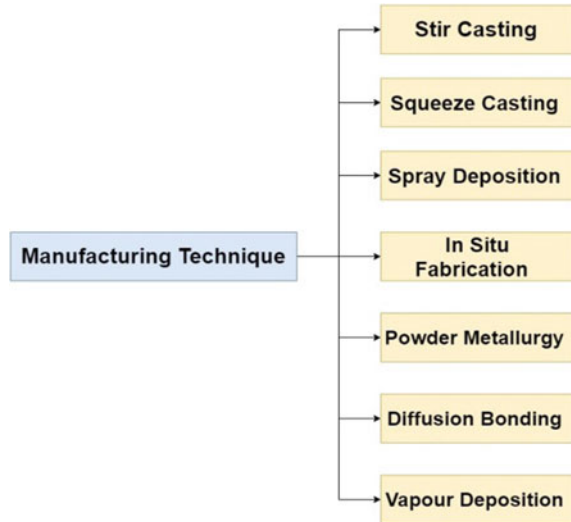
transition from solid to liquid throughout the process [32] is involved in the above-mentioned procedures, and this process may affect the mechanical characteristics of the composite due to interface response between matrix and reinforcement [39].

3.1   Friction Stir Processing (FSP)

FSP is the most promising approach for changing the surface microstructure of Mg alloys [41]. Insert a spinning tool with a pin at the end and plunge along a thickness direction with a suitable axial load to customise the surface of the Mg alloy. In the stir zone, the revolving tool creates friction heat and strong plastic deformation. As a result, dynamic recrystallization occurs in the stir zone (SZ) [42], resulting in fine microstructure [42]. To make surface composites, the reinforcing particles can be incorporated and disseminated in the top surface of the metal during FSP. Fine grain size at the top surface can be achieved in conjunction with reinforcing particles, which is another advantage of FSP. Figure 4 shows how a fine groove or holes are made on the metal top surface and the reinforcing particles are packed before FSP.

However, as illustrated in Fig. 4, certain ways for introducing reinforcement particles into the matrix material during FSP have been discovered. Reinforcement particles are delivered in situ through a groove or hole in the tool. Direct friction stir processing [43] is a technique that uses a pinless FSP tool to create a surface composite. When comparing the different approaches, hole filling consumes more reinforcement particles than groove filling [32]. The reinforcement particles are disseminated on the workpiece surface throughout the SZ area during FSP, resulting in MMC. The size of the nano reinforcement particles and the dimensions of the
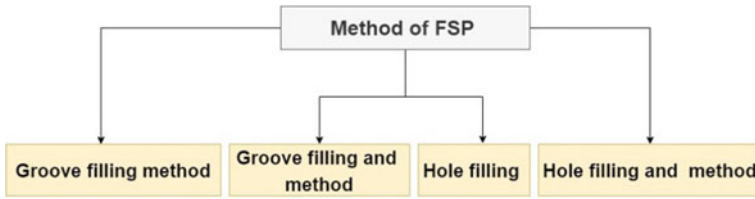
Fig. 4 Methods of FSP

groove or hole determine the volume of reinforcement particles within the matrix surface. The material flow mechanism and deformation during FSP are quite similar to the forging and extrusion processes [44, 45]. The quality of FSP surface composites is determined by machine factors (tool rotational speed, transverse speed, and axial load), tool design variables (tool geometry, tool pin, and shoulder size), and material qualities (mechanical and thermal properties).

FSP without reinforcement results in a significant transform the microstructure of the Mg alloy in and around the SZ region. This results in extreme changes in the mechanical and corrosion properties. These sections try to investigate the microstructure evolvement and the grain refinement around the SZ region during FSP. Lan et al. [46] demonstrated the effect of tool rotational speed on FSP AZ31 alloy. The fine and homogenous grains were achieved in the SZ for FSP specimens with the tool rotational speed range from 1300 to 1700 rpm. FSP enhanced the ductility and damping capacity of the AZ31 alloy. Liu et al. [47] fabricated the single and multi-pass FSP AZ3. After FSP, they compared the microhardness and corrosion properties of FSP AZ31 alloy. It is found from this literature that subsequent FSP passes reduced the grain size and enhanced the hardness compared with the single-pass FSP. Moreover, multi-pass FSP also improved the corrosion resistance of Mg alloy. The corroded area of multi-pass FSP was smaller than the single-pass FSP and base material (BM). Ma et al. [48] grain refinement and break up of reinforcement particles can be obtained simultaneously by the FSP. Similar studies have been found in AZ61 alloy, Luo et al. [49] compared the mechanical properties of single and double pass FSP AZ61 alloys. The elongation of double pass FSP AZ61 alloy was 25% and 75% higher than the single-pass FSP and BM. The homogeneous microstructure and texture evolution in the FSP region is the primary reason for the improvement in ductility. Wang et al. [50] noticed that FSP process significantly enhanced the mechanical properties of the cast AZ31 alloy. The large breakup and dissolution of the eutectic (β-$Mg_{17}Al_{12}$) phase into the Mg and the grain refinement was the major reason for the improvement of mechanical properties. From the work of Sheng et al. [51] found that four passes of FSP significantly reduced the grain size of AZ61 alloy. The grain size of the FSP processed AZ61 alloy was 90% lower than the BM. FSP process also modifies the microstructure and enhance the properties of cast and thin sheets of Mg alloy. Hassani et al. [52] understand the metallurgical and corrosion behaviour of FSP processed cast AZ91C Mg alloy. The broken and dissolution of coarse dendrites were observed after FSP. The FSP enhanced the corrosion resistance

properties because of two main reasons: First, the grain refinement helps to enhance repassivation kinetics and leads to the development of adhesive and constant passive layer. Second, the removal of segregations and casting defects helps to reduce the stress corrosion cracking. Darras et al. [53] studied the effect of FSP on the thin sheets of AZ31B-H24 alloy. The homogenous and fine grain size has been obtained in the SZ region of FSP thin sheets. It improved the formability and ductility of the Mg alloy at higher temperatures and enhances the superplastic behaviour. FSP without reinforcement is often preferred to refine the grain size and improve the mechanical and corrosion properties. FSP with reinforcement particles of AZ Mg alloys has been reviewed later in this article.

The AZ31 alloy is the most often utilised Mg alloy in the AZ series for FSP surface composites. FSP was utilised by Azizieh et al. [54] to make an AZ31/Al_2O_3 surface nanocomposite. Surface composites made with a non-threaded tool produce cavities and microvoids, according to the authors. At higher tool rotating speeds, the Al_2O_3 particles do not effectively delay grain boundary and grain growth motion. Authors observed that choosing the right tool rotational speed increased particle distribution and refined the grain size of matrix material. Similarly, Lan et al. [46] found that increasing the rotational speed of the FSP tool leads in big grain size. FSP produced a surface composite of AZ31 alloy using multi walled carbon nanotubes (MWCNTs) by Morisada et al. [55]. When compared to other processed surface composites, the surface composite that was manufactured at a tool transverse speed of 25 mm/min had a larger dispersion of MWCNTs particles. The transverse feed plays a crucial role in generating Mg-based surface composites via FSP, according to Morisada et al. [55]. Balakrishnan et al. [56] used FSP to create AZ31 matrix surface composites by inserting 6–18 vol.% TiC particles into the surface of an AZ31 alloy. The FSP process was performed with a tool rotational speed of 1200 rpm, a transverse feed of 40 mm/min, and an axial load of 40 mm/min (10 kN). There was no interfacial response between the matrix (AZ31) and the reinforcement (TiC) particles, according to the author. The Mg alloy was properly bound to all of the TiC particles. Few researches have looked into the impact of FSP on the corrosion and wear of the AZ31 alloy. Muralimanokar et al. [57] used FSP to create AZ31 alloy-niobium carbide (NbC) surface composite. The microhardness of the AZ31 alloy was improved by the fine distribution of NbC with fine grains. Authors also briefed about how surface composites wear and corrode. The surface composite had a 15.6% lower wear rate than the BM. The created surface composite, on the other hand, had a higher corrosion rate than the BM. Dinaharan et al. [58] used two stir casting and FSP procedures to make the AZ31 composites. The FSP composite has better fly ash (FA) particle dispersion and fine grains than other composites. They also noticed that the FSP composite has a higher wear resistance than the stir cast composite. Higher wear resistance was mostly due to an increase in hardness.

Faraji et al. [59] investigated the microstructure and mechanical properties of AZ91/Al_2O_3 surface composites using FSP process settings. The surface composite generated with the square pin tool at 900 rpm tool rotational speed and 80 mm/min transverse feed created fine and homogenous grain structure. It is obvious from the study of Faraji et al. [59] that the grain size and particle distribution during FSP are

highly dependent on the process parameters. The transverse feed has a big impact on how the reinforcement particles are distributed in the matrix. To make the AZ91/SiC composite, Asadi et al. [27] used the surface composite processing technique (FSP). Gain size refinement was obtained from 150 m to 600 nm, according to the authors. The nano-grain structure was obtained with the use of nanoSiC particles for reinforcement. It was noticed that increasing the tool rotational speed produces more heat, which induces grain formation and lowers the surface hardness. Increased transverse feed, on the other hand, results in smaller grain size and higher hardness. When compared to the AZ91 with SiC reinforcement particles, the surface composite had a 45% higher hardness. By changing the tool rotational orientation, an advanced level of reinforcing homogeneity was achieved. Abbasi et al. [60] investigated the influence of FSP on the mechanical, wear, and corrosion behaviour of AZ91 Mg alloy surface composites. In comparison with the BM, FSP treated specimens containing SiC and Al_2O_3 reinforcement particles improved mechanical, wear, and corrosion characteristics. They also found that FSP specimens processed with SiC reinforcement particle had better mechanical and corrosion properties than FSP specimens processed with Al_2O_3 reinforcement particle. The sort of particle, on the other hand, had no effect on the wear qualities. The effect of stainless steel powder as a reinforcement particle for AZ61 surface composite on FSP was examined by Sithole and Madushele [61]. The corrosion resistance of the surface composite was 20% higher than that of the BM. Lee et al. [62] used the FSP technique to create AZ61 surface composites by introducing nano-SiO_2 particles. The FSP process was carried out at an 800 rpm tool rotating speed and a 45 mm/min transverse feed rate. The particles were observed to be clustered in a size range (0.1–3 nm) after FSP, with the extent of clustering varying substantially depending on the number of FSP passes. The SiO_2 reinforcement particles were definitely not converted to crystalline phase during the transmission electron microscope (TEM) analysis. The presence of MgO and Mg_2Si particles in the AZ61 matrix is another interesting finding from the TEM tests. In the FSP processed samples, the high strain rate superplasticity behaviour was found.

3.2 Strengthening Mechanisms

Strengthening mechanisms active in the preparation of friction-based Mg composites are related to those in large metal matrix composites. There are two important strengthening mechanisms in particle reinforced friction-based welding and composite materials. Orowan and sub-grain boundary strengthening are two important mechanisms that are critical for improving mechanical properties. The mechanisms that work in FSP surface composites are similar to those that work in bulk metal matrix composites [39]. Orowan strengthening, work hardening, variation in coefficient of thermal expansion (CTC) between matrix and reinforcement particles, and sub-grain boundary strengthening are the four main strengthening mechanisms in metal matrix composites. The dispersed particles and grain boundary strengthening was the major reason for improvement in hardness of FSP processed AZ31 surface

composites [52]. The microhardness was higher after FSP of cast AZ31 alloy due to solid solution strengthening and grain size reduction [49]. Orowan strengthening mechanism helps to increase the surface hardness properties of Mg surface composites [28]. Figure 5 illustrates the improvement in microhardness of the AZ Mg alloy surface composites processed via FSP [43–61]. It was found that FSP without reinforcement also enhanced the microhardness properties. However, multi-pass FSP showed superior hardness value compared to the single-pass FSP. The subsequent passes of FSP significantly reduce the grain size and enhanced the microhardness value compared with the single-pass FSP [55]. From the microhardness results of different FSP studies, it was observed that addition of reinforcement particles (NbC, Al_2O_3, SiC, and fly ash) in the surface of the Mg matrix via FSP increased the hardness value. However, another important observation was noticed that nano surface composite (SiC and MWNT) via FSP significantly enhanced the microhardness of Mg matrix. The dispersion strengthening mechanism and grain size reduction are the reason for higher hardness in the surface composites [29]. Jiang et al. [63] found that addition of nano-SiO_2 reinforcement particles by FSP of AZ31 alloy refined the grain size less than 1 μm and enhanced hardness (50%) as compared with BM. The dispersed particles and grain boundary strengthening was the major reason for the improvement in the hardness of FSP processed AZ31 surface composites [52]. The microhardness was higher after the FSP of cast AZ31 alloy due to solid solution strengthening and grain size reduction [49]. Orowan strengthening mechanism helps to increase the surface hardness properties of Mg surface composites [28]. Figure 5 illustrates the improvement in microhardness of the AZ Mg alloy surface composites processed via FSP [43–61]. It was found that FSP without reinforcement also enhanced the microhardness properties. However, multi-pass FSP showed a superior hardness value compared to the single-pass FSP. The subsequent passes of FSP significantly reduce the grain size and enhance the microhardness value compared with the single-pass FSP [55].

From the microhardness results of different FSP studies, it was observed that the addition of reinforcement particles (NbC, Al_2O_3, SiC, and fly ash) in the surface of the Mg matrix via FSP increased the hardness value. However, another important observation was noticed that nano surface composite (SiC and MWNT) via FSP significantly enhanced the microhardness of Mg matrix. The dispersion strengthening mechanism and grain size reduction are the reason for higher hardness in the surface composites [57]. Jiang et al. [63] found that the addition of nano-SiO_2 reinforcement particles by FSP of AZ31 alloy refined the grain size less than 1 μm and enhanced hardness (50%) as compared with BM. Table 3 lists the improvement happened in fabricating AZ series Mg-based surface composite by FSP.

Processing of Mg alloys using conventional method like welding and casting supplies higher heat input and processing difficulties [64–68]. This increases the feasibility of FSW to join the cast and rolled plates of AZ series Mg alloy, AZ Mg alloy with other materials such as aluminium and copper and high melting point alloys like steel and titanium is currently being comprehensively researched. Similarly, FSP has also shown good results in different studies carried out by fabricating numerous surface composites of different non-ferrous materials [1].
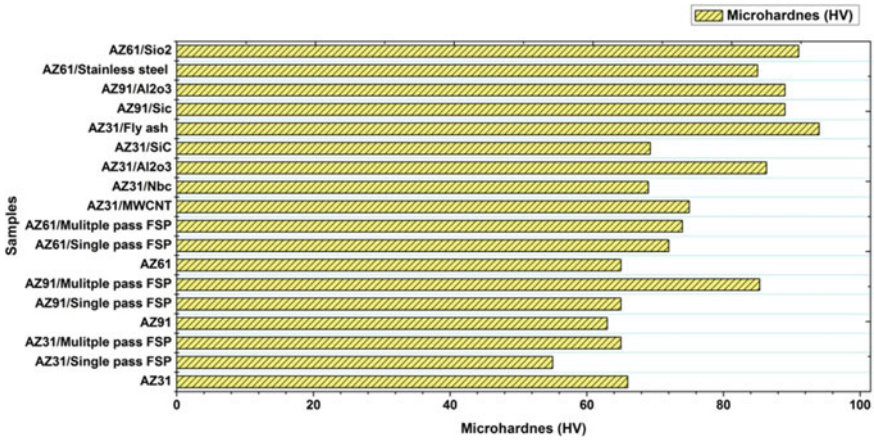
Fig. 5 Microhardness of BM and AZ series Mg alloy surface composites fabricated via FSP

Table 3 AZ series Mg-based FSP surface composite

Base material	Reinforcement particles	Maximum number of FSP passes	Grain refinement	Observation	References
AZ31	TiC	1	Not studied	FSP surface composite of AZ31/TiC fabricated without any defects TiC particles were correctly bonded to the Mg matrix	Balakrishnan et al. [56]
	Fly ash	1	4 μm	Homogenous distribution of fly ash particles The hardness and wear properties of FSP composite were superior compare to the stir casting composite	Dinaharan etal. [58]
	Al_2O_3nano particles	4	0.35 μm	Cavities and micro-void were noticed in non-threaded The grain size refinement was more effective in nano composite compare to the micro-composite	Azizieh et al. [54]

(continued)

Table 3 (continued)

Base material	Reinforcement particles	Maximum number of FSP passes	Grain refinement	Observation	References
	MWCNT	1	500 nm	Defect free nano surface composite was obtained using tool rotational speed (1500 rpm) and welding speed (25 mm/min) Hardness of the surface composite was increased up to 78 HV that was higher than the base material (51 HV)	Morisada et al. [55]
	NbC	1	Not studied	The fine distribution of NbC particles was obtained at the tool rotational speed of 1200 rpm and traverse speed of 45 mm/min Hardness, wear, and corrosion behaviour of the surface composite were higher than the BM	Muralimanokar et al. [57]
AZ161	Stainless steel	1	Not studied	The hardness of the AZ61 Mg alloy-based surface composite enhanced by 12.01% than that of the BM Corrosion resistance of AZ61 Mg alloy-based surface composite enhanced by 20% than that of the BM	Sithole and Madushele [61]
	Nano-SiO$_2$	4	0.8 µm	Super plasticity was achieved 400% higher than the BM Nano-SiO$_2$ improved the tensile strength	Lee et al. [62]

(continued)

Table 3 (continued)

Base material	Reinforcement particles	Maximum number of FSP passes	Grain refinement	Observation	References
AZ91	SiC	1	0.07 µm	Higher tool rotational speed and traverse speed reduced the grain size The hardness in the SZ increased from 63 to 96 HV	Asadi et al. [60]
	Al_2O_3 nano particles	1	6 µm	Defect free surface composite was produced using square tool with tool rotational speed (900 rpm) and traverse speed (80 mm/min). The grain refinement was mainly depending upon FSP parameters	Faraji et al. [59]

4 Summary and Conclusion

The major aspects of friction-based processing Mg alloys were covered in this work. The following conclusions were presented as follows.

I.   It has been understood that FSP is the most promising method for producing Mg-based surface composites and also helps to modify large surface areas by multiple passes. The proper selection of tool profile, process parameters, and reinforcement particles makes better Mg FSW joints and tailored FSP Mg surface composites.

II. Poor control over the number of reinforcement particles that can be on the matrix surface is a drawback in the FSP. The volume of distribution of the reinforcement particles along the thickness direction is also not uniform.

III. Certain areas such as welding of composite materials and dissimilar Mg alloys, material flow, and temperature distribution during FSW are needed to be further analysed.

IV. The optimization techniques and modern finite element analysis (FEA) tools help to find the optimum process parameters, temperature distribution, and flow of the reinforcement particles during friction base processing which is inadequate in the literature.

V.   Developing multi-physics FEA macro- and micromodels is one of the approaches that could be used to predict the temperature distribution and microstructure changes.

VI.   The majority of the work has been carried out using AZ31B Mg alloys. It is expected that different series of Mg alloys also will be processed by friction-based processing in future for an extensive range of applications.

VII. Overall, it can be brief that FSW and FSP have enormous industrial applications in producing AZ series Mg alloys for lightweight applications that required high hardness, wear, and corrosion-resistant surface.

References

1. Janiec-AnwarJ TGE, Zhou XR, Curioni M, Turski M, Wilks T (2013) Galvanic corrosion between magnesium alloys and steel. Mat Sci Forum 765:648–652
2. Song G, StJohn DH (2005) Corrosion of magnesium alloys in commercial engine coolants. Mater Corros 56:15–23
3. Golabczak M (2011) Estimation of carbon coatings manufactured on magnesium alloys. In: Special issues on magnesium alloys, 41
4. Luo AA (2013) Magnesium casting technology for structural applications. J Magn Alloys 1:2–22
5. Mironov S, Inagaki K, Sato YS, Kokawa H (2015) Effect of welding temperature on microstructure of friction-stir welded aluminum alloy 1050. Met Mat Trans A 46:783–790
6. Shigematsu I, Kwon YJ, Saito N (2009) Dissimilar friction stir welding for tailor-welded blanks of aluminum and magnesium alloys. Mat Trans:0812150622
7. Aonuma M, Nakata K (2009) Effect of alloying elements on interface microstructure of Mg–Al–Zn magnesium alloys and titanium joint by friction stirs welding. Mater Sci Eng, B 161(1–3):46–49
8. Venkateswaran P, Reynolds AP (2012) Factors affecting the properties of friction stir welds between aluminum and magnesium alloys. Mat Sci Eng A 545:26–37
9. Luo C, Li X, Song D, Zhou N, Li Y, Qi W (2016) Microstructure evolution and mechanical properties of friction stir welded dissimilar joints of Mg–Zn–Gd and Mg–Al–Zn alloys. Mat Sci Eng A 664:103–113
10. Mironov S, Onuma T, Sato YS, Kokawa H (2015) Microstructure evolutions during friction stir welding of AZ31 magnesium alloy. Acta Mater 100:301–312
11. Singh K, Singh G, Singh H (2018) Review on friction stir welding of magnesium alloys. J Magn Alloys 6(4):399–416
12. Luo AA (2013) Magnesium casting technology for structural applications. J Magn Alloy 1(1):2–22
13. Liu Z, Ji S, Meng X (2018) Improving joint formation and tensile properties of dissimilar friction stir welding of aluminum and magnesium alloys by solving the pin adhesion problem. J Mater Eng Perform 27(3):1404–1413
14. Khodir SA, Shibayanagi T (2007) Dissimilar friction stir welded joints between 2024–T3 aluminum alloy and AZ31 magnesium alloy. Mater Trans 48(9):2501–2505
15. Bruni C, Buffa G, Fratini L, Simoncini M (2010) Friction stir welding of magnesium alloys under different process parameters. Mater Sci Forum 638:3954–3959
16. Chen J, Fujii H, Sun Y, Morisada Y, Kondoh K, Hashimoto K (2012) Effect of grain size on the microstructure and mechanical properties of friction stir welded non-combustive magnesium alloys. Mater Sci Eng, A 549:176–184
17. Singh K, Singh G, Singh H (2019) Microstructure and mechanical behaviour of friction-stir-welded magnesium alloys: as-welded and post weld heat treated. Mater Today Commun 20
18. Forcellese A, Martarelli M, Simoncini M (2016) Effect of process parameters on vertical forces and temperatures developed during friction stir welding of magnesium alloys. Int J Adv Manuf Technol 85(1):595–604

19. Zhang YN, Cao X, Larose S, Wanjara P (2012) Review of tools for friction stirs welding and processing. Can Metall Q 51(3):250–261
20. Dialami N, Cervera M, Chiumenti M (2019) Effect of the tool tilt angle on the heat generation and the material flow in friction stir welding. Metals 9(1):28
21. Sahu PK, Pal S, Pal SK, Jain R (2016) Influence of plate position, tool offset and tool rotational speed on mechanical properties and microstructures of dissimilar Al/Cu friction stir welding joints. J Mater Process Technol 235:55–67
22. Klag O, Gröbner J, Wagner G, Schmid-Fetzer R, Eifler D (2014) Microstructural and thermo-dynamic investigations on friction stir welded Mg/Al-joints. Int J Mater Res 105(2):145–155
23. Firouzdor V, Kou S (2010) Al-to-Mg friction stir welding: effect of material position, travel speed, and rotation speed. Metall Mater Trans A 41(11):2914–2935
24. Thakur A, Sharma V, Bhadauria SS (2021) Effect of tool tilt angle on weld joint strength and microstructural characterization of double-sided friction stir welding of AZ31B magnesium alloy. CIRP J Manuf Sci Technol 35:132–145
25. Zhou M, Morisada Y, Fujii H, Ishikawa T (2018) Mechanical properties optimization of AZX612-Mg alloy joint by double-sided friction stir welding. J Mater Process Technol 254:91–99
26. Chen S, Wang L, Jiang X, Yuan T, Jiang W, Liu Y (2021) Microstructure and mechanical properties of AZ31B Mg alloy fabricated by friction stir welding with pulse current. J Manuf Process 71:317–328
27. Mehta KP, Carlone P, Astarita A, Scherillo F, Rubino F, Vora P (2019) Conventional and cooling assisted friction stir welding of AA6061 and AZ31B alloys. Mater Sci Eng, A 759:252–261
28. Motalleb-Nejad P, Saeid T, Heidarzadeh A, Darzi K, Ashjari M (2014) Effect of tool pin profile on microstructure and mechanical properties of friction stir welded AZ31B magnesium alloy. Mater Des 59:221–226
29. Kumar DS, Sundaram SK (2020) Experimental ballistic performance determination of friction stir welded magnesium (AZ31B) targets. Mech Based Des Struct Mach
30. Kumar SD, Magarajan U, Kumar SS, Balasubramani S (2021) Effect of shot peening on mechanical properties and ballistic resistance of magnesium alloy AZ31B. Met Sci Heat Treat 63(3):197–202
31. Subramani V, Jayavel B, Sengottuvelu R, Lazar PJL (2019) Assessment of microstructure and mechanical properties of stir zone seam of friction stir welded magnesium AZ31B through nano-SiC. Materials 12(7):1044
32. Sunil BR, Reddy GPK, Patle H, Dumpala R (2016) Magnesium based surface metal matrix composites by friction stir processing. J Magn Alloys 4(1):52–61
33. Radhika K, Lakshminarayanan AK (2020) An insight into the stress corrosion cracking resistance of friction stir processed and micro arc oxidation coated ZE41 grade magnesium alloy. Proc Inst Mech Eng, Part C: J Mech Eng Sci:0954406220920315
34. Singla S, Kang AS, Sidhu TS (2020) Development and characterization of WE43/nano-TiC surface composite by friction stir processing technique. Meas Control 53(3–4):730–741
35. Joshi S, Singh RC, Chaudhary R (2021) Effect of friction stir processing (FSP) on the wear behavior of cast AS21A magnesium alloy. Surf Rev Lett 28(01):2050037
36. Kainer KU (2006) Basics of metal matrix composites. In: Metal matrix composites, pp 1–54
37. Hort N, Kainer KU (2006) Powder metallurgically manufactured metal matrix composites. In: Metal matrix composites: custom-made materials for automotive and aerospace engineering, pp 243–274
38. Fridrich HE, Mordike BL (2006) Magnesium technology
39. Kumar SD, Kumar SS (2021) Effect of heat treatment conditions on ballistic behaviour of various zones of friction stir welded magnesium alloy joints. Trans Nonferrous Metals Soc China 31(1):156–166
40. Sharma V, Prakash U, Kumar BM (2015) Surface composites by friction stir processing: a review. J Mater Process Technol 224:117–134
41. Ma J, Wang G, Li Y, Qin C, Ren F (2019) Electrochemical investigations on AZ series magnesium alloys as anode materials in a sodium chloride solution. J Mater Eng Perform 28(5):2873–2880

42. Peng J, Zhang Z, Liu Z, Li Y, Guo P, Zhou W et al (2018) The effects of texture and grain size on improving the mechanical properties of Mg-Al-Zn alloys by friction stir processing. Sci Rep 8(1):2–10
43. Shamanian M, Mostaan H, Safari M, Dezfooli MS (2017) Friction-stir processing of Al–12% Si alloys: grain refinement, numerical simulation, microstructure evolution, dry sliding wear performance and hardness measurement. Metall Res Technol 114(2):213
44. Govindaraju M, Prasad KR, Chakkingal U, Balasubramanian K (2012) Effect of distance between passes in friction stir processing of magnesium alloy. Adv Mater Res 585:397–401
45. Huang Y, Wang T, Guo W, Wan L, Lv S (2014) Microstructure and surface mechanical property of AZ31 Mg/SiCp surface composite fabricated by direct friction stir processing. Mater Des 59:274–278
46. Liu D, Shen M, Tang Y, Hu Y, Zhao L (2019) Evaluation of corrosion resistance of multipass friction stir processed AZ31 magnesium alloy. Mater Corros 70(9):1553–1560
47. Lan FY, Chen HM, Guo WP, Zhang J, Jin YX (2017) Effects of friction stir processing on mechanical properties and damping capacities of AZ31 magnesium alloys. IOP Conf Ser Mater Sci Eng 230(1)
48. Ma ZY, Xiao BL, Yang J, Feng AH (2010) Friction stir processing: a novel approach for microstructure refinement of magnesium alloys. Mater Sci Forum 638–642:1191–1196
49. Luo XC, Zhang DT, Zhang WW, Qiu C, Chen DL (2018) Tensile properties of AZ61 magnesium alloy produced by multi-pass friction stir processing: effect of sample orientation. Mater Sci Eng A 725:398–405
50. Wang W, Wang K, Guo Q, Wu N (2012) Effect of friction stir processing on microstructure and mechanical properties of cast AZ31 magnesium alloy. XiyouJinshuCailiao Yu Gongcheng/Rare Met Mater Eng 41(9):1522–1526
51. Sheng SX, Guo YL, Liu SF, Wu SL (2014) Superplasticity Mg alloy fabricated by friction stir processing. Adv Mater Res 941–944:93–96
52. Hassani B, Vallant R, Karimzadeh F, Enayati MH, Sabooni S, Pradeep K (2019) Effect of friction stir processing on corrosion behavior of cast AZ91C magnesium alloy. Surf Rev Lett 26(6)
53. Darras BM, Khraisheh MK, Abu-Farha FK, Omar MA (2007) Friction stir processing of commercial AZ31 magnesium alloy. J Mater Process Technol 191(1–3):77–81
54. Azizieh M, Kokabi AH, Abachi P (2011) Effect of rotational speed and probe profile on microstructure and hardness of AZ31/Al$_2$O$_3$ nanocomposites fabricated by friction stir processing. Mater Des 32(4):2034–2041
55. Morisada Y, Fujii H, Nagaoka T, Fukusumi M (2006) MWCNTs/AZ31 surface composites fabricated by friction stir processing. Mater Sci Eng A 419(1–2):344–348
56. Balakrishnan M, Dinaharan I, Palanivel R, Sivaprakasam R (2015) Synthesize of AZ31/TiC magnesium matrix composites using friction stir processing. J Magnes Alloy 3(1):76–78
57. Muralimanokar M, Vaira VR, Padmanaban R, Suganya PG (2020) Characterization of AZ31-NbC surface composite fabricated by friction stir processing. KorozeaOchr Mater 64(1):29–37
58. Dinaharan I, Vettivel SC, Balakrishnan M, Akinlabi ET (2019) Influence of processing route on microstructure and wear resistance of fly ash reinforced AZ31 magnesium matrix composites. J Magnes Alloy 7(1):155–165
59. Faraji G, Dastani O, AkbariMousavi SAA (2011) Microstructures and mechanical properties of Al$_2$O$_3$/AZ91 surface nanocomposite layer produced by friction stir processing. Proc Inst Mech Eng Part B J Eng Manuf 225(8):1331–1345
60. Asadi P, Givi MKB, Rastgoo A, Akbari M, Zakeri V, Rasouli S (2012) Predicting the grain size and hardness of AZ91/SiC nanocomposite by artificial neural networks. Int J Adv Manuf Technol 63(9–12):1095–1107
61. Sithole LM, Madushele N (2019) Surface treatment of magnesium AZ61 alloy with stainless steel powder by friction stir processing. Procedia Manuf 35:1047–1053
62. Lee CJ, Huang JC, Hsieh PJ (2006) Mg based nano-composites fabricated by friction stir processing. Scr Mater 54(7):1415–1420
63. Jiang Y, Yang X, Miura H, Sakai T (2013) Rev Adv Mater Sci 33:29–32

64. Arulmurugan B, Balaji D, Rajkumar S et al (2021) Influence of filler wire and welding process to mitigate the micro segregation of Alloy C-2000 using continuous and pulsed current gas tungsten arc welding techniques. J Materi Eng Perform 30:6050–6067
65. Arulmurugan B, Kumar MS, Kannan T, Karuppiah S, Kumaraguru N, Ponsundar E, Manikandan M (2021) Investigation on mechanical and microstructure characteristics of nickel based C-2000 super alloy using laser beam welding. Mater Today: Proc 43:3044–3049
66. Manikandan M, Arivarasu M, Arivazhagan N, Puneeth T, Sivakumar N, Murugan BA, Sivalingam S (2016, Sept) High temperature corrosion studies on pulsed current gas tungsten arc welded alloy C-276 in molten salt environment. IOP Conf Ser: Mater Sci Eng 149(1):012020
67. Kannan T, Arulmurugan B, Kathiresan G, Amarnath V, Akilesh G, Arhath S, Dhanajjayan R (2021, April) Friction stir welding of dissimilar materials (AA2024 & AA6063) and investigation of mechanical properties. IOP Conf Ser: Mater Sci Eng 1145(1):012029
68. Shah PH, Badheka VJ (2019) Friction stir welding of aluminium alloys: an overview of experimental findings–process, variables, development and applications. Proc Inst Mech Eng, Part L: J Mater: Des Appl 233(6):1191–1226

Chapter 14
An Investigation on Friction Stir Processing of Aluminum Alloy-Boron Carbide Surface Composite

Sampath Boopathi

1 Introduction

Friction stir processing (FSP) is a solid-state external surface hardening method using thermo-mechanical principles to change the microstructure of the surfaces of metals and non-metals. The working principles of FSP are similar to the friction stir welding process, wherein non-consumable tools have been employed [1, 2]. The base material is subjected to plastic deformation by localized frictional heat beet wen the tool and work material [3, 4]. The ceramic particles in the groove/slot of base material have uniformed been dispersed on the materials by rotating the FSP tool. Finally, the particles reinforced/coated surface composite components have been made by the friction stir processing method [5]. The research activities on FSP have been performed using some significant factors: revolving speed, travel speed and the tilting angle of the tool, axial load, depth of slot, number of processes, grain size, and volume /weight percentage of mixed particles. The rotational speed and grain size are the most significant factors in the aluminum-based surface modification method [6]. The wear rate and micro-hardness values have been minimized by enhancing tool revolving speed. TiC particles were imposed on the Al plate by the FSP method to improve the wear resistance and micro-hardness values. A356-cast aluminum alloy surface defects have been eliminated by adding ceramic particles using the FSP method due to improve fatigue strength [7]. The depth of slots should be optimized to improve the uniform distributions of particles on the base materials during FSP [8]. The grain structure of the modified FSP surface has been improved by changing tool pin shape like thread/taper/grooved structure [9]. While increasing the traveling speed of a tool, the surface defects have been increased by inadequate material flows. Thus, low

S. Boopathi (✉)

Department of Mechanical Engineering, Muthayammal Engineering College (Autonomous), Rasipuram, Namakkal (District) 637408, India

e-mail: boopasangee@gmail.com

URL: https://www.webofscience.com/wos/author/record/363875

traveling with the maximum revolving speed of the tool is recommended for making quality FSP [10]. While an increasing number of tool passes, high micro-hardness, uniformly dispersed particles, and defect-free surfaces have been attained [5]. It was found that insufficient heat for melting materials at low rotational speed and high feed rate tool and leads to defects formations on the surface [11]. Surface modification has been improved by increasing speed, complex tool profile, and number passes. The refinements of microstructure, resignification, and homogeneity are called important merits of FSP [12].

While reinforcement of fine nanoparticles on the material surfaces, the grain size distribution rate and micro-hardness have greatly been improved during FSP [13]. It was found that the glass fiber reinforced on the Al alloy metals is investigated to improve the ductile and tensile strength by the FSP method [14]. The carbon nanotubes imposed into the aluminum alloy metal were investigated to enhance the overall mechanical properties and yield strength is improved to 70%. It was found that the micro-hardness and mechanical strength of AL5083 alloy using nanoparticles of cerium oxide have been improved to 120% and 45%, respectively [15]. BN particles imposed on Mg alloy materials have been investigated to improve the ultimate strength using high speed and low tool feed rate. The hybrid particles (AlO_3 + SiC) have been dispersed in Al metal to improve the brittle nature using the FSP method [16]. Very recently, the B_4C particle in Al alloy dispersed by the FSP method has been investigated to improve the micro-hardness and tensile strength using various volume percentage reinforced particles [17]. The influences of B_4C particles on the aluminum alloy had been examined using the Taguchi design of experimentation to improve the wear resistance and microstructure [18]. The influence of mixed magnesium and chromium particles in the joining of the AA5052 alloy matrix had also been analyzed to enhance the corrosion resistance and tensile strength [19].

In this article, B_4C particles are imposed on the Al2014 alloy using the friction stir process. The effect of the volume percentage of B_4C on the tensile strength and wear rate had been investigated.

2   Experimental Method

Al2014 and B_4C powder are considered as matrix and reinforced particles in this study. The pictorial representation of FSP is illustrated in Fig. 1. The dimensions of the Al2014 plate used are $150 \times 50 \times 8$ mm. The size of B_4C powder is used from 1 to 10 μm for reinforcement [18]. The various metal elements and mechanical properties of Al2014-T6 are shown in Tables 1 and 2, respectively. The scanning electron microscopy (SEM) images of AA2014 alloy and B_4C Particle are shown in Fig. 2a, b, respectively.

A slot was formed in the middle of the base plate with dimensions of 150 mm in length and 4 mm in thickness. Three composite specimens with 5, 10, and 15 vol% of B_4C have been prepared for tensile and micro-hardness testing purposes. The width of the groove has been modified to change the volume percentage of B_4C on the top
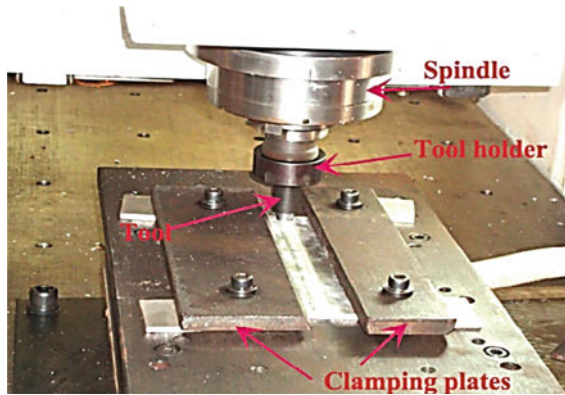
Fig. 1   Friction stir processing of Al2014 using B$_4$C powder

Table 1   Various metal elements of Al2014-T6 alloy

Metal	Al	Cu	Si	Mn	Mg	Fe	Zn	Ti	Ni
Percentage of weight	93.24	4.64	0.668	0.58	0.358	0.223	0.199	0.02	0.019

Table 2   Mechanical properties of Al2014-T6 material

Density (kg/m^3)	Tensile strength (MPa)	Melting point (°C)	Specific heat (J/kg °C)	Vickers hardness (H$_v$)	Thermal conductivity (W/mK)
2800	470	638	880	155	154
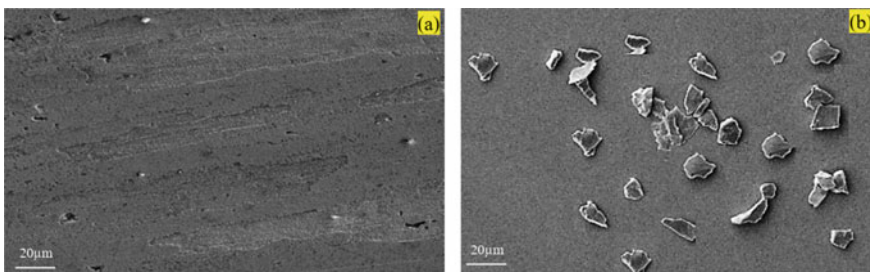
Fig. 2   SEM image of **a** A12014 alloy and **b** B$_4$C powder

surface, which is called FSP. The FSP tool was made with H13 tool steel hardened to 65 HRC. The length of 4, 6 mm pin diameter, and 20 mm shoulder diameter of the tool were used for FSP. The FSP was done in the computer-integrated friction stir welding machine. During FSP, a contact-frictional heat was developed between the revolving tools to the base material. The Al2014 was transformed to a plastic

state, and B_4C particles were reinforced by frictional heat. The tool was uniformed for smooth conduction of the FSP to proper distributions of particles. The tool's revolving speed has played an important role in generating heat and reinforcement of B_4C. Initially, the B_4C powder was packed inside the groove of the alloy plate. The rotating tool was connected over the slot opening and compact reinforcement powder. Experiments were done by 40 N of axial trust, 1200 rpm of tool revolving speed, and 60 mm/min of welding speed. The welding samples with 5% of B_4C (Sample 1), 10% of B_4C (Sample 2), and 15% of B_4C (Sample 3) are shown in Fig. 3.

The SEM view of the 15% B_4C surface composite specimen with EDS analysis is shown in Fig. 4a, b, respectively. The fabricated composites were tested to evaluate tensile, and micro-hardness characteristics. The test specimen cut for the tensile test was machine using a wire-cut thermo-electric process as per the dimensions of ASTM-E8 standard [20–22]. The wear rate has been tested by a pin-on-disk instrument. The parameter used for testing wear characteristics were 30 N of force, 350 rpm of sliding speed, and 1000 m sliding length at room temperature. ASTM G99-05 standard specimen was prepared for wear testing of the composite material. The wear loss was determined by the weight changes in the pin after and before the testing processes. The wear loss principle was applied to compute the wear rate by Eq. (1).
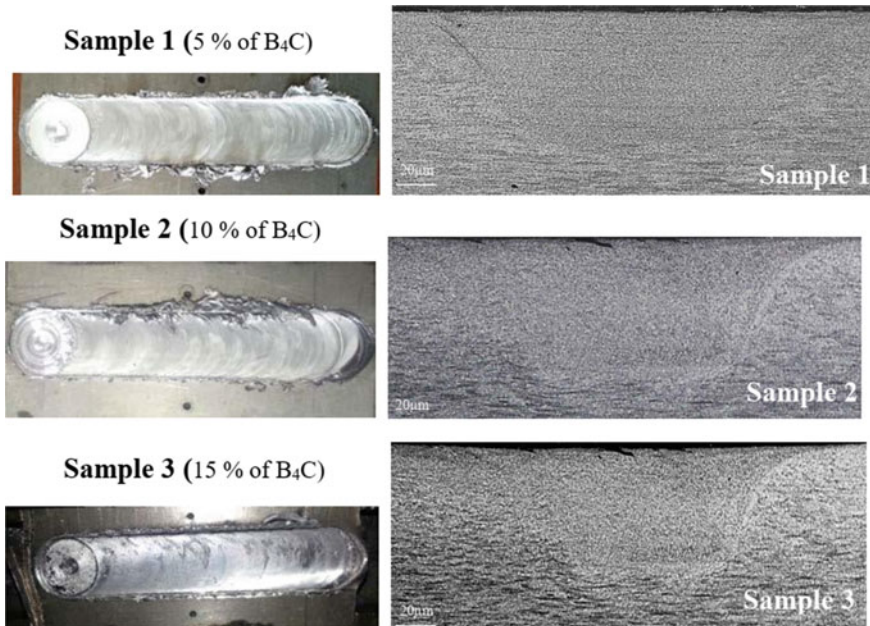

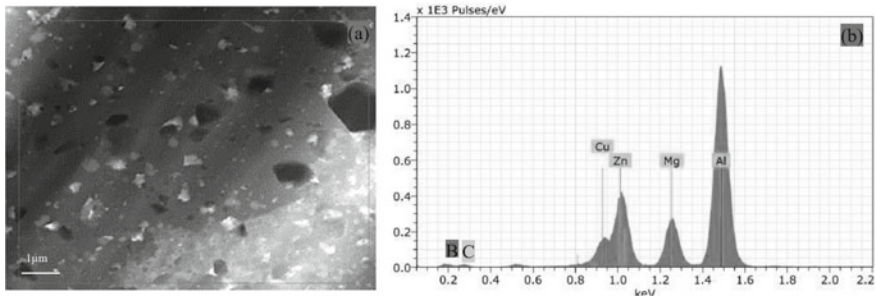**Fig. 3** Surface images of FSP surface composite of three samples

Fig. 4 **a** SEM image and **b** EDS analysis of volume percentage 15% B_4C on Al2014 surface

$$Wear\ rate\ =\ (Initial\ weight\ before\ the\ test - final\ weight\ after\ the\ test)/$$
$$(sliding\ distance\ \times\ force \times\ density\ of\ composite\ )\ mm^3/Nm \quad (1)$$

3 Results and Discussions

The maximum tensile stress of Al2014 base material is 470 MPa. The tensile strength of the fabricated Al2014 surface composite is exposed in Table 3. Effects of B_4C on the tensile strength are exposed in Fig. 5. The tensile strength of base Al2014 is initially very lesser and gradually increased by adding the volume percentage of the B_4C powder reinforcement. The thermal coefficient of Al2014 and B_4C particles produce the density dislocations. The free-moving of dislocations is restricted by dislocated molecules. According to the Orowan mechanism, the homogeneous dispersion of particles in base metal during the tensile test is observed. Some portion of the tensile load was withstood by B_4C particles in the composite. Thus, the tensile strength has been improved by adding B_4C during FSP. During the FSP, the outer surface of base materials was plasticized by the frictional heat using which the B_4C was also reinforced with base materials. The grain structure of the composite was dynamically refined by a rotating tool during FSP.

The fractography views of the fracture surface of tensile test specimens (Sample 1, 2, and 3) were scanned to analyze the causes of failure are illustrated in Fig. 6a–c. The fractured image consists of a cup cone structure which is an indication of

Table 3 Tensile strength of surface composite specimens

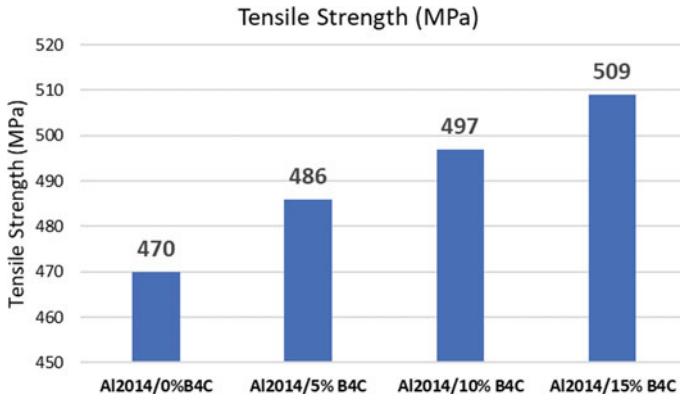| Composite	Sample	Tensile strength (MPa)
Al2014/0%B_4C	Sample 0	470
Al2014/5% B_4C	Sample 1	486
Al2014/10% B_4C	Sample 2	497
Al2014/15% B_4C	Sample 3	509

Fig. 5 Variation of tensile strength of surface composite

the ductility of the developed composite. Upon increase in volume percentage of B_4C, the occurrence of cup cone structure gradually decreases, and a flat fracture zone was observed. The occurrence of a flat fracture zone is the indication of the transition of composite material from ductile to brittle nature. The wear rate of the established composite specimen of FSP is exhibited in Table 4. The wear rate of unreinforced Al2014 matrix material was recorded to be 2.1 mm^3/Nm. The wear rate of composite with 5, 10, and 15 volume percentage of B_4C are observed as 2.7, 2.4, and 2.1 mm^3/Nm, respectively. The addition of B_4C particles increases its wear resistance characteristics as the wear rate was reduced as exposed in Fig. 7. The wear rate of material is diminished by adding hardness. As discussed earlier, the addition of hard B_4C particles in the Al2014 matrix limits grain growth by dynamic recrystallization. The restriction of modified grain results in the formation of finer grain structure in the composite. The microstructure of worn-out surfaces of three samples is illustrated in Fig. 8a–c. The hardness of the composite has also been improved by nanoparticles in the B_4C powder. It is well-known fact that material with smaller grains possesses a higher hardness. During the sliding of composite and steel, the softer material around the B_4C particle plastically deformed and detached from the surface as debris. This made the B_4C particle protrude out of the surface and made direct contact with the rotating counter body. The effective contact area between composite and counter body gets reduced and results in a lower wear rate.

4 Conclusions

The effects of reinforcement of B_4C in the Al2014 surface composite had been analyzed through the specimens prepared by FSP to investigate the tensile strength and wear rate by varying volume percentages (5, 10, and 15%) of B_4C particles. The quality uniform spreading of reinforcement of B_4C particles on base materials

(a) Al2014 / 5% B₄C (Sample 1)   (b) Al2014 / 10% B₄C (Sample 2)   (c) Al2014 / 15% B₄C (Sample 3)
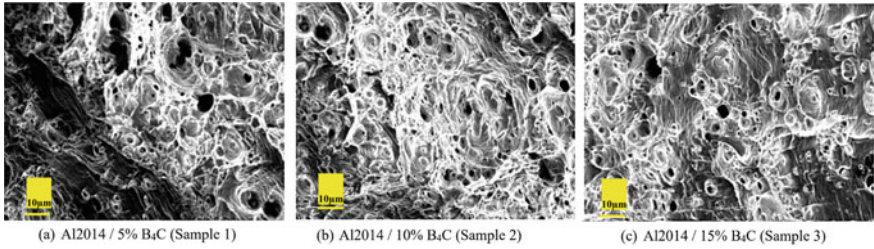
Fig. 6 Fractography views of tensile fractured surface composite materials

Table 4 Wear rate of surface composite material

Surface composite composition	Sample	Wear rate (mm^3/Nm)
Al2014/0% B_4C	Sample 0	2.7
Al2014/5% B_4C	Sample 1	2.4
Al2014/10% B_4C	Sample 2	2.1
Al2014/15% B_4C	Sample 3	1.8
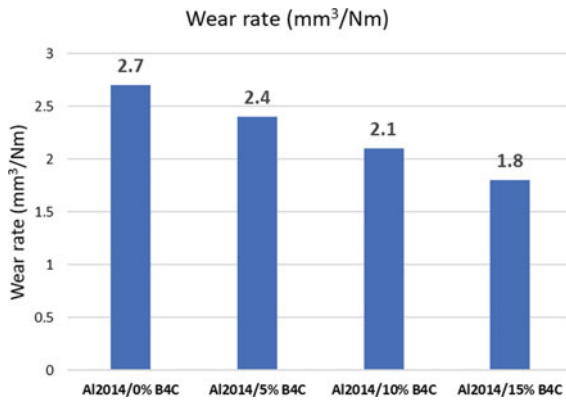
Fig. 7 Variations of wear rate by adding volume % of B_4C

(a) Sample 1   (b) Sample 2   (c) Sample 3
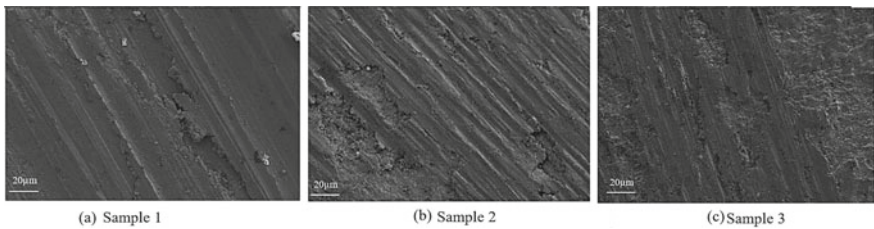
Fig. 8 Microstructure of worn-out surface of three samples

has been attained by FSP. The tensile strength of the composite has been enhanced by adding B_4C particles and optimum tensile strength of 509 MPa was achieved by imposing 15% of the volume of B_4C. The wear rate of the composite was greatly minimized by adding B_4C particles and the minimum wear rate (1.8 mm^3/Nm) was also achieved by 15% of volume percentage of B_4C. The EDS, SEM, and fractography analyses had been performed to illustrate the particle distributions, tensile strength, and worn-out surface behaviors.

References s

1. Sampath B, Haribalaji V (2021) Influences of welding parameters on friction stir welding of aluminum and magnesium: a review. Mater Res Proc 19:222–230. https://doi.org/10.21741/9781644901618-28
2. Haribalaji V, Boopathi S, Mohammed Asif M, Jeyakumar M, Subbiah R, Anton Savio Lewise K (2022) Influences of friction stir tool parameters for joining two similar AZ61A alloy plates. Mater Today: Proc 50:2547–2553. https://doi.org/10.1016/j.matpr.2021.12.074
3. Haribalaji V, Boopathi S, Asif MM (2021) Optimization of friction stir welding process to join dissimilar AA2014 and AA7075 aluminum alloys. Mater Today: Proc. https://doi.org/10.1016/j.matpr.2021.09.499
4. Boopathi S, Kumaresan A, Manohar N, Krishna Moorthi R (2017) Review on effect of process parameters-friction stir welding process. Int Res J Eng Technol (IRJET) 4:272–278
5. Sharifitabar M, Kashefi M, Khorshahian S (2016) Effect of friction stir processing pass sequence on properties of Mg–ZrSiO₄–Al₂O₃ surface hybrid micro/nano-composites. Mater Des 108:1–7. https://doi.org/10.1016/j.matdes.2016.06.087
6. Sathiskumar R, Dinaharan I, Murugan N, Vijay SJ (2015) Influence of tool rotational speed on microstructure and sliding wear behavior of Cu/B4C surface composite synthesized by friction stir processing. Trans Nonferrous Metals Soc China 25:95–102
7. Tajiri A, Uematsu Y, Kakiuchi T, Tozaki Y, Suzuki Y, Afrinaldi A (2015) Effect of friction stir processing conditions on fatigue behavior and texture development in A356–T6 cast aluminum alloy. Int J Fatigue 80:192–202
8. Rathee S, Maheshwari S, Siddiquee AN, Srivastava M (2017) Effect of tool plunge depth on reinforcement particles distribution in surface composite fabrication via friction stir processing. Defence Technol 13:86–91
9. Leal RM, Galvão I, Loureiro A, Rodrigues DM (2015) Effect of friction stir processing parameters on the microstructural and electrical properties of copper. Int J Adv Manuf Technol 80:1655–1663
10. Dolatkhah A, Golbabaei P, Givi MKB, Molaiekiya F (2012) Investigating effects of process parameters on microstructural and mechanical properties of Al5052/SiC metal matrix composite fabricated via friction stir processing. Mater Des 37:458–464
11. Salekrostam R, Givi MK, Asadi P, Bahemmat P (2010) Influence of friction stir processing parameters on the fabrication of SiC/316L surface composite. In: Defect and diffusion forum, pp 221–226
12. Thangarasu A, Murugan N, Dinaharan I, Vijay SJ (2012) Microstructure and microhardness of AA1050/TiC surface composite fabricated using friction stir processing. Sadhana 37:579–586
13. Shafiei-Zarghani A, Kashani-Bozorg SF, Zarei-Hanzaki A (2011) Wear assessment of Al/Al₂O₃ nano-composite surface layer produced using friction stir processing. Wear 270:403–412
14. Arab SM, Karimi S, Jahromi SAJ, Javadpour S, Zebarjad SM (2015) Fabrication of novel fiber reinforced aluminum composites by friction stir processing. Mater Sci Eng, A 632:50–57
15. Zeidabadi SRH, Daneshmanesh H (2017) Fabrication and characterization of in-situ Al/Nb metal/intermetallic surface composite by friction stir processing. Mater Sci Eng A 702:189–195

16. Selvakumar S, Dinaharan I, Palanivel R, Babu BG (2017) Development of stainless steel particulate reinforced AA6082 aluminum matrix composites with enhanced ductility using friction stir processing. Mater Sci Eng A 685:317–326
17. Boopathi S, Thillaivanan A, Pandian M, Subbiah R, Shanmugam P (2022) Friction stir processing of boron carbide reinforced aluminium surface (Al-B4C) composite: mechanical characteristics analysis. Mater Today: Proc 50:2430–2435. https://doi.org/10.1016/j.matpr. 2021.10.261
18. Boopathi S, Haribalaji V, Mageswari M, Asif MM (2022) Influences of boron carbide particles on the wear rate and tensile strength of AA2014 surface composite fabricated by friction-stir processing. Materiali in tehnologije/Mater Technol 56:263–270. https://doi.org/10.17222/mit. 2022.409
19. Haribalaji V, Boopathi S, Mohammed Asif M, Yuvaraj T, Velmurugan D, Anton Savio Lewise K, Sudhagar S, Suresh P (2022) Influences of Mg–Cr filler materials in friction stir process of aluminium-based dissimilar alloys. Mater Today: Proc. https://doi.org/10.1016/j.matpr.2022. 04.668
20. Boopathi S (2022) An extensive review on sustainable developments of dry and near-dry electrical discharge machining processes. ASME: J Manuf Sci Eng 144
21. Myilsamy S, Sampath B (2021) Experimental comparison of near-dry and cryogenically cooled near-dry machining in wire-cut electrical discharge machining processes. Surf Topogr Metrol Prop 9:035015. https://doi.org/10.1088/2051-672X/ac15e0
22. Sampath B, Myilsamy S (2021) Experimental investigation of a cryogenically cooled oxygen-mist near-dry wire-cut electrical discharge machining process. Strojniski Vestnik/J Mech Eng 67:322–330. https://doi.org/10.5545/sv-jme.2021.7161

Chapter 15
Performance Studies of Process Parameters on Friction Stir Processed AA5052 by Grey Analysis

S. V. Alagarsamy, C. Chanakyan, P. Prabhakaran, Adarsh Abi Mathew, and K. Senthamarai

1 Introduction

Friction stir processing (FSP) is very necessity technique to develop the mechanical properties with enhanced surface finishing of processed materials. Out of the different welding and processing techniques, FSP is appropriated technique to establish the material properties [1]. Normally, the material properties depend upon the properties of the parent metal, various processed zones, most heat influencing zones on the processed metal, some metallurgical modification while in friction stir process. It is called as solid-state process [2]. This solid-state method had some extraordinary benefits when compared to other traditional fusion joining process. Due to that process, some benefits are followed by enhanced mechanical characteristics, no consumables, ease in process, and employed in all the position [3]. The various researches were accomplished by friction stir process with different features and

S. V. Alagarsamy
Department of Mechanical Engineering, Mahath Amma Institute of Engineering and Technology, Pudukkottai, Tamil Nadu 622101, India

C. Chanakyan (✉)
Department of Mechanical Engineering, R.V.S. College of Engineering and Technology, Kumaran Kottam Campus, Coimbatore, Tamil Nadu 641402, India
e-mail: chanmech89@gmail.com

P. Prabhakaran
Department of Mechanical Engineering, J. J. College of Engineering and Technology, Trichy, Tamil Nadu 620009, India

A. A. Mathew
Pimpri Chinchwad College of Engineering, Pune, Maharashtra 411044, India

K. Senthamarai
Department of Mechanical Engineering, Sri Raaja Raajan College of Engineering and Technology, Karaikudi, Tamil Nadu 630301, India

broad in variety. The strengthened friction stir processed materials were attained by speed of tool rotation, traverse speed, and axial load [4]. Most of the mechanical applications like railway section, marine, aerospace, and transportation segments are utilized by the FSP [5].

Chanakyan et al. [6] studied the process parameter of FSWed AA5052 to carry out the mechanical properties by various tool pin profiles. It is concluded that the enhanced mechanical characteristics are achieved by pentagonal tool pin profile. Sivasankar et al. [7] investigated the process parameters of friction stir process on AA5052. The central composite design was arranged the process parameters and to examine the developed mechanical attributes. The entire process was obtained by the pentagonal tool pin profile. Jagathesh et al. [8] produced the dissimilar friction stir welded AA2024 and AA6061 by the three tool pin profiles. The FSW parameters are validated by ANOVA, and finally, GRA method was utilized to accomplish the optimal parameters. Bharathikanna et al. [9] carried out the experiments on AA6082 aluminium alloy with cylindrical tool pin profile by friction stir process. In this study, process parameters are arranged by the box-behnken design and ANOVA outcomes prove the optimal parameter. Palanivel et al. [10] carried out the friction stir processed on AA6351 with square tool pin profile. The central composite design was analysed the FSP parameters to carry out the optimal with RSM procedures. Vijayan et al. [11] analysed the FSW parameters on AA5083 by grey relational analysis. It is concluded that the FSW parameters are successfully optimized by GRA. Periyasamy et al. [12] successfully optimized the FSW parameters on MMCs by multi-objective approach. Similarly, this approach achieved better mechanical characteristics. Sudhagar et al. [13] conducted the FSW on AA2024 with various input of process parameters. Strengthened mechanical properties were achieved with selected optimal parameter of GRA method. From the complete analysis of literature, there is insufficient study was made on friction stir process with Taguchi framed parameters. Grey relational analysis does not employ with friction stir process parameters so far.

In this study, experimental results were carried out by the GRA and ANOVA from the structured parameters of Taguchi to predict the optimal process parameters. The outcomes of tensile strength and hardness were enhanced by the following combinational process parameters like speed of tool rotation, traverse speed and axial load.

2 Materials and Methods

In this study, AA5052 is considered as a parent metal. AA5052 is normally having super plastic behaviour due to that AA5052 highly possess magnesium content. Also this alloy proposed tremendous formability characteristics with better weldability. The following mechanical properties of AA5052 are 251 MPa of tensile, 19% of elongation, and 70 VHN of microhardness. Similarly, the chemical composition is 2.5 of Mg, 0.3 of Fe, 0.2 of Cr, 0.1 of Mn, 0.1 of Si, 0.1 of Zn, 0.1 of Cu, and remaining of Al. During this research, AA5052 plate was prepared with 100 ×
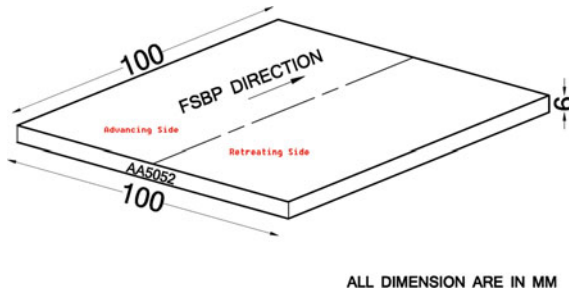
Fig. 1 Configuration of FSP with AA5052 dimension

100×6 mm dimensions and prepared pentagonal tool pin profile was carried out the friction stir process [7]. Pin was made with high carbon high chromium die steel due to greater toughness and higher hardness. The pin having dimensions 5.7 mm pin length and 18 mm shoulder diameter [14]. The pentagonal pin plunged in the beginning centerline of the base plate to be processed. Therefore, the processed base material has softened due to the frictional heat. After that period (pre-heat time), the processing table has given forward movement, resulting in about formation of friction stir processing or friction stir bead on plate processing (FSBPP). The tool pulled back after the processing fabricated. The configuration of FSP processing was displayed in Fig. 1. FSP and tool pin profile were displayed in Fig. 2a, b, respectively. Friction stir processed images and tensile image were showed in Fig. 3a, b, respectively. The Taguchi L9 was prepared the arrangements of friction stir process parameters [15]. Taguchi helps to reduce lesser amount of experiment out of large numbers of decision variables. The three level process parameter of FSP and nine levels are listed in Tables 1 and 2, respectively.

3 Results and Discussions

3.1 Macrostructure

The entire nine processed samples of macrostructures were taken as per the below schematic representation which is displayed in Fig. 4. Table 3 exhibits the macrostructure of processed samples with their suggestions. Moreover, all the samples get fine structure with lesser number of pores. Especially, all the processed specimens produce defect-free zones. From Fig. 4, SZ, TMAZ, HAZ, and PM represent the stirred zone, thermomechanically affected zone, heat affected zone, and parent metal, respectively. From Table 3, it is clearly understood that the all zones were indicated in the respective specimens.
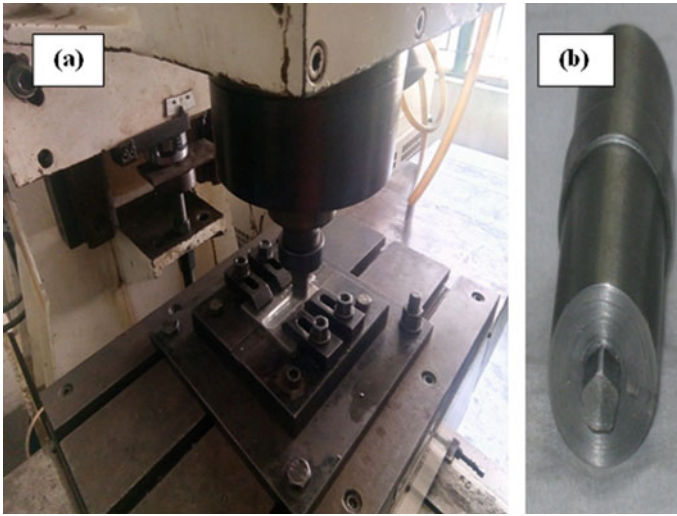
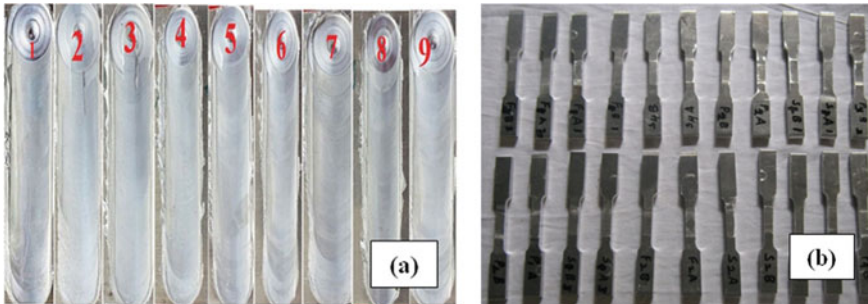**Fig. 2** **a** Frictions stir processing and **b** pentagonal tool pin profile

Fig. 3 **a** Friction stir processed specimen and **b** prepared tensile specimen

Table 1 FSP parameters and factors level

Process parameters	Symbols	Factors levels		
		1	2	3
Speed of tool rotation (rpm)	R	800	1000	1200
Traverse rate (mm/min)	T	20	25	30
Axial load (kN)	A	3	5	7

Table 2 Nine level experiments with process parameters
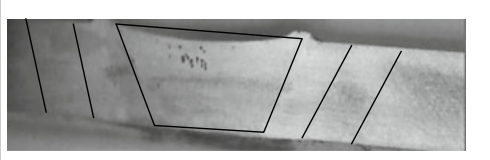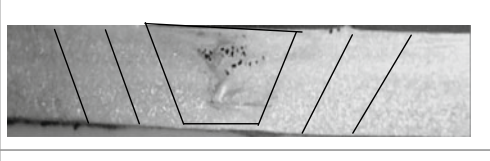
Runs	R (rpm)	T (mm/min)	A (kN)
1	800	20	3
2	800	25	5
3	800	30	7
4	1000	20	5
5	1000	25	7
6	1000	30	3
7	1200	20	7
8	1200	25	3
9	1200	30	5
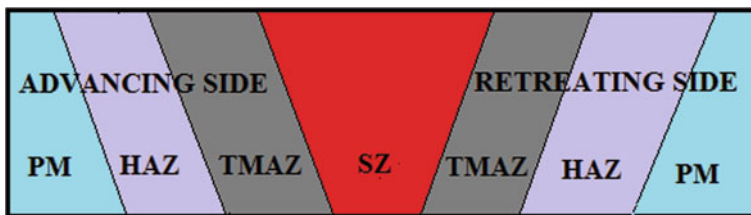
Fig. 4 Schematic diagram of macrostructure

3.2 Microstructure

Optical microstructure was carried out on the optimal specimen. From the macrostructure analysis, moreover most of the specimens achieved minute defects. Figure 5 displayed the base metal AA5052. It is showed that the grain structure was granular. From the GRG rank order, most (rank 1) and least (rank 9) optimal specimen were carried out by OM. The OM was examined on the various regions (SZ, TMAZ, HAZ, and PM) of the processed AA5052. The rank 1 parameter 1000 rpm, 20 mm/min and 5 kN and rank 9 parameters 1200 rpm, 20 mm/min, and 7 kN micrographs were showed in Fig. 6a, b, respectively. From Fig. 6a, the stirred or processed zone exhibits better grain structure by the accomplishment of intermetallic compounds between base metal and tool pin profile material which are well blended [16]. It was also employed to dynamic recrystallization during the FSP. Orowan strengthening into FSBP process correlates to standardize the dispersion. The configuration of superior grain structure provides to prolong the additional tensile force earlier to fracture [17]. The dispersion of grain was homogeneous in the nugget zone. The TMAZ advancing and retreating side were much finer than the both side of HAZ. Optimal process parameter is a major significant reason to enhance the better grains. From Fig. 6b, it is implicit that the stirred zone is poorer grain structure as well as other two sides (AS and RS) of both the TMAZ and HAZ achieved coarse grain. It is revealed

Table 3 Macrostructure with their effect of process parameters

Runs	Macrostructure	Remarks
1		Maximum pore was produced in the SZ. In this zone, lower hardness was produced
2		Higher number of pores was attained by the improper heat generation
3		Minute crack was identified in SZ
4		Defect-free zone was observed in the SZ due to sufficient of heat generation and higher hardness achieved
5		No defects. Sufficient of heat generation was improved. In this zone, maximum hardness was occurred
6		Flaw less was achieved due to proper plastic deformation occurs. Tensile was greater in this zone
7		Minute cracks due to less generation of heat in the nugget zone. In this zone, less tensile was achieved
8		Small hole was produced due to improper plastic deformation. Less hardness

(continued)

Table 3   (continued)

Runs	Macrostructure	Remarks
9		Minute hole was observed in the SZ

Fig. 5 Base metal AA5052

100X / 100μm
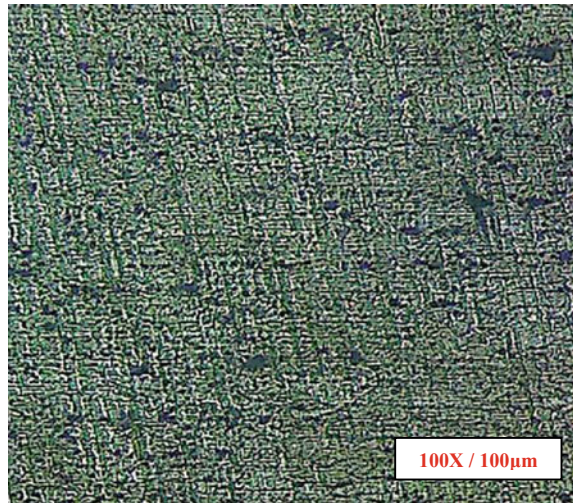
that the process parameter is one of the causes to diminish the grain structure with inadequate heat generation [18].

3.3   Tensile and Hardness Strength

The tensile strength and hardness of processed AA5052 values are presented in Table 4. The tensile with effect of process parameters is displayed in Fig. 7. From Fig. 7, it is understood that the tensile strength is improved at the parameters of 1000 rpm, 20 mm/min, and 5 kN. Due to that medium level of tool rotation with low level traverse achieved better tensile [19]. During the process, sufficient heat was generated to produce between the pin and magnesium base alloy so the process was well developed with severe plastic deformation [20]. The lesser tensile was achieved at the parameters 1200 rpm, 20 mm/min, and 7 kN. It is revealed that the higher tool rotation with low level of traverse and high level of axial force gets lesser tensile [21]. Because, the insufficient heat was generated while in process to carried out lesser severe plastic deformation [22]. In the hardness survey, the values
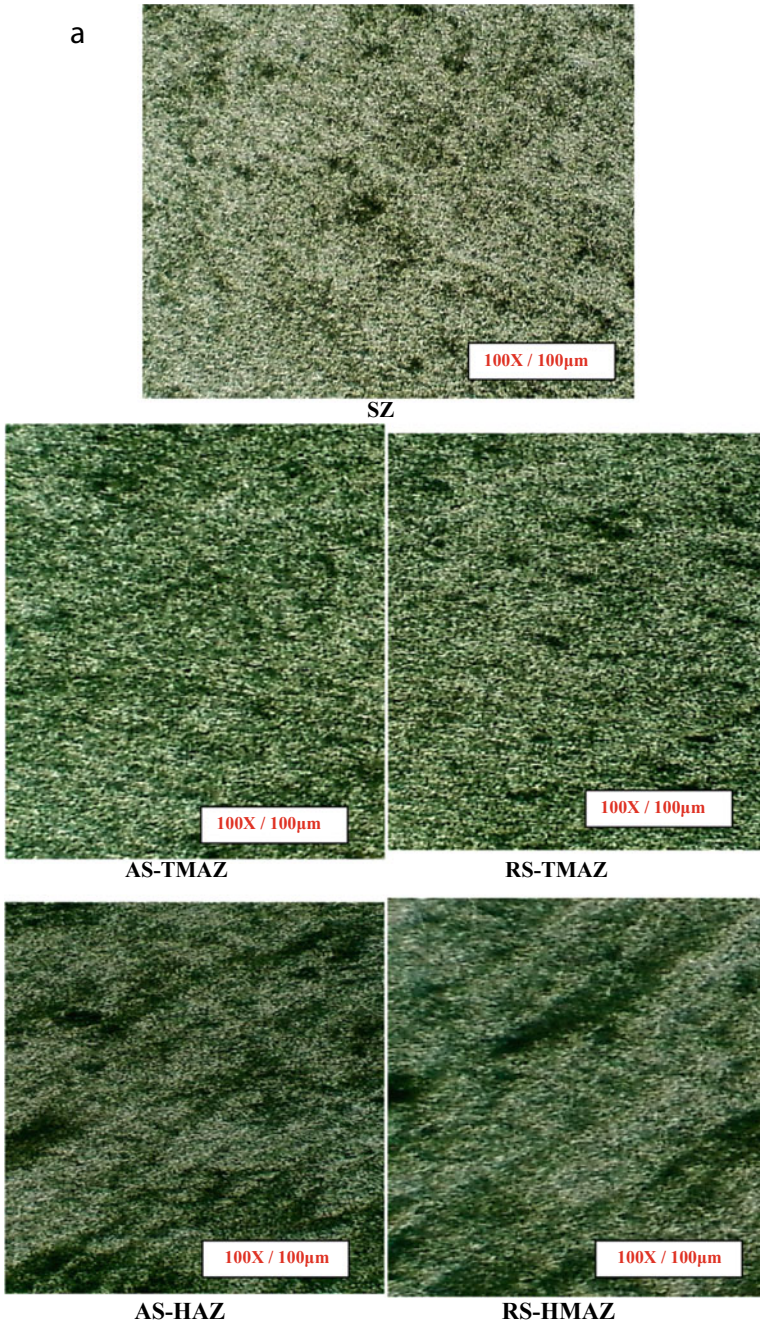
Fig. 6 a Microstructure of rank 1 optimal specimen with various zones. **b** Microstructure of rank 9 optimal specimen with various zones

b

NZ

AS-TMAZ

RS-TMAZ

AS-HAZ

RS-HMAZ
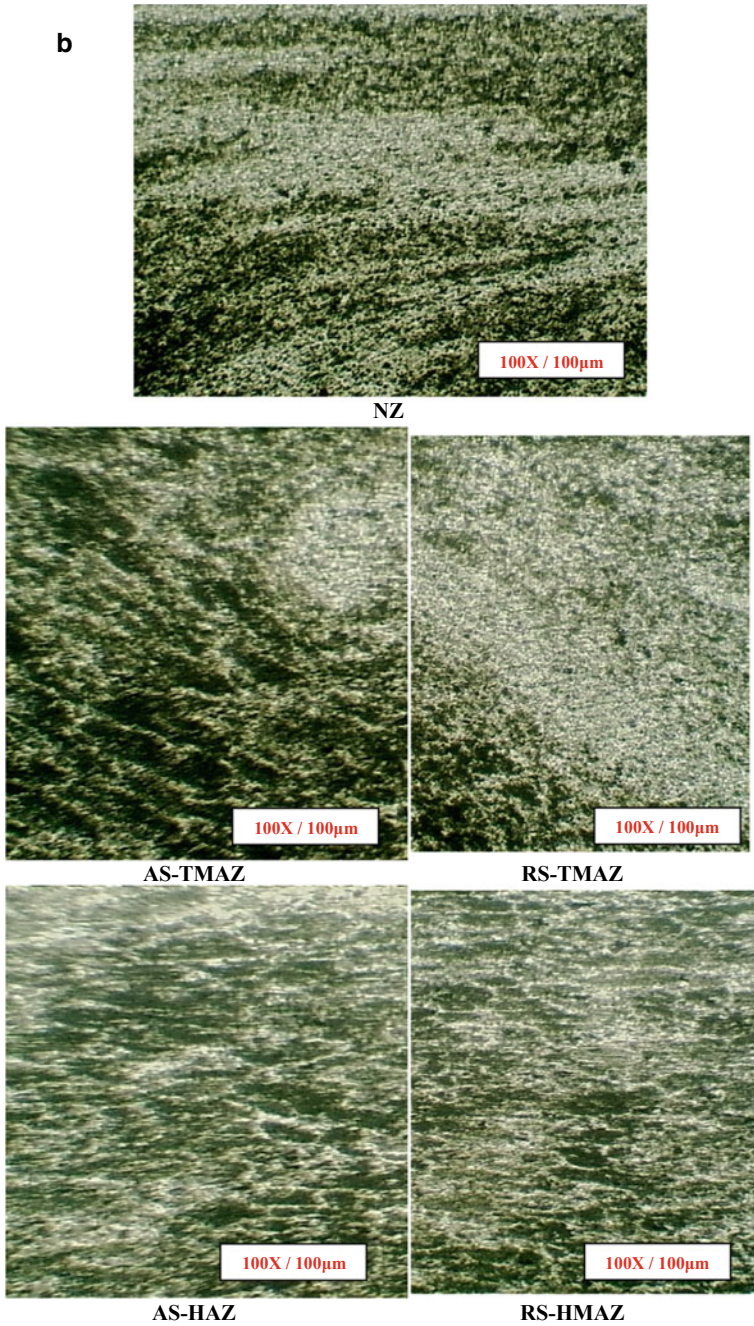
Fig. 6 (continued)

Table 4 Taguchi L9 with process parameters and their responses

Runs	R (rpm)	T (mm/min)	A (kN)	Tensile strength (MPa)	Hardness (VHN)
1	800	20	3	173	61
2	800	25	5	184	66
3	800	30	7	183	64
4	1000	20	5	215	69
5	1000	25	7	213	68
6	1000	30	3	212	67
7	1200	20	7	169	61
8	1200	25	3	170	62
9	1200	30	5	185	66
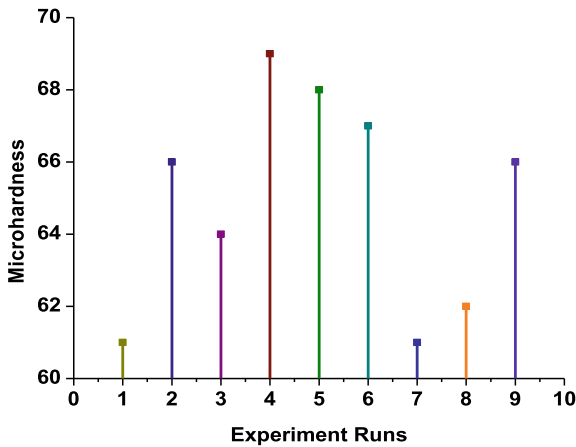
Fig. 7 Tensile strength with effect of FSP parameters

were taken on the different zones in the processed material. Those zones are nugget zone, thermomechanically affected zone, heat affected zone, and parent metal. The microhardness with effect of FSP parameters was illustrated in Fig. 8. From Fig. 8, it is clearly indicated that the 1000 rpm, 20 mm/min, and 5 kN achieve greater hardness. Orowan strengthening mechanism is major reason to enhance the hardness on the processed specimen [23]. It has highly densified and evenly scattered grain structure.

3.4 Fractography and EDS Studies on Optimal Specimen

The fractography was examined on the tensile fractured optimal specimen by SEM which was displayed in Fig. 9a, b. Figure 9a shows the tensile fracture of 1000 rpm,

Fig. 8 Microhardness with their effect of FSP parameter

20 mm/min, and 5 kN processed AA5052. From Fig. 9a, fracture surface clearly indicates that the surfaces were occupied by the small size of dimples with regular dispersion of intermetallic particles. It is understood that the fracture was observed with ductile mode failure [24]. Figure 9b shows the tensile fracture of 1200 rpm, 20 mm/min, and 7 kN processed AA5052. From Fig. 9b, it is understood that the fracture surfaces indicate larger void with bigger dimples were appeared. It is revealed that the fracture was observed with brittle mode failure [25].

The electron dispersion spectroscopy (EDS) was analysed on fractured surface of optimal specimen which is displayed in 10a, b. Figure 10a shows the EDS of rank 1 parameter 100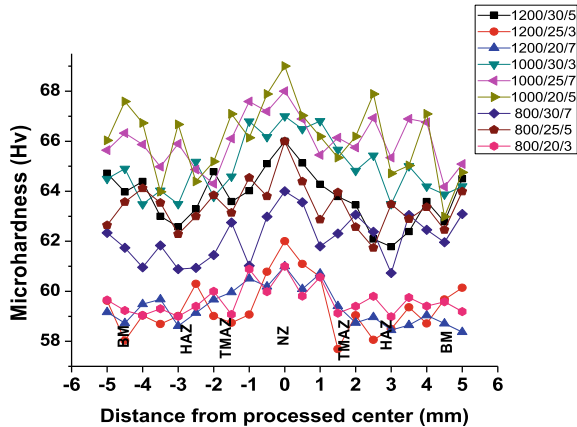0 rpm, 20 mm/min, and 5 kN processed AA5052. From Fig. 10a, it is explored that the chromium and carbide were majorly present in the fractured area due to processing of tool pin profile. The tool pin profile had highly presented by chromium and carbide so that intermetallic compounds are composed by the aluminium magnesium and chromium carbide compounds [26, 27]. Figure 10b exhibits the EDS of rank 9 parameter 1200 rpm, 20 mm/min, and 7 kN processed AA5052. From Fig. 10b, it is understood that the fractured area is fully accompanied by aluminium with less number of chromium and carbide. The chosen parameter is a major reason to lack of compounds on the fractured area.

4   Grey Relation Analysis (GRA)

Grey relation analysis is a straightforward way for developing the recognized key system factors. It is valuable for fluctuating independent analysis and also transformed the single response from the multi-response values. Grey boundaries were no evidence of data—no solution and entire data with evidence—distinctive solution. This technique is an appropriate arrangement for incomplete evidence of data
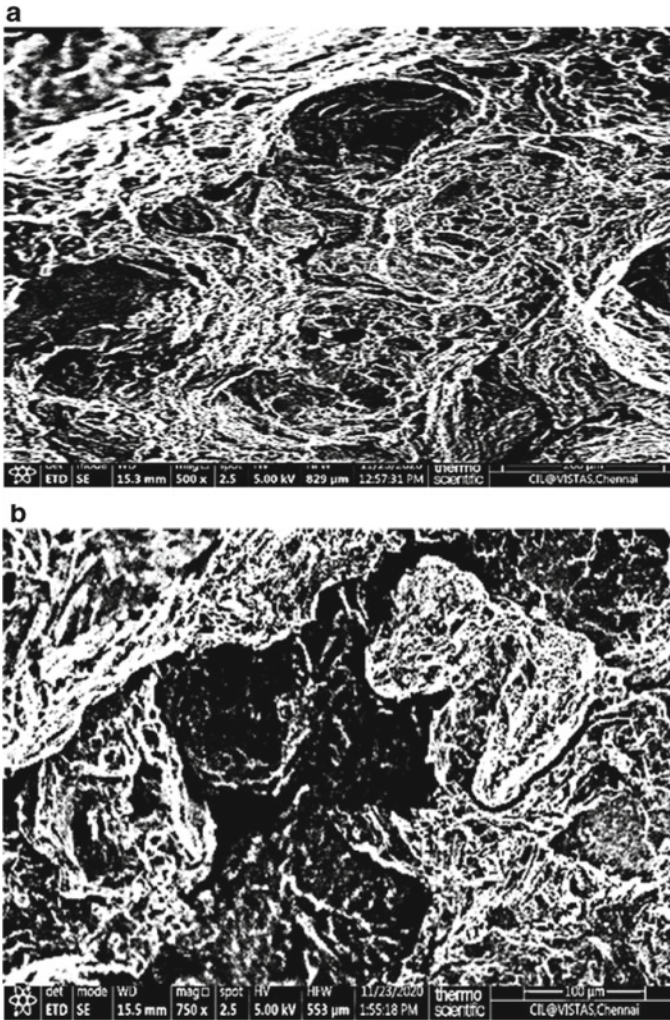
Fig. 9 **a** SEM fractograph of rank 1 optimal specimen. **b** SEM fractograph of rank 9 optimal specimen

in between the boundaries. A grey relation system is trying to locate the most elegant solution and also provide good clarification for critical problems. In this analysis, the appearance of estimated qualities is standardized, i.e. start from 0 to 1. The standardized outcomes used to perform the qualities at the condition more significant are best. In this study, output responses like tensile (TS) and hardness (VHN) which were utilized to determine larger the better solution [28, 29]. This solution was used to perform the qualities of standardized outcomes which are suggested by below the eqn.
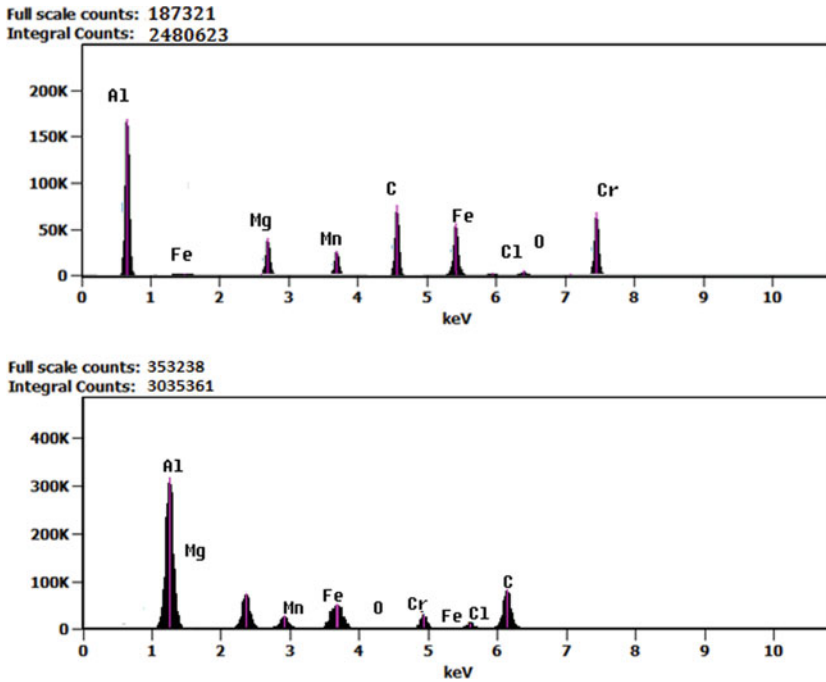
Fig. 10 a EDS of rank 1 optimal specimen for fractured surface. b EDS of rank 9 optimal specimen for fractured surface

$$X_i^0(k) = X_i^*(k) - \min X_i^*(k)/\max X_i^*(k) - \min X_i^*(k) \tag{1}$$

After the assembly of grey relation method, min $X_i(k)$ and max $X_i(k)$ are the least and biggest value of $X_i(k)$ for the kth response. Ideal arrangement for the responses is $X_i^0(k)(k = 1, 2, 3, \ldots 9)$, and the actual and preferred experimental data were determined by grey relational coefficient. It can be suggested by (ξ).

$$\xi = \frac{\Delta_{\min} + \psi \Delta_{\max}}{\Delta_{0i}(k) + \psi \Delta_{\max}} \tag{2}$$

From above the equation, grey relational coefficient (GRC) was computed. By taking the average of the grey relational coefficient was used to compare the selected responses and establishing values of grey relational grade and to execute different responses. The weighting strategy of ψ is taken as 0.5 and its coordinate the GRC into grey relational grade for every individual experiment.

$$y_j = \sum_{k=1}^{n} w_i \xi_i(k) \tag{3}$$

Table 5 GRG and rank order for tensile and microhardness

Ex. No	Standardized S/N ratio		GRC		Grey relational grade	Rank
	TS	VHN	TS	VHN		
1	0.087	0.000	0.354	0.333	0.344	8
2	0.326	0.625	0.426	0.571	0.499	5
3	0.304	0.375	0.418	0.444	0.431	6
4	1.000	1.000	1.000	1.000	1.000	1
5	0.957	0.875	0.920	0.800	0.860	2
6	0.935	0.75	0.885	0.667	0.776	3
7	0.000	0.000	0.333	0.333	0.333	9
8	0.022	0.125	0.338	0.364	0.351	7
9	0.348	0.625	0.434	0.571	0.503	4

Above the Eq. 3 utilized to compute the grey relational grade, where y_j as the grey relational grade for identify the experiment of jth value, n is the quantity of responses, and ith characteristics were performed by the weighting factor w_i. The performance characteristics were predicted and confirmed by utilizing the consolidation of optimal friction stir processing parameters [30], and it can be determined by underneath the equation.

$$\hat{y} = y_m + \sum_{i=1}^{q} (\overline{y_i} - y_m) \tag{4}$$

Above the Eq. 4 utilized to identify the validation of predicted values, where y_m and y_i are the overall mean and mean of the grey relational grade at the level of optimum, and the multiple performance characteristics influenced by the number of friction stir process parameters, which is denoted by (q). The purpose of the total grey relational grade is used to change over a process of multi-response into single response optimization. The Taguchi technique used to perform the evaluating of uppermost and maximizing results in grey relation grade. Table 5 shows the standardized ratios, grey relational coefficient, GRG, and rank. From Table 5, it is clearly indicated that the 4th experiments compose the greater grey relational grade and higher mechanical properties. So that the 4th experiment was indicated as rank 1. Those rank 1 correlated parameter is 1000 rpm, 20 mm/min, and 5 kN, which was the optimal parameter also.

5 Contour Plot of GRG with FSP Parameters

The contour plots of GRG values with three process parameters are displayed in Fig. 11a–c. It is clearly understood that the effect of process parameters on GRG during FSP. Figure 11a shows the relations between the rotation speed and traverse

speed on GRG values. It is revealed that the GRG values are improved at medium level of rotation speed (1000 rpm) and low level of traverse speed (20 mm/min), respectively. Figure 11b displays the effect of traverse speed and axial load on GRG estimated values. It is explored that the maximum GRG was occurred at low level of traverse speed (20 mm/min) and medium level of axial load (5 kN), respectively. Figure 11c explored the effect of axial load and rotation speed on computed GRG mean values. It is revealed that the greater GRG was attained at the moderate level of tool rotation (1000 rpm) and axial load (5 kN), respectively. From these figures, it is understood that the most influencing parameters are tool rotation with moderate range of speed, intermediate level of axial load and low level of traverse speed composes the better mechanical properties [31, 32].

5.1   Computing the Mean Values of GRG and S/N Ratios

The FSP parameters are independent by the calculated GRG values. By taking the average (three levels 1–3) of the GRG from their respective runs (speed of tool rotation), $1 + 2 + 3$, $4 + 5 + 6$, and $7 + 8 + 9$ were used to determine the mean of the GRG. Similarly, the runs (traverse speed) $1 + 4 + 7$, $2 + 5 + 8$, and $3 + 6 + 9$ and the runs (axial load) $1 + 6 + 8$, $2 + 4 + 9$, and $3 + 5 + 7$ used to determine the mean of grey relational grade. The calculated mean responses of GRG are presented in Table 6. From the maximization of GRG, 3 level mean table was initiated from the FSP parameters. From Table 6, the level 2–3-2 of speed of tool rotation, traverse speed, and axial load is the significant. It is revealed that the most influenced parameter id speed of tool rotation. The GRG means are necessity to improve the robustness with S/N ratio values. So that the GRG means are transformed into the S/N ration values with help of MINITAB software [33]. The signal and noise are indicating the average response and variation from the investigational outputs. In this investigation, the 'Larger-is-better' precedent preferred for S/N proportion to maximize the responses and its summary of data presented in Table 7. Table 8 represented the average responses of signal-to-noise ratio and mean of grey relation grade for a friction stir processing at the 3 levels. The maximum grey relational grade obtained at the second, third, and second levels of 1000 rpm, 20 mm/min, and 5 kN, respectively. The average response of maximum grey relation grade was the most exceptional level, which recommended by the signal-to-noise ratio for the process parameters.

Fig. 11 **a** Rotation speed and traverse speed on GRG. **b** Traverse speed and axial load on GRG. **c** Axial load and rotation speed on GRG
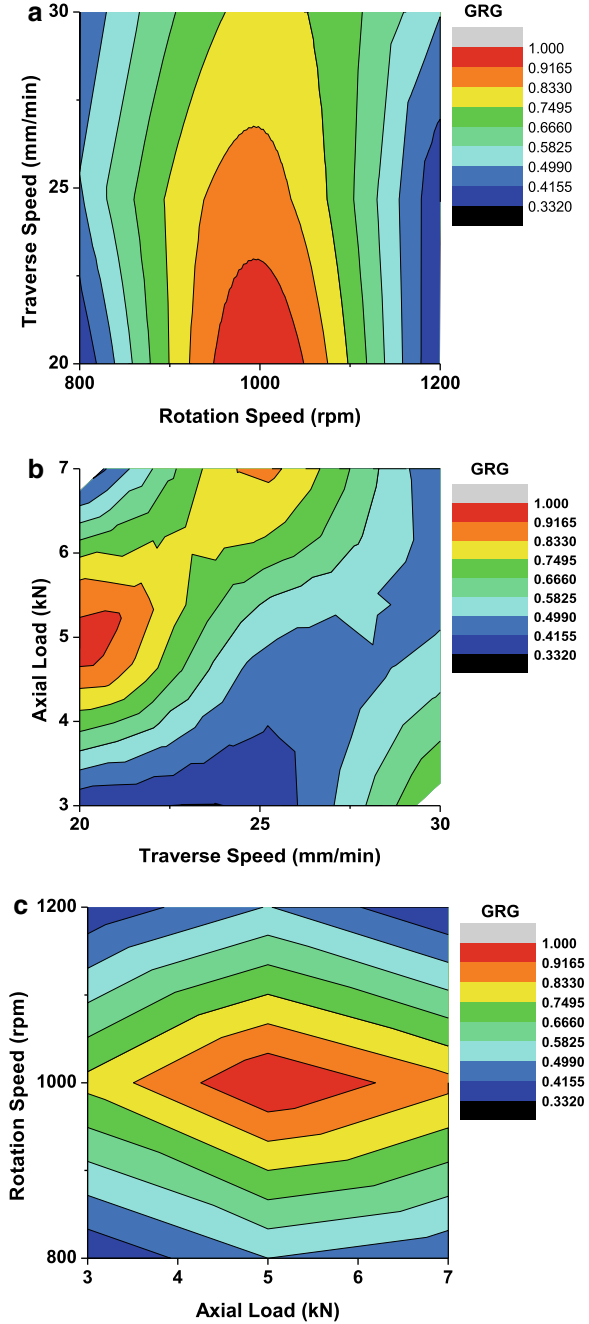
Table 6 Response tables for grey relation grade at three Levels

Process parameters	Grey relation grade				
	Level 1	Level 2	Level 3	Max–Min	Rank
Tool spinning speed (Rpm)-TSS	0.425	0.879	0.396	0.483	1
Traverse speed (mm/min)-TS	0.559	0.568	0.570	0.011	3
Axial load (kN)-AL	0.490	0.667	0.542	0.177	2

Table 7 Mean of GRG and S/N ratio

Runs	TSS	TS	AL	Mean value of GRG	S/N ratio
1	800	20	3	0.344	−9.269
2	800	25	5	0.499	−6.038
3	800	30	7	0.431	−7.310
4	1000	20	5	1.000	0.000
5	1000	25	7	0.860	−1.310
6	1000	30	3	0.776	−2.203
7	1200	20	7	0.333	−9.551
8	1200	25	3	0.351	−9.094
9	1200	30	5	0.503	−5.969
Average				0.566	−5.638

Table 8 Mean of S/N ratio and GRG at three level

Level	For S/N ratio			For GRG mean		
	TSS	TS	AL	TSS	TS	AL
1	−7.539	−6.273	−6.855	0.425	0.559	0.490
2	−1.171	−5.481	−4.002	0.879	0.568	0.667
3	−8.205	−5.161	−6.057	0.396	0.570	0.542
Delta	7.034	1.113	2.853	0.483	0.011	0.177
Rank	1	3	2	1	3	2

5.2 ANOVA

The method ANOVA is used to test the efficiency of the grey relational grade for the optimal consolidation of FSP parameters [34]. The ANOVA analysed the grey relational grade outputs represented in Table 9. Out of the various parameters, tool spinning speed obtained a maximum of 78.05%, and next to axial load reaches 15.55%, respectively. The percentage contribution of tool spinning speed has a maximum, which is significant than other parameters. Figures 12a–c and 13a–c contributed to the main effects of friction stir processing versus the means of GRG and means of S/N ratios. The grey relational grade proposed the second, third, and second levels

Table 9 ANOVA for GRG

Parameters	DOF	SS	MS	F	P	Percentage contribution (%)
R	2	3.76857	1.88428	399.21	0.002	78.05
T	2	0.29991	0.14995	31.77	0.031	6.21
A	2	0.75076	0.37538	79.53	0.012	15.55
Error	2	0.00944	0.00472			0.20
Total	8	4.82867				100.00

of 1000 rpm TSS, 20 mm/min TS, and 5 kN AL as the best level for the friction stir processed joints.
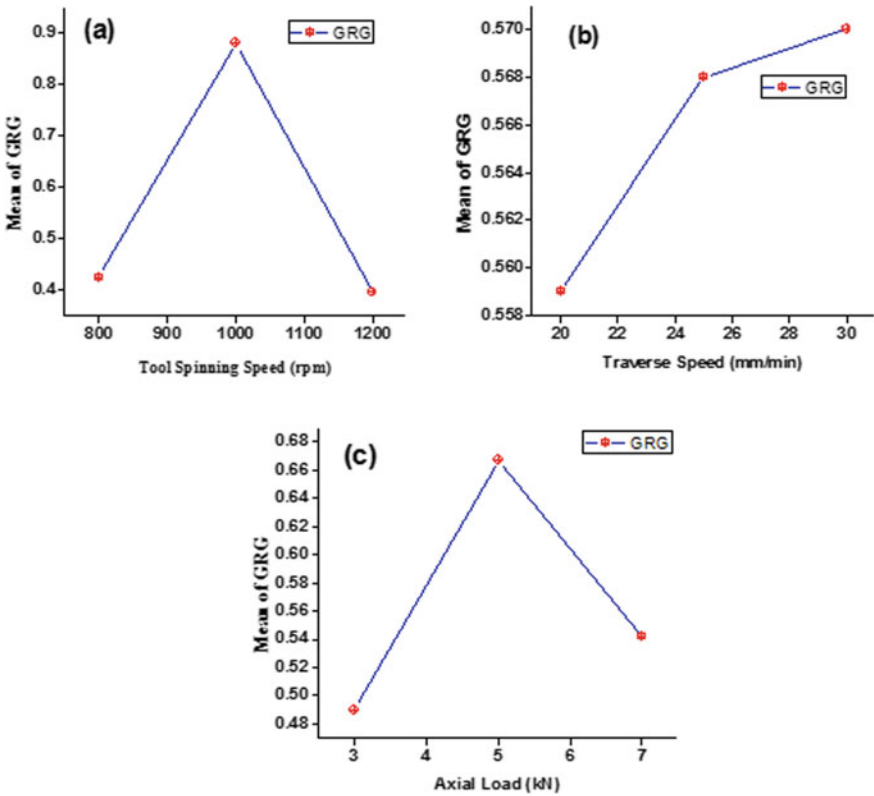
Fig. 12 **a** Effect of tool spinning speed versus mean of GRG, **b** effect of traverse speed versus mean of GRG and **c** effect of axial load versus mean of GRG
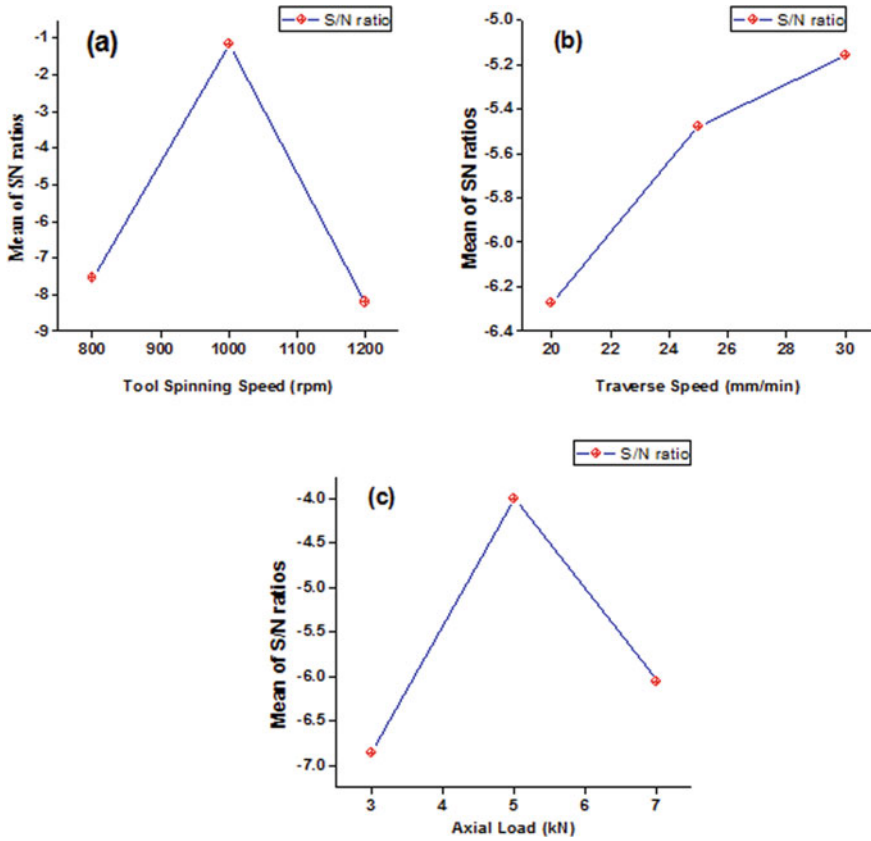
Fig. 13 a Effect of tool spinning speed versus mean of S/N ratios, **b** effect of traverse speed versus mean of S/N ratios, **c** effect of axial load versus mean of S/N ratios

5.3 Validation Test of Optimal Parameters

The optimal processing parameters, i.e. $R = 1000$ rpm, $T = 20$ mm/min, and $A = 5$ kN. The average means value of grey relational grade, tensile, and microhardness properties of processed samples was initiated with grey relational analysis and its confidence interval is presented in Table 10.

6 Conclusion

- The friction stir process was successfully employed with Taguchi and GRA. Also identifies the optimal process parameter with L9 arrays. The nine experiments were effectively fabricated by FSP.

Table 10 Validation test using optimum level of process parameters

Initial processing parameters	Initial designated levels of processing parameters	Optimal condition of process parameter using GRA
Factor level	R2, T1, A2	R2, T3, A2
tensile strength (Mpa)	215	218.7
Microhardness-Hv	69	67.87
Grey relational grade	0.979	0.984

- The maximum grey relational grade was obtained in the optimal process parameters 1000 rpm of rotation speed, 20 mm/min of traverse speed, and 5 kN of axial load.
- Mechanical properties of friction stir processed AA5052 have extremely upgraded by Taguchi and grey relational techniques.
- Speed of tool rotation (78.05%) was exceedingly substantial parameter for the grey relational grade, whereas traverse speed (15.55%) and axial load (6.21%) are next partial significant parameters in the grey relational analysis.
- Optimal specimen microstructure was successfully carried out by optical micrographs and fractured surfaces are clearly indicated by SEM analysis. Similarly, EDS was conducted effectively to prove the presence of particles.

References

1. Chanakyan C, Sivasankar S, Meignanamoorthy M, Ravichandran M, Mohanavel V, Alfarraj S, Almoallim HS, Manikandan V, Issac JoshuaRamesh Lalvani J (2021) Optimization of FSP process parameters on AA5052 employing the S/N ratio and ANOVA method. Adv Mater Sci Eng. https://doi.org/10.1155/2021/6450251,1-15
2. Dinaharan I (2016) Influence of ceramic particulate type on microstructure and tensile strength of aluminum matrix composites produced using friction stir processing. J Asian Ceram Soc 4:209–218
3. Mohammed MH, Subhi AD (2020) Exploring the influence of process parameters on the properties of SiC/A380 Al alloy surface composite fabricated by friction stir processing. Eng Sci Technol Int J. https://doi.org/10.1016/j.jestch.2021.02.013
4. Dinaharan I, Zhang S, Chen G, Shi Q (2020) Titanium particulate reinforced AZ31 magnesium matrix composites with improved ductility prepared using friction stir processing. Mater Sci Eng A 772:138793
5. Abbasi M, Givi M, Bagheri B (2019) Application of vibration to enhance efficiency of friction stir processing. Trans Nonferrous Met Soc China 29:1393–1400
6. Chanakyan C, Dineshbabu P, Jagathesh K, Jenarthanan MP (2014) An experimental investigation on mechanical properties and microstructure of friction stir welding of AA5052. Appl Mech Mater 592–594:48–52
7. Sivasankar S, Chanakyan C (2019) Parametric advancement of numerical model to predict the mechanical properties of friction stir processed AA5052. Int J Rapid Manuf 8(1/2):147–160
8. Jagathesh K, Jenarthanan MP, Dineshbabu P, Chanakyan C (2017) Analysis of factors influencing tensile strength in dissimilar welds of AA2024 and AA6061 produced by friction stir welding (FSW). Aust J Mech Eng 15(1):19–26

9. Bharathikanna R, Elatharasan G (2019) Investigation of mathematical model to optimise the mechanical properties of friction stir processed AA6082. Int J Rapid Manuf 8(1/2):133–146

10. Palanivel R, Koshy Mathews P, Murugan N (2011) Development of mathematical model to predict the mechanical properties of friction stir welded AA6351aluminium alloy. J Eng Sci Technol Rev 4(1):25–31

11. Vijayan S, Raju R, Rao SR (2010) Multiobjective optimization of friction stir welding process parameters on aluminum alloy AA 5083 using Taguchi-based grey relation analysis. Mater Manuf Processes 25(11):1206–1212

12. Periyasamy P, Mohan B, Balasubramanian V, Rajakumar S, Venugopal S (2013) Multi-objective optimization of friction stir welding parameters using desirability approach to join Al/SiC p metal matrix composites. Tran Nonfer Met Soci China 23(4):942–955

13. Sudhagar S, Sakthivel M, Prince Mathew J, Ajith Arul Daniel S (2017) A multi criteria decision making approach for process improvement in friction stir welding of aluminium alloy. Measurement 108:1–8

14. Chanakyan C, Sivasankar S (2021) Parametric optimization of mechanical properties via FSW on AA5052 using Taguchi based grey relational analysis. INCAS Bull 13(2):21–30

15. Sivam SPSS, Karuppaiah SM, Yedida BK, Atluri JR, Mathur S (2018) Multi response optimization of setting input variables for getting better product quality in machining of magnesium AM60 by grey relation analysis and ANOVA. Periodica Polytech Mech Eng 62(2):118–125

16. Heinz Z, Skrotzki B (2002) Characterization of a friction-stir-welded aluminum alloy 6013. Metall Mater Trans B 33(3):489–498

17. Balakrishnan M, Dinaharan I, Palanivel R, Sathiskumar R (2019) Effect of friction stir processing on microstructure and tensile behavior of AA6061/Al3Fe cast aluminum matrix composites. J All Comp 785:531–541

18. Charit I, Mishra R (2003) High strain rate superplasticity in a commercial 2024 Al alloy via friction stir processing. Mater Sci Eng A 359(1–2):290–296

19. Satya Kumar D, Tripathi MK, Manoj MK (2020) Effect of welding speeds on microstructure and mechanical properties of dissimilar friction stir welding of AA7075 and AA5083 alloy. Mater Today: Proc 27(3):2713–2717

20. Fonda RW, Lambrakos SG (2002) Analysis of friction stir welds using an inverse problem approach. Sci Technol Weld Joining 7(3):177–181

21. Mehri A, Abdollah-zadeh A, Habibi N, Hajian M, Wang JT (2020) The effects of rotational speed on microstructure and mechanical properties of friction stir-welded 7075-T6 thin sheet. J Mater Eng Perform 29:2316–2323

22. Fuller CB, Mahoney MW, Calabrese M, Micona L (2010) Evolution of microstructure and mechanical properties in naturally aged 7050 and 7075 Al friction stir welds. Mater Sci Eng A 527:2233–2240

23. Wang X-h, Wang K-s, Shen Y, Yang X-r, Xu k-w (2006) Evaluation of microstructure and mechanical property of fsw welded MB3 magnesium alloy. J Iron Steel Res Int 13(4):75–78

24. Kwon YJ, Saito N, Shigematsu I (2002) Friction stir process as a new manufacturing technique of ultrafine grained aluminum alloy. J Mater Sci Lett 21:1473–1476

25. Jata K, Semiatin S (2000) Continuous dynamic recrystallization during friction stirs welding of high strength aluminum alloys. Scripta Mater 43(8):743–749

26. Sharma V, Prakash U, ManojKumar BV (2015) Surface composites by friction stir processing: a review. J Mater Process Technol 224:117–134

27. Shahraki S, Khorasani S, Behnagh RA (2013) Producing of AA5083/ZrO2 nanocomposite by friction stir processing (FSP). Metall Mater Trans B 44:1546–1553

28. Shanmuga SN, Murugan N (2010) Tensile behavior of dissimilar friction stir welded joints of aluminium alloys. Mater Des 31(9):4184–4193

29. Prabhakar GVNB, Ravi Kumar N, Ratna Sunil B (2018) Surface metal matrix composites of Al5083-fly ash produced by friction stir processing. Mater Today: Proc 5:8391–8397

30. Babu S, Elangovan K, Balasubramanian V (2009) Optimizing friction stir welding parameters to maximize tensile strength of AA2219 aluminum alloy joints. Metals Mater Int 15:321–330

31. Koilraj M, Sundareswaran V, Vijayan S, Koteswara Rao SR (2012) Friction stir welding of dissimilar aluminum alloys AA2219 to AA5083—optimization of process parameters using Taguchi technique. Mater Des 42:1–7
32. Elangovan K, Balasubramanian V, Valliappan M (2008) Influence of pin profile and axial force on the formation of friction stir processing zone in AA6061 aluminum alloy. Int J Adv Manuf Technol 38:285–294
33. Kumar S, Kumar S, Kumar A (2012) Optimization of process parameters for friction stir welding of joining A6061 and A6082 alloys by Taguchi method. Proc Inst Mech Eng Part C: J Mech Eng Sci 227(6):1150–1163
34. Rajendran C, Srinivasan K, Balasubramanian V, Balaji H, Selvaraj P (2017) Identifying combination of friction stir welding parameters to maximize strength of lap joints of AA2014-T6 aluminum alloy. Arch Mech Technol Mater 37:6–21

Chapter 16
Analysis into Mechanical Properties and Microstructural Behavior of Friction Stir Welded Al 6061-T6 Alloy Joints

Saurabh Dewangan, Ramneek Yadav, Anirudh Sharma, and Siddharth Vohra

1 Introduction

FSW has emerged as a widely used solid state joining process since its inception. It is applicable for all the metals, especially those which have low melting point, e.g., aluminum and its alloys. Later on, other engineering materials like copper, steel, titanium, and other metal matrix composition were also taken under consideration for this welding. FSW, in butt joint configuration, was patented by Thomas et al. (1991) at The Welding Institute (TWI) in 1991 [1]. FSW is relatively simple to process. In this, a tool of high strength containing a shoulder and a pin is rotated and fed between the adjoining surfaces of plate. As the tool plunges inside the edges, it starts to make the edges plastically deformed. The pin of the tool stirs this semisolid structure. The plastically deformed and stirred part of the material is pressurized by the tool shoulder. Hence, splashing of the material is completely arrested. In this way, the tool is moved from a leading part to trailing part of the adjoining edges. As a result, upon cooling, a very good bonding between two edges is observed [2–5]. A schematic of FSW process is shown in Fig. 1.

S. Dewangan (✉)
Department of Mechanical Engineering, Manipal University Jaipur, Dehmi Kalan, Jaipur, Rajasthan 303007, India
e-mail: saurabh22490@gmail.com

R. Yadav
Delhi Technological University (East Campus), M893+JHM, Vivek Vihar, Delhi 110095, India

A. Sharma
Automotive Systems Engineering, University of Michigan, Dearborn 48126, USA

S. Vohra
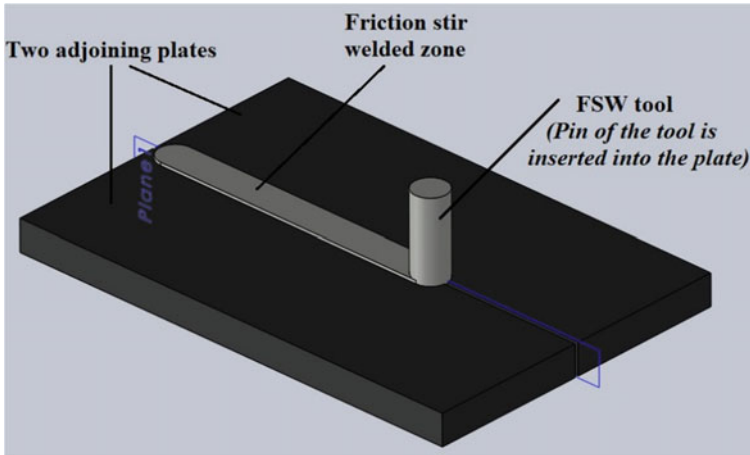NewSpace Research and Technologies, Bengaluru 560092, India

281

Fig. 1 Schematic of friction stir welding process

In traditional fusion welding process, a lot of problems come into picture during solidification due to significant post welding thermal gradients. Defects like embrittlement of microstructure, hydrogen cracking, welding fumes, distortion at larger scale, and significant residual stresses are usually reported in traditional welding. As the solid state welding is done below melting point (about 100 °C less), it has the ability to minimize the discussed defects to a great extent. Among different SSW, FSW seems to be more advantageous because it does not contain extra filler metal, hence additional weight gain into the welded part is prevented. As the heat is generated by friction of the tool and plates, there is no need of extra arrangement of heat addition as in case of FW process. The mechanical mixture of the metals of the joining plates, through stirring process, takes place by specially designed tool called probe. In addition, the pressure exerted by tool shoulder confirms a fine welding surface. FSW process can be employed to produce various joints like butt joint, lap joint, T-joint, L-joint, etc. Application of FSW includes various fields like aerospace industry, automobile industry, ship building industry, etc. [2, 3]. The quality of the FSW joint depends on various parameters like tool rotational speed, welding speed, plunge depth, etc. These parameters are responsible for making a semisolid structure of the metals being welded. Higher the welding speed, better will be the stirring process [6–8]. Some review of the previous research works has been done this work.

As the FSW is not a very old development, continuous research is going on to establish the new facts and results. Initially, it was applied for soft materials only but nowadays advanced machinery overcame this issue. Now, the materials with high yield point can also be taken under FSW process. As it is basically a joining process, research is mainly focused on the effects of yield parameters in mechanical properties of the joints. FSW deals with high strain rate deformation and simultaneous increment in temperature, various microstructural zones could be observed in the welded plate. These zones include: (1) nugget zone (NZ), in the center of the weld

where stirring takes place; (2) thermo-mechanical-affected zone (TMAZ), next to NZ; and (3) heat affected zone (HAZ). With the change in microstructural behavior, the mechanical properties also differ. It has been an interesting topic of research to analyze the microstructural changes and mechanical properties after welding the specimen. Some previous research works are summarized here.

Dawood et al. (2014) compared the FSW and gas metal arc welding process in joining 1030 Al alloys. The comparison was done on the basis of power consumption, mechanical properties, and microstructural behavior. The results showed that FSW is eco-friendly, comparatively safer, and a better joining technique according to mechanical behavior of the joint [9]. Carlone and Palazzo (2013) investigated the effect of process parameters like tool rotating speed and welding speed on joint quality, microstructure, and mechanical properties in FS-welded AA2024-T3. For this purpose, numerical and experimental both the techniques were applied. Smaller grains were reported when rotational speed was low and welding speed was high and vice-versa [10]. Saravanan et al. (2016) investigated the effects of rotational speed, welding speed, axial load and ratio of shoulder diameter to pin diameter (*D/d*) on tensile strength, microhardness, and microstructure of the friction stir welded dissimilar joints of AA6061-T6 and AA7075-T6. This work was basically performed with many parameters. An optimized set of parameters were selected on the basis of experimental results. The best set of parameters on high tensile strength and hardness basis, for this experiment, were: 1100 RPM rotational speed, 26 mm/min welding speed, 7 kN axial load; and *D/d* ratio of 3. A reduction in grain size was reported in stir zone due to improved mechanical properties [11]. Rodriguez et al. performed the FSW of dissimilar Al-alloys, graded 6061 and 7050. They concluded that the microstructure of stir zone is dependent on the tool rotational speed. They observed various distinct lamellar structure at NZ which was associated with tool rotation [12]. With regard to dissimilar FSW joint of Al 6061 and Al-7075, Guo et al. (2014) reported a proper mixing of materials and thereby good mechanical properties at NZ, whereas HAZ was reported as the weakest area in the plates. In addition, there was improved mechanical properties toward Al 6061 plate when placed in advancing side [13]. Sinhmar and Dwivedi (2019) performed thermo-mechanical, mechanical, and microstructural testing of FS-welded Al-AA2014 alloy. The experiments were carried out at various combination of speeds. According to measurement of weld-thermal cycle, it was found that the maximum temperature was reported at higher tool rotation and lower welding speed. However, hardness and corrosion resistance properties were reported at their higher values when rotational speed was low and welding speed was high. In addition, a good correlation among microstructural behavior, mechanical properties, and corrosion phenomena was observed in this study [14]. Research on effect of FSW yield parameters, such as tool RPM, welding speed, tool pin profile, and shoulder to pin diameter ratio. On mechanical properties and microstructural attributes of the final welded plates was carried out by many researchers [4–14]. For many years, FSW process has been focused into Al-alloys in butt configuration. Some important grades of Al-alloys, which were taken under consideration by researchers, are: AA2219 [15], AA5083 [16], AA2198-Li [17], AA2024 [18], and AA6061 [19].

Nowadays, the research is being carried out on dissimilar materials in lap and tee configuration also [10–12, 20–23].

As an original FSW machine is comparatively costlier, the FSW machine can be developed by using an augmented vertical milling machine in view of economic feasibility. For soft materials like Al-alloys, the developed set up has become a successful approach to carry out FSW. In the present work, an augmented milling machine was used as a FSW machine to weld the Al 6061-T6 alloy. The successfully joined Al-alloys, at different welding parameters, were analyzed on the basis of mechanical properties and microstructural behavior.

2 Experiment

2.1 Material Selection

Al 6061-T6 alloy was chosen as the work-piece material for the experiment. This grade of aluminum is widely used in heavy duty construction purposes, most commonly rail coaches, truck frames, shop building, bridges and military bridges, aerospace applications, etc. It has melting point of about 617 °C. For fulfilling, the criteria of specification provided by the American Society of Testing Materials (ASTM), the work-piece dimensions were selected as $150 \times 50 \times 10$ mm. The chemical and mechanical properties of Al 6061-T6 alloy are mentioned in Tables 1 and 2.

Table 1 Chemical composition of Al 6061-T6 alloy

Element	Cu	Mg	Si	Fe	Mn	Al
Content	0.05	0.65	0.50	0.50	0.03	98.27

Table 2 Mechanical properties of Al 60–61-T6 alloy

Material	UTS (MPa)	TYS (MPa)	Elongation (%)	Hardness (RHN)
6061-T6	310	276	12	40

2.2 Tool Specifications

AISI D2, a high carbon steel, was selected for manufacturing the FSW tool. It is a strong non-consumable material with high wear resisting properties. It can retain its hardness at high temperature generated during the process. The ratio of shoulder

Table 3 Chemical composition of AISI D2 steel

Element	C	Mn	Si	Co	Cr	Mo	V	Ni	Cu
Content	1.4–1.6	0.6	0.6	1.0	11.0–13.0	0.7–1.2	1.1	0.3	0.25

Table 4 Mechanical properties of AISI D2 steel

Properties	Density (kg/m^3)	Hardness (RHN)	Ultimate tensile strength (MPa)	Melting point (°C)	Thermal expansion (unit/°C)
Values	7.7×10^3	62	1736	1421	10.4×10^{-6}

diameter to pin diameter (*D/d*) is 3:1. The pin was designed into a plain cylindrical shape with length and diameter value of 9.00 mm and 7.33 mm, respectively. The chemical and mechanical properties of the tool are mentioned in Tables 3 and 4, respectively. The image of the tool with dimensions of shoulder and pin is shown in Fig. 2.

Tool Dimension	
Pin	
Length	**Diameter**
9.00 mm	7.33 mm
Shoulder	
Length	**Diameter**
43.30 mm	22.00 mm
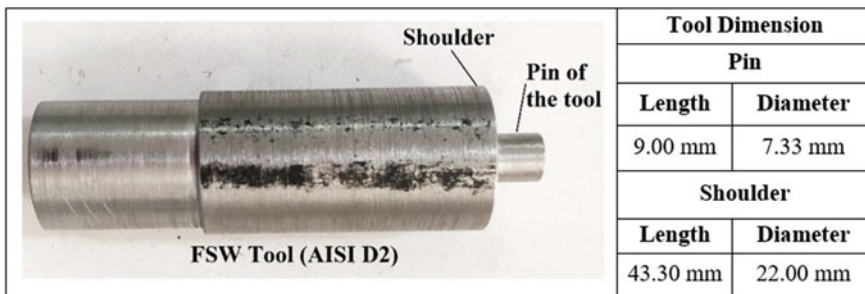
Fig. 2 FSW tool and its dimension

2.3 Experimental Procedure

The FSW was performed using an augmented vertical milling machine as a FSW machine. The specifications of the selected machine are mentioned in Table 5. The experimental setup is shown in Fig. 3.

The tool was properly machined so that it can be fitted into the chuck of the developed FSW machine. Turning operation was performed to attain the proper pin and shoulder dimensions. Once the tool was ready, it was fixed in the tool post. In addition, the Al-alloy plates were properly clamped on the table so that no movements of the adjoining edges could occur due to vibration. The developed FSW machine was, then, operated at different RPMs, and the table of the augmented milling machine was traversed with varying speeds. The selected rotational speeds of the tool and

Table 5 Specification of the augmented milling machine as a FSW setup

Spindle speed control	Variable speed pulley
Spindle taper size	NT40
Maximum RPM	5440
Minimum RPM	70
Table width	15 in.
Table length	60 in.
Horsepower	3
Phase	3
Longitudinal travel	41.34 decimal inch
Cross travel	19.69 d in.
Knee travel	23.62 d in.
Number of spindle speed	2
Voltage	415 V
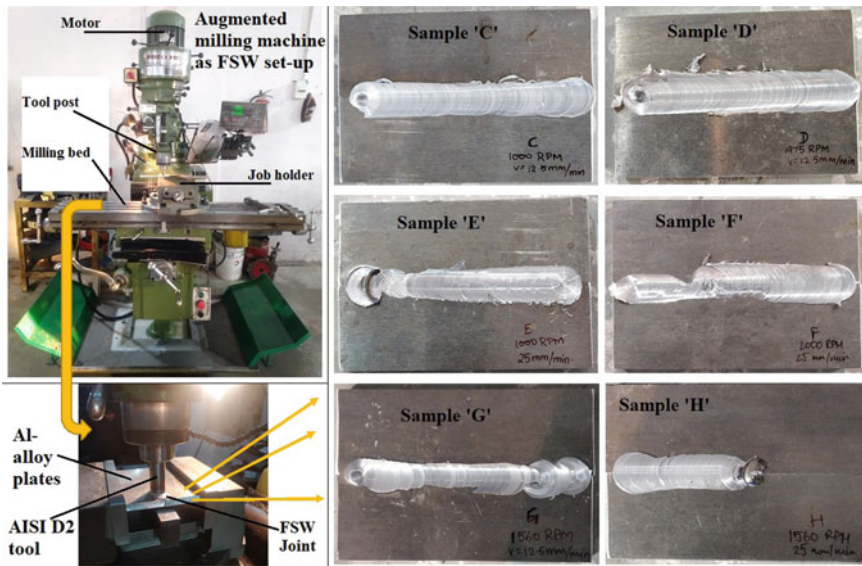
Fig. 3 FSW experimental setup; six pairs of plates were welded at different tool rotational and welding speeds

various traverse speeds are given in Table 6. As the revolving tool, which includes shoulder and pin, advances toward the abutting edges of the plates, high heat is generated due to high frictional contact. The contacting materials get soften at this high degree of frictional heat. In this condition, the pin of the tool stirs soft materials of both the abutting plates. The shoulder pressurizes plastically deformed soft materials between the plates, and hence, very less flashing effect could be seen. As soon as

Table 6 Input parameters during FSW process

S. no	Samples	Rotational speed of tool, N in rpm	Speed of table or welding speed, v in mm/min	Temperature generated due to friction, T in °C
1	Sample C	1000	25	509.90
2	Sample G	1560	25	542.66
3	Sample H	1560	45	520.78
4	Sample D	1975	25	560.88
5	Sample F	1975	45	538.27

the tool moved from leading edge to trailing edge, a very fine FS-welded joint was created. Different qualities of weld were obtained by applying various combinations of tool rotation (rpm) and welding speed (mm/min). All the welded samples are shown in Fig. 3. Initially, the FSW was performed on six pairs of plates, namely sample C, sample D, sample E, sample F, sample G, and sample H. Mainly three different rotational speeds were adopted. For samples C and E, 1000 RPM was selected. 1560 RPM was selected for samples G and H. Similarly, the tool was rotated at 1975 RPM for the samples D and F. It was noticed that the welding quality in sample E was very poor. Also, the joint bonding was too weak due to some mechanical defects during welding. Hence, the sample E was rejected for further analysis. According to different input parameters, the necessary temperature generated due to friction was, also, calculated analytically for each welding process (Table 6). The analytical expression for calculating the temperature is given in Eq. 1 [24].

$$\frac{T}{T_{\text{melt}}} = K \left[\frac{N}{v \times 10^4} \right]^{\alpha} \tag{1}$$

where T = Maximum temperature reached at given conditions, T_{melt} = Melting temperature of the material (for AA6061-T6, melting temp = 617 °C), N = Rotational speed (RPM), v = Traverse speed or welding speed (mm/min), and α = Constant (≈ 0.07), K = Constant (≈ 0.75).

2.4   Mechanical Testing and Result Analysis

To check the bonding strength and feasibility of the joint, it is important to carry out some destructive testing of the welded samples. After welding the Al-alloy plates, proper sample preparation was carried out to analyze various mechanical properties. In this work, mainly three mechanical tests were performed: Tensile testing, hardness testing, and impact testing for toughness analysis.

2.4.1 Tensile Test

For tensile testing, a digital universal tensile testing machine (INSTRON 8800 UTM) was used. The maximum load capacity of this machine is 90 kN. The specimen was tested until failure. Tensile test was performed to measure the tensile strength, maximum load, elongation, and Young's modulus. To perform the test, all the work-pieces were prepared according to specified dimensions as per ASTM E-8M standard [25]. For the purpose, wire cut electric discharge machining was used. The required dimensions for tensile testing and the images of prepared tensile specimen are shown in Fig. 4a, b, respectively. All the tests were performed at room temperature (28 °C). The rate of deformation of all the test samples was 0.0001/s. All the results obtained by tensile tests are given in Table 7. The tensile stress vs. tensile strain graphs for all the specimen are shown in Fig. 5.

According to results obtained by stress–strain graphs, it can be seen that the tensile strength (133.28658 MPa) and Young's modulus (23,215.30617 MPa) of sample C is the highest among all. Sample C was welded by lower values of input parameters, i.e., 1000 RPM and 25 mm/min welding speed. With these conditions, the maximum temperature generated in sample C is also the lowest among all. Hence, by this
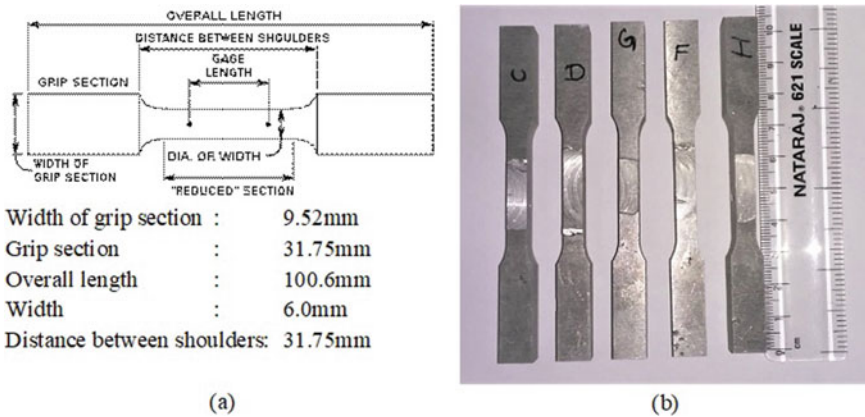

Fig. 4 **a** ASTM standard of tensile test specimen; **b** tensile test specimen taken under study

Table 7 Tensile test results

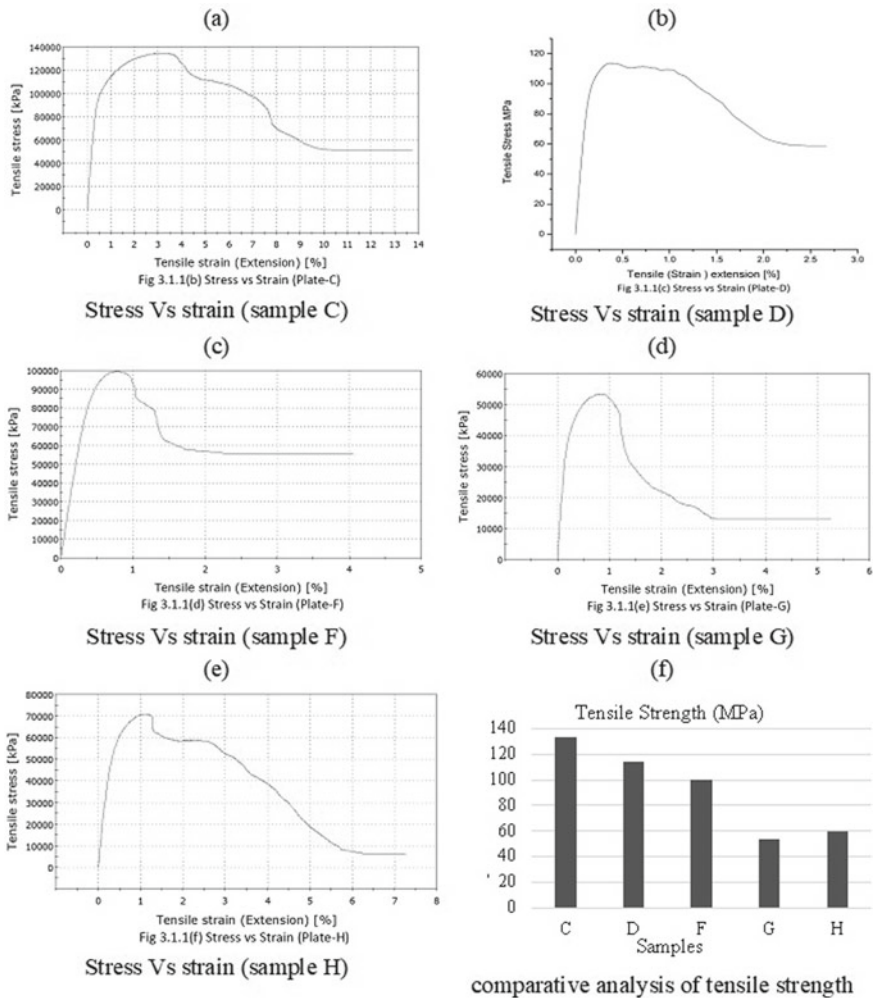| Name of plate	Tensile strength (MPa)	Maximum load (N)	Elongation (mm)	Young's modulus (MPa)
C	133.28658	10,263.06641	1.19273	23,215.30617
D	113.68954	8754.09448	2.66883	13,962.03498
F	99.57011	7666.89844	0.25486	21,551.36478
G	53.33393	4106.71240	0.27432	16,721.09878
H	58.74121	4523.07324	0.75266	14,211.85891

Fig. 5 Stress versus strain diagrams of different welded specimen; **a** sample C; **b** sample D; **c** sample F; **d** sample G; **e** sample H; and **f** comparative analysis of tensile strength among all samples

experimental results, it can be predicted that comparatively lower values of tool rotation and welding speed give higher tensile strength.

By observing the bar chart, it is clear that sample D has higher value of tensile strength. In this case, low welding speed comes out as a beneficial yield parameter for better tensile strength. In contrary, samples H and F, with higher welding speed (45 mm/min) than that of sample G (25 mm/min), are showing slight increment in tensile strength. As the tunnel defect in sample G was predominant as compared to other samples, it possesses the lowest tensile strength among all samples. With the

above analysis, it can be concluded that the tensile strength depends more on welding speed in comparison with tool rotation.

The finite element analysis of tensile test specimen was carried out in ANSYS software to compare the experimental data. By using fundamental relationships of stress and strain, i.e., strain = change in length/original length and stress = tensile force/nominal area, tension test was simulated. For the purpose, a total of 16,833 elements were selected and they were divided into 28,390 nodes. Element size was taken as 1 mm. The meshed specimen and its stress analysis are shown in Fig. 6. In simulation process, the material properties of AA6061-T6 were selected for the specimen. The maximum stress of 265.81 MPa was reported during simulation. In addition, stress was dominant at the fillet corners. In contrary, the experimental analysis showed a maximum stress of 133.28 MPa (sample C). The reasons behind difference between simulated data and experimental data are: (1) Simulation work considered single piece specimen without any joining and therefore, the effect of stress was concentrated at fillet section. (2) During experiment, some defects like improper stirring and air gaps generated which reduced the actual tensile strength of the joint.
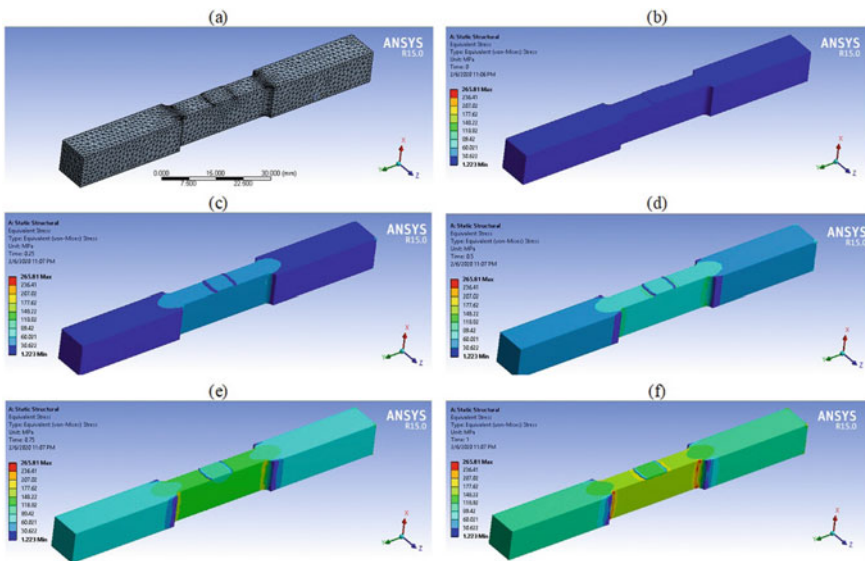

Fig. 6 Tensile test simulation of AA6061-T6 alloy (relevance = 100, relevance center: fine, element size = 1 mm, nodes = 28,390, elements = 16,833): **a** Meshing of the standard sized specimen; **b–f** tension test has been captured in five different frames

Table 8 Impact test results

Sample	Initial energy (E_1) in Joule	Residual energy (E_2) in Joule	Absorb energy or energy required to break the specimen ($E_2 - E_1$) in Joule
C	4	140	136
D	4	86	82
F	4	42	38
G	4	22	18
H	4	38	34

2.4.2 Impact Test (Toughness Test)

The toughness test was performed by Charpy impact method. This test consists of breaking the specimen by a single blow from swinging hammer under prescribed test conditions. The test piece is simply supported at the two ends. The energy absorbed is determined by striking the specimen with a hammer at the center from which the impact value is obtained. Initially, the hammer was released freely without keeping the sample. It is required to know the error of the manual impact test machine. It was found that there was an error of 4 J in the machine. For all the samples, the impact test results are written in Table 8. The test setup and tested samples are shown in Fig. 7a, b.

The toughness test uncovers the fact that how much energy is getting absorbed in the material before fracture. In other words, it is also a measure of ductility with strength. In this work, this test was performed to check the toughness of FS-welded joints in all the samples. From Fig. 7c, it can be noted that the highest value of toughness, i.e., 136 J belongs to sample C, whereas the sample G possesses the lowest toughness of 18 J. It is important to note that proper mixing of materials at stirring zone plays a vital role to determine the toughness of the welded sample. If the tunnel defects are predominantly available inside the WZ, the toughness becomes greatly reduced. The sample G was welded with the tool rotation and welding speed of 1560 RPM and 25 mm/min, respectively. On the basis of macroscopic observation, a higher degree of tunnel defects was found in sample G. With this comparatively higher dimension of void formation, the impact toughness of sample G was greatly affected. Hence, for this study, it can be reported that lower welding speed tends to enhance the toughness if tunnel defects are negligible.

2.4.3 Hardness Test

Hardness of the materials was checked in various locations of the FS-welded plates. Hardness test imparts an indenter which is allowed to penetrate the specimen under a specific loading condition for a fixed period of time. Hardness of the material comes out as a result of resistance to penetration. In this work, Rockwell hardness
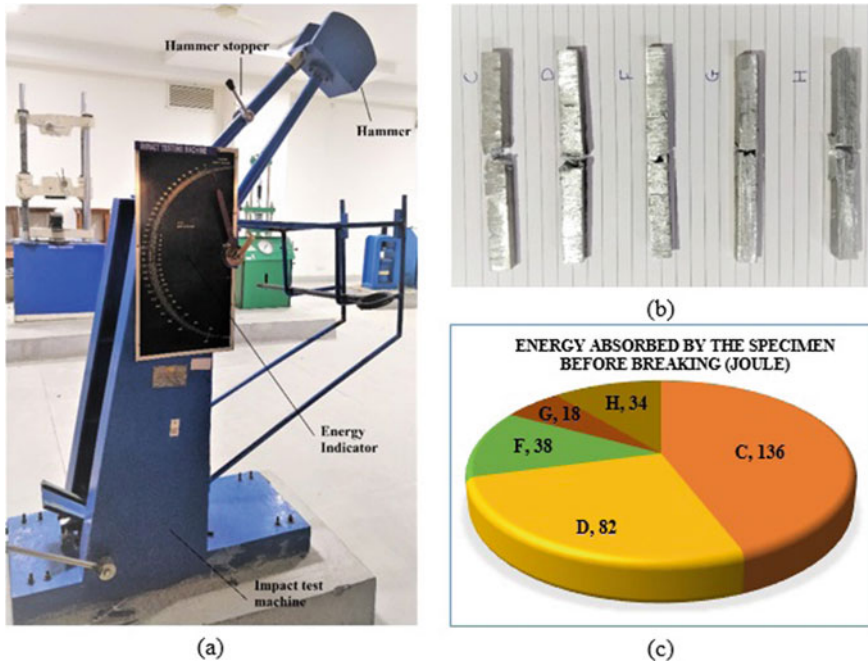
Fig. 7 Charpy impact test of welded specimen; **a** Impact test machine; **b** tested specimen; **c** comparative analysis of energy absorbed by different samples

test method was taken under study. It includes a ball indenter, called "Brale" by its trade name, of diameter 1/16″ to make the indentation. This test was carried out on the cross sectional area of the samples. For the purpose, the welded plates were cut along the breadth and the cut section was smoothened properly prior to indentation. A load value of 150 kgf was selected for each indentation. In each plate, multiple indentations were performed starting from the weld center line to both sides of the plate. A fixed gap of 2 mm was kept between two consecutive indentations. Hence, excluding the center point, there were total nine indentations on both the sides of the weld center line. In this way, all the necessary zones, i.e., WZ, TMAZ, HAZ, and PM were undergone through hardness test. A comparative analysis of hardness variation from weld center line to parent metal is shown in Fig. 8a. Also, all the tested samples are shown in Fig. 8b.

By the hardness profile from −18 mm to +18 mm distance in each plate, it can be seen that all the samples show a similar trend of variation (Fig. 7a). Hardness values are the lowest at the center point (0) or WZ in all the welded samples. At a very little distance (−3 and +3 mm) from center point, there is a slight increment in hardness in all the samples except D. This zone, where hardness gets slightly enhanced, is near about TMAZ. Since this zone is just aside of the welded zone, the effect of strain hardening makes it comparatively harder. At some more distance, 4–6 mm on both side from center point, hardness values are suddenly decreased. These zones are
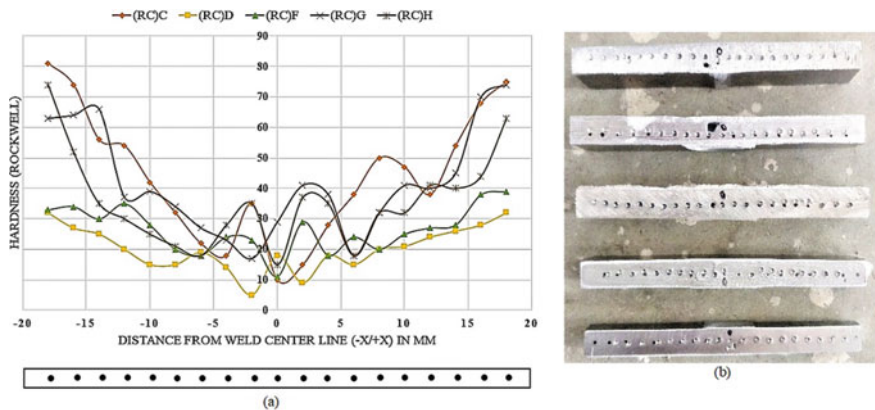
Fig. 8 Hardness test; **a** A comparative graph showing hardness variations in different points of the welded plates; **b** five plates used for hardness analysis

pertaining to HAZ which become the weakest part on hardness basis. The PM part is clamped properly so that no movement can happen during welding. When high degree of friction creates plastic deformation into abutting edges, the HAZ (available between WZ and PM) faces a high degree of shocks and vibrations during FSW. This causes decrease in hardness in HAZ. As the indentation moves away from HAZ, high hardness is achieved in all the samples. In other words, hardness of PM parts of all the samples is higher than other parts. In comparison with other samples, sample C was reported to possess higher hardness at all the points whereas the lowest hardness was reported in sample D in every point of study.

2.5   Microscopic Characterization

For microstructural study, the samples were cut across the welded zone. The cross sectional area of the samples was highly polished as the microstructural observation was carried out on this surface. For this purpose, different grades of polishing papers (grit size of 100, 500, and 1000) were used. After polishing the samples, Keller's etch (distilled water 190 ml + nitric acid 5 ml + hydrochloric acid 3 ml + hydrofluoric acid 2 ml) was applied on the polished surfaces. After proper etching, the samples were observed through an optical microscope *Motic Images Plus 3.0(×64)* make Germany. Mainly three regions were taken under consideration: welded zone (WZ); heat affected zone (HAZ); and parent metal part (PM). All the microstructural images of five welded samples, i.e., C, D, F, G, and H are shown in Fig. 9a–e, respectively. As the present study does not include mapping of the microstructures, it is very hard to comment on the grain size and related properties of the microstructures. However, by observing the microstructural images, it can be concluded that all images follow a similar trend. As the material mixing was done in WZ, clear differences between

microstructural appearance in WZ and PM could be observed. In the WZ area, lots of pores and crack-like structures were observed because the material mixing at the stirring zone was not up to the mark. Application of plain tool, rather than threaded tool, was the main reason behind this issue. It is contrary with the results obtained by Lorrain et al. [26].
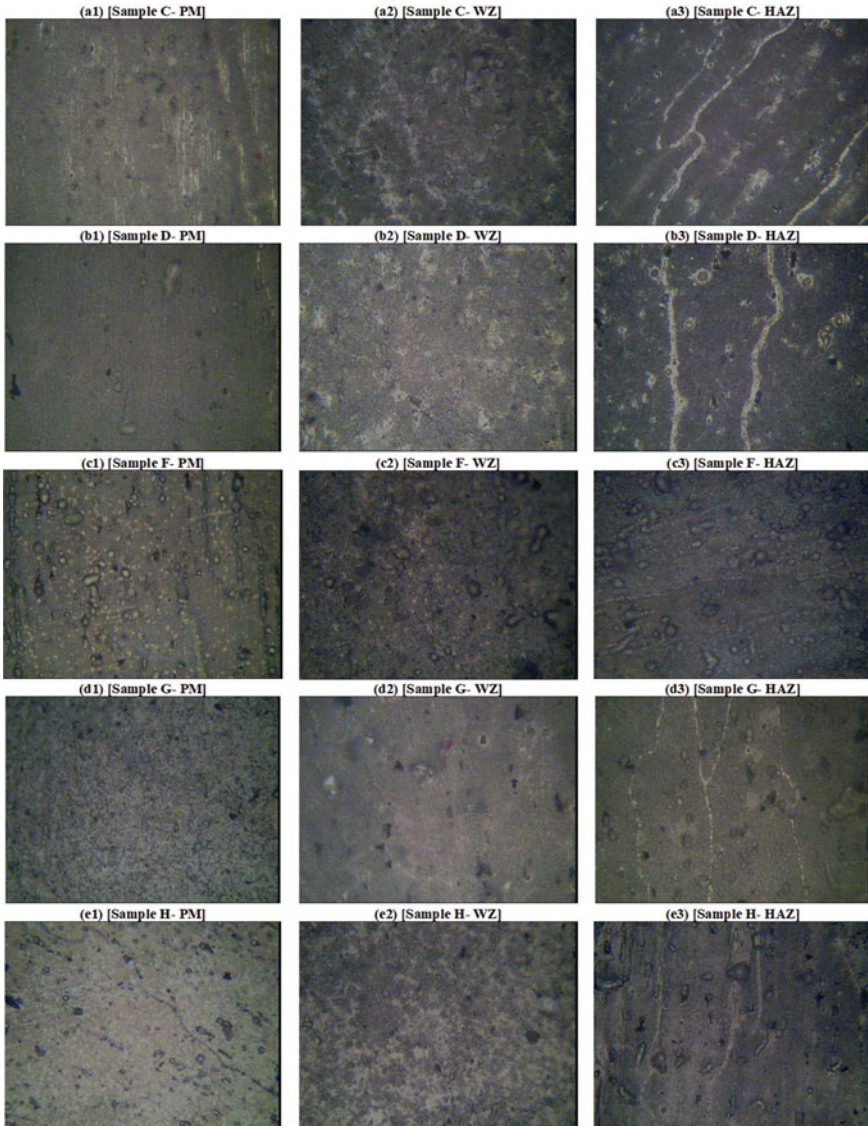

Fig. 9 Microstructures of the FS-welded plates; All the five samples were observed in three different zones-parent metal part (PM), welded zone (WZ), and heat affected zone (HAZ)

With regard to HAZs, all the images can be easily recognized in comparison with PM and WZ. Like observations done in WZ, a similar trend exists in the microscopic image of the HAZ. White colored dendritic structures were reported in HAZs of the samples. These structures are defects due to residual stresses generated during welding. The formation of these white structures depends on welding speed. As two different welding speeds, i.e., 25 and 45 mm/min were selected in this study, it was found that lower welding speed (25 mm/min) is responsible for defects in HAZ. Therefore, whitish structures are predominant in samples 'C', 'D', and 'G', whereas samples 'F' and 'H' do not show such defects as they were welded at higher welding speed (45 mm/min).

3 Discussion

According to this work, the main problem with FSW was reported as insignificant mixing of the joining metal parts. In previous studies, it was concluded that improper mixing caused reduction in metallurgical bonding and thereby a lot of defects come into picture [3, 4, 27, 28].

In the field of defect analysis of FS-welded joints, Podrzaj et al. (2015) reported a number of damage behavior, such as tunnel formation, pores and voids generation, grooves formation on surface, high weld flash, cavity produced by abnormal stirring, surface galling, nugget collapse, and kissing bond [27]. These defects may be caused by individual or joint effects of yield parameters, such as tool rotation, traverse speed, high heat generation, D/d ratio, pin length, and pin profile. In the present work, tunnel defect or void formation was found in all the samples except sample 'C'. This result is similar to the work of Zhao et al. (2019) [28]. The most probable reason behind void formation defect is plain pin profile. As the pin was selected as plain cylindrical projection, additional stirring, and thereby mixing were prevented. As a result, the cavity formed at one position was carry forward till trailing edge of the abutting plates. *Bulging out of edge* and *pin collapsing* are the two different defects which were reported in this study. The trailing edges of the Samples 'C' and 'D' were found to get *bulged out* due to excessive plastic deformation. In sample 'H', *pin collapsing* was reported due to high heat generation during welding. Due to this defect, pin gets adhered to the plastically deformed stirred zone (Fig. 10).

The present research work imparts a primary analysis as compare to other works of similar kind. Even after a number of research work in the field pf FSW, a lot of problems are existing [29]. A detailed analysis consisting of load value calculation, pin profile variation, analysis to nullify the defects, etc., are required to carry out in the future.
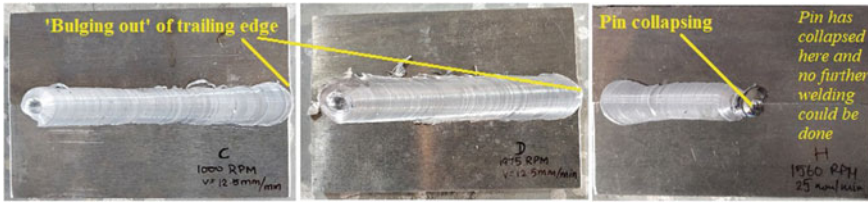
Fig. 10 Defects found in FS-welded samples; *Bulging out* trailing edges in samples C and D; *Pin collapsing* in sample H

4 Conclusion

An attempt was made to carry out FSW of Al 6061-T6 alloys and to analyze the joint characteristics on the basis of mechanical properties measurement and microstructural assessment. Tensile test, hardness test, and toughness test were considered under the mechanical property analysis. The following points are concluded by this research work:

- An augmented vertical milling machine was used as a FSW machine. A successful welding of five pairs of plates named sample C, sample D, sample F, sample G, and sample H was performed by using AISI D2 (HSS) as a FSW tool with plain cylindrical pin. Tool rotation and welding speed were selected as variable input parameters. Three different rotations, 1000, 1560, and 1975 RPM were applied on the tool. Two different welding speeds were 25 and 45 mm/min. In addition, the maximum temperature generation in each sample was obtained by analytical approach. The highest and the lowest temperatures were obtained in sample D (560.88 °C) and sample C (509.90 °C), respectively.
- The tensile strength (133.28658 MPa) and Young's modulus (23,215.30617 MPa) of sample C was higher than other samples. It was seen that comparatively lower values of input parameters, i.e., 1000 RPM of tool, 25 mm/min of welding speed and 509.90 °C of temperature were responsible for higher tensile strength of the joint. In addition, it is also concluded that welding speed greatly influences the tensile strength.
- The Charpy impact test was performed to measure the toughness of the samples. The toughness value of sample C, i.e., 136 J, was higher than other samples. Sample G possessed the lowest toughness of 18 J. A high degree of tunnel defects in sample G inversely affected the toughness. If the formation of tunnel defect is avoided, toughness is found to enhance with a decrease in welding speed.
- On the basis of hardness test, a similar trend of hardness profile in all the samples was observed. Starting from weld center point to parent metal part, a zig-zag profile of hardness was obtained. The lowest hardness was obtained in weld center point. An increment in hardness was observed in TMAZ, whereas a sudden decrement in hardness was noted in HAZ. Finally, hardness reached to comparatively higher

values in PM zone in all the samples. Among all, sample C was found to possess higher hardness at every indentation of the test.

- The microstructural images of three zones, WZ, HAZ, and PM zone showed three different characteristics. The grain appearance in WZ and HAZ could be easily recognized. In the WZ, the material mixing was reported with some defects like cracks and pores. These defects are indication of insignificant stirring. In the HAZ, defects in white colored dendritic structures were reported. The most probable reason behind these phenomena was residual stress generation. It is concluded that these defects are negligible at higher welding speeds.

By observing all the data discussed above, it can be established that welding speed predominates the weld quality when compared to rotational speeds.

References

1. Thomas WM, Nicholas ED, Needham JC, Murch MG, Temple-Smith P, Dawes CJ (1991) Friction-stir butt welding. GB Patent No. 9125978.8, International patent application No. PCT/GB92/02203
2. Jene T, Dobmann G, Wagner G, Eifler D (2008) Monitoring of the friction stir welding process to describe parameter effects on joint quality. Weld World 52:47–53
3. Shankar S, Saw K, Chattopadhyaya S, Hloch S (2018) Investigation on different type of defects, temperature variation and mechanical properties of friction stir welded lap joint of aluminum alloy 6101–T6. Mater Today: Proc 5:24378–24386
4. Kumar R, Bora B, Chattopadhyaya S, Krolczyk G, Hloch S (2018) Experimental and mathematical evaluation of thermal and tensile properties of friction stir welded joint. Int J Mater Product Technol 57(1/2/3):204–229
5. Kumar R, Chattopadhyaya S, Dixit AR, Bora B, Zelenak M, Foldyna J, Hloch S, Hlavacek P, Scucka J, Klich J, Sitek L (2017) Surface integrity analysis of abrasive water jet-cut surfaces of friction stir welded joints. Int J Adv Manuf Technol 88:1687–1701
6. Silva-Magalhães A, De Backer J, Martin J, Bolmsjö G (2019) In-situ temperature measurement in friction stir welding of thick section aluminium alloys. J Manuf Process 39:12–17
7. Lin H, Wu Y, Liu S, Zhou X (2018) Effect of cooling conditions on microstructure and mechanical properties of friction stir welded 7055 aluminium alloy joints. Mater Charact. https://doi.org/10.1016/j.matchar.2018.04.029
8. Sashank JS, Sampath P, Krishna PS, Sagar R, Venukumar S, Muthukumaran S (2018) Effects of friction stir welding on microstructure and mechanical properties of 6063 aluminium alloy. Mater Today: Proc 5:8348–8353
9. Dawood HI, Mohammed KS, Rajab MY (**2014**) Advantages of the green solid state FSW over the conventional GMAW process. Adv Mater Sci Eng 10, Article ID 105713. https://doi.org/10.1155/2014/105713
10. Carlone P, Palazzo GS (2013) Influence of process parameters on microstructure and mechanical properties in AA2024-T3 friction stir welding. Metall Microstruct Anal 2:213–222
11. Saravanan V, Rajakumar S, Muruganandam A (2016) Effect of friction stir welding process parameters on microstructure and mechanical properties of dissimilar AA6061-T6 and AA7075-T6 aluminum alloy joints. Metall Microstruct Anal. https://doi.org/10.1007/s13632-016-0315-8
12. Rodriguez RI, Jordon JB, Allison PG, Rushing T, Garcia L (2015) Microstructure and mechanical properties of dissimilar friction stir welding of 6061-to-7050 aluminum alloys. Mater Des 83:60–65

13. Guo JF, Chen HC, Sun CN, Bi G, Sun Z, Wei J (2014) Friction stir welding of dissimilar materials between AA6061 and AA7075 Al alloys effects of process parameters. Mater Des 56:185–192
14. Sinhmar S, Dwivedi DK (2019) Effect of weld thermal cycle on metallurgical and corrosion behavior of friction stir weld joint of AA2014 aluminium alloy. J Manuf Process 37:305–320
15. Xu W, Liu J, Zhu H, Fu L (2013) Influence of welding parameters and tool pin profile on microstructure and mechanical properties along the thickness in a friction stir welded aluminum alloy. Mater Des 47:599–606
16. Peel M, Steuwer A, Preuss M, Withers PJ (2003) Microstructure, mechanical properties and residual stresses as a function of welding speed in aluminium AA5083 friction stir welds. Acta Mater 51:4791–4801
17. Ma YE, Xia ZC, Jiang RR, Li WY (2013) Effect of welding parameters on mechanical and fatigue properties of friction stir welded 2198 T8 aluminum-lithium alloy joints. Eng Fract Mech 114:1–11
18. Trimble D, O'Donnell GE, Monaghan J (2015) Characterisation of tool shape and rotational speed for increased speed during friction stir welding of AA2024-T3. J Manuf Process 17:141–150
19. Liu F, Fu L, Chen H (2018) High speed friction stir welding of ultra-thin AA6061-T6 sheets using different backing plates. J Manuf Process 33:219–227
20. Ambroziak A, Korzeniowski M, Kustron P, Winnicki M, Sokolowski P, Harapinska E (**2014**) Friction welding of aluminium and aluminium alloys with steel. Adv Mater Sci Eng 2014:15, Article ID 981653. https://doi.org/10.1155/2014/981653
21. Viscusi A, Astarita A, Prisco U (**2019**) Mechanical properties optimization of friction stir welded lap joints in aluminium alloy. Adv Mater Sci Eng 2019:9, Article ID 3832873. https://doi.org/10.1155/2019/3832873
22. Anganan K, Prabagaran S, Muthukrishnan M (2018) Experimental study and analysis of the wear properties of friction-stir-welded AA-T6 and A384.0-T6 dissimilar aluminium alloys of butt joints. Mater Technol 52(2):201–205
23. Palani K, Elanchezhian C, Avinash K, Karthik C, Chaitanya K, Sivanur K, Reddy KY (2018) Influence of friction stir processing parameters on tensile properties and microstructure of dissimilar AA 8011-H24 and AA 6061-T6 aluminum alloy joints in Nugget Zone. IOP Conf Ser: Mater Sci Eng 390:012108
24. Bisadi H, Tavakoli A, Sangsaraki MT, Saragaraki KT (2013) The influences of rotational and welding speeds on microstructures and mechanical properties of friction stir welded Al5083 and commercially pure copper sheets lap joints. Mater Des 43:80–88
25. ASTM E8M-13: Standard test methods for tension testing of metallic materials. http://www.galvanizeit.com/uploads/ASTM-E-8-yr-13.pdf. (Date of access: 10 Feb 2020)
26. Lorrain O, Favier V, Zahrouni H, Lawrjaniec D (2010) Understanding the material flow path of friction stir welding process using unthreaded tools. J Mater Process Technol 210(4):603–609
27. Podrzaj P, Jerman B, Klobcar D (2015) Welding defects at friction stir welding. Metalurgija 54(2):387–389
28. Han J, Domblesky JP, Yang Z, Li Z, Liu X, Zhao Y (2019) Investigation of void formation in friction stir welding of 7N01 aluminum Alloy. J Manuf Process 37:139–149
29. Arab MA, Zemri M, Blaoui MM (2018) Experimental Investigation on the effect of tool rotational speed on mechanical properties of AA6082-T6 friction stir-welded butt joints. J Fail Anal Prev 18:1625–1630

Chapter 17
Microstructure, Tribology, and Corrosion Characteristics of Hot-Rolled AZ31 Magnesium Alloy

R. Lokesh Kumar, B. G. Yashwanth Kumar, R. Vaira Vignesh, J. Kaasi Viswanath, M. Muralimanokar, Shabbir Memon, and M. Govindaraju

1 Introduction

The principal lightweight alloys that are widely utilized in aircraft, aerospace, automotive, and structural applications include aluminum alloys and magnesium alloys. Aluminum alloys are the preferred choice of materials for structural applications, because of their high strength-to-weight ratio. However, magnesium alloys have a lesser density than aluminum alloys. Hence, aircraft and automotive industries have been replacing aluminum alloys with magnesium alloys to achieve light-weighting of structures. Magnesium alloys also have high strength-to-weight ratio, high stiffness to weight ratio, good formability, machinability and castability, and excellent damping characteristics. Some of the magnesium alloys like AE42 are used for high-temperature applications [1]. Hence, magnesium alloys play an important and useful role in developing components with good mechanical properties [2].

Typically, engine blocks, casings, seat frames, wheels, support brackets in clutches and brakes, and transmission housings in automotive are made of magnesium alloys. Besides, magnesium alloy sheet metal is utilized in seating frames, door frames, pedals, steering wheel, and manifolds to reduce the curb-weight of automotives. In addition, magnesium alloys also provide more vibrational damping than conventional

R. Lokesh Kumar · B. G. Yashwanth Kumar · R. Vaira Vignesh (✉) · J. Kaasi Viswanath · M. Muralimanokar · M. Govindaraju
Department of Mechanical Engineering, Amrita School of Engineering, Amrita Vishwa Vidyapeetham, Coimbatore, India
e-mail: r_vairavignesh@cb.amrita.edu

M. Govindaraju
e-mail: m_govindaraju@ch.amrita.edu

S. Memon
Department of Mechanical Engineering, Wichita State University, Wichita, KS, USA
e-mail: sxmemon@shockers.wichita.edu

materials. Hence, usage of magnesium alloys in automotive reduces fuel consumption and hence emissions. However, the high activity of magnesium results in a high corrosion rate.

Conventionally, magnesium is alloyed with various alloying elements to form magnesium alloys with desired properties. Magnesium is alloyed with Al, Zn, Si, Cu, Mg, and rare earth metals [3, 4]. AZ91, AZ31, AM50, Elektron 21, ZK51, and WE54 are some of the prominent magnesium alloys. AZ31 is one of the most used magnesium alloys in the automotive sector. AZ31 alloy has 3% aluminum, 1% zinc, and the rest magnesium. AZ31 alloys are lightweight, durable, and easily formable. They also have high tensile strength and vibrational damping [5]. Generally, AZ31 alloys are heat-treated for improvising the microstructure and mechanical properties [6]. However, wear resistance and corrosion resistance of AZ31 alloy could not be improved by heat treatment methods [7].

Rolling is one of the several adopted methodologies to enhance the mechanical properties of AZ31 alloy [8]. Rolling of AZ31 alloy is challenging, as magnesium has an HCP crystal structure. A hexagonal structure has basal slip as its dominant slip system. A basal slip system has only two independent modes. According to the von Mises criterion for the deformation, a uniform deformation requires five slips at room temperature. Since magnesium has a basal slip system that has only two slips, the von Mises criterion is undue. Hence, it is very difficult to deform AZ31 alloy at room temperature. The alloy breaks instead of deforming during cold rolling [9].

As cold rolling of AZ31 alloy is challenging, the hot rolling technique can be employed. Hot rolling activates additional slip systems and thereby providing sufficient ductility for deformation. Besides, hot rolling mechanically fragments the secondary intermetallic phase (β-$Mg_{17}Al_{12}$) and induces dynamic recovery and dynamic recrystallization [10]. This, in turn, is metallurgically advantageous, as refined grains with homogeneous dispersion of β-$Mg_{17}Al_{12}$ are achieved. Hence, the hot-rolled AZ31 alloy would have augmented mechanical, tribological, and corrosion properties. In the course of hot rolling AZ31 alloy, oxidation may deteriorate the material properties. Hence, precautionary steps must be taken to curb the oxidation effects. A brief overview of the research work carried out on hot rolling of AZ31 alloy is discussed below.

Vespa et al. [11] performed hot rolling on magnesium alloy AZ31. The microstructure obtained was of two types: partially recrystallized state (banded structure of fine equiaxed grains with few pancaked grains) and recrystallized state (coarser equiaxed grains without banding or pancaked grains). After hot rolling, the sheets were subjected to a tensile test at a temperature range of 573–723 K at a strain rate from 0.1 to 0.001 s^{-1}. The grain boundary sliding was observed at 723 K and a strain rate of 0.001 s^{-1}. Dynamic recrystallization was observed at 673 K and a strain rate of 0.1 s^{-1}. Miao et al. [12] also performed the same study. The microstructure revealed that the grain size was reduced to about 5 μm after five rolling passes attributed to dynamic recrystallization. The yield strength, tensile strength, and tensile fracture strain were improved from 200 MPa, 268 MPa, and 0.32 to 211 MPa, 280 MPa, and 0.28, respectively, after five rolling passes.

Jager et al. [13] performed hot rolling in magnesium alloy AZ31 sheets. The microstructure revealed non-uniform grain size (average grain size of 53 μm) distribution with the presence of twins. The tensile strength of the hot-rolled specimens was decreased to 14 MPa at 623 K, whereas 343 MPa was obtained at room temperature. The ductility of the material increased to 420% at 673 K. The tensile strength dependency on temperature was attributed to the activity of the non-basal slip system and dynamic recovery. It is seen that Zhang et al. [14] performed hot rolling at 593 K on AZ31 magnesium alloy and observed formability. The microstructure revealed fine grains after the rolling process. Limit drawing ratio (LDR) and limit dome height (LDH) were used to measure material draw-ability and stretch-ability, respectively. A maximum LDR of 2.65 was obtained at 473 K, and a maximum LDH of 10.8 mm was obtained at warm working conditions. AZ31 alloy showed good deep draw-ability and poor stretch-ability. This was also researched by Choi et al. [15] and Jiang et al. [16].

Similarly, Huang et al. [17] performed rolling at a high temperature at 823 K followed by warm rolling at 498 K and observed the stretch formability improvement. The Erichsen value, which is the quality index of forming process, was increased from 3.7 to 9.5. The good formability was obtained as a result of hot rolling and the weak basal texture with a largely tilted basal pole caused by static recrystallization. Sun et al. [18] performed a hot rolling operation on AZ31 magnesium alloy and observed mechanical properties and texture evolution at 673 K. The microstructure of as-rolled specimens revealed twins and as-received specimens contained coarse grains. During hot rolling, the basal texture intensity showed a decreasing trend with an increase in deformation ratio. While low strain hot rolling, a strong texture {0002} <10–10> was developed. At intermediate strain hot rolling, a double peak-type basal structure was seen. In large strain hot rolling, a weak type texture {0002} <11–20> was formed. The properties tend to vary concerning the change in basal texture. This study was also performed by Jin et al. [19], Kim et al. [20], and Tighiouret [21].

Fatemi-Varzaneh et al. [22] performed hot rolling in AZ31 magnesium alloy at three variant temperatures 573, 648, and 723 K followed by the evaluation of mechanical properties at room temperature. The microstructure of the rolled specimens revealed the presence of homogeneously distributed grains (with an average grain size of 5 μm). From the shear punch test and uniaxial tensile reports, it was evident that lower rolling temperature and higher rolling strain had an impact on strength and ductility at room temperature. Similarly, Miao et al. [23] performed rolling at 433–523 K in AZ31 magnesium alloy followed by annealing. The microstructure revealed fine grains of size 2.8 μm. Dynamic recrystallization occurred in sheets temperature above 473 K and temperature below 473 K required annealing to obtain fine recrystallized grains. The yield strength obtained was 350 MPa, and the elongation was about 35% in the hot-rolled specimen.

Bohlen [24] performed hot rolling on AZ31 magnesium alloy and observed acoustic emission during tensile testing. The microstructure of the sheet revealed a large number of residual stresses and lattice defects. The acoustic emission showed a better correlation with stress–strain curves, which revealed a sharp peak close to the macroscopic yield point followed by a decrease in acoustic emission activity.

The dislocation glide and deformation twinning were the mechanisms responsible for plastic deformation and corresponding acoustic emission. Kawalla et al. [25] fabricated AZ31 alloy by twin-roll casting followed by hot rolling. The microstructure of twin-roll cast alloy revealed large dendritic columnar grains with some fine grains near the surface and in the mid-thickness of the strip. The intermetallics were present in the inter-dendritic region. The average yield strength of 200 MPa, the average tensile strength of 270 MPa, and ductility in the range of 20–25% elongation were obtained.

Wang et al. [26] fabricated magnesium alloy by squeeze casting method and further processed by hot rolling at 643 K and equal channel angular pressing (ECAP). The microstructure of hot-rolled specimens revealed an equiaxed microstructure. The grain refinement caused by hot rolling improved fatigue resistance, corrosion resistance (from 0.87 to 0.74 μm/day), and endurance limit (from 40 to 95 MPa). ECAP leads to deterioration of desired properties because of textural softening. Similar to AZ31 alloy, the AZ91 alloy also showed good texture evolution properties [27]. Chang et al. [28] fabricated an AZ31 magnesium alloy sheet using asymmetric hot extrusion at 673 K. The microstructure showed fine grains with some gradient in grain size and the texture was distributed in-homogeneously throughout the thickness. Nene et al. [29] performed hot rolling at 573 K in ultra-light Mg–4Li–1Ca (LC41) and observed the refinement in the microstructure. The microstructure revealed grain refinement up to 5 μm and the presence of fine dispersed eutectic phases. The specific strength obtained was 142 kN m/kg, and the bio-corrosion resistance was found to be improved in simulated body fluid ($R_p = 0.266$ k ohm cm^2). The improved corrosion resistance was also seen on AZ91 alloy studies in simulated body fluids [30, 31]. Bio-corrosion studies on other magnesium alloys also proved bio-corrosion resistance [32, 33].

From the above literature, it is evident that hot rolling is an efficient technique to improve the microstructure and strength of AZ31 alloy. The rolled magnesium implants showed good resistance to bio-corrosion. The influence of rolling temperature on tribological and corrosion properties of the hot-rolled AZ31 magnesium alloy is seldom discussed in the open literature. Hence, studies on sliding wear and saltwater immersion corrosion properties of hot-rolled AZ31 alloy become essential. In this present work, the AZ31 alloy is hot-rolled at three temperature variants of 150, 300, and 400 °C. The influence of rolling temperature on the microstructural evolution and hence the microhardness, sliding wear, and corrosion rate of the AZ31 alloy are analyzed. The manuscript also includes a comprehensive analysis of the wear mechanism and corrosion mechanism of the specimens.

Table 1 Chemical composition of AZ31 magnesium alloy (wt%)

Element	Mg	Al	Zn	Mn	Si	Fe	Cu	Ni
% Composition	Bal	3.3	1.1	0.25	0.6	0.007	0.01	0.0005

Table 2 Fabricated specimens at different conditions

Sl	Workpiece nomenclature	Fabrication
1	BM	Normal as-cast AZ31 alloy
2	HR1	AZ31 alloy hot-rolled at 150 °C
3	HR2	AZ31 alloy hot-rolled at 300 °C
4	HR3	AZ31 alloy hot-rolled at 400 °C

2   Materials and Methods

2.1   Material

Cast magnesium alloy AZ31 plate of dimension $150 \times 50 \times 4$ mm was used for rolling studies. The chemical composition of AZ31 alloy was obtained using optical emission spectroscopy, and the composition is given in Table 1.

2.2   Hot Rolling

The workpiece of dimension $150 \times 50 \times 4$ mm was cleaned, and the grease was removed using acetone before the hot rolling process. The workpieces were hot-rolled in a 2-high rolling mill setup that is available at Amrita Vishwa Vidyapeetham. The rolling mill setup was operated at speed of 200 rpm. The workpiece was heated in the furnace at the specific temperature (150, 300, and 400 °C) and was immediately rolled by passing through the gap between the rollers. The workpiece was hot-rolled for multiple passes until the desired thickness of 3.5 mm was achieved. After the rolling process, the workpiece was allowed to cool at room temperature. Table 2 shows the nomenclature of the specimens that were rolled at the various temperatures.

2.3   Microstructure

The rolled workpieces were cut along the transverse section and mounted using a cold setting compound. The specimens were prepared according to the standard ASTM E3-11. The specimens were ground using 400, 600, 800, and 1000 grit emery papers. Then, a mirror polish was obtained by using a disk polisher containing velvet

cloth and alumina colloidal suspension. The polished specimens were cleaned using acetone and etched using acetic picral solution (4.2 g picric acid, 10 ml acetic acid, and 10 ml distilled water, and 70 ml ethanol) for 30 s. The microstructure was observed in an optical microscope (Make: Carl Zeiss; Model: Axiovert 25).

2.4 Microhardness

The hot-rolled specimens (HR1, HR2, and HR3) along with base material were prepared as per the standard ASTM E3-11. The Vicker's microhardness was measured using a microhardness tester with a diamond intender (Make: Mitutoyo, Model: MVK-H1) as per ASTM standard E384. The load applied was 0.981 N (100 gf) for a period of 15 s. The hardness was measured at five different locations, and the average microhardness was reported for each specimen.

2.5 Tribological Characterization

The specimens of dimension 10×10 mm were cut from the rolled workpiece. The specimens were polished as per the standard ASTM E3-11. The specimens were mounted in a cylindrical tube of dimension φ 12 mm and length 50 mm using a cold setting compound. The wear rate was determined using a pin-on-disk apparatus (Make: DUCOM, Model: TR20LE). The specimen surface was degreased with acetone and weighed using a precision weighing balance with the least count of 0.0001 g.

The sliding wear rate was calculated for certain parameters like the velocity of 0.6 m/s, the rotating disk speed of 50 rpm, a varying load of 1, 1.5, and 2 kg, and a duration of 16 min 36 s (996 s). The wear rate of the specimens was calculated from Eq. (1), respectively.

$$\text{Wear Rate} = \frac{\Delta M}{L \times \text{SD}} \tag{1}$$

where ΔM is a mass loss, L is the load applied, and SD is the sliding distance.

2.6 Corrosion Testing

The specimens of dimension 10×10 mm were cut from the base material and hot-rolled workpieces. The specimens were polished as per the standard ASTM E3-11. The specimens were cleaned and were degreased with ethanol. The immersion corrosion test was conducted as per ASTM G31-72 standard. The specimens were

weighed using a precision balance of resolution 0.0001 g. The immersion tests were performed in the artificial seawater solution (3.5% of NaCl solution). The artificial seawater solution was prepared by mixing 3.5 g of NaCl in 100 ml of distilled water. The temperature of the solution was maintained using a water bath, fitted with a digital temperature controller. After the immersion period, the specimens were ultrasonicated in 15 ml ethanol for 3 min to remove the corrosion products. The specimens were allowed to dry and weighed in precision balance to calculate the mass loss. The corrosion rate was calculated using Eq. (2).

$$\text{Corrosion rate} = \frac{K \times \Delta M}{A \times T \times D} \tag{2}$$

where $K = 8.76 \times 10^{-4}$, ΔM is mass loss, A is surface area, T is time, and D is the material density.

2.7 Surface Morphology, Elemental Analysis, and TEM Analysis

The surface morphology of the worn-out and corroded specimens was observed using a high-resolution scanning electron microscope (FE-SEM) (Make: Zeiss Sigma). The elemental composition analysis of the worn-out and corroded specimens was carried out using an energy-dispersive X-ray electron spectroscope (Make: Bruker). Conventional metallurgical preparation techniques followed by ion beam etching were performed to prepare specimens for high-resolution transmission electron microscope analysis (TEM). The images observed through TEM were analyzed using CrysTBox analytical software.

3 Results and Discussion

3.1 Hot Rolling

The AZ31 alloy plate was hot-rolled at 150 °C (HR1), 300 °C (HR2), and 400 °C (HR3). A 12.5% reduction in specimen thickness (4–3.5 mm) was achieved in four passes. The microstructural evolution, tribological, and corrosion characteristics of the specimens are discussed below.
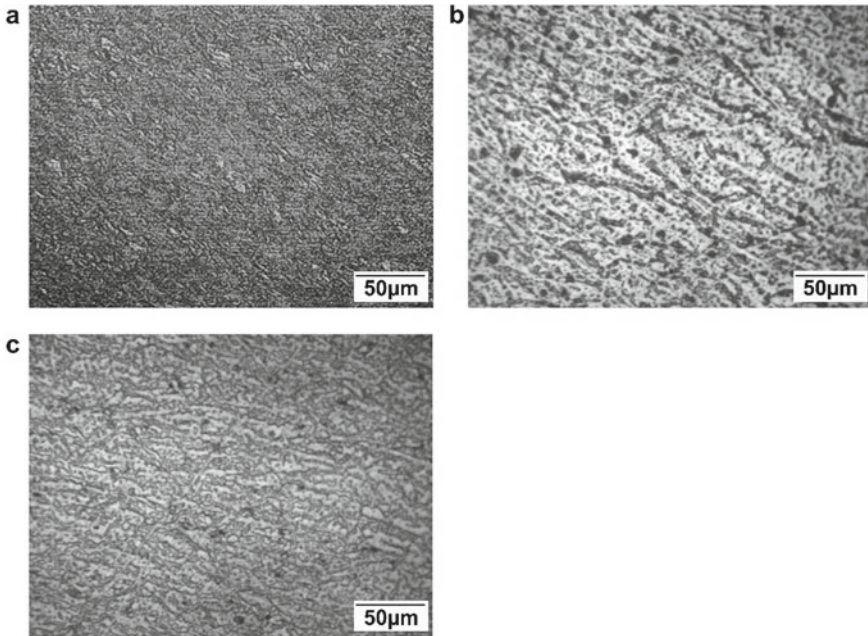
Fig. 1 Optical microstructure of the specimen **a** HR1; **b** HR2; and **c** HR3

3.2 Microstructure

3.2.1 Optical Microscopy

The phase diagram of the Al–Mg system in the ASM handbook indicates that the primary phase of AZ31 alloy is α-Mg, and the secondary intermetallic phase is β-$Mg_{17}Al_{12}$. In the as-cast AZ31 alloy, the $Mg_{17}Al_{12}$ phase is present as a continuous networked structure [34]. The microstructure of the specimen HR1 that was rolled at 150 °C is shown in Fig. 1a. The microstructure shows the absence of the networked structure of β-$Mg_{17}Al_{12}$. The microstructure of the specimen HR2 that was rolled at 300 °C is shown in Fig. 1b. A more homogeneous dispersion of the mechanically fragmented β-$Mg_{17}Al_{12}$ phase was observed in the microstructure. Besides, β phases were elongated and dispersed along the rolling direction. The microstructure of HR3 illustrates the semi-networked fashion of β phase and elongation α-Mg grains along the rolling direction, as shown in Fig. 1c.

3.2.2 High-Resolution Transmission Electron Microscopy

The typical microstructure of the hot-rolled specimens as observed using a high-resolution transmission electron microscope is presented in Fig. 2. In Fig. 2, bright

regions indicate the α-Mg matrix and the dark regions indicate the β-$Mg_{17}Al_{12}$ phase or the dislocation tangles. Figure 2a confirmed the presence of mechanically fragmented β-$Mg_{17}Al_{12}$ phase particles that are embedded in the α-Mg matrix. Figure 2b, c show the bright field and dark field image of the particle in the specimen HR2. The results confirm the formation of sub-micron size β particles in the α-Mg matrix. The formation of such sub-micron size β particles is the result of dynamic recovery and dynamic recrystallization. As observed from Fig. 2d, most of the β phase particles were homogeneously dispersed in the matrix and of spheroid shape.

This geometrical aspect of β particles enables less stress concentration sites, and hence, the fracture initiation does not occur more often. Therefore, the hot-rolled AZ31 alloy (specimen HR2) is metallurgically proven to exhibit better mechanical properties. In addition, the triple point junction is shown in Fig. 2d. As hot rolling encompasses large plastic deformation of the material at high temperature, the formation of controlled deformation features such as high-density dislocations like tangles or low-density dislocations such as cells and low angle grain boundary were observed in the microstructure. Figure 2e shows the SAED pattern of the grain shown in Fig. 2d. The spot pattern confirms that the matrix is α-Mg.

3.3   Microhardness

The average microhardness of the base material and hot-rolled specimens HR1, HR1, and HR3 are shown as a bar graph in Fig. 3a. The average microhardness of the base material was 56.15 HV and that of the specimens HR1, HR2, and HR3 were 49.11 HV, 70.43HV, and 46.82 HV, respectively. The sufficient dynamic recovery and dynamic recrystallization resulted in refined grains, homogeneous dispersion of sub-micron-sized β-$Mg_{17}Al_{12}$ phase particles, and formation of sub-grain boundaries (dislocation tangles) in the specimen HR2. Besides, partial dissolution of β-$Mg_{17}Al_{12}$ particles improvised the microhardness of the specimen HR2. Hence, the microhardness of the specimen HR2 that was hot-rolled at 300 °C was 25% higher than that of the base material. The microhardness HR1 and HR3 specimens were lesser than that of the base material. This is attributed to the non-uniform distribution and semi-networked fashion of β-$Mg_{17}Al_{12}$ phase particles in the specimen HR1 and HR3.

3.4   Tribological Characterization

3.4.1   Wear Rate

The wear rate of the base material and the hot-rolled specimens HR1, HR2, and HR3 were calculated by performing a sliding wear test at various axial loads (1, 1.5, and 2 kg). The wear rate of the specimens is shown as a bar graph in Fig. 3b–d. Under all the testing conditions, the base material exhibited a higher wear rate than
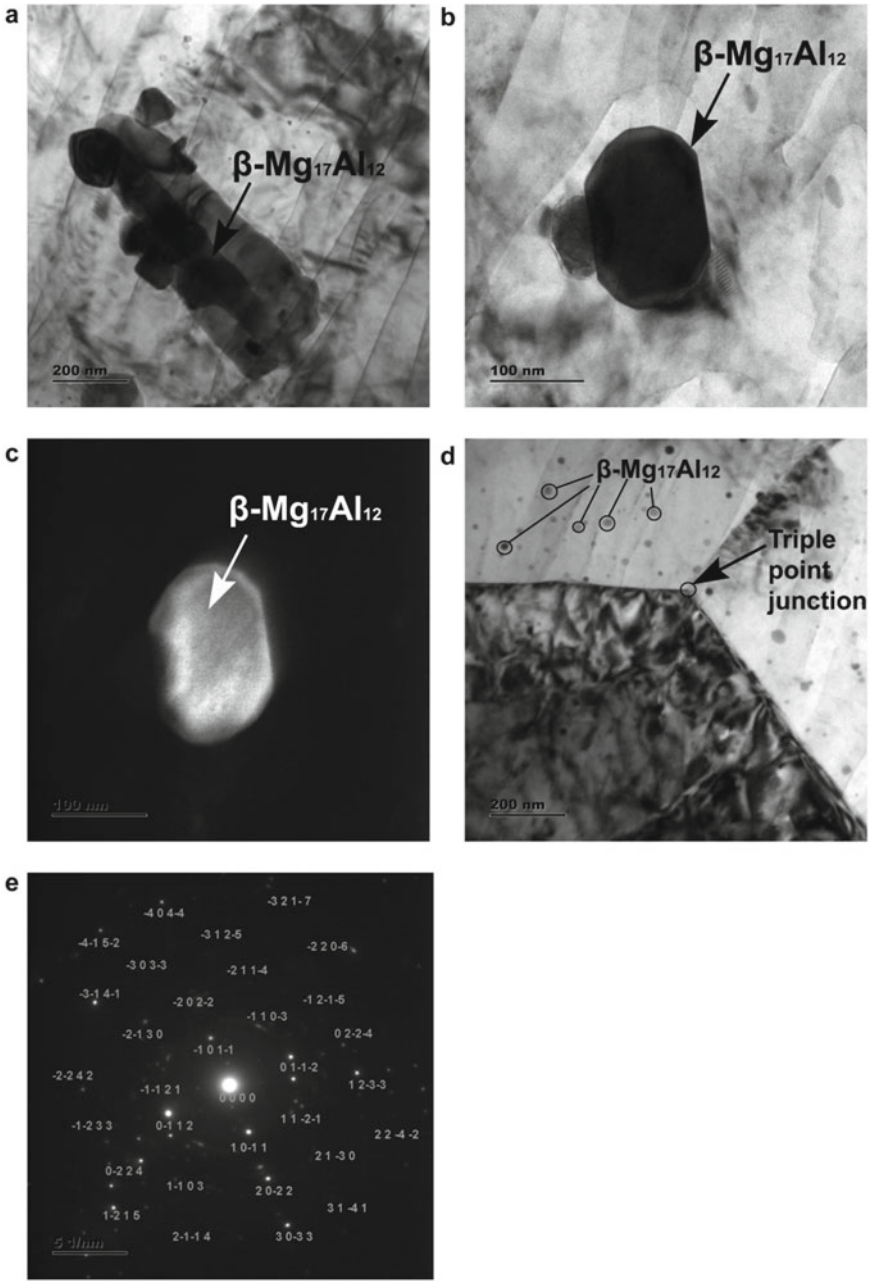
Fig. 2 High-resolution transmission electron microscopy of the specimen HR2 **a** β-Mg$_{17}$Al$_{12}$ phase; **b** Bright-field image; **c** Dark field image; **d** Triple point junction and dislocation tangles; and **e** SAED pattern
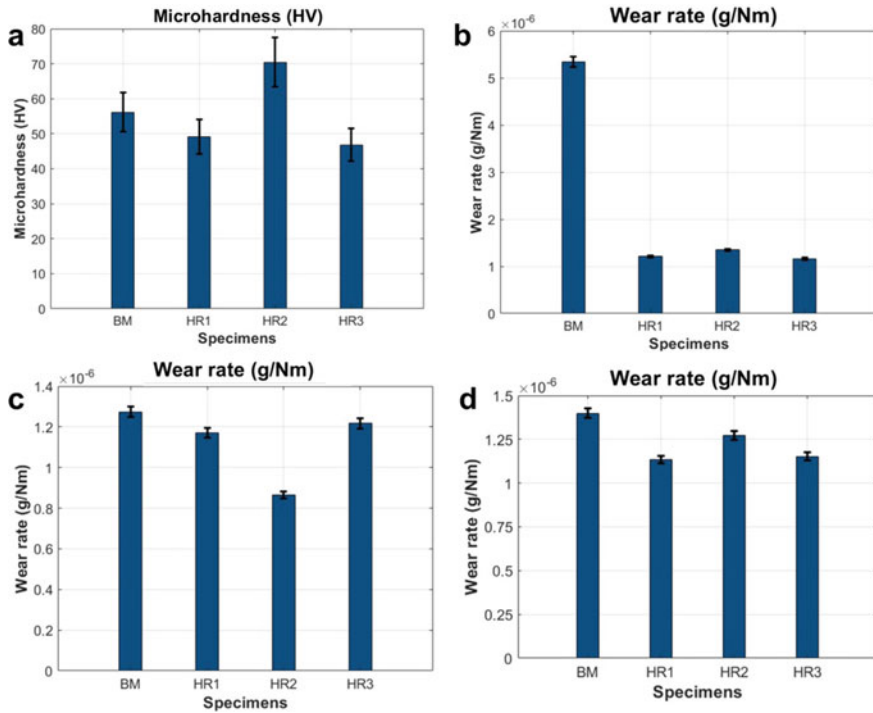
Fig. 3 a Average microhardness of the base material and hot-rolled specimens; Wear rate of the specimens that were worn at an axial load of **b** 1 kg; **c** 1.5 kg; and **d** 2 kg

that of the hot-rolled specimens. The bar graph representing the wear test performed at an axial load of 1 kg is shown in Fig. 3b. Among the specimens tested at 1 kg axial load, the base material exhibited the highest average wear rate of 5.339×10^{-6} g/Nm. The specimen HR3 exhibited the least average wear rate of 1.1599×10^{-6} g/Nm. Comparatively, the specimen HR3 had a 78% lesser wear rate than that of the base material. Similarly, the average wear rate of the specimen HR1 was 77% and specimen HR2 was 75% lesser than that of the base material. The results indicate that the wear rate of the hot-rolled specimens HR1, HR2, and HR3 are significantly similar under the axial load of 1 kg.

The wear rate of the specimens tested at an axial load of 1.5 kg is shown as a bar graph in Fig. 3c. The results show base material had the highest average wear rate of 1.2736×10^{-6} g/Nm, whereas the specimen HR2 had the least average wear rate of 0.8642×10^{-6} g/Nm. The specimen HR2's average wear rate was 32% lesser than that of the base material. The average wear rate of the specimen HR1 was 8% and the specimen HR3 was 5% lesser than that of the base material. The results confirm that the average wear rate of the specimens HR1 and HR3 was almost similar to that of the base material at 1.5 kg. For the wear test performed at an axial load of 2 kg shown as a bar graph in Fig. 3d, the base material exhibited the highest wear rate of

1.3987 × 10^{-6} g/Nm. The least wear rate of 1.1343 × 10^{-6} g/Nm was observed in specimen HR1. In comparison with the base material, 19% wear rate reduction was obtained in the HR1 specimen. Similarly, the average wear rate of the specimen HR3 was 17% and the specimen HR2 was 9% lesser than that of the base material. The results show that the average wear rate of the specimen HR1 and HR3 was almost similar.

The results show that the base material had a higher wear rate than any hot-rolled specimens irrespective of the loads. The absence of sub-grain boundaries and the presence of a continuous network of β-$Mg_{17}Al_{12}$ phase reduced the hardness, which in turn increased the wear rate. Among all the specimens, the HR2 specimen exhibited the lowest wear rate at an axial load of 1.5 kg attributed to the homogeneous dispersion of sub-micron-sized β phase particles and formation of sub-grain boundaries (dislocation tangles) in the specimen HR2.

3.5 Wear Mechanism

The surface morphology and elemental composition of the worn base material and hot-rolled specimens were analyzed using a high-resolution scanning electron microscope and energy-dispersive x-ray spectroscopy, respectively. The wear mechanism was deduced for the specimens that exhibited the least and highest wear rate.

3.5.1 Base Material

The worn surface morphology of the base material that was worn at an axial load of 1.5 kg (low wear) is shown in Fig. 4. The wear debris formed by the plunging of particles from the discontinuous and deformed surface and cracks are shown in Fig. 4a. Figure 4b shows delamination caused by the continued impact of load, and spalling effect. The crater and cracks are shown in Fig. 4c. The scratches and the remains of the eroded particle as chips are shown in Fig. 4d. The wear mechanism could be concluded as predominantly adhesive wear. The worn surface morphology of the base material that was worn at an axial load of 1 kg (high wear) is shown in Fig. 5. The hollow spots that were formed as a result of localized stress in the course of the tribological test are known as pits.

The pits and spalling defect that was formed in the course of the wear test by ejection of material is shown in Fig. 5a. Figure 5b shows cracks developed and delamination caused by layer-by-layer removal of the specimen by the counter disk. In addition to delamination, shallow grooves were observed in the specimen, as shown in Fig. 5c. The wear debris and cracks are depicted in Fig. 5d. From the morphology analysis, it could be concluded that both mild (adhesive) and severe (abrasive) wear happened in the course of wear testing of base material at an axial load of 1 kg. Figure 6a shows the EDS spectrograph of the worn-out base material specimen. The base material with a severe wear rate was taken for EDS analysis. The
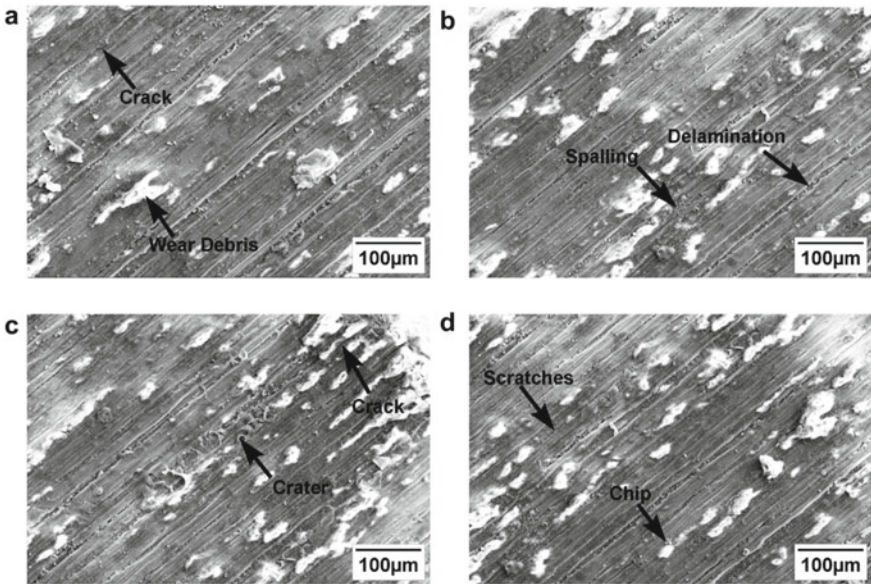
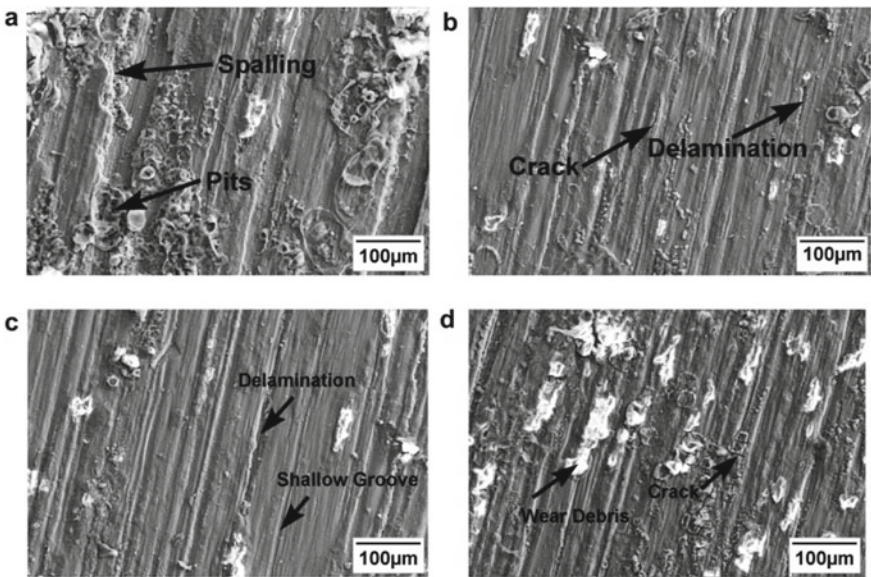Fig. 4 Worn surface morphology of the base material with the mild wear rate

Fig. 5 Worn surface morphology of the base material with the severe wear rate
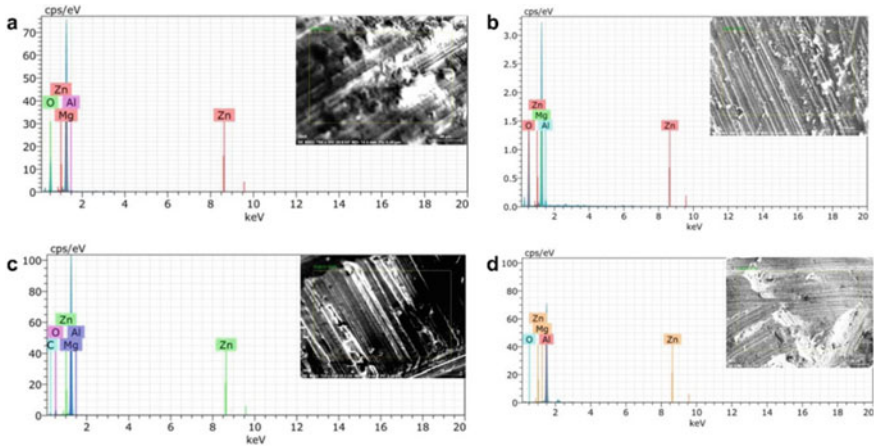
Fig. 6 Elemental composition of the worn specimens **a** BM; **b** HR1; **c** HR2; and **d** HR3

elements like Mg of 37%, O of 62%, Al, and Zn of negligible amounts were present. The high concentration of O confirms the oxidative wear of the specimen under the test axial load of 1 kg.

3.5.2 Hot-Rolled Specimen at 150 °C

The worn surface morphology of the specimen HR1 that was worn at an axial load of 2 kg (low wear) is shown in Fig. 7. Figure 7a shows the spalling defect. The shallow groove caused by the localized load at a particular area and delamination caused by the cyclic impact centered on the contact region is shown in Fig. 7b. Besides shallow grooves, pits were observed in Fig. 7c. The bright spots are the wear debris on the worn surface of the specimen, as observed in Fig. 7a–d. The cracks and delamination, which are indicative of combined adhesive and abrasive wear mechanism, were observed in the worn specimen HR1, as shown in Fig. 7d.

The worn surface morphology of the specimen HR1 that was worn at an axial load of 1 kg (high wear) is shown in Fig. 8. The secondary cracks that were formed in the worn specimen are shown in Fig. 8a. The crater and the spalling defect, which is caused by the removal of material as particles is shown in Fig. 8b. In addition to the spalling defect, the galling effect is attributed to the adhesive phenomenon which occurs during the sliding contact between the surfaces. The surface galling is shown in Fig. 8c. The accumulation of wear debris on the surface of the specimen is depicted in Fig. 8a–d. The pits and deep grooves on the worn specimen are shown in Fig. 8d. From the images shown in Fig. 8, it can be concluded that the wear mechanism is predominantly abrasive. The presence of elements Mg of 47%, O of 50%, Al of 3%, and Zn at negligible amounts was evident from the elemental analysis of the specimen
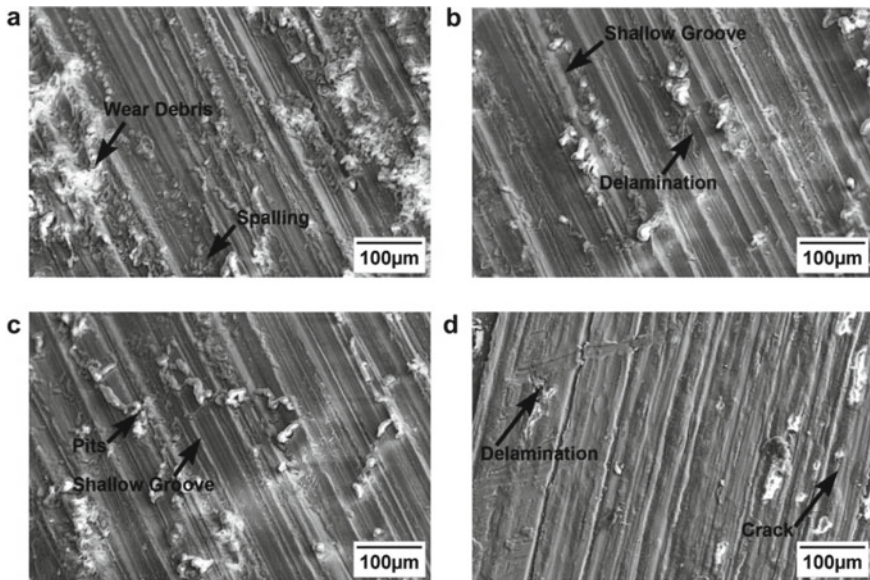
Fig. 7   Worn surface morphology of the specimen HR1 with the mild wear rate

HR1, as shown in Fig. 6b. The high concentration of O confirms the oxidative wear of the specimen under the test axial load of 1 kg.

3.5.3   Hot-Rolled Specimen at 300 °C

The worn surface morphology of the specimen HR2 that was worn at an axial load of 1.5 kg (low wear) is shown in Fig. 9. The pits and shallow grooves caused by the localized concentration of load on the surface are shown in Fig. 9a. Wearing of particles followed by their interaction with the surface produces chips. The chips and development of cracks are indicated in Fig. 9b. The delamination and spalling effect can be observed in Fig. 9c. In addition to spalling affect the presence of a deep groove, which confirmed the severe wear rate in HR2 specimens, and it is shown in Fig. 9d. The specimen was worn by both adhesive and abrasive wear mechanisms.

The worn surface morphology of the specimen HR2 that was worn at an axial load of 1 kg (high wear) is shown in Fig. 10. The shallow grooves are shown in Fig. 10a. The primary and secondary cracks and the delamination on the worn surface are depicted in Fig. 10b. The presence of shallow grooves and delamination, which is the combination of severe (abrasive) and mild (adhesive) wear mechanism, is shown in Fig. 10c. The pits and depression on the surface (spalling) are shown in Fig. 10d. Figure 10a–d shows the wear debris (bright spots) on the worn surface of the specimen. It can be concluded that the wear mechanism is predominantly abrasive wear at an axial load of 1 kg. The elemental composition of the worn HR2 specimen
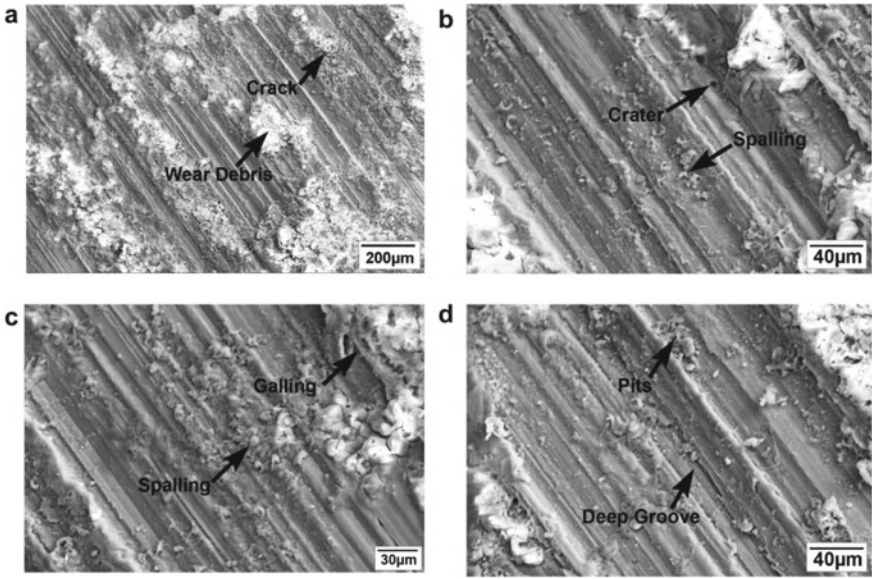
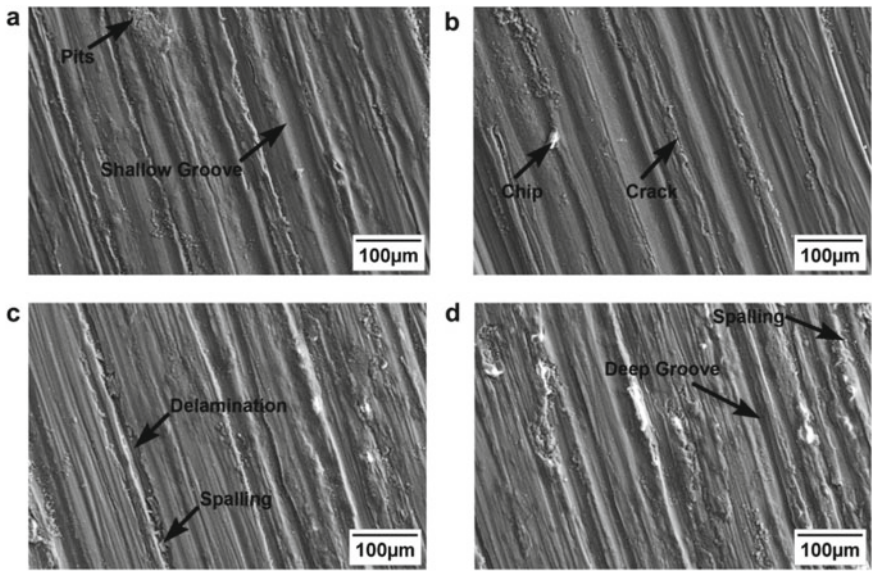**Fig. 8** Worn surface morphology of the specimen HR1 with the severe wear rate

Fig. 9 Worn surface morphology of the specimen HR2 with the mild wear rate
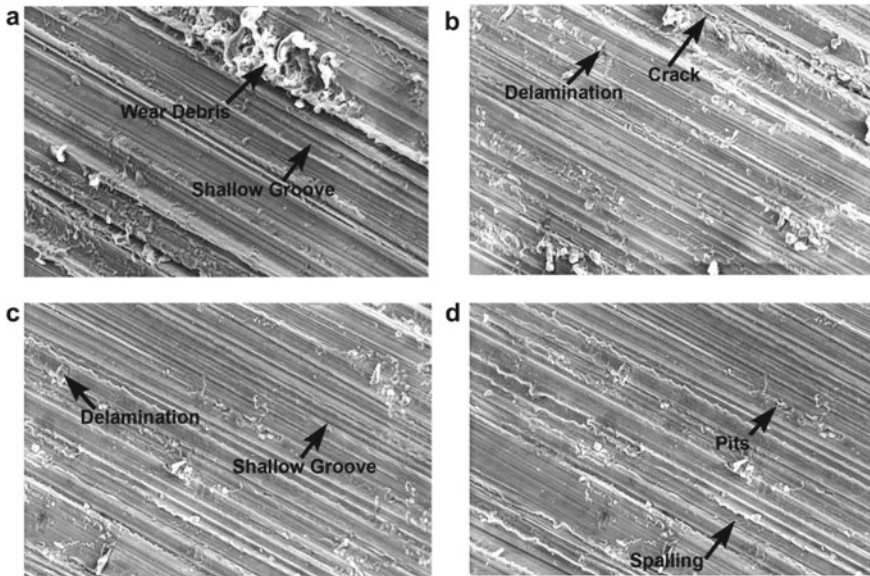
Fig. 10 Worn surface morphology of the specimen HR2 with the severe wear rate

is shown in Fig. 6c. The elements like Mg of 66%, O of 14%, Al, and Zn at negligible amounts were present. The composition indicates the partial oxidative wear of the HR2 specimen under the test axial load of 1 kg.

3.5.4 Hot-Rolled Specimen at 400 °C

The worn surface morphology of the specimen HR3 that was worn at an axial load of 2 kg (low) is shown in Fig. 11. The pits and spalling effect as a result of the removal of particles during the course of wear is shown in Fig. 11a. The furrows were caused by the dragging of particles in the course of the wear test. Figure 11b shows the presence of furrows and chips. Besides spalling, wear debris is depicted in Fig. 11c. The scratches and crack formation are shown in Fig. 11d. The worn-out HR2 specimen shows a predominantly adhesive wear mechanism.

The worn surface morphology of the specimen HR3 that was worn at an axial load of 1.5 kg (high) is shown in Fig. 12. The presence of cracks and the spalling effect observed as depression on the surface is shown in Fig. 12a. Figure 12b shows the crater and shallow groove caused by the localized load at a particular area. The pits and spalling defect are shown in Fig. 10c. The wear debris and chips are shown in Fig. 12d. The wear mechanism can be concluded as a predominantly abrasive wear mechanism. Figure 6d shows a spectrograph of the worn-out specimen HR3. The concentration of O was ~6%. The low concentration of O indicates partial oxidative wear of the specimen under the test axial load of 1.5 kg.
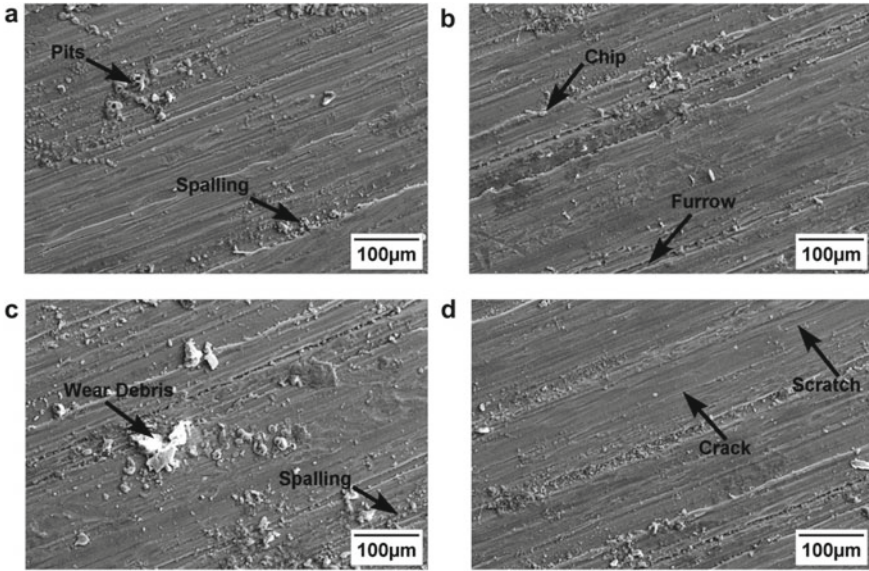
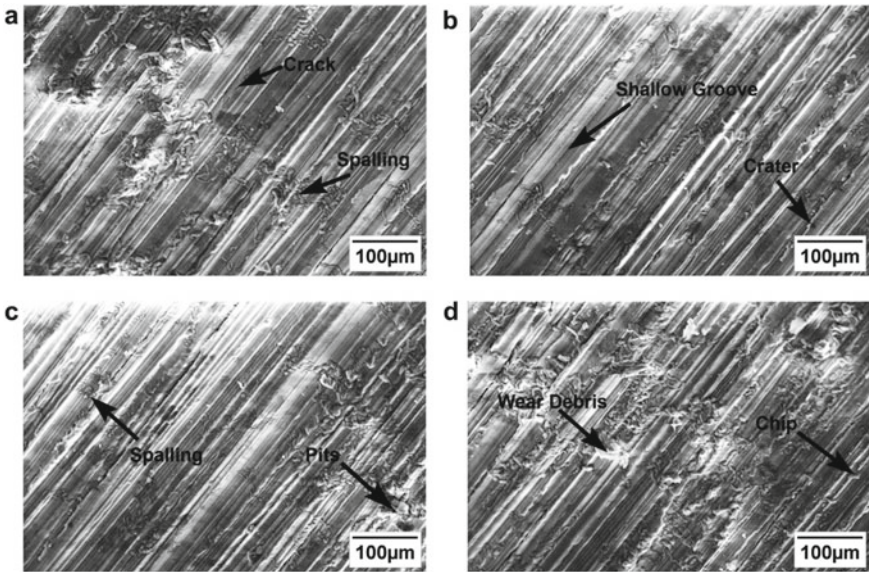**Fig. 11** Worn surface morphology of the specimen HR3 with the mild wear rate

Fig. 12 Worn surface morphology of the specimen HR3 with the severe wear rate
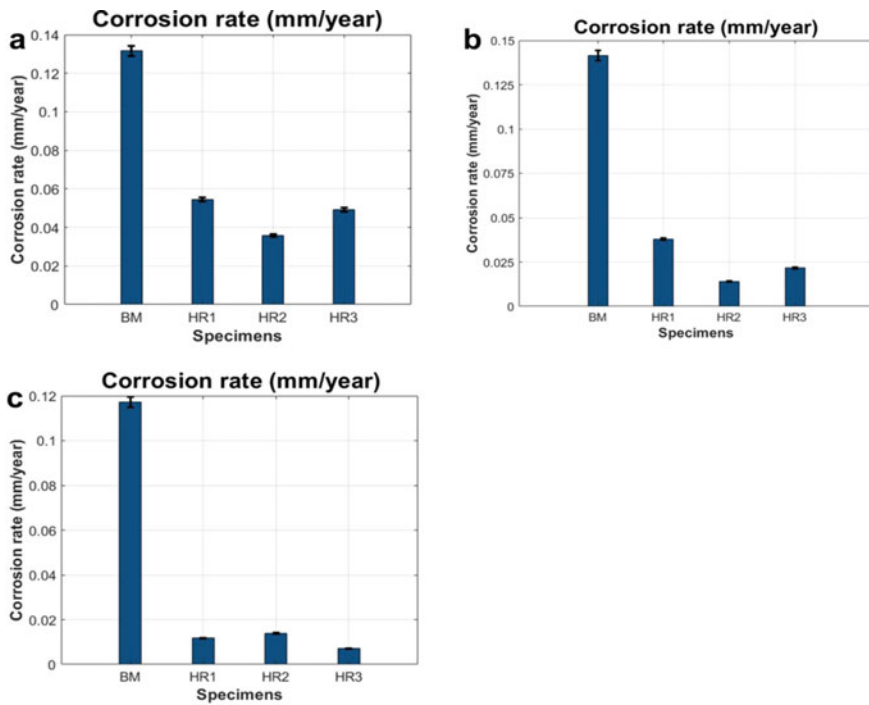
Fig. 13 Corrosion rate of the specimens after **a** 24 h; **b** 48 h; and **c** 96 h of immersion

3.6   Corrosion Test

The average corrosion rate (three specimens) of the base material and hot-rolled specimens after 24, 48, and 96 h are shown as a bar graph in Fig. 13a–c, respectively. From Fig. 13a, a maximum corrosion rate of 0.1316 mm/year was observed in the base material and a minimum corrosion rate of 0.0357 mm/year was observed in the specimen HR2 after 24 h. The corrosion rate of the specimen HR1 was 58.58% lesser than that of the base material. The specimen HR2 exhibited a 72.87% lesser corrosion rate than that of the base material. The corrosion rate of the specimen HR3 was 62.68% lesser than that of the base material. The results indicate that the corrosion rate of the specimens HR1 and HR3 were significantly similar. The specimen HR2 exhibited the greatest corrosion resistance among the tested specimens after 24 h.

Figure 13b shows the corrosion rate of the specimens after 48 h. The results show that a maximum corrosion rate of 0.1414 mm/year was observed in the base material. The least corrosion rate of 0.0140 mm/year was observed in the specimen HR2. The specimen HR1 had a 73.26% lesser corrosion rate than that of the base material. The corrosion rate of the specimen HR2 was 90.09% lesser than that of the base material. When compared to the base material, the specimen HR3 had an 84.72% lesser corrosion rate. According to the corrosion test results, the specimens HR2 and

HR3 had an insignificant difference in the corrosion rate. Hence, it is concluded that both specimens HR2 and HR3 showed high resistance to corrosion after 48 h

The corrosion rate of the specimens after 96 h of immersion is shown in Fig. 13c. The highest corrosion rate of 0.1173 mm/year was observed in the base material. The least corrosion rate was observed after 96 h in the specimen HR3 (0.0070 mm/year). The specimen HR1 had a 90.01% lesser corrosion rate than that of the base material. The corrosion rate of the specimen HR2 was 88.23% lesser than that of the base material. It was also observed that the specimen HR3 also had a 94.03% lesser corrosion rate than that of the base material. All the hot-rolled specimens HR1, HR2, and HR3 exhibited significantly similar less corrosion rates after 96 h. Hence, it could be concluded that the specimens HR1, HR2, and HR3 were highly corrosion resistant.

The base material had the highest corrosion rate compared to all the hot-rolled specimens after 24, 48, and 96 h. The base material AZ31 alloy in the as-cast condition has a continuous network of β phase [35]. The previous studies confirm that the α phase exhibits the anodic behavior and the β phase exhibits the cathodic behavior [36]. Hence, a significant potential difference exists between the α phase and β phase [37]. Hence, the corrosion rate of AZ31 alloy is not only governed by dissolution but also by the formation of a micro-galvanic couple in the matrix. The presence of a continuous network of β phase augments the corrosion rate of the base material by high dissolution rates through the micro-galvanic coupling effect, as well.

As attested from the microstructure analysis (optical microscopy and high-resolution transmission electron microscopy), the β phase was fragmented and dispersed as sub-micron size particles in the hot-rolled specimens. That in turn resulted in a lesser micro coupling galvanic effect. Hence, the corrosion rate of the hot-rolled specimens was lesser than that of the base material. Among the hot-rolled specimens, specimen HR2 exhibited the highest corrosion resistance. Hence, hot rolling at 300 °C is recommended for augmenting the corrosion resistance of AZ31 alloy. It is also observed that among all the specimens, the specimens exhibited the least corrosion rate after 96 h. Hence, surface morphology and elemental composition analysis were performed on those specimens to deduce the corrosion mechanism.

3.7   Surface Morphology and Elemental Composition of Corroded Specimens

The surface morphology of the corrosion specimens was observed using a high-resolution scanning electron microscope. The surface morphology of the base material after 96 h of immersion is shown in Fig. 14. Figure 14a–d shows the extensive corrosion of the specimen. The bright regions (white patches) indicate the corrosion products that were formed over the surface of the specimen. The dark regions are the uncorroded sites (apparently) that may become a new corrosion site. The dark regions

could also be pits, in which the corrosion products were dissolved in the course of immersion. It could be observed that the specimen had more dark regions than the bright region. Hence, it could be concluded that there are more corrosion sites for corrosion or there may be pits caused by the dissolving of corrosion products. Thus, the base material shows an elevated corrosion rate. Figure 15a shows the elemental composition of the base material after 96 h of immersion. The elements present in the corrosion layers were Al, Mg, Zn, O, Na, and Cl. The percentage of Mg, Cl, and Na were higher than any other elements. Hence, the probable corrosion products that were deposited on the surface of the specimen could be MgCl or NaCl.
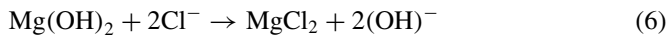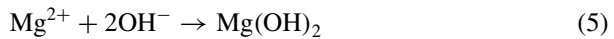
The surface morphology of the specimen HR1 after 96 h of immersion corrosion test is shown in Fig. 16. The mild corrosion in the specimen HR1 is shown in Fig. 16a–d. Similar to the base material, the bright regions indicate corrosion products, and the dark regions indicate the uncorroded sites or pits. Figure 16a–d confirmed more corrosion products on the specimen. The formation of such corrosion products retards the corrosion rate of HR1 after 96 h of immersion. Figure 15b shows the elemental composition image of the specimen HR1 after 96 h of corrosion. The elements present were Mg, Cl, Na, Zn, O, and Al. The elements Na, Cl, and Mg were found more in the corrosion layers. Hence, the corrosion products that were deposited on the specimen surface could probably be MgCl or NaCl.

Figure 17 is the surface morphology of HR2 specimens after 96 h of immersion. The mild corrosion is shown in Fig. 17a–d. Similarly, the bright regions depict corrosion products and the dark regions depict the uncorroded sites or pits. Besides, Fig. 17a–d shows the formation of corrosion products on the specimen surface. Hence, the specimen HR2 after 96 h of immersion showed less corrosion rate. Figure 15c displays the elemental composition images of the HR2 specimen after 96 h of immersion. The corrosion products consisted of the following elements: Mg, Cl, Na, Zn, O, and Al. The concentration of Na, Mg, and Cl elements was higher than the other elements. Therefore, the corrosion products formed on the specimen surface may be MgCl or NaCl.

Figure 18 shows the surface morphology images of HR3 specimens after 96 h of immersion. Figure 18a–d shows the formation of a fine layer of corrosion products on the specimen surface. The dark regions in the image represent the uncorroded sites. The specimen HR3 after 96 h of immersion showed the least corrosion rate, among the tested specimens. Figure 15d shows the elemental composition image of the specimen HR3 after 96 h of immersion. The elements present were Mg, Cl, Na, Zn, O, and Al. Similar to the previous specimens, Na, Mg, and Cl were the prominent elements present in the corrosion products. Hence, the phase composition of the corrosion product could probably be MgCl or NaCl. The summary of the corrosion test results is as follows: The base material had a very high corrosion rate, even after 96 h displayed. The corrosion rate of the specimens HR1, HR2, and HR3 was almost similar and lesser than that of the base material. The corrosion products could be MgCl or NaCl in all the specimens.

3.8 Corrosion Mechanism

The reactions of magnesium with the artificial seawater solution are shown in Eqs. (3–5). The high activity of Mg enables dissociation of Mg into Mg^{2+} ions, as soon as the AZ31 alloy specimens are immersed in the artificial seawater solution environment. This dissociation reaction is given in Eq. (3). After the dissociation, the electrons formed in Eq. (3) react with water to form H_2 gas and OH^- ions.

$$Mg \rightarrow Mg^{2+} + 2e^- \tag{3}$$

$$2H_2O + 2e^- \rightarrow H_2 \uparrow + 2OH^- \tag{4}$$

$$Mg^{2+} + 2OH^- \rightarrow Mg(OH)_2 \tag{5}$$

$$Mg(OH)_2 + 2Cl^- \rightarrow MgCl_2 + 2(OH)^- \tag{6}$$

The artificial seawater solution could be regarded as an electrolyte with abundant H^+, Na^+, OH^-, and Cl^- ions [38]. The formation of $Mg(OH)_2$ is thermodynamically favored with a ΔG value of -359 kJ/mol [39]. Hence, Mg^{2+} reacts with OH^- ions in the solution to form $Mg(OH)_2$, as given in Eq. (5). The formation of $Mg(OH)_2$ (HCP, hp3) distorts the crystal lattice of Mg (HCP). This transformation was attributed to the formation of cracks in the specimen. The solubility of $Mg(OH)_2$ is limited with a solubility product value of 5.61×10^{-12} (more or less, insoluble in water at room temperature) [40]. However, $Mg(OH)_2$ is not so stable in the sea water environment that has Cl^- ions. The small radius of Cl^- ions permit the easy-penetration of Cl^- ions into $Mg(OH)_2$. Subsequently, the reaction of Cl^- ions with $Mg(OH)_2$ results in the formation of $MgCl_2$, as shown in the Eq. (6).

$MgCl_2$ has a solubility of 54.3 g in 100 ml at 20 °C [41]. Hence, $MgCl_2$ that was formed in the course of the corrosion phenomenon, is also highly solvable in the artificial seawater solution. That in turn created newly exposed sites for corrosion. Hence, the corrosion rate of the AZ31 alloy was initially higher (after 24 h). However, the corrosion products (salts such as NaCl or $MgCl_2$) settled over the specimen's surface in the course of testing. The formation of the layer of corrosion product limited the contact of Cl^- ions with the specimen surface. Hence, no new sites were exposed for corrosion phenomenon. As a result, the corrosion rate of the specimens decreased subsequently after 48 h of immersion in all the tested specimens. However, $MgCl_2$ has high solubility. Hence, the formation of passivation or protective film of corrosion products is impossible for AZ31 alloys (as-cast or hot-rolled) in seawater solution. Therefore, the corrosion rate will increase once the corrosion products are removed from the surface by convection or dissolution of $MgCl_2$. Hence, the specimens should be subjected to a corrosion test with a convective flow of fluid over the surface to evaluate the actual corrosion rate.
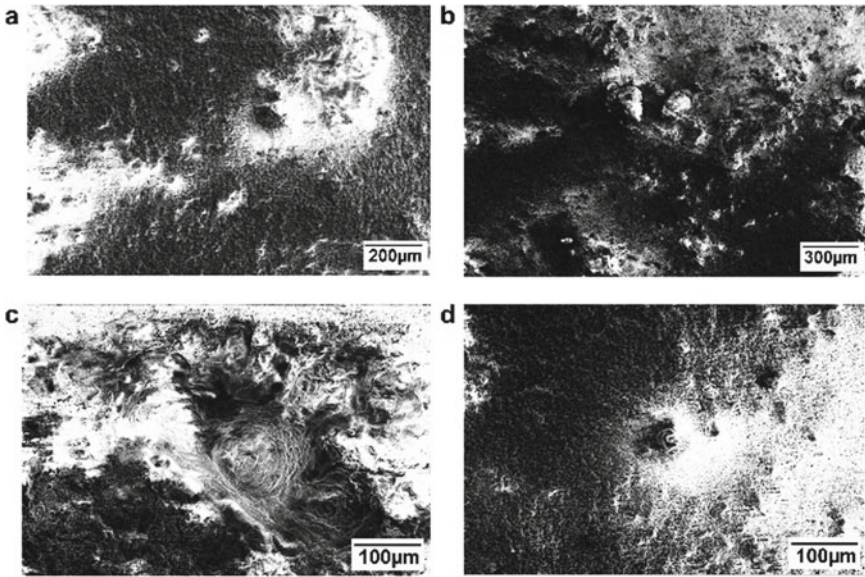
Fig. 14   Corroded surface morphology of the specimen BM after 96 h
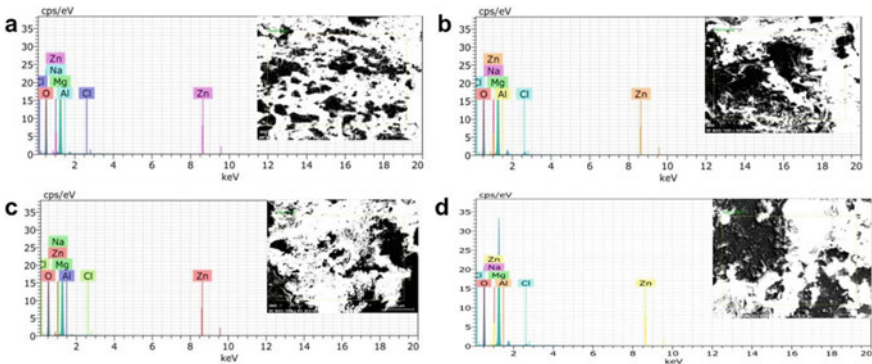
Fig. 15   Elemental composition of the corroded specimens **a** BM; **b** HR1; **c** HR2; and **d** HR3

4   Conclusion

The as-cast AZ31 alloy was hot-rolled at 150, 300, and 400 °C successfully. The hot-rolled specimens along with the base material were analyzed for microstructure, microhardness, wear rate, and corrosion rate. The results demonstrated the following:

1. Hot rolling of AZ31 alloy at 300 °C replaced the continuous networked β-$Mg_{17}Al_{12}$ phase of AZ31 alloy with homogeneously fragmented and dispersed β-$Mg_{17}Al_{12}$ phase. The microhardness of the hot-rolled specimens was higher
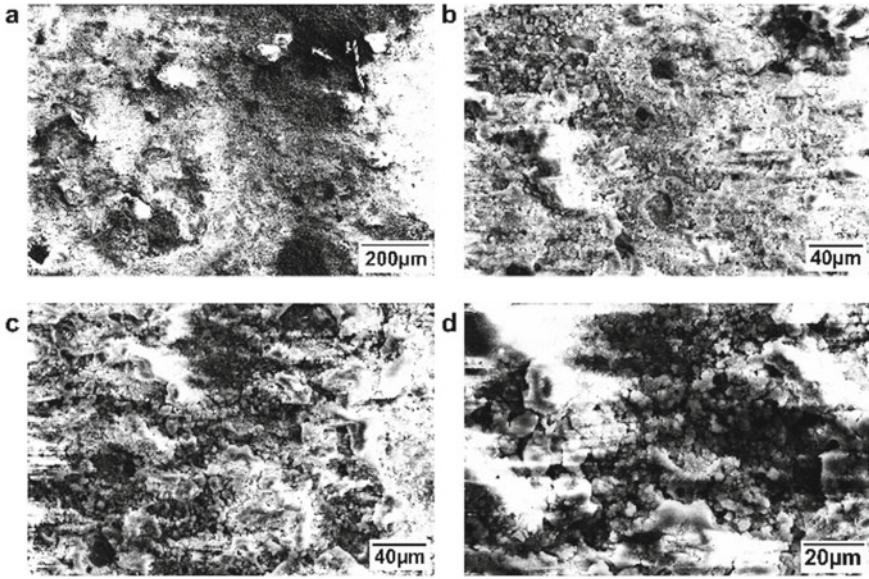
Fig. 16 Corroded surface morphology of the specimen HR1 after 96 h
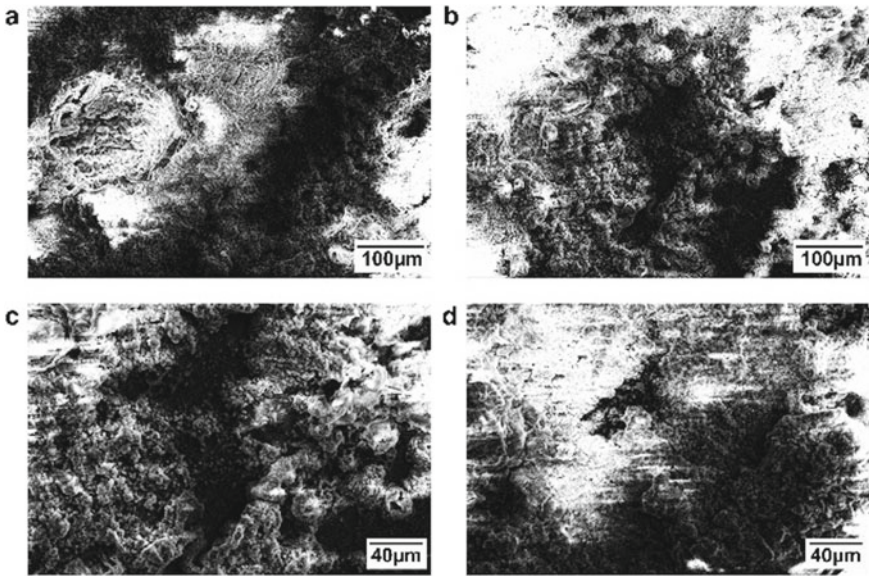
Fig. 17 Corroded surface morphology of the specimen HR2 after 96 h
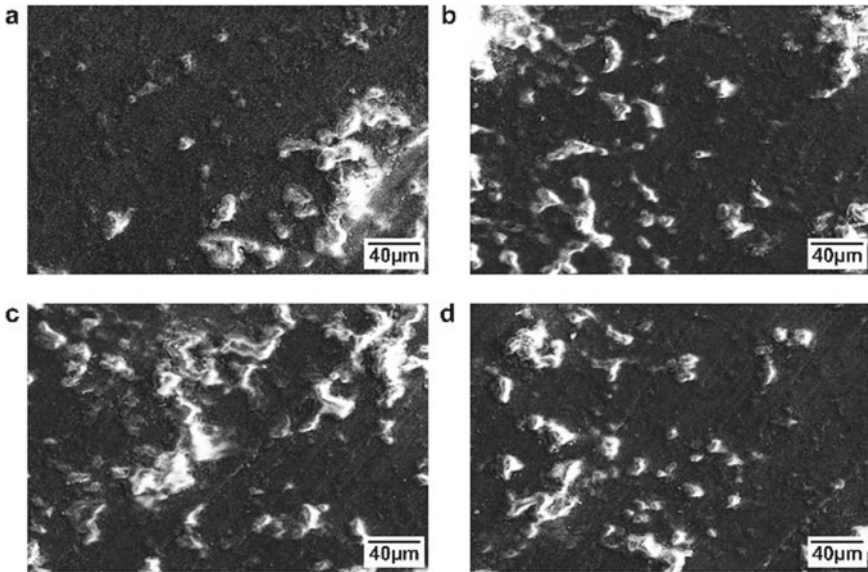
Fig. 18 Corroded surface morphology of the specimen HR3 after 96 h

than that of the base material. Among the tested specimens, HR2 exhibited the highest microhardness of 70.43 HV. This was attributed to the homogeneous distribution of fragmented and sub-micron β-$Mg_{17}Al_{12}$ phase in the specimen HR2.

2. The wear rate of the hot-rolled specimens was lesser than that of the base material. Almost all the hot-rolled specimens exhibited a similar wear rate under the axial loads of 1, 1.5, and 2 kg. The specimen HR2 that was hot-rolled at 300 °C exhibited the least corrosion rate (almost similar to that of the specimen HR3 after 96 h of immersion).

3. The results indicate that the optimum temperature to maximize the microhardness, wear resistance, and corrosion resistance in the hot rolling of AZ31 alloy is 300 °C.

References

1. Govindaraju M, Chakkingal U, Kalvala PR, Vignesh RV, Balasubramanian K (2020) Investigations on the creep behavior of friction-stir-processed magnesium alloy AE42. J Mater Eng Perform 29(5):3172–3182. https://doi.org/10.1007/s11665-020-04848-0
2. Vaira Vignesh R, Padmanaban R (2018) Modelling of peak temperature during friction stir processing of magnesium alloy AZ91. In: Conference series: materials science and engineering, vol 310, p 12019. https://doi.org/10.1088/1757-899x/310/1/012019

3. Vignesh RV, Padmanaban R (2018) Forecasting tribological properties of wrought AZ91D magnesium alloy using soft computing model. Russ J Non-Ferrous Met 59(2):135–141. https://doi.org/10.3103/S1067821218020116

4. Vaira Vignesh R, Padmanaban R, Govindaraju M, Suganya Priyadharshini G (2019) Mechanical properties and corrosion behaviour of AZ91D-HAP surface composites fabricated by friction stir processing. Mater Res Express 6(8):85401. https://doi.org/10.1088/2053-1591/ab1ded

5. Watanabe H, Mukai T, Sugioka M, Ishikawa K (2004) Elastic and damping properties from room temperature to 673 K in an AZ31 magnesium alloy. Scr Mater 51:291–295. https://doi.org/10.1016/j.scriptamat.2004.04.032

6. Govindaraju M, Vignesh RV, Padmanaban R (2019) Effect of heat treatment on the microstructure and mechanical properties of the friction stir processed AZ91D magnesium alloy. Met Sci Heat Treat 61(5):311–317. https://doi.org/10.1007/s11041-019-00422-1

7. Gl S, Zq X (2010) The surface, microstructure and corrosion of magnesium alloy AZ31 sheet. Electrochim Acta 55(13):4148–4161. https://doi.org/10.1016/j.electacta.2010.02.068

8. Yim CD, Seo YM, You BS (2009) Effect of the reduction ratio per pass on the microstructure of a hot-rolled AZ31 magnesium alloy sheet. Met Mater Int 15(4):683–688. https://doi.org/10.1007/s12540-009-0683-6

9. Panicker R, Chokshi A, Mishra R, Verma R, Krajewski P (2009) Microstructural evolution and grain boundary sliding in a superplastic magnesium AZ31 alloy. Acta Mater 57:3683–3693. https://doi.org/10.1016/j.actamat.2009.04.011

10. Shin B, Kang H, Bae D (2012) Texture development and deformation behavior of a statically recrystallized Mg–Al–Zn alloy sheet. Met Mater Int 18(1):23–27. https://doi.org/10.1007/s12540-012-0003-4

11. Vespa G, Mackenzie LWF, Verma R, Zarandi F, Essadiqi E, Yue S (2008) The influence of the as-hot rolled microstructure on the elevated temperature mechanical properties of magnesium AZ31 sheet. Mater Sci Eng A 487(1):243–250. https://doi.org/10.1016/j.msea.2007.10.064

12. Miao Q, Hu L, Sun H, Wang E (2009) Grain refining and property improvement of AZ31 Mg alloy by hot rolling. Trans Nonferrous Met Soc China 19:s326–s330. https://doi.org/10.1016/S1003-6326(10)60063-5

13. Jäger A, Lukáč P, Gärtnerová V, Bohlen J, Kainer KU (2004) Tensile properties of hot rolled AZ31 Mg alloy sheets at elevated temperatures. J Alloys Compd 378(1):184–187. https://doi.org/10.1016/j.jallcom.2003.11.173

14. Zhang KF, Yin DL, Wu DZ (2006) Formability of AZ31 magnesium alloy sheets at warm working conditions. Int J Mach Tools Manuf 46(11):1276–1280. https://doi.org/10.1016/j.ijmachtools.2006.01.014

15. Choi SC, Kim HY, Hong SM, Shin YS, Lee GH, Kim HJ (2009) Evaluation and prediction of the forming limit of AZ31B magnesium alloy sheets in a cross-shaped cup deep drawing process. Met Mater Int 15(4):575–584. https://doi.org/10.1007/s12540-009-0575-9

16. Jiang P et al (2020) Microstructure, tensile properties and free bulge formability of Sr- and Y-containing AZ31 alloy sheet produced by twin-roll casting and sequential hot rolling. Rare Met 39(10):1202–1209. https://doi.org/10.1007/s12598-020-01381-w

17. Huang X, Suzuki K, Saito N (2009) Enhancement of stretch formability of Mg–3Al–1Zn alloy sheet using hot rolling at high temperatures up to 823K and subsequent warm rolling. Scr Mater 61(4):445–448. https://doi.org/10.1016/j.scriptamat.2009.04.042

18. Sun H, Liang S, Wang E (2009) Mechanical properties and texture evolution during hot rolling of AZ31 magnesium alloy. Trans Nonferrous Met Soc China 19:s349–s354. https://doi.org/10.1016/S1003-6326(10)60067-2

19. Jin L, Dong J, Wang R, Peng LM (2010) Effects of hot rolling processing on microstructures and mechanical properties of Mg–3%Al–1%Zn alloy sheet. Mater Sci Eng A 527(7):1970–1974. https://doi.org/10.1016/j.msea.2009.11.047

20. Kim YJ, Lee JU, Kim S-H, Yoon J, Kim YM, Park SH (2019) Variation in crystallographic orientation and twinning activation with size of individual grains in rolled magnesium alloy. Met Mater Int 25(6):1541–1547. https://doi.org/10.1007/s12540-019-00321-3

21. Tighiouaret S et al (2021) On the evolution of microstructure, texture and corrosion behavior of a hot-rolled and annealed AZ31 alloy. Mater Chem Phys 267:124598. https://doi.org/10.1016/j.matchemphys.2021.124598

22. Fatemi-Varzaneh SM, Zarei-Hanzaki A, Haghshenas M (2009) The room temperature mechanical properties of hot-rolled AZ31 magnesium alloy. J Alloys Compd 475(1):126–130. https://doi.org/10.1016/j.jallcom.2008.06.162

23. Miao Q, Hu L, Wang G, Wang E (2011) Fabrication of excellent mechanical properties AZ31 magnesium alloy sheets by conventional rolling and subsequent annealing. Mater Sci Eng A 528(22):6694–6701. https://doi.org/10.1016/j.msea.2011.05.023

24. Bohlen J et al (2004) Orientation effects on acoustic emission during tensile deformation of hot rolled magnesium alloy AZ31. J Alloys Compd 378(1):207–213. https://doi.org/10.1016/j.jallcom.2003.10.102

25. Kawalla R, Ullmann M, Schmidt C, Dembińska J, Vogt HP (2011) Properties of magnesium strips produced by twin-roll-casting and hot rolling. Mater Sci Forum 690:21–24. https://doi.org/10.4028/www.scientific.net/MSF.690.21

26. Wang H, Estrin Y, Fu H, Song G, Zúberová Z (2007) The effect of pre-processing and grain structure on the bio-corrosion and fatigue resistance of magnesium alloy AZ31. Adv Eng Mater 9(11):967–972. https://doi.org/10.1002/adem.200700200

27. Suh JS, Suh B-C, Choi JO, Kim YM, You BS (2020) Effect of extrusion temperature on mechanical properties of AZ91 alloy in terms of microstructure and texture development. Met Mater Int. https://doi.org/10.1007/s12540-020-00642-8

28. Chang LL, Wang YN, Zhao X, Huang JC (2008) Microstructure and mechanical properties in an AZ31 magnesium alloy sheet fabricated by asymmetric hot extrusion. Mater Sci Eng A 496(1):512–516. https://doi.org/10.1016/j.msea.2008.06.015

29. Nene SS, Kashyap BP, Prabhu N, Estrin Y, Al-Samman T (2014) Microstructure refinement and its effect on specific strength and bio-corrosion resistance in ultralight Mg–4Li–1Ca (LC41) alloy by hot rolling. J Alloys Compd 615:501–506. https://doi.org/10.1016/j.jallcom.2014.06.151

30. Vaira Vignesh R, Padmanaban R, Govindaraju M (2019) Study on the corrosion and wear characteristics of magnesium alloy AZ91D in simulated body fluids. Bull Mater Sci 43(1):8. https://doi.org/10.1007/s12034-019-1973-3

31. Vaira Vignesh R, Padmanaban R, Govindaraju M (2019) Investigations on the surface topography, corrosion behavior, and biocompatibility of friction stir processed magnesium alloy AZ91D. Surf Topogr Metrol Prop 7(2):25020. https://doi.org/10.1088/2051-672x/ab269c

32. Yan H, Gong X, Chen J, Cheng M (2020) Microstructure, texture characteristics, mechanical and bio-corrosion properties of high strain rate rolled Mg–Zn–Sr alloys. Met Mater Int. https://doi.org/10.1007/s12540-019-00601-y

33. Zhu T, Gong X, Xiong Y, Hu X (2020) Effect of initial orientation on corrosion behavior of AZ80 magnesium alloy in simulated body fluid. Met Mater Int. https://doi.org/10.1007/s12540-020-00611-1

34. Guan R, Zhao Z, Wang X, Dai C, Liu C (2013) Process parameter optimizing and studies on microstructure and properties of AZ31 alloy prepared by semisolid rolling process. Acta Metall Sin (English Lett) 26(3):293–298. https://doi.org/10.1007/s40195-012-0190-5

35. Kim HL, Chang YW (2011) Deformation mechanism temperature-dependence of AZ31 magnesium alloy. Met Mater Int 17(4):563. https://doi.org/10.1007/s12540-011-0806-8

36. Bharathi BM, Vignesh RV, Padmanaban R, Govindaraju M (2020) Effect of friction stir processing and heat treatment on the corrosion properties of AZ31 alloy. Aust J Mech Eng 1–10. https://doi.org/10.1080/14484846.2020.1815999

37. Vaira Vignesh R, Padmanaban R (2019) Modelling corrosion phenomenon of magnesium alloy AZ91 in simulated body fluids BT. In: Singh VK, Gao D, Fischer A (eds) Advances in mathematical methods and high performance computing. Springer International Publishing, Cham, pp 471–486

38. Sherif E-S (2012) Corrosion behavior of magnesium in naturally aerated stagnant seawater and 3.5% sodium chloride solutions. Int J Electrochem Sci 7:4235–4249

39. Song G-L (2011) 1-Corrosion electrochemistry of magnesium (Mg) and its alloys. In: G. B. T.-C. of MA Song (ed) Woodhead publishing series in metals and surface engineering. Woodhead Publishing, pp 3–65
40. Ropp RC (2013) Chapter 3—group 16 (O, S, Se, Te) alkaline earth compounds. In: R. C. B. T.-E. of the Ropp AEC (ed). Elsevier, Amsterdam, pp 105–197
41. Website reference: http://www.inchem.org/documents/icsc/icsc/eics0764.htm

Chapter 18
Investigations on the Texture, Formability, and Corrosion Characteristics of AA3003-Y$_2$O$_3$ Surface Composite Fabricated by Friction Stir Processing

S. Kamaleshwar, S. Jagadeesh Kumar, K. Naveen Kumar, S. Keerthana, R. Vaira Vignesh, and R. Padmanaban

1 Introduction

Aluminum alloys are frequently employed in a variety of applications such as aerospace, marine, automotive, and structural applications owing to their lightweight, high specific strength, and better corrosion resistance. One of the primary alloys employed in the fabrication of household utensils includes AA3003 alloy. The major alloying elements of AA3003 alloy include Mn, Cu, and Fe. The microstructure of AA3003 alloy possesses α-Al primary phase with dispersed Al$_{15}$ (Fe, Mn)$_3$Si and Al$_6$Mn second phase particles. The primary dendrites of α-Al form until the nucleation of the Al$_6$Mn phase occurs in the course of normal solidification. The slow cooling retards the nucleation of Al–Fe–Si–Mn particles and therefore dendrites of α-Al and Al$_6$Mn phase grow competitively. The formability of AA3003 alloy is limited by the presence of form hard and brittle intermetallic particles (Al–Fe–Si–Mn intermetallic) in the grain boundaries. Also, simultaneous recrystallization and deformation and controlling texture in a hot rolling process possess a challenge.

Friction stir processing (FSP) is one of the most effective solid-state processing methods for altering the microstructure and texture of the alloys and for the fabrication of surface composites. FSP tool, that has a specifically constructed pin and shoulder, is plunged into the workpiece until the tool shoulder rests and establishes a
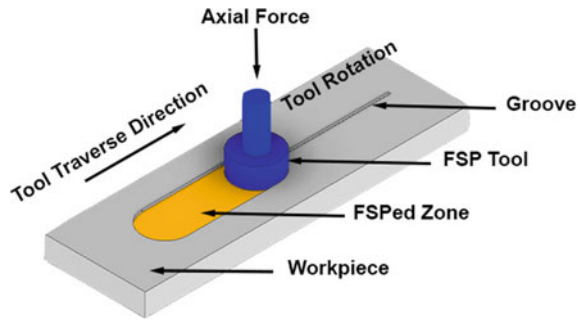
S. Kamaleshwar · S. Jagadeesh Kumar · K. Naveen Kumar · S. Keerthana · R. Vaira Vignesh (✉) · R. Padmanaban
Department of Mechanical Engineering, Amrita School of Engineering, Amrita Vishwa Vidyapeetham, Coimbatore, India
e-mail: r_vairavignesh@cb.amrita.edu

R. Padmanaban
e-mail: dr_padmanaban@cb.amrita.edu

contact with the workpiece surface (Fig. 1). The rubbing action of the tool shoulder
and tool pin generates frictional heat energy, which in turn softens and plasticizes the
workpiece. The rotary motion coupled with the translatory motion of the tool stirs and
transfers the plasticized mass within the stir zone (region of the workpiece beneath
the tool) of the workpiece. During this process, the subjection of the stir zone (SZ) to
intensive localized heat and severe plastic deformation results in dynamic recrystal-
lization (DRX). Consequently, significant grain refinement is achieved. However, a
regulated manufacturing procedure and controlled dynamic recrystallization through
the addition of the reinforcement phase could improve the properties further (Fig. 1).

Many sheet metal industries are working on material advancements such as
alloy research, coating development, and other techniques to improve the forma-
bility of high strength and light gage goods, as the demand for lighter equipment
grows. Recently, manufacturers focus on the development of aluminum metal matrix
composites that are reinforced with particulates such as C_g, SiC, WC, Al_2O_3, Si_3N_4,
TiB_2, B_4C, TiO_2, TiC, and AIN. However, rare-earth metal (RE) oxide-based rein-
forcements are not discussed in the open literature. In particular, this work focus on
the development of AA3003 alloy-based surface composite. In particular, the influ-
ence of yttrium oxide (Y_2O_3) on the microstructure, texture, microhardness, strength,
and formability of AA3003 was investigated.

Surendra Kumar et al. [1] investigated on mechanical and microstructural proper-
ties of AA3003 which was reinforced with the tungsten carbide (WC) micro-particles
by multi-pass friction stir processing (FSP). The microstructural analysis of the inter-
face showed very good intermetallic particles that bind to AA3003/WC matrices and
solid solutions. Kotiyani et al. [2] reinforced the rolled AA3003 aluminum alloy with
Zr that eventually formed Al_3Zr aluminide nanoparticles in the course of friction stir
processing. By increase in the FSP passes, in aluminide, many Al_3Zr nanoparticles
were formed, and it is more evenly dispersed throughout the metal matrix. There was
an increase in tensile strength and hardness after 6 passes on the fabricated specimen.

Kumar et al. [3] performed the synthesis, characterization, and mechanical
behavior of AA3003-TiO_2 surface composites using friction stir processing. The
composite formed by reinforced particles exhibits a rise in the hardness and tensile
strength of the weld increment from fractography results tells us the brittle to ductile
transformation in addition with TiO_2 particles. The aluminum grains have refined by

dynamic recrystallization with intensified localized plastic deformation. Yahya and Serdal [4] investigated the impact of parameters in welding on the mechanical and the microstructural properties of dissimilar friction stir welded AA3003-H24 and 2124/T4/SiC alloy joints. Results proved the good quality of welded joints which was acquired with a TRS of 900 rpm and at a TTS of 125 mm/min.

Takhakh et al. [5] investigated the fatigue properties of friction stir welded AA3003-H14 alloy. FSW trials were performed by varying the rotational and welding speeds. The joints were devoid of voids, cracks, and distortion. The FSW welds fatigue strength was higher than fusion TIG weld by 22%. Tan et al. [6] investigated the microstructure and mechanical properties of AA3003 alloy that was joined using underwater friction stir welding. With a decrease in the welding ambient and sub-ambient temperature for $-25\ °C$ liquid medium, in the weld nugget zone, the decrease in size of recrystallized grain for the annealed hot bands and the hot bands.

Shinde et al. [7] have performed multi-response optimization in the friction stir welding process with dissimilar AA3003-H12 and C12200-H01 alloys. The full factorial design was set up at different process parameters, like shoulder diameter, welding speed, rotational speed, and tool pin profiles. The maximum UTS is 135 MPa, % elongation is 14%, and the yield strength of 98 MPa was with the joint which is fabricated along tapered pin having the diameter of the shoulder up to 22.5 mm, with 1800 rpm of tool rotation speed, and 16 mm/min of welding speed. The large elongated grain in the base metal was 37 μm for AA3003-H12 and about 37.5 μm for C12200-H01, equiaxed grains along with fine grains were analyzed at NZ is to be 4 microns. The microhardness was a maximum of 505 HV at the nugget zone.

Aydin et al. [8] examined the impact of welding parameters regarding the fatigue behavior of friction stir welded AA3003-O alloy. The FSW welds exhibited less fatigue life compared to the base material. FSW welds' fatigue behavior was dependent on the welding parameters such as rotational speed as well as welding speed. The fatigue performance of AA3003-O alloy is improved by lower welding speeds and greater rotational speeds. With a lower welding speed and a faster rotational speed, the fatigue life of friction stir welds may be extended. This could be due to an increase in the amount of heat given to the weld per unit length. For all the fractured specimens, cracks initiated from the root of part between TMAZ and the stirred zone at the retreating side of the welds.

Dehghani et al. [9] investigated the effect of friction stir welding parameters on the properties of AA3003-H18 alloy to mild steel. By increasing of heat input factor, the intermetallic layer thickness was increased from 0.8 to 7.8 μm. The weld zone heat input was increased by increasing the tool rotation speed from 450 to 700 rpm. By lowering the heat input factor and increasing the welding speed, the ultimate tensile strength improved from 28 to 100 MPa.

Yadav et al. [10] fabricated Al–Zn solid solution using the FSP technique. Multi-pass FSP was used to incorporate Zn into commercially pure Al, resulting in its dissolution and the formation of a supersaturated solid solution. The hardness of Zn-rich sections was higher (82 Hv) than that of Zn-free parts (43 Hv), with an average hardness of 57 Hv. Following the second pass of FSP, the pinning action of the grain boundary precipitate improved the thermal stability of the microstructure

against aberrant grain development. FSP has produced in grain refinement in the alloy, resulting in fine equiaxed grains with a higher fraction less than 67% of large-angle grain boundaries in a span of 4–6 μm.

Chekalil et al. [11] analyzed the influence of friction stir welding process parameters through mechanical behavior of AA3003 alloy by the design of experiments approach. The enhanced friction stir welding parameters to obtain maximum strength include the parameters of 1423.93 rpm, 400 mm/min, and the tool tilt angle was 1.2885°. Tensile strength of 121.18 MPa which was 75% that of the base material was obtained in the specimen welded.

Kotiyani et al. [12] analyzed the effect of heat treatment on the microstructure and mechanical properties of an in situ hybrid composite made of $Al/Al_3Zr + Al_3Ti$ and formed using FSP. The base material's elongated and large grains were changed to equiaxed and fine grains, according to microstructural testing. In addition, at the interface between the aluminum matrix and the metallic powders, chemical reactions took place, resulting in the formation of in situ aluminides of Al3Zr and Al3Ti.

Abdulrehman et al. [13] investigated the mechanical properties of friction stir welded AA3003-H14 alloy. The strength of a maximum 134.4 MPa is acquired in the specimens that were welded at 1600 rpm rotation speed and 30 mm/min traverse speed (joint strength had 84% efficiency). X-ray analysis depicted the non-appearance of defects in the welding line. FSW had enhanced properties that were attributed to the refined grain microstructure in the nugget zone that caused.

Mumin Tutar et al. [14] optimized the process parameters of friction stir spot-welded AA3003-H12 aluminum alloy using the Taguchi orthogonal array. The tool plunge depth had the greatest impact on the tensile shear load, accounting for 69.26% of the total, followed by dwell duration and rotating speed. All of the joint cracks during tensile testing occurred in the stir zone, where the bonded section was the smallest. The FSW joints' tensile load and tensile deformation rose linearly as the bonded size increased. Higher hardness came from the finer grain size of the stir zone, which led to higher fracture strength.

The formability of AA3003 alloy is limited by the presence of form hard and brittle intermetallic particles (Al–Fe–Si–Mn intermetallic) in the grain boundaries [15–19]. The microstructure and mechanical properties of AA3003 alloy-based surface composite that is reinforced with yttrium oxide (Y_2O_3) through friction stir processing are seldom discussed in the open literature. Hence, the project aims to evaluate AA3003 alloy that is reinforced with Y_2O_3 particles on the microstructural aspects (grain size, grain orientation, and composition/morphology of intermetallic phases), mechanical properties (microhardness, tensile strength), and formability.

Table 1 Composition of AA3003 (base material)

Element	Cu	Fe	Mn	Si	Zn	Al
Composition (wt%)	0.08	0.64	1.21	0.45	0.10	Balance

Table 2 Processing parameters

Trial. no	TRS (rpm)	TTS (mm/min)	No. of passes
FSP01	750	60	1 pass
FSP02	750	40	1 pass
FSP03	750	20	1 pass
FSP04	750	20	2 passes

2 Materials and Method

2.1 Materials

AA3003 alloy plate of 5 mm thickness was sheared into workpieces of 150 × 50 × 5 mm in dimension. The composition of the AA3003 alloy is shown in Table 1. The workpiece was machined having a groove of 100 × 1 × 1 mm in dimension. The reinforcement was yttrium oxide (Y_2O_3) which had an average particle size of 30 μm and 99.99% purity.

2.2 Methodology

2.2.1   Friction Stir Processing

A customized friction stir welding setup at Amrita Vishwa Vidyapeetham was utilized to perform friction stir processing trials. The grooves were filled and compacted with Y_2O_3 after degreasing with ethanol. FSP tools were made of high carbon and high chromium steel that had geometric configurations as follows: tool shoulder diameter of 18 mm, pin diameter of 5 mm, and pin height of 3.5 mm. After 60 s of dwell time, the tool was inserted into the workpiece and traversed for the fabrication of surface composite. The experimental layout is shown in Table 2.

2.2.2   Microstructure and Grain Orientation Analysis

The transverse section of the processed workpieces was used to create specimens of dimensions 10 × 10 × 5 mm for microstructure investigation. The specimen was prepared according to the standard ASTM E3-11 including polishing with standard metallographic sheets (600, 800, 1000 and 2000 grit), followed by fine polishing in

diamond suspension. The polished specimens were electropolished with an etchant (80% ethanol and 20% perchloric acid) for 11 s at 9 V. The etched specimens were observed under a high-resolution scanning electron microscope (Make: FEI Model: Quanta 200). Texture analysis (grain size, crystallographic orientation, positions and intensities of specific crystallographic orientations, and mis-orientation angle) was performed using an electron backscattered diffraction (EBSD) technique in the TSL-EDX OIM system that was coupled with the high-resolution scanning electron microscope.

2.2.3 Microhardness

The microhardness of the base material and the fabricated specimen along the transverse sections was analyzed using the Vickers's microhardness tester (Make: Mitutoyo; Model: HVT –M1). The specimen was indented using a diamond indenter under an axial load of 300 g for 15 s, in accordance with the standard ASTM E92. The average of ten microhardness measurements was reported.

2.2.4 Tensile Strength and Ductility

The sub-size specimens (base material and the fabricated specimen) for the tensile test were prepared according to the standard ASTM B557. The tensile test was performed using a computerized universal tensile testing machine (Make: Tinius Olsen) at a cross head speed of 0.5 mm/min. The tensile test was performed in triplicates, and the average result was reported. The engineering stress–engineering strain curve was plotted to analyze the ductility, yield strength, and ultimate tensile strength. The engineering stress and engineering strain were calculated using Eqs. (1) and (2), respectively.

2.2.5 Formability Test

The formability and strain hardening exponent (n) of the base material and fabricated specimen was evaluated through the tensile test. The sub-size specimens for the formability test were prepared according to the standard ASTM B557 (gage length of 45 mm and gage width of 8 mm). Circles of diameter 3 mm were inscribed on the test specimens. The inscribed test specimen was then subjected to a formability test, as described in the previous section. True stress–true strain was plotted to determine the strain hardening exponent. The engineering stress and engineering strain were calculated using Eqs. (1) and (2), respectively. The true stress and true strain were calculated using Eqs. (4) and (5), respectively.

$$\sigma_{\text{eng}} = \frac{F}{A_0} \tag{1}$$

$$\varepsilon_{\text{eng}} = \frac{l_{\text{ext}}}{l_0} \tag{2}$$

$$l_i = l_{\text{ext}} + l_0 \tag{3}$$

$$\sigma_{\text{true}} = \sigma_{\text{eng}}(1 + \varepsilon_{\text{eng}}) \tag{4}$$

$$\varepsilon_{\text{true}} = \ln \frac{l_i}{l_0} \tag{5}$$

where F is force, A is cross-sectional area, σ_{eng}— engineering stress, ε_{eng}—engineering strain, σ_{true}—true stress, $\varepsilon_{\text{true}}$—true strain, l_{ext}—extension length, l_0—original length.

2.2.6 Electrochemical Corrosion

Samples of dimensions $10 \times 5 \times 5$ mm were prepared from base and surface composite workpieces for corrosion tests. The specimen was prepared by polishing with standard metallographic sheets (600, 800, 1000, and 2000 grit), followed by fine polishing. The samples were covered using an insulation tape, leaving an exposed area of 1 mm^2. The corrosion rate and corrosion potential of specimens in artificial seawater solution (accelerated environment) were analyzed using potentiodynamic polarization test in an electrochemical work station. The preparation of electrolyte was done by adding 3.5 wt% of sodium chloride (NaCl) to distilled water. The test was carried out in an electrochemical cell containing a workpiece sample as a working electrode; a platinum rod as a counter electrode, and standard calomel electrodes as a reference electrode. During a sixty minute immersion period, an open-circuit potential was established for the base material and surface composite specimens. Tafel plots were obtained which were used to determine the corrosion rates and corrosion current density. The anodic and cathodic Tafel constants were used to examine the corrosion current density using Eq. (6), and corrosion current I_{corr} using Eq. 7.

$$i_{\text{corr}} = \frac{\beta_a \times \beta_c}{(\beta_a \times \beta_c) \times 2.3} \times \frac{1}{R_p} \tag{6}$$

$$I_{\text{corr}} = i_{\text{corr}} \times A \tag{7}$$

A smooth curve was interpolated from the polarization plot. The Tafel area is the part of the curve where a decade of current varies linearly with potential. The slopes of anodic (β_a) and cathodic (β_c) polarization curves were determined by drawing tangents to the smoothened curve in the Tafel region, as the ratio of change in potential (V) per unit decade change in current (A). The slope lines were extended to intersect at a point in the Tafel region, which corresponds to corrosion potential

E_{corr} and corrosion current density i_{corr}. The corrosion rate was calculated using Eq. (8).

$$\text{CorrosionRate} = \frac{k \times I \times E'}{A \times \rho} \tag{8}$$

where k is a constant for expressing the corrosion rate in mm/year, I is the corrosion current, and E' is the equivalent weight of the corroding specimen, calculated from the molecular weight (M) to the number of electrons (n) involved in the electrochemical reaction.

2.2.7 Advanced Instrumental Characterization

The microstructures of the specimens and the evolution of microstructures after the FSP were examined by scanning electron (SEM) microscopes, high-resolution transmission electron microscope (HR-TEM), and the X-ray diffraction method (XRD). The SEM examinations were performed in a scanning electron microscope (Make: Zeiss Sigma; Model: Gemini 300) with an accelerating voltage of 10 kV to examine the fractured surface of the specimens. The elemental composition and elemental maps of the specimens were obtained using EDS (Make: Oxford Instruments; Model: Ultim Max). The XRD analysis was performed using an x-ray diffractometer (Make: Rigaku; Model: Ultima 4) in the Cu–Kα radiation at a scanning rate of 0.5° per minute to identify the phases in the base and surface composite specimens. Standard metallurgical preparation techniques followed by ion beam etching were performed to prepare the specimens for microstructure analysis using HR-TEM (Make: Jeol; Model: JEM 2100). CrystTBox analytical software was used to analyze the selected area electron diffraction pattern.
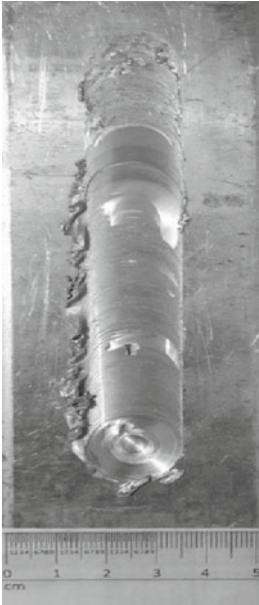
3 Results and Discussion

3.1 Defect Analysis

The defect analysis is comprehensively presented in Table 3.
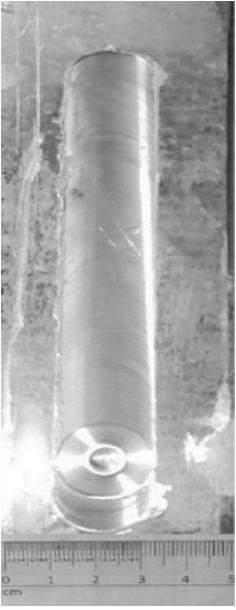
FSP01 was performed with TRS of 750 rpm and TTS of 60 mm/min [10]. As the process parameter combination resulted in inadequate heat generation (high TTS), futile plastic deformation occurred in the specimen FSP01. The meager plastic deformation resulted in ineffective material flow that sequentially caused surface defects. To intensify the plastic deformation, the FSP trial was performed at TTS of 40 mm/min (FSP02). However, specimen FSP02 exhibited considerable defect. The defect also had characteristic features of ineffective plasticization and poor material flow (onion-ring patches on the surface). Specimen FSP03 was performed at

Table 3 Defect analysis of the specimen

Sl. No	Specimen	Macro image of the specimen	Defects	Reason for defect
1	FSP01		Voids, flash scalloping	Inadequate heat generation
2	FSP02		Surface lack of fill	Patchy plastic deformation and also rugged material flow

Table 3 (continued)

Sl. No	Specimen	Macro image of the specimen	Defects	Reason for defect
3	FSP04		No defect	Optimum FSP parameters

a low TTS of 20 mm/min to augment the heat input and then to assist the plastic deformation. Further to improve the surface finish and homogeneous dispersion of reinforcement particles, FSP trial was performed for 2 passes. The specimen FSP04 that was processed at TRS of 750 rpm, TTS of 20 mm/min, and 2 passes appeared to be devoid of defects. Hence, the specimen FSP04 was subjected to microstructure analysis (along the transverse section).

3.2 Microstructure

The microstructure of base material AA3003 alloy and the fabricated surface composite specimen is shown in Fig. 2. AA3003 alloy had an average grain size of 25 μm. Also, grains of size ranging between 20 and 33.5 μm covered an area fraction of 0.60 in the microstructure. The incorporation of reinforcement particles and dynamic recovery-recrystallization phenomenon in the course of FSP reduced the average grain size of the surface composite specimen to 2 μm. The surface composite had a homogeneous microstructure with fine equiaxed grains, as observed in Fig. 2. The recrystallized grains growth was effectively inhibited, which resulted in the fine grains in the stir zone [20–22]. The surface composite material had a dominant α phase and fewer intermetallic phases.

In the inverse pole figure [001] of the base material, as shown in Fig. 3, most of the grains were oriented between (001) and (111) of the crystallographic planes. The surface composite specimen had most of the grains well oriented near to the (001) plane.

Figure 4 shows the bright field and dark field image of the surface composite specimen. The presence of distinguishable phases, deformation, and dislocation region was observed. Figure 5a shows the grain boundaries and sub-grain boundaries (prominent hair-like strands present within the matrix). Multiple clusters of thread-like structures known as dislocation tangles were observed in Fig. 5b. Sub-micron secondary phase β particles were observed in Fig. 5c. The dynamic recovery and recrystallization phenomena resulted in sub-grain structure. The SAED pattern (Fig. 6) confirmed the presence of α-Al and Y_2O_3. The XRD graph of the base material is shown in Fig. 7, which indicated the presence of two distinct phases. In addition to the existing phases, Y_2O_3 was observed in the surface composite specimen [9].

3.3 Microhardness

The hardness of the base material and fabricated surface composite specimen was obtained at equidistant points by applying 300 gf. The average hardness for the base material was 45.82 ± 2.6 HV and that of the surface composite specimen was 84.1 ± 5.4 HV. The hardness of the surface composite specimen increased by 83.54% compared to the base material (45.82 HV). Optimum heat generation coupled
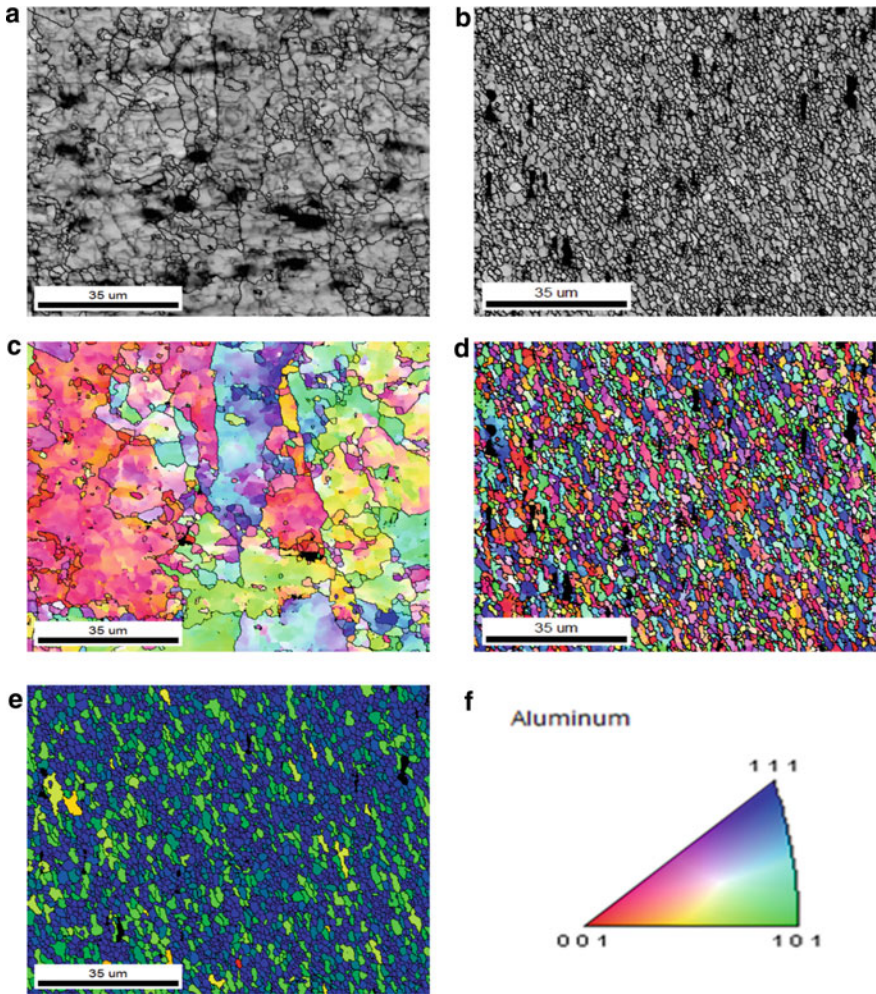
Fig. 2 **a** Microstructure of base material; **b** microstructure of surface composite specimen; **c** grain orientation of base material; **d** grain orientation of surface composite specimen; **e** grain mis-orientation of surface composite specimen

with dynamic recovery and recrystallization in FSP specimens resulted in a high microhardness value. The hardness gain was attributed grain refinement at the stir zone compared to the base metal [8]. In the surface composite specimens, the dynamic recrystallization event resulted in fine grains, disintegrated, and dispersed tougher phase particles, which operated as dislocation movement impediments. Therefore, most of the surface composite specimens had a higher hardness than the base material.
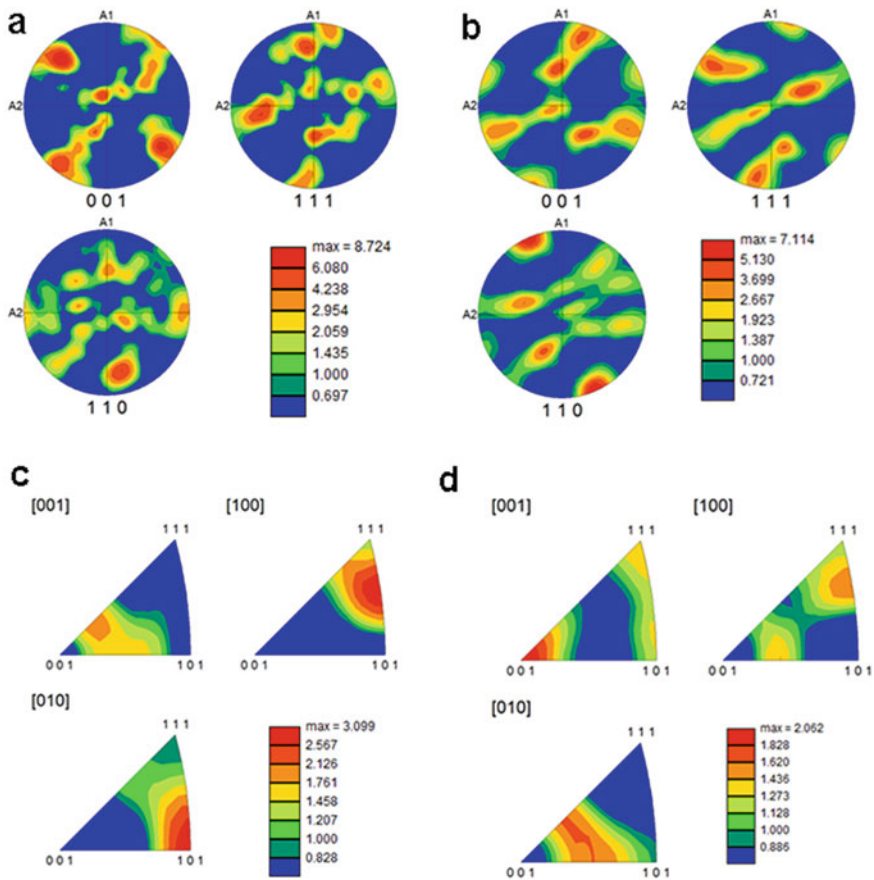
Fig. 3 a Pole figure of base material; **b** pole figure of surface composite specimen; **c** inverse pole figure of base material; **d** inverse pole figure of surface composite specimen

3.4 Tensile Test

The engineering stress–engineering strain graph was utilized to determine the ultimate tensile strength, ductility, and yield strength of the base material and fabricated surface composite. The ultimate tensile strength of the base material was 152.16 ± 5.02 MPa. The fabricated surface composite specimen exhibited an ultimate tensile strength of 171.57 ± 4.08 MPa which was 12.7% higher than the base material [11]. The increase in strength was due to the grain refinement, fragmentation of secondary phases, and fine dispersion of reinforcement. Similarly, the yield strength of the fabricated surface composite specimen (149 MPa) was 7.1% higher than that of the base material (139 MPa). In line with the increase in ultimate tensile strength and yield strength, the ductility of the fabricated surface composite specimen (16.2%) was 8% higher than the base material (15%).
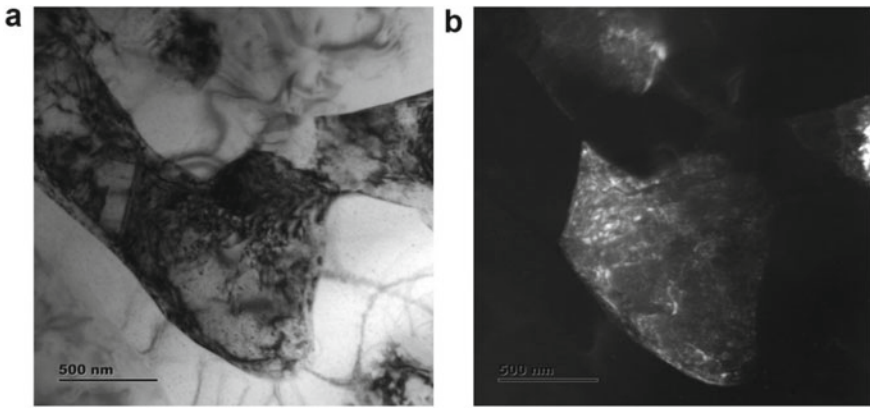
Fig. 4 TEM micrograph images **a** bright field image; **b** dark field image
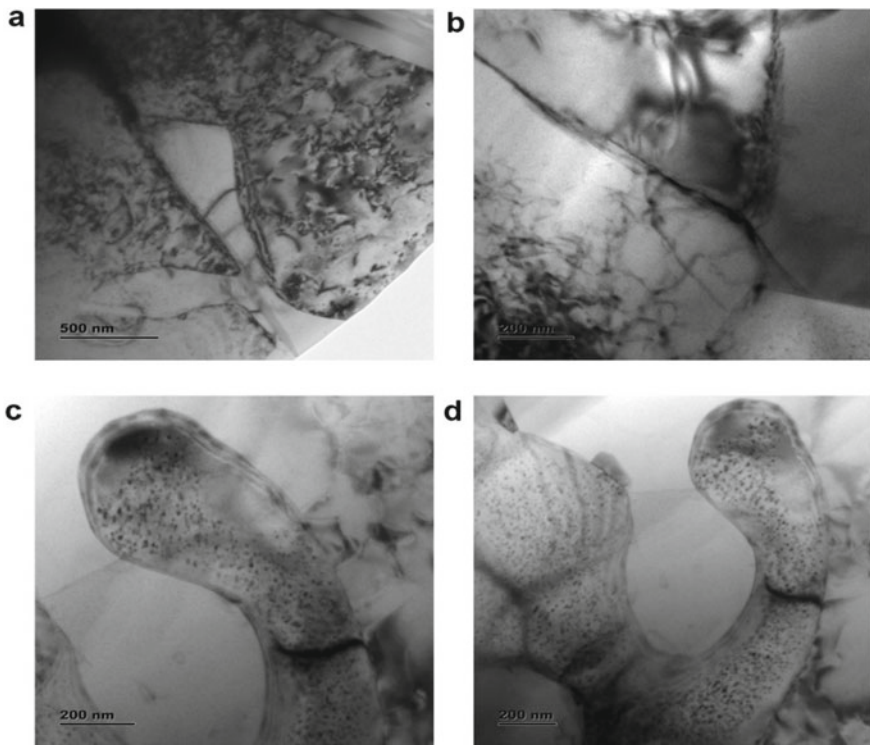
Fig. 5 **a** Phase boundaries, **b** dislocation tangles, **c** secondary phase β particles
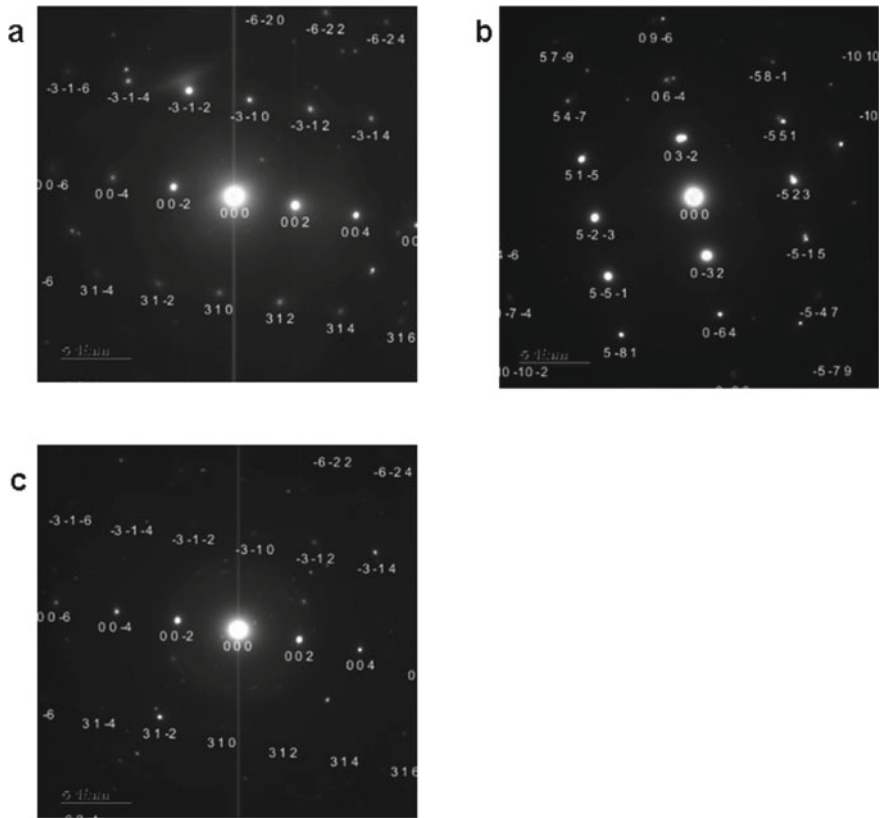
Fig. 6   SAED pattern **a** α-Al phase; **b** Y₂O₃ phase; **c** α-Al phase

3.5   Fractography

The fractography of the base material is shown in Fig. 8. In the fractured base material, dimples were observed in Fig. 8a, b that was characterized by the emergence of micro-voids along the granular boundary of the specimen. Also, intergranular fracture with secondary cracks was observed (marked as B in Fig. 8b). As shown in Fig. 8c, a small zone of plastic deformation (marked by C) was observed. The quasi-cleavage fracture (marked as D) was observed on the non-cleavage plane, parallel to the crack propagation direction in Fig. 8d. The presence of a small deformation zone and few cleavages attest to the low strength of the base specimen.

Fractography of surface composite specimen exhibited characteristic features of a high tensile strength specimen. Dimples (Fig. 9a marked as A) and a large zone of plastic deformation compared to the base specimen (Fig. 9b marked as C) were observed. However, quasi-cleavage dimple (Fig. 9d marked as D) was also observed on the fractured surface. The dominance of equiaxed dimples confirmed that the
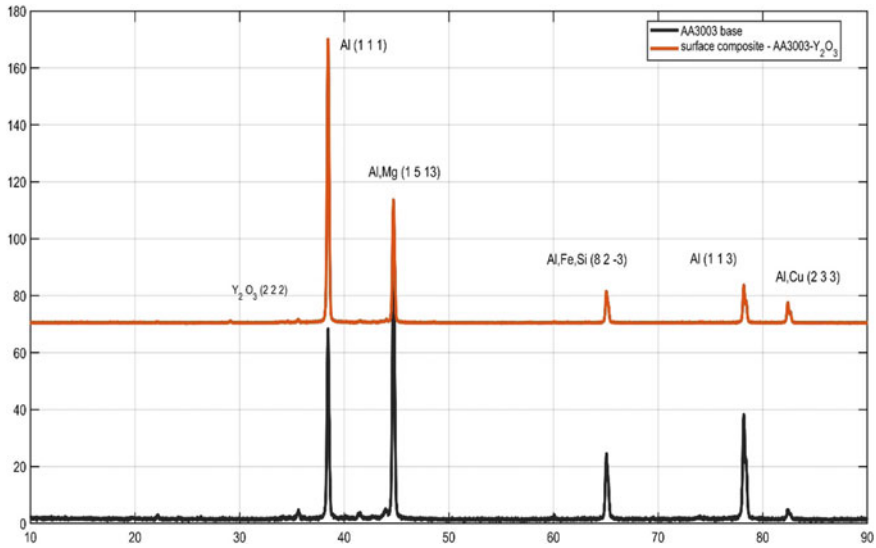
Fig. 7 Phase composition analysis of the base material and surface composite specimen

specimen yielded before fracture. The fracture features attested the improved ductility of the surface composite than the base material.

3.6 Formability

The strain state and level of strain that was accumulated prior to the necking or fracture were referred to as formability. The true stress and true strain were calculated from the force-extension plot that was obtained from the formability test. The slope for the linear portion of the elastic region corresponded to the strain hardening index of the specimen. The elastic region was fitted using a linear equation, which was utilized to determine the strength coefficient K. The strain hardening coefficient for the base material and surface composite specimen was 0.37 and 0.79, respectively. The strength coefficient for base and surface composite specimens was observed to be 432 and 782 MPa. Cumulatively, the surface composite specimen had an increased strain hardening by 53% and strength coefficient by 82%. The improved strength of the surface composite specimen was attributed to the fine grains which lead to grain boundary strengthening. The reduction in grain size was caused by simultaneous input of heat and severe plastic deformation that resulted in dynamic recrystallization. The increment in ductility of the surface composite specimen was linked to strain hardening ability. The surface composite specimen had relatively more modest deformation even at minimal load application. Hence, an increase in formability was anticipated.
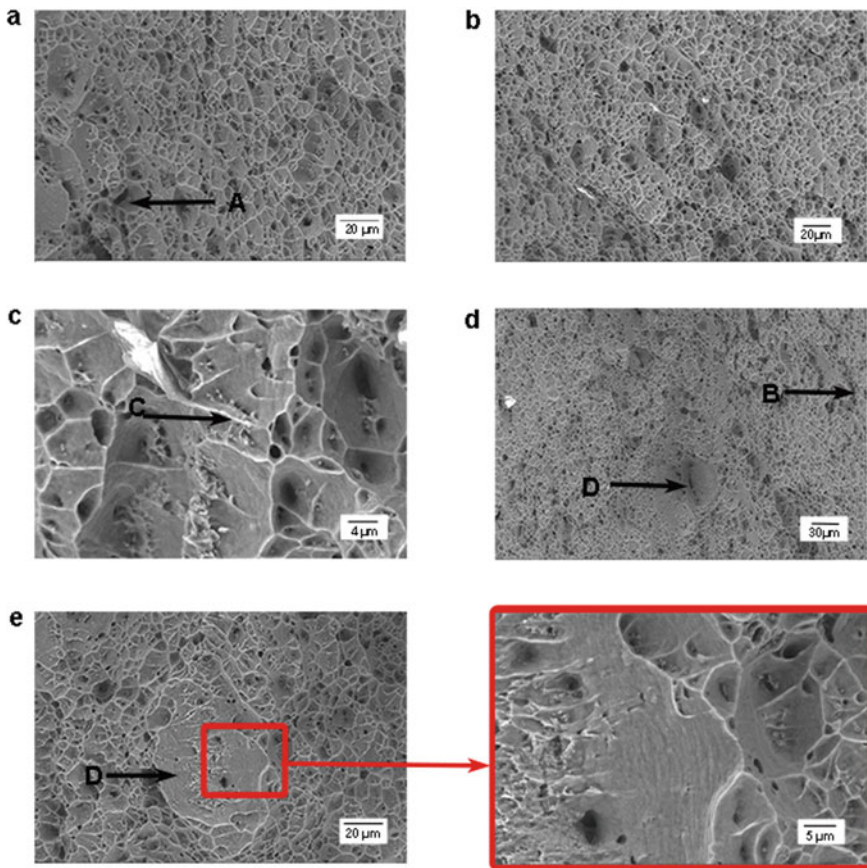
Fig. 8 Fractography of the base material (*A* indicates dimple fracture, *B* indicates secondary cracks, *C* indicates plastic deformation, *D* indicates quasi-cleavage fracture)

The true major strain and true minor strain were calculated from the inscribed circles that were elongated to an ellipse in the course of formability test. Forming limit diagram (FLD) graphically represented the limits for forming the base material and surface composite specimen, as shown in Fig. 10. Also, the minor and major stresses corresponding to local necking phenomenon were depicted. The formability of surface composite increased as the strength increases.

3.7   Electrochemical Corrosion Analysis

The potentiodynamic polarization tests were performed utilizing the electrochemical cell arrangement depicted in the segment electrochemical corrosion. Prior to
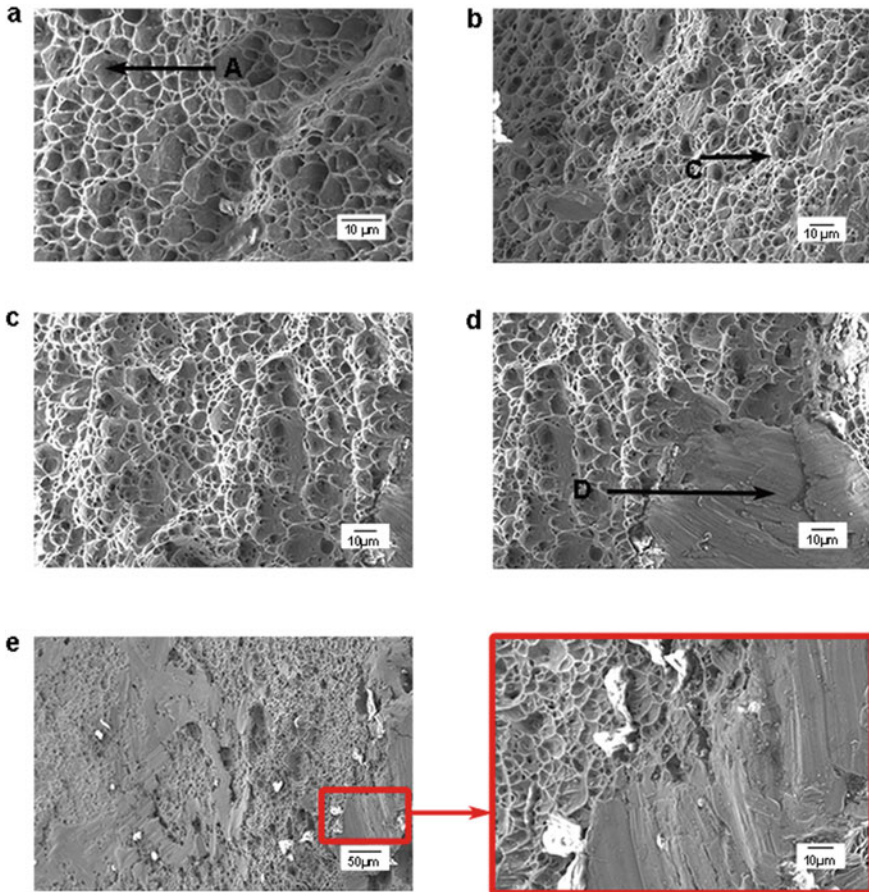
Fig. 9 Fractography of the surface composite specimen (*A* indicates dimple fracture, *B* indicates secondary cracks, *C* indicates plastic deformation, *D* indicates quasi-cleavage fracture)

polarization experiments, the steady-state open-circuit potential (OCP) of the base material was measured to be -0.4728 V whereas, for surface composite specimens, it was observed as -0.4636 V. Typical plots of potentiodynamic polarization obtained are shown in Fig. 11. The decrease in i_{corr} attested to the improvement in corrosion resistance of surface composite specimens.

The corrosion rates for the base and surface composite specimens were observed as 0.305 mm/year and 0.1175 mm/year, respectively. The corrosion resistance of surface composite specimens was superior to the base specimen by 61%. The optimal heat generation causes dynamic recovery and dynamic recrystallization, resulting in fine grains with dispersed secondary phases, which improved the corrosion resistance of surface composites. Also, the presence of yttrium oxide which had high electron work function increased the corrosion resistance of the surface composite specimen.
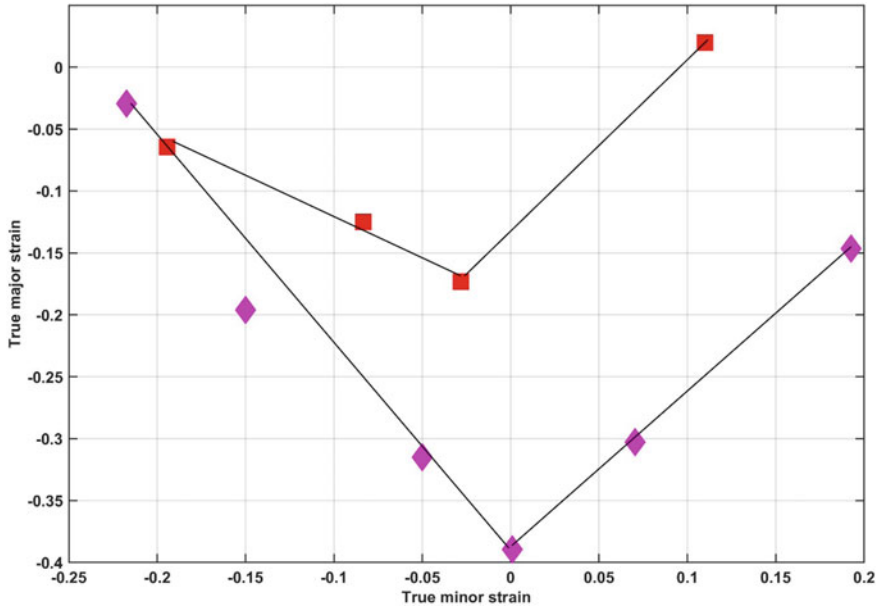
Fig. 10 Forming limit diagram
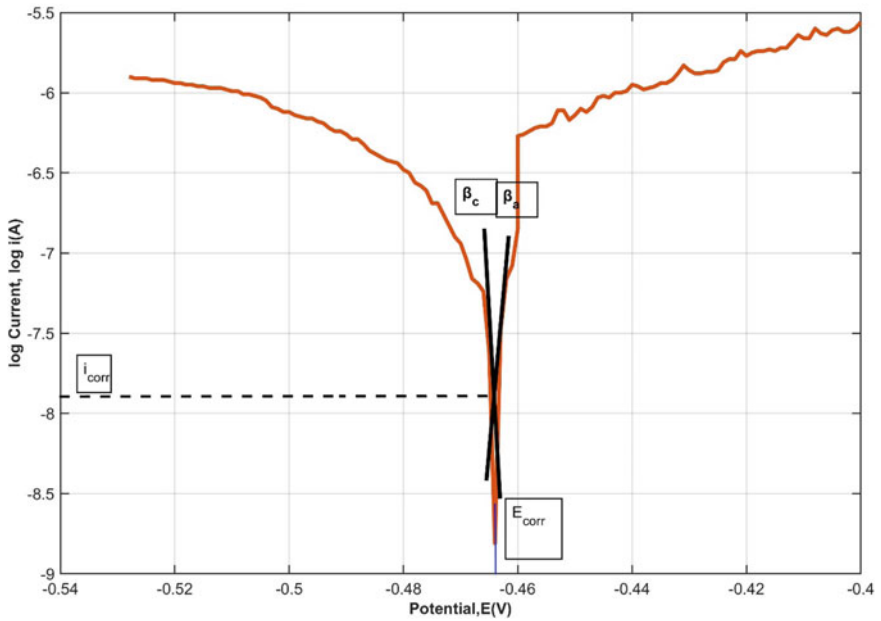
Fig. 11 Typical Tafel plot of the surface composite specimen

4   Conclusion

Friction stir processing was successfully applied to fabricate surface composite of AA3003-Y_2O_3. The microstructure, microhardness, tensile strength, ductility, formability, and corrosion characteristics of base material and surface composite were analyzed. The investigation arrives following conclusion:

- Reinforcement Y_2O_3 was homogeneously dispersed in the AA3003 alloy matrix after FSP. The cumulative effect dynamic recovery, dynamic recrystallization, and presence of Y_2O_3 resulted in grain refinement.
- The hardness of the surface composite specimen was increased by 83.54% compared to the base metal. The ultimate tensile strength/yield strength of the surface composite specimen was 12.7%/7.1% higher than the base material. The strain hardening coefficient for the base material and surface composite specimen was 0.37 and 0.79, respectively.
- Modest deformation at minimal load application and high strength of surface composite specimen concluded an increase in formability.

Authors' Contributions
S. Kamaleshwar: Investigation, Validation, Writing—Original Draft

S. Jagadeesh Kumar: Data Curation, Visualization, Resources

K. Naveen Kumar: Conceptualization, Methodology, Formal Analysis, Writing—Original Draft

S. Keerthana: Investigation, Data Curation

Dr. R. Padmanaban: Resources, Formal Analysis, Methodology, Review, Supervision

Dr. R. Vaira Vignesh: Conceptualization, Formal Analysis, Project administration, Writing—Review.

Highlights of AA3003 - Y$_2$O$_3$

1. Grain refinement
2. Uniform dispersion of Y$_2$O$_3$ particles
3. Corrosion resistance
4. Formability
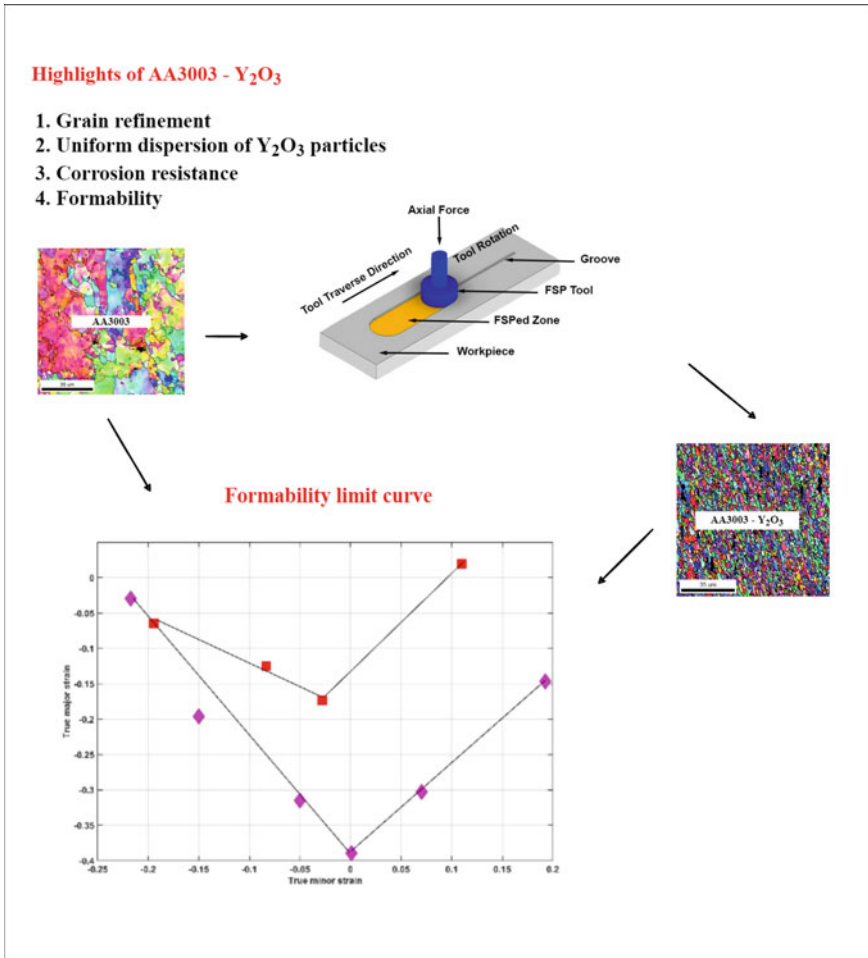
References

1. Surendra Kumar P et al (2020) Microstructural and mechanical behaviour of WC reinforced particles A3003 surface composite fabricated through friction stir processing. Prot Met Phys Chem Surf 56(5):998–1007
2. Kotiyani MZM et al (2017) In-situ fabrication of Al$_3$ Zr aluminide reinforced AA3003 alloy composite by friction stir processing. Mater Charact 131:78–90
3. Kumar KA et al (2019) Synthesis, characterization and mechanical behavior of Al 3003—TiO$_2$ surface composites through friction stir processing. Mater Manuf Processes 34(2):183–191
4. Yahya B, Serdal D (2011) The effect of welding parameters on the mechanical and microstructural properties of friction stir welded dissimilar AA 3003–H24 and 2124/SiC/25p-T4 alloy joints. Sci Res Essays 6(17):3702–3716

5. Takhakh A, Abdullah A (2012) An experimental investigation on fatigue properties of AA3003-H14 aluminum alloy friction stir welds. J Eng **17**

6. Tan YB et al (2017) A study on microstructure and mechanical properties of AA 3003 aluminum alloy joints by underwater friction stir welding. Mater Charact 127:41–52

7. Shinde GV, Arakerimath RR (2021) Multi-response optimization of friction stir welding process of dissimilar AA3003-H12 and C12200–H01 alloys using the full factorial method. Proc Inst Mech Eng, Part E: J Process Mech Eng 235(5):1555–1564

8. Aydin H et al (2010) Influence of welding parameters on the fatigue behaviours of friction stir welds of 3003-O aluminum alloys. Medziagotyra 16:311–319

9. Dehghani M et al (2013) Effects of welding parameters and tool geometry on properties of 3003–H18 aluminum alloy to mild steel friction stir weld. Trans Nonferrous Metals Soc China 23(7):1957–1965

10. Yadav D et al (2017) Fabrication of Al–Zn solution via friction stir processing. Mater Charact 136

11. Chekalil I et al (2020) Prediction of mechanical behavior of friction stir welded joints of AA3003 aluminum alloy. Frattura ed Integrità Strutturale 54:153–168

12. Kotiyani M, Ranjbar K (2019) The effect of heat treatment on the microstructure and mechanical properties of Al/Al3Zr + Al3Ti in-situ hybrid composite fabricated by friction stir processing. J Adv Materi Eng 38:49–64

13. Abdulrehman MA et al (2020) Investigation of mechanical and numerical properties of friction stir welding (FSW) for 3003–H14 aluminum alloys. Defect Diffusion Forum 398:106–116

14. Vaira Vignesh R et al (2018) Influence of FSP on the microstructure, microhardness, intergranular corrosion susceptibility and wear resistance of AA5083 alloy, Tribology. Mater Surf Interfaces

15. Xu A (2020) Properties of friction stir welded 3003–H17 aluminum alloy at high travel speeds. J Phys: Conf Ser 1676:012114

16. Abnar B et al (2015) Effects of heat input in friction stir welding on microstructure and mechanical properties of AA3003H18 plates. **25**:2147−2155

17. Viswanath Allamraju K (2019) Mechanical properties and contact stress analysis between pin and sidewall of AA3003 during dwelling by using FSW. Mater Today: Proc 18:3643–3650

18. Abnar B et al (2014) The effect of cu powder during friction stir welding on microstructure and mechanical properties of AA3003-H18. Metall Mater Trans A 45

19. Nait Salah A et al (2021) Optimization of process parameters of friction stir welded joints of dissimilar aluminum alloys AA3003 and AA6061 by RSM. Mater Today: Proc

20. Govindaraju M et al (2019) Effect of heat treatment on the microstructure and mechanical properties of the friction stir processed AZ91D magnesium alloy

21. Suganya Priyadharshini G et al (2021) Influence of tool traverse speed on microstructure and mechanical properties of CuNi/B4C surface composites. Trans IMF (Int J Surf Eng Coatings) 99:38–45

22. Padmanaban R et al (2020) Effect of friction stir welding process parameters on the tensile strength of dissimilar aluminum alloy AA2024-T3 and AA7075-T6 joints. Materialwisss Werkstofftech 51:17–27

Machinability Characteristics of Lightweight Alloys and Composites

Chapter 19
Machinability Study of Amorphous Bulk Metallic Glass in Micro Milling

Debajyoti Ray and Asit Baran Puri

1 Introduction

Miniaturization is emerging largely in various industrial products for catering the needs in different application areas, such as biomedical engineering, microelectronics, aerospace, etc. Micro cutting is a key process for fabrication of the micro products. Amongst several micro-cutting processes, mechanical micro milling represents a flexible and economical micro-cutting process, suitable for the fabrication of complex-shaped three-dimensional micro products [1]. Micro cutting refers to material removal and creating machined features in micro scales with no constraint on the size of the component (macro/micro) being machined. Micro cutting involves micro tools, where the cutting edge radius is generally maintained in the range of 1–10 µm. The uncut material thickness in micro cutting is often comparable to the grain size or short range atomic orders in the work material and the cutting edge radius. Material removal predominantly takes place in front of the rounded cutting edge, and the material flow around the cutting edge need to be considered to analyse the cutting mechanics. The cutting edge radius in micro cutting influences the cutting process as the effective rake angle is highly negative at low depths of cut. The work material below a certain level of uncut thickness or depth of cut is significantly ploughed by the rounded cutting edge [2]. As shown in Fig. 1, for uncut chip thickness 'h' less than '$h*$', the rounded edge of the cutting tool is involved in micro cutting. For very low feed rates, the uncut layer thickness can be so low that the inflowing work material hardly finds a way to rise over the rake face to be removed as chip. There exists

D. Ray (✉)
Sanaka Educational Trust's Group of Institutions, Durgapur 713212, India
e-mail: debajyoti_ray2002@yahoo.co.in

A. B. Puri
National Institute of Technology Durgapur, Durgapur 713209, India
e-mail: abpuri2000@yahoo.co.in

a critical uncut thickness referred as minimum uncut chip thickness (MUCT) that determines the formation of chip. This limiting uncut chip thickness referred as the minimum uncut chip thickness (h_m) is the removable material layer and is illustrated in Fig. 2. For cutting a particular work material, minimum uncut chip thickness may be within 5–40% of the cutting edge radius [3, 4] depending on tool-work material and cutting conditions. The ploughing phenomenon significantly contributes to the increased cutting forces, larger specific cutting energy, poor surface quality, burr formation, etc. The size effect on the machining characteristics in micro cutting is mainly attributed to increased ploughing and work material strengthening at low cut size [5]. All these aforementioned aspects cause machinability characteristics to differ significantly between the micro cutting and the conventional cutting. The micro-cutting force signatures contain fluctuations particularly in micro milling that arise from the minimum chip thickness effect, ploughing, elastic recovery, tool tip runout, regenerative effects, etc. Cutting edge radius of the micro-cutting tool, cutting process geometry, cutting conditions, ploughing and elastic recovery effects, influence surface roughness, profile accuracy and burr formation that affect the quality of the micro features. Micro parts are made of materials that need to have improved properties to meet the specific requirements. Innovation of gold–silicon amorphous alloys in early 1960's and further development of numerous metallic glasses provided solutions to some of the limitations of aluminium and titanium alloys that are commonly used materials for many micro applications. Bulk metallic glass (BMG) belongs to a new class of light material having amorphous atomic structure. Bulk metallic glasses (BMGs) have density around 6 gm/cc, comparatively lighter than steel. Metallic glasses have high fracture toughness and the ratio of strength to weight of bulk metallic glasses may be typically twice than that of titanium, aluminium, etc. BMGs have typically high hardness that is almost twice the hardness of most stainless steels and titanium, and at least four times the hardness of aluminium. BMGs may be three times more elastic or resilient than practically all crystalline metallic alloys with high elastic limit [6]. BMGs can be also readily cast into near net shapes. High strength and elasticity, excellent wear and corrosion resistance, bio-compatibility in physiological environment, etc., have made BMGs suitable to be used in biomedical applications [7–9]. The enhanced mechanical properties of BMGs bring challenges in the cutting process. Therefore, exploring the machinability characteristics of bulk metallic glass in micro milling is useful to enable effective application of micro cutting to make complex shaped micro parts made of this material. Scientific investigation on micro-scale cutting exploring the machining characteristics has been done through modelling and experimental studies. In this respect, a number of studies analysing several machining aspects of bulk metallic in micro milling and micro turning are available in literatures [10–16]. In this chapter, the machining characteristics and machinability aspects of amorphous bulk metallic glass in micro milling have been highlighted. The machining characteristics discussed here are limited to micro-milling forces, specific cutting energy, surface roughness and burr formation. As machining characteristics depend largely on the process geometry, a brief overview of the micro-milling process is explained in the next section.
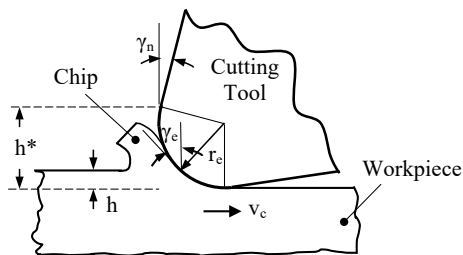
Fig. 1 Schematic of the effective rake angle (γ_e) in micro-scale cutting; (nominal rake angle γ_n, cutting edge radius r_e, cutting velocity v_c)
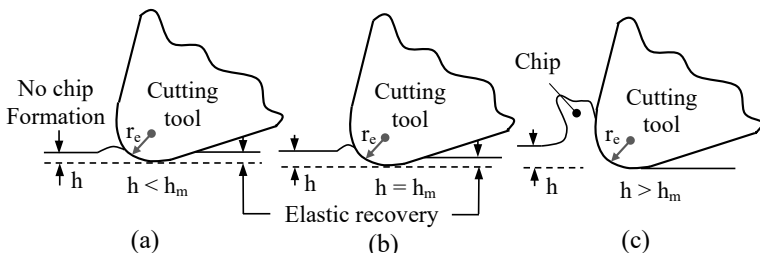
Fig. 2 Influence of minimum uncut chip thickness, cutting edge radius on chip formation

2   Micro-milling Process Overview

Micro channels are common micro features that are often fabricated in micro compo-nents and devices. These micro features of several shapes are produced by full immer-sion micro-milling process, where the micro-cutter diameter determines the width of the micro channel and the axial depth of cut determines the micro-channel depth. If a full immersion micro-end milling process geometry is observed as shown in Fig. 3, it is found that the instantaneous uncut chip thickness is not constant; rather it varies with the rotation of the cutting tool and the immersion angle of the cutting point. At the entry of the cutting edge into the cut, the region from the entry point to the point where clear chip separation starts to occur (region 1), and at the exit of the cutting edge from the cut, the region from the point where clear chip separation seizes to occur to the exit point (region 3), are predominantly ploughing dominant regions. The middle of the micro-channel passage (region 2), where chip separation takes place clearly (provided feed per tooth value is more than MUCT), is the shearing dominant region as the chip formation occurs mainly due to shearing. One side of the micro channel experiences up-milling cut, while the other side experiences down-milling cut.
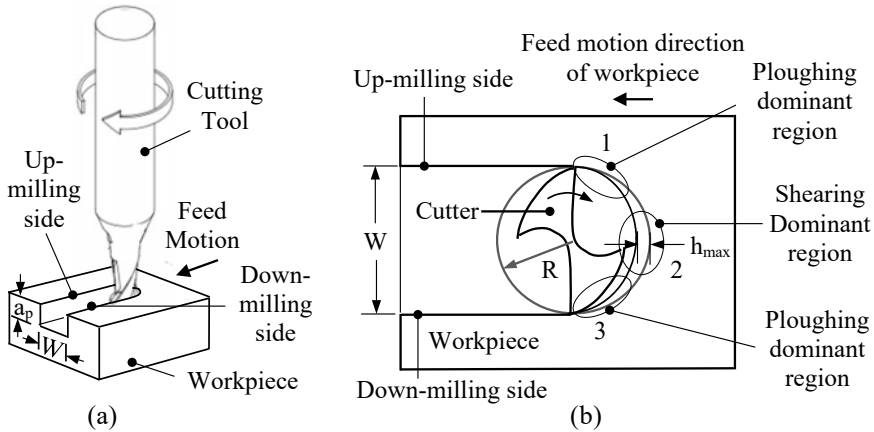
Fig. 3 **a** Full immersion micro-end milling; **b** Geometry of micro-channel (slot) cutting in end milling process by two fluted micro-end mill of radius R; width of the micro channel W, axial depth of cut a_p, maximum uncut chip thickness h_{max}

3   Micro-milling Process Enabling Elements

Micro milling is a powerful and cost-effective process to fabricate miniature components made of various materials such as metals and its alloys, composites, ceramics, polymers, etc. The accuracy of these micro components and the cutting process efficiency largely depend on two fundamental elements in micro milling. They are micro-milling machines and micro-milling cutting tools. The dynamic performance and overall accuracy of a machine tool determine the quality of the machined components and influence the productivity of the micro-machining process. In some micro-milling studies, large-scale ultraprecision machines have been utilized for micro fabrication. These large-scale precision machine tools have highly developed configuration with multi-axis position control, high motion accuracy, increased stiffness and high dynamic stability. These precision machining centres are useful to produce micro parts commercially. However, the cost of these machines is very high. Researchers have also utilized self-developed specialized miniature machine tools. Some miniature machine tools of this type are shown in Fig. 4. These customized machine tools are small in size and are built by assembling and integrating several machine tool components for carrying out specific designed experiments. The components of a machine tool used for micro milling are machine structure, spindle, positioning stages and control system, fixtures and clamping devices. The machine structure includes machine base, column and connecting structural members, work-table, etc. Spindle is a key driving component for rotational motion in a precision micro-machining system. The spindle speeds need to be reasonably high due to low diameter tools used in micro milling. Positioning system is another key component in a micro-machining system. It has a significant impact on machined components in terms of form, dimensional accuracy and surface quality. Control system is a necessary
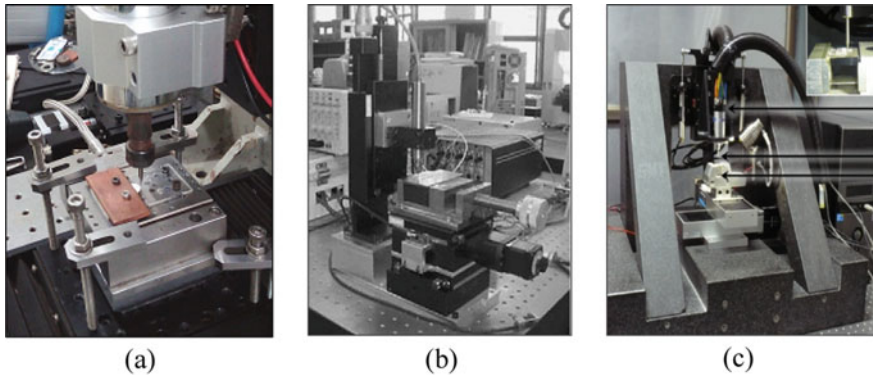
Fig. 4 Miniaturized micro-machine tools, **a** Constructed micro-milling machine [11]; **b** Miniaturized 3-axis machine tool [17]; **c** High-speed micro-machining centre [18]

element that ensures smooth cutting tool and workpiece movements without variation in the subjected feed rate. Clamping devices and fixtures are important elements of a micro-machining system for precise positioning of the workpiece.

Micro-milling tool with cutting edges that removes material from the work piece is an essential element in the mechanical micro-milling process. Micro-milling cutting tool geometry influences the material removal and the generated surface characteristics of the micro parts. Micro milling uses small diameter end mills, where the diameter of these micro-milling tools ranges from 50 µm to 1 mm. The size and geometry of the micro-milling tool determine the size and shape of the micro features [19]. Figure 5 depicts the micro-end milling tool. Cutting edge radius of these micro-milling tools is normally of a few microns. Advanced technologies like micro-EDM, focussed ion-beam machining (FIB) and ultra-precision grinding are the machining methods that are commonly utilized in fabricating these miniature tools. Tungsten carbide is a common material for the commercially available micro-end milling tools. Tungsten carbide is a composite material made of tungsten carbide powders and a binder material. The ultrafine sub-micron grain size and the binder content influence the cutting tool properties. Tungsten carbide micro-end mills are available in coated and uncoated form. Common coating materials include TiAlN, TiCN, TiN, etc. Coating improves tool life by reducing tool wear. Several machinability issues related to micro milling of bulk metallic glass are discussed in the next section.

4   Study of Micro-milling Forces and Specific Cutting Energy

Cutting forces are important process outputs in mechanical micro-cutting processes. Improper cutting conditions may lead to excessive cutting force generation, tool
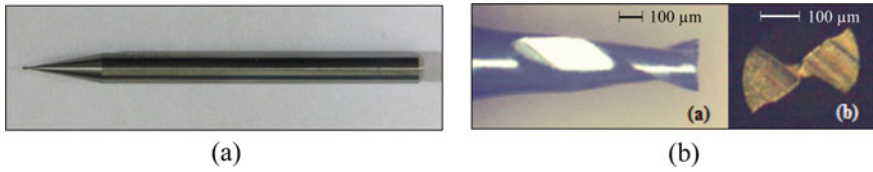
Fig. 5 A Micro-milling cutting tool, **B** Enlarged (*a*) side view and (*b*) Top view of tool tip of micro-end mill [14]

deflection and bending causing tool failure. Gradual tool wear causes increase in the cutting edge radius resulting in higher cutting forces. Cutting force signatures in micro milling contain fluctuations and show erratic behaviour particularly at low feed rates when ploughing effect is significant and difficulty arises in chip formation. Dynamic chip thickness, non-uniformity in material micro structure, vibration, tool runout, regenerative effects, etc. influence the process dynamics and are responsible for the cutting force fluctuations. Micro-machined surface characteristics are also influenced by the static and dynamic characteristics of the cutting forces. A study on mechanistic modelling of cutting forces in micro milling of bulk metallic glass with carbide micro-end mills [10] showed that the values of the cutting force coefficients for Zr-based bulk metallic glass are comparably higher than that estimated for the materials such as structural steels [20] and aluminium alloys [21, 22]. Higher cutting force coefficients indicated higher cutting forces associated to the amorphous metallic alloys than the aforementioned crystalline materials. Higher resistance to the shear deformation and plastic flow in BMGs may be attributed to the higher values of the coefficients. According to this study, the comparison of the predicted and the experimental in-plane cutting force components F_x and F_y in micro-milling bulk metallic glass at cutting speed of 0.062 m/s and feed rates of 0.5 and 6 µm/tooth is shown in Fig. 6. The cutting force profile seems erratic at lower feed rates and the expected periodicity of the cutting force signatures at tooth passing intervals is not clearly observed. Another study of the parametric influences on the cutting forces [11] indicated that the cutting parameters significantly influenced the cutting forces. This study considered cutting parameters such as feed per tooth in the range of 3.3–6.7 µm, axial depth of cut in the range of 11.6–28.4 µm and cutting velocity corresponding to the spindle speed range of 2318–5682 rpm using 0.3 mm diameter micro-end mill. Figure 7 depicts the variation of the in-plane cutting force components within the specific range of the cutting parameters. According to this study, the cutting forces tend to exhibit a nonlinear trend with decrease in the feed rate and tend to increase with the decrease in the feed rate at very low feed rates in contrary to the observation at higher feed rates and showed higher values than anticipated at lower chip load. This might be due to the dominance of ploughing over shearing in the cutting process due to large effective negative rake angles at low feed rates. Cutting force components increased with the increase in feed per tooth at higher feed rates when the feed per tooth was higher than the cutting edge radius. The study further showed that cutting force components increased with the increase in

the axial depth of cut due to increase in the engagement of the work material with the cutting tool and increase in the chip load. Increase of cutting speed that increases the temperature in the cutting zone and also increases the strain rate in the localized shear bands of the bulk metallic glass might have interactive influence on the flow stress and cutting forces. Selection of appropriate cutting parameters using optimisation techniques is a useful option to adopt appropriate machining strategy in achieving optimal cutting performance and improved productivity. Cutting forces are related to the material deformation in cutting and chip formation. Segmented chips are observed in machining of BMGs even at low cutting speeds due to the periodic formation of the localized shear bands [23]. Deformation in metallic glasses is localized into shear bands. Multiple shear band formation along with their branching and interactions is observed in the deformation zone. In bulk metallic glasses, crystalline particles that may form within the amorphous matrix during machining, blocks crack growth and propagation and initiates formation of multiple shear bands [8]. Suppression of shear band propagation due to lack of the preferential sites from where the shear banding develops leads to increased strength and certain degree of ductility of the material in micro cutting. Experimental study of cutting forces in macro turning process of amorphous BMG, Al-alloy and stainless steel also indicated greater cutting forces in amorphous material in comparison with the crystalline materials [24].
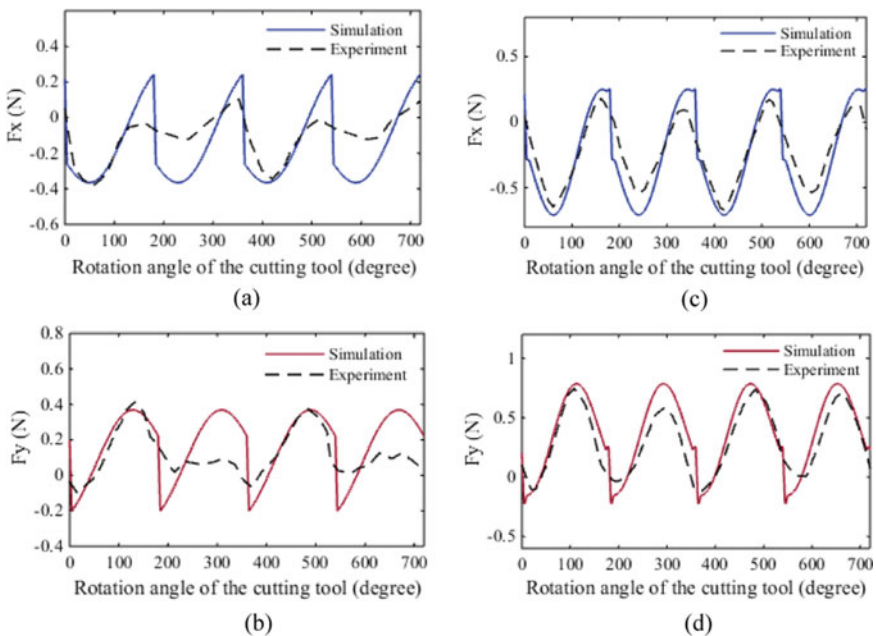
Fig. 6 Predicted and experimental cutting forces **a**, **b** at feed rate 0.5 μm/tooth; and **c**, **d** at feed rate 6 μm/tooth, cutting velocity 0.062 m/s, axial depth of cut 20 μm [10]
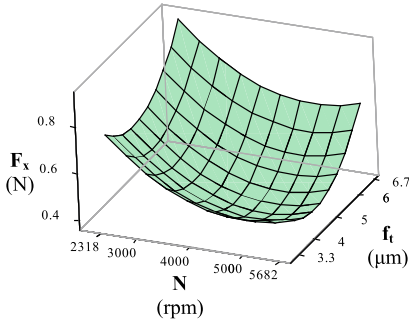
(a) Response surface plot of F_x with spindle speed (N) and feed per tooth (f_t) at axial depth of cut (a_p) equal to 20 μm.
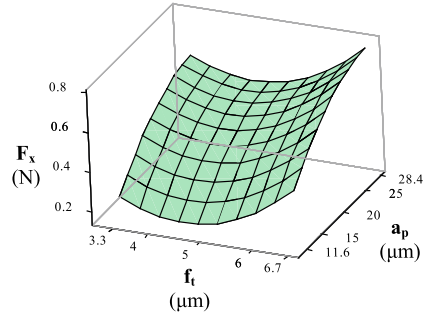
(b) Response surface plot of F_x with feed per tooth (f_t) and axial depth of cut (a_p) at spindle speed (N) equal to 4000 rpm.
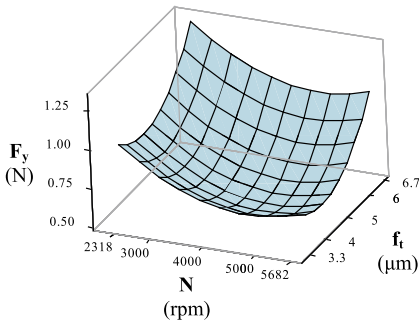
(c) Response surface plot of F_y with spindle speed (N) and feed per tooth (f_t) at axial depth of cut (a_p) equal to 20 μm.
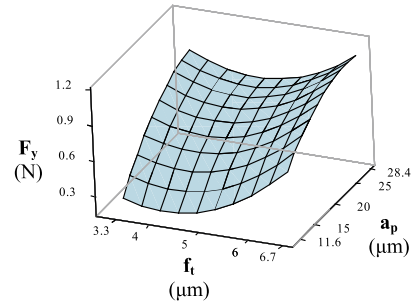
(d) Response surface plot of F_y with feed per tooth (f_t) and axial depth of cut (a_p) at spindle speed (N) equal to 4000 rpm.

Fig. 7 Variation of in-plane cutting force components (F_x, F_y) within the specific range of cutting parameters, namely spindle speed (N), feed per tooth (f_t) and axial depth of cut (a_p) [11]

Specific cutting energy is an important characteristic that assesses the machinability of a work material for a particular process and is a measure of the energy expended to remove unit amount of material. A study related to the analysis of specific cutting energy in micro milling of bulk metallic glass [12] indicated that specific cutting energy values are influenced by the ratio of uncut material thickness to the cutting edge radius. In this analysis for the assessment of energy dissipation, a micro-cutting model was considered that takes into account the forces in the cutting direction of the shearing region and the rubbing region that lies beneath the rounded cutting edge. In this study, the experimental results of the specific cutting energy estimated by dividing the average resultant in-plane cutting force by the average chip load showed a sharp increase in the specific cutting energy at very low feed rates when feed per tooth is less than the cutting edge radius indicating size effect in specific cutting energy. For feed per tooth larger than the cutting edge radius, a marginal decrease in specific cutting energy with increase in feed rate was observed.
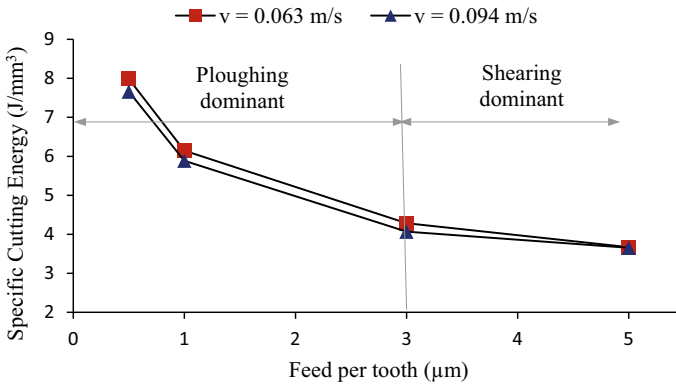
Fig. 8 Specific cutting energy versus feed per tooth (f_t) at axial depth of cut (a_p) of 20 μm [12]

According to the aforementioned study, the variation of average in-plane specific cutting energy is shown in Fig. 8.

The 'size effect' is typically characterized with the abrupt nonlinear increase of specific cutting energy with the decrease of uncut chip thickness at values below the edge radius of the cutting tool in micro cutting. Several research studies have been carried out to understand the size effect in micro cutting. The size effect in micro-milling bulk metallic glass may be attributed to the increased strengthening of the work material in small size deformation processes such as micro cutting. In several studies [25–27], it has been observed that small size deformation of micro-sized samples of bulk metallic glasses showed increased strength and transition from brittle to ductile state. In metallic glasses, shear transformation zones develop embryonic shear bands that propagate rapidly leading to failure. The sites that develop shear banding gets substantially reduced in micro-deformation processes as in micro cutting due to reduced deforming volume, thereby reducing shear banding events and propagation leading to increased strengthening effect of the work material.

5   Study of Surface Quality

Surface roughness is a parameter to quantify the quality of the generated surface. Micro-machining processes aim to generate functional surfaces having good surface finish. Process kinematics affects surface quality in micro milling. Excessive ploughing in micro cutting leads to work material side flow and elastic recovery, resulting in abrupt non-uniform rise of the machined surface and increase in surface roughness. Process dynamics and stability, motion errors of different linear and rotary drives greatly influence the achievable surface quality. Several other stochastic factors such as abrupt loss of edge geometry and cutting edge serrations also affect the surface roughness. In an experimental study of micro-milling bulk metallic glass
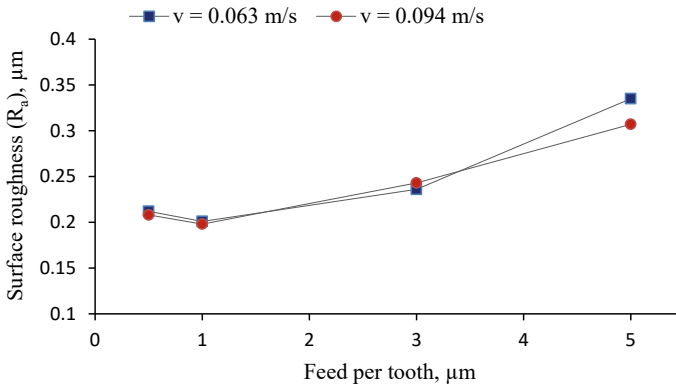
Fig. 9 Variation of surface roughness (R_a) at different feed rates [12]

[12] using uncoated micro-end mill of edge radius 3 µm, surface roughness (R_a) for two different cutting speeds was measured. The surface roughness was measured at the floor of the micro channels. The results of the study as depicted in Fig. 9 indicated that surface roughness decreased with the decrease in the feed rate when feed rate is greater than the cutting edge radius. For the two cutting speeds, the surface roughness remained approximately same for feed per tooth value up to 3 µm/flute. Surface roughness showed an increasing tendency with the decrease in feed rate at very low feed rates. The surface generation involved the secondary cutting edge at the tip of the micro tool. Low uncut chip thickness with respect to cutter edge radius possibly had resulted in intense ploughing at very low feed rates. Some of the plastically deformed material was ploughed aside and material side flow occurred [28–32] at very low feed rates. Material side flow caused abrupt material accumulation on the feed mark ridges that resulted in the increased roughness values.

6 Study of Burr Formation in Micro Milling

Formation of burrs creates an undesirable edge condition of the machined feature. It is necessary to understand the burr formation mechanism and the characterization of burrs formed under different cutting conditions. Two types of burrs form in micro-slotting process. They are Poisson burrs and roll-over burrs. Roll-over burrs are formed at the entry and the exit of the micro channels. However, Poisson burrs are difficult to remove and occur over an extended length of the machined edge [33, 34]. The top Poisson burrs are formed at the top edges of the micro channels when the sidewall material is severely ploughed and bulges out upwards due to the indenting pressure of the rounded cutting edge and intense plastic deformation of the side wall material. The extent of bulging and correspondingly the burr size depends on the material properties, the pressure developed due to the radial force applied by the

cutting tool and the micro-cutter edge radius. The cutting parameters influence the indenting pressure that depends on the radial force applied on the sidewall [14]. The burr formation in micro milling is influenced by the micro-cutting mechanics, inter-action effects between the cutting tool and the work material. Ductility of the work material enhances the development of burrs. An experimental study that analyses the parametric influences on the generation of top burrs in full immersion micro-milling process [15] indicated that the cutting parameters significantly influenced the width of top burrs in both up-milling and down-milling sides. This experimental study used 0.3 mm diameter micro-end mill having average edge radius of 3 µm and considered cutting parameters such as feed per tooth in the range of 3.3–6.7 µm, axial depth of cut in the range of 11.6–28.4 µm and cutting velocity of 0.036 and 0.090 m/s. Figure 10 depicts some scanning electron microscope (SEM) images of top burrs in micro milling of bulk metallic glass. According to this study, the variation of the width of top burrs in up-milling and down-milling sides is depicted in Fig. 11. The plots indicate that the top burr width developed in down-milling side was lower than in the up-milling side. Observing the variation of top burr width with the cutting parameters shows that decrease in feed rate resulted in the increase of top burr width. Ploughing might have occurred for a longer time at low feed per tooth than for higher feed per tooth values. Thus, the lateral bulging of material occurred more intensely at low feed rates. Cutting action with chip formation started earlier at higher feed rates than in lower feed rates due to which action of lateral deformation at the sidewall diminished quickly resulting in lower sized burrs. It is further revealed from Fig. 11 that increase in axial depth of cut caused an increase of top burr width. Increase in depth of cut resulted in increased amount of work material being displaced by the cutting edge due to plastic deformation and increased lateral rise of work material in the direction of minimum restraint, thereby increasing the burr width.

(a)   (b)
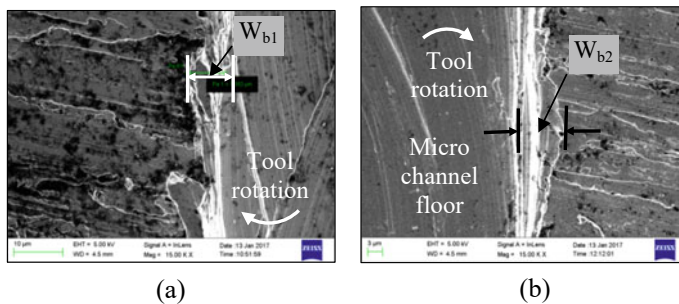
Fig. 10 SEM images of top burrs in micro-slot milling **a** Burr formation at up-milling side (W_{b1}), $v_c = 0.047$ m/s, $f_t = 4$ µm, $a_p = 15$ µm; **b** Burr formation at down-milling side (W_{b2}), $v_c = 0.079$ m/s, $f_t = 6$ µm, $a_p = 15$ µm [15]

Surface plot of W_{b1} with f_t and a_p
at $v_c = 0.63$ m/s.

Surface plot of W_{b2} with f_t and a_p
at $v_c = 0.63$ m/s.

Surface plot of W_{b1} with v_c and a_p
at $f_t = 5$ μm.

Surface plot of W_{b2} with v_c and a_p
at $f_t = 5$ μm.
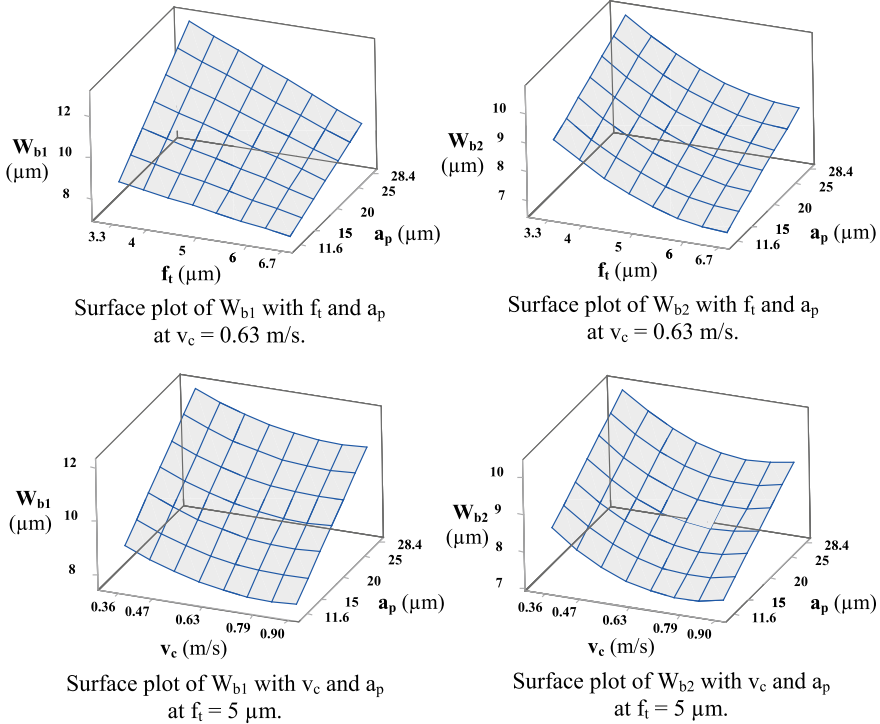
Fig. 11 Influence of cutting parameters (cutting speed v_c, feed per tooth f_t, axial depth of cut a_p) on the width of top burrs in up-milling side (W_{b1}) and down-milling side (W_{b2}) [15]

7 Conclusions

This chapter discusses the micro machinability of bulk metallic glass in terms of micro-cutting forces, specific cutting energy, surface roughness and micro-burr formation. A brief overview of the full immersion micro-milling process is also presented. Different critical issues that influence the micro-cutting process have been discussed. According to the results of different studies carried out, it may be concluded that feed rate influences the different machining characteristics significantly. At low feed rates, cutting forces were higher than anticipated at low chip loads. Specific cutting energy exhibited the size effect. The micro mechanism that is relevant in exhibiting size effect of amorphous materials is discussed. Experimental results also indicated the 'size effect' in the surface roughness when surface roughness decreased with the decrease in the feed rate, reached a minimum and then tended to increase with further reduction in feed rate. At low temperatures though metallic glasses exhibit brittleness, however, in micro-cutting metallic glass, significant burrs were formed indicating increased ductility in small-scale high rate deformation processes. Experimental studies showed that lower feed rate augmented

higher width of top burrs in micro milling. Micro cutting being an emerging technology with limited knowledge in process mechanisms and limited experience in productive manufacturing confronts the challenge of effective industrial utilization. However, the discussion made in this chapter would help the industries and future researchers to understand micro-milling process mechanisms better and utilize the knowledge for cost-effective fabrication of micro parts made of specialized materials such as amorphous bulk metallic alloys.

References

1. Chae J, Park SS, Freiheit T (2006) Investigation of micro-cutting operations. Int J Mach Tools Manuf 46(3–4):313–332
2. Waldorf DJ, Devor RE, Kapoor SG (1999) An evaluation of ploughing models for orthogonal machining. ASME J Manuf Sci Eng 121(4):550–558
3. Ikawa N, Shimada S, Tanaka H (1992) Minimum thickness of cut in micromachining. Nanotechnology 3(1):6–9
4. Yuan ZJ, Zhou M, Dong S (1996) Effect of diamond tool sharpness on minimum cutting thickness and cutting surface integrity in ultraprecision machining. J Mater Process Technol 62(4):327–330
5. Huo D, Cheng K (2013) Overview of micro-cutting. In: Cheng K, Huo D (eds) Micro-cutting: fundamentals and applications. Wiley, UK, pp 1–16
6. https://materion.com/media/files/beryllium/materion-bulk-metallic-glass-data-sheet
7. https://www.liquidmetal.com/info-center, Liquidmetal® Technologies Design Guide Rev. 4.0
8. Chen M (2011) A brief overview of bulk metallic glasses. NPG Asia Mater 3(9):82–90
9. Wang WH, Dong C, Shek CH (2004) Bulk metallic glasses. Mater Sci Eng R 44(2–3):45–89
10. Ray D, Puri AB, Hanumaiah N, Halder S (2020) Mechanistic modelling of dynamic cutting forces in micro end milling of Zr-based bulk metallic glass. Int J Mach Mach Mater 22(6):527–550
11. Ray D, Puri AB, Nagahanumaiah (2019) Investigation on cutting forces and surface finish in mechanical micro milling of Zr-based bulk metallic glass. J Adv Manuf Syst 18(1):113–132
12. Ray D, Puri AB, Hanumaiah N, Halder S (2020) Analysis on specific cutting energy in micro milling of bulk metallic glass. Int J Adv Manuf Technol 108(1):245–261
13. Ray D, Puri AB, Hanumaiah N (2020) Experimental analysis on the quality aspects of micro-channels in mechanical micro milling of Zr-based bulk metallic glass. Measurement 158(1):107622/1–14
14. Ray D, Puri AB, Hanumaiah N, Halder S (2019) Modelling of top burr formation in micro-end milling of Zr-based bulk metallic glass. ASME J Micro Nano-Manuf 7(4):041004/1–12
15. Ray D, Puri AB, Hanumaiah N (2019) An experimental investigation on the formation of burrs in micro milling of Zr-based amorphous bulk metallic glass. Int J Mater Prod Technol 59(2):140–171
16. Chen X, Xiao J, Zhu Y, Tian R, Shu X, Xu J (2017) Micro-machinability of bulk metallic glass in ultra-precision cutting. Mater Des 136:1–12
17. Wang W, Kweon SH, Wang SH (2005) A study on the roughness of the micro-end milled surface produced by a miniaturized machine tool. J Mater Process Technol 162–163:702–708
18. Bajpai V, Kushwaha AK, Singh RK (2013) Burr formation and surface quality in high speed micro milling of titanium alloy (Ti6Al4V). In: Proceedings of the ASME 2013 international manufacturing science and engineering conference MSEC2013, pp 1–8
19. Aramcharoen A, Mativenga PT, Yang S, Cooke KE, Teer DG (2008) Evaluation and selection of hard coatings for micro milling of hardened tool steel. Int J Mach Tools Manuf 48(14):1578–1584

20. Srinivasa YV, Shanmugam MS (2013) Mechanistic model for prediction of cutting forces in micro-end milling and experimental comparison. Int J Mach Tools Manuf 67:18–27
21. Malekian M, Park SS, Jun MBG (2009) Modelling of dynamic micro-milling cutting forces. Int J Mach Tools Manuf 49(7–8):586–598
22. Moges TM, Desai KA, Rao PVM (2017) On modelling of cutting forces in micro-end milling operation. Mach Sci Technol 21(4):562–581
23. Jiang MQ, Dai LH (2009) Formation mechanism of lamellar chips during machining of bulk metallic glass. Acta Mater 57(9):2730–2738
24. Bakkal M, Shih AJ, Scattergood RO (2004) Chip formation, cutting forces, and tool wear in turning of Zr-based bulk metallic glass. Int J Mach Tools Manuf 44:915–925
25. Jang D, Greer JL (2010) Transition from a strong-yet-brittle to a stronger-and-ductile state by size reduction of metallic glass. Nat Mater 9:215–219
26. Kuzmin OV, Pei YT, Chen CQ, Hosson JTMD (2012) Intrinsic and extrinsic size effects in the deformation of metallic glass nanopillars. Acta Mater 60(3):889–898
27. Lee CJ, Huang JC (2007) Sample size effect and microcompression of $Mg_{65}Cu_{25}Gd_{10}$ metallic glass. Appl Phys Lett 91:161913
28. Kishawy HA, Elbestawi MA (1999) Effects of process parameters on material side flow during hard turning. Int J Mach Tools Manuf 39:1017–1030
29. Xu F, Fang F, Zhang X (2018) Effects of recovery and side flow on surface generation in nano-cutting of single crystal silicon. Comput Mater Sci 143:133–142
30. Liu K, Melkote SN (2006) Effects of plastic side flow on surface roughness in micro-turning process. Int J Mach Tools Manuf 46:1778–1785
31. El-Wardany TI, Elbestawi MA (1998) Phenomenological analysis of material side flow in hard turning: causes, modelling and elimination. Mach Sci Technol 2(2):239–251
32. He CL, Zong WJ, Sun T (2016) Origins for the size effect of surface roughness in diamond turning. Int J Mach Tools Manuf 106:22–42
33. Aurich, JC, Dornfield, D, Arrazola, PJ, Franke V, Leitz, L, Min S (2009) Burrs–analysis, control and removal. CIRP Ann–Manuf Technol 58(2):519–542
34. Gillespie LK, Blotter PT (1976) The formation and properties of machining burrs. Trans ASME 98(1):66–74

Chapter 20
Machinability Studies on Al–Fe–Si Alloy-Based Composites

C. Chanakyan, S. V. Alagarsamy, C. Sivakandhan, and K. Senthamarai

1 Introduction

Wire electrical discharge machining (WEDM) is a nontraditional machining method that is used to manufacture difficult-to-machine materials such as composites and intermetallic compounds. It is commonly used to cut plates up to 300 mm thick, as well as punches, tools, and dies from hard metals that are difficult to process using conventional techniques [1]. This process also known as a thermo-electrical process in which material is eroded off the work piece by a succession of discrete sparks that occur between the work piece and the wire electrode. A thin film of dielectric fluid separates the tool and is continually delivered to the region being machined to flush away the eroded particles [2]. Discharge current, pulse duration, wire speed, wire tension, type of dielectric fluid are the most important variables for evaluation of WEDM performance [3]. However, because to the vast number of variables and stochastic nature of the operation, even a highly trained operator would struggle to achieve optimal processing and prevent wire breakage when using WEDM. Hence, it

C. Chanakyan
Department of Mechanical Engineering, R.V.S. College of Engineering and Technology, Coimbatore 641402, India

S. V. Alagarsamy (✉)
Department of Mechanical Engineering, Mahath Amma Institute of Engineering and Technology, Pudukkottai 622101, India
e-mail: s.alagarsamy88@gmail.com

C. Sivakandhan
Department of Mechanical Engineering, Nadar Saraswathi College of Engineering and Technology, Theni 625531, India

K. Senthamarai
Department of Mechanical Engineering, Sri Raaja Raajan College of Engineering and Technology, Karaikudi 630301, India

is essential to choose machining settings for the WEDM process in order to achieve optimal machining performance [4]. The necessary machining parameters are usually selected based on previous experience or values from a handbook. However, this does not ensure that the chosen machining parameters produce optimal or near-optimal machining results for that specific wire electrical discharge machine and environment. Mahapatra et al. [5] Described how to use the Taguchi approach to optimize WEDM process parameters. It has been demonstrated that the gray-based Taguchi approach may be used to optimize multi-response processes by adjusting process parameters. Alagarsamy et al. [6] studied the machining performances like MRR and SR of Al7075-10wt.% TiO_2 composite while the wire EDM process by using Taguchi coupled desirability function approach. They stated that pulse current was the most prominent factor with a contribution of 51.96%, followed by pulse-on time 34.59% and pulse-off time 12.21%, respectively. Anand Babu et al. [7] investigated the effect if wire cut EDM parameters on MRR and SR of hybrid Al metal matrix composites. They noticed that the pulse-on time was a highly influential factor on MRR, whereas pulse-off time shows high impact factor for SR. Sondararajan et al. [8] studied the machining performance of A413 with 12wt.% B_4C composites during WEDM process. They reported that the higher amount of MRR produced when the maximum setting of peak current and pulse-on time, respectively. Similarly, the better SR was acquired for higher values of pulse-off time. Dineshkumar et al. [9] investigated the effect of machining parameters on the combined objective of maximum MRR and minimum SR during WEDM of AA7178-10wt.% ZrB_2 composite. They found that as the 11A of peak current, 112 µs of pulse-on time, 45 µs of pulse-off time and 7 m/min of wire feed rate gives the higher MRR with lesser SR. Venkatesan et al. [10] carried out the WEDM process of aluminum metal matrix composites by chosen four input parameters like pulse-on time (T_{on}), pulse-off time (T_{off}), servo voltage (V_s) and peak current (A), and output response such as MRR, SR and kerf width. They noted that as the voltage and peak current increased the MRR increases. Subramaniam et al. [11] presented the influence of WEDM processing parameters on SR for Al/10wt.% SiO_2 composite by Taguchi method and they concluded that the pulse-off time (44.69%) was the preliminary dominant factor affecting the SR, subsequently by current (14%) and pulse-on time (4.58%), respectively. Thella Babu et al. [12] optimized the wire EDM process variables on Al7075/SiC_p composites using integrated statistical approach. According to the ANOVA results, the particle size, pulse-on time and wire tension has more significant on the overall quality of the process. Rajyalakshmi et al. [13] analyzed the WEDM process parameters on Inconel 825 by employing Taguchi gray relational analysis. They understood that a Taguchi approach is well appropriate method to obtain the optimum parameters condition for maximization of MRR and minimization of SR. Geetha et al. [14] determined the influence of machining parameter on MRR and SR for Al6061/MoS_2 composites during WEDM process. They revealed that the wire feed and pulse-off time were primary dominant variables on SR and pulse-on time and peak current were more impact factors for the MRR. Sonia Ezeddini et al. [15] predicted the WEDM machining parameters on SR of Ti–Al intermetallic-based composites using Taguchi combined response surface method. They concluded that the pulse-on time,

flushing pressure and the cutting speed are the most noteworthy factors, whereas the servo voltage is found to be less significant for obtaining the less SR.

Therefore, the aim of the present study is to obtain the optimum condition of WEDM process parameters for the higher MRR and lower SR of AA8011/10wt.% TiO_2 composite fabricated by stir casting technique. Furthermore, ANOVA was employed to explore the order of significant effect of parameters on the response and also observed the percentage contribution.

2 Materials and Methods

2.1 Composite Fabrication

In this work, Al–Fe–Si alloy (AA8011) was chosen as matrix alloy and TiO_2 (10wt.%) was used as reinforcement ceramic particles. The compositions of matrix alloy are presented in Table 1. In matrix alloy, Fe and Si are the primary elements which are given the better strength and stiffness property. To synthesize the AA8011-TiO_2 composite, stir casting method is used. Figure 1 illustrates the methodology of present study.

Table 1 Chemical elements of AA8011

Elements	Fe	Si	Cu	Mn	Mg	Cr	Zn	Ti	Al
Weight (%)	0.6–1.0	0.5–0.9	0.10	0.20	0.05	0.05	0.10	0.08	Remaining
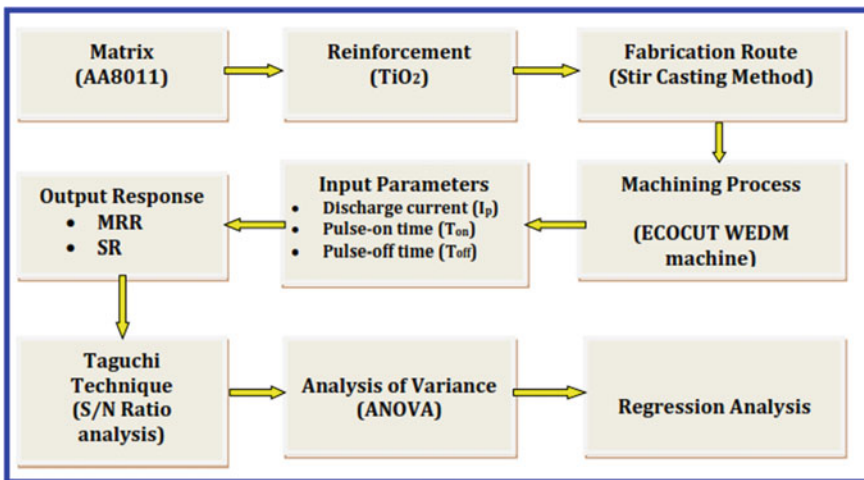
Fig. 1 The layout of current investigation

Fig. 2 SEM image of AA8011-10wt.% TiO$_2$ composite
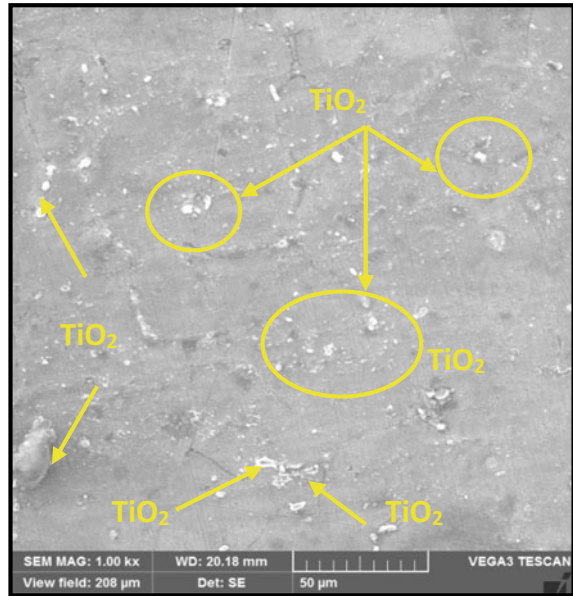
The stir casting process was used to make the composite in this work, since mechanical stirring ensured homogeneous distribution of reinforcement particles in the matrix alloy. The weighted amount of AA8011 ingots was first placed in the crucible of the electrical furnace, which was retained at 750 °C until the entire metal was completely melted. An TiO$_2$ particles at 10wt.% was preheated for 1 h at 200 °C [16] to eliminate moisture content and increase wettability with the molten alloy. Simultaneously, mechanical stirring is started by immersing a three-blade stainless steel stirrer in the molten alloy, generating a vortex in the melt. The heat-treated TiO$_2$ particles were then continually injected into the vortex slurry of molten metal. In the meantime, the stirring speed was increased to 280 rpm and held for 10 min [17]. The blended composite slurry was then put into the warmed mold and allowed to harden at room temperature in the air. After solidification, the composite specimens were removed from the mold and the required form was achieved by preferred machining. Figure 2 shows the microstructure of processed composite taken by scanning electron microscopy and it was ensure the presence of TiO$_2$ particles evenly distributed within the matrix alloy.

2.2 Design of Experiments

The selection of suitable process parameters is even more important, when predicting machining performance for newly suggested composite materials. Many parameters have been shown to have a significant impact on the machining performance of

Table 2 Machining parameters and its levels

Machining Parameters	Notations	Units	Level 1	Level 2	Level 3
Discharge current	I_p	amps	4	6	8
Pulse-on time	T_{on}	μs	110	114	118
Pulse-off time	T_{off}	μs	50	54	58

Al matrix composites in previous research [18]. As a result, three input machining parameters and three levels were chosen from prior research for this investigation and are shown in Table 2.

2.3 WEDM of Composite

ECOCUT wire EDM machine was used to machined the suggested AA8011-10wt.% TiO$_2$ composite. The cutting tool was a brass wire with a diameter of 0.25 mm, which was connected to the negative terminal. The workpiece is 100 mm long, 100 mm wide and 10 mm thick, and it was connected to the positive terminal. De-ionized water was utilized as a dielectric medium during the machining process, and it was kept at a temperature of 20 °C. The studies were carried out using a L9 (3^3) orthogonal array, as shown in Table 3. The WEDM machining performance is examined using output responses such as MRR and SR. The MRR is calculated as the ratio of the difference in workpiece weight before and after machining during a given time period [19]. The SR of the machined composite is measured at three seperate places on the machined surfaces by using the Mextech SRT-6200 digital portable surface roughness tester.

Table 3 L9 orthogonal array design of experiments

Ex. No	Input parameters			Output responses		S/N ratios (dB)	
	I_p (amps)	T_{on} (μs)	T_{off} (μs)	MRR (g/min)	SR (μm)	MRR	SR
1	4	110	50	0.016279	3.212	−35.7674	−10.1355
2	4	114	54	0.016827	3.068	−35.4799	−9.7371
3	4	118	58	0.017327	3.581	−35.2257	−11.0801
4	6	110	54	0.018421	3.112	−34.6937	−9.8608
5	6	114	58	0.018919	3.257	−34.4621	−10.2564
6	6	118	50	0.020349	3.686	−33.8292	−11.3311
7	8	110	58	0.019886	3.982	−34.0289	−12.0020
8	8	114	50	0.021472	4.150	−33.3624	−12.3610
9	8	118	54	0.023026	4.621	−32.7555	−13.2947

2.4 Taguchi Technique

Taguchi technique is an effective statistical tool used for determining the significant relationships between the input parameters and the output responses in an experiment based upon the computations of the signal-to-noise (SN) ratio [20]. Minitab 17 software was used to analyze the parameters and their estimated responses. In the current study, Taguchi methodology is adopted to obtain the optimized parameters, which would result in the highest MRR and lowest SR for the AA8011-10wt.% TiO$_2$ composite during WEDM process. Therefore, "higher the better" SN ratio approach was used for MRR and "lower the better" SN ratio approach was applied for SR by using Eqs. (1) and (2). Table 3 shows the L$_9$ orthogonal array design, measured response and their SN ratios.

$$\text{S/N ratio} = -10\log_{10}(1/n)\sum_{k=1}^{n}\frac{1}{Y_{ij}^2} \tag{1}$$

$$\text{S/N ratio} = -10\log_{10}(1/n)\sum_{k=1}^{n}Y_{ij}^2 \tag{2}$$

where n—number of replications, Y_{ij}—measured response values where $i = 1, 2, 3\ldots n; j = 1, 2, 3\ldots k$.

3 Results and Discussion

3.1 Effect of Machining Parameters on MRR

The main effect plot of SN ratio value for MRR is illustrated in Fig. 3. From the plot, the optimum condition of each factor and their effects on the MRR of the machined AA8011-10wt.% TiO$_2$ composite can be observed. In the SN ratio analysis, the optimum range of parameters on the MRR is chosen from the larger the better SN ratio value. According to Fig. 3, the higher MRR is obtained at the high level of I_p (8 amps), the high level of T_{on} (118 µs) and the middle level of T_{off} (110 µs), respectively. It can be also seen that the MRR increases with an increasing trends in I_p and T_{on}. This can be attributed to the increase in the delivered spark energy with increasing discharge time, which results in the melting of the composite leading to easier removal of the metal from the work piece. Similar results were previously reported by Shyam Lal et al. during WEDM process of Al7075/Al$_2$O$_3$/SiC composites [21].

The S/N ratio and means of MRR for the machined AA8011-TiO$_2$ composite are depicted in Tables 4 and 5. From the tables, it can be seen that the order of significant parameters which affecting the MRR of the machined composite is indicated through a particular rank. This rank is assigned by delta value which is computed between the

Main Effects Plot for SN ratios
Data Means
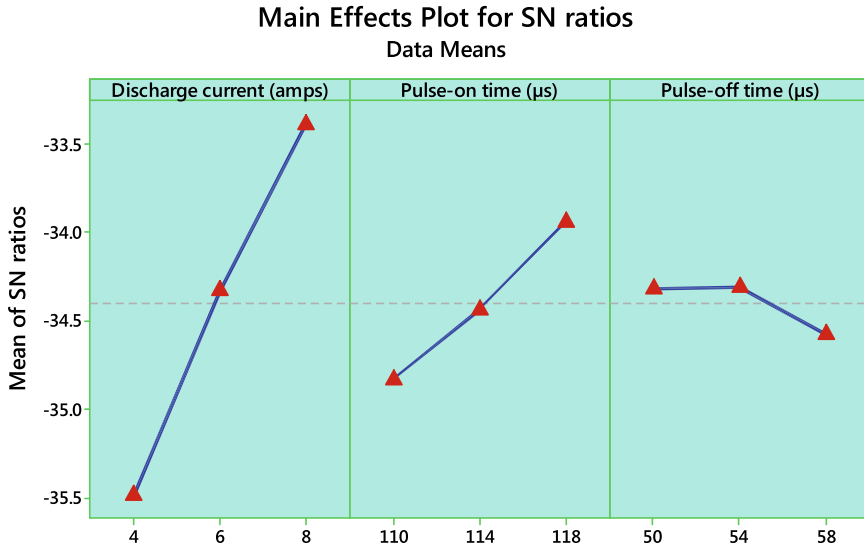
Signal-to-noise: Larger is better

Fig. 3 Main effect plot for MRR

higher and lower value of concerned column of parameters. According to Tables 4 and 5, it can be reveal that the I_p is the primary influencing factor affecting the MRR followed by T_{on} and T_{off}, respectively. This can be attributed to the fact that the supply of discharge current improves the melting temperature that shows enhanced the vaporization of metal from the work piece which result in improve the MRR. However, the T_{on} increases the MRR due to longer spark energy between the work piece and the wire electrode, which leads to an increase in the MRR.

The contour graphs for MRR is shown in Fig. 4a–c. It clearly explored the interactive effect of process parameters on MRR while machining of AA8011-10wt.%TiO$_2$ composite. The interaction of I_p with T_{on} on MRR is illustrates in Fig. 4a. It can be seen that the MRR increasing with an increase in I_p and T_{on} at higher level. Therefore, the higher MRR (>0.023 g/min) obtained at 8 amps of I_p with 118 µs of T_{on}, respectively. Figure 4b explored that the effect of I_p with T_{off} on MRR. It is observed that the maximum MRR (>0.023 g/min) attained at 8 amps of I_p with 54 µs of T_{off}.

Table 4 Response table for S/N ratio of MRR

Level	I_p (amps)	T_{on} (µs)	T_{on} (µs)
1	−35.49	−34.83	−34.32
2	−34.33	−34.43	−34.31
3	−33.38	−33.94	−34.57
Delta	2.11	0.89	0.26
Rank	1	2	3

Table 5 Response table for mean of MRR

Level	I_p (amps)	T_{on} (μs)	T_{on} (μs)
1	0.01681	0.01820	0.01937
2	0.01923	0.01907	0.01942
3	0.02146	0.02023	0.01871
Delta	0.00465	0.00204	0.00071
Rank	1	2	3

By considering the T_{off}, the MRR is achieved at higher T_{off} with middle I_p. However, the average MRR (0.019 to 0.020 g/min) is produced at 6 amps of I_p with 58 μs of T_{off}. Therefore, T_{off} is acted as an insignificant factor than the others while machining of AA8011-TiO$_2$ composite. In Fig. 4c reveal the influence of T_{on} with T_{off} on MRR. It is noticed that the less amount of MRR (<0.017 g/min) produced at medium level of T_{off} (54 μs) and T_{on} (114 μs), respectively. Furthermore, with an increase in T_{on} with middle level of T_{off} (54 μs) gives the higher MRR (0.022–0.023 g/min).

3.2 Effect of Machining Parameters on SR

Figure 5 displays the main effect plot for the SN ratio of SR. From the graph, it can be understood that the optimal level and influence of machining parameters such as discharge current (I_p), pulse-on time (T_{on}) and pulse-off time (T_{off}) on SR of the AA8011-10wt.% TiO$_2$ composite during WEDM process. In the SN ratio analysis, the optimum range of parameters on the desired response is chosen from the smaller the better SN ratio value. Based on the Fig. 5, it can be found that the low level of I_p (4 amps), the low level of T_{on} (110 μs) and the middle level of T_{off} (110 μs) produce less SR. It can be also clearly noticed that the SR decreases with decreasing the I_p and T_{on}. The high current tends to increase the delivered consecutive spark energy thus improving the SR. Similar observations were previously reported by Gopalakrishnan et al. during WEDM process of AA7075-9wt.% of activated carbon composites [22].

Tables 6 and 7 presented the response table for SN ratio and means of SR with respect to each level of machining parameters. From the tables, it can be revealed that the order of significant parameters which affecting the SR of the proposed composite is indicated through a particular rank. Based on the results (Tables 6 and 7), it has been observed that the rank 1 is placed for I$_p$ which is the primary dominant factor affecting the SR, subsequently by T_{on}, and T_{off}, respectively. Similar observations were previously reported by et al. while WEDM of composites. They concluded that the IP and T_{on} are more preferable factors for WEDM processes because of the development of SR is mainly depend on it.

Figure 6a–c demonstrates the contour plots for SR and these plots clearly reveals the interaction effect of input parameters on the response characteristics. From Fig. 6a, it can be noticed that the SR value is gradually increased with an increase
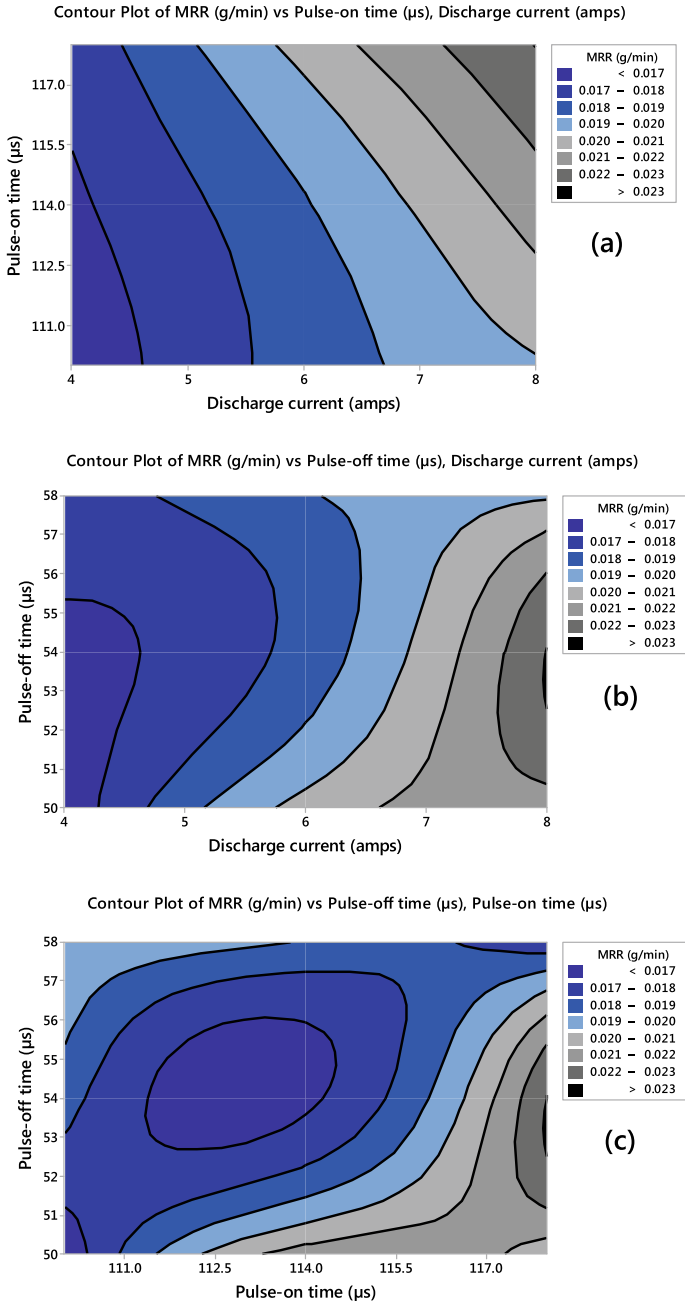
Contour Plot of MRR (g/min) vs Pulse-on time (µs), Discharge current (amps)

(a)

Contour Plot of MRR (g/min) vs Pulse-off time (µs), Discharge current (amps)

(b)

Contour Plot of MRR (g/min) vs Pulse-off time (µs), Pulse-on time (µs)

(c)

Fig. 4 Contour plot for MRR **a** I_p versus T_{on}, **b** I_p versus T_{off} and **c** T_{on} versus T_{off}

Main Effects Plot for SN ratios
Data Means
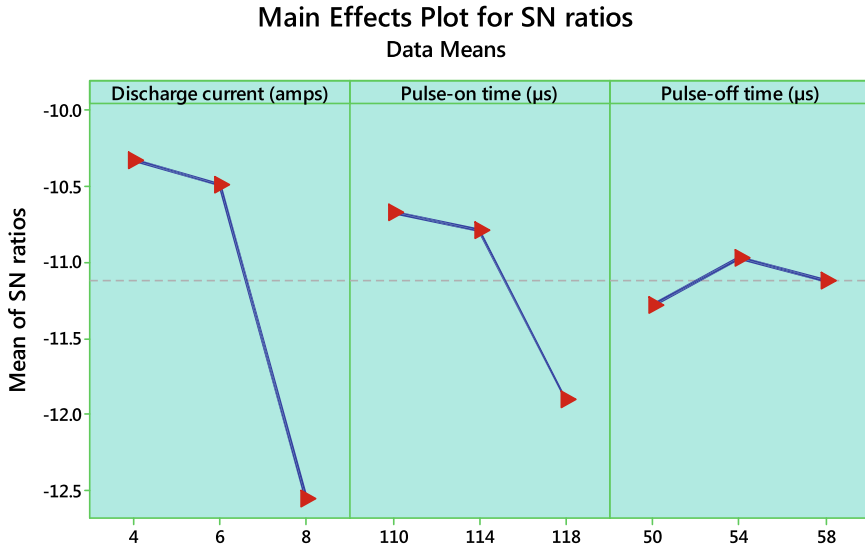
Signal-to-noise: Smaller is better

Fig. 5 Main effect plot for SR

Table 6 Response table for S/N ratio of SR

Level	I_p (amps)	T_{on} (µs)	T_{on} (µs)
1	−10.32	−10.67	−11.28
2	−10.48	−10.78	−10.96
3	−12.55	−11.90	−11.11
Delta	2.24	1.24	0.31
Rank	1	2	3

Table 7 Response table for mean of SR

Level	I_p (amps)	T_{on} (µs)	T_{off} (µs)
1	3.287	3.435	3.683
2	3.352	3.492	3.600
3	4.251	3.963	3.607
Delta	0.964	0.527	0.082
Rank	1	2	3

in I_p and T_{on}, respectively. Here, the less SR (<3.3 µm) was achieved at moderate level of I_p (6 amps) and T_{on} (116 µs). After that, SR was significantly improved from 3.6 µm to 4.5 µm when an increase in I_p and T_{on}. The higher SR (>4.5 µm) is obtained at 8amps I_p with 118 µs T_{on}. Due to higher I_p and T_{on} delivered more spark energy between the gaps thus produce more crates on the machined surface

which result in poor surface finish obtained. The interaction effect of I_p with T_{off} on SR is shown in Fig. 6b. It ensure that the middle level of I_p (6 amps) with high level of T_{off} (58 µs) produce less SR. Based on the Tables 6 and 7, it is also confirmed that the T_{off} has insignificant factor than the others. However, the higher SR (>4.5 µm) developed at moderate level of T_{off} when high level setting of I_p (8 amps). In Fig. 6c reveal the interactive influence of T_{on} with T_{off} on SR. It can be clearly seen that the maximum SR (>4.5 µm) produced at high level setting of T_{on} (118 µs) with middle level of T_{off} (54 µs). Meanwhile, at high level of T_{off} (58 µs) with the moderate level of T_{on} (114 µs) produce less SR.

3.3 Analysis of Variance (ANOVA)

ANOVA is a statistical design tool focused on a least square approach, commonly applied to break up the specific effects from all the process parameters [23]. In this study, ANOVA was carried out to compute the order of significant parameters at a level of significance of 5%. If the P-value of a factor is less than 0.05, then it confirms that the machining parameter has a statistically significant effect on the response [23]. Tables 8 and 9 shows the ANOVA result for the MRR and SR of the machined AA8011-10wt.% TiO₂ composite. From Table 8, it can be seen that the P-values for I_p and T_{on} are less than 0.05, suggesting that these two parameters do have a significant effect on MRR. Moreover, it can also be noted that the percentage contribution of I_p has an influence of 81.45% T_{on} has an influence of 15.78% on the MRR of the machined composites. Similarly, it is clearly revealed from Table 9, that the P-values for I_p and T_{on}, are less than 0.05, suggesting that these two factors have the most significant effect on SR with contributions of 76.41% and 22.06%, respectively. Similar findings were previously reported by Mythili et al. [24] during the WEDM process of Al6061/Al₂O₃ composites developed by stir casting technique.

3.4 Regression Model

To predict the MRR and the SR value of WEDM process parameters, regression equation was developed. A first order polynomial regression equation for MRR and SR is derived with R-sq values of 98.45% and 93.51% and R-sq (adj) values of 97.51% and 94.38%, respectively. The regression equations are given as (3) and (4),

$$\text{MRR (g/ min)} = -0.01243 + 0.001163\, I_p(\text{amps}) \\ + 0.000255\, T_{on}(\mu s) - 0.000082\, T_{off}(\mu s) \tag{3}$$

$$SR(\mu m) = -4.82 + 0.2410\, I_p(\text{amps}) + 0.0659 T_{on}(\mu s) \\ - 0.0095 T_{off}(\mu s) \tag{4}$$
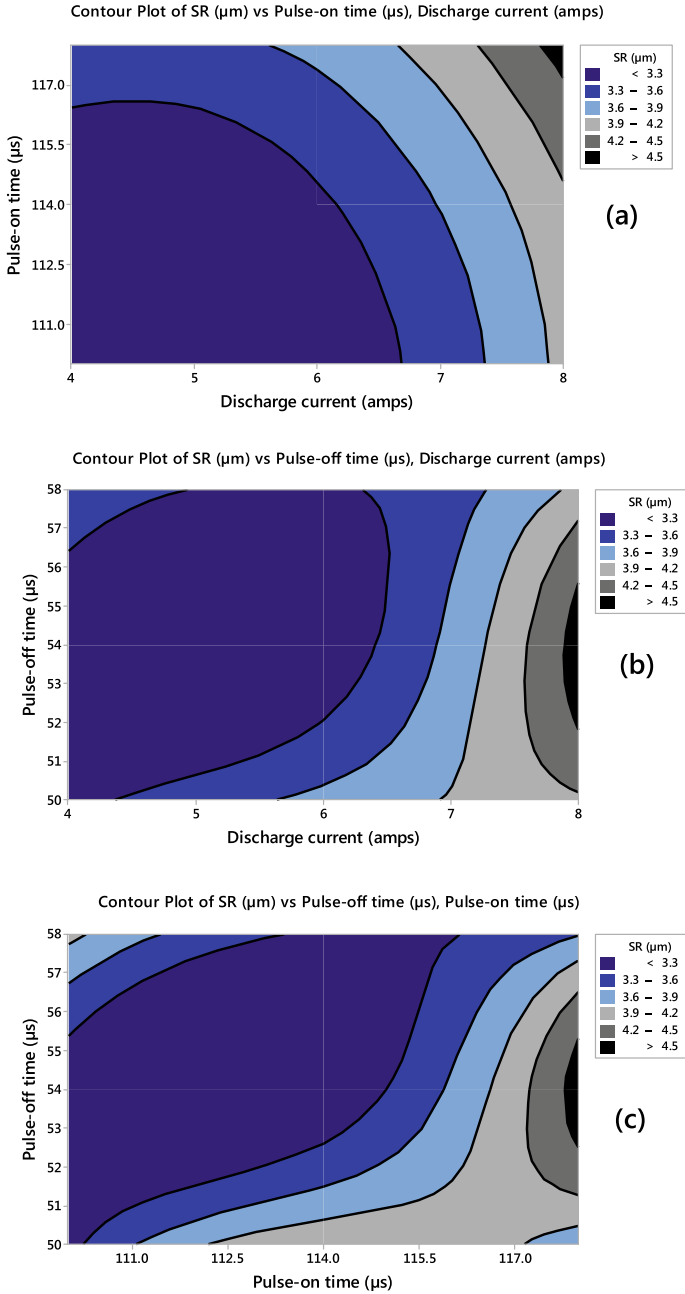
Fig. 6 Contour plot for SR **a** I_p versus T_{on}, **b** I_p versus T_{off} and **c** T_{on} versus T_{off}

Table 8 ANOVA table for MRR

Source	DF	Seq SS	Adj MS	F-ratio	P-value	P (%)
I_p	2	0.0000325	0.0000162	122.57	0.008	81.45
T_{on}	2	0.0000063	0.0000031	23.70	0.040	15.78
T_{off}	2	0.0000009	0.0000005	3.56	0.219	2.25
Error	2	0.0000003	0.0000001	–	–	0.75
Total	8	0.0000399	–	–	–	100

$S = 0.000363870$; R-Sq = 99.34%; R-Sq (adj) = 97.35%

Table 9 ANOVA table for SR

Source	DF	Seq SS	Adj MS	F-ratio	P-value	P (%)
I_p	2	1.74228	0.87114	79.28	0.012	76.41
T_{on}	2	0.50309	0.25155	22.89	0.042	22.06
T_{off}	2	0.01259	0.00630	0.57	0.636	0.55
Error	2	0.02197	0.01099	–	–	0.96
Total	8	2.27994	–	–	–	100

$S = 0.104821$; R-Sq = 99.04%; R-Sq (adj) = 96.14%

Figure 7a, b shows the comparison plot for the predicted and experimental value of MRR and SR and also it can be seen that both the values are very close to each other

3.5   Surface Morphology of Machined Surface

Figure 8 and 9 shows the SEM micrographs of machined surface for the AA8011-10wt.% TiO_2 composite. From the graphs, it can be clearly examined the WEDMed surface characteristics such as cracks, craters, ridges, recast layer and presence of reinforcement particles. The machined surface of the suggested composite is depicted in Fig. 8 for parameter conditions of 8 amps of I_p, 118 µs of T_{on} and 54 µs of T_{off}, respectively. It clearly reveals the generation of micro crack and micro craters on the machined surface. The reason for this is because sparks are generated in a certain zone. The WEDMed surface of the developed composite is shown in Fig. 9 under parameter conditions of 4 amps of I_p, 110 µs of T_{on} and 54 µs of T_{off}, respectively. It is noticed that the formation of macro crack and also evident the presence of reinforcement particles on the machined surface.

Fig. 7 Comparison plot **a**
MRR and **b** SR
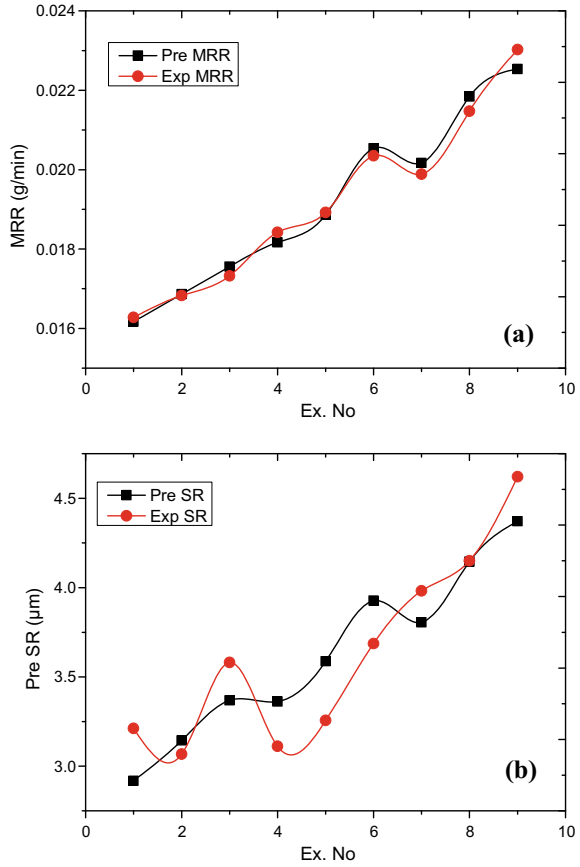
4 Conclusion

- Al–Fe-Si (AA8011) alloy matrix reinforced with 10wt.% TiO_2 particulates composite was effectively fabricated by stir casting method. The SEM micrograph reveals the presence of TiO_2 content within the matrix alloy and it was distributed uniformly.
- Machinability studies of the developed composite was performed by WEDM process and the effect of machining parameters namely, discharge current (I_p), pulse-on time (T_{on}) and pulse-off time (T_{off}) on MRR and SR were analyzed.
- Based on the SN ratio results, the maximum MRR obtained at 8 amps of I_p, 118 μs of T_{on} and 54 μs of T_{off}, respectively. Subsequently, the minimum SR achieved at 4 amps of I_p, 110 μs of T_{on} and 54 μs of T_{off}, respectively.
- ANOVA result showed that the I_p was more significant parameter which affecting the MRR (81.45%) and SR (76.41%) of the proposed composite during WCEDM process, followed by T_{on} with contribution of 15.78% and 22%, respectively.

Fig. 8 SEM image of
machined surface at 8 amps
I_p, 118 μs T_{on} and 54 μs
T_{off}
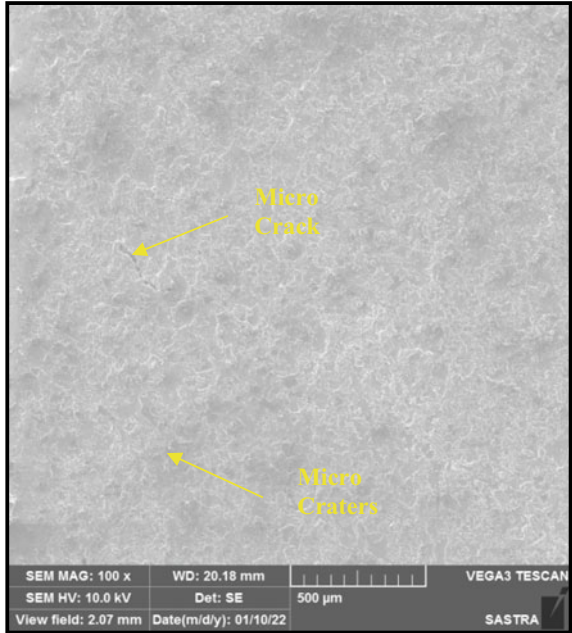
Fig. 9 SEM image of
machined surface at 4 amps
I_p, 110 μs T_{on} and 54 μs
T_{off}
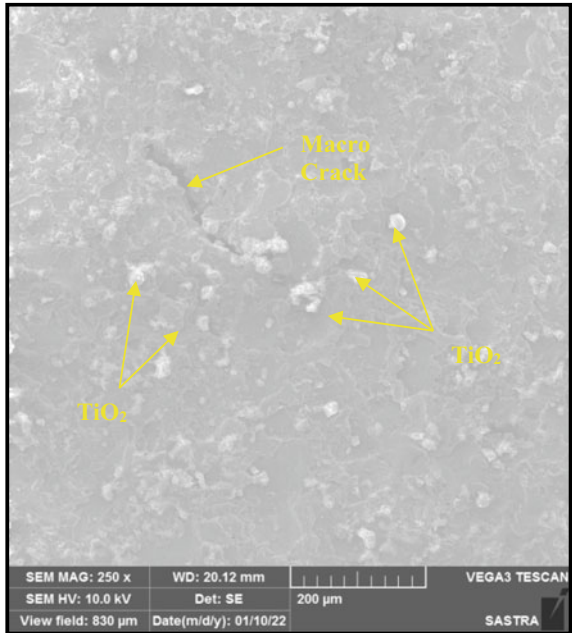
- Finally, the predicted values for the MRR and SR were computed by the regression equations and these values are well agreed with the experimental results.

References

1. Habib S (2017) Optimization of machining parameters and wire vibration in wire electrical discharge machining process. Mech Adv Mater Mod Process 3(3):1–9
2. Huang JT, Liao YS, Hsue WJ (1999) Determination of finish cutting operation number and machining parameters setting in wire electrical discharge machining. J Mater Process Technol 87:69–81
3. Scott D, Boyina S, Rajurkar KP (1991) Analysis and optimization of parameter combination in wire electric discharge machining. Int J Prod res 29(11):2189–2207
4. Tarng YS, Ma SC, Chung LK (1995) Determination of optimal cutting parameters in wire electrical discharge machining. Int J Mach Tool Manuf 35(12):1693–1701
5. Mahapatra SS, Patnaik A (2006) Optimization of wire electrical discharge machining (WEDM) process parameters using Taguchi method. Int J Adv Manuf Technol 34:911–925
6. Alagarsamy SV, Ravichandran M, Dinesh Kumar S, Sakthivelu S, Meignanamoorthy M, Chanakyan C (2020) A Taguchi coupled desirability function analysis of wire cut EDM behaviour of titanium dioxide filled aluminium matrix composite. Mater Today Proc 27:853–858
7. Anand Babu K, Venkata Ramaiah P (2019) Optimization in wire-cut EDM of aluminium hybrid metal matrix composite using Taguchi coupled deng's similarity based approach. UPB Sci Bull Ser D 81(3):169–186
8. Soundararajan R, Ramesh A, Ponappa K, Sivasankaran S, Arvind D (2020) Optimization of WEDM process parameters by RSM in machining of stir cum squeeze cast A413–B_4C composites. SN Appl Sci 2(1768):1–21
9. Dinesh Kumar S, Ravichandran M (2018) Synthesis, characterization and wire electric erosion eehaviour of AA7178-10 wt.% ZrB_2 composite. SILICON 10:2653–2662
10. Venkatesan S, Ravindran D (2020) Experimental studies on micro machining of aluminium based hybrid metal matrix composite materials. Taga J 14:2455–2470
11. Subramaniam K, Natarajan A, Vinayagam A, Muthiya N et al (2020) Optimization of wire cut EDM process parameters of Al/SiO_2 composites using Taguchi method. SAE Technical Paper, 2020-28-0426, pp 1–8
12. Rao TB (2016) Optimizing machining parameters of wire-EDM process to cut Al7075/SiCp composites using an integrated statistical approach. Adv Manuf 4(3):202–216
13. Rajyalakshmi G, Venkata Ramaiah P (2013) Multiple process parameter optimization of wire electrical discharge machining on Inconel 825 using Taguchi grey relational analysis. Int J Adv Manuf Technol 69:1249–1262
14. Geeta Rani M, Parameswara Rao ChSP, Rama Kotaiah K (2017) Experimental investigation on optimization of the controlling factors for machining Al 6061/MoS_2 metal matrix composites with wire EDM. Int J Appl Eng Res 12(22):12023–12028
15. Ezeddini S, Boujelbene M, Bayraktar E, Salem SB (2020) Optimization of the surface roughness parameters of Ti–Al intermetallic based composite machined by wire electrical discharge machining. Coatings 10(900):1–19
16. Alagarsamy SV, Ravichandran M (2019) Investigations on tribological behaviour of AA7075-TiO_2 composites under dry sliding conditions. Ind Lubr Tribol 71(9):1064–1071
17. Alagarsamy SV, Ravichandran M (2019) Synthesis, microstructure and properties of TiO_2 reinforced AA7075 matrix composites via stir casting route. Mater Res Express 6:1–15
18. Sarkar S, Mitra S, Bhattacharyya B (2006) Parametric optimisation of wire electrical discharge machining of γ titanium aluminide alloy through an artificial neural network model. Int J Adv Manuf Technol 27:501–508

19. Alagarsamy SV, Raveendran P, Ravichandran M (2020) Investigation of material removal rate and tool wear rate in spark erosion machining of Al-Fe-Si alloy composite using Taguchi coupled TOPSIS approach. SILICON 13:2529–2543
20. Vinoth Kumar M, Meignanamoorthy M, Sakthivelu S, Dinesh Kumar S, Chanakyan C, Alagarsamy SV (2020) Optimization of material removal rate in CNC turning of AA2024 via Taguchi technique. Mater Today Proc 27:1163–1167
21. Lal S, Kumar S, Khan ZA, Siddiquee AN (2015) Multi-response optimization of wire electrical discharge machining process parameters for Al7075/Al$_2$O$_3$/SiC hybrid composite using Taguchi-based grey relational analysis. Proc IMechE Part B J Eng Manuf 229(2):229–237
22. Ramanan G, Elangovan R (2018) Parametric optimization of wire cut electrical discharge machining on Al-9% PAC composites using desirability approach. Int J Veh Struct Syst 10(6):467–470
23. Chanakyan C, Sivasankar S, Meignanamoorthy M, Alagarsamy SV (2021) Parameteric optimization of mechanical properties via FSW on AA5052 using Taguchi based grey relational analysis. Incas Bulletin 13(2):21–30
24. Mythili T, Thanigaivelan R (2020) Optimization of wire EDM process parameters on Al6061/Al composite and its surface integrity studies. Bull Polish Acad Sci Tech Sci 68(6):1403–1412

Chapter 21
Optimization of Machining Parameters in EDM Using GRA Technique

S. Balaji, P. Maniarasan, C. Sivakandhan, and S. V. Alagarsamy

1 Introduction

In recent decades, the growing demand for novel, lightweight materials with higher strength and toughness has resulted in the establishment of a new generation of composite materials. In comparison to traditional monolithic materials, metal matrix composites (MMCs) exhibit multifunctional features such as better stiffness, toughness and reduced density [1]. However, due to the existence of hard reinforcements, precision machining of these materials is very difficult and thus necessitating the adoption of cost-effective machining processes. Electrical discharge machining (EDM) is a vitally essential non-traditional machining method that has recently been developed [2]. Because the EDM method does not use the mechanical energy, the removal rate is unaffected by the work piece hardness, strength, or toughness. EDM is a non-traditional machining method that removes material by precisely controlling sparks that fall between the electrode and an electrically conductive work piece [3]. The benefits of the EDM process are most obvious when machining MMCs, which have the highest hardness in reinforcement. In EDM process, some variables such as peak current, discharge energy, tool material, duty cycle, and other process factors have a significant impact on performance attributes MRR, TWR and SR [4,

---

S. Balaji · P. Maniarasan
Department of Aeronautical Engineering, Nehru Institute of Engineering and Technology, Coimbatore 641105, India

C. Sivakandhan
Department of Mechanical Engineering, Nadar Saraswathi College of Engineering and Technology, Theni 625531, India

S. V. Alagarsamy (✉)
Department of Mechanical Engineering, Mahath Amma Institute of Engineering and Technology, Pudukkottai 622101, India
e-mail: s.alagarsamy88@gmail.com

5]. Gopalakannan et al. [6] have studied the EDM behavior of Al7075/10wt.% Al_2O_3 composite synthesized by stir casting route. They stated that pulse current and pulse-on time have more significance variables on the output responses such as MRR, SR and TWR and also observed that SR increased when setting of 50 V voltage after that SR slightly reduced with a further increase in voltage. Mehdi Hourmand et al. [7] investigated the effect of EDM factors namely, voltage, current, pulse-on time and duty factor on MRR and electrode wear ratio (EWR) while machining of Al-Mg_2Si MMC. They noticed that voltage and current are the most impact factors on MRR, whereas the pulse-on time has significantly affecting the EWR. Alagarsamy et al. [8] have reported the EDM process of AA7075-10wt.% TiO_2 composite developed through stir casting method and observed that electrode material and pulse current were highly affecting the machining performances such as MRR, SR and EWR. Tripathy et al. [9] have optimized the EDM performances of H-11 die steel using Cu electrode with addition of chromium (Cr) powder to the dielectric fluid. They observed that the SR values are decreased to a range of 2.4 µm to 5.04 µm due to addition of Cr powder at 6 gm/l. Mujibur Rahman et al. [10] have performed the EDM process of AA6061-cenospheres MMCs using multi-criteria decision making (MCDM) method. They noticed that the optimal level of pulse current 10 A, pulse-on time 1010 µs, percentage of reinforcement as 2% and flushing pressure as 0.6 MPa. Lin Tang et al. [11] applied the Taguchi method and GRA to optimize the multiple performance characteristics of the Ti–6Al–4 V alloy during EDM. When using the GRA approach, it was discovered that the optimized parameters enhanced the MRR by 2%, the TWR by 59% and the SR by 4%. Kachhap et al. [12] studied the machinability characteristics of Al6063/SiC/Gr/Al_2O_3 hybrid MMCs using solid and hollow electrode tool made of Cu and brass (Br). They reported that the higher MRR is obtained when using hollow Br electrode, whereas the less TWR is acquired when using solid Cu electrode tool. Yan et al. [13] analyzed the influence of EDM factors on the machining performances of Al_2O_3/6061 Al composite using a disklike electrode. The statistical results found that the peak current has the most noteworthy factor for the MRR and EWR. Vikas Gohil Yogeh et al. [14] have reported about the EDM process of titanium alloy (Ti-6Al-4V) using statistical analysis. The results showed that peak current and gap voltage were most decisive factors on MRR that contributes more than 90%. Similarly, the peak current and pulse-on time are more important for SR that contributes 82%. Murahari Kolli and Kumar Adepu [15] employed GRA-Taguchi approach for optimizing EDM parameters on MRR and SR during machining of Ti-6Al-4V alloy. They concluded that the MRR and SR was improved by 20.69% and 11.09% when using the multi-optimization technique. Dey et al. [16] examined the machinability of Al6061/cenosphere composite using gray-based hybrid approach. The MRR, EWR and SR were selected as the machining performances for this study. The experimental results revealed that 9.9126A pulse current, 210.002 µs pulse-on time, 3.6936% volume fraction of reinforcement and 0.5999 MPa flushing pressure gives the better machining performances during EDM process. Venkadesh et al. [17] have optimized the machining parameters on MRR, SR and TWR while EDM of superni-800 alloy by using Cu–Ti electrode. They stated that the higher value of grey relational grade (GRG) was selected as the optimal conditions of parameters.

Avijeet Satpathy et al. [18] attempted the EDM process of Al–SiC MMC using Cu tool and reported that the effect of input factors on the machining responses such as MRR, TWR, SR and diametral overcut. They observed that the input current was the main factor for controlling the machining performances.

Hence in this research, EDM input parameters of pulse current (I_p), pulse-on time (T_{on}) and pulse-off time (T_{off}) have been optimized to acquire maximum MRR with minimum SR and TWR for stir casted AA8011-10wt.% TiO$_2$ composite by employing GRA technique. Furthermore, the effect of each parameter on the performances are determined by ANOVA.

2 Experimental Details

2.1 Matrix and Reinforcement

In this research, the AA8011 was taken as matrix alloy having a composition of 1.0% Fe, 0.9% Si, 0.10% Cu, 0.20% Mn, 0.10% Zn, 0.08% Ti, 0.05% Mg, 0.05% Cr and the rest being Al. The titanium dioxide (TiO$_2$) particles were utilized as reinforcement having a hardness of 1121 Hv and a density of 4.23 g/cm^3.

2.2 Fabrication of Composite

A liquid metallurgy technique like stir casting route have been adopted to fabricate the composite specimen. In the beginning, pure AA8011 ingot was melted in a graphite crucible furnace at the temperature 750 °C. Similarly, 10wt.% TiO$_2$ particles were preheated at 200 °C to remove the moisture and also to improve the wettability of the TiO$_2$ particles with molten AA8011. The molten AA8011 was stirred with a motorized agitator at the speed of 200 rpm constantly. Subsequently, the preheated TiO$_2$ particles were added slowly in the vortex of the AA8011 pool. In order to blend the reinforcements in AA8011 pool, the mixture was constantly stirred at 280 rpm around 10 min. After stirring, the slurry was poured into the preheated steel die immediately.

2.3 Design of Experiments

Design of experiments (DOE) offers a particular array design that allows researchers to investigate all parameters with the minimum number of experiments. Hence, DOE is the preferred approach for experimenting in order to improve the performance of goods and processes [19]. In this study three machining parameters are used such

Table 1 Input parameters and its levels

Machining parameter	Notation	Unit	Level		
			1	2	3
Peak current	I_p	amps	5	10	15
Pulse-on time	T_{on}	μs	100	200	300
Pulse-off time	T_{off}	μs	30	60	90

Table 2 Properties of Cu electrode

Density (g/cm^3)	Thermal conductivity (W/m.K)	Melting point (°C)	Specific heat capacity (J/kg-K)	Electrical resistivity (Ω/m)
8.96	391	1085	385	1.67×10^{-8}

Table 3 L9 (3^3) orthogonal array with output responses

Ex. No	I_p (amps)	T_{on} (μs)	T_{off} (μs)	MRR (g/min)	SR (μm)	TWR (g/min)
1	5	100	30	0.05144	5.270	0.00372
2	5	200	60	0.10711	3.602	0.00688
3	5	300	90	0.03280	5.211	0.00242
4	10	100	60	0.04609	4.798	0.00372
5	10	200	90	0.12126	3.357	0.00912
6	10	300	30	0.27619	5.206	0.01304
7	15	100	90	0.02716	1.765	0.00260
8	15	200	30	0.23929	2.827	0.01492
9	15	300	60	0.38544	3.686	0.03576

as pulse current (I_p), pulse-on time (T_{on}) and pulse-off time (T_{off}), each with three levels, as shown in Table 1. The most appropriate array for the given machining settings is L9 (3^3) orthogonal array as shown in Table 3 (Table 2).

2.4 EDM of Composite

The experiments were conducted on die sinking EDM machine (Model: Sparkonix, Pune, India) containing a separate dielectric tank and jet flushing setup for ease of dielectric flow toward workpiece and electrode interface. Before the experimentation, the work specimen (50 × 50 × 10 mm) was ground to make them perfectly flat on both sides to avoid dimensional accuracy and impart a good machined surface. A electrolyte Cu in cylindrical form of diameter 12 mm and a length of 80 mm was used as an electrode tool during machining. Table 2 shows the properties of Cu electrode

Table 4 Normalized S/N ratio and deviation sequence

Ex. No	Normalized S/N ratio			Deviation sequence		
	MRR	SR	TWR	MRR	SR	TWR
1	0.067768	0	0.961008	0.932232	1	0.038992
2	0.223149	0.475892	0.866227	0.776851	0.524108	0.133773
3	0.015742	0.016833	1	0.984258	0.983167	0
4	0.052836	0.134665	0.961008	0.947164	0.865335	0.038992
5	0.262644	0.545792	0.79904	0.737356	0.454208	0.20096
6	0.695071	0.01826	0.681464	0.304929	0.98174	0.318536
7	0	1	0.994601	1	0	0.005399
8	0.592079	0.697004	0.625075	0.407921	0.302996	0.374925
9	1	0.451926	0	0	0.548074	1

tool. Commercial grade of kerosene was utilized as the dielectric fluid throughout the machining because of its benefits, including high flash point, low viscosity, increased dependability and enhanced stability. These experiments were performed to find out the effect of each parameters on the performances (MRR, SR and TWR). The initial and final weight of the specimen and elctrode were acquired using the weighing machine. Furthermore, SR was assessed using a Mitutoyo Talysurf SJ-210 surface roughness tester. The MRR and TWR were estimated by using Eqs. (1) and (2) [20].

$$MRR = \frac{W_{bj} - W_{aj}}{T_m} \tag{1}$$

$$TWR = \frac{W_{be} - W_{ae}}{T_m} \tag{2}$$

where W_{bj} and W_{aj}—weight of work piece before and after machining (g), W_{be} and W_{aj}—weight of the electrode before and after machining (g), T_m—machining time (min). Table 3 depicted the estimated output responses.

2.5   GRA Technique

In this study, GRA technique was applied to determine the optimum condition of EDM parameters such as pulse current (I_p), pulse-on time (T_{on}) and pulse-off time (T_{off}) on multiple performances with an objective to maximize the MRR and minimize the SR and TWR of AA8011-10wt.% TiO$_2$ composite. The given steps are to be carried out in the GRA techniques:

Step 1:   The responses of MRR, SR and TWR are normalized in the ranging from 0 to 1. If the objective has the response value of "lower-the-better" the

response values can be normalized by the Eq. (3)

$$x_i^*(k) = \frac{\max x_i^o(k) - x_i^o(k)}{\max x_i^o(k) - \min x_i^o(k)} \tag{3}$$

If not, in case the response value of "higher-the-better" the response values can be normalized by the Eq. (4)

$$x_i^*(k) = \frac{x_i^o(k) - \min x_i^o(k)}{\max x_i^o(k) - \min x_i^o(k)} \tag{4}$$

where $i = 1,\dots m$; $k = 1,\dots, n$. M—is the number of data items in the experiment, and n—is the number of input parameters. $x_i^o(k)$ represents the reference sequence; $x_i^*(k)$ the sequence after normalized processing data; max $x_i^o(k)$ & min $x_i^o(k)$—are the maximum and minimum value in the reference sequence of $x_i^o(k)$. The normalized S/N ratio and deviation sequence are depicted in Table 4.

Step 2: After normalizing the response, grey relational coefficient $\xi_i(k)$ can be determined for the kth performances in the ith experiment by the Eq. (4)

$$\xi_i(k) = \frac{\Delta \min + \zeta \cdot \Delta \max}{\Delta_{0i}(k) + \zeta \cdot \Delta \max} \tag{5}$$

where Δ_{0i}—is the deviation sequence, ζ—is the distinguished coefficient generally taken as 0.5.

Step 3: Once the grey relational coefficient (GRC) was computed, later proceeds to estimate the grey relational grade (GRG) by using Eq. (5)

$$\gamma_i = \frac{1}{n} \sum_{k=1}^{m} \xi_i(k) \tag{6}$$

where γ_i—is the GRG for the ith experiment, ξ_i—is the GRC and n—is the number of responses. Table 5 shows the computed GRC and GRG with rank in order.

From Table 5, the greater value of GRG represents the optimal combination of machining parameters on the output performances. The last column of Table 5 shows that the rank assigned for all the experiments conducted during the EDM process. According to Table 5, it has proved that experiment number 7 has a higher GRG (0.77422), which identifies the best combination of optimal EDM parameters on proposed AA8011-10wt.% TiO_2 composite.

Table 5 GRC, GRG and their rank

Ex. No	GRC ($\xi_i(k)$)			GRG (γ_i)	Rank
	MRR	SR	TWR		
1	0.349106	0.333333	0.927657	0.53670	8
2	0.391589	0.48823	0.788926	0.55625	5
3	0.336869	0.337116	1	0.55800	4
4	0.345503	0.36621	0.927657	0.54646	7
5	0.404087	0.523995	0.713308	0.54713	6
6	0.621173	0.337441	0.610846	0.52315	9
7	0.333333	1	0.989318	0.77422	1
8	0.550709	0.622668	0.571478	0.58162	3
9	1	0.477065	0.333333	0.60347	2

3   Result and Discussion

3.1   Analysis of EDM Parameters on GRG

Figure 1 shows the effects of machining parameters such as pulse current (I_p), pulse-on time (T_{on}) and pulse-off time (T_{off}) on GRG. From the plot, it is clearly revealed that the most significant parameters on response could be easily identified. In the plot, the level of machining parameters is represented in x-axis and the obtained mean GRG denoted in y-axis. In this graph, the red dot indicated as the optimal level of machining parameters. According to Fig. 1, it is clearly seen that the optimal experimental conditions at which maximum MRR with minimum SR and TWR obtained are found to be pulse current (I_p) at level 3 (15 amps), pulse-on time (T_{on}) at level 1 (100 µs) and pulse-off time (T_{off}) at level 3 (90 µs). During this condition, the maximum MRR with minimum SR and TWR for the set of optimum machining parameters are 0.02716 g/min, 1.765 µm and 0.00260 g/min, respectively.

Table 6 shows the response table for mean GRG. The ranking of machining parameters on the influence of machining performances is found based on the delta (Δ) value. The high delta (Δ) value possesses the primary dominant parameter among the others. According to Table 6, the prime noteworthy parameter for GRG is exerted by pulse current (I_p) subsequently by pulse-off time (T_{off}) and pulse-on time (T_{on}). The increase in pulse current (IP) produces the higher MRR with SR and TWR due to more spark between the workpiece and tool electrode thus delivers more heat energy on the work material. This will cause the workpiece and tool materials are extremely eroded and also more craters are formed on the machined surface. This related observation also earlier reported by Alagarsamy et al. during EDM process of AA7075-10wt.% TiO$_2$ composite [21].
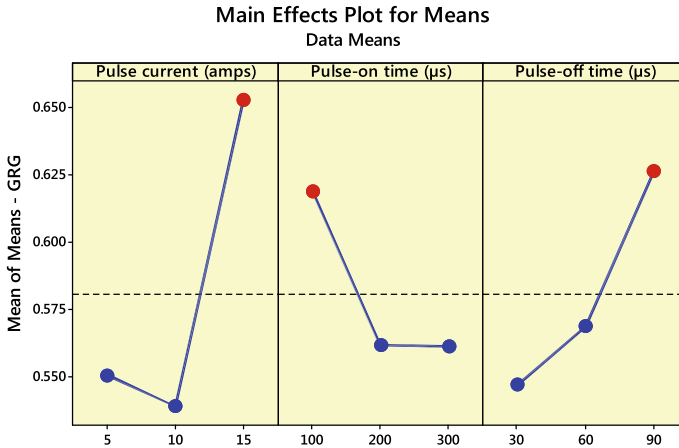
Fig. 1 Effect of machining parameters on GRG

Table 6 Response table for mean of GRG

Level	I_p (amps)	T_{on} (μs)	T_{off} (μs)	Average mean GRG
1	0.5503	0.6191	0.5472	0.58078
2	0.5389	0.5617	0.5687	
3	0.6531	0.5615	0.6264	
Delta	0.1142	0.0576	0.0793	
Rank	1	3	2	

3.2 Anova

ANOVA is used to determine which machining factors have a substantial impact on the output performances [22]. The ANOVA separates the total volatility of the means into contributions from each of the machining parameters as well as the errors. The sum of the squared deviations from the overall mean of the response is used to compute the total volatility of mean [23]. In this study, ANOVA has been made to determine the percentage contribution of EDM parameters toward machining performance. The ANOVA result for GRG is depicted in Table 7 and also Fig. 2 reveals the percentage contribution of machining parameters on GRG while EDM process of AA8011-10wt.% TiO$_2$ composite. As it can be stated that the I_p is the more dominant parameter on output performances with contribution of 50.89%, trailed by T_{off} and T_{on} with contribution of 21.62% and 14.19%, respectively. The same observations were previously noticed by Ponappa et al. during the EDM process of Al7075/TiC/B$_4$C composite [24].

Table 7 ANOVA table for GRG

Source	DF	Seq SS	Adj SS	Adj MS	F-ratio	P (%)
I_p	2	0.023734	0.023734	0.011867	3.83	50.89
T_{on}	2	0.006618	0.006618	0.003309	1.07	14.19
T_{off}	2	0.010084	0.010084	0.005042	1.63	21.62
Error	2	0.006193	0.006193	0.003097	–	13.28
Total	8	0.046629	–	–	–	100

(DF—Degrees of freedom, Seq SS—Squential sum of square, Adj SS—Adjusted sum of square, Adj SS—Adjusted mean square)
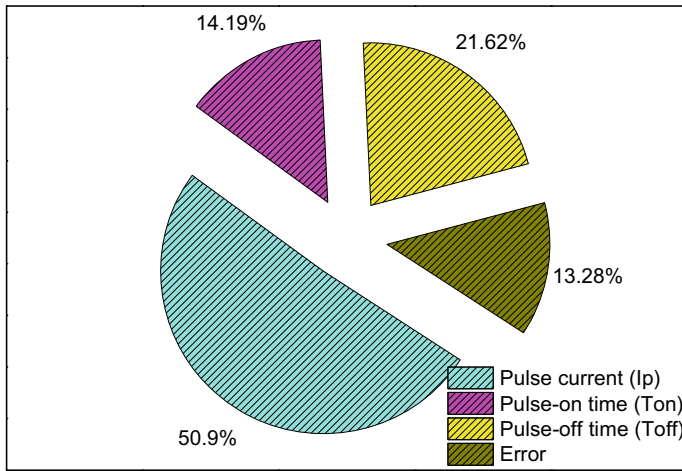
Fig. 2 Contribution of parameters on GRG

3.3   Effect of the Machining Parameters on MRR

The influence of input parameters such as pulse current (I_p), pulse-on time (T_{on}) and pulse-off time (T_{off}) on MRR while EDM of AA8011-10wt% TiO$_2$ composite is shown in Fig. 3a–c. The interplay of I_p and T_{on} on MRR is shown in Fig. 3a, where it is obvious that the MRR rises as I_p and T_{on} increase. Because it produces more spark at the interface and so melts and evaporates the metal from the work piece, 15 amps of I_p with 300 µs T_{on} gives the greater MRR (0.35 g/min). The effect of I_p and T_{off} on MRR is seen in Fig. 3b. The larger MRR (0.35 g/min) produced at 15 amps I_p with 60 µs T_{off} may be noted. Similarly, the MRR (0.25 g/min) is improved by a moderate I_p (10 amps) and an initial level of T_{off} (30 µs). Furthermore, when T_{off} is increased from 30 to 60 µs at 10 amps of I_p, MRR drops to 0.05 g/min. The effect of T_{on} and T_{off} on MRR is seen in Fig. 3c. It was clearly established that the MRR grows with increasing T_{on} from 100 to 300 µs at the intermediate level of

T_{off} (60 μs). Meanwhile, the MRR (0.05 g/min) is lower at the intermediate level of 60 μs T_{off} with initial level of T_{on}.

3.4   Effect of Machining Parameters on SR

The contour impact of EDM settings on the SR of the machined composite is shown in Fig. 4a–c. Figure 4 shows the interaction of I_p with T_{on} on SR (a). The maximum SR (5.0 m) was achieved with the I_p of 10 amps and 30 μs of T_{on}, as shown in the diagram. We do, however, demand a minimum SR that will be attained at a higher I_p (15 amps) and a reasonable T_{on} (200 μs). The influence of I_p and T_{off} on SR is seen in Fig. 4b. The low SR attained at the initial level of I_p (5 amps) with 90 μs of T_{off} is noticeable. It was also discovered that when T_{off} was increased at a modest level of I_p (10 amps), SR reduced linearly. Figure 4 shows the effect of T_{on} with T_{off} on SR (c). It can be seen that at 100 μs of T_{on} with 30 μs of T_{off}, there is less SR created. Furthermore, as T_{on} and T_{off} increased, SR improved dramatically.

3.5   Effect of Machining Parameters on TWR

The interactive influence of EDM settings on TWR during machining was shown in Fig. 5a–c. The less TWR (0.005 g/min) obtained at the starting level of T_{on} (100 μs) with the middle level of I_p (10 amps) is clearly shown in Fig. 5a. Furthermore, as I_p and T_{on} rise, TWR rises as well. The impact of I_p and T_{off} on TWR may be shown in Fig. 5 b. At the intermediate level of T_{off} (60 μs), the TWR steadily increases with an increase in I_p from 10 to 15 amps. The lowest TWR (0.005 g/min) is reached when I_p (5 amps) is low and T_{off} (90 μs) is high. Similar patterns may be seen in Fig. 5c. It was a clear representation of T_{on} and T_{off} impact on TWR. At the middle level of T_{off} (60 μs), the TWR increases as T_{on} increases from 100 to 300 μs.

3.6   Verification Test

The final step is to verify the EDM performance improvement of AA8011-10wt.% TiO$_2$ composite using optimal condition of the process parameters (I_p-3T_{on}-1T_{off}-3). In Eq. (7) has been applied to find out the predicted output response [25].

$$\eta_{pre} = \eta_m + \sum_{k=1}^{n} (\eta_i - \eta_m) \qquad (7)$$
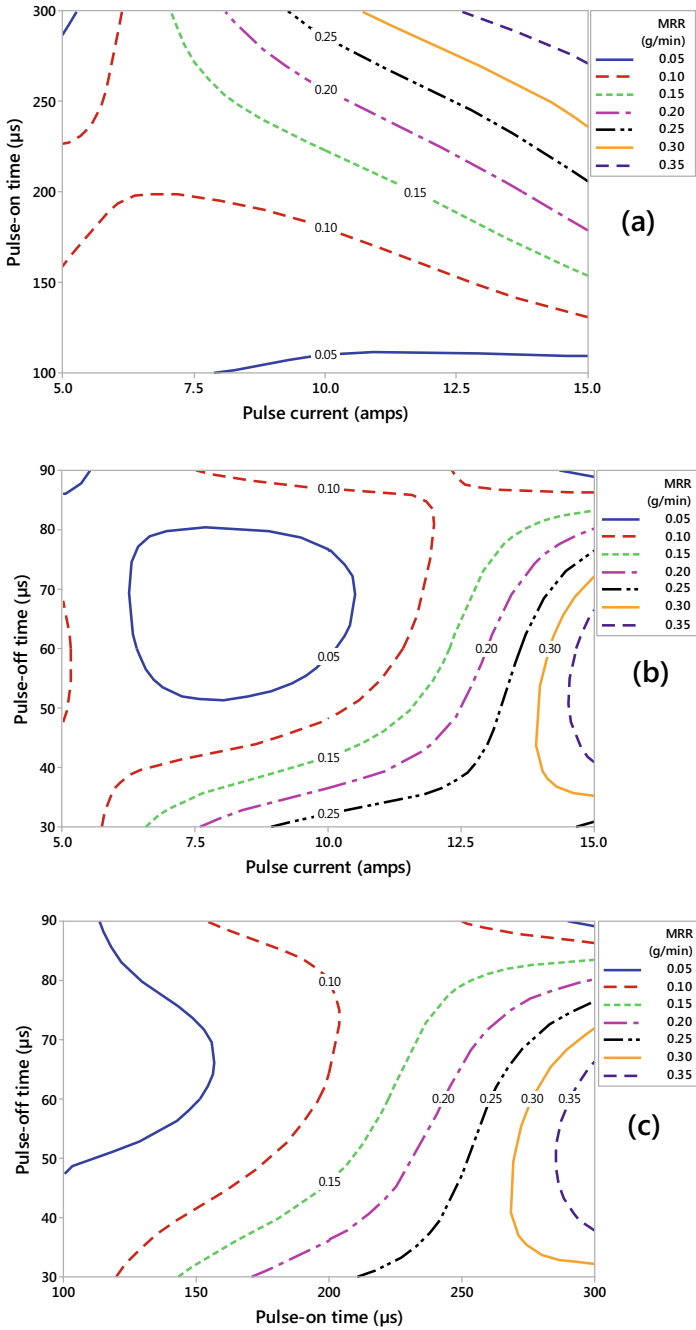
Fig. 3 Contour plot for MRR **a** I_p versus T_{on}, **b** I_p versus T_{off} and **c** T_{on} versus T_{off}
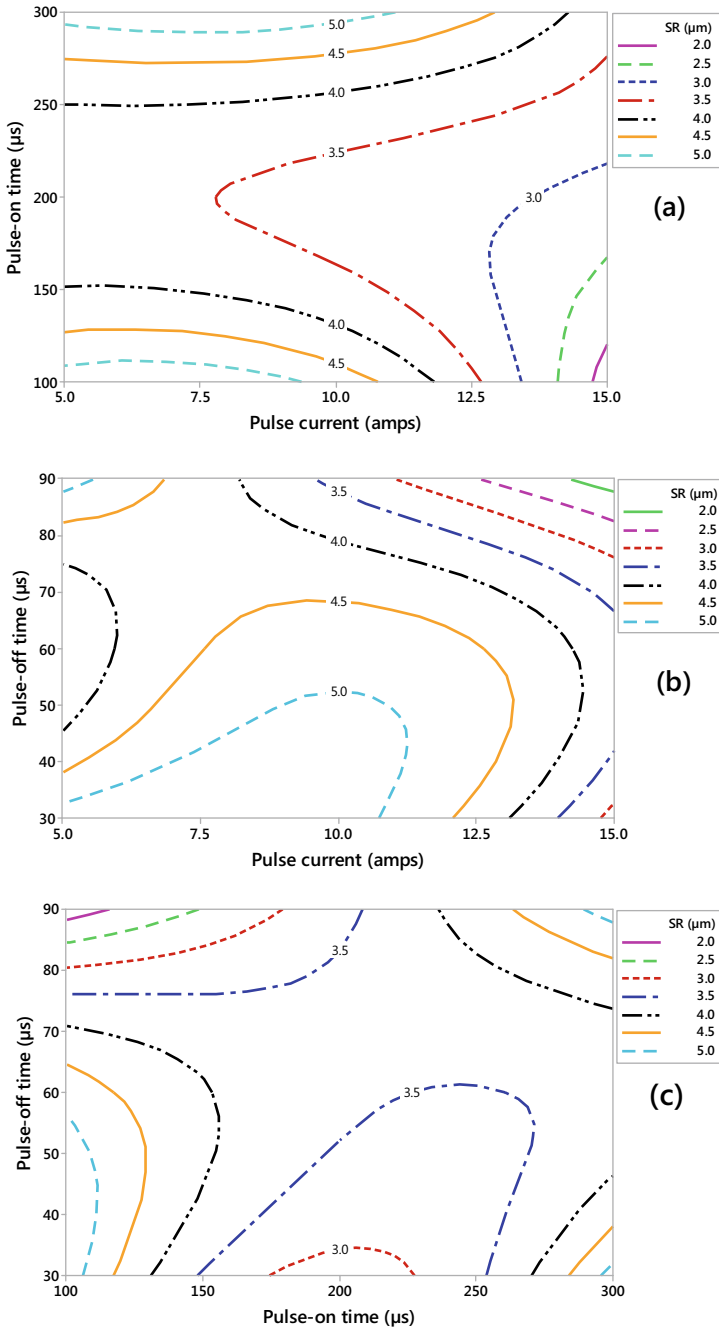
Fig. 4 Contour plot for SR **a** I_p versus T_{on}, **b** I_p versus T_{off} and **c** T_{on} versus T_{off}
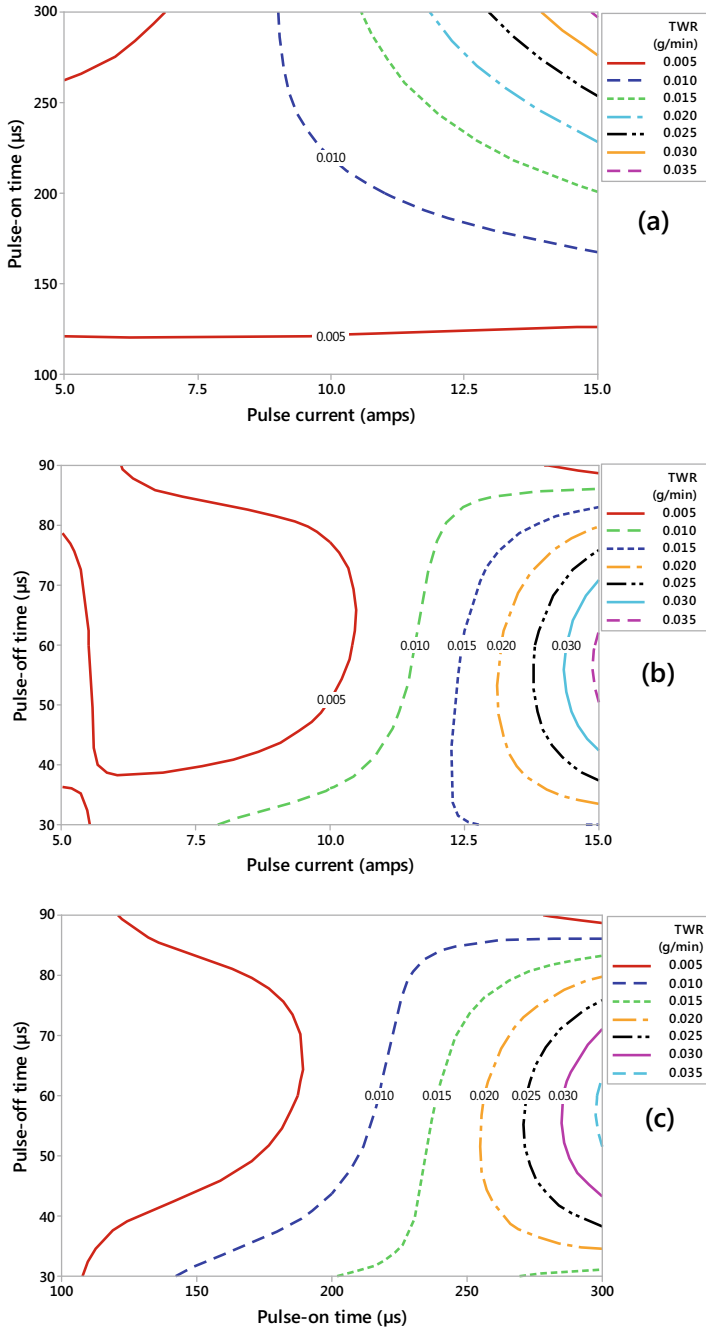
Fig. 5 Contour plot for TWR **a** I_p versus T_{on}, **b** I_p versus T_{off} and **c** T_{on} versus T_{off}

Table 8 Results of confirmation test

Parameter setting	Optimal level	MRR (g/min)	SR (μm)	TWR (g/min)	GRG	Error (%)
Predicted	$I_p\text{-}3\,T_{on}\text{-}1\,T_{off}\text{-}3$	–	–	–	0.73704	4.8
Experimental	$I_p\text{-}3\,T_{on}\text{-}1\,T_{off}\text{-}3$	0.02716	1.765	0.00260	0.77422	
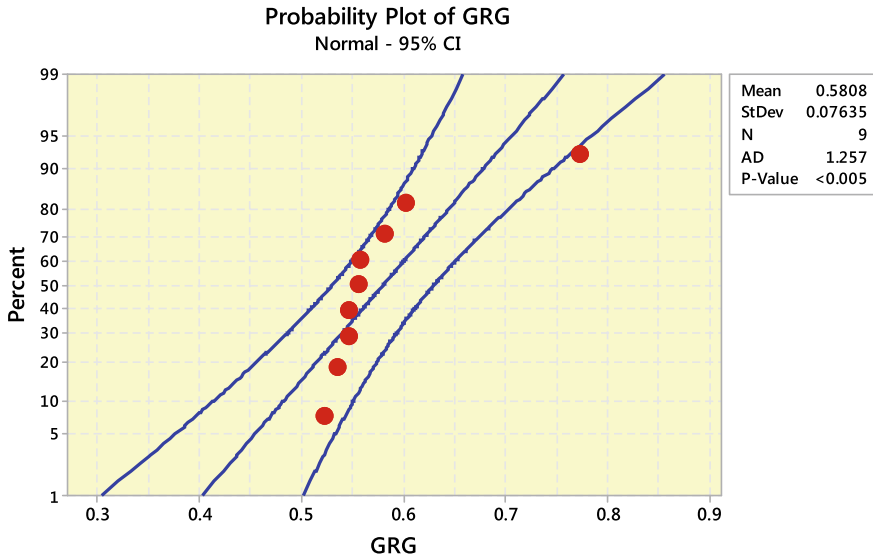
Fig. 6 Probability plot for GRG

where η_{pre}—predicted response, η_m—total mean response value, η_i—mean response value at the optimum condition and k—no. of parameters. Table 8 depicts a comparison of predicted and the experimental results. It is observed that the GRG for the experimental and predicted values are 0.73704 and 0.77422 respectively, and it has ensured the very good correlation due to a minor error of 4.8% is obtained. Figure 6 illustrates the probability graph for GRG, it is found that the errors are normally scattered along the straight line within limits.

4   Conclusion

The EDM performance of the AA8011-TiO$_2$ composite was studied in this work, and the following observations were made.

- The stir casting process was used to successfully produce the AA8011 matrix reinforced with 10wt.% TiO$_2$ particles.

- The GRA approach was used to optimize the EDM parameters with multi-response characteristics such as MRR, SR and TWR using a L9 (3^3) orthogonal array.
- According to the main effect graph, the optimal condition for best multi-response was identified as 15 amps I_p, 100 μs T_{on} and 90 μs T_{off} (i.e., I_p-3T_{on}-1T_{off}-3).
- According to the ANOVA results, the most prominent parameter was I_p, which contributed 50.9%, followed by T_{off} (21.62%) and T_{on} (14.19%).
- The verification experiment was carried out under optimal parameter conditions, and the experimental response was found to be extremely near to the predicted response, with a tiny error of 4.8%.

References

1. Alagarsamy SV, Ravichandran M (2019) Synthesis, microstructure and properties of TiO$_2$ reinforced AA7075 matrix composites via stir casting route. Mater Res Express 6:1–15
2. Sharma A, Kumar V, Dhawan ABV, Kotecha K, Prakash C (2021) Experimental investigation and optimization of electric discharge machining process parameters using grey-fuzzy-based hybrid techniques. Materials 14:1–21
3. Patel Gowdru Chandrashekarappa M, Kumar S, Pimenov DY, Giasin K (2021) Experimental analysis and optimization of EDM parameters on HcHcr steel in context with different electrodes and dielectric fluids using hybrid Taguchi-based PCA-utility and CRITIC-utility approaches. Metals 11:1–23
4. Kumar R, Singh I, Kumar D (2013) Electro discharge drilling of hybrid MMC. Procedia Eng 64:1337–1343
5. Meignanamoorthy M, Ravichandran M, Sakthivelu S et al (2020) Optimization of electric discharge machining process parameters on AA6351-Al$_2$O$_3$. Mater Today Proc 27:1051–1054
6. Gopalakannan S, Senthilvelan T, Kalaichelvan K (2012) Modeling and optimization of EDM of Al 7075/10wt% Al$_2$O$_3$ metal matrix composites by response surface method. Adv Mater Res 488–489:856–860
7. Hourmand M, Farahany S, Sarhan AAD, Noordin MY (2015) Investigating the electrical discharge machining (EDM) parameter effects on Al-Mg2Si metal matrix composite (MMC) for high material removal rate (MRR) and less EWR–RSM approach. Int J Adv Manuf Technol 77:831–838
8. Alagarsamy SV, Ravichandran M (2021) Variation of electrode materials and parameters in the EDM of an AA7075-TiO$_2$ composite. Mater Test 63(2):182–189
9. Tripathy S, Tripathy DK (2016) Multi-attribute optimization of machining process parameters in powder mixed electro-discharge machining using TOPSIS and grey relational analysis. Eng Sci Technol Int J 19:62–70
10. Rahman M, Dey A, Pandey KM (2018) Machinability of cenosphere particulate–reinforced AA6061 aluminium alloy prepared by compocasting. Proc IMechE Part B J Eng Manuf 232:1–11
11. Tang L, Du YT (2014) Multi-objective optimization of green electrical discharge machining Ti–6Al–4V in tap water via grey-Taguchi method. Mater Manuf Process 29:507–513
12. Kachhap S, Singh A, Debnath K (2018) Electric discharge drilling of hybrid metal matrix composites using different tool electrodes. J Sci Ind Res 77:325–3289
13. Yan BH, Wang CC, Liu WD, Huang FY (2000) Machining characteristics of Al$_2$O$_3$/6061Al composite using rotary EDM with a disklike electrode. Int J Adv Manuf Technol 16:322–333
14. Gohil V, Puri YM (2018) Statistical analysis of material removal rate and surface roughness in electrical discharge turning of titanium alloy (Ti-6Al-4V). Proc IMechE Part B J Eng Manuf 232:1–12

15. Kolli M, Adepu K (2016) Optimization of the parameters for the surfactant-added edm of a Ti–6Al–4V alloy using the GRA-Taguchi method. Mater Technol 50:229–238
16. Dey S, Debnath K, Pandey M (2017) Optimization of electrical discharge machining process parameters for Al6061/cenosphere composite using grey-based hybrid approach. Trans Nonferrous Met Soc China 27:998–1010
17. Venkatesh S, Prakash S, Durairaj RB et al (2021) Machinability of SUPERNI-800 during PMEDM using the Taguchi method. Mater Today Proc 44:3851–3855
18. Satpathy A, Tripathy S, Pallavi Senapati N, Brahma MK (2017) Optimization of EDM process parameters for Al- 20% SiC reinforced metal matrix composite with multi response using TOPSIS. Mater Today Proc 4:3043–3052
19. Meena VK, Azad MS, Singh S, Singh N (2017) Micro-EDM multiple parameter optimization for C_p titanium. Int J Adv Manuf Technol 89:897–904
20. Alagarsamy SV, Raveendran P, Ravichandran M (2020) Investigation of material removal rate and tool wear rate in spark erosion machining of Al-Fe-Si alloy composite using Taguchi coupled TOPSIS approach. SILICON 13:2529–2543
21. Alagarsamy SV, Ravichandran M, Saravanan H (2021) Development of mathematical model for predicting the electric erosion behaviour of TiO_2 filled Al-Zn-Mg-Cu (AA7075) alloy composite using RSM-DFA method. J Adv Manuf Syst 20:1–26
22. Vinoth Kumar M, Meignanamoorthy M, Sakthivelu S et al (2020) Optimization of material removal rate in CNC turning of AA2024 via Taguchi technique. Mater Today Proc 27:1163–1167
23. Dinesh Kumar S, Ravichandran M, Meignanamoorthy M et al (2020) Prediction of optimum electric discharge machining parameters for AA7075-SiC composites. Mater Today Proc 27:1192–1196
24. Ponappa K, Sasikumar KSK, Sambathkumar M, Udhayakumar M, Multi-objective optimization of EDM process parameters for machining of hybrid aluminum metal matrix composites (Al7075/TiC/B_4C) using genetic algorithm. Surf Rev Lett 26:1–12
25. Alagarsamy SV, Ravichandran M, Dinesh Kumar S et al (2020) A Taguchi coupled desirability function analysis of wire cut EDM behaviour of titanium dioxide filled aluminium matrix composite. Mater Today Proc 27:853–858

Chapter 22
Parametric Optimization of Dry Turning on Zirconia-Reinforced Magnesium Matrix Composites Using Taguchi-GRA Approach

D. Sreekanth and R. Radha

1 Introduction

Magnesium is the lightest of all metals with specific features like good castability, machinabiility, weldability which makes it more attractive for the automotive, electronics, and aerospace sectors in many applications. However, it cannot be extensively used in structural applications due to its limited strength and ductile properties. Therefore, it is alloyed with other elements such as Ca, Zn, Sn, Al, Mn, and rare earth elements to improve its mechanical properties. Henceforth, the ceramic reinforcements like Al_2O_3, TiO_2, ZrO_2, SiC, TiC, etc., have been used extensively to improve its ductile and strength. Magnesium matrix composites can be processed by various methods such as casting, powder metallurgy, and severe plastic deformation. Squeeze casting is a technique of utilizing pressure during solidification can improve the wettability and bonding at the reinforcement-matrix interface. This prevents the shrinkage and gas porosity and produces sound casting. Squeeze casting is an attractive method for processing Mg-based alloys/composites [1]. Mg/Mg alloys with hexagonally closely packed (HCP) structure exhibit good machining characteristics at elevated temperature rather than room temperature. The cutting energy required for machining Mg is much lower than for other materials. Machining MMCs is difficult as the ceramic reinforcements build them stronger and stiffer than the base matrix [2]. The decrease in cutting forces with a large clearance angle helps in the reduction of friction and increases tool life [3]. The feed is a significant parameter for minimization of surface roughness and power consumption followed by depth of cut and cutting speed whilst machining steel with uncoated tungsten carbide [4]. The minimum power consumption during turning of metal matrix composite can be

D. Sreekanth · R. Radha (✉)
School of Mechanical Engineering, Vellore Institute of Technology, Chennai 600127, India
e-mail: radha.r@vit.ac.in

analyzed by desirability analysis of process parameters [5]. Lower power consumption and surface roughness were obtained at the lowest cutting speed and feed rate whilst machining of austenitic stainless steel with uncoated carbide tool [6]. The magnitude of cutting forces generated whilst machining hardened HSS than annealed HSS was high owing to the rise inflow of shear stress on the shear plane of the hardened HSS [7]. The cutting forces generated during machining can be used to calculate the power consumption [8]. The influence of cutting velocity, feed, cutting time on surface roughness, power, and flank wear on turning metal matrix composites has been investigated by orthogonal array and ANOVA [9, 10]. Taguchi technique is a standard protocol for analyzing machining parameters within minimum experimental runs. Taguchi method is a systematic design for improving product quality with less cost involved [11, 12]. The drawback of this technique is that it can be used only for single objective optimization scenarios. Grey system theory can be used to analyze data which has uncertain/incomplete information [13]. Unlike Taguchi's technique, grey relational analysis (GRA) can be used multi-objective optimization problems [14]. The combination of Taguchi techniques and GRA will simplify the process of optimization [15]. The surface finish of machined Al7075 MMCs is better with lower feed rate and higher cutting speed [16]. The turning process is one of the primary machining operations for shaping the component to the desired dimensions [17]. The research on machinability of Mg composites is gaining attention in recent times because of the positive effect of reinforcement on improvising its characteristics and very limited numbers in machinability studies on magnesium matrix composites. The optimization of turning parameters of Mg–ZrO_2 for better removal rate with minimum power consumption and study of chip morphologies are not reported elsewhere. The present work is to analyze dry turning of zirconia-reinforced magnesium matrix composite using low-cost HSS tool using a hybrid approach that combines Taguchi methodology and grey relational analysis (TM-GRA).

2 Materials and Method

2.1 Fabrication of Magnesium Matrix Composite

Pure Mg was used as a matrix material and 2 vol% ZrO_2 were chosen as the reinforcements to fabricate magnesium matrix composite. The composite was fabricated using squeeze casting technique. The monolithic pure Mg was loaded inside the furnace, and it was super-heated to the temperature of 800 °C. The preheated ZrO_2 particles were preheated which are added gradually in Mg matrix and stirred firmly at a speed of 500 rpm for 15 min so that the reinforcements will be distributed uniformly. Pouring temperature was maintained at 800 °C, and composite melt was transferred to the preheated graphite coated steel die. The squeeze casting process was performed by applying a uniform pressure using a 40 t hydraulic press to ensure defect free casting.

2.2   Measuring Cutting Forces, Power Consumption, and MRR

The experiments were carried out in accordance with machining parameters and their levels as shown in Table 1. The experiment runs were designed based on Taguchi L9 orthogonal array as shown in Table 2. The magnesium matrix composite was turned on a lathe machine using HSS tool with the cutting conditions shown in Table 3. For each test run, cutting forces (F_x), thrust forces (F_y), and radial forces (Fz) are measured using a lathe tool dynamometer (Kistler type 9272) as shown in Fig. 1. The turning of specimen was performed for 20 s for each run. The cutting forces measured are shown in Fig. 2. The turning operations were carried out on the composites for the different combination of parameters. The forces were measured using Lathe tool dynamometer, and the performance measures such as MRR and power were obtained as shown in Table 4.

Table 1 Factors and their levels

Factors	Level 1	Level 2	Level 3
Spindle speed (N)	330	510	770
Feed (f)	0.15	0.25	0.37
Depth of cut (d)	1	1.5	2

Table 2 Taguchi L9 orthogonal array

Levels of parameters			
S. No.	Spindle speed (N)	Feed (f)	Depth of cut (d)
1	1	1	1
2	1	2	2
3	1	3	3
4	2	1	2
5	2	2	3
6	2	3	1
7	3	1	3
8	3	2	1
9	3	3	2

Table 3 Cutting conditions

Cutting tool	HSS
Tool geometry	0-10-6-6-8-75-1 mm (ORS)
Machining environment	Dry
(N) rpm	330, 510, 770
(f) mm/rev	0.15, 0.25, 0.37
(d) mm	1, 1.5, 2
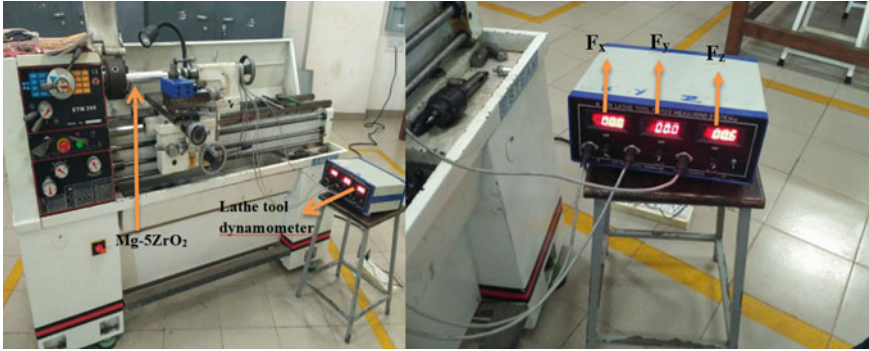
Fig. 1 Lathe with tool dynamometer
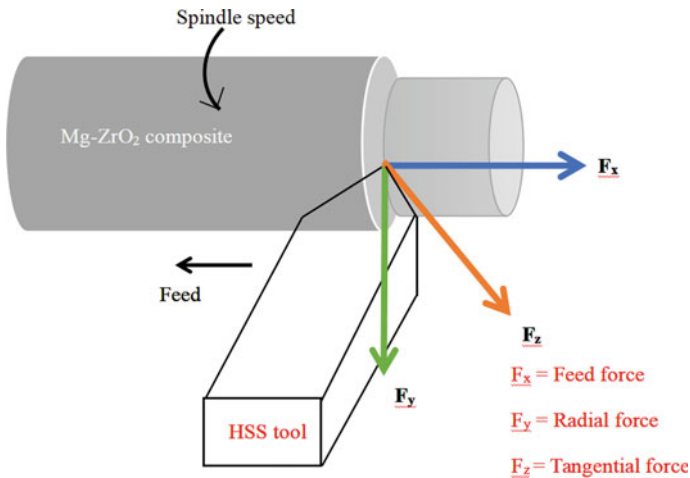
Fig. 2 Cutting forces

2.3 Optimization Using GRA

The data sequences may have different quantities, and levels of parameters and the range of sequence may be scattered widely. Therefore, the raw data should be pre-processed. Hence, the original sequence is transferred to comparable one. The experimental results obtained from GRA are normalized in a range of 0–1. Then, data pre-processing is carried out for normalizing the inputs of the characteristics. In case of MRR, it should be more for better machining. When the "larger-the-better" is a characteristic of the original sequence, then the original sequence should be normalized by substituting the values of the sequence obtained from pre-processing of data $X_i(k)$ Eq. (1).

Table 4 Experimental runs using an L9 OA and performance results: (Mg–ZrO$_2$)

Exp. No.	N	f	d	F_xN	F_yN	F_zN	MRR mm^3/min	P watt	t_1 uncut chip thickness	t_2 chip thickness	r chip thickness ratio
1	1	1	1	1.96	12.75	15.69	7305	813	0.15	0.75	0.2
2	1	2	2	2.55	22.56	19.61	17,777	1016	0.25	0.96	0.1562
3	1	3	3	2.90	35.30	25.50	33,739	1321	0.37	1.25	0.12
4	2	1	2	1.46	17.65	18.63	15,223	1492	0.15	1.01	0.2475
5	2	2	3	2.06	27.46	25.50	32,428	2042	0.25	1.19	0.21008
6	2	3	1	4.77	21.57	20.59	23,108	1649	0.37	0.76	0.3289
7	3	1	3	1.49	18.63	17.65	27,200	2134	0.15	0.99	0.3737
8	3	2	1	3.41	14.71	14.71	21,760	1778	0.25	0.72	0.51383
9	3	3	2	3.63	27.46	18.63	46,630	2252	0.37	1	0.37

Table 5 Sequences of each performance characteristics after data processing

Exp. No.	F_x	F_y	F_z	MRR	Power
Reference sequence	1.0000	1.0000	1.0000	1.0000	1.0000
1	0.8571	1	0.909090	0	1
2	0.42857	0.56521	0.545454	0.2663	0.8138
3	0	0	0	0.6721689	0.5526
4	0.42857	0.78260	0.636363	0.20135	0.4419
5	0	0.34782	0	0.63886	0
6	0.571428	0.60869	0.454545	0.401856	0.4128
7	0.42857	0.73913	0.727272	0.50592	0.0607
8	1	0.913043	1	0.367577	0.4197
9	0.28571	0.34782	0.636363	1	0.095

$$x_i(k) = \frac{X_i(k) - \min X_i(k)}{\max X_i(k) - \min X_i(k)} \tag{1}$$

Minimum cutting forces and power are desirable for better machining performance (smaller-the-better). The sequence obtained in pre-processor is normalized using Eq. (2)

$$x_i(k) = \frac{\max X_i(k) - X_i(k)}{\max X_i(k) - \min X_i(k)} \tag{2}$$

where k denotes the sequence of forces and i represents power. Deviation for the normalized sequences is done to reduce the deviation of result from the optimized one. The deviation sequence $\Delta_{0i}(k)$ is calculated using Eq. (3)

$$\Delta_{0i}(k) = |X_0\Delta(k) - X_i(k)| \tag{3}$$

The data after pre-processing is given in Table 5.

2.4 Calculation of Grey Relational Grade from Grey Relational Coefficient

The coefficient for grey relation was calculated using the sequence of pre-processing which reveals the relation between the actual normalized results and ideal normalized results. Coefficient for grey relation is given by Eq. (4) by substituting the values for identification coefficient ($x*I(k)$), reference, and deviation sequences ($x_0* (k)$, $\Delta_{0i}(k)$).

$$\xi(k) = \frac{\Delta \min + \xi \Delta \max}{\Delta_{0i}(k) + \xi \Delta \max} \tag{4}$$

Grey relational grade is computed using the grey relational coefficient by taking the average of the grey relational coefficient corresponding to each performance characteristics. In this approach, the multi-objective of optimizing will be transformed into a mono grey relational grade. The grey relational coefficient and mean of the grey relational grade for each level of the machining parameters are found out.

3 Results and Discussion

3.1 Material Removal Rate

This section focusses on analyzing the effects of spindle speed, feed rate, and depth of cut on material removal rate, chip thickness ratio, and cutting power. Also the cutting forces generated during machining and their impact were analyzed in detail. Figure 3a–h shows the plots of MRR. The main effect plot shows that material removal rate increases as the levels of the cutting parameters are increased (Fig. 3a). Spindle speed seems to play a lesser role in MRR compared to feed rate Fig. 3b. Higher MRR is shown in green in the contour plots Fig. 3b–h. Medium depth of cut combined with higher feed rate is giving better MRR. Radial force and tangential forces got increased when there is increase in MRR (Fig. 3e–h). The radial force dominates significantly than the other forces when the MRR is high. Cutting forces are predominantly influenced by depth of cut.

3.2 Cutting Forces

Cutting forces generated with respect to feed rate, depth of cut, and spindle speed are shown in Fig. 4(a–i). Increase in spindle speed seems to raise the tangential force and feed force, and then, there is sudden drop when it reaches higher rpm (Fig. 4a, b, g). This may be attributed due to thermal softening of workpiece. There is significant reduction in feed force when spindle speed is increased. The density of dislocation at the matrix-reinforcement interface plays a vibrant role on decrement in the cutting forces whilst machining the composite. When the cutting tool passes through these dislocations, there will be less effort needed which in turn reduces the magnitude of cutting forces. The increase in radial force can be observed at higher feed rate. Feed force never reached its maximum at higher feed rate and depth of cut but the other two forces reached the peak (Fig. 4c–f). Even though feed force did not reach its maximum, there are instances in which feed force is little higher than the other two forces.
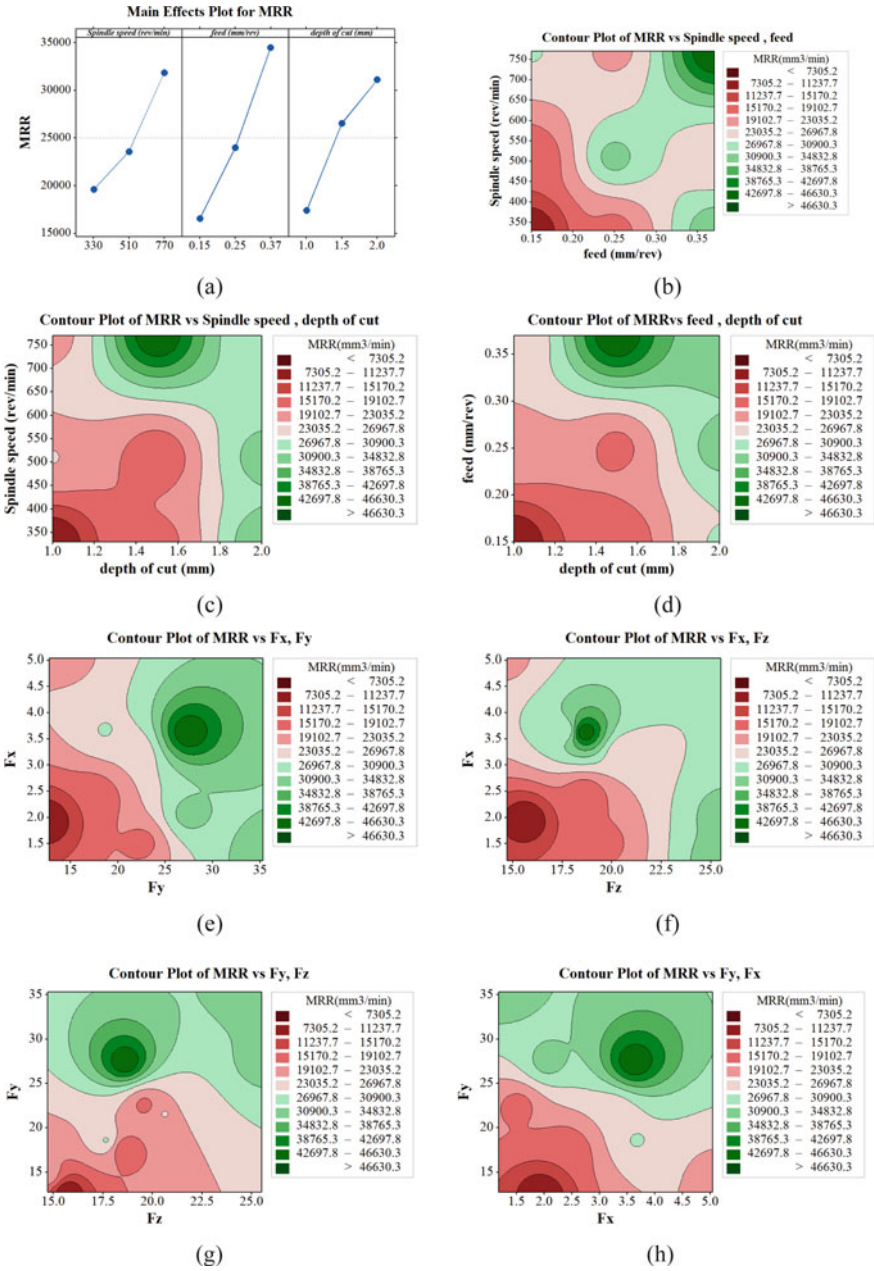
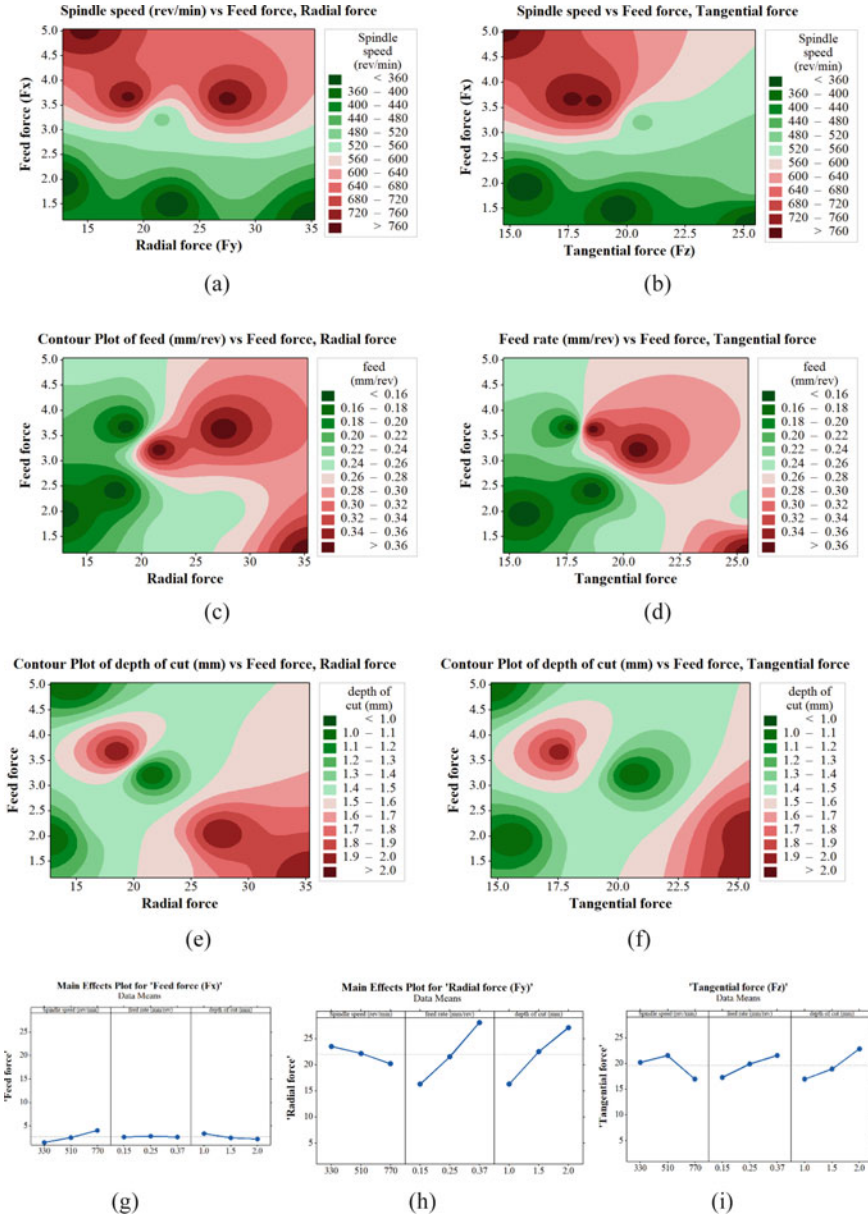Fig. 3 MRR versus F_x, F_y, and F_z

Fig. 4 Effect of turning parameters on cutting forces

3.3 MRR Versus Power, Cutting Forces

The main effects plots of MRR and power (Figs. 4a, 5a) and the contour plots (Fig. 5b, c) give a unique insight about the contribution of spindle speed, feed rate, and depth of cut. Feed rate has higher influence in MRR but less influence in power consumption. Spindle speed is the major power consuming factor. Feed force consumes huge power (Fig. 5d, e). Strategies to reduce feed force can significantly reduce power required for cutting. The better chip thickness ratio was obtained with lower spindle speed and higher depth of cut (Fig. 6a). Lower MRR and higher cutting power corresponds to better chip thickness ratio (Fig. 6b). Minimal spindle speeds and higher feed rates and lower depth of cuts are favourable for better chip thickness ratio (Fig. 6c–d). The contour plots of power are shown in Fig. 4b–5h. Increase in spindle speed increases power, however, the increase in feed rate and depth of cut contributes to MRR (Fig. 6f–h). With the increase in feed rate, the section of sheared chips is increasing, and consequentially, the removal of material requires more effort which in turn raises the cutting force requirement. At higher speed of machining, the temperature in the cutting zone causes plasticity of the metal which in turn reduces the efforts necessary for machining with less power requirement.

3.4 Chip Analysis

The type of chip formations is determined by the joined effects of tool geometry, work material, speed, feed, depth of cut, and uncut chip thickness. Discontinuous chip formation was noted at lower speed due to the increase in tool-chip contact length. Serrated chip at higher feed rate was observed owing to the deformation and shear slip phenomenon occurred in the primary deformation zone. Whilst cutting metals generally shorter and thick chip flow can be observed due to plastic deformation before the cutting action. This deviation in dimension can be quantified by thickness ratio which is the ratio of the thickness of chip before and after cutting. Chip thickness ratio varies with respect to many pentameters like cutting speed, feed, and depth of cut, type of material/cutting fluid and the geometry of the cutting tool. Higher chip thickness ratio indicates good cutting action. The corresponding plots are shown in Fig. 6 (green indicates favourable higher values of chip thickness ratio). The ductility of magnesium matrix increases when machining at high cutting speeds facilitates the reinforcement transport in Mg matrix. Hence, particles are aligned on the direction of shear zone results in the serrated discontinuous chips. The increase in cutting speed promotes the crack propagation results in reduction of chip length and finally broken in to smaller segments. The distribution of reinforcement particles with in the matrix influences the crack propagation along the shear zone. The de-bonding of particles creates voids propagates micro-cracks would be the reason for the formation of serrated chips. The higher cutting temperature at high cutting speed and low thermal
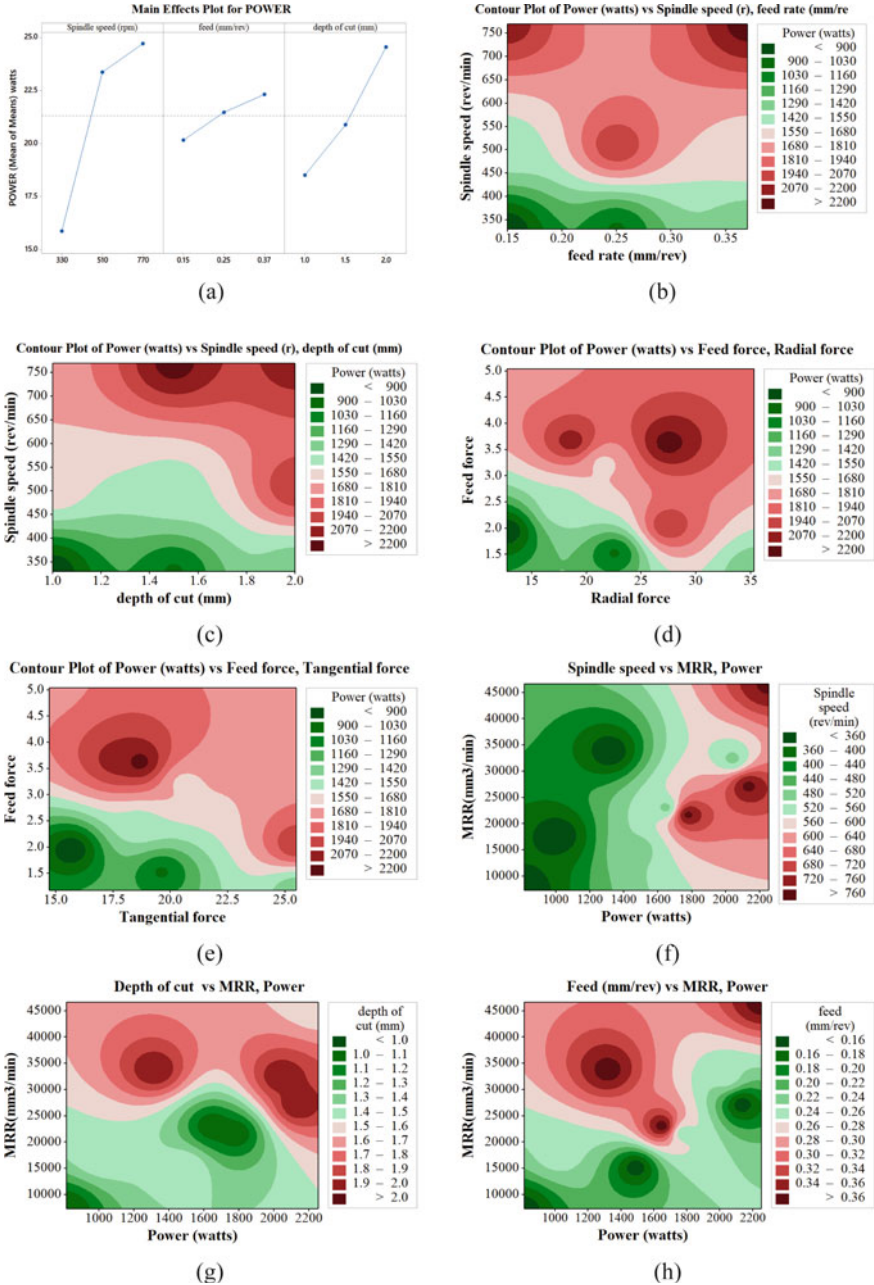
Fig. 5 Cutting power analysis
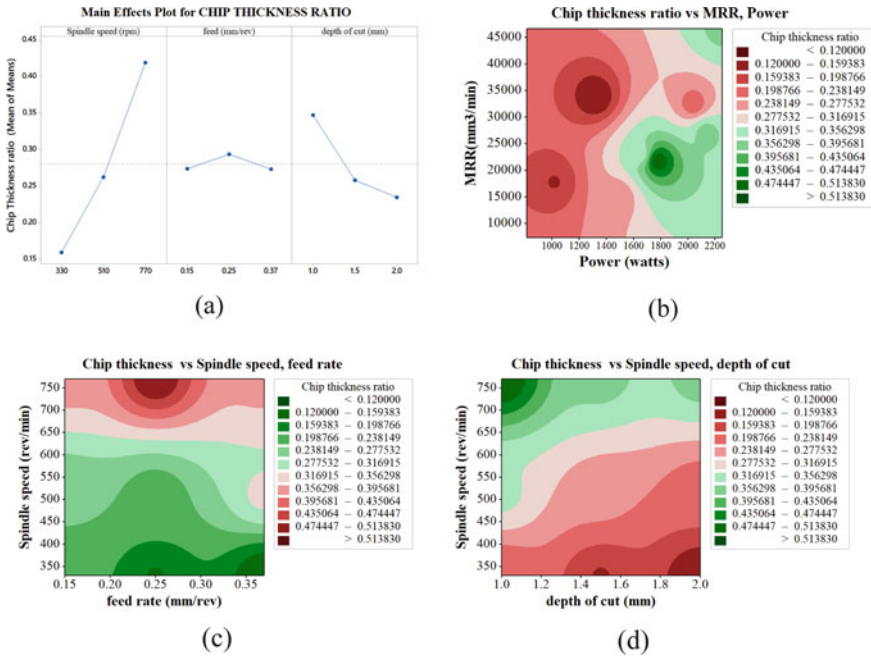
Fig. 6 Chip thickness ratio plots

conductivity of MMC led to high strain at shear zone yields serrated discontinuous chips.

3.5 Grey Relational Analysis

For "larger-the-better" MRR, the original sequence can be normalized by Eq. (1), where $X_i(k)$ and $x(k)$ are the sequence after the data pre-processing and comparability sequence, respectively, $k = 1$ for MRR; $i = 1, 2, 3…, 9$ for experiment numbers 1–9. Similarly for forces and power consumption should be minimum for optimal cutting performance, thus the "smaller-the-better" quality characteristic has been used. When "smaller-the-better" is a characteristic of the original sequence, then it should be normalized by Eq. (2), where $X_i(k)$ and $x(k)i$ are the sequence after the data pre-processing and comparability sequence, respectively, $k = 2$ and 3 for forces and power; $i = 1, 2, 3…, 9$ for experiment numbers 1–9. So the calculations are done, and all the sequences after data pre-processing using Eqs. 1 and 2 are presented in Table 5. The deviation sequences are calculated by Eq. 3 as shown in Table 6. After data pre-processing is carried out, a grey relational coefficient can be calculated with the pre-processed sequence by Eq. 4, where $\Delta_{0i}(k)$ is the deviation sequence of the reference sequence $x_0^*(k)$, and the comparability sequence is $x^*I(k)$, distinguishing

Table 6 Deviation sequences Mg–ZrO$_2$

Deviation sequences/Exp No.	$\Delta_{0i}(1)$	$\Delta_{0i}(2)$	$\Delta_{0i}(3)$	$\Delta_{0i}(4)$	$\Delta_{0i}(5)$
1	0	0	0	1	0
2	0.5	0.375	0.3847	0.7304	0.192
3	1	1	1	0.32039	0.4822
4	0.5	0.20054	0.1539	0.7972	0.4659
5	0.666	0.333	0.3847	0.35663949	0.5839
6	0.1666	0.375	0.3077	0.596559	0.4709
7	0.666	0.29167	0.23077	0.4928762	1
8	0	0.16666	0	0.6329389	0.6853
9	0.833	0.8333	0.23077	0	0.8556

or identification coefficient. If all the parameters are given equal preference, it is taken as 0.5. The grey relational coefficient for each experiment of the L9 OA can be calculated using Eq. 4, and the same is presented in Table 8. The higher grey relational grade represents that the corresponding experimental result is closer to the ideally normalized value. After obtaining the grey relational coefficient, the grey relational grade is computed by averaging the grey relational coefficient corresponding to each performance characteristic. Since the experimental design is orthogonal, it is then possible to separate out the effect of each machining parameter on the grey relational grade at different levels. For example, the mean of the grey relational grade for the pulse-on time at levels 1, 2, and 3 can be calculated by averaging the grey relational grade for the experiments 1–3, 4–6, and 7–9, respectively, as shown in Table 7. The mean of the grey relational grade for each level of the machining parameters is summarized and shown in Table 8. The larger the grey relation grade is, the closer will be the product quality to the ideal value. Thus, larger grey relational grade is desired for optimum performance. Therefore, the optimal parameters setting for better MRR and lesser forces and power consumption are (A3B1C1).

4 Conclusion

The experimental investigations on turning of Mg–ZrO$_2$ composites were studied using HSS tool under dry cutting conditions by varying machining parameters, based on that the following conclusions are drawn: The feed rate is found to be more significant than spindle speed for better MRR. The depth of cut has notable influence in generation of cutting forces than feed rate and spindle speed. The increase in tangential force and feed forces is caused by increase in spindle speed, thereby increases the power consumption. The optimal machining parameters have been determined by the grey relational grade for multi-objectives like better MRR, lesser power consumption,

Table 7 Grey relational coefficient and grey relational grade (Mg–ZrO$_2$)

Exp. No.	Grey relational coefficient					Grey relational grade	Rank
	F_x $\xi_i(1)$	F_y $\xi_i(2)$	F_z $\xi_i(3)$	MRR $\xi_i(4)$	Power $\xi_i(5)$	$\Gamma i = (1/5)(\xi i(1) + \xi i(2) + \xi i(3) + \xi i(4) + \xi i(5))$	
1	0.7777	1	0.8461	0.3333	1	0.79142	1
2	0.4666	0.5348	0.5238	0.4052	0.7286	0.5318	7
3	0.3333	0.3333	0.3333	0.6039	0.5274	0.4214	9
4	0.4666	0.6969	0.5789	0.3850	0.4725	0.5198	3
5	0.3333	0.4339	0.3333	0.5806	0.3333	0.4040	8
6	0.5384	0.5609	0.4782	0.4553	0.4598	0.4985	4
7	0.4666	0.6571	0.6470	0.5029	0.3474	0.5242	6
8	1	0.8518	1	0.4415	0.4628	0.7512	2
9	0.4117	0.4339	0.5791	1	0.3552	0.555	5

Table 8 Response table for the grey relational grade (Mg–ZrO$_2$)

Symbol	Machining parameters	Grey relational grade			Main effect (Max–Min)	Rank
		Level 1	Level 2	Level 3		
A	N	0.5815	0.4741	0.6101	0.1731	2
B	f	0.6118	0.5623	0.4916	0.10258	3
C	d	0.6472	0.5286	0.4498	0.1974	1

and it was found that the optimal values are larger value of spindle speed (770 rpm), lower depth of cut (1 mm), and lower feed rate (0.15 mm/rev).

References

1. Goh CS, Soh KS, Oon PH, Chua BW (2010) Effect of squeeze casting parameter on the mechanical properties of AZ91–Ca Mg alloys. Mater Des 31:S0–S53
2. Aggarwal A, Singh H, Kumar P, Singh M (2008) Optimizing power consumption for CNC turned parts using response surface methodology and Taguchi's technique—a comparative analysis. J Mater Process Tech 200:373–384
3. Bagaber SA, Yusoff AR (2017) Multi-objective optimization of cutting parameters to minimize power consumption in dry turning of stainless steel 316. J Clean Prod 157:30–46
4. Bhushan RK (2013) Optimization of cutting parameters for minimizing power consumption and maximizing tool life during machining of Al alloy SiC particle composites. J Clean Prod 39:242–254
5. Davim JP (2003) Design of optimization of cutting parameters for turning metal matrix composites based on the orthogonal arrays. J Mater Process Tech 132:340–344
6. Hsiao YF, Tarng YS, Huang WJ (2007) Optimization of plasma arc welding parameters by using the Taguchi method with the grey relational analysis. Mater Manuf Process 23:51–58
7. Ghani JA, Rizal M, Haron CHC (2014) Performance of green machining: a comparative study of turning ductile cast iron FCD700. J Clean Prod 85:289–292

8. Juang SC, Tarng YS (2002) Process parameter selection for optimizing the weld pool geometry in the tungsten inert gas welding of stainless steel. J Mater Process Tech 122:33–37
9. Kant G, Sangwan KS (2014) Prediction and optimization of machining parameters for minimizing power consumption and surface roughness in machining. J Clean Prod 83:151–164
10. Lan J, Yang Y, Li X (2004) Microstructure and microhardness of SiC nanoparticles reinforced magnesium composites fabricated by ultrasonic method. Mater Sci Eng A 386:284–290
11. Lin CL (2003) Use of the Taguchi method and grey relational analysis to optimize turning operations with multiple performance characteristics. Mater Manuf Process 19:209–220
12. Loovey LA, Monaghan JM, Reilly PO, Taplin DMR (1992) The turning of an Al/SiC metal matrix composite. J Mater Process Tech 33:453–468
13. Montgomery DC (2001) Design and analysis of experiments. Wiley, New York
14. Selvaraj DP, Chandramohan P, Mohanraj M (2014) Optimization of surface roughness, cutting force and tool wear of nitrogen alloyed duplex stainless steel in a dry turning process using Taguchi method. Measurement 49:205–215
15. Rajeswari B, Amirthagadeswaran KS (2017) Experimental investigation of machinability characteristics and multi-response optimization of end milling in aluminium composites using RSM based grey relational analysis. Measurement 105:78–86
16. Kumar R, Chauhan S (2015) Study on surface roughness measurement for turning of Al 7075/10/SiCp and Al 7075 hybrid composites by using response surface methodology (RSM) and artificial neural networking (ANN). Measurement 65:166–180
17. Rathod NJ, Chopra MK, Chaurasiya PK, Vidhate US, Dasore A (2022) Optimization on the turning process parameters of SS 304 using Taguchi and TOPSIS. Annals of Data Science 1–15

Current Trends in Additive Manufacturing of Materials

Chapter 23
Light Metals and Composites in Additive Manufacturing

A. T. Erturk

1 Introduction

Additive manufacturing (AM) or 3D printing is a manufacturing process to obtain parts from a CAD design. It was the late 1980s when AM entered the industry under the name of rapid prototyping. In the process of technological development for AM, many other names were put forward and adopted by developers and users [15]. To avoid the complexity of naming production methods, the American Society of Mechanical Engineers (ASME) and the American Society for Testing and Materials (ASTM) adopted "Additive Manufacturing" nomenclature as the standard terminology in 2009 [17].

AM process steps start with the data set which is obtained by virtual CAD design or imaging a part model. Thus, the computer software takes the information of each layer contour. Any geometry can be produced with AM. Each layer is built with equal thickness according to the contour information. The quality of a product increases with getting thinner layer. As a negative result, the production time increases. AM parts show stair-stepping formation because of the layer-based process. Next layer bonds with the previous one [14, 22].

Today many types of AM machines are available and they work on the same process route. Different layer generation methods are used in AM. Figure 1 shows the standard categorization for all AM processes. Generation of a layer can be done using light metals is generally powder forms. Existing AM machines consist of an energy source that provides melting and sintering effects. An additional system component that provides coordinate control for contouring. Laser is the most used energy source of AM processes for light metals. Laser melting provides metal part processing. Although it is also a sintering process, laser sintering designation is used

A. T. Erturk (✉)
Department of Mechanical Engineering, Kocaeli University, 41001 Izmit, Turkey
e-mail: tamer.erturk@kocaeli.edu.tr
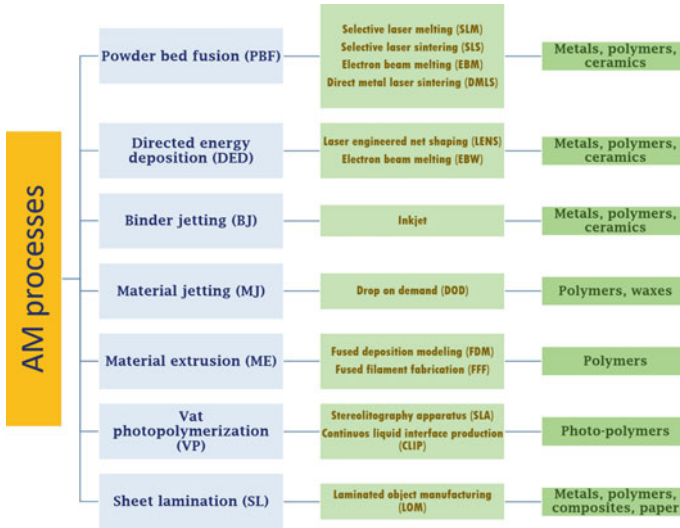
Fig. 1 AM process classifications based on ISO/ASTM 52900 standard

for plastic materials building machines. Identical machine designs can be used for processing plastics and metals. The main subsystems of an AM machine are a build chamber, a moving platform, and a laser source. The laser source selectively melts the raw materials and generates dense (>99%) sectors. AM machines can operate with a broad range of types of ferrous and non-ferrous metals [3, 15, 23].

2 Applications of Light Metals and Composites in AM

Design engineers create a part using professional design software and get STL file format data set in most industrial productions. Then after the proper raw material is selected according to the ability of the AM machine and product needs. Before building part, process parameters are determined and set with software by the operator of AM machine. When the process and cooling-down stage finish, the final part is taken from the machine, and sandblasting is applied as post-processing. Machining operations such as drilling, threading, or surface treatments such as coating, and polishing are also optional finishing operations. Figure 2 shows a typical workflow of part production through AM route [27, 28, 31].

Fig. 2 A typical workflow of part production through AM route

Industrial applications of AM have become widespread and diversified rapidly today. Innovative parts produced by the actors of the automotive, aerospace, medical implants, consumer goods, art, and toy industries accelerate the spread of AM technology and provide different perspectives [2].

Lightweight metal alloys and composites have been in use with AM. Attempts to obtain AM products with more advanced properties for different types of such materials are ongoing. Light metals such as Al and Mg are difficult to process with AM technology due to their high reflectivity and high thermal conductivity features. Especially Mg is highly reactive, so it is crucial to avoid free oxygen in the AM process [2].

Titanium-based Ti6Al4V is an alloy frequently used in AM production. It is preferable in the biomedical and aerospace industries for its corrosion resistance, deformation ability, and suitability of specific strength properties. The product properties of this alloy are affected by the thermal conditions during the AM process. The microstructure of Ti6Al4V consists of primary and secondary α grains and β phases. Increasing α phase composition also increases the elastic behavior. Therefore, both phase composition and mechanical properties change due to the thermal effect of phase structures in the AM process. Due to the rapid thermal cycle heating and cooling, especially in the PBF and DED process, needle-shaped marten-site α' phases can also form. Needle-shaped martensite α' increases strength and decreases ductility. In the EBM process, where comparatively lower cooling rates confront, a microstructure occurs in the mixture of α and β phases. A microstructure is a mixture of α and β phases that reduces the strength while increasing ductility. In general, the mechanical properties of the AM product exhibit low ductility compared to the Ti6Al4V material wrought condition. β-stabilizers such as Nb, Ta, Zr, and Mo are added to the Ti6Al4V alloy composition to improve biocompatibility al-so reduce the elastic modulus. Achieving the balance between strength and ductility according to the expected mechanical properties of the final product is possible with heat treatment applied at a temperature above the β transformation temperature after AM [8].

Although many aluminum alloy compositions are in industrial use, there are a limited number of aluminum alloys suitable for AM technology. It is hard to manufacture AM parts with Al alloys due to their high reflectivity, especially in processes with laser melting. On the other hand, Al alloys are prone to high-speed parts production in AM technology thanks to their high thermal conductivity. Accompanying elements of an Al alloy such as Sn and Zn with low melting temperatures also cause pore defects due to unbalanced phase changes in the melt pool. Some other accompanying elements like Li and Mg remove from the composition in the AM process, just like in the casting process. Therefore, it is complex to remain in the desired percentage composition ratios in the product. Since AM parts produced with Al alloys have fine microstructure, they have higher mechanical properties than wrought conditioning. The most frequently preferred aluminum alloys in SLM processes are eutectic. After AM production of eutectic Al–Si alloy contains primary Al, primary silicon, and eutectic phases. The phases are coaxial and columnar. Al–Cu alloys come to the fore in the directed-energy deposition method.

Another light metal is Mg. General usage of Mg alloys is biodegradable part production in AM process. This type of implant is discarded by decomposing over time with the recovery period in the body. If necessary, Sr, Y, and Zr adding elements give a slowing down role of the biodegradability feature in Mg-based alloy compositions. These alloys are the material for intravascular and extravascular stents and orthopedic implants. Porous or lattice structures are at the forefront in the design of compatibility with biodegradability. Mg-based alloys are difficult to process in the AM because Mg is a highly flammable light metal.

3 Powder Bed-Based Technologies for AM Processing of Light Metals and Composites

The layer-based process supports obtaining complex geometries with customizable internal structures. The resulting geometry cannot thereby be realized using conventional manufacturing techniques. Figure 3 shows a complex production sample overview with scanning electron microscopy and energy-dispersive X-ray spectroscopy (EDS) analysis. Different PBF methods have their respective advantages and disadvantages. The criteria by which a method should be evaluated are raw material availability, construction volume, geometric completeness of the resulting product, product manufacturing time, pretreatment, and post-treatment requirements [7, 29].
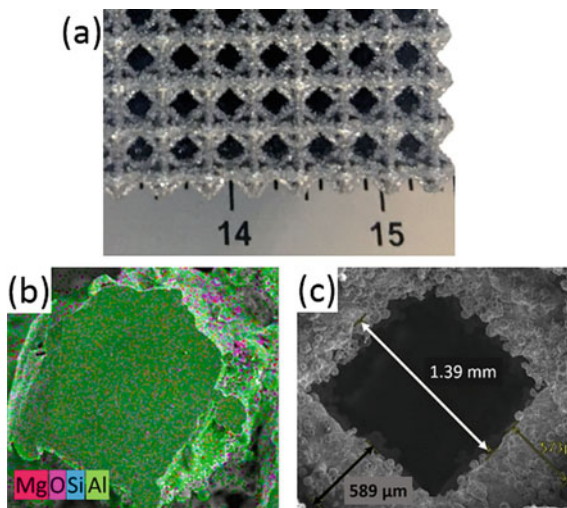

Fig. 3 An example of DMLS production: double pyramid lattice with the lateral structure of AlSi10Mg material **a** overview, **b** EDS analysis, **c** SEM micrograph

SLM and EBM are based on powder bed fusion (PBF). Selective laser melting (SLM), electron beam melting (EBM), and directed energy deposition (DED) processes are used for the fabrication of light metals and their composites. These methods produce with raw materials in powder form. The energy source (laser or electron beam) and its effect on the metal powder (sintering or melting) are different for SLM and EBM methods. SLM provides complex geometric and structural characters. A high-power laser is the energy source of SLM in which metal powder melts and fuses. Due to the complexity of the part designs and the high thermal energy provided by the laser, the thermal stress problem arises, a simple precaution applied to prevent this problem is to preheat the powder bed up to 250 °C under an inert atmosphere. The powder sizes used as raw materials are generally 10–60 μm in size. The 3D CAD data that gives the part contour is divided by the slice thickness in a range of 20–100 μm [10, 22].

The energy source of the EBM is the electron beam. The process is carried out under a high vacuum. The powder size as in raw material used in EBM is larger than SLM and is in the range of 60–105 μm. Hence, EBM parts are rougher due to the larger powder size. To avoid thermal distortions, the inside of the building chamber is at a temperature of 700 °C. Therefore, metals with a low melting temperature cannot be processed with the EBM method. The divergence brings about the microstructure and strength differences between the parts produced with SLM and EBM [5].

Unlike these methods, raw material is added to the melt pool from a nozzle in the DED method. DED technique processes powder and wire from metals as raw materials with a more concentrated energy source. It is also possible to obtain composite structure products by transferring powder and wire with different content from the multi-feeding point to the processing area. Thanks to its high energy source and multiple feeding possibilities, it provides the advantage of large-size part production with a high deposition rate. In addition, the DED technique can be used for repair and coating. However, it is not conducive to precise dimensional accuracy and complex geometric designs.

4 Wire-Arc Welding-Based Technologies for AM Processing of Light Metals and Composites

The WAAM manufacturing process allows for complex designs. It stands out for the industrial production of aluminum, titanium, and other light metal alloys with low production costs thanks to its high deposition capability. WAAM is a production method that continues to work on material applicability, microstructural formation, and damage prevention in both industrial and academic fields. Among light metal alloys, many aluminum alloys (2024, 2219, 2319, 4043, 5087, 5183) and titanium alloys (Ti–6Al–4V) are applicable. This production method includes arc formation, wire feeding, and deposition of molten liquid metal onto the previous layer, the whole process takes place under shielding gas. The processing steps continue until the part
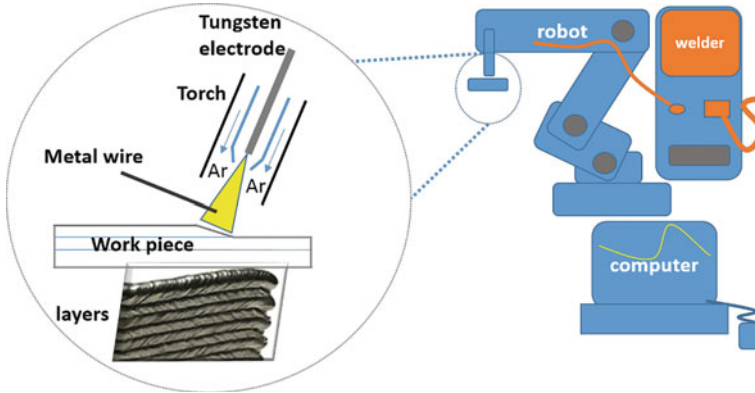
Fig. 4 Schematic representation of the WAAM process

geometry is complete. The geometric accuracy of the product depends on the layer thickness, electrode-wire distance, wire feeding speed, and wire angle parameters. Using a low wire-feed angle causes improvement with smoothing of the deposition surface. The current and cycle time of the TIG process used in melting affect the strength and hardness of the product. Figure 4 shows a schematic representation of the WAAM process. Differences in solidification also cause changes in microstructure. The rapid arc progression provides smooth layers with fine grain. The cold working at the interlayer removes micropores in the structure. Hence, inter-layer rolling and post and post-deposition heat-treatment increase the mechanical strength of the part. However, in post-deposition heat-treated, the pores will enlarge if hydro-gen diffusion is not avoided. The precipitations in the inner/inter layers also increase the strength of aluminum-based wire + arc additive manufactured (WAAM) products. The microstructure of aluminum alloys consists of coarse columnar grains between layers. Besides, equiaxed and finner grains form in the inner layer regions [15].

5   Input Material Properties for AM Processes of Light Metals and Composites

In AM processes, raw materials generally are used in powder form. The physical property of raw material affects to mechanical properties of the final product. The ability of products produced by AM processes to achieve the predicted properties reproducibly is also related to the raw material properties. The reusing of raw material not processed in the production area has been examined for this purpose. Therefore, the quantitative properties of recycled raw materials should be kept under control. The main factors that have been used to control powder material properties are chemical composition, powder morphology, powder density, and powder fluidity. Although there are many

different metal powder production methods, the most preferred method is atomization. Each of the particular powder production techniques provides powder products with various characters, sizes, and shapes. Therefore, the production technique of the powder used as a raw material reflects in the AM part properties. Metal powder atomization techniques in AM part production are gas and plasma rotating electrode atomization. Because the powder products obtained by water atomization are irregular in shape, coarse, rough, and contain a high amount of oxide. Since gas and plasma atomization occur under a controlled vacuum and inert gas atmosphere, these techniques are more suitable for powder production of reactive Al and Mg light metals. The metal powders obtained are more homogeneous, low in oxide, and have a smooth surface. Metal powders produced by the gas atomization method are not the primary choice to obtain AM raw materials. They can contain gas pores trapped inside. Plasma atomization results in smaller grain, more spherical, and smoother than gas atomization. In recent years, new metal powder production techniques have been developed a suitable for the widespread use of AM productions. The main methods used to characterize the shape and surface structure of the particles are sieve analysis, laser diffraction measurement, SEM, and micro-CT analysis [10, 14, 25].

The particle size distribution (PSD) of a powder is a mathematical function that gives information about the volume fraction of different particle sizes. Hall flow rate testing determines density and powder fluidity. The more spherical the metal powders provide a higher strength properties of AM parts. The other metal powder particle shapes like rounded, angular, and cylindrical form result in poor strength. However, in AM production processes, due to the repeated use cycle of the metal powder raw material, some particles change shape by exposure to high energy. Unused powders participate in the production process as a raw material with the preferred powder size by sieving at the recycling. Chemical and physical property changes are inevitable in the powder particles adjacent to the contours of the part being produced. For this reason producing high-quality AM parts, the particles that have lost their desired properties in metal powder recovery must be removed from the system. The production technique of metal particles also affects their flowability. The fine-grained metal powder shows higher flowability. Since the production methods used to obtain smooth and fine metal powder are more expensive, it also increases the raw material prices used for AM.

The flowability of a powder is characterized by a Hall flowmeter. Gas pores in metal powder particles affect the properties of AM products. The volumetric and weight analysis of the metal powder feedstock, which is in the micrometer range, is most effective by determining the mass of the powder in a known volume. Pycnometer density measurements are required to control the product differences and the structural changes of the recycled powders. The helium pycnometer method is often used to determine metal powder density. This measurement provides information on internal voids within feedstock powder. In the pycnometer method, helium at a certain pressure and temperature flows from the chamber where the metal powder sample is located, replacing the air present in this chamber. Thus, the volume of helium filling the chamber is calculated using the ideal gas law. The volume of metal powder can be easily found by subtracting the calculated volume of helium gas placed in the spaces

in the chamber from the total chamber volume. In this method, possible internal voids of metal powder particles are neglected. Density measurement is carried out to control the amount of shrinkage after production due to the porosity of metal powders. The pycnometer method is also used for composition control of composite powder blends. A metal composite part is obtained from different powder blend compositions by in-situ alloying in AM processes. The production of metal composites in AM processes provides new possibilities for design and strength [10, 14, 15].

6 The Processing Parameters of AM Technologies

The production of an AM part with the desired properties necessarily depends on the optimum process parameters. Many process parameters depend on the process type of AM and the control capabilities of a production machine. The main parameters affecting the product quality are the power of the source, laser or beam diameter, spacing, scanning speed, scan route, and preheating temperature. Achieving desired quality requirements and consistency between manufactured AM parts is only possible with appropriate parametric control. There are many studies on optimization studies with process parameter control in specific part productions. This knowledge continues to increase. It should be noted that these researches are both design and machine specific. Current research findings guide manufacturers in producing high-quality parts [6, 7, 10].

7 Quality Assessment of AM Parts

It is possible to produce AM parts with higher mechanical properties, microstructural formations, and dimensional stability than conventional production techniques with the usage of high-quality raw materials and the correct setting of production parameters. Similar to the success criterion of the production method with powder metallurgy technique, in the production success of AM parts is the level of access to the theoretical density, identical criteria. A value of 99.5% or more of the theoretical density value must be reached for a manufactured AM part to be successfully attributed. It is understood that the parts have defects resulting in lower density ratios. As an example that could cause this, gas entrapment in a produced part due to rapid cooling is a common problem in AM. Internal pores encountered due to gas entrapment can generally occupy 1 vol% and are in the range of 10–50 μm in diameter. Mechanical properties, especially fatigue strength, are weakened by trapped gas pores. The presence of micropores in the structure is related to the level of energy in the AM process. In AM production, if the energy level is fewer or more than necessary, the rate of gas pores trapped in the structure will increase [14] (Fig. 5).

The dimensional accuracy of a part is also one of the key indicators of product quality, which depends on processing parameters and raw material properties. Also,
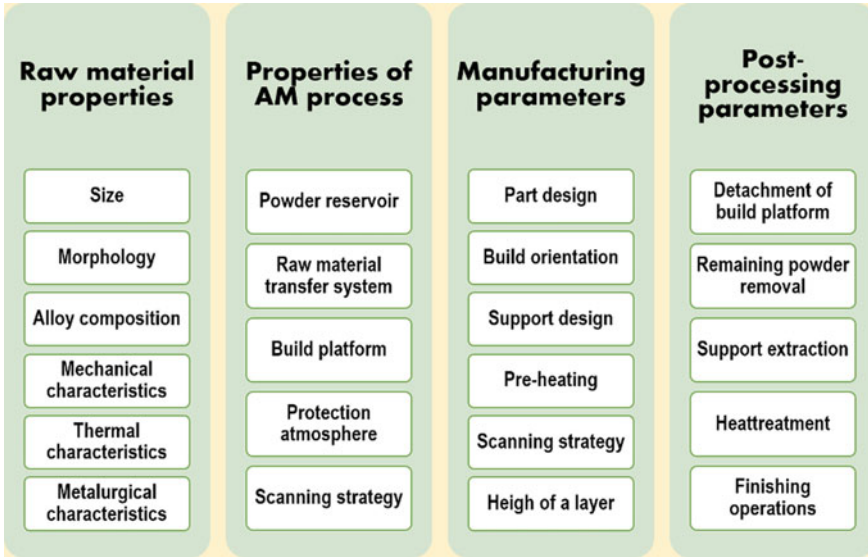
Fig. 5 Main parameters influencing AM part quality

processing apart with a different AM process type will have different geometric accuracy values. Namely, PBF processes enable the production of parts with higher geometric accuracy than the DED process. The dimensional accuracy of a part is one of the primary indicators of product quality, and quality also depends on machining parameters and raw material properties. A geometric accuracy value can be expressed by statistically evaluating different measurements on a part. Geometric accuracy is very important, especially in metal foams, lattice structures, and parts in designs with internal channel space20.

Raw material storage conditions are essential for a high-quality AM part. The storage environment preserves at appropriate humidity and temperature values, and the atmosphere should be provided, such as protective Ar gas, in the boxing used. In addition, if adequate protection from oxidation fails to provide in the building environment during the AM process, the mechanical properties decrease in most cases. The high energy and temperature conditions applied in the AM process may disrupt the elemental composition in production and cause oxidation [14].

Different AM technologies result in different surface properties. Surface roughness is another materialization of part quality. Poor quality due to surface roughness stems from reused defective metal powders, incorrect choice of process parameter variable level (particularly scanning speed level), and insufficient or over-melted powders on counter lines. Various surface roughness measurement methods are available. There are differences between these methods in terms of ease of use, obtaining quantitative information, three-dimensional (3D) topography data, lateral and vertical resolution capability, and cost. The choice among these methods is related to the roughness of information desired to be achieved by the measurement.

In-process roughness measurement is mainly based on reflection principles. There are the stylus profilometer, digital optical profilometer, and AFM methods to obtain detailed measurement data. A customer ordering AM Parts also states quality requirements in the technical specification [18]. This is expressed as the average roughness value for the parts. The best surface quality AM part production is generally produced with SLM, while the fabrication with EBM and DED gives slightly lower surface quality. Because SLM uses finner metal powder (<20 μm) feedstock and its layer is thinner (30 μm) than the others. After AM production, one of the post-production processes such as shot peening, grinding, and polishing is applied to further improve the surface quality of the part [19].

Microstructural characterizations of AM parts are the same as metal-based parts produced by conventional methods. It includes OM, SEM, and TEM microscopy examinations after standard metallographic preparation and appropriate chemical etching. Unlike metal parts produced by conventional methods, AM parts provide fine grain structure. Because in AM processes, the melting and solidification time of the metal is generally quite fast. Factors such as pre-heating applied to the raw material and built table in the thermal cycle in production, energy power density in the melting stage, and the coolant flow rate in the cooling stage affect the maximum/minimum and time variables of the thermal cycle. The cooling rate differences due to these variables will affect the microstructure formation. In general, AM parts with fine grain structure are obtained with low melting energy and high feeding speed, while the opposite levels of these parameters lead to coarse columnar grain structure. Depending on the chemical composition of the alloy, the solidification mechanisms also differ. Different solidification mechanisms affect the microstructural character. Heterogeneous nucleation of partially melted grains causes coaxial grains formations. Besides, solidification mechanisms can induce a growing epitaxial layer. Rapid solidification also enables the formation of a metastable phase with highly elastic properties. Therefore, the different solidification mechanisms can vary between layers due to different cooling rates in an entire AM part. This situation may result in the formation of a graded microstructure. Microstructural anisotropy occurs in grain growth because of the directional heat flow inherent in the layer-by-layer progress of part production in the AM process [15].

8 AM Part Design of Light Metals and Composites

AM technology has removed conventional engineering design limits and eliminated stereotypical geometric criteria in terms of mechanical properties. Thus, industrial product designers have come to make bespoke designs for exclusive purposes. Some researchers state that design complexity for AM processes will not result in an additional fee increase. However, the main factors that determine the cost of AM parts are the amount of raw material and the measure of processing time. So only if design complexity requires less raw material and time of the process. There will be a cost reduction. It is a well-known fact that the cost per piece decreases with

the increase in batch size in conventional production. But in AM production, the bach-size-indifference phenomenon comes to the fore [32]. Batch-size independency provides a notable advantage in the production of implants and surgical instruments suitable for the individual characteristics and needs of the patient in the production of biomaterials. Engineers use AM technology to design and manufacture metamaterials. The micro-scale structural design of metamaterial provides access to innovative mechanical, electrical, magnetic, thermal, corrosion, or optical properties to achieve the expected macro properties and functionalities of engineering structures [21]. The topology optimization (TO) approach serves for optimum material distribution in the part design space. TO evaluates design performance with gradient-based or non-gradient-based mathematical algorithms. TO is also possible to use in a conventional production method, but the complex geometry will increase the cost of production. TO approach is the primary mathematical tool in part design, as AM technology is cost-effective for producing complex part geometry [24]. However, if there are long protrusions in a part design, it is necessary to use additional support struts in the structure for error-free production. Algorithms generally used in TO are optimality criterion, genetic algorithms, particle swarm optimization, simulation annealing, Nelder–Mead simplex, and moving asymptotes. TO is indicative in determining microstructure and mechanical properties in terms of suitability for manufacturing with AM and product performance [9]. Metal foams have been included in industrial designs for the last few decades in terms of their functions [12]. Metal foams have two basic cell structures, open and closed [13]. Production processes with the PBF method are not suitable for the production of closed-cell metal foam because of the dust particles that remain unprocessed in the cell. AM is currently the undisputed leading production method in a homogeneous lattice structure and functionally graded parts with open-cell metal foams [10]. Such configuration structures are particularly suitable for a component that provides increased efficiency in engineering systems with flow control (for example, in a fuel cell system) and an implant that provides increased fixation and integration [11].

9 Post-Processing of AM Parts from Light Metals and Composites

After the AM process, various post-processing methods are applied to metal parts to eliminate the deteriorating effects caused by production and to gain different properties required for use. Microporosity and lack of fusion are the principal defects in products with AM processes. In particular, sudden heating and cooling cycle also causes residual thermal stresses in SLM and DED processes. Residual thermal stress is existing stress in the structure without any external force acting on a part. Residual stresses are resulting from the very high heating and cooling rates in AM process and unstable thermal gradients in the part design. The effect level of these causes determines the magnitude of the residual stress in the size part. Distortion of the

part by residual stresses causes geometric mismatches such as out-of-size trouble in construction or the balance problem of a cylindrical component. Moreover, residual stresses change mechanical properties and affect tensile strength and fatigue life. The process parameters and properties of the alloy composition that affect the heating and cooling stages in AM processes also affect the residual stress. Therefore, process parameters such as melting source power, scanning strategy, and protrusions of a part are the leading factors in the formation of residual stress. Also, the properties of the alloy composition that affect residual stresses are modulus of elasticity, yield stress, thermal conductivity, and thermal expansion. The most frequently applied considerations in AM processes to avoid residual stresses are parametric optimization, pre-heating build table, and part-specific scanning strategy. Because of the preheating of the build table in the EBM process, this method is suitable for production with inherently lower residual stress. In addition, support struts for protruding parts are also a precaution against distortion [25].

Another AM post-process method is a heat treatment, in which the microstructural design is made by adjusting the grain size and precipitates. Stress relaxation occurs with heat treatment, and residual stresses are either reduced or completely removed. The annealing process has become almost standard for SLM and DED parts where post-production residual stresses are intense [15].

Hot isostatic pressing (HIP) is another post-processing method for AM parts. The HIP is preferred for removing micropore-type defects in AM parts due to its high temperature and high-pressure effect. It is also applied for configuring microstructural properties under the influence of high temperature and pressure. This also improves the fatigue and mechanical properties of the part. HIP process parameters are determined according to the part material and dimensions to be applied [25].

There are also post-processings to improve the surface properties of the parts removed from the AM machine after production. These post-processes are coating, mechanical polishing, and chemical etching. Apart from visuality, smoothness is at the forefront in parts where fatigue life is critical. The AM method used in production defines the surface treatment process. It is possible to achieve a smooth part when fine metal powders of 15–30 μm work in the SLM process. Therefore, these parts may not require a post-processing surface treatment. However, parts produced by the EBM and DED methods are characteristically rough. A thin coating layer on surfaces improves the wear and corrosion properties of AM parts. There is also a surface coating to improve the biocompatibility of the implants and speed up the healing process [15].

10 Mechanical Properties of AM Parts from Light Metals and Composites

In the determination of mechanical properties of AM parts, tensile and compression tests are primarily applied, just like conventional metal parts. Mechanical properties

of AM parts show anisotropy due to building direction. In general, metal AM parts have a poor tensile strength in the direction perpendicular to the build plate. Therefore, AM part design and manufacture must be considered the direction of force under operating conditions. In addition to these tests, hardness, creep, and fracture toughness are other main characterization methods [23, 30].

Elemental composition and microstructure are the determinants of the mechanical properties of AM parts. Therefore, raw material properties and process variables influence these two determinants. They are the control course for target mechanical properties. It is possible to exceed the mechanical properties of conventionally manufactured parts with precise control over the determinants. Possible defects due to sudden thermal cycling (heating/cooling) in AM processes will adversely affect the mechanical properties. Achieving high mechanical properties is quite delicate because of light metal activeness and contaminants like oxygen, nitrogen, and moisture in AM processes. Each type of AM process results in parts with specific defects, microstructure, residual stress, and mechanical properties. While the EBM method builts high-ductility Ti6Al4V materials, other methods cannot. Table 1 gives comparative mechanical properties data of conventional and AM manufacturing Ti6Al4V alloy parts [14, 15].

Since ancient times, human beings have encountered the porous structures of some animals and plants such as bone, wood, and fruit cocoon in nature. However, engineers have used metal foam and lattice designs in a technical sense for a few decades. It takes advantage of the mechanical properties of porous structures, especially in the design of parts, as in nature. Cellular structures serve in the main fields such as aerospace, biomaterials under tensile, compression, and torsional stress conditions [5, 20]. Porous materials exhibit three typical behavior zones under compression conditions. These are the linear elastic region, plateau region, and densification region. It may be possible to achieve the mechanical properties expected from porous materials thanks to different unit cell geometries with the advantages of AM technology in design and production. The mechanical behavior of lattice structures is either stress dominated or bending dominated. The damage mechanisms that occur under overloading conditions are different between these structural categories. While damage

Table 1 Mechanical properties of Ti6Al4V alloy parts fabricated with various AM processes [16]

AM process	Mechanical properties			
	Elastic modulus (Gpa)	Tensile yield stress (MPa)	Tensile strength (MPa)	Ductility (%)
DED (CO_2 laser)	–	1070	1150	5
PBF(SMYb:YAG)	110	1110	1270	7
DMLS	–	1180	1220	7
LENS	–	1120	1170	8
Commercial (conventional)	106	950	1050	15

occurs between layers in an AM part with a stress-dominated building, shear band damage arises in an AM part with a bending-dominated framework [15, 26].

11 Fatigue Behavior of AM Parts from Light Metals and Composites

Today AM technology can produce many system elements that can operate under repetitive load cycles. The ASTM E466 standard describes the fatigue test method for such parts. S–N curves and fatigue strength value reveal the fatigue life. Fatigue crack growth AM is the primary indicator of the fatigue behavior characteristics of an AM part under a maximum/minimum cycling loading with a frequency. Since the structural formations of the product change according to AM processes, the fatigue life also changes depending on the production method. Residual stress in a component due to thermal cycling in AM processes is another major factor influencing fatigue life. The surface roughness of the final product is as effective in the fatigue life of the AM product parts as it is in conventional production parts. The microstructure and the defects of the part also determine the fatigue life. The unstable martensitic phase reduces the fatigue life of Ti6Al4V parts produced using LENS. The production method is also effective in fatigue life as it will result in different structural characteristics. Production of Ti6AL4V parts by the SLM method shows better fatigue life than EBM. Defects reduce fatigue life by causing stress concentration, as in conventionally manufactured parts. In the face of these negativities, it is also possible to slightly increase the fatigue life with post-process applications [1, 15].

There is fatigue exposure in biomedical applications of lattice structures. Biomedical AM-parts in lattice or foam structures exhibit tensile-dominated or bending-dominated behavior under variable compression loading conditions, depending on their part design. As in conventional production parts, microcracks develop under the loading cycle, especially in the regions of struts where tensile stress is dominant, causing fatigue damage. Therefore, the lattice structure design is effective in fatigue life. In addition, the plastic deformation ability of porous materials changes according to the elemental composition and microstructure. Therefore, porous AM parts in materials with high plastic deformation properties exhibit higher fatigue life [4].

12 Conclusion

The production of AM parts from light metals and composites attracts great attention from both industrial applications and academic researchers. A reliable and repeatable product is possible with the current technological development in the production of AM parts from light metal alloys and composite materials. This chapter of the book

comprehensively explains the production of AM parts from light metal alloys and composite materials in terms of design, application, raw material, and properties of a final product. Future research for the development of AM technology focuses on powder raw materials produced from light metal alloys and composites. The progress of light metal alloys and composite raw materials to obtain functional products that can provide the required property performance will be the main objective of future research.

References

1. Ahmadi SM, Kumar R, Borisov EV et al (2019) From microstructural design to surface engineering: a tailored approach for improving fatigue life of additively manufactured meta-biomaterials. Acta Biomaterialia 83(January 2019):153–166. https://doi.org/10.1016/j.actbio.2018.10.043

2. Balasubramanian KR, Senthilkumar V (2020) Additive manufacturing applications for metals and composites

3. Bikas H, Stavropoulos P, Chryssolouris G (2016) Additive manufacturing methods and modeling approaches: a critical review. Int J Adv Manuf Technol 83(1–4):389–405. https://doi.org/10.1007/s00170-015-7576-2

4. Bose S, Ke D, Sahasrabudhe H et al (2018) Progress in materials science additive manufacturing of biomaterials. Prog Mater Sci 93:45–111. https://doi.org/10.1016/j.pmatsci.2017.08.003

5. Bulduk ME, Ertürk AT, Coşkun M et al (2019) The microstructure and mechanical properties of porous structures produced from Alsi10mg by direct metal laser sinterıng. Amc Turkey (Oct)

6. Cagatay Z, Coskun M, Akca Y et al (2019) Optik support optimization for overhanging parts in direct metal laser sintering. Optik—International Journal for Light and Electron Optics 181(November 2018):575–581. https://doi.org/10.1016/j.ijleo.2018.12.072

7. Çalışkan Cİ, Özer G, Coşkun M et al (2021) Investigation of direct metal laser sintering downskin parameters' sagging effect on microchannels. The International Journal of Advanced Manufacturing Technology 114(9):2567–2575. https://doi.org/10.1007/s00170-021-07057-8

8. Dang J, Liu G, Chen Y et al (2019) Experimental investigation on machinability of DMLS Ti6Al4V under dry drilling process. Mater Manuf Processes 34(7):749–758. https://doi.org/10.1080/10426914.2019.1594254

9. Enes M, Cemal B, Çalışkan İ et al (2022) Comparison of the effect of different topological designs and process parameters on mechanical strength in gears 6707–6716. https://doi.org/10.1007/s00170-021-08405-4

10. Erturk AT, Bulduk ME, Tarakçi G et al (2022) Investigation of the microstructure and mechanical characteristics of lattice structures produced by laser powder bed fusion Method. Met Mater Int 28(1):155–167. https://doi.org/10.1007/s12540-021-01038-y

11. Erturk AT, Ergin U, Kadıoglu T et al (2022) ScienceDirect metal foams as a gas diffusion layer in direct borohydride fuel cells. Int J Hydrogen Energy 47(55):23373–2338. https://doi.org/10.1016/j.ijhydene.2022.05.118

12. Ertürk AT (2016) Production of aluminum glass fiber reinforced foam synthesized by space-holder technique. Acta Physica Polonica A 129(4). https://doi.org/10.12693/APhysPolA.129.592

13. Ertürk AT, Aydin I (2017) Enhanced mechanical performance of aluminum glass fiber reinforced foam material by Cu modification. Acta Physica Polonica A 131(3). https://doi.org/10.12693/APhysPolA.131.470

14. Frazier WE (2014) Metal additive manufacturing: a review. J Mater Eng Perform 23(6):1917–1928. https://doi.org/10.1007/s11665-014-0958-z

15. Gebhardt A (2011). Understanding additive manufacturing. https://doi.org/10.3139/978344643 1621.fm
16. Gisario A, Kazarian M, Martina F et al (2019) Metal additive manufacturing in the commercial aviation industry: a review. J Manuf Syst 53(June):124–149. https://doi.org/10.1016/j.jmsy. 2019.08.005
17. ISO/ASTM (2013) Additive manufacturing—general principles terminology (ASTM52900). Rapid Manufacturing Association 10–12. https://doi.org/10.1520/F2792-12A.2
18. Khan HM, Tarakçi G, Bulduk ME et al (2021) Estimation of the compression strength and surface roughness of the as-built SLS components using weibull distribution 2:1–6. https://doi. org/10.14744/ytu.jame.2021.00001
19. Khan HM, Sirin TB, Tarakci G et al (2021) Improving the surface quality and mechanical properties of selective laser sintered PA2200 components by the vibratory surface finishing process. SN Applied Sciences. https://doi.org/10.1007/s42452-021-04371-4
20. Khoda B, Ahsan AMMN, Shovon AN et al (2021) 3D metal lattice structure manufacturing with continuous rods. Scientific Reports 1–17. https://doi.org/10.1038/s41598-020-79826-6
21. Mahmood H, Gökhan K, Safa M et al (2022) Corrosion of additively manufactured metallic components: a review. Arab J Sci Eng 47(5):5465–5490. https://doi.org/10.1007/s13369-021-06481-y
22. Özer G, Özbay B, Öter ZÇ et al (2020) Investigation of the surface quality and dimensional accuracy of polymer patterns produced by selective laser sintering (SLS) method for investment casting (IC). Int J Cast Met Res 33(2–3):146–152. https://doi.org/10.1080/13640461.2020.177 3053
23. Pelleg J (2020). Testing: comparison of AM data with traditionally fabricated. https://doi.org/ 10.1016/B978-0-12-821918-8.00003-6
24. Ramadani R (2021) Topology optimization and additive manufacturing in producing lightweight and low vibration gear body 3389–3399
25. Safa M, Özer G, Ça Z (2021) Effects of hot isostatic pressing and heat treatments on structural and corrosion properties of direct metal laser sintered parts. 5(April):1059–1067. https://doi. org/10.1108/RPJ-10-2020-0245
26. Sciences H (2016) https://www.taylorfrancis.com/books/edit/https://doi.org/10.1201/978042 9466236/additive-manufacturing-amit-bandyopadhyay-susmita-bose
27. Shahid S, Ismail M (2020) FA design framework for build process planning in DMLS. Progress in Additive Manufacturing 5(2):125–137. https://doi.org/10.1007/s40964-020-00110-0
28. Thompson MK, Moroni G, Vaneker T et al (2016) Design for additive manufacturing: trends, opportunities, considerations, and constraints. CIRP Annals—Manufacturing Technology 65(2):737–760. https://doi.org/10.1016/j.cirp.2016.05.004
29. Yang L, Hsu K, Baughman B et al (2017) Electron beam. Technology. https://doi.org/10.1007/ 978-3-319-55128-9_4
30. Yilmaz MS (2019) Investigation of the effects of different heat treatment parameters on the corrosion and mechanical properties of the AlSi10Mg alloy produced with direct metal laser sintering (July). https://doi.org/10.1002/maco.201911171.
31. Zadpoor AA (2018) Frontiers of additively manufactured metallic materials. Materials 11(9):1–10. https://doi.org/10.3390/ma11091566
32. Zhou B, Tian T (2021) A path planning method of lattice structural components for additive manufacturing. The International Journal of Advanced Manufacturing Technology 1467–1490

Chapter 24
Additive Manufacturing of Titanium Alloys for Aerospace and Biomedical Applications

Salwa El Baakili, Abd Baghad [ORCID], Meriame Bricha, and Khalil El Mabrouk

1 Introduction

Additive manufacturing (AM) is a new processing technology that uses a three-dimensional CAD model. This allows the creation of 3D parts. This technique is used for the first time as an innovative resource for prototyping. Moreover, AM is a quick manufacturing process to produce complete parts layer by layer [1, 2]. The AM method is relatively different from conventional and formative manufacturing methods. Therefore, it can produce thousands of component layers with high accuracy and precision [3].

AM technology is increasingly requested to improve operational resiliency, precision, and durability. This is because of its ability to manufacture highly complex parts without tools or molds in a short time frame [4–6]. Furthermore, it solves the dilemma of design feasibility and manufacturing personalized implants [7]. This has rapidly changed small- and long-scale production in aerospace and biomedical sectors. Nevertheless, this technology's most prevalent drawbacks are defects included during processing. However, parts suffer from high porosity and rough surfaces resulting from unmelted powder particles [5, 8].

Very recently, the bio-manufacturing research community made remarkable progress in implementing AM. This is for the creation of patient-specific implants for hard tissue engineering [8, 9]. On one hand, biomedical industries are mostly using fully dense 3D metallic materials. Among them, only a few have proven their long-term biological compatibility with the human body. Biocompatibility, osseointegration, and mechanical properties of metal compounds are some of the main issues. For example, their elastic modulus is higher than that of bone tissue. This results in

S. El Baakili · A. Baghad (✉) · M. Bricha · K. El Mabrouk
Euromed Research Center, Euromed Polytechnic School, Euromed University of Fes, Route de Meknes, Rond-point de Bensouda, BP 51, 30030 Fes, Morocco
e-mail: abd.baghad@ueuromed.org

stress protection of adjacent tissues, complicating their integration into human bone. Overall, the material must be suitable for casting and welding techniques. It must also be industrially rigid in the input processing [10, 11]. These are according to the general parameters for efficiently processing powder-fused metal parts. Accordingly, specific AM techniques, such as SLM, frequently supply commercially available metal powders [3].

Titanium alloys are among the most advanced materials in the aerospace and biomedical industries. Moreover, the promising on-demand is now predicted because of its excellent properties. This makes them a viable option for different applications. They are also highly resistant to fatigue loading and corrosion in the physiological environment [12]. The present chapter reviews AM as a process for manufacturing high-quality titanium alloy structures. It discusses recent advances in the aeronautical and biomedical fields. Moreover, an overview of the main advantages and disadvantages of using metallic AM based on titanium alloy powders is given.

2 Additive Manufacturing (AM) Processes

A key motivator for AM improvement is the increased demand for complex shapes and excellent quality. AM has shifted to new alloys for specific applications. This is because pure metals are rarely adapted to unique needs. The American Society for Testing and Materials divides AM of metallic materials into two primary categories: directed energy deposition (DED) and powder bed fusion (PBF). These technologies are based on similar concepts. However, they use a layered concept to build parts directly from CAD data [13]. DED technology is divided into four sub-methodologies depending on the thermal energy source [14–16]:

- Direct metal deposition (DMD) uses a laser to melt powders or wires as a close loop process deposits them,
- Laser engineered net shaping (LENS) also uses a laser for deposition,
- Wire and arc additive manufacturing (WAAM) uses an electric arc to melt metal wires, and
- Direct manufacturing (DM) melts metal wires using an electron beam.

The DED processes have a bigger build envelope and a faster deposition rate (construction rate higher than 300 cm^3/h). Moreover, this technique is commonly used with titanium alloys for aerospace and coatings applications [16, 17]. However, the DED process has limitations and difficulties, including the following [18]:

- The ability to produce hollow cooling tunnels,
- Manufacture of finer geometries,
- Higher surface resolution,
- Manufacturing of complex parts,
- Low-dimensional resolution, and
- Shrinkage and deformation due to the local temperature variation.

On the other hand, PBF can also be divided into four categories:

- Selective laser melting (SLM),
- Selective laser sintering (SLS),
- Direct metal laser sintering (DMLS), and
- Electron beam melting (EBM).

These technologies use laser or beam as an energy source to melt the powder. Except for SLS, which concerns polymers and nylon, all these technologies use metallic powders. Moreover, during the PBF process, the part is built in a powder bed. Then, the energy source sinters the necessary locations to create the selected portion. This process enables the building of complex features at elevated densities with high precision [8].

3 Additive Manufacturing of Titanium Alloys

Metal AM approaches improve wear performance by altering the surface of Ti-based materials. Moreover, they also promote osseointegration by using structurally graded parts [19, 20]. The directed energy technologies may add metal to existing parts. The purpose is to reconfigure or add functionality and repair broken parts. Undeniably, metallic alloys can be manufactured using a variety of AM methods. SLM and EBM, both powder bed fusion processes, are the most widely used. They provide the advantage of printing a part with complex design and micro-architecture.

3.1 Selective Laser Melting (SLM)

SLM was developed in 2002. It was used in various industries as a non-classical method for manufacturing complex parts [1]. Nowadays, it is the most prevalent metal PBF process for generating metallic biomaterials. This situation agrees with the expansion of the SLM system in development and innovation. The aim is to make it more productive and economically appealing. Indeed, the ultimate attributes are determined by design (process manufacturing) and material composition. For example, the produced commercially pure titanium (Cp-Ti) has a closer elastic modulus (105 GPa) to the bone than Ti6Al4V (110–114 GPa) [21]. Nevertheless, it is still rather high. Indeed, this process brings new opportunities to develop new parts. Parts with specific porosities and graded structures for the case of titanium. Therefore, the primary purpose of SLM is to create porous and defect-free parts.

SLM has many parameters to control the process and produce a high-quality product [11]. However, the lack of mechanical stress in SLM, melt pool surface tension, and thermal effects induced defects in the final parts [22]. Some characteristics, such as wavelength and laser mode, cannot be controlled for specific SLM systems. For example, the critical laser energy densities of Ti-6Al-4V and Ti2448

are about 40–120 J/mm^3. However, varying techniques produce different densities and mechanical qualities for the same material. For example, the relative density of SLM-produced Ti-6Al-4V samples with a cross-hatching zigzag scanning pattern can reach 99.9% [23].

3.2   Electron Beam Melting (EBM)

EBM technique was firstly developed for steel processing. It is mostly known as metal PBF techniques. Like SLM, the system includes a rake, build platform, powder hoppers, and an energy source. However, instead of a laser, the system processes data with electron beam energy. The emitted electron beam scans the powder bed at high speed. This melts it to form a molten pool. The liquid metal then solidifies rapidly [24]. Electron beams must operate in a high vacuum. However, this is due to the fundamental features of electron beams. In addition, some highly reactive metals and alloys absorb contaminants when exposed to air [25]. The vacuum chamber is used to create a vacuum environment during the process. This ensures the integrity of the EBM manufactured part [26]. The main difference with SLM is that the EBM uses a different heat source. The heat source of EBM is an electron beam with a voltage of 60 kV. This beam preheats the substrate plate to a pre-setting temperature before dropping the powder [27]. Some prior works on metal AM manufactured porous structures are listed below (Table 1). This table reveals that Ti6Al4V is the most popular biomaterial for porous structure creation in orthopedics.

Table 1 Metal AM manufactured porous structures of titanium and its alloys

Material	AM process	Elastic modulus (GPa)	References
Porous Ti6Al4V	EBM	0.9–1.6	[28]
	EBM	2.5 ± 0.5	[29]
	EBM	0.5–9.9	[30]
Dense Cp-Ti	SLM	106 ± 3	[31]
Porous pure titanium	SLM	2.61 ± 0.05	[32]
Porous Ti6Al4V	SLM	11.9	[33]
Porous Ti-Ta-Nb-Zr alloys	SLM	2.35	[34]
Porous Ti-25Ta	SLM	14	[35]
Porous Ti6Al4V	SLM	22	[36]

3.3 Properties of Additively Manufactured Titanium Alloy Materials

In the earth's mantle, titanium is the fourth prevalent structural metal. It is an excellent candidate for use in several industries due to its features [37]. Moreover, Nb, Ta, and Zr elements are among the safest alloying elements for biocompatible Ti alloys [38]. Titanium structures can exist under two forms: a hexagonal α phase and a centered-cubic β phase [39]. Thus, low modulus beta Ti alloys with non-allergic and non-toxic alloying elements are developed to reduce the stress shielding effect [40]. Titanium alloys are among the commonly used metals in traditional biomaterials and aerospace engines. They continue to be the material of choice for biocompatible applications. Additionally, they have become the most used metallic biomaterial for metal AM processing. However, titanium is more expensive than other metallic biomaterials (such as cobalt-based alloys and stainless steel), but it is more durable [41]. The first titanium-based materials were reportedly developed in the USA in the 1940s [23]. The aerospace and biomedical industries have used titanium alloys because of their specific properties, namely [13, 40, 42]:

- High melting pool (1668 °C),
- Density (4.5 g/cm^3),
- High tensile strength at room temperature (1400 MPa), and
- Available in four grades classified by strength. This facilitates the selection of the appropriate material based on the desired strength and workability.

The Cp-Ti has acceptable biocompatibility, but its low strength (500 MPa) limits its use [30]. Titanium alloys are used in non-structural applications where corrosion resistance and formability are important. Such examples include water supply systems for galleys, ducts, and pipelines. Commonly used titanium materials in industries and their properties are summarized in Table 2. Recently, many attempts are undertaken to create alloys with high mechanical properties and biocompatibility. Today's most widely used titanium alloy is an $\alpha + \beta$ type Ti-6Al-4V. A material that is initially produced for aerospace applications. Following further investigation, it was found to have excellent corrosion resistance and strength. These specific properties make it ideal for various applications [1].

Arcam's ongoing partnership with Adler Ortho Group resulted in the CE-certifying EBM-manufactured titanium hip implants. This marks a significant step forward in titanium AM [43]. Recently, Hazwani et al. [12] highlighted the crucial role of titanium alloys in the biomedical field. They show the appropriate composition and phase for novel 3D printed titanium alloys. In addition, porous Ti6Al4V is a favored material over stainless steel and Co-Cr alloys as implants. This can be explained by their low modulus, excellent biocompatibility, and high corrosion resistance. However, the porous structure of titanium alloy can improve biocompatibility and reduce Young's modulus. Likewise, EBM Ti6Al4V structures promote cell ingrowth and proliferation. They also prevent the release of cytokines compared to the Cp-Ti alloy disk [44]. Moreover, the effect of SLM-Ti6Al4V pore geometry on

Table 2 Titanium and its alloys for different applications [47, 48]

Titanium alloys	Properties	Applications
Ti-6Al-4V	Yield strength of annealed material: 825 MPa Tensile strength: 895 MPa Elongation: $\geq$10%	Airframe, engine parts, wing box, fastener, and orthopedic implants
Ti-6Al-2Sn-4Zr-2Mo	Improve oxidation resistance and creep property with the addition of Si Yield strength of annealed material: 860 MPa Tensile strength: 930 MPa Elongation: $\geq$10%	Compressor disks and automotive industry
Ti-8Al-1Mo-1 V	Heat resistant temperature: 400 °C Yield strength of the annealed material: $\geq$930 MPa Tensile strength: 1000 MPa Elongation: $\geq$10%	Compressor blades
Ti-5Al-2Sn-2Zr-4Cr-4Mo/(Ti-17)	Yield strength (solution treatment and aging)/ 1055–1193 MPa Tensile strength: 1124–1265 MPa Elongation: $\geq$5%	Aircraft engines
Ti-6Al-2Sn-4Zr-6Mo	Yield strength: 1105 MPa Tensile strength: 1170 MPa Elongation: $\geq$10%	Turbine and race car engines and compressor disks
Ti-15 V-3Cr-3Sn-3Al	Yield strength of the solution heat treated material: 690–835 MPa Tensile strength: 745–945 MPa Elongation: 12%	Airframes welded pipes and ducts are made by welding thin sheets
Ti-10 V-2Fe-3Al	Yield strength: 1105 MPa Tensile strength: 1240 MPa Elongation: $\geq$4%	Landing gear (part of the main landing gear for takeoff and landing)
Ti-6Al-7Nb	Elastic modulus: 100–110 GPa Coefficient of thermal expansion: 8–9.8 (10^{-6} K^{-1})	Loading as an orthopedic implant (hip prostheses)

the in vitro biological behavior of human cells has been documented by Bael et al. [45]. They concluded that functionally graded SLM-produced Ti6Al4V scaffolds must combine two types of pores: small pores for initial cell attachment and wider non-circular pores to avoid pore occlusion. In addition, Arabnejad et al. [46] proposed tetrahedron and octet truss as cell topologies for porous SLM-produced Ti6Al4V. A structure that can be employed for load-bearing orthopedic applications. The complex structures created by AM provide superior mechanical qualities and improved bone

ingrowth. Altogether, the process parameters play a critical role in enhancing properties. Therefore, more studies should concentrate on improving the roughness of AM parts. This should be done through surface treatment and eliminating flaws through process optimization. Likewise, Depboylu et al. [39] reviewed recently the critical drawbacks of LPBF technologies applied to titanium and its alloys. They include induced defects and residual stresses. Furthermore, this review focused on titanium material as a promising biomaterial for bone replacement. They concluded that porous implant production is crucial and beneficial for tissue engineering.

The economic performance of the AM is particularly well suited to aerospace applications compared to other industries, thus facilitating the production of customized and complex parts [41]. For aerospace components, the proportional ratio between the weight of the raw material and the weight of the final part (flight-to-buy ratio) is between 20:1 and 40:1 [49]. By adopting the AM processes, this ratio can be reduced to 1:1. A result was demonstrated for the bleed air leak detector manufactured by Lockheed Martin using the PBF process [50]. In this example, the potential reduction in substrate production costs is 50%. The reduction is achieved by using an AM-treated titanium alloy [51]. Another advantage favoring titanium alloys is their electrochemical compatibility with the fibers reinforced polymers [52]. A material that is widely used in the aviation industry. Furthermore, cryogenic applications found in rocket propellant tanks are also potential use cases [53]. The reason is that they do not exhibit a transition at low temperatures.

4 Conclusion and Future Trends

Metal additive manufacturing has revolutionized the designing and processing of metallic materials for specific needs. It solves the dilemma of design structures and parameters process without counterbalancing the material's properties. Titanium alloys are extensively employed in both aerospace and medical applications. A variety of applications in these domains are discussed in this chapter. The titanium alloys and their particular qualities are then described in depth. This chapter focuses on one powder metallurgy technique: additive manufacturing (AM). It provides an overview of AM and the current state of the method. It is mainly about titanium and its alloys using SLM and EBM. Some essential qualities for a titanium alloy to qualify as a biomedical implant or an aircraft engine are the desired phase, uniformity in microstructure, good mechanical strength, correct pores creation, and bioactivity (with surface modification). Therefore, technology selection is crucial before alloy manufacturing to guarantee these qualities. However, different processes result in varying final properties of the alloy.

Finally, new research and development directions in metallic materials would be interesting. Indeed, porous materials 3D printing has already opened a new door to personalized medicine. Furthermore, modern metal 4D printing techniques can adapt implant structures to long term. Similarly, a better knowledge of degradable

metallic biomaterials is also required. In addition, the creation of predictive models for different applications is needed.

References

1. Harun WSW, Kamariah MSIN, Muhamad N, Ghani SAC, Ahmad F, Mohamed Z (2018) A review of powder additive manufacturing processes for metallic biomaterials. Powder Technol 327:128–151
2. Emmelmann C, Herzog D, Kranz J (2017) Design for laser additive manufacturing. Laser Addit Manuf Mater Des Technol Appl. https://doi.org/10.1016/B978-0-08-100433-3.00010-5
3. Bandyopadhyay A, Traxel KD, Lang M, Juhasz M, Eliaz N, Bose S (2022) Alloy design via additive manufacturing: advantages, challenges, applications and perspectives. Mater Today. https://doi.org/10.1016/j.mattod.2021.11.026
4. Haeri S, Wang Y, Ghita O, Sun J (2017) Discrete element simulation and experimental study of powder spreading process in additive manufacturing. Powder Technol 306:45–54
5. Cao Y, Bai P, Liu F, Hou X, Guo Y (2020) Effect of the solution temperature on the precipitates and grain evolution of IN718 fabricated by laser additive manufacturing. Materials (Basel). https://doi.org/10.3390/ma13020340
6. Margueray C, Vollard L, Breteau T, Barbe F (2015) Fabrication additive métallique: technologies et opportunités
7. Zhang L, Yang G, Johnson BN, Jia X (2018) Three-dimensional (3D) printed scaffold and material selection for bone repair. Acta Biomater. https://doi.org/10.1016/j.actbio.2018.11.039
8. Zadpoor AA (2019) Additively manufactured porous metallic biomaterials. J Mater Chem B 7:4088–4117
9. Putra NE, Mirzaali MJ, Apachitei I, Zhou J, Zadpoor AA (2020) Acta biomaterialia multi-material additive manufacturing technologies for Ti-, Mg-, and Fe-based biomaterials for bone substitution. Acta Biomater 109:1–20
10. Attar H, Ehtemam-Haghighi S, Soro N, Kent D, Dargusch MS (2020) Additive manufacturing of low-cost porous titanium-based composites for biomedical applications: advantages, challenges and opinion for future development. J Alloys Compd 827:154263
11. Aboulkhair NT, Everitt NM, Ashcroft I, Tuck C (2014) Reducing porosity in AlSi10Mg parts processed by selective laser melting. Addit Manuf 1:77–86
12. Siti Nur Hazwani MR, Lim LX, Lockman Z, Zuhailawati H (2022) Fabrication of titanium-based alloys with bioactive surface oxide layer as biomedical implants: opportunity and challenges. Trans Nonferrous Met Soc China 32:1–44
13. Yusuf SM, Cutler S, Gao N (2019) Review: the impact of metal additive manufacturing on the aerospace industry. Metals (Basel). https://doi.org/10.3390/met9121286
14. Yilmaz O, Ugla AA (2016) Shaped metal deposition technique in additive manufacturing: a review. Proc Inst Mech Eng Part B J Eng Manuf 230:1781–1798
15. Dutta B, Froes FH (2016) Additive manufacturing technology. Addit Manuf Titan Alloy 25–40
16. Ngo TD, Kashani A, Imbalzano G, Nguyen KTQ, Hui D (2018) Additive manufacturing (3D printing): a review of materials, methods, applications and challenges. Compos Part B Eng 143:172–196
17. Sun C, Wang Y, McMurtrey MD, Jerred ND, Liou F, Li J (2021) Additive manufacturing for energy: a review. Appl Energy 282:116041
18. Davoodi E, Montazerian H, Mirhakimi AS et al (2021) Additively manufactured metallic biomaterials. Bioact Mater. https://doi.org/10.1016/j.bioactmat.2021.12.027
19. Torun G, Momose T, Sun X, Zhou W, Kikuchi K, Nomura N, Kawasaki A (2022) Microstructure and mechanical properties of MRI-compatible Zr-9Nb-3Sn alloy fabricated by a laser powder bed fusion process. Addit Manuf 102647

20. Muthaiah VMS, Indrakumar S, Suwas S, Chatterjee K (2022) Surface engineering of additively manufactured titanium alloys for enhanced clinical performance of biomedical implants: a review of recent developments. Bioprinting 25:e00180

21. Ataee A, Li Y, Wen C (2019) A comparative study on the nanoindentation behavior, wear resistance and in vitro biocompatibility of SLM manufactured CP–Ti and EBM manufactured Ti64 gyroid scaffolds. Acta Biomater 97:587–596

22. Ford S, Despeisse M (2016) Additive manufacturing and sustainability: an exploratory study of the advantages and challenges. J Clean Prod 137:1573–1587

23. Zhang LC, Attar H (2016) Selective laser melting of titanium alloys and titanium matrix composites for biomedical applications: a review. Adv Eng Mater 18:463–475

24. Zhong Y, Rännar LE, Liu L, Koptyug A, Wikman S, Olsen J, Cui D, Shen Z (2017) Additive manufacturing of 316L stainless steel by electron beam melting for nuclear fusion applications. J Nucl Mater 486:234–245

25. Gao W, Zhang Y, Ramanujan D, Ramani K, Chen Y, Williams CB, Wang CCL, Shin YC, Zhang S, Zavattieri PD (2015) The status, challenges, and future of additive manufacturing in engineering. CAD Comput Aided Des 69:65–89

26. Ahmed N, Abdo BM, Darwish S, Moiduddin K, Pervaiz S, Alahmari AM, Naveed M (2017) Electron beam melting of titanium alloy and surface finish improvement through rotary ultrasonic machining. Int J Adv Manuf Technol 92:3349–3361

27. Avila JD, Bose S, Bandyopadhyay A (2018) Additive manufacturing of titanium and titanium alloys for biomedical applications. Titan Med Dent Appl 325–343

28. Heinl P, Mu L, Singer RF, Mu FA, Ko C (2008) Cellular Ti–6Al–4V structures with inter-connected macro porosity for bone implants fabricated by selective electron beam melting 4:1536–1544

29. Li X, Wang C, Zhang W, Li Y (2009) Fabrication and characterization of porous Ti6Al4V parts for biomedical applications using electron beam melting process. Mater Lett 63:403–405

30. Murr LE, Gaytan SM, Medina F, Martinez E, Martinez JL, Hernandez DH, Machado BI, Ramirez DA, Wicker RB (2010) Characterization of Ti-6Al-4V open cellular foams fabricated by additive manufacturing using electron beam melting. Mater Sci Eng A 527:1861–1868

31. Attar H, Calin M, Zhang LC, Scudino S, Eckert J (2014) Manufacture by selective laser melting and mechanical behavior of commercially pure titanium. Mater Sci Eng A 593:170–177

32. Wauthle R, Ahmadi SM, Amin Yavari S, Mulier M, Zadpoor AA, Weinans H, Van Humbeeck J, Kruth JP, Schrooten J (2015) Revival of pure titanium for dynamically loaded porous implants using additive manufacturing. Mater Sci Eng C 54:94–100

33. Bagheri ZS, Melancon D, Liu L, Johnston RB, Pasini D (2017) Compensation strategy to reduce geometry and mechanics mismatches in porous biomaterials built with Selective Laser Melting. J Mech Behav Biomed Mater 70:17–27

34. Guo Y, Wu J, Xie K, Tan J, Yang Y, Zhao S, Wang L, Jiang W, Hao Y (2019) Study of bone regeneration and osteointegration effect of a novel selective laser-melted titanium-tantalum-niobium-zirconium alloy scaffold. ACS Biomater Sci Eng 5:6463–6473

35. Soro N, Attar H, Brodie E, Veidt M, Molotnikov A, Dargusch MS (2019) Evaluation of the mechanical compatibility of additively manufactured porous Ti–25Ta alloy for load-bearing implant applications. J Mech Behav Biomed Mater 97:149–158

36. Soro N, Attar H, Wu X, Dargusch MS (2019) Investigation of the structure and mechanical properties of additively manufactured Ti-6Al-4V biomedical scaffolds designed with a Schwartz primitive unit-cell. Mater Sci Eng A 745:195–202

37. Zhong C, Liu J, Zhao T, Schopphoven T, Fu J, Gasser A, Schleifenbaum JH (2020) Laser metal deposition of Ti6Al4V-A brief review. Appl Sci 10:1–12

38. Niinomi M (2007) Recent research and development in metallic materials for biomedical, dental and healthcare products applications. Mater Sci Forum 539–543:193–200

39. Depboylu FN, Yasa E, Poyraz Ö, Minguella-Canela J, Korkusuz F, De los Santos López MA (2022) Titanium based bone implants production using laser powder bed fusion technology. J Mater Res Technol 17:1408–1426

40. Svetlizky D, Das M, Zheng B, Vyatskikh AL, Bose S, Bandyopadhyay A, Schoenung JM, Lavernia EJ, Eliaz N (2021) Directed energy deposition (DED) additive manufacturing: physical characteristics, defects, challenges and applications. Mater Today 49:271–295
41. Altıparmak SC, Xiao B (2021) A market assessment of additive manufacturing potential for the aerospace industry. J Manuf Process 68:728–738
42. Moghadasi K, Mohd Isa MS, Ariffin MA et al (2022) A review on biomedical implant materials and the effect of friction stir based techniques on their mechanical and tribological properties. J Mater Res Technol 17:1054–1121
43. Wohlers T, Gornet T (2014) History of Additive Manufacturing 2014. Wohlers Rep 2014—3D Print Addit Manuf State Ind 1–34
44. Tuomi JT, Björkstrand RV, Pernu ML, Salmi MVJ, Huotilainen EI, Wolff JEH, Vallittu PK, Mäkitie AA (2017) In vitro cytotoxicity and surface topography evaluation of additive manufacturing titanium implant materials. J Mater Sci Mater Med 28:1–6
45. Van Bael S, Chai YC, Truscello S, Moesen M, Kerckhofs G, Van Oosterwyck H, Kruth JP, Schrooten J (2012) The effect of pore geometry on the in vitro biological behavior of human periosteum-derived cells seeded on selective laser-melted Ti6Al4V bone scaffolds. Acta Biomater 8:2824–2834
46. Arabnejad S, Johnston RB, Ann J, Singh B, Tanzer M, Pasini D (2015) Acta Biomaterialia High-strength porous biomaterials for bone replacement: a strategy to assess the interplay between cell morphology, mechanical properties, bone ingrowth and manufacturing constraints. ACTA Biomater. https://doi.org/10.1016/j.actbio.2015.10.048
47. Inagaki I, Takechi T, Shirai Y, Ariyasu N (2014) Application and features of titanium for the aerospace industry. Nippon Steel Sumitomo Met Tech Rep 106:22–27
48. Han Q, Wang C, Chen H, Zhao X, Wang J (2019) Porous tantalum and titanium in orthopedics: a review. ACS Biomater Sci Eng 5:5798–5824
49. Plocher J, Panesar A (2019) Review on design and structural optimisation in additive manufacturing: Towards next-generation lightweight structures. Mater Des. https://doi.org/10.1016/j.matdes.2019.108164
50. Dehoff R, Duty C, Peter W, Yamamoto Y, Chen W, Blue C, Tallman C (2013) Case study: additive manufacturing of aerospace brackets. Adv Mater Process 171:19–22
51. Frazier WE (2014) Metal additive manufacturing: a review. J Mater Eng Perform 23:1917–1928
52. Blakey-Milner B, Gradl P, Snedden G, Brooks M, Pitot J, Lopez E, Leary M, Berto F, du Plessis A (2021) Metal additive manufacturing in aerospace: a review. Mater Des 209:110008
53. Williams JC, Boyer RR (2020) Opportunities and issues in the application of titanium alloys for aerospace components. Metals (Basel) 10:705

Chapter 25
Process Modeling of Laser-Based Metal Additive Manufacturing of Metal Alloy

Ananya Nath

1 Introduction to Laser-Based Metal Additive Manufacturing

Additive manufacturing (AM) is a relatively new advanced manufacturing technology that includes a large number of processes based on the layer-by-layer material deposition strategy to fabricate complex components. It is a kind of flexibility that has attracted the attention of many fields like automobile, aerospace, medical [1], etc., because of its high advantages over other conventional manufacturing processes. The industrial adoption of the metal AM process has accelerated in the past few decades; laser-based direct energy deposition (DED) or laser cladding [2] is one of them. This process produces metallic products by feeding powder through a nozzle onto the build platform over which the substrate material is to be mounted. (Fig. 1) [3].

The nozzle which is used to deposit the metal powder along with the laser beam onto the substrate can also be of many types such as coaxial nozzle and off-axis nozzle systems. In the coaxial nozzle, the powder flows circumferentially and the laser beam focuses centrally [4]. In off-axis systems, the laser beam and powder meet at a certain angle over the depositing substrate [5]. In both cases, a carrier gas continuously feeds with the powder from the hopper to the substrate to maintain the powder flow ability and to control the powder feed rate. The coaxial nozzle consists of three annular channels through which inner shielding gas, carrier gas, and outer shielding gas flow [6]. The inner shielding gas is used for laser optics protection. Outer shielding gas protects the process from atmospheric contamination. It also helps to reduce the extra high-power density in the melt pool [7].

Laser-based DED enables new complex geometry production where it is difficult to make by conventional manufacturing processes [2]. However, the complex physics

A. Nath (✉)
Department of Mechanical Engineering, National Institute of Technology, Durgapur, India
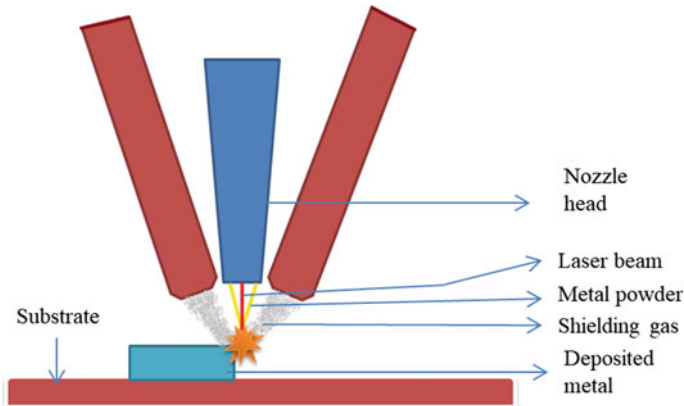e-mail: nath.ananya99@gmail.com

Fig. 1 Schematic of direct energy deposition (DED)

behind the laser–material interaction causes a lot of difficulty at the time of understanding the methodology. The cyclic thermal loading due to layer-by-layer manufacturing may also cause quality issues such as low mechanical strength, residual stresses, pore defects, and poor dimensional fidelity [8].

However, a lot of process parameters are responsible for good product quality. Process parameters like laser power, scan speed, laser beam diameter, powder flow rate, bead overlap ratio, etc., can be controllable, whereas parameters such as each powder particle dimensions and environmental factors like temperature and humidity are uncontrollable. These all parameters are highly accountable to predict the deposition characteristics or clad quality. The deposition can be characterized by its deposition width, height, penetration depth, residual stress, surface roughness, microstructures, and other mechanical properties. Therefore, selecting the correct process parameters and their operating ranges is a challenging task.

Many researchers have done an investigation on process parameters to obtain preferable outputs. Dai et al. [3] observed an increase in the surface roughness with the increase of laser energy, and this was attributed to surface over melting due to increased melt pool velocity and the repetitive heat accumulation. Caiazzo and Caggiano [9] studied the process parameters of the DED process and implemented a metaheuristic artificial neural networks (ANN) model to predict the process parameters. Kersten et al. [10] investigated the build orientation effect over the mechanical properties of the building part which was produced by the DED process. Isquierdo et al. [11] has shown the effect of the initial substrate temperature on heat transfer and related phenomena of a stainless steel sample fabricated by the DED process. Temmler et al. [12] studied the effect of shielding gas in laser surface polishing technique in H1 tool steel product. Rosa et al. [13] investigated the effect of the number of passes over the deposition characteristics. Marimuthu et al. [14] investigated the effect of laser energy and other process parameters over surface roughness. Lian et al. [15] analyzed the effects of the laser power, scanning speed, carrier gas flow

rate, and lap ratio on the cladding width, flatness, and dilution rate of multi-track cladding layers and established a prediction model. Tang and Landers [16] demonstrated a layer height control model using particle swarm optimization (PSO) in the laser metal deposition process. Kats et al. [17] used a machine learning method for predicting grain structure characteristics in the directed energy deposition process. Neural network-based models are used for predicting the grain size and grain aspect ratios.

However, an attempt has been made in this chapter to provide a few process of modeling methodologies. A brief literature review has been given on the process modeling methodologies to model the DED process. Also, an experimental input–output data set of DED process of metal alloy has been used to illustrate the above-mentioned process modeling techniques.

2 Process Modeling of Laser-Based Metal Additive Manufacturing

Due to the complexity of the process, the study of the process parameters and process modeling of laser-based metal AM is very important and is still under research. Process modeling deals with the mapping between input and output factors to predict the responses for given input parameters. This modeling is mainly done by three methods, such as multi-physics-based modeling, statistical modeling, and data-driven artificial intelligence (AI)-based modeling. In physics-based modeling, the process is simulated using finite element methods [18, 19]. This type of modeling is done to predict the process signatures, such as the melt pool temperature profile, density, cooling and solidification rate of the specific material, mechanical properties of the final part, deposition geometry, and microstructure of the deposited model. In statistical modeling, the design of experiments, regression analysis, analysis of variance, etc., is carried out to build the relationship between the input and output parameters. In data-driven AI modeling, the neural network-based approaches are mainly used to predict the process output values for a given input parameters. Moreover, bio-inspired metaheuristics algorithms are used for process parameter optimization.

2.1 Multi-Physics-Based Modeling

Multi-physics-based modeling is the royal discipline of numerical modeling to solve engineering problems. As the AM process involves a lot of complication and several process parameters are involved to get desired product, multi-physics modeling can help out in this regard. Finite element analysis (FEA) and computational fluid dynamics (CFD) are used recently to model the conventional manufacturing processes as well as the AM processes. Keller and Parekh et al. [20] reported a

two-dimensional simulation of the laser cladding process to understand the influence of process parameters on clad geometry formation for better process optimization. Li et al. [21] combined the FEA and thermal-metallurgical-mechanical analysis to predict the influence of solid-state phase transformation. Jin et al. [18] developed a multi-physics-based model to determine the effect of the solidification microstructures on the strength and mechanical properties of the building part by laser cladding process. In multi-physics-based modeling techniques, a finite element model can be developed to simulate the effect of various pertinent parameters (e.g., laser beam size, boundary conditions, laser scan speed, etc.) on the temperature gradients at different locations of the part.

2.2 Experimental Data-Driven Statistical Modeling

Statistical modeling-based experimental design techniques are very frequently used techniques in the field of engineering to model the input–output relationship. However, it has a good impact on the AM field. It has been used widely for process modeling of different AM processes. By using designed experiments, the number of experiments conducted can be minimized and it can be decided whether the chosen parameters have an effective influence on the outcome of the experiment or not. It also reduces the time and cost of the experiment.

The design of experiment (DOE) technique is used to study the process parameters such as input or predictor and output or response. This technique enables the facts about the relationship between predictors and responses. The effect of individual predictors can also be studied. It helps to understand the process performance accurately. This statistical approach also includes analysis of variance (ANOVA), response surface methodology (RSM), etc. After a thorough literature survey and systematic studies, the process parameters are chosen before conducting any experiment. The response or output parameters are also got decided. Understanding the actual influence of the selected input factors over the output is very important.

However, to build a relationship between the process input and output parameter, first, a regression analysis is done. Few experimental data sets are used to build these regression equations. A nonlinear equation can be made between the predictor, i.e., input parameters, and response, i.e., output parameters. For example, a generalized second-order regression equation can be expressed as follows:

$$y = \beta_0 + \sum_{j=1}^{k} \beta_j X_j + \sum_{j=1}^{k} \beta_{jj} X_j^2 + \sum \sum_{j<i}^{k} \beta_{ji} X_j X_i + \varepsilon \tag{1}$$

where y is the process response, X is the process control parameter, β is the regression coefficient, the experimental error is denoted by ε, and the investigated process control parameters are represented by i and j. In Eq. 1, the linear effect of process

parameters is captured by X_j; the nonlinear effect is represented by X_{j2}, and parametric interaction is exhibited by X_i X_j. Equation 1 is then expanded with one response variable and three control parameters. Thus, the equation will be expressed as follows:

$$
\begin{aligned}
y = {} & \beta_0 + \beta_1 X_1 + \beta_2 X_2 + \beta_3 X_3 + \beta_{11} X_{11} + \beta_{22} X_{22} \\
& + \beta_{33} X_{33} + \beta_{12} X_1 X_2 + \beta_{13} X_1 X_3 + \beta_{23} X_2 X_3
\end{aligned}
\tag{2}
$$

β factors can be determined using the least square method by solving some normal set of equations. For more detail, interested readers can refer to [22].

2.3 Data-Driven Artificial Intelligence (AI)-Based Modeling

Data-driven AI-based modeling is a useful tool to predict responses. It mainly includes the neural network-based machine learning approaches, neuro-fuzzy, genetic-fuzzy approaches, etc. ANN is the most commonly used modeling methodology in the machine learning domain. Many researchers have already worked on different types of neural networks to model and predict the response or output factors.

Other than model prediction which predicts the respective output results for a given set of input parameters, Caiazzo and Caggiano [9] implemented a meta-heuristic ANN model to predict the laser DED process parameters. A back propagation neural network (BPNN) and genetic algorithm optimization were used for the prediction purpose. Few researchers have investigated the application of other newly implemented algorithms, for example GA-ANN [23–26]

In this section, the BPNN and recurrent neural network (RNN) are briefly discussed. Besides these, networks' adaptive neuro-fuzzy inference system (ANFIS) architecture is also explained in a brief.

2.3.1 Back Propagation Neural Network (BPNN)

BPNN was first introduced by Werbos in 1974 [27]. The batch mode of training is used for optimization. It adaptively gets trained by each loop with the help of a huge input–output data set which is fed to the network and minimizes the error. The training data sets are first normalized between one and zero before feeding to the network. After the training is done, few experimental test data sets are sent to the network to test and validate them. The data can be normalized by using Eq. 3 as follows:

$$
X_{\text{norm}} = \frac{X - X_{\min}}{X_{\max} - X_{\min}};
\tag{3}
$$

The output which is got from the network is also in the normalized form. Before doing further operations with the network output results, the output should be demoralized first. The demoralized form can be written like (Eq. 4).

$$X = \{X_{\text{norm}} \times (X_{\text{max}} - X_{\text{min}})\} + X_{\text{min}} \tag{4}$$

The learning rate parameter is used to avoid over fitting and the error vibration, whereas to speed up the training process when the networks stuck with local optima region, the term momentum constant will be used (Eq. 5).

$$\Delta W_{jk}(t) = -\eta \frac{\partial E}{\partial W_{jk}}(t) + \alpha \Delta W_{jk}(t-1) \tag{5}$$

The network weights need to be updated with learning rate (η) and momentum parameters (α). The term t indicates the iteration number, and $\frac{\partial E}{\partial W_{jk}}$ can be determined using the chain rule of differential equation as shown in Eq. 6:

$$\frac{\partial E}{\partial W_{jk}} = \frac{\partial E}{\partial Y_k} \cdot \frac{\partial Y_k}{\partial U_k} \cdot \frac{\partial U_k}{\partial W_{jk}} \tag{6}$$

The terms U_k and Y_k represent input and output of the kth neuron lying on the output layer, respectively.

It is to be noted that a huge set of input–output training data is used to train the network using the batch mode. The parametric study is to be carried out to optimize the neural network parameters during training (refer to Fig. 2). The parametric study is carried out by varying the neural network parameters (such as hidden neurons number, learning rate, momentum constant, activation function constants, and the bias value) one at a time and keeping the rest at their respective mid values
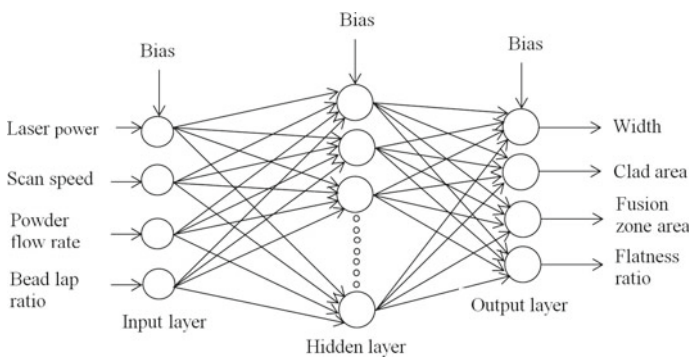

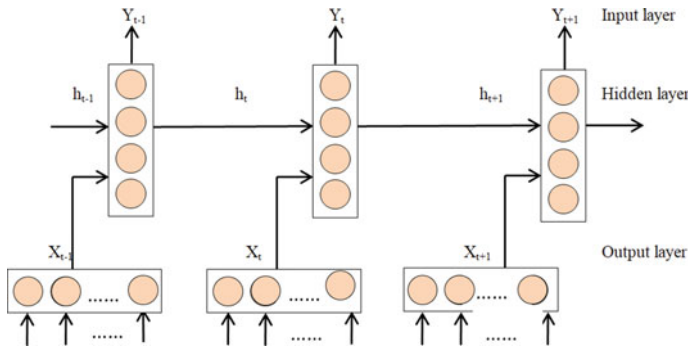**Fig. 2** Schematic representation of back propagation neural network

Fig. 3 Schematic representation of recurrent neural network

2.3.2 Recurrent Neural Network (RNN)

RNN or recurrent neural network is another variant of the neural network [27], where the neuron of each layer is sequenced by connecting the preceding and succeeding layers of neurons. This network consists of two or more layers. Each layer is containing a specific number of nodes or neurons. RNN s dispense a rigid baseline in machine learning applications. Therefore, this network is expected to be very sophisticated in terms of architecture verification. The work of RNN is based on a memory function that is used for producing sequential information [28]. This memory detains all the information about the network and works on the calculations that have been done in the present state. This network also consists of input, hidden, and output layers. All the neurons of the hidden layer are connected and arranged in a chain. The output results depend upon the present input as well as the past state of the architecture. The RNN architecture is shown in Fig. 3.

In engineering as well as other industries also, this type of neural network is useful for modeling and prediction purposes. However, the biggest disadvantage of this type of network is they work on point prediction instead of time series prediction. Point predictions require a context-aware method, whereas time series prediction does not need that one. The RNN is widely used in machine translation, text classification, image analysis, language recognition, etc.

2.3.3 Adaptive Neuro-Fuzzy Inference System (ANFIS)

ANFIS is a machine learning algorithm that uses Takagi, Sugano, and Kang's fuzzy logic-based system [29]. It uses the inputs and outputs of the data that are fed to the ANFIS architecture to build a relationship between them. ANFIS consists of five layers out of which two layers are adaptive in nature where the optimization of the required parameters is done. Each of the layers has its specific governing equations by which each layer output is got. The ANFIS predicted outputs also depend upon the type of membership functions (MF). The five layers of ANFIS are the fuzzy layer,
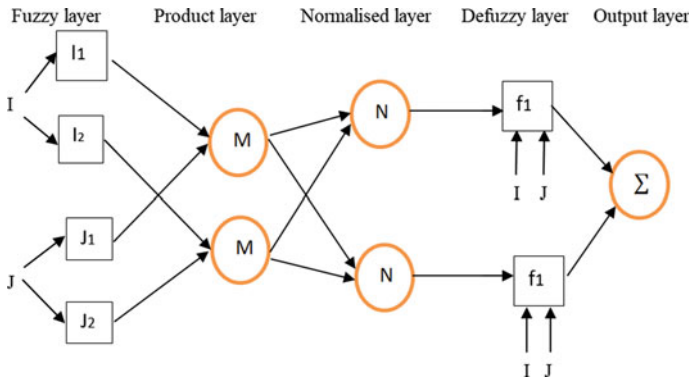
Fig. 4 Schematic of ANFIS architecture

product layer, normalized layer, de-fuzzy layer, and total output layer (Fig. 4). The predicted output of ANFIS is sent back to the system as feedback to optimize the error after each loop. Optimization refers to the minimization of the weight factors of two adaptive layers. The number of iterations is called an epoch. The number of epochs can be changed or increased as per the need for a better result.

3 Result and Discussion

In this section, the above-mentioned process modeling methodologies such as statistical modeling and AI modeling approaches have been implemented for the laser-based DED process [30]. In the work, the material used in DED was Fe–Cr-based alloy powder which was deposited over the substrate of the AISI 4340 plate specimen with dimensions of 40 mm × 30 mm × 20 mm [30]. The powder material was 30–200 μm in diameter. The substrate was first to get cleaned using alcohol and acetone. Argon has been used as the flowing gas and shielding gas. The whole DED system consists of one laser unit (LDF-3000, Laserline, Germany) and its integrated control unit S7-1200, Siemens, Germany, an industrial robot for the deposition purpose (KR30-3 HA, KUKA, Germany), coaxial nozzle for the powder material feeding (OTS-2, Laserline, Germany), powder delivery system (RC-PGF-D-2, Raychem, China), and the water cooling channels (TFLW-3000WDR, Sanhe Tongfei, China). For more detail about experimentation, interested readers can refer to [30].

After systematic study of the process parameters, the input parameters and their operating ranges are chosen and given in Table 1 [30].

In this given study, the input parameters are laser power (P), scan speed (V), powder flow rate (F), and bead overlap ratio (L), whereas the response parameters are deposited width (W), clad area (A_c), fusion zone area (A_m), and flatness ratio (S).

Table 1 Operating ranges of input parameters

Input factors	Range		Unit
	High	Low	
Laser power (P)	1400	1000	W
Scan speed (V)	1100	700	mm/min
Powder flow rate (F)	3.8	2.6	rad/s
Bead overlap ratio (L)	60	20	%

3.1   Data-Driven Statistical Modeling of DED

To model any process output in terms of its input parameters, a relationship equation is made between these two parameters. Regression equations are developed for the same.

To establish a relationship between the process parameters, experimental data sets [30] are used to build the regression model. A second-order regression equation has been made. The equations for each response such as deposited width (W), clad area (A_c), fusion zone area (A_m), and flatness ratio (S) are obtained below:

$$W = 219.1 - 0.0523P - 0.1184V - 33.2F$$
$$- 2.300L + 0.001557P \times L + 0.0351V \times F$$

$$A_c = -275 + 1.375 \text{ P} - 0.841 \text{ V} - 0.000552 \text{ P} \times \text{P}$$
$$+ 0.000392 \text{ V} \times \text{V}$$

$$A_m = 4.26 - 0.00445 \text{ V} - 0.796 \text{ F} + 0.001125 \text{ V} \times \text{F}$$

$$S = -4.2 + 0.0077P + 0.1674V - 0.550L$$
$$- 0.000090V \times V + 0.000576P \times L$$

where P is laser power (W), V is the scan speed (mm/min), F is the powder flow rate (rad/min), and L is the bead overlap ratio (%).

However, using the regression equations mentioned earlier, the output corresponding to experimental input data set is calculated. The absolute error percentage between the regression analysis result and the experimental result is evaluated. The average absolute error percentage is obtained as 4.22%, 4.54%, 3.81%, and 0.92% for width (W), clad area (A_c), fusion zone area (A_m), and flatness ratio (S), respectively.

3.2   Data-Driven AI Modeling Result of DED

The successfully constructed neural network can predict the output result very accurately with minimum error. Hence, the experimental data set is fed to the each network to test the accuracy. Prediction accuracy is measured (using Eq. 7) in terms of absoluter percentage error of the predicted outcome with the experimental results.

$$E = \left| \frac{W_e - W_p}{W_e} \times 100\% \right| \tag{7}$$

where E is the absolute error percentage, W_e is the experimental result of width, and W_P is the model predicted width value.

In the data-driven AI modeling, BPNN, RNN, and ANFIS are designed and tested with a few experimental data set. In the case of ANFIS architecture, the four outputs are modeled differently for each of the four different MF. The optimal ANFIS architecture is developed using the training data set. After the network is properly built, the test experimental data sets are fed to the network. The predicted results are compared with the experimental results. The absolute error percentage between the same is calculated. ANFIS offers only one output modeling at a time with any number of inputs. Therefore, for ANFIS modeling, four output parameters are modeled separately. For different inputs, the MF are used to model each output, i.e., triangular, trapezoidal, Gaussian, and bell-shaped MF. For each output model, the comparison between the predicted output and experimental output is done by calculating the absolute error percentage. For four different MF, each model prediction accuracy is given in Table 2 in terms of average absolute percentage error.

However, similarly BPNN and RNN networks are also being trained using same set of input–output data set and tested with the experimental data sets. Each network predicted results is compared with the experimental output values, and the average absolute error percentage for each case has been calculated and given in Table 3.

In every output factor prediction, Gaussian MF outperforms the rest of the MFs for its nonlinear characteristics. Therefore, in Table 3, only the error percentage for using Gaussian MF is given in ANFIS predicted result.

Table 2 ANFIS architecture prediction accuracy in terms of average absolute percentage error

Output parameter	Average absolute error percentage			
	Triangular MF	Trapezoidal MF	Gaussian MF	Bell-shaped MF
Width (W)	4.35	6.75	1.27	5.09
Clad area (A_c)	1.11	1.11	1.05	1.07
Fusion zone area (A_m)	1.12	1.12	1.08	1.11
Flatness ratio (S)	0.27	0.27	0.26	0.27

Table 3 BPNN, RNN and RBFNN architecture prediction accuracy in terms of average absolute percentage error

Network	Error % in predicting W	Error % in predicting A_c	Error % in predicting A_m	Error % in predicting S
BPNN	15.65	20.59	18.30	3.21
RNN	14.78	17.61	19.21	1.64
ANFIS	1.273	1.055	1.087	0.27

4 Conclusion

DED is a well-known method under AM mostly used in printing metallic components or surface cladding purposes. In this chapter, the process modeling of DED is elaborated. The performance of different process modeling techniques such as the statistical method and data-driven AI methods are evaluated by predicting four different process outputs, and both methods can predict the results with good accuracy. In case of data-driven AI modeling, the performance of two different neural networks, i.e., BNN and RNN, was not very significantly different from each other in predicting each of the four responses. However, computational efficiencies are also more or less the same of BPNN and RNN. It has been observed that the time taken by each network to predict the result was almost the same. On the other hand, the network efficiency of these two networks has been compared with the fuzzy logic-based network, i.e., ANFIS. The absolute error percentage is 0.27%, 0.27%, 0.26%, and 0.27% in predicting the deposited width, clad area, fusion zone area, and flatness ratio, respectively. These absolute average error percentages for each output parameter are less than other neural network results such as BPNN and RNN. Therefore, the ANFIS predicted results showed more accuracy in terms of error percentage between experimental and network predicted results.

5 Future Scope

Future possibilities for this approach are vast. In the future scope, feedback control systems can be developed under every technique to control the deposition characteristics at that time only. In this work, the relationship between each output factor with the input factor is empirically made during this process, but the characterization of each output factor with the input parameters with their detailed empirical relationships is of utmost importance to get a better result in terms of print quality or the expected output values. This improvement will be very much beneficial for more advances of this process in the future scope. However, a lot of research on process parameter and their effect on metallurgical properties are ongoing.

References

1. Paul S et al (2021) Additive manufacturing of multi-functional biomaterials for bioimplants: a review. IOP Conf Ser: Mater Sci Eng 1136:012016
2. Toyserkani E, Khajepour A, Corbin SF (2004) Laser cladding. CRC Press, Boca Raton
3. Saboori A, Gallo D, Biamino S, Fino P, Lombardi M (2017) An overview of additive manufacturing of titanium components by directed energy deposition: microstructure and mechanical properties. Appl Sci 7(9):883
4. DeWitte L, Saldana C, Kurfess T, Fu K (2022) Effect of coaxial nozzle wear on catchment efficiency in direct energy deposition built components. J Manuf Syst 63:524–538
5. Wen S, Shin YC (2011) Modeling of the off-axis high power diode laser cladding process. Journal of Heat Transfer 133(3)
6. Thompson SM, Bian L, Shamsaei N, Yadollahi A (2015) An overview of direct laser deposition for additive manufacturing; part I: transport phenomena, modeling and diagnostics Addit Manuf
7. Ahn J, He E, Chen L, Dear J, Davies C (2017) The effect of Ar and He shielding gas on fibre laser weld shape and microstructure in AA 2024–T3. J Manuf Process 29:62–73
8. Fu J, Li H, Song X, Fu MW (2022) Multi-scale defects in powder-based additively manufactured metals and alloys. Journal of Materials Science and Technology
9. Caiazzo F, Caggiano A (2018) Laser direct metal deposition of 2024 Al alloy: trace geometry prediction via machine learning. Materials 11(3). https://doi.org/10.3390/ma11030444
10. Kersten S, Praniewicz M, Kurfess T, Saldana C (2020) Build orientation effects on mechanical properties of 316SS components produced by directed energy deposition. Procedia Manufacturing 48:730–736
11. Isquierdo DV, Siqueira RHM, Carvalho SM, Lima MSF (2022) Effect of the initial substrate temperature on heat transfer and related phenomena in austenitic stainless steel parts fabricated by additive manufacturing using direct energy deposition. J Market Res 18:5267–5279
12. Temmler A, Liu D, Preußner J, Oeser S, Luo J, Poprawe R, Schleifenbaum JH (2020) Influence of laser polishing on surface roughness and microstructural properties of the remelted surface boundary layer of tool steel H11. Mater Des 192:108689
13. Rosa B, Mognol P, Hascoët J (2015) Laser polishing of additive laser manufacturing surfaces. J Laser Appl 27:S29102
14. Marimuthu S, Triantaphyllou A, Antar M, Wimpenny D, Morton H, Beard M (2015) Laser polishing of selective laser melted components. Int J Mach Tool Manu 95:97–104
15. Lian GF, Yao MP, Zhang Y et al (2018) Analysis and prediction on geometric characteristics of multi-track overlapping laser cladding. Int J Adv Manuf Technol 97:2397–2407
16. Liu H, Qin X, Huang S et al (2018) Geometry characteristics prediction of single track cladding deposited by high power diode laser based on genetic algorithm and neural network. Int J Precis Eng Man 19:1061–1070
17. Kats D, Wang Z, Gan Z, Liu WK, Wagner GJ, Lian Y (2018) A physics-informed machine learning method for predicting grain structure characteristics in directed energy deposition. Comput Mater Sci 202:110958
18. Jin K, Yang Z, Chen P, Huang G, Qiao X (2022) Dynamic solidification process during laser cladding of IN718: multi-physics model, solute suppressed nucleation and microstructure evolution. Int J Heat Mass Transf 192:122907
19. Li C, Yu Z, Gao J, Zhao J, Han X (2019) Numerical simulation and experimental study of cladding Fe60 on an ASTM 1045 substrate by laser cladding. Surf Coat Technol 357:965–977

20. Parekh R, Buddu RK, Patel RI (2016) Multiphysics simulation of laser cladding process to study the effect of process parameters on clad geometry. Procedia Technol 23:529–536
21. Li S, Ren S, Zhang Y, Deng D, Murakawa H (2017) Numerical investigation of formation mechanism of welding residual stress in P92 steel multi-pass joints. J Mater Process Technol 244:240–252
22. Shucai Y, Chunsheng H, Minli Z (2018) A prediction model for titanium alloy surface roughness when milling with micro-textured ball-end cutters at different workpiece inclination angles. Int J Adv Manuf Technol
23. Zhang Y, Cheng W, Sun Y, Xu Y, Li Z (2022) Surface quality optimization of laser cladding based on surface response and genetic neural network model. Available at SSRN 4096082
24. Solati A, Hamedi M, Safarabadi M (2019) Combined GA-ANN approach for prediction of HAZ and bearing strength in laser drilling of GFRP composite. Opt Laser Technol 113:104–115
25. Singh A, Nath A, Roy SS., Lohar AK (2022) Modeling of laser aided direct metal deposition of stainless steel using supervised deep learning algorithms. Materials Today: Proceedings
26. Dhar AR, Gupta D, Roy SS, Lohar AK (2022) Forward and backward modeling of direct metal deposition using metaheuristic algorithms tuned artificial neural network and extreme gradient boost. Progress in Additive Manufacturing 1–15
27. Lin JCW, Shao Y, Djenouri Y, Yun U (2021) ASRNN: a recurrent neural network with an attention model for sequence labeling. Knowl-Based Syst 212:106548
28. Yang Z-L, Guo X-Q, Chen Z-M, Huang Y-F, Zhang Y-J (2019) RNN-Stega: linguistic steganography based on recurrent neural networks. IEEE Trans Inf Forensics Secur 14(5):1280–1295
29. Najafzadeh M, Azamathulla HM (2015) Neuro-fuzzy GMDH to predict the scour pile groups due to waves. J Comput Civ Eng 29:4014068
30. Guo C et al (2021) Prediction modeling and process optimization for forming multi-layer cladding structures with laser directed energy deposition. Opt Laser Technol 134:1007